Phone : +90 (312) 201 10 00
Fax : +90 (312) 287 91 88
Adress : MTA 06520 - Ankara - TURKEY
www.mta.gov.tr

161

BULLETIN OF THE MINERAL RESEARCH AND EXPLORATION

2020

BULLETIN OF THE MINERAL RESEARCH AND EXPLORATION

Foreign Edition | 2020 | 161 | ISSN : 0026-4563 E-ISSN : 2651-3048

CONTENTS

Research Articles

Uncertainty-volume fractal model for delineating copper mineralization controllers using geostatistical simulation in Nohkouhi volcanogenic massive sulfide deposit, Central Iran
..... Saeid HAJSADEGHI, Omid ASGHARI, Mirsaleh MIRMOHAMMADI, Peyman AFZAL and Seyed Ahmad MESHKANI 1

The role of Variscan shortening in the control of mineralization deposition in Tadaout-Tizi N'rsas mining district (Eastern Anti-Atlas, Morocco)
.....Mustapha AIT DAOUD, Abdelhafid ESSALHI, Mourad ESSALHI and Abdeslam TOUMMITE 13

2D inverse modeling of the gravity field due to a chromite deposit using the Marquardt's algorithm and forced neural network
.....Ata ESHAGHZADEH, Sanaz SEYEDI SAHEBARI and Alireza DEHGHANPOUR 33

Usability of PC-ash as lightweight aggregate in foam concrete
.....Metin DAVRAZ and Şemsettin KILINÇARSLAN 49

Determination of the origin and recharge process of water resources in Salda Lake Basin by using the environmental, tritium and radiocarbon isotopes (Burdur/Turkey)
..... Simge VAROL, Ayşen DAVRAZ, Fatma AKSEVER, Şehnaz ŞENER, Erhan ŞENER, Bülent KIRKAN and Ahmet TOKGÖZLÜ 57

Investigation on geoarchaeological structure of ancient port cities in the Lycia region
..... Su Güneş KABAKLI and M. Erkan KARAMAN 71

Geochemical features and petrogenesis of Gökçeada volcanism, Çanakkale, NW Turkey
.....Pınar ŞEN, Ramazan SARI, Erdal ŞEN, Cahit DÖNMEZ, Serkan ÖZKÜMÜŞ and Şahset KÜÇÜKEFE 81

Geology and formation of Nevruztepe Fe-Cu skarn mineralization (Kayseri-Turkey)
.....Deniz TİRİNGA, Bülent ATEŞÇİ, Yılmaz ÇELİK, Güvenç DEMİRKIRAN, Cahit DÖNMEZ, Aytekin TÜRKEL and Taner ÜNLÜ 101

Drilling and core data from the Gulf of Gemlik (SE Sea of Marmara): Holocene fauna and flora assemblages
Engin MERİÇ, Zeki Ü. YÜMÜN, Atike NAZİK, Enis K. SAGULAR, M. Baki YOKEŞ,
.....Yeşim BÜYÜKMERİÇ, Ayşegül YILDIZ and Gülin YAVUZLAR 121

Precise monitoring of temporal topographic change detection via unmanned air vehicle
..... Serkan KARAKIŞ, Umut Guneş SEFERCİK, Turhan BİLİR and Can ATALAY 151

An example study on re-evaluation of historical earthquakes: 1789 Palu (Elazığ) earthquake, Eastern Anatolia, Turkey
.....Mehmet KÖKÜM and Fatih ÖZÇELİK 157

Early Miocene seed like plant remain fossils and facies associations from the Nallıhan district (NW Turkey)
.....Muhittin GÖRMÜŞ, Yusuf Kağan KADIOĞLU, Baki Erdoğan VAROL and Muhammed Sami US 171

Utilization of pumice of Burdur region and zeolite of Bigadiç - Balıkesir region as fine aggregate in construction materials
.....Özge BEYCAN TATANOĞLU and Niyazi Uğur KOÇKAL 191

Bulletin of the Mineral Research and Exploration Notes to the Authors..... 201

BULLETIN OF THE MINERAL RESEARCH AND EXPLORATION

Foreign Edition | 2020 | 161 | ISSN : 0026-4563 E-ISSN : 2651-3048

CONTENTS

Research Articles

Uncertainty-volume fractal model for delineating copper mineralization controllers using geostatistical simulation in Nohkouhi volcanogenic massive sulfide deposit, Central Iran
..... Saeid HAJSADEGHI, Omid ASGHARI, Mirsaleh MIRMOHAMMADI, Peyman AFZAL and Seyed Ahmad MESHKANI 1

The role of Variscan shortening in the control of mineralization deposition in Tadaout-Tizi N'rsas mining district (Eastern Anti-Atlas, Morocco)
..... Mustapha AIT DAOUD, Abdelhafid ESSALHI, Mourad ESSALHI and Abdeslam TOUMMITE 13

2D inverse modeling of the gravity field due to a chromite deposit using the Marquardt's algorithm and forced neural network
..... Ata ESHAGHZADEH, Sanaz SEYEDI SAHEBARI and Alireza DEHGHANPOUR 33

Usability of PC-ash as lightweight aggregate in foam concrete
..... Metin DAVRAZ and Şemsettin KILINÇARSLAN 49

Determination of the origin and recharge process of water resources in Salda Lake Basin by using the environmental, tritium and radiocarbon isotopes (Burdur/Turkey)
..... Simge VAROL, Ayşen DAVRAZ, Fatma AKSEVER, Şehnaz ŞENER, Erhan ŞENER, Bülent KIRKAN and Ahmet TOKGÖZLÜ 57

Investigation on geoarchaeological structure of ancient port cities in the Lycia region
..... Su Güneş KABAKLI and M. Erkan KARAMAN 71

Geochemical features and petrogenesis of Gökçeada volcanism, Çanakkale, NW Turkey
..... Pınar ŞEN, Ramazan SARI, Erdal ŞEN, Cahit DÖNMEZ, Serkan ÖZKÜMÜŞ and Şahset KÜÇÜKEFE 81

Geology and formation of Nevruztepe Fe-Cu skarn mineralization (Kayseri-Turkey)
..... Deniz TİRİNGA, Bülent ATEŞÇİ, Yılmaz ÇELİK, Güvenç DEMİRKIRAN, Cahit DÖNMEZ, Aytekin TÜRKEL and Taner ÜNLÜ 101

Drilling and core data from the Gulf of Gemlik (SE Sea of Marmara): Holocene fauna and flora assemblages
Engin MERİÇ, Zeki Ü. YÜMÜN, Atike NAZİK, Enis K. SAGULAR, M. Baki YOKEŞ,
..... Yeşim BÜYÜKMERİÇ, Ayşegül YILDIZ and Gülin YAVUZLAR 121

Precise monitoring of temporal topographic change detection via unmanned air vehicle
..... Serkan KARAKIŞ, Umut Guneş SEFERCİK, Turhan BİLİR and Can ATALAY 151

An example study on re-evaluation of historical earthquakes: 1789 Palu (Elazığ) earthquake, Eastern Anatolia, Turkey
..... Mehmet KÖKÜM and Fatih ÖZÇELİK 157

Early Miocene seed like plant remain fossils and facies associations from the Nallıhan district (NW Turkey)
..... Muhittin GÖRMÜŞ, Yusuf Kağan KADIOĞLU, Baki Erdoğan VAROL and Muhammed Sami US 171

Utilization of pumice of Burdur region and zeolite of Bigadiç - Balıkesir region as fine aggregate in construction materials
..... Özge BEYCAN TATANOĞLU and Niyazi Uğur KOÇKAL 191

Bulletin of the Mineral Research and Exploration Notes to the Authors..... 201

LOCATION OF MANAGEMENT
Redaksiyon Kurulu Başkanlığı
Maden Tetkik ve Arama Genel Müdürlüğü
D Block Room Number:2-3
Üniversiteler Mah. Dumlupınar Bulvarı No:139
06800 Çankaya/ANKARA/TURKEY
e-mail: redaksiyon@mta.gov.tr

The translations of Şen et al., Meriç et al. were made by M. Kerem AVCI. The translation of Tiringa et al. was made by Catherine YİĞİT. The translation of Köküm and Özçelik was made by Hakan PEHLİVAN.

Bull. Min. Res. Exp. is indexed and abstracted in TR Dizin, Emerging Source Citation Index (ESCI), Scopus, The ICI Journals Master List (Copernicus), Directory of Open Access Journals (DOAJ), Clarative Analytics Master List (OAJI), Georef, Geological Abstracts, MIAR and Zoological Record. The Bulletin of the Mineral Research and Exploration is published in three issues in a year. Each bulletin is printed in Turkish and English languages as two separate issues. The English and Turkish issues of the "Bulletin of the Mineral Research and Exploration" can be obtained from "BDT Department" free of charge, either directly or ordered by adding postage fee from the correspondence address. Typesetting and printing operations are carried out and followed by the Publication Service of the Scientific Documentation and Publicity Department. Typesetting and Print Review: Yaşar ÖZKAN, Tuğba UĞUR. e-mail: bdt@mta.gov.tr

The section of "notes to the authors", format, copyright and other information can be obtained from www.mta.gov.tr as PDF files.

Printed Date: 21/04/2020

Printing House: Kuban Matbaacılık - İvedik Organize Sanayi Matbaacılar Sitesi 1514. Sokak No: 20 Phone: 0312 395 2070 Fax: 0312 395 3723 www.kubanmatbaa.com

Periodical

ISSN: 0026-4563
E-ISSN: 2651-3048

Bulletin of the Mineral Research and Exploration

http://bulletin.mta.gov.tr

Uncertainty-volume fractal model for delineating copper mineralization controllers using geostatistical simulation in Nohkouhi volcanogenic massive sulfide deposit, Central Iran

Saeid HAJSADEGHI[a], Omid ASGHARI[b*], Mirsaleh MIRMOHAMMADI[a], Peyman AFZAL[c] and Seyed Ahmad MESHKANI[a]

[a]*School of Mining Engineering, University of Tehran, Iran.*
[b]*Simulation and Data Processing Laboratory, School of Mining Engineering, University of Tehran, Tehran, Iran.*
[c]*Department of Mining Engineering, South Tehran Branch, Islamic Azad University, Tehran, Iran.*

Research Article

Keywords:
Sequential Gaussian simulation, Sequential indicator simulation, Concentration–volume fractal modeling, Uncertainty-volume fractal modeling, Volcanogenic massive sulfide, Nohkouhi copper deposit.

Received Date: 29.07.2018
Accepted Date: 14.11.2018

ABSTRACT

The aim of this study was to delineate copper mineralization controllers in Nohkouhi volcanogenic massive sulfide (VMS) deposit by using geostatistical and fractal simulation. In this study, concentration-volume (C-V) fractal model has been used to indicate various copper populations related to different host rocks and copper minerals. Accordingly, uncertainty-volume (U-V) fractal model was applied to probability values achieved through sequential indicator simulation (SIS). Copper ores of Nohkouhi deposit including chalcopyrite and malachite were simulated in 30 realizations. The U-V fractal model obtained by using a probability map was divided into four probability zones (high, moderate, low, and very low) for copper minerals. Furthermore, copper grades were simulated for 10 times by sequential Gaussian simulation (SGS). Combination of C–V and U-V fractal modeling resulted in a hybrid method which could be properly employed to determinate various mineralization zones based on the relationship between quantitative (e.g. copper grade) and qualitative (e.g. copper minerals) variables. Moreover, integrating the results of C–V and U-V fractal modeling with the most frequent occurrence of rock type modeling helps identify copper mineralization controllers in a VMS deposit.

1. Introduction

Fractal models, presented by Mandelbrot (1983), has been used in many different cases to explain geological and mineralization processes. Considering spatial information of mineral deposit data, it can be noted that fractal models are useful tools which reveal the relationships among geological, geochemical, and mineralogical settings (Afzal et al., 2016; Carranza, 2009; Daneshvar Saein et al., 2012; Goncalves et al., 2001; Gumiel et al., 2010; Soltani et al., 2014). Famous fractal models include number–size (N-S: Mandelbrot, 1983; Sadeghi et al., 2012), concentration-area (C-A: Cheng et al., 1994), spectrum-area (S-A: Cheng et al., 1999), concentration- distance (C-D: Li et al., 2003), concentration–volume (C-V: Afzal et al., 2011), concentration-number (C-N: Hassanpour and Afzal, 2013), and simulated size–number (SS–N: Sadeghi et al., 2015).

Concentration-volume fractal models has been widely used in porphyry deposit (e.g. Afzal et al., 2011; Yasrebi et al., 2013; Soltani et al., 2014; Sun and Liu, 2014) and lesser another type of deposit such as gold deposit (Afzal et al., 2013; Lin et al., 2014), Zn-Pb MVT deposit (Delavar et al., 2012), iron deposit (Sadeghi et al., 2012; Afzal et al., 2015; Rahmati et al., 2015). Grade distribution of block

Citation info: Hajsadeghi, S., Asghari, O., Mirmohammadi, M., Afzal, P., Meshkani, A. A. 2020. Uncertainty-volume fractal model for delineating copper mineralization controllers using geostatistical simulation in Nohkouhi volcanogenic massive sulfide deposit, Central Iran. . Bulletin of the Mineral Research and Exploration, 161, 1-11. https://dx.doi.org/10.19111/bulletinofmre.495753

* *Corresponding author: Omid ASGHARİ, o.asghari@ut.ac.ir*

models can be generated by geostatistical methods such as the Ordinary Kriging, Multi-Gaussian Kriging and Sequential Gaussian simulation. Geostatistical simulations are designed to overcome the smoothing effect of estimation methods (such as ordinary kriging and simple kriging) (e.g., Chiles and Delfiner, 2009). These methods are applied to continuous and indicator variables of respectively sequential Gaussian simulation (SGS e.g., Deutsch and Journel, 1998) and sequential indicator simulation (SIS e.g., Journel, 1983). Recently, geological phenomena e.g., mineralization, and alteration are separated effectively by combining simulation methods with fractal modeling (Afzal et al., 2014; Soltani et al., 2014; Sadeghi et al,. 2015).

The main aim of this paper was to indicate the relationship between copper grade, the probability of occurrence of copper ore minerals and host rocks in a VMS deposit. For this purpose, C-V fractal model was applied to Cu realizations produced from sequential Gaussian simulation. Also, U-V fractal model was used to distinguish different probability zones in two copper minerals of Nohkouhi deposit (i.e. chalcopyrite and malachite) using sequential indicator simulation.

2. Regional Geology of Mineral Deposit

The Nohkouhi copper deposit is located in Posht- e-Badam block as a part of Central Iran microcontinent (Figure 1a). This deposit contains 1.5 Mt measured of ore at average grades of 1% Cu (Karmania, 2013). Black shale and rhyodacite are main host of copper mineralization (Figure 1b). Based on Hajsadeghi et al (2017) studies copper mineralization occurred during three stages. Firstly, pyrite and minor chalcopyrite are deposited in the black shale, synchronously (Figure 2a, b, c). Second stage occurred during intrusion of rhyodacite in black shale. Copper enriched in black shale as a result of circulation of hydrothermal fluid (Figure 2d). Chalcopyrite formed as semi massive and veinlet with euhedral pyrite, lesser sphalerite and galena. During third stage, sulfide minerals oxidized and produced malachite, limonite, goethite, hematite ± azurite ± gypsum.

3. Applied Methods

3.1. Concentration-Number Fractal Model

Concentration- number (C-N) fractal model is one of the fractal models (Mandelbort, 1983) which it is used to separate geochemical background and anomaly in a geochemical dataset. The model is defined as (1):

$$N(\geq\rho) \propto \rho^{-\beta} \quad (1)$$

where N (≥ρ) denotes the sample number with concentration values greater than ρ value. ρ is

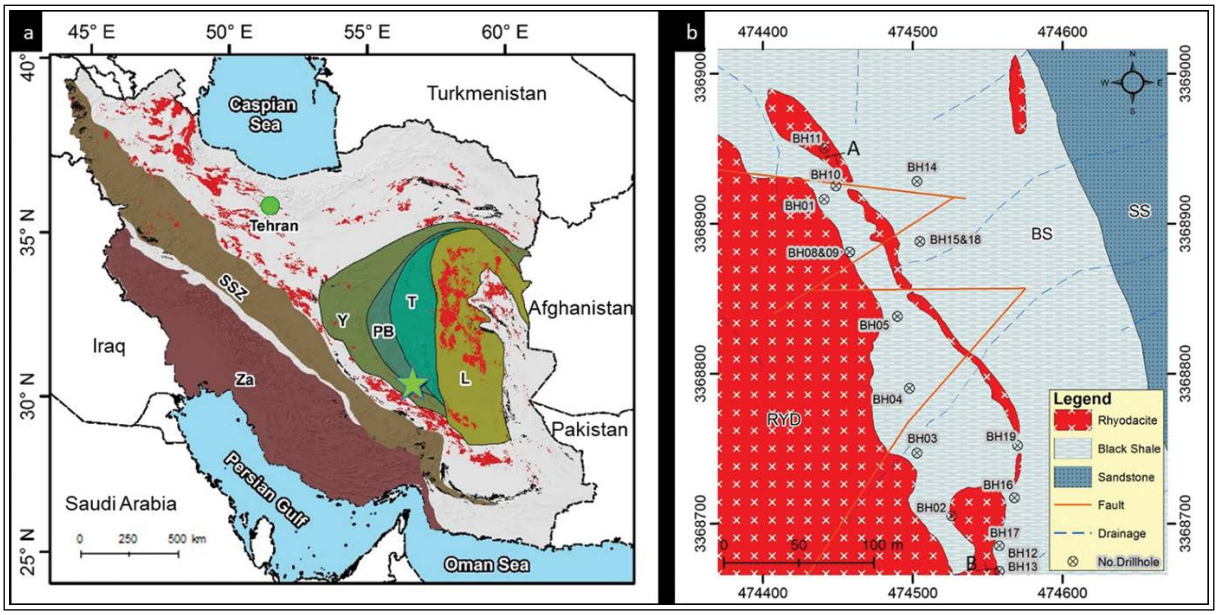

Figure 1- a) The location of Nohkouhi deposit in the regional geology map of Iran (Green stars; Simplified from Sahandi et al., 2002), b) Geology of the Nohkouhi deposit. Abbreviations: SSZ = Sanandaj-Sirjan zone, Za = Zagros, Y = Yazd block, PB = Posht-e-Badam block, T = Tabas block, L = Lut block.

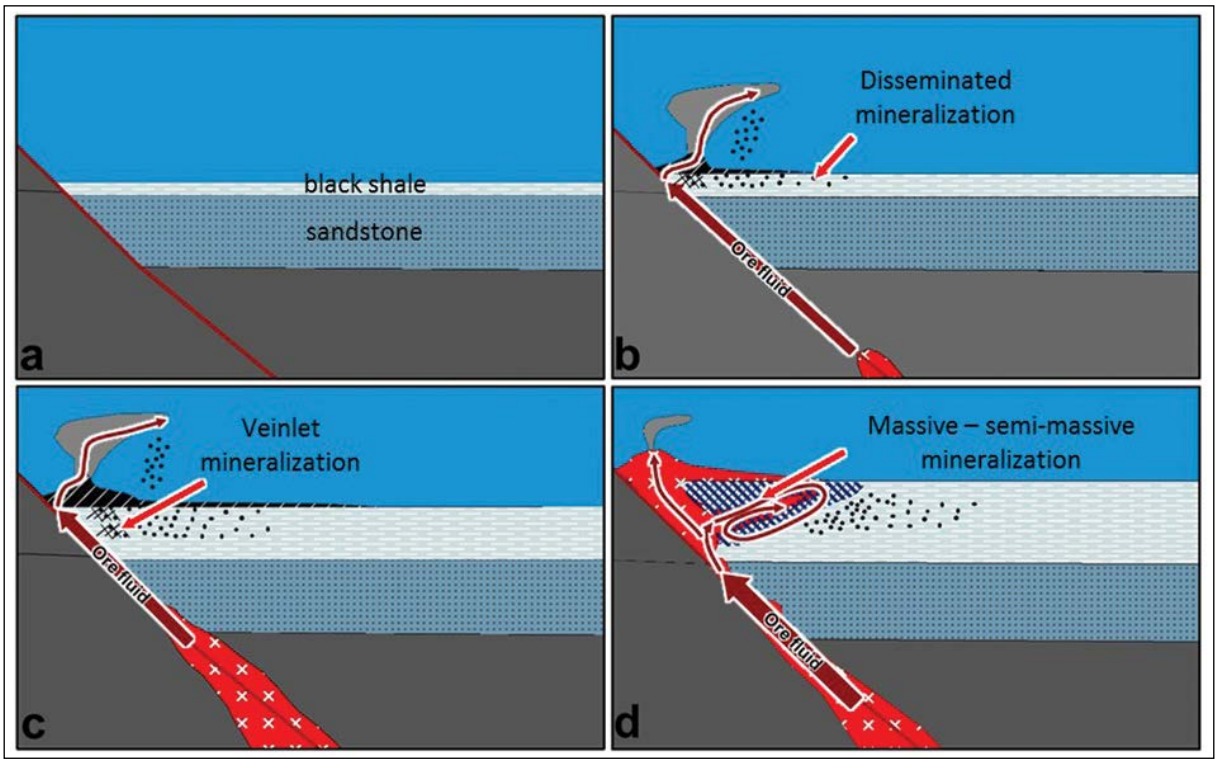

Figure 2- Schematic block diagram illustrating the most probable geodynamic scenario of the formation of Nohkouhi deposit (Hajsadeghi et al., 2017), a) sandstone and barren black shale are deposited, b-c) black shale and pyrite rich ± chalcopyrite had been deposited synchronously during first stage of mineralization while felsic magma ascended to the ground, d) copper mineralization is enriched as a result of circulation of magmatic fluid (second stage).

concentration of element, and β is the fractal dimension. The main advantage of this method is classification of geochemical populations before their estimation (Sadeghi et al., 2012; Rezaei et al., 2015).

3.2. Concentration-Volume (C-V) Fractal Model

The C-V fractal model was first introduced by Afzal et al. (2011) for separation of mineralization host rocks in different types of ore deposits. It has to be added here that in the C- V model, "C" can be replaced by either "concentration" (e.g. grade, or tonnage), or "probability" (e.g. uncertainty). In this paper, the researchers used "C" to refer to concentration. C- V fractal model can be expressed as:

$$V(c \leq \nu) \propto c^{-a1}; V(c > \nu) \propto c^{-a2} \quad (2)$$

where V ($c \leq \nu$) and V ($c > \nu$) indicate volumes (V) with concentration values (c) smaller and greater than contour values (ν), respectively; a1 and a2 are characteristic exponents.

3.3. Sequential Gaussian Simulation

Sequential Gaussian simulation (SGS) is a conditional simulation of continuous variable (Goovaerts, 1996; Chiles and Delfiner, 1999). In this algorithm, data are transformed to a Gaussian distribution with a zero mean and a unit variance. In this method, hard data are obtained by moving conditioning data to the nearest grid nodes. The other nodes are simulated and considered as soft data. The procedure of sequential Gaussian simulation is as follows:

- Simulated node is randomly selected in the grid (1st randomness);
- Simulated value is selected from interval calculated from zero-realization (2nd randomness);
- Final histogram and distribution in each realization can be calculated from both hard and soft data:

$$Z^*_{SGS}=Z^*_{SK} +/- s_K(U) \quad (3)$$

where Z^*_{SK} calculate from simple kriging estimate; $s_K(U)$ signifies standard deviation of kriging estimate; and (U) is a random value from normal function and Z^*_{SGS} is simulated value (Rossi and Deutsch, 2013).

3.4. Sequential Indicator Simulation

Sequential indicator simulation (SIS) is deployed for categorical variables (e.g., Journel and Isaaks 1984). The realization is achieved through the following procedure:

- A random path is defined through the grid nodes to be simulated (target nodes). This part also includes data points (data nodes);
- Conditional cumulative distribution function is determined (ccdf) by the Indicator Kriging;
- Order relations is corrected to build a complete ccdf model;
- A simulation value draw from the corrected ccdf;
- Add the simulated value to the conditioning dataset;
- Proceed to the next node on the random path and repeat the above steps.

4. Experimental Dataset

The dataset consists of 559 rock samples with intervals of 2m gathered from 17 drill holes. The drill holes locations are provided on the geological map (Figure 1b). Drill hole samples were analyzed for 26 elements (Table 1) using inductively coupled plasma optical emission spectrometry (ICP-OES).

The copper grade histogram and C-N log-log plots for Cu were generated as depicted in figure 3a and 3b. Based on C-N fractal model, there are six populations for Cu. The first population for Cu appeared at grades below 160 ppm. The second population occurred between grades 160 ppm and 900 ppm. These populations are related to black shale and rhyodacite with very weak mineralization (Figure 3c).

The third and fourth populations are related to low grade mineralization in rhyodacite and black shale (Figure 3d), ranging between 900 to 3100 ppm and 3100 to 6300 ppm, respectively. The fifth population included major Cu mineralization which occurred in Cu grades between 6300 and 17800 ppm (Figure 3e). Eventually, the sixth population for the C-N log-log plot of Cu illustrates both extreme mineralization (Figure 3f) and enrichment in samples with Cu values higher than 17800 ppm.

5. C-V Fractal Modeling of Copper Grade Based on SGS

Sequential Gaussian simulation was used for generating 10 realizations of the copper grade. Nohkouhi deposit is simulated using 600.000 cells, which have a cell dimension of 2 m×2 m×2 m in the X, Y, and Z directions, respectively.

The grade data are transformed into Gaussian distribution, on which the semi-variogram analysis is performed. Due to the lack of boreholes in azimuth 70°, no experimental variogram has been obtained. Hence, based on geological knowledge (e.g. ratio between structural axis), the range of the second direction (Az 70°) was considered equal to 75% of the range of the major axis.

Consequently, the following semi-variogram model, consisting of a nugget effect and a nested spherical model, was obtained (Figure 4):

Table 1- Detection limits for analyzed elements.

Element	Ag	Al	As	Ca	Cd	Ce	Co	Cr	Cu	Fe	La	Li	Mg
Unit	ppm	ppm	ppm	ppm	ppm	ppm	ppm	ppm	ppm	ppm	ppm	ppm	ppm
Detection limit	0,1	100	0,5	100	0,1	1	1	1	1	100	1	1	100
Element	Mn	Mo	Ni	P	Pb	S	Sb	Sc	Th	V	Y	Yb	Zn
Unit	ppm	ppm	ppm	ppm	ppm	ppm	ppm	ppm	ppm	ppm	ppm	ppm	ppm
Detection limit	5	0,5	1	5	1	50	0,5	0,5	0,5	1	0,5	0,2	1

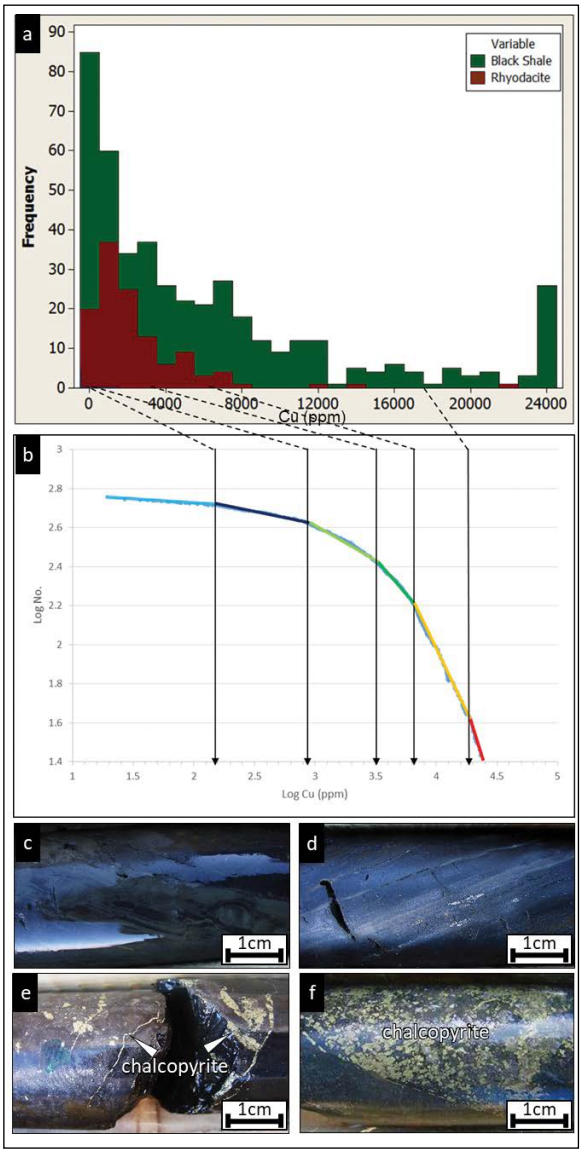

Figure 3- a) Histogram of Cu, b) C-N log-log plot for Cu concentrations in Nohkouhi deposit, c) barren black shale, d) disseminated chalcopyrite, e) veinlet of chalcopyrite, f) Massive-semi-massive chalcopyrite hosted by black shale.

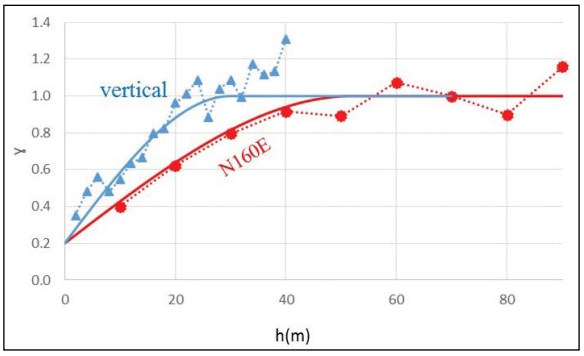

Figure 4- Experimental (dashed lines) and theoretical (solid lines) semi variograms along major (N160E) and minor (vertical) anisotropy axis (Gaussian transformed grade data).

$$\gamma_{N160E} = 0.2 \text{ nugget} + 0.8 \text{ Sph } (52) \quad (4)$$

$$\gamma_{N070E} = 0.2 \text{ nugget} + 0.8 \text{ Sph } (40) \quad (5)$$

$$\gamma_{horizental} = 0.2 \text{ nugget} + 0.8 \text{ Sph } (32) \quad (6)$$

where the distances into brackets denote the ranges along each directions.

Thresholds values of simulated Cu grades were identified using C-V log-log plots of the simulations (Figure 5). The simulations indicate four or five populations with different thresholds, as depicted in figure 5 and table 2. The enriched zones in the different simulated data are higher than 2,23%. Moreover, the main mineralization of Cu commences from 0,5% for sim 1, 3, 6, 7, 8, 9, and 10. In addition, the major Cu mineralized zones occurred in Cu values greater than 0,3% in sim 2, 4 and 5. One can see that, there is similar threshold with minor difference between them. So just two realization will be investigated.

6. U-V Fractal Modeling Of Copper Mineralization Based On SIS

In this study, SIS is used to simulate two copper ore minerals of chalcopyrite and malachite, separately. Indicator variables for copper minerals are defined as:

$$I_{malachite} = \begin{cases} \textit{if malachite present} \\ \textit{0 other} \end{cases} \quad (7)$$

$$I_{chalcopyrite} = \begin{cases} \textit{1 if chalcopyrite present} \\ \textit{0 other} \end{cases} \quad (8)$$

The experimental variogram are fitted by nugget effect and spherical model (Figure 6). However, as in the previous section, due to the lack of boreholes in azimuth 70°, no experimental variogram has been obtained. So, the range of the second direction (Az 70°) was considered equal to 75% of the range of the major axis.

$$\text{chalcopyrite} = \begin{cases} \gamma_{K160E} = 0.02 \text{ nugget} + 0.18 \text{ Sph } (144) \\ \gamma_{K070E} = 0.02 \text{ nugget} + 0.18 \text{ Sph } (108) \\ \gamma_{vertical} = 0.02 \text{ nugget} + 0.18 \text{ Sph } (40) \end{cases} \quad (9)$$

$$\text{malachite} = \begin{cases} \gamma_{K160E} = 0.02 \text{ nugget} + 0.16 \text{ Sf } (200) \\ \gamma_{K070E} = 0.02 \text{ nugget} + 0.16 \text{ Sf } (150) \\ \gamma_{vertical} = 0.02 \text{ nugget} + 0.16 \text{ Sf } (21) \end{cases} \quad (10)$$

where the distances into brackets represent the ranges along the directions.

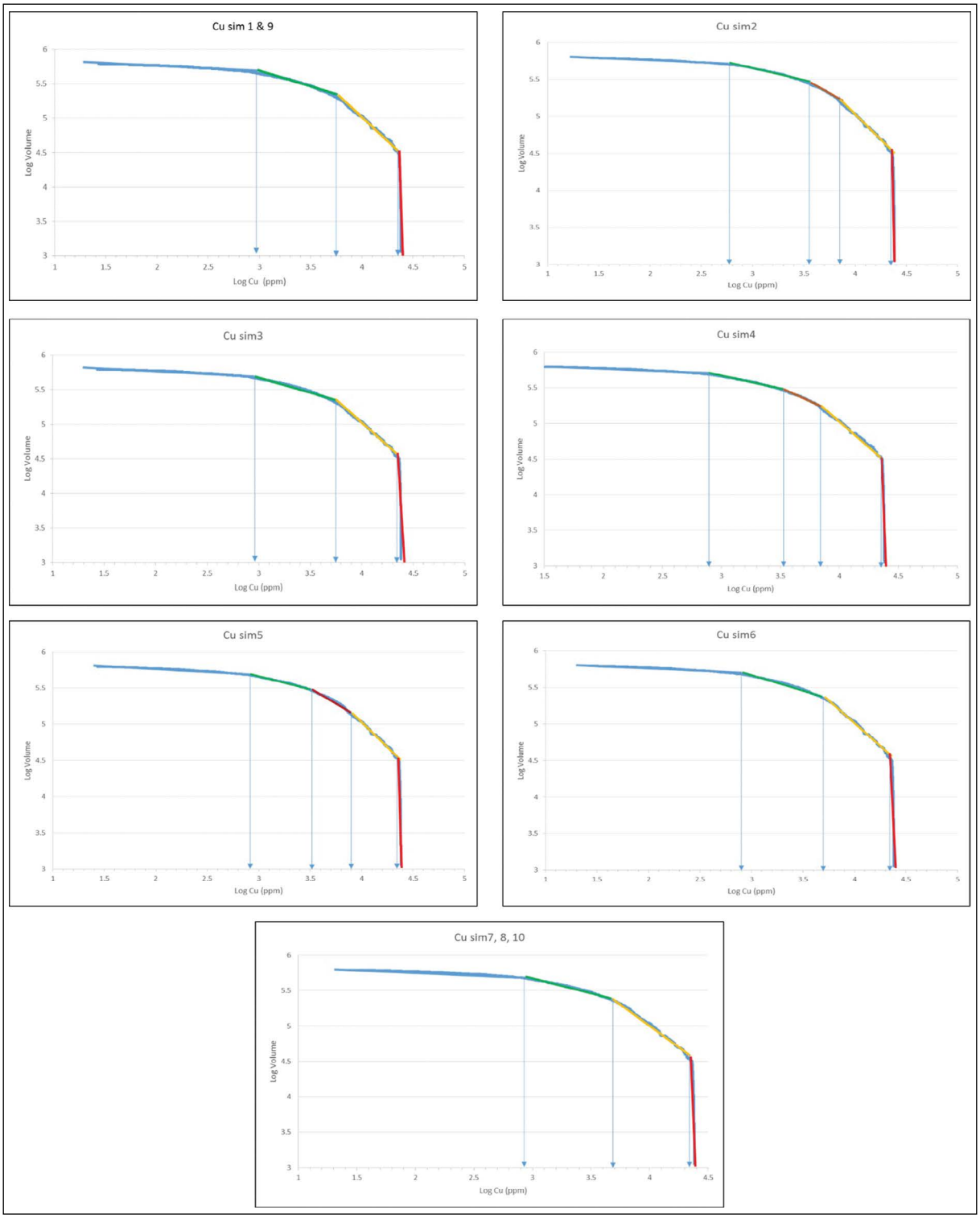

Figure 5- C-V log–log plots of different realizations of SGS and E-type.

Table 2- Cu threshold values (ppm) were recognized using C–V fractal model for different realizations.

Realization no.	First	Second	Third	Forth
Sim 1	1000	5623	22387	-
Sim 2	630	3548	7079	22387
Sim 3	891	5623	22387	-
Sim 4	794	3162	7079	22387
Sim 5	794	3162	7943	22387
Sim 6	794	5011	22387	-
Sim 7	891	5011	22387	-
Sim 8	891	5011	22387	-
Sim 9	1000	5623	22387	-
Sim 10	891	5011	22387	-

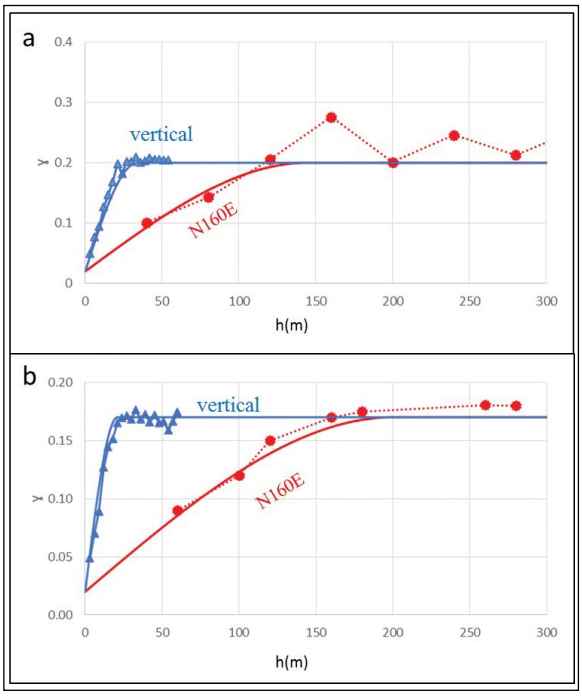

Figure 6- Sample (dashed lines) and modeled (solid lines) semi variograms along main anisotropy directions, a) chalcopyrite, b) malachite.

The probability maps of chalcopyrite and malachite were calculated and U-V fractal modeling was obtained for these ores. Threshold values were determined in the U-V log-log plot as breakpoints which reveal a power-law relationship between probability of minerals and the volumes occupied (Figure 7). Three breakpoints (0,13, 0,6, 0,83 and 0,13, 0,52, 0,83 for chalcopyrite and malachite respectively) appeared in the U-V log-log plots which represent four populations for chalcopyrite and malachite (Figure 7). As a result, the plots revealed four zones with variable probabilities, ranging from low to highly probable zones (Figure 8).

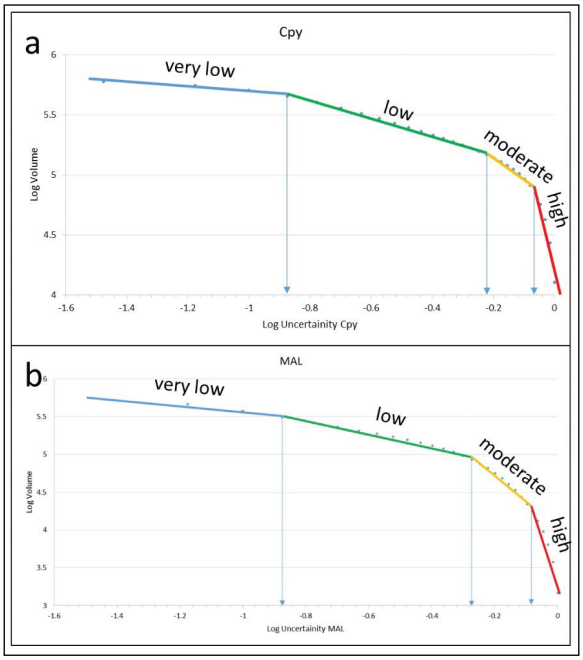

Figure 7- U–V log–log plots of copper ore minerals in the Nohkouhi deposit (Cpy: Chalcopyrite; Mal: Malachite).

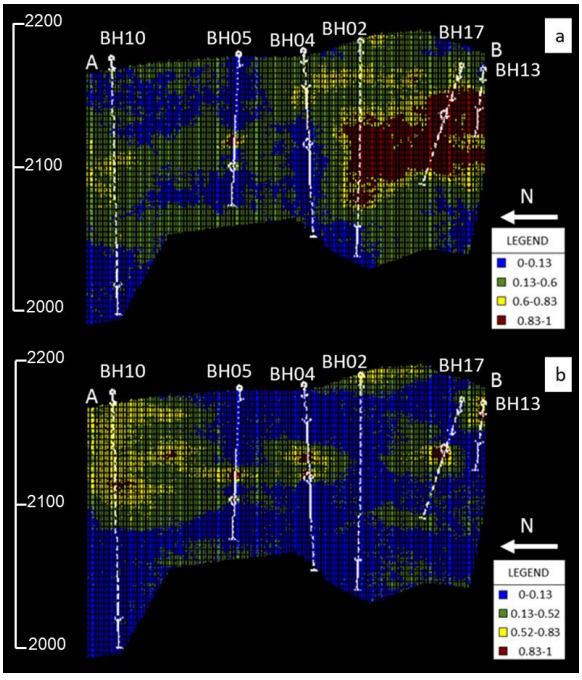

Figure 8- Different probability mineralization zones for a) chalcopyrite b) malachite based on the U–V fractal modeling and probability map of 30 realizations of copper ores. Section A-B is provided on figure 1.

7. Comparison of Fractal and Host Rock Models of the Deposit

The results derived from C-V fractal modeling of the deposit are correlated with U-V fractal model of copper minerals. Confusion matrix is utilized to calculate spatial correlations between the results provided by U-V and C-V fractal models (Table 3; Carranza, 2011). Due to similar results, only two realizations were reviewed (realization 1 and 10). Based on confusion matrix (Tables 4-5), generally, the realizations represent the proper results of a highly probable delineation (CPY≥0,83 and Mal

Table 3- Matrix for comparing performance of fractal modeling results with geological model. A, B, C, and D represent numbers of voxels in overlaps between classes in the binary geological model and the binary results of fractal models (Carranza, 2011).

		Geological model	
		Inside zone	Outside zone
Fractal model	Inside zone	True positive (A)	False positive (B)
	Outside zone	False negative (C)	True negative (D)
		Type I error = C/(A +C)	Type II error = B / (B + D)
		Overall accuracy =(A+D)/(A+B+C+D)	

Table 4- Overall accuracy (OA), Type I and Type II errors (T1E and T2E, respectively), resulted from U-V fractal models of copper minerals and C–V fractal modeling of realizations 1.

	CPY ≥ 0,83			0,6 ≤ CPY < 0,83			0,13 ≤ CPY < 0,6			CPY < 0,13	
Cu ≥ 22387	A	B	5623≤ Cu<22387	A	B	1000 ≤ Cu<5623	A	B	Cu < 1000	A	B
	5484	76172		18807	47278		122502	183239		49481	120350
	C	D		C	D		C	D		C	D
	28372	513285		153233	403995		120559	187688		121067	332414
	OA	0,83		OA	0,67		OA	0,50		OA	0,61
	ETI	0,83		ETI	0,89		ETI	0,49		ETI	0,70
	ETII	0,13		ETII	0,11		ETII	0,49		ETII	0,26
	Mal ≥ 0,83			0,52 ≤ Mal < 0,83			0,13 ≤ Mal < 0,52			Mal < 0,13	
Cu ≥ 22387	A	B	5623≤ Cu<22387	A	B	1000≤ Cu<5623	A	B	Cu < 1000	A	B
	2772	14651		27082	41265		87388	137662		111560	200933
	C	D		C	D		C	D		C	D
	31084	574806		144958	410008		159481	238782		58988	251831
	OA	0,92		OA	0,70		OA	0,52		OA	0,58
	ETI	0,91		ETI	0,84		ETI	0,64		ETI	0,34
	ETII	0,02		ETII	0,09		ETII	0,36		ETII	0,44

Table 5- Overall accuracy (OA), Type I and Type II errors (T1E and T2E, respectively), resulted from U-V fractal models of copper minerals and C–V fractal modeling of realizations 10.

	CPY ≥ 0,83			0,6 ≤ CPY < 0,83			0,13 ≤ CPY < 0,6			CPY < 0,13	
Cu ≥ 22387	A	B	5011 ≤ Cu < 22387	A	B	891 ≤ Cu < 5011	A	B	Cu < 891	A	B
	1820	79836		21417	44668		119453	186288		33030	136801
	C	D		C	D		C	D		C	D
	32036	509621		170285	386943		118973	189274		122538	330944
	OA	0,82		OA	0,66		OA	0,50		OA	0,58
	ETI	0,95		ETI	0,89		ETI	0,50		ETI	0,79
	ETII	0,14		ETII	0,10		ETII	0,50		ETII	0,29
	Mal ≥ 0,83			0,52 ≤ Mal < 0,83			0,13 ≤ Mal < 0,52			Mal < 0,13	
Cu ≥ 22387	A	B	5011≤ Cu < 22387	A	B	891≤ Cu < 5011	A	B	Cu < 891	A	B
	1847	15576		28187	40160		82580	142470		90390	222103
	C	D		C	D		C	D		C	D
	32009	573881		163515	391451		159607	238656		65178	245642
	OA	0,92		OA	0,67		OA	0,52		OA	0,54
	ETI	0,95		ETI	0,85		ETI	0,66		ETI	0,42
	ETII	0,03		ETII	0,09		ETII	0,37		ETII	0,47

≥0,83). Moreover, C–V modeling of realizations is appropriate for moderate probability (0.6≤CPY<0.83 and 0,52≤Mal<0,83). On the other hand, C–V fractal modeling provides relatively poor results for low and very low probabilities (0,13≤CPY<0,6, CPY<0,13, 0,13≤Mal<0,52, Mal<0,13) of copper minerals. Hence, this finding can be used to show the relationship between two probability zones (i.e. high and moderate) and copper grades. 3D models of the rock types (black shale, rhyodacite, and sandstone) were generated by employing SIS and geological drill core data (Hajsadeghi et al., 2016). Figure 9a displays the most frequently occurring model of rock types.

Merging C-V and U-V fractal models with the most frequent model of rock types helps delineate different copper populations in this deposit (Figure 9). Based on the log–log plots, Cu concentrations in massive, semi-massive, and oxide zones, hosted by black shale and partly by rhyodacite, are shown to be greater than 22387 ppm. The disseminated and veinlet zones have a concentration range varying between 5011 and 7943 ppm. This zone is hosted by black shale and rhyodacite. Besides, it was observed that low-grade host rocks had a Cu concentration between 1000 and 5011 ppm which is hosted by both of the host rocks. Finally, the barren part of all three host rocks (black shale, rhyodacite, and sandstone) is characterized by a Cu concentration lower than 1000 ppm. Geostatistical-fractal simulations conform to the hydrothermal and mineralization process of Nohkouhi copper deposit.

8. Conclusion

C-V fractal model revealed different copper grade mineralization's which are related to various copper ores and accumulations in Nohkouhi VMS deposit. U-V fractal model was used to obtain different probability zones for occurrence of copper minerals. C-V fractal modeling provided four or five populations. Several copper populations were delineated based on the results of U-V and C–V fractal modeling and the most frequently occurring model of rock types. Massive, semi-massive, and oxide zones - hosted by black shale

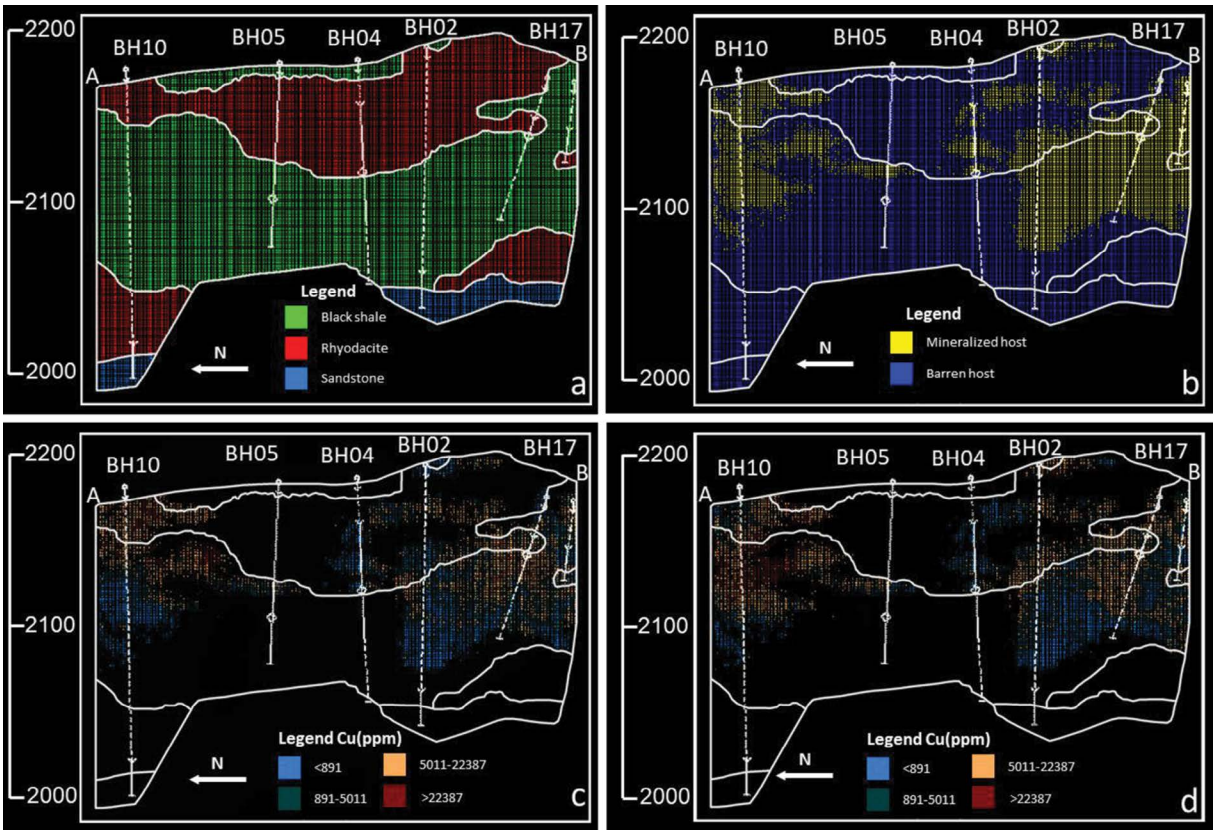

Figure 9- a) Most frequent occurrence model of rock types obtained by SIS (Hajsadeghi et al., 2016), b) Mineralized host rock characterized by MAL> 0.52 or CPY> 0.6, c) different Cu populations based on C–V fractal modeling in a simulation in realization 1, d) different Cu populations based on C–V fractal modeling in a simulation in realization 10. Section A-B is provided on figure 1.

were found to be higher than 2,24%. The disseminated and veinlet zones, hosted by black shale and rhyodacite, each showed a concentration range of 1,99-2,24% and 0,31-0,56%, respectively. Additionally, low-grade host rocks, occurring in black shale and rhyodacite, exhibited a Cu concentration ranging between 0.1-0,31 %. Eventually, the barren part of all host rocks, consisting of black shale, rhyodacite, and sandstone, were featured by a Cu concentration lower than 0.1%. These are related to characterize of Nohkouhi VMS deposit which suggested in pervious study (Hajsadeghi et al., 2017). However a 3D model can be more useful in exploration than a simple schematic model.

Acknowledgments

The authors are grateful to Zarmesh Group for providing the dataset used in this study.

References

Afzal, P., Alghalandis, Y.F., Khakzad, A., Moarefvand, P., Omran, N.R. 2011. Delineation of mineralization zones in porphyry Cu deposits by fractal concentration–volume modeling. Journal of Geochemical Exploration 108(3), pp.220-232.

Afzal, P., Ahari, H.D., Omran, N.R., Aliyari, F. 2013. Delineation of gold mineralized zones using concentration–volume fractal model in Qolqoleh gold deposit, NW Iran. Ore Geology Reviews 55, pp.125-133.

Afzal, P., Alhoseini, S.H., Tokhmechi, B., Ahangaran, D.K., Yasrebi, A.B., Madani, N., Wetherelt, A. 2014. Outlining of high quality coking coal by concentration–volume fractal model and turning bands simulation in East-Parvadeh coal deposit, Central Iran. International Journal of Coal Geology 127, pp.88-99.

Afzal, P., Madani, N., Shahbeik, S., Yasrebi, A.B. 2015. Multi-Gaussian kriging: a practice to enhance delineation of mineralized zones by Concentration–Volume fractal model in Dardevey iron ore deposit, SE Iran. Journal of Geochemical Exploration 158, pp.10-21.

Afzal, P., Tehrani, M.E., Ghaderi, M., Hosseini, M.R. 2016. Delineation of supergene enrichment, hypogene and oxidation zones utilizing staged factor analysis and fractal modeling in Takht-e-Gonbad porphyry deposit, SE Iran. Journal of Geochemical Exploration, 161, pp.119-127.

Carranza, E.J.M. 2009. Controls on mineral deposit occurrence inferred from analysis of their spatial pattern and spatial association with geological features. Ore Geology Reviews 35(3), pp.383-400.

Carranza, E.J.M. 2011. Analysis and mapping of geochemical anomalies using logratio-transformed stream sediment data with censored values. Journal of Geochemical Exploration 110(2), pp.167-185.

Cheng, Q. 1999. Spatial and scaling modelling for geochemical anomaly separation. Journal of Geochemical Exploration 65(3), pp.175-194.

Cheng, Q., Agterberg, F.P., Ballantyne, S.B. 1994. The separation of geochemical anomalies from background by fractal methods. Journal of Geochemical Exploration 51(2), pp.109-130.

Chilés, J.P., Delfiner, P. 2012. Geostatistics: modeling spatial uncertainty (Vol. 497). John Wiley & Sons.

Daneshvar Saein, L., Rasa, I., Rashidnejad Omran, N., Moarefvand, P., Afzal, P. 2012. Application of concentration-volume fractal method in induced polarization and resistivity data interpretation for Cu-Mo porphyry deposits exploration, case study: Nowchun Cu-Mo deposit, SE Iran. Nonlinear Processes in Geophysics 19(4), pp.431-438.

Delavar, S.T., Afzal, P., Borg, G., Rasa, I., Lotfi, M., Omran, N.R. 2012. Delineation of mineralization zones using concentration–volume fractal method in Pb–Zn carbonate hosted deposits. Journal of Geochemical Exploration 118, pp.98-110.

Deutsch, C.V., Journel, A.G. 1998. Geostatistical software library and user's guide. Oxford University Press, New York.

Goncalves, M.A., Mateus, A., Oliveira, V. 2001. Geochemical anomaly separation by multifractal modelling. Journal of Geochemical Exploration 72(2), pp.91-114.

Goovaerts, P. 1996. Geostatistics for natural resources evaluation. Oxford University Press on Demand.

Gumiel, P., Sanderson, D.J., Arias, M., Roberts, S. Martín-Izard, A. 2010. Analysis of the fractal clustering of ore deposits in the Spanish Iberian Pyrite Belt. Ore Geology Reviews 38(4), pp.307-318.

Hajsadeghi, S., Asghari, O., Mirmohammadi, M., Meshkani, S.A. 2016. Indirect rock type modeling using geostatistical simulation of independent components in Nohkouhi volcanogenic massive sulfide deposit, Iran. Journal of Geochemical Exploration 168, pp.137-149.

Hajsadeghi, S., Mirmohammadi, M., Asghari, O., Meshkani, S.A. 2017. Geology and mineralization at the copper-rich volcanogenic massive sulfide deposit in Nohkouhi, Posht-e-Badam block, Central Iran. Ore Geology Review doi:https://doi.org/10.1016/j.oregeorev.2017.11.030.

Hassanpour, S., Afzal, P. 2013. Application of concentration–number (C–N) multifractal modeling for geochemical anomaly separation in Haftcheshmeh porphyry system, NW Iran. Arabian Journal of Geosciences 6(3), pp.957-970.

Journel, A.G. 1983. Nonparametric estimation of spatial distributions. Journal of the International Association for Mathematical Geology 15(3), pp.445-468.

Journel, A.G., Isaaks, E.H. 1984. Conditional indicator simulation: Application to a Sachatchewan uranium deposits. Marhematical Geology 16 (7):685-718.

Karmania, A. 2013.Company, Preliminary Exploration Report in Nohkouhi Area, Tehran (73 pp., (In Persian)).

Li, C., Ma, T., Shi, J. 2003. Application of a fractal method relating concentrations and distances for separation of geochemical anomalies from background. Journal of Geochemical Exploration 77(2), pp.167-175.

Lin, X., Zhang, B., Wang, X. 2014. Application of factor analysis and concentration-volume fractal modeling to delineation of 3D geochemical patterns: a case study of the Jinwozi gold field, NW China. Geochemistry: Exploration, Environment, Analysis 14(4), pp.359-367.

Mandelbrot, B.B. 1983. The fractal geometry of nature (Vol. 173). Macmillan.

Rahmati, A., Afzal, P., Abrishamifar, S.A., Sadeghi, B. 2015. Application of concentration–number and concentration–volume fractal models to delineate mineralized zones in the Sheytoor iron deposit, Central Iran. Arabian Journal of Geosciences 8(5), pp.2953-2965.

Rezaei, S., Lotfi, M., Afzal, P., Jafari, M.R., Meigoony, M.S. 2015. Delineation of Cu prospects utilizing multifractal modeling and stepwise factor analysis in Noubaran 1: 100,000 sheet, Center of Iran. Arabian Journal of Geosciences 8(9), pp.7343-7357.

Rossi, M.E., Deutsch, C.V. 2013. Mineral resource estimation. Springer Science & Business Media.

Sadeghi, B., Moarefvand, P., Afzal, P., Yasrebi, A.B., Saein, L.D. 2012. Application of fractal models to outline mineralized zones in the Zaghia iron ore deposit, Central Iran. Journal of Geochemical Exploration 122, pp.9-19.

Sadeghi, B., Madani, N., Carranza, E.J.M. 2015. Combination of geostatistical simulation and fractal modeling for mineral resource classification. Journal of Geochemical Exploration 149, pp.59-73.

Sahandi, M. R., Soheily, M., Sadeghi, M., Delavar, S.T., Jafari Rad, A. 2002. Geological Map of Iran, 1:1,000,000. Geological Survey of Iran, Tehran, Unpublished

Soltani, F., Afzal, P., Asghari, O. 2014. Delineation of alteration zones based on Sequential Gaussian Simulation and concentration–volume fractal modeling in the hypogene zone of Sungun copper deposit, NW Iran. Journal of Geochemical Exploration 140, pp.64-76.

Sun, T., Liu, L. 2014. Delineating the complexity of Cu–Mo mineralization in a porphyry intrusion by computational and fractal modeling: A case study of the Chehugou deposit in the Chifeng district, Inner Mongolia, China. Journal of Geochemical Exploration 144, pp.128-143.

Yasrebi, A.B., Afzal, P., Wetherelt, A., Foster, P., Esfahanipour, R. 2013. Correlation between geology and concentration-volume fractal models: significance for Cu and Mo mineralized zones separation in the Kahang porphyry deposit (Central Iran). Geologica Carpathica 64(2), pp.153-163.

Bulletin of the Mineral Research and Exploration

http://bulletin.mta.gov.tr

The role of variscan shortening in the control of mineralization deposition in Tadaout-Tizi N'rsas mining district (Eastern Anti-Atlas, Morocco)

Mustapha AIT DAOUD[a]*, Abdelhafid ESSALHI[a], Mourad ESSALHI[a] and Abdeslam TOUMMITE[a]

[a]*Géophysique, Géoresources et Patrimoine, Faculté des Sciences et Techniques, Université Moulay Ismaïl, BP. 509, Boutalamine, 52000 Errachidia, Maroc*

Research Article

Keywords:
Tadaout-Tizi n'Rsas Anticline, Tafilalet, Eastern Anti-Atlas, Variscan Shortening, Normal Faults.

ABSTRACT

The abundance of the NE-SW direction veins mineralized in barite, copper, lead and zinc in the Tadaout-Tizi n'Rsas (TTR) anticline make this area one of the principal vein fields in Tafilalet (easternmost border of the Eastern Anti-Atlas). Reactivation of faults and alternation of competent (thicks Ordovician series, Silurian limestone and Devonian limestone) and incompetent levels (Silurian shales and Devonian marls) have an important role in the deformation of the TTR anticline during the NE-SW Variscan shortening. Our work based on lineaments extraction using a Landsat 8 OLI combined with some geological cross sections, shows a N130° major fold corresponding to TTR anticline. This big fold shows internal N130°, N95° and N20° minor folds. This structure indicates that the TTR area was formed in the hinge between the Anti-Atlas and the Ougarta belts. A number of these folds are the consequence of the underlying Precambrian faults reactivation and alternation of competent and incompetent levels. Brittle tectonics is dominated by NE-SW normal faults which result from the NE-SW shortening consequence of the Gondwana and Eurasia continents collision. Consequently, the mineralization of TTR is necessarily related to late or post-Variscan orogeny.

Received Date: 19.07.2018
Accepted Date: 16.01.2019

1. Introduction

The Tafilalet region corresponds to the easternmost part of the Moroccan Anti-Atlas. This region, principally formed by Paleozoic formations, was the subject of several studies; biostratigraphic and sedimentological ones (Choubert, 1943; Termier ve Termier, 1948; Destombes, 1963, 1968, 1971, 2006; Hollard, 1967, 1974, 1981; Wendt, 1985; Raddi vd., 2007; Brachert vd., 1992), and paleogeographic, paleobathymmetric or paleoecological ones (Mounji et al., 1998; Belka, 1998; Hilali et al., 1999; 2001). The geological mapping of this area corresponds to 1/200.000 map sheet of Tafilalet-Taouz (Destombes and Hollard, 1986), whereas the most important metallogenic work was realized on the M'Fis deposit (Makkoudi, 1995). More recently, some tectonic and magmatic studies were performed (Baidder et al., 2016; Pouclet et al., 2017; Robert-Charrue, 2006). Over the last two decades, the National Geological Mapping Program [Programme Nationale de la Cartographie Nationale (PNCG)] produced several geological maps with the scale of 1/50.000, like Irara, Marzouga, M'Fis, Taouz and El Atrous which contains our study area (TTR).

This work focusses on the tectonic control of the TTR deposit and discusses the role of Variscan shortening in the formation of a geometric trap, and the rock mechanical behavior changing. A structural

Citation Info: Ait Daoud, M., Essalhi, A., Essalhi, M., Toummite, A. 2020. The role of variscan shortening in the control of mineralization deposition in Tadaout-Tizi N'rsas mining district (Eastern Anti-Atlas, Morocco). Bulletin of the Mineral Research and Exploration, 161, 13-32. https://doi.org/10.19111/bulletinofmre.524167

* *Correponding Author: Mustapha AIT DAOUD, aitdaoud.mus@gmail.com*

model of the deposit will be considered as an exploration guide in the Tafilalet region.

The Tafilalet region has a big mining vocation; it has been the site of lead-zinc production in the past, but now the exploitation concerns mainly the barite ore bodies. The main vein fields of Tafilalet are M'Fis, Shayb Arras, Njakh, Bouizrane, Ras Kammouna, Bou Mayz, Tijekht and TTR. The latter comprises more than twenty veins of Cu, Pb, Zn and barite. The present paper aims to analyze and understand the relationship between the Variscan tectonics and the large distribution of mineralized veins in TTR.

2. Geological Framework and Previous Works

Geographically, The TTR anticline is located in the south of Erfoud, and in the southwest of the touristic dunes of Merzouga, precisely in the NW part of Taouz village. It extends more than 16 km between 30°54' and 31°00'N latitudes, and between 4°00'W and 4°14'W longitudes. It is located in the easternmost part of the Anti-Atlas belt, in the south-eastern part of Ougnat-Ouzina Ridge, between the Tafilalet plain (east) and the Maider basin (west) (Figure 1).

Moroccan Anti-Atlas, located at the northern rim of the West African Craton (WAC), is laterally limited by the Atlantic Ocean to the west and by the Hamada in the east. This chain corresponds to a large Paleozoic folded belt formed by a number of Precambrian inliers affected by Eburnean and Pan-African orogeneses. As a result of the post-Variscan erosion, the Precambrian rocks are exposed in the center of all inliers. The Anti-Atlas is considered as an arch continued southwest into the Zemour belt and southeast into the Ougarta belt (Haddoum et al., 2001) (Figure 2).

The Anti-Atlas belt display an ENE-striking where Precambrian basement is exposed in an ENE–WSW series that outcrops in several inliers (Bas Draâ, Ifni, Kerdous, Tagragra of Akka, Tagragra of Tata, Igherm, Sirwa, Zenaga, Bou Azzer, Saghro and Ougnat). All these inliers are distributed along two major fault zones: the South Atlas Fault (SAF) and the Anti-Atlas Major Fault (AAMF) (Choubert, 1964; Gasquet et al., 2008, 2005; Thomas et al., 2004) (Figure 3). This Precambrian basement is an assemblage of crystalline, metamorphic and sedimentary rocks. We can, then, distinguish two assemblages: (i) an older Paleoproterozoic substratum (~2 Ga) structured during the Eburnian orogenesis and (ii) a more recent Neoproterozoic cover associated with the Pan-African cycle (800 - 560 Ma). Classically, the Precambrian formations of the Anti-Atlas are divided into two domains from west to east: (i) a cratonic domain where Proterozoic substratum outcrop and belong to the WAC, and (ii) a Pan-African mobile domain where only the Neoproterozoic formations outcrop (Choubert, 1964). Cratonic and mobile domains are separated by the AAMF (Choubert, 1947).

The Paleozoic cover of the Anti-Atlas Precambrian inliers is predominantly deposited in a shallow marine environment. During the Lower Cambrian, an important carbonate platform was deposited in the western Anti-Atlas (Boudda et al., 1979; Geyer and Landing, 1995). Deposits from Middle Cambrian to

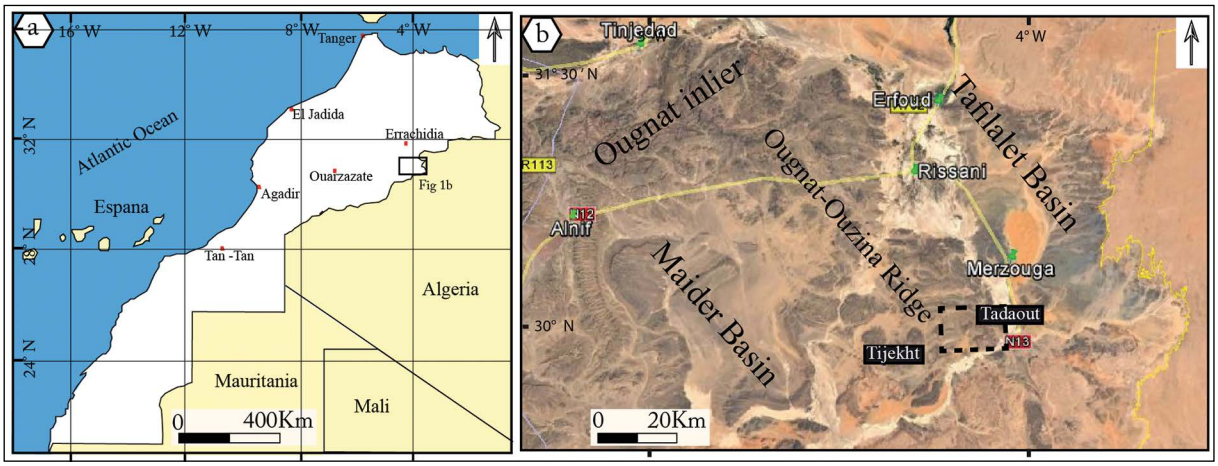

Figure 1- a) Geographic map of Morocco and b) Google maps image showing the eastern part of the Eastern Anti-Atlas. Dashed black rectangle in b indicates the study area.

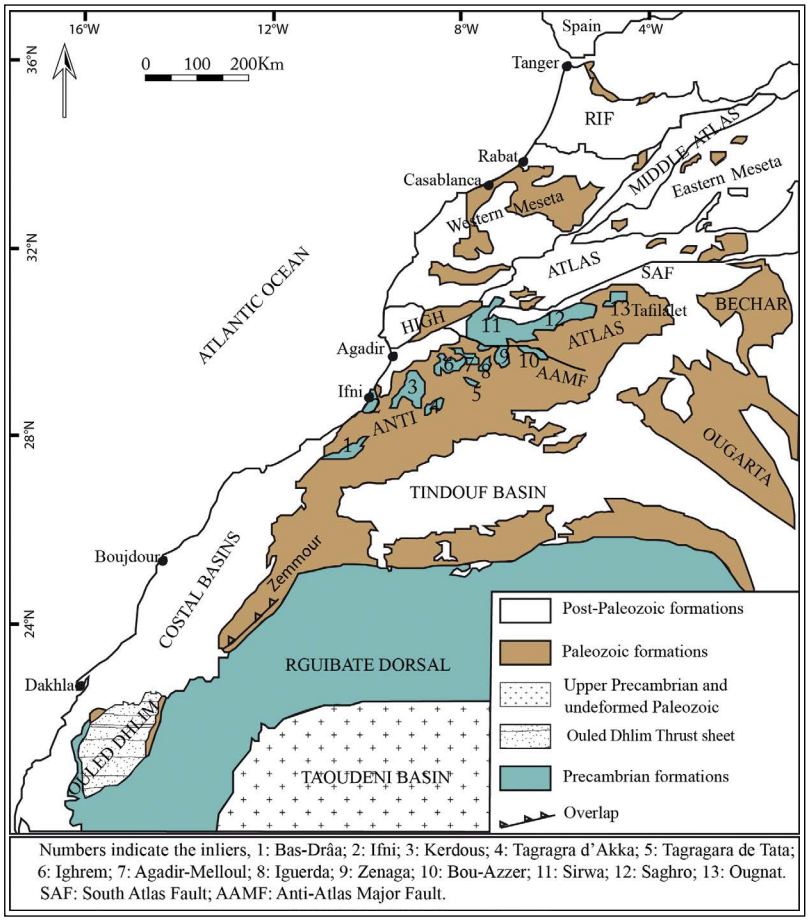

Figure 2- Moroccan structural domains. The Anti-Atlas belt is located between Zemmour and Ougarta belts (Pique, 1994).

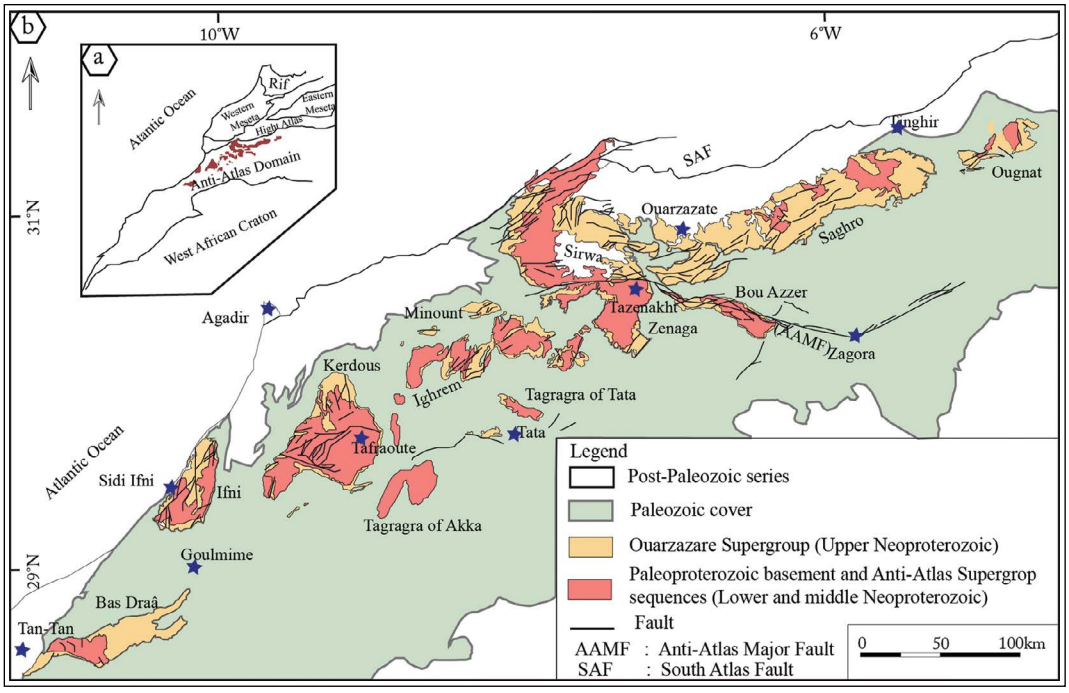

Figure 3- a) Moroccan geological domains, b) Anti-Atlas geological map showing all Precambrian inliers surrounded by Paleozoic rocks, adapted from 1/1.000.000-scale geological map of Morocco (Service Géologique du Maroc, 1985).

Late Silurian are dominated by WAC sedimentary inputs (Buggisch and Siegert, 1988; Destombes, 1976). The carbonate sedimentation restarted at the end of Silurian (Hollard, 1981) and continued during the Devonian, being combined with clastic inputs, throughout the Anti-Atlas region and beyond (Wendt, 1985). A renewed increase in detrital input is marked in the lower Carboniferous from the east, south and in places from the north (Michard et al., 1982; Pique and Michard, 1989).

In the Eastern Anti-Atlas, Paleozoic sequences overlie the Precambrian basement that crops out widely in the Saghro and the Ougnat massifs. This continental basement formed through the Pan-African orogeny was converted into an extending metacratonic domain in the latest Neoproterozoic times (Ennih and Liégeois, 2001; Gasquet et al., 2005). From Early/Middle Cambrian to early Carboniferous, the whole area was flooded by the Paleozoic seas (Raddi et al., 2007) (Figure 4). Around the Precambrian culminations, the sediments of Cambrian/Ordovician are exposed and constitute a SE-trending folded ridge (Ougnat-Ouzina Ridge) between Tafilalet basin to the east and Maider basin to the west, respectively (Hollard, 1981, 1974; Raddi et al., 2007; Wendt, 1985) (Figure 1b).

Before Variscan orogeny which affects the Paleozoic formations, the Anti-Atlas knew an extension, during the Cambrian, generated in the eastern part by a N70° normal and NW-SE left-lateral faults. In Tafilalet and Ougnat-Ouzina Ridge, the Caradoc tectonic is well-expressed where a fracturing zone differed between the Tafilalet and the Maider basins with NW-SE directions (Baidder, 2007). Throughout the Variscan orogeny, the Paleozoic series of the Anti-Atlas basin were involved in folding tectonics. This tectonics coincides with the uplift of Proterozoic basement blocks bounded by inherited basement faults (Soulaimani et al., 2014). During the Devonian, the extension and dislocation of the platform, produced the differentiation of basins (Baidder et al., 2008). Variscan tectonics in this age is called Eovarisc, they are controlled by Devonian paleofaults recognized in Tafilalet-Maider area with ENE, NW, NNE and ENE to ESE directions (Baidder, 2007; Baidder et al., 2007; 2008). During the Visean, the Eastern Anti-Atlas is marked by a tectonic instability (the Mesovarisc), as a prelude to the major Variscan phase (Baidder, 2007), controlled by three families of accidents E-W, SW-NE and NW-SE in extensive left-lateral faults (pull-apart system) (Soualhine et al., 2003).

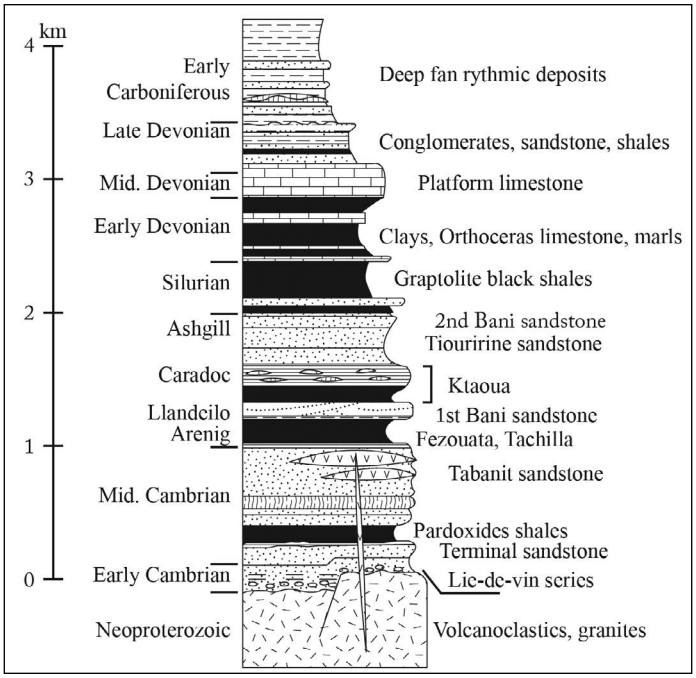

Figure 4- Synthetic stratigraphic column of the Paleozoic formations of the eastern Anti-Atlas, synthesized by (Raddi et al., 2007).

Neovarisc tectonic in the Eastern Anti-Atlas is characterized by NW-SE Namuro-Westphalian compression, responsible for E-W to NE-SW axis folds and right-lateral movements dominant associated with inverse or normal movements along major Pan-African accidents. The NE-SW Stephanian-Permian compression is responsible for the fault inversions and their dominant strike-slip throw (Raddi et al., 2007).

The folds trend analysis in the Eastern Anti-Atlas allowed to underline two preferential directions; the first with an E-W axis and the second with a NW-SE axis. The first direction dominates the west part and the last one dominates the eastern part, whereas in the south of the Precambrian inliers, both directions coexist (in the Tazzarine region; Figure 5). The E-W direction also dominates north of Ougnat and Saghro inliers with an ENE-WSW trend. However, there is an exception of isolated case to the north of the Ougnat inlier that has a N-S axis (Robert-Charrue, 2006).

According to Baidder (2007), the eastern part of Saghro and the northwestern of Ougnat show the presence of a fold system with different axis; N-S to NNE-SSW. This one characterizes the area between the northeastern of Saghro and the northwestern of Ougnat, with subhorizontal axes (Figure 5). In addition, the ENE-WSW to E-W folds are visibles between Tizi n'Boujou in the south and Jbel Tachtafacht in the north. In the south of the Ougnat inlier, the deformation of the Paleozoic sequences is strongly heterogeneous. Over tens of square kilometers, this deformation coexists with more restricted folded and faulted zones. The largest folds are observed in the Angal-Guerghis Lozenge (Raddi et al., 2007).

In the Ougnat-Ouzina Ridge, Baidder et al. (2016) distinguished between Cambrian- and Ordovician-cored folds. Three Cambrian-cored folds are identified from the north to the south of the Ougnat-Ouzina Ridge: (i) the NW-SE axis fold of Jbel Taklimt, (ii) the N120 axis fold of Jbel Renneg and (iii) the NNE axis fold of Jbel Tijekht. The Ordovician-cored folds are the (i) E-W anticline of Bou Maïz, (ii) the NW-SE axis fold of Shaïb Ras and (iii) the E-W axis fold of Tadaout (Figure 5).

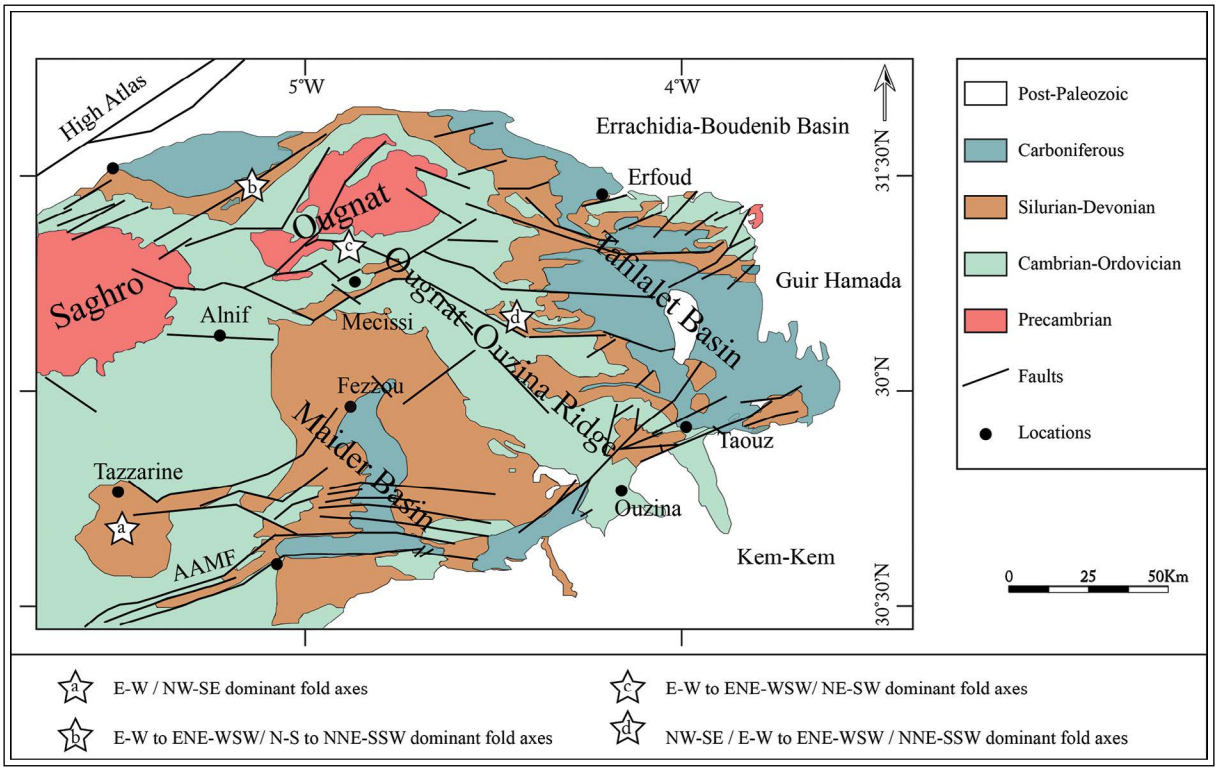

Figure 5- Geological maps of Eastern Anti-Atlas with major folds and faults located at the Eastern Anti-Atlas Paleozoic series. The starts represent the dominant fold axes by locations according to a) Robert-Charrue, 2006, b) Baidder, 2007; Robert-Charrue, 2006; Robert-Charrue and Burkhard, 2008, c) Michard et al., 2008; Raddi et al., 2007; Robert-Charrue and Burkhard, 2008 and d) Baidder et al., 2016; Benharref et al., 2014; Michard et al., 2008.

Numerous dykes and sills of the Central Atlantic Magmatic Province (CAMP), intruded the Anti-Atlas Paleozoic fold, were dated 200-195 Ma by place (Hailwood ve Mitchell, 1971; Hollard, 1973; Sebai vd., 1991; Derder vd., 2001; Youbi vd., 2003; Verati vd., 2007; Chabou vd., 2010). The Anti-Atlas belt was influenced by Variscan and Alpine orogenies. These two orogenesis affected hardly the Meseto-Atlasic domain situated at the north of the SAF and to a lesser degree, the Anti-Atlasic domain, located south of the SAF (Gasquet et al., 2005). According to the 1/200 000 Tafilalet-Taouz map (Destombes and Hollard, 1986), the massif of TTR is approximately a N120-trending anticlinal which affects the Middle Paleozoic series from Ordovician to Devonian. This massif contains doleritic intrusions localized within the Silurian, Devonian and Ordovician formations.

3. Methods

The Landsat image used in this work consists of the Landsat 8 OLI image (Operational Land Imager) acquired on 27/06/2014. The image has been downloaded from the USGS website page. It composes nine spectral bands with 30 m spatial resolution for bands 1 to 7 and 9. The resolution for band 8 (Panchromatic) is 15 m. The methodology followed for extracting lineaments from the Landsat 8 OLI image is summarized in figure 6a. After preprocessing of the Landsat 8 OLI image (radiometric calibration

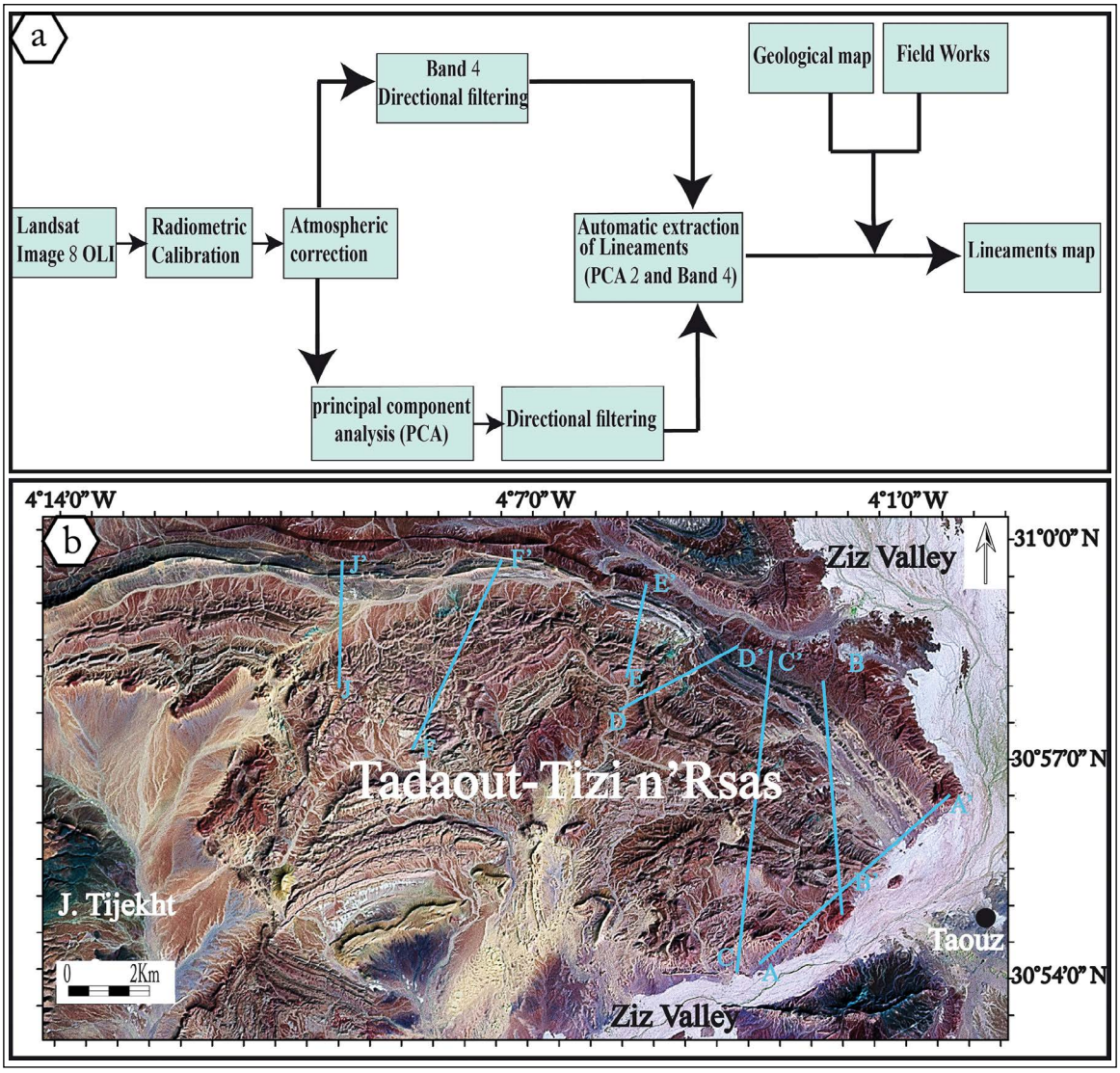

Figure 6- a) Major steps of lineaments extraction and analysis, b) landsat image of the TTR anticline showing the location of the geological cross sections.

and atmospheric correction), we calculated the principal component (PC) of the bands (from 1 to 7). Subsequently, the directional filters were applied to all bands and also on these principal component analysis (PCA) using the matrix 7-7. Many tests of automatic extraction of the lineaments are carried out on the 7 bands and on the results of the PCA. Following these tests, we selected the PCA2 and the band 4 filtered with the directional filter 45, because they give the best results. The compilation of two lineament maps extracted from PCA2 and band 4 makes it possible to establish a synthetic study area map of the lineaments. Several corrections are made to eliminate the linear structures (rivers, roads, scrapings, line of ridges, etc.

Results obtained from the automatic extraction of lineaments on the bands from 1 to 7 of the image OLI and on the results of the PCA, have been compared with the geological map of the region, and with data from our field missions. The field work is based on geological mapping following the method of cross sections whose objective is to intersect all structures of the studied area. Several cross sections were realized in order to collect as much of information as possible about the direction and the dip of tectonic structures (Figure 6b). Subsequently, the data collected are treated and presented using appropriate diagrams (Dips program).

4. Results

Stratigraphically, The TTR anticline is formed by Devonian, Silurian and Ordovician sedimentary terrains (Figure 7a). The Ordovician formations start with the "Feijas Externe" group ("Fezouata and Tachilla" shales), folowed by the "1st Bani" sandstone. This competent layer is surmounted by the "Ktaoua" shales and the "2nd Bani" sandstone (Figure 7b).The Silurian formations are composed of shales, orthoceras and crinoids limestone. These formations have a very small thickness compared to Ordovician ones (Figure 7b). The Devonian formations, which cover the north part of the region, are characterized by carbonate rocks with enormous enrichment in paleontological fossils. They are mainly composed by an alternation of marls and limestone forming the "Erfoud" and "Tafilalet" groups, and by sandstone of "Aoufilal" formations (Figure 7b).

In addition, all the Paleozoic formations of TTR are crosscut by the magmatic activity expressed by dykes and sills of the late Devonian-Early Carboniferous age (Pouclet et al., 2017) (Figures 7 and 8). Evidently, the Paleozoic sedimentary formations in the TTR are affected by a brittle tectonics at the north part of the Oumejrane-Taouz Fault (OJTF), which is the continuity of the AAMF towards Tafilalet (Baidder, 2007; Baidder et al., 2008). AAMF is considered as one of the more important major structures that impressed the Eastern Anti-Atlas (Choubert, 1947).

4.1. Extraction of Structural Lineaments from Satellite Image Landsat 8 OLI

The lineaments map, extracted automatically from the image processing, shows the dominance of a NE-SW direction. Other directions (NNE-SSW and ENE-WSW) are present but are less abundant (Figure 9a). The illustrated rose diagram of lineaments trends confirms the dominance of the NE-SW direction (Figure 9b). To validate these results we compared, in the first step, the extracted lineaments with the pre-existing 1/50.000 geological map of El Atrous (Benharref et al., 2014). The comparison with this geological map shows the presence of many analogies, although we notice the existence of a few disagreements in some segments. During the second stage of validation of our extracted lineaments, we observed linear structures on the field. This stage allowed us to confirm some linear structures, as well as to determine their movements (Figure 10).

4.2. Field Work and Structural Analysis

The TTR anticline is a WNW-ESE-trending fold with an Ordovician cored (Baidder et al., 2016; Destombes, 1963) and curved axis. It represents the hinge between the Anti-Atlas and the Ougarta belts. It is characterized by a long north limb and a short southern limb (asymetric fold). Structurally, the TTR anticline is limited to the east by the big fault of Ziz and to the northwest by a N70° fault which lodges the vein of Tizi-n'Rsas (Clariound, L, 1944; Destombes, 1963).

A set of disharmonic or entrainment folds are generated at the long limb of the TTR anticline; the majority of these folds are located in the Devonian formations. However, other folds are observable in the core of the anticline within Ordovician formations. Disharmonic folds are generated in formations as a

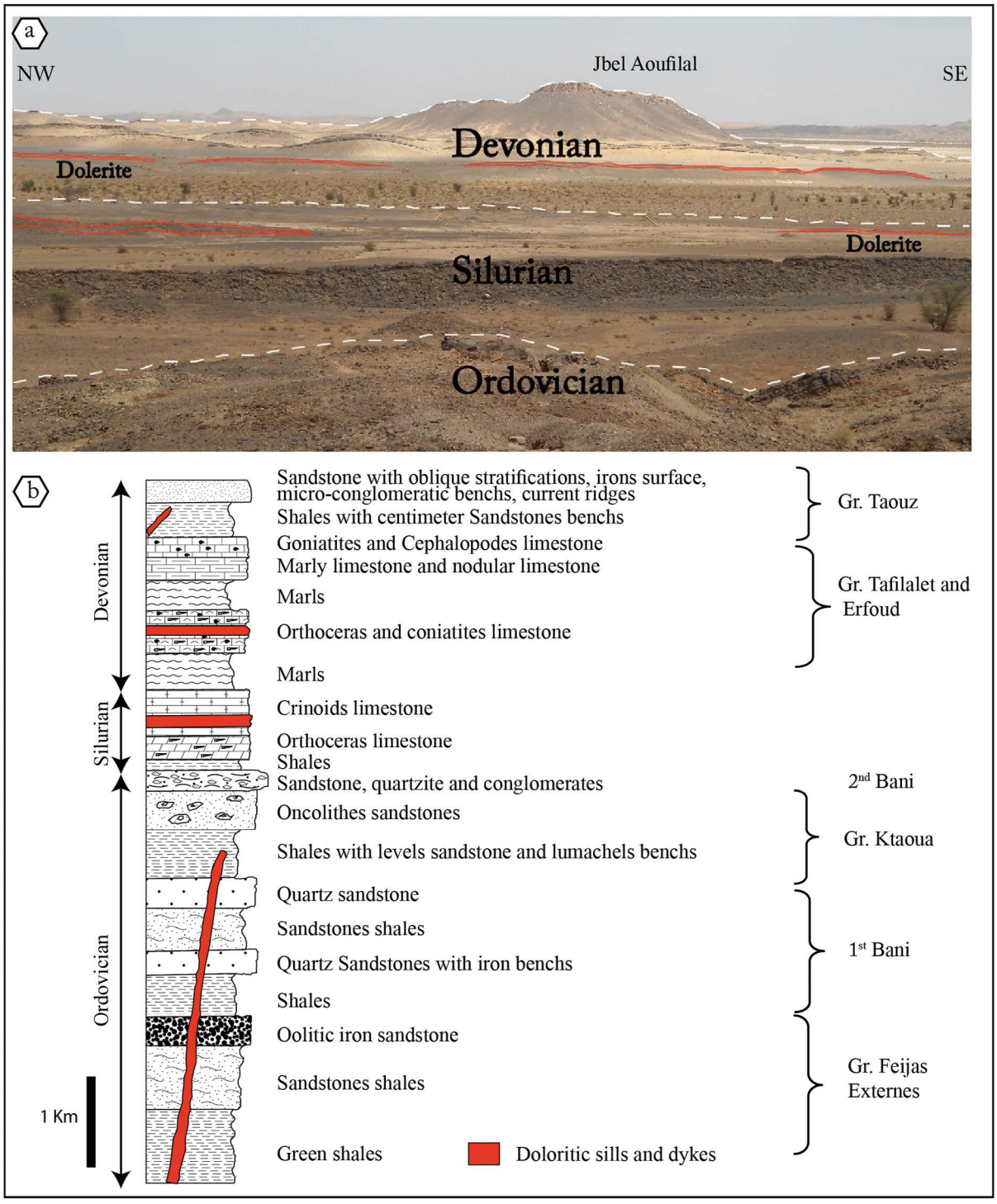

Figure 7- a) Panoramic view of the north limb of TTR anticline and b) synthetic stratigraphic column of the study area.

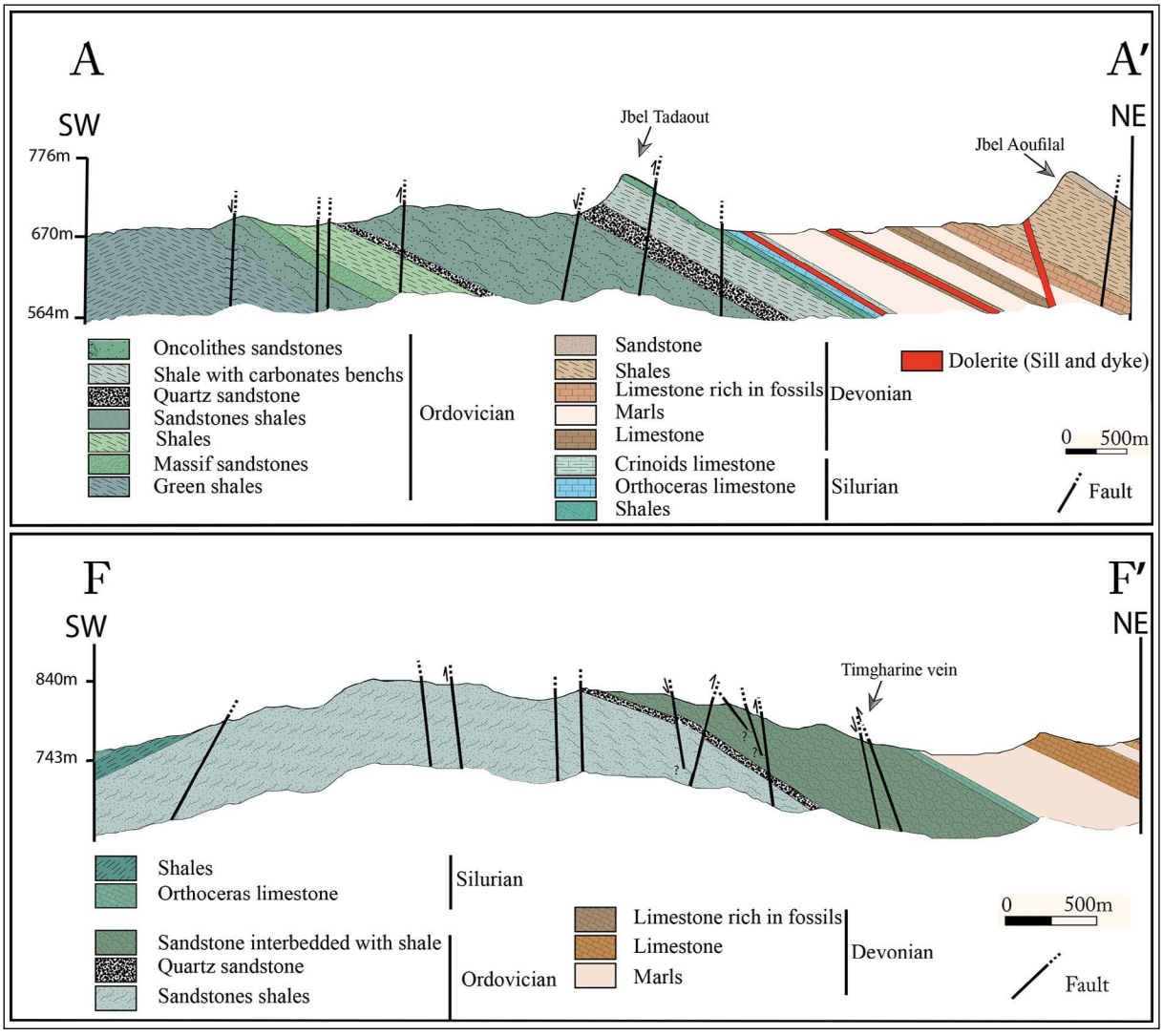

Figure 8- Geological cross sections realized in the study area. A-A' and F-F': in the Eastern and Western part of the study area, respectively. Cross sections B-B', C-C', D-D' and E-E' (in the figure 6) give similar informations.

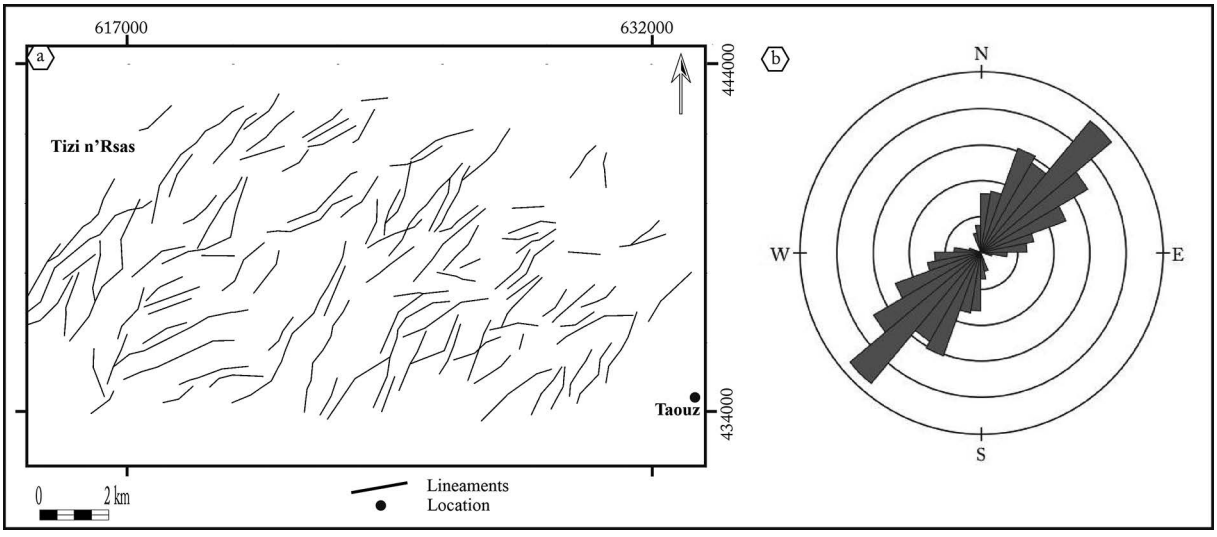

Figure 9- Results after Landsat 8 OLI image processing, a) synthetic map of lineaments and b) rose diagram of lineaments trend.

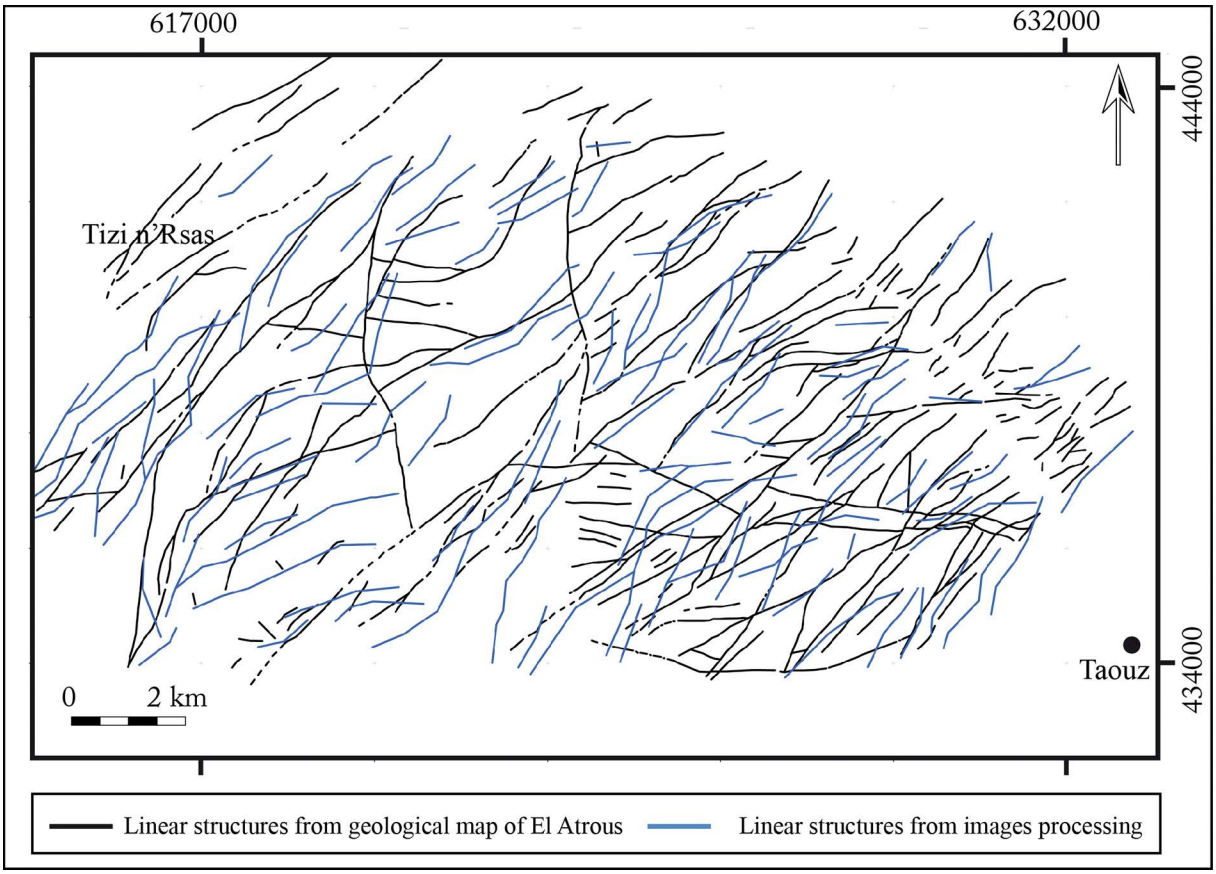

Figure 10- Superposition of the results and the geological map of El Atrous (Benharref et al., 2014).

result of the contrast of their rheologies: competent and incompetent layers. Also, there are small-wavelength folds called parasitic folds. Observed on field, this type of folding is manifested in limestone and marl formations of Devonian (Famennian, Eifelian and Emsian age formations). They are repeated more on the northern limb of the anticline of TTR. Many folds have an axis varying between N95° and N130° with a fold axis plunge of 30° to the west and northwest, respectively (Figures 11a-11e). These folds are well observed in competent layers, while incompetent ones does not show any folding structures. Other folds are generated at the Ordovician age formations; they have N20° and N130° axes exhibited in sandstone shales (Figure 11f). Silurian formations in the study area do not show any indication of folding, although these formations are located between two folded sets, Devonian and Ordovician.

The TTR anticline shows some internal structures, we can distinguish three types of fold axes; N130°, N95° and N20°. The N130° and N95° trend axes generally reflect the TTR major fold axis (WNW-ESE), which is considered as one of Variscan structures. The presence of minor disharmonic folds (N130° and N95°) within Devonian formations is probably related to (i) the folding of thick and competent Ordovician formations, which produces large folds, and (ii) the presence of incompetent formations (clays and limestone) at the bottom of the Devonian series, within the Silurian and at the bottom of Upper Devonian formations. The Devonian formations decollement involved its detachment from the Ordovician basement, this latter is characterized by the presence of rigid terrains (sandstone). The N20° directional folds within the Ordovician formations may be related to the faults crossing the TTR anticline.

North of the OJTF, TTR anticline is intensely fractured. Cartographic surveys have emphasized the important brittle tectonics whose statistical analysis has distinguished only one major fault family NE-SW. The ENE-WSW and NNE-SSW faults families are less abundant compared to the NE-SW family (Figures 8, 12a and 13). These families of faults is also reported on the rose diagram obtained by processing

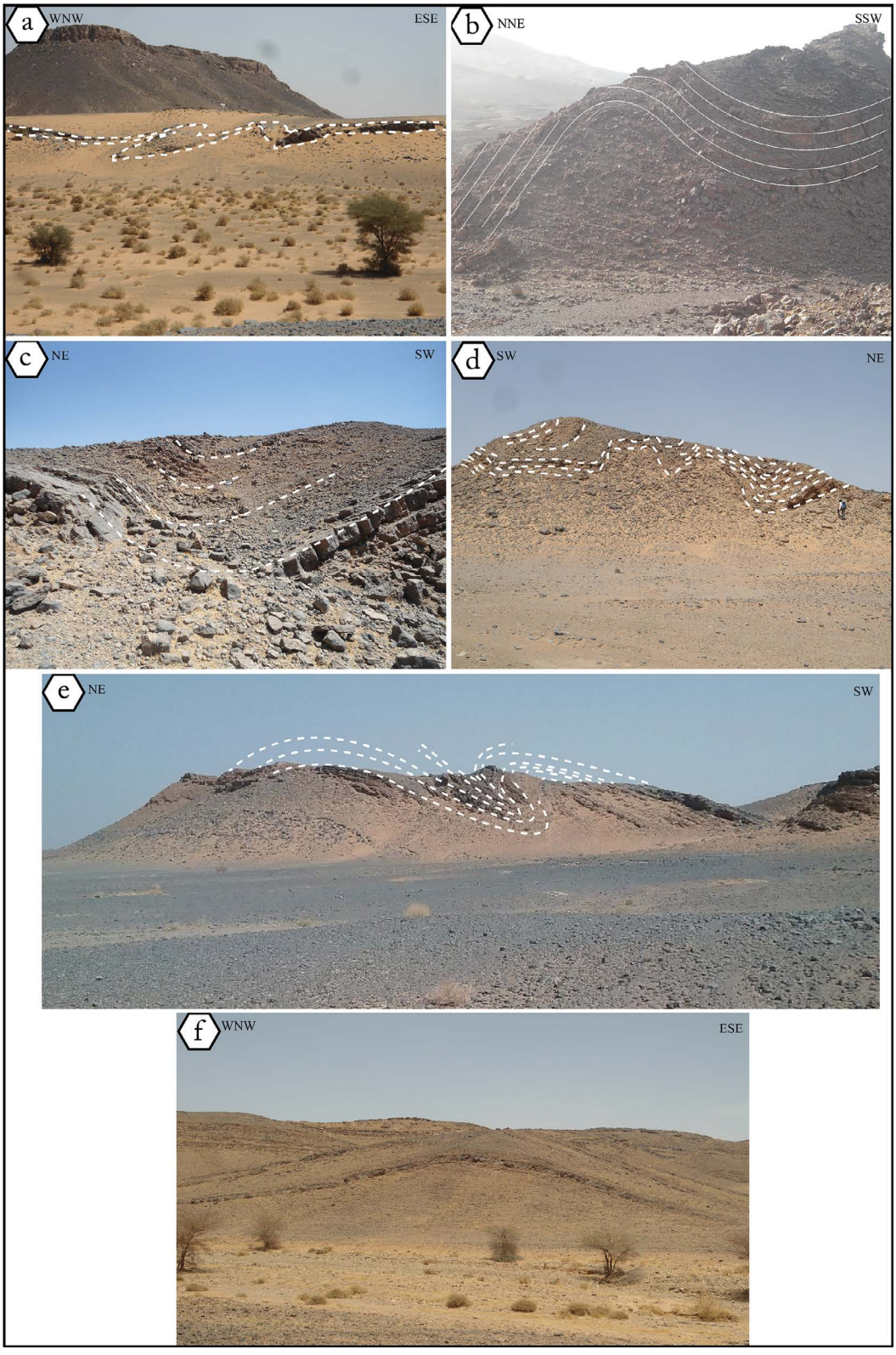

Figure 11- Photos of disharmonic folds located on the northern limb of the TTR anticline. a) N100°-trend folds within nodular limestone formations of Eifelian age, b) E-W folds at the Upper Devonian (Famenian) limestones and marls, c) NW-trend folds at the Emsian limestone formations, d) NW-trend folds in limestones and marls of Upper Devonian (Famenian), e) fold with N130° axis and f) folding of Ordovician formations with N20° axis.

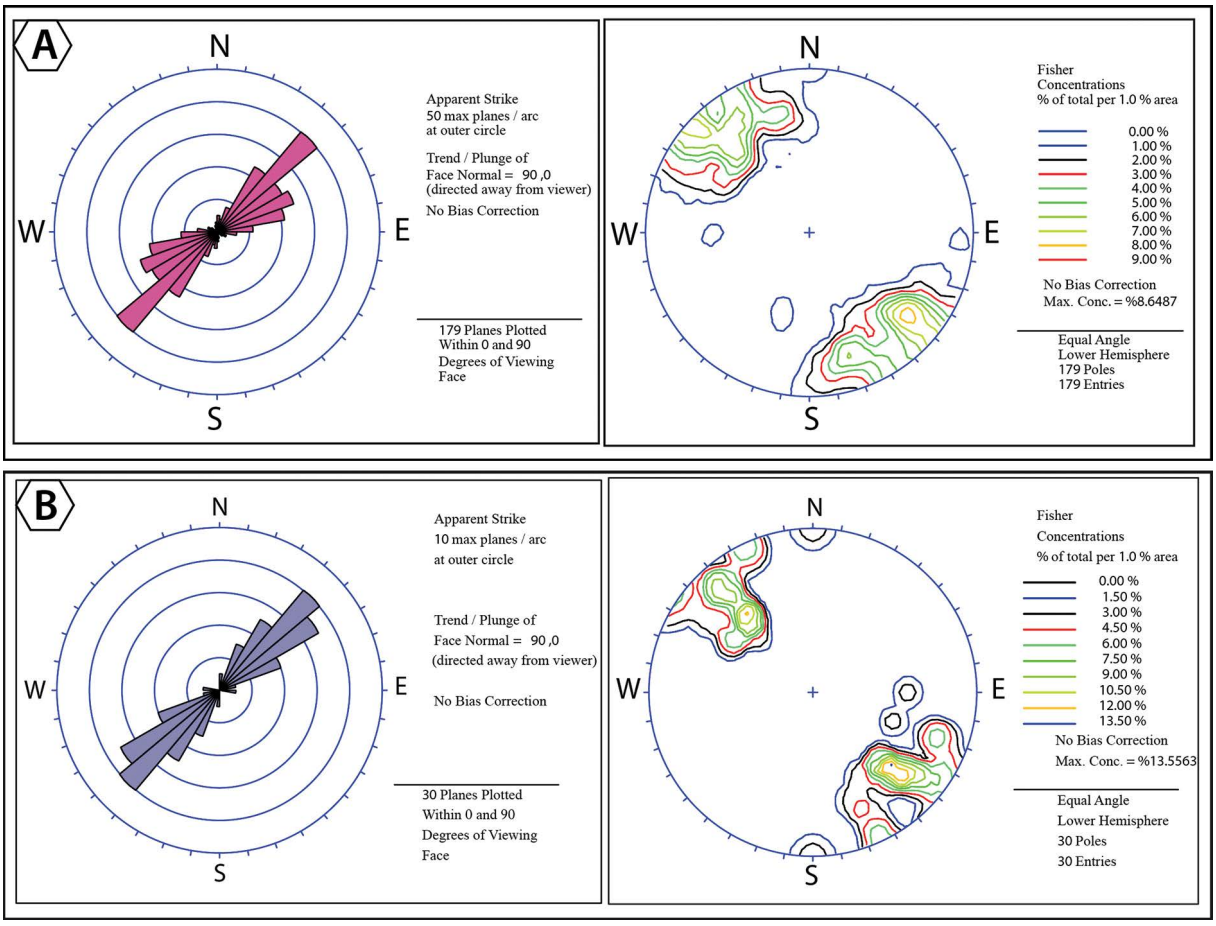

Figure 12- Statistical orientation of fracturing data of TTR anticline (equal angle, lower hemisphere), a) faults and b) veins.

of the Landsat 8 OLI image. However, the ENE-WSW family is less represented in the rose of Landsat image processing diagram. The NE-SW family (N40° to N55° trend), shows a 70° with both opposite dips to the NW and the SE. It is the most predominant family in the TTR anticline. Normal faults are predominant in this direction, but inverse and transcurrent faults exist too. Geometrically, the throw of this family of faults is low and can not reach ten metres in general (Figure 14).

Structural analysis of this fault family allows to emphasize a polyphase structuring. Here, we distinguish: (i) a reverse and strik-slip faults probably forward and can be linked to a compression perpendicular to the fault direction. It is well observed in striaes and slickensides at the mirror surface of faults. From a frequency point of view, the left-lateral faults are more dominant than the right-lateral ones in this region. These movements are probably attributed to the NW-SE major compression of Namuro-Westphalian age related to the Variscan orogeny. (ii) More dominant late normal faults are distributed along the anticline. The presence of vertical to sub-vertical striaes, slickensides in the mirror surface and also the net displacement of the layers indicate that the vertical movement is dominant in this family. Moreover, in order of frequency, the normal faults are more abundant than the inverse or transcurrent ones.

The vein field of TTR consists of more than twenty mineralized veins. From east to west, the main vein structures are: Tadaout, Bou Itberne, Bou Amane, Filon 12, Bou Faddouz, Filon 15, Bou Zeggar, El Atrous, Timgharine, Bou lmyour and Tizi n'Rsas (Figure 15). The NE-SW direction is the main carrier of barite, copper, lead and zinc mineralization in our study area, in the form of fissure veins, arranged into echelon and forming a vein field which is part of the mining domain of Tafilalet. It is important to note that these veins have been the subject of old artisanal exploitation for lead and barite mineralizations

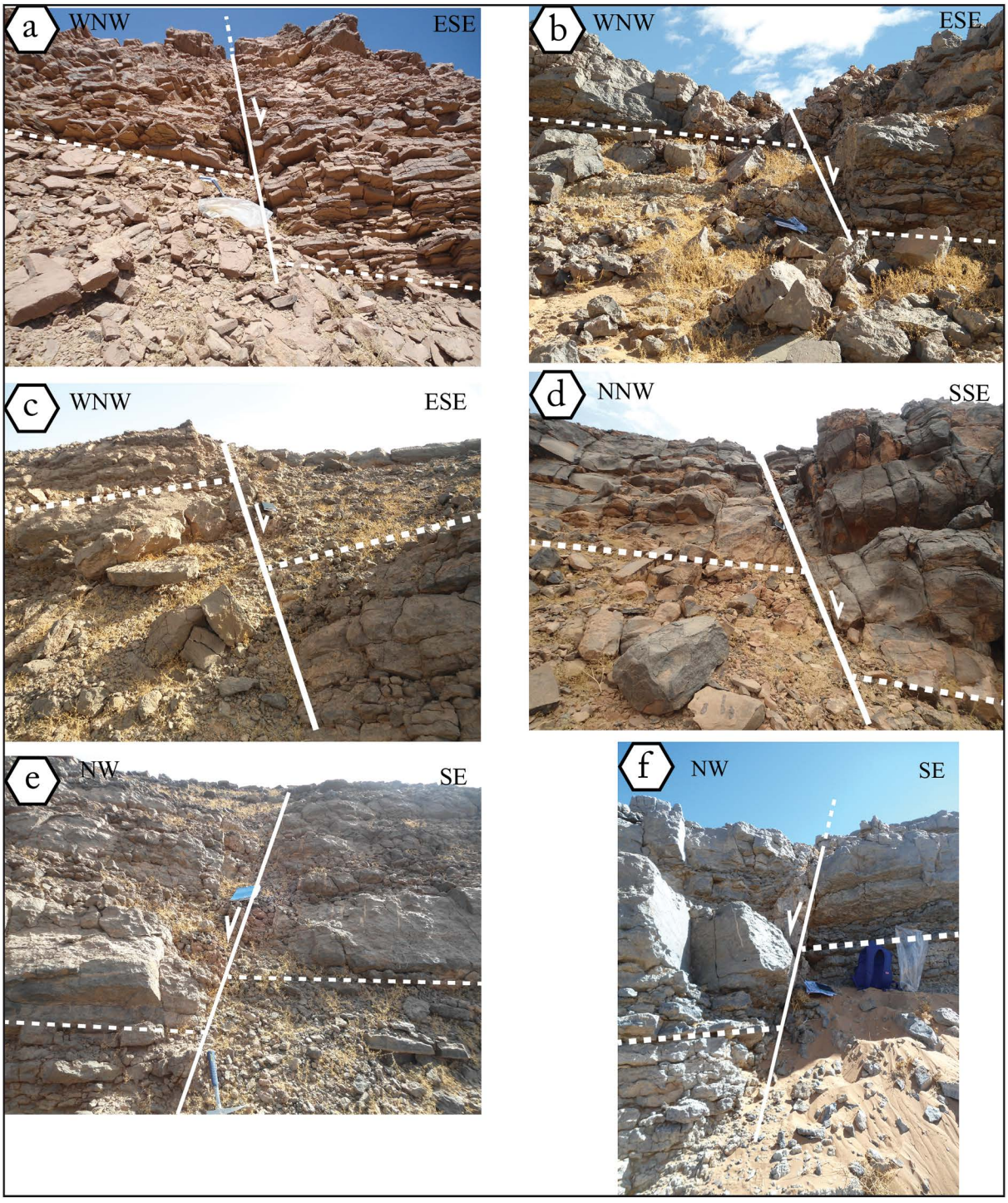

Figure 13- Faults of TTR anticline. a), b) and c) NNE direction fault families, d) ENE fault families and e) and f) NE-SW fault families.

(Figures 12b and 16). The normal movement of NE-SW direction faults is probably associated with the reactivation of this fault family during the NE-SW Late-Variscan (Stephanian-Permian) compression of the Variscan orogeny (Figure 17).

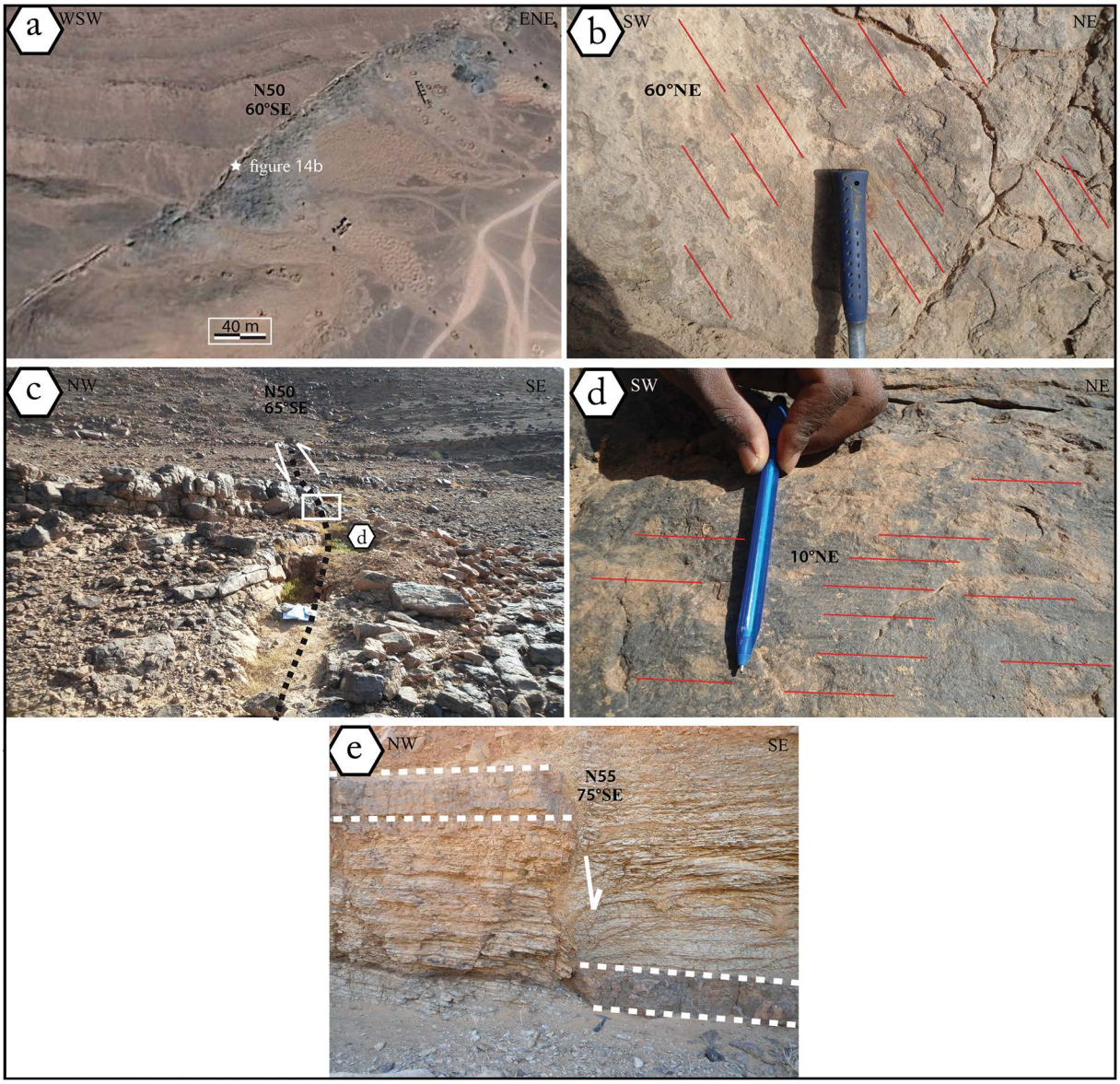

Figure 14- NE-SW directional faults: a) N50°, 60°SE mineralized vein (Tizi-n'Rsas vein), b) striaes (60°NE) on the mirror surface, c) N50°, 60°SE fault with left-lateral movement, d) striaes (10°NE) at the mirror surface, e) N55°,75°SE fault showing a vertical movement.

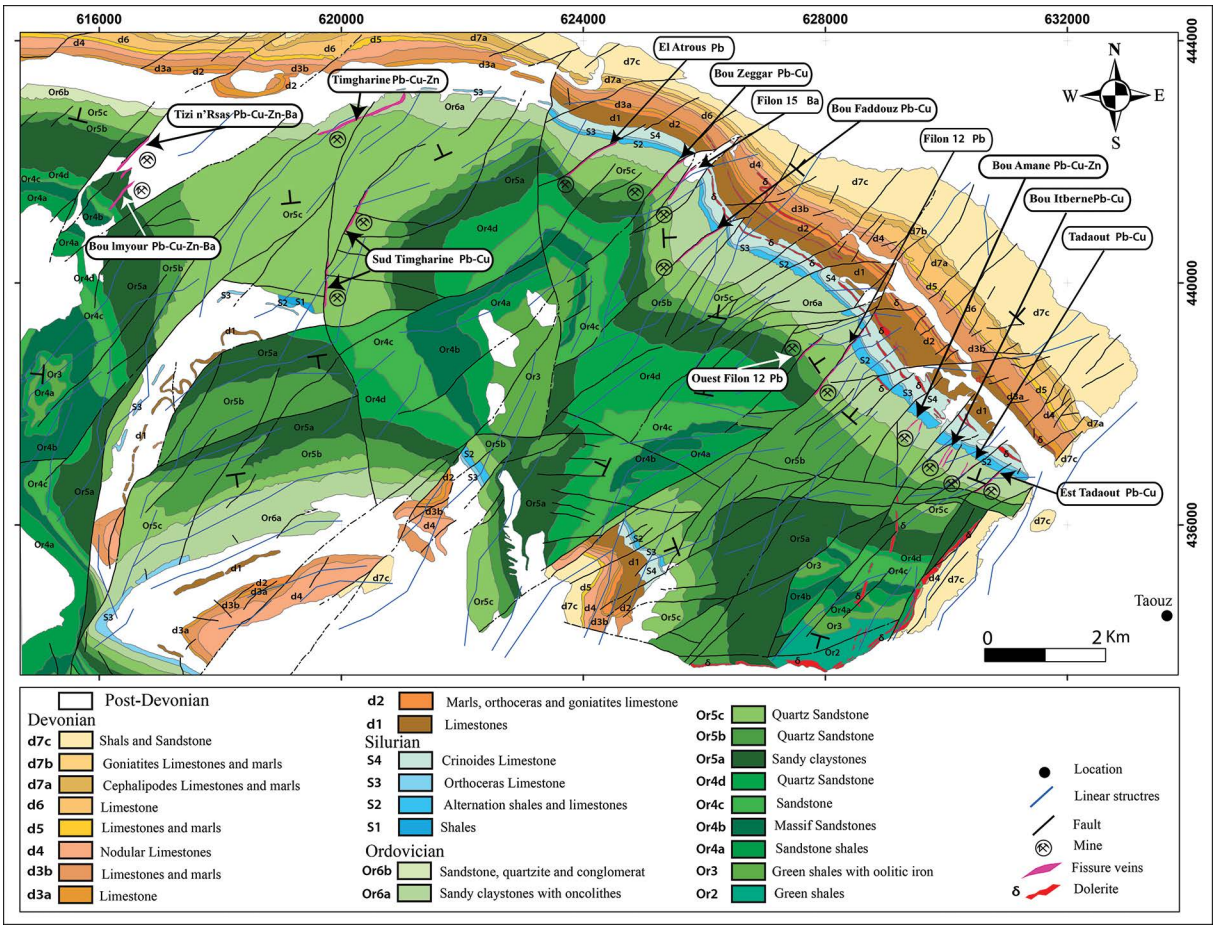

Figure 15- Geological map of study area showing the relationship between NE-trending structures and base metal mineralization (Geological map 1/50.000 of El Atrous in Benharref et al., 2014, modified).

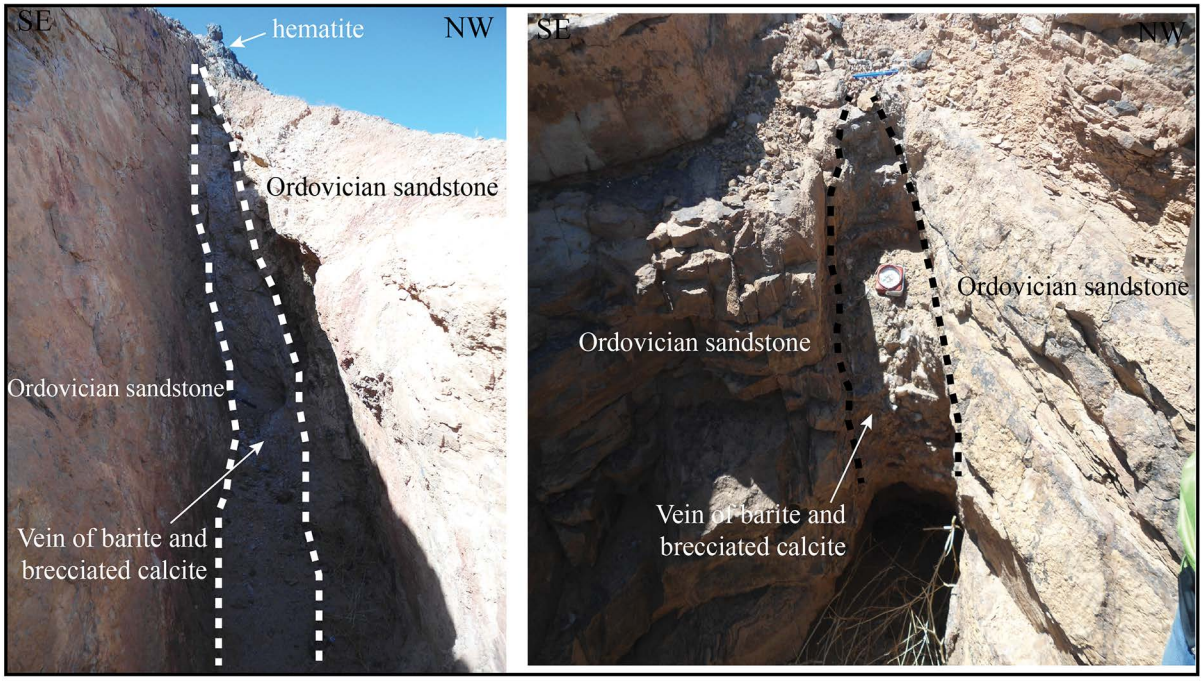

Figure 16- NE-SW barite veins in the TTR anticline.

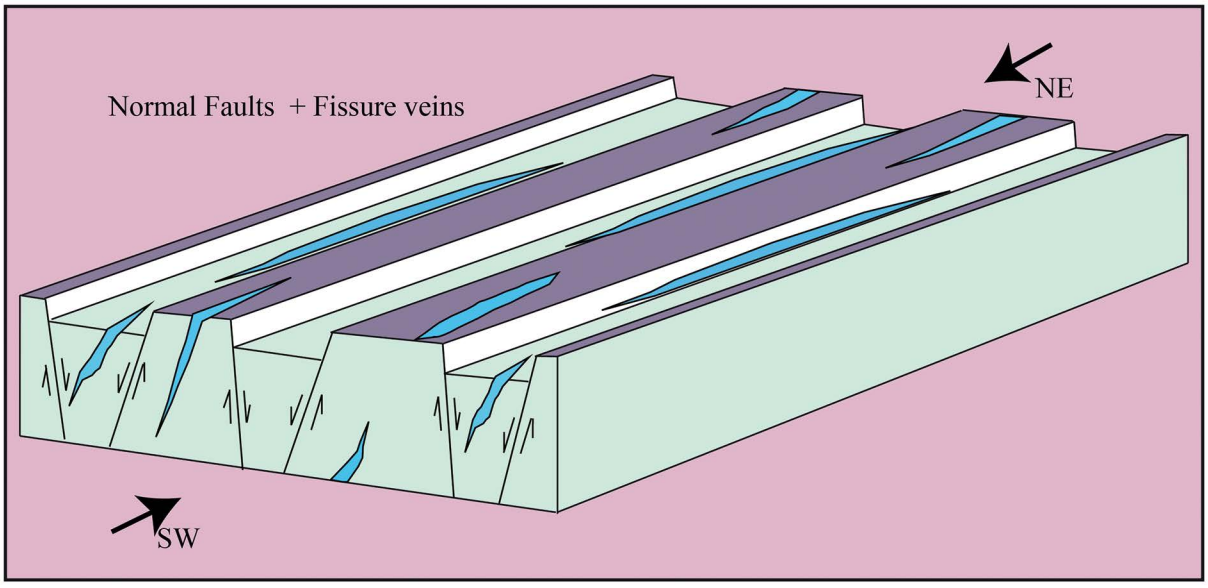

Figure 17- Bloc-diagram showing the fault movements during the Variscan orogeny (NE-SW shortening).

5. Discussion

TTR anticline is one of the major folded structures located in the Ougnate-Ouzina Ridge. It corresponds to the junction zone between Anti-Atlas and Ougarta mountains, and shows a WNW-ESE directional axis at Ordovician core. These open types of folds are well presented at the scale of the Eastern Anti-Atlas, and are consistent with a NE-trending direction of shortening (Michard et al., 2008). These pluri-kilometric regional folds are characterized by a strong thinning of limbs and an important hinge thickening and also by the presence of an intense disharmonic folding with decametric folds (Benharref et al., 2014). Baidder et al. (2016) assumes that major structures of Tafilalet and Maider, in particular the most complicated fold structures (Tijekht and Tadaout anticlines), can be explained by a combination of paleofault control of folding orientation, and superimposed compression events with different compression directions. South of the Ougnat Massif (Bouadil area), the Paleozoic cover series show a mosaic of tilted basement blocks associated with the dominance of NE- and SE-trending folds (Raddi et al., 2007).

Internal structures; minor disharmonic folds (N130° and N95°), are observed in the long north limb of TTR anticline. Likewise in the south of Eastern Anti-Atlas inliers, small scale NW-SE structures are observed. This orientation is similar to that observed in the major structures (Baidder et al., 2016; Robert-Charrue and Burkhard, 2008). The N20° axes trend is another trend of fold axes observed in the TTR anticline. These folds are late and related to the faults crossing the anticline (Baidder et al., 2016).

Like other folded structures of Tafilalet, TTR anticline shows a very intense fracturing with the dominance of NE-SW direction filled by barite, copper, lead and zinc. The Tijekht anticline located in the western part of TTR shows a N35° to N70° faults system mainly mineralized in barite. In addition, the anticline of Bou Mayz, situated in the northern part of the Ougnat-Ouzina Ridge, shows a NE-SW direction of barite mineralized faults. Likewise, the Shayb Arras anticline, located at the north of the study area, is also pierced by NE to ENE faults frequently mineralized in barite. In addition, the Znaigui and M'fis anticlines show both an ENE-trend structure (Baidder et al., 2016; Makkoudi, 1995).

The NE-SW faults are the most important and the most frequent faults in the TTR anticline, these structures are probably inherited from the Precambrian basement (Rjimati et al., 1992; Soulaimani et al., 2014; Walsh et al., 2012). During the evolution of the Lower Cambrian basin, the role of the NE-SW direction faults in extensional tectonics has been emphasized, this direction generates a NW-SE extension (Algouti et al., 2001; Baidder, 2007; Benssaou and Hamoumi, 2003;

Chbani et al., 1999; Gasquet et al., 2005; Soulaimani et al., 2003; Soulaimani and Piqué, 2004). In the Middle-Late Devonian, the Eastern Anti-Atlas was characterized by a dislocation and an extension of the Saharan platform (Baidder, 2007; Baidder et al., 2008; Wendt and Belka, 1991). According to Soulaimani et al. (2014), Devonian paleofaults are inherited from the Precambrian. The most important faults recognized in the Tafilalet-Maider area are qualitatively ordered into first order ENE-trending faults, second order NW- and NNE-trending faults and third order ENE to ESE-trending faults (Baidder et al., 2008). After Devonian, the sedimentation of the Lower Carboniferous is controlled by some old faults of the Upper Devonian (Baidder, 2007; Soulaimani et al., 2014). The Visean tectonics is controlled by three families of accidents; E-W, NE-SW and NW-SE (Soualhine et al., 2003).

In the study area, the polyphase movements of the faults are expressed by the reactivation of old faults during the Variscan orogeny, and has already been shown in the section of ductile tectonics, this zone is affected by a deformation during the Variscan collision which resulted in the reactivation of old structures. The main shortening stage responsible for the folding recognized in Eastern Anti-Atlas and Ougarta is the NE-SW Late Variscan (Stephanian-Permian) compression of the Variscan orogeny (Michard et al., 2008). This shortening corresponding to NE-SW Ouagarta compression (Donzeau, 1974; Fabre, 2005; Haddoum et al., 2001). It interferes with the NNW-SSE compression between the Meseta Block and its foreland at the regional scale, particularly well observed in the north of Saghro inlier (Malusà et al., 2007; Michard et al., 1982; Raddi et al., 2007; Robert-Charrue, 2006). The collision responsible for the Variscan deformation can be estimated to Late Carboniferous, and it results from the collision of Gondwana and Eurasia plates (Stampfli and Borel, 2002).

The majority of NE-SW faults in our study area have a normal movement, likewise Robert-Charrue, (2006); Robert-Charrue and Burkhard, (2008) announced that the Paleozoic series of the Eastern Anti-Atlas at Tafilalet and Maider are intersected by a set of normal faults that have probably result of the Central Atlantic opening related to the breakup of Pangea supercontinent. In the south-east of TTR anticline, the Cretaceous plateau is crosscut by several ENE-striking faults, parallel to the basement OJTF (Soulaimani et al., 2014), which indicates the reactivation of the paleofaults in this region at the north-south shortening alpine stage.

6. Conclusion

Our study area, TTR anticline, is one of the major folds at the Tafilalet region, it is a WNW-ESE axis fold whose represents the hinge between Anti-Atlas and Ougarta belts. At the northern limb of this anticline, three types of minor fold axes are present, (i) N20° fold can be related to the reactivation of fault crossing the anticline, (ii) N130° and N95° disharmonic folds generally reflect the TTR major fold. These folds are probably related to the folding of a serie incorporated the competent (Ordovician, Silurian and Devonian limestone) and incompetent (Silurian shales and Devonian marls) formartions. The results of ductile tectonic show that TTR anticline constitues the hinge of the arc (Zemmour, Anti-Atlas, Ougarta) that goes rounded the West African Craton. The TTR major fold shows a very intense fracturing with dominance of NE-SW normal faults. This dominance is confirmed by the lineaments extracted automatically from the Landsat 8 OLI image processing. Late Variscan NE-SW shortening is the main folding and reactivation mechanism of paleofault in this area. The NE-SW fault family is the main carrier of barite, copper, lead and zinc mineralization. We consider present results as a valuable target for advanced metallogenic researches and mineral exploration in the TTR and more generally at the Eastern Anti-Atlas.

Acknowledgements

We would like to thank Dr. A. Babni and Dr. H. Si Mhamdi for their contribution to enhancing the quality of the English language of the article. The author also wishes to thank the two reviewers for their constructive feedback, and insightful comments and recommendations.

References

Algouti, A., Algouti, A., Chbani, B., Zaim, M. 2001. Sedimentation et volcanisme synsedimentaire de la serie de base de l'adoudounien infra-cambrien a travers deux exemples de l'Anti-Atlas du Maroc. Journal of African Earth Sciences 32, 541–556.

Baidder, L. 2007. Structuration de la bordure septentrionale du Craton Ouest-Africain du Cambrien à l'Actuel : cas de l'Anti-Atlas oriental du Maroc. (Thèse d'Etat). Université Hassan II Aïn Chock, Faculté des sciences, Casablanca, Maroc.

Baidder, L., Raddi, Y., Tahiri, M., Michard, A. 2008. Devonian extension of the Pan-African crust north of the West African craton, and its bearing on the Variscan foreland deformation: evidence from eastern Anti-Atlas (Morocco). Geological Society, London, Special Publications 297, 453–465. https://doi.org/10.1144/SP297.21

Baidder, L., Michard, A., Soulaimani, A., Fekkak, A., Eddebbi, A., Rjimati, E.-C., Raddi, Y. 2016. Fold interference pattern in thick-skinned tectonics; a case study from the external Variscan belt of Eastern Anti-Atlas, Morocco. Journal of African Earth Sciences 119, 204–225. https://doi.org/10.1016/j.jafrearsci.2016.04.003

Belka, Z. 1998. Early Devonian Kess-Kess Carbonate Mud Mounds of the Eastern Anti-Atlas (Morocco), and Their Relation to Submarine Hydrothermal Venting. Journal of Sedimentary Research 68.

Benharref, M., Álvaro, J.J., Hibti, M., Pouclet, A., El Hadi, H., Koukaya, A., Ettachfini, E.M. 2014. Carte géologique du Maroc au 1/50 000, feuille Al Atrous-Mémoire explicatif. Notes Mém. Serv. Géol. Maroc 555.

Benssaou, M., Hamoumi, N. 2003. Le graben de l'Anti-Atlas occidental (Maroc) : contrôle tectonique de la paléogéographie et des séquences au Cambrien inférieur. Comptes Rendus Geoscience 335, 297–305. https://doi.org/10.1016/S1631-0713(03)00033-6

Boudda, A., Choubert, G., Faure-Muret, A. 1979. Essai de stratigraphie de la couverture sédimentaire de l'Anti-Atlas: Adoudounien-Cambrien inférieur. Editions du Service géologique du Maroc.

Brachert, T.C., Buggisch, W., Flügel, E., Hüssner, H.M., Joachimski, M.M., Tourneur, F., Walliser, O.H. 1992. Controls of mud mound formation: the Early Devonian Kess-Kess carbonates of the Hamar laghdad, Antiatlas, Morocco. Geologische Rundschau 81, 15–44.

Buggisch, W., Siegert, R. 1988. Paleogeography and facies of the 'gres terminaux'(uppermost Lower Cambrian, Anti-Atlas/Morocco), in: The Atlas System of Morocco. Springer, pp. 107–121.

Chabou, M.C., Bertrand, H., Sebaï, A. 2010. Geochemistry of the Central Atlantic Magmatic Province (CAMP) in south-western Algeria. Journal of African Earth Sciences 58, 211–219. https://doi.org/10.1016/j.jafrearsci.2010.02.009

Chbani, B., Beauchamp, J., Algouti, A., Zouhair, A. 1999. Un enregistrement sédimentaire éocambrien dans un bassin intracontinental en distension: le cycle «conglomérats de base—unité calcaire—grès de Tikirtde Bou-Azzer El Graara (Anti-Atlas central, Maroc). Comptes Rendus de l'Académie des Sciences-Series IIA-Earth and Planetary Science 329, 317–323.

Choubert, G. 1943. Quelques réflexions sur la terminaison orientale de l'Anti Atlas. Bulletin de la Société d'Histoire Naturelle 61–79.

Choubert, G. 1947. L'accident majeur de l'Anti-Atlas. Comptes Rendus de l'Académie des Sciences, Paris 224, 1172–1173.

Choubert, G. 1964. Histoire géologique du Précambrien de l'Anti-Atlas. Éditions du Service géologique du Maroc.

Clariound, L.1944. Carte géologique provisoire des plateaux et chaines du Saghro et Maider.

Derder, M.E.M., Smith, B., Henry, B., Yelles, A.K., Bayou, B., Djellit, H., Ait ouali, R., Gandriche, H. 2001. Juxtaposed and superimposed paleomagnetic primary and secondary components from the folded middle carboniferous sediments in the Reggane Basin (Saharan craton, Algeria). Tectonophysics 332, 403–422. https://doi.org/10.1016/S0040-1951(00)00298-5

Destombes, J. 1963. Le Cambrien et la base de l'Ordovicien dans la partie orientale et meridionale du Tafilalt (Maroc). Bulletin de la Société Géologique de France S7-V, 938–945. https://doi.org/10.2113/gssgfbull.S7-V.6.938

Destombes, J. 1968. Sur la presence d'une discordance generale de ravinement d'age Ashgill superieur dans l'Ordovicien terminal de l'Anti-Atlas (Maroc). Comptes Rendus de l'Academie de Sciences, Paris 267, 565–567.

Destombes, J. 1971. L'Ordovicien au Maroc. Essai de synthèse stratigraphique. Mémoires de la BRGM, Paris 73, 237–263.

Destombes, J. 1976. The Ordovician of the Moroccan Anti-Atlas. The Ordovician System 411–413.

Destombes, J. 2006. Carte géologique au 1/200 000 de l'Anti-Atlas marocain. Paléozoïque inférieur: Cambrien moyen-Ordovicien-base du Silurien.

Feuille régions de Tan-Tan–Jbel Zini (Province de Tarfaya). Mémoire explicatif, Chapitre J (Anti-Atlas sud-occidental au sud de l'oued Dra)[written in 2003]. Notes Mém. Serv. Géol. Maroc 90.

Destombes, J., Hollard, H. 1986. Carte géologique du Maroc au 1/200 000, feuille Tafilalt-Taouz. Notes et Mémoires du Service Géologique du Maroc 244.

Donzeau, M. 1974. L'Arc Anti-Atlas–Ougarta (Sahara nord-occidental, Algérie-Maroc). CR Acad. Sci. Paris 278, 417–420.

Ennih, N., Liégeois, J.-P. 2001. The Moroccan Anti-Atlas: the West African craton passive margin with limited Pan-African activity. Implications for the northern limit of the craton. Precambrian Research 112, 289–302.

Fabre, J. 2005. Géologie du Sahara occidental et central. Série/Reeks: Tervuren African Geosciences Collection. MRAC Tervuren, Belgique.

Gasquet, D., Levresse, G., Cheilletz, A., Azizi-Samir, M.R., Mouttaqi, A. 2005. Contribution to a geodynamic reconstruction of the Anti-Atlas (Morocco) during Pan-African times with the emphasis on inversion tectonics and metallogenic activity at the Precambrian–Cambrian transition. Precambrian Research 140, 157–182. https://doi.org/10.1016/j.precamres.2005.06.009

Gasquet, D., Ennih, N., Liégeois, J.-P., Soulaimani, A., Michard, A. 2008. The Pan-African Belt, in: Continental Evolution: The Geology of Morocco. Springer, pp. 33–64.

Geyer, G., Landing, E. 1995. The Cambrian of the Moroccan Atlas regions. Morocco 95, 7–46.

Haddoum, H., Guiraud, R., Moussine-Pouchkine, A. 2001. Hercynian compressional deformations of the Ahnet–Mouydir Basin, Algerian Saharan Platform: far-field stress effects of the Late Palaeozoic orogeny. Terra Nova 13, 220–226.

Hailwood, E.A., Mitchell, J.G. 1971. Palaeomagnetic and radiometric dating results from Jurassic intrusions in South Morocco. Geophysical Journal International 24, 351–364.

Hilali, A., Lachkem, H., Boulvain, F. 1999. Comparaison des Kess-Kess de Hmar Lakhdad (Emsien, Maroc) et des monticules micritiques de l'anticlinorium de Philippeville (Frasnien, Belgique). Geologica Belgica 1.

Hilali, A, Lachkhem, H, Tourneur, F. 2001. Répartition des tabulés dans les Kess-Kess emsiens de Hmar Lakhdad (SE d'Erfoud, Tafilalt, Maroc). Geologica et Palaeontologica 35,8,53-61.

Hollard, H. 1967. Le Dévonien du Maroc et du Sahara nord-occidental.

Hollard, H. 1973. La mise en place au Lias des dolérites dans le Paléozoïque moyen des plaines du Drâa et du bassin de Tindouf (Sud de l'Anti-Atlas central, Maroc). CR Acad. Sci. Paris 277, 553–556.

Hollard, H. 1974. Recherches sur la stratigraphie des formations du Dévonien moyen, de l'Emsien supérieur au Frasnien, dans le Sud du Tafilalt et dans le Ma'der (Anti-Atlas oriental). Notes et Mémoires du Service Géologique du Maroc 264, 7–68.

Hollard, H. 1981. Principaux caractères des formations dévoniennes de l'Anti-Atlas. Notes et Mémoires du Service géologique du Maroc 42, 15–22.

Makkoudi, D. 1995. Les minéralisations Pb-Ba de M'Ifiss, Etude Géologique et Contribution à la gitologie des Gisement du Tafilalet. (Thèse de 3ème cycle). Université Mohamed V, Faculté des Sciences, Rabt, Maroc.

Malusà, M.G., Polino, R., Feroni, A.C., Ellero, A., Ottria, G., Baidder, L., Musumeci, G. 2007. Post-Variscan tectonics in eastern Anti-Atlas (Morocco). Terra Nova 19, 481–489. https://doi.org/10.1111/j.1365-3121.2007.00775.x

Michard, A., Yazidi, A., Benziane, F., Hollard, H., Willefert, S. 1982. Foreland thrusts and olistromes on the pre-Sahara margin of the Variscan orogen, Morocco. Geology 10, 253–256.

Michard, A., Hoepffner, C., Soulaimani, A., Baidder, L. 2008. The Variscan Belt, in: Continental Evolution: The Geology of Morocco, Lecture Notes in Earth Sciences. Springer, Berlin, Heidelberg, pp. 65–132. https://doi.org/10.1007/978-3-540-77076-3_3

Mounji, D., Bourque, P.-A., Savard, M.M. 1998. Hydrothermal origin of Devonian conical mounds (kess-kess) of Hamar Lakhdad Ridge, Anti-Atlas, Morocco. Geology 26, 1123–1126.

Pique, A. 1994. Les domaines régionaux et leur évolution structurale. PUMAG (ed.): Géologie du Maroc.

Pique, A., Michard, A. 1989. Moroccan Hercynides; a synopsis; the Paleozoic sedimentary and tectonic evolution at the northern margin of West Africa. Am J Sci 289, 286–330. https://doi.org/10.2475/ajs.289.3.286

Pouclet, A., El Hadi, H., Bardintzeff, J.-M., Benharref, M., Fekkak, A. 2017. Devonian to Early Carboniferous magmatic alkaline activity in the Tafilalt Province, Eastearn Morocco: An Eovariscan episode in the Gondwana margin, north of the West African Craton. Journal of African Earth Sciences 129, 814–841. https://doi.org/10.1016/j.jafrearsci.2017.01.030

Raddi, Y., Baidder, L., Tahiri, M., Michard, A. 2007. Variscan deformation at the northern border of the West African Craton, eastern Anti-Atlas, Morocco: compression of a mosaic of tilted blocks. Bulletin de la Société géologique de France 178, 343–352.

Rjimati, E., Derre, C., Lecolle, M., Lillie, F., Nerci, K., Azza, A., Bennani, A. 1992. Caractéristique de la tectonique panafricaine dans le Jbel Saghro (Anti Atlas, Maroc). Notes et Mkmoires du Service Geologique du Maroc 366.

Robert-Charrue, C. 2006. Géologie structurale de l'Anti-Atlas oriental, Maroc (PhD Thesis). Université de Neuchâtel.

Robert-Charrue, C., Burkhard, M. 2008. Inversion tectonics, interference pattern and extensional fault-related folding in the Eastern Anti-Atlas, Morocco. Swiss Journal of Geosciences 101, 397–408. https://doi.org/10.1007/s00015-008-1266-0

Sebai, A., Feraud, G., Bertrand, H., Hanes, J. 1991. 40Ar/39Ar dating and geochemistry of tholeiitic magmatism related to the early opening of the Central Atlantic rift. Earth and Planetary Science Letters 104, 455–472.

Service Géologique du Maroc, 1985. Carte géologique du Maroc au 1/1 000,000.

Soulaimani, A., Piqué, A. 2004. The Tasrirt structure (Kerdous inlier, Western Anti-Atlas, Morocco): a late Pan-African transtensive dome. Journal of African Earth Sciences 39, 247–255. https://doi.org/10.1016/j.jafrearsci.2004.07.043.

Soualhine, S., de Leon, J.T., Hoepffner, C. 2003. Les faciès sédimentaires carbonifères de Tisdafine (Anti-Atlas oriental): remplissage deltaïque d'un bassin en «pull-apart» sur la bordure méridionale de l'Accident sud-atlasique. Bull. Inst. Sci. Rabat 25, 31–41.

Soulaimani, A., Bouabdelli, M., Piqué, A. 2003. L'extension continentale au Néo-Protérozoïque supérieur-Cambrien inférieur dans l'Anti-Atlas (Maroc).

Soulaimani, A., Michard, A., Ouanaimi, H., Baidder, L., Raddi, Y., Saddiqi, O., Rjimati, E.C. 2014. Late Ediacaran–Cambrian structures and their reactivation during the Variscan and Alpine cycles in the Anti-Atlas (Morocco). Journal of African Earth Sciences 98, 94–112. https://doi.org/10.1016/j.jafrearsci.2014.04.025.

Stampfli, G.M., Borel, G.D. 2002. A plate tectonic model for the Paleozoic and Mesozoic constrained by dynamic plate boundaries and restored synthetic oceanic isochrons. Earth and Planetary Science Letters 196, 17–33.

Termier, H., Termier, G. 1948. Un biotope à bryozoaires dans l'ordovicien du tafilalet (Maroc). C.R. Somm. Soc. Biogéogr. Paris 25, 26.

Thomas, R.J., Fekkak, A., Ennih, N., Errami, E., Loughlin, S.C., Gresse, P.G., Chevallier, L.P., Liégeois, J.P. 2004. A new lithostratigraphic framework for the Anti-Atlas Orogen, Morocco. Journal of African Earth Sciences 39, 217–226. https://doi.org/10.1016/j.jafrearsci.2004.07.046

Verati, C., Rapaille, C., Féraud, G., Marzoli, A., Bertrand, H., Youbi, N. 2007. 40Ar/39Ar ages and duration of the Central Atlantic Magmatic Province volcanism in Morocco and Portugal and its relation to the Triassic–Jurassic boundary. Palaeogeography, Palaeoclimatology, Palaeoecology 244, 308–325. https://doi.org/10.1016/j.palaeo.2006.06.033

Walsh, G.J., Benziane, F., Aleinikoff, J.N., Harrison, R.W., Yazidi, A., Burton, W.C., Quick, J.E., Saadane, A. 2012. Neoproterozoic tectonic evolution of the Jebel Saghro and Bou Azzer—El Graara inliers, eastern and central Anti-Atlas, Morocco. Precambrian Research 216–219, 23–62. https://doi.org/10.1016/j.precamres.2012.06.010

Wendt, J. 1985. Disintegration of the continental margin of northwestern Gondwana: Late Devonian of the eastern Anti-Atlas (Morocco). Geology 13, 815–818.

Wendt, J., Belka, Z. 1991. Age and depositional environment of Upper Devonian (early Frasnian to early Famennian) black shales and limestones (Kellwasser facies) in the eastern Anti-Atlas, Morocco. Facies 25, 51–89.

Youbi, N., Martins, L.T., Munhá, J.M., Ibouh, H., Madeira, J., Aït Chayeb, E.H., El Boukhari, A. 2003. The Late Triassic-Early Jurassic volcanism of Morocco and Portugal in the framework of the Central Atlantic Magmatic Province: An overview, in: Hames, W., McHone, J.G., Renne, P., Ruppel, C. (Eds.), Geophysical Monograph Series. American Geophysical Union, Washington, D. C., pp. 179–207. https://doi.org/10.1029/136GM010.

Bulletin of the Mineral Research and Exploration

http://bulletin.mta.gov.tr

2D inverse modeling of the gravity field due to a chromite deposit using the Marquardt's algorithm and forced neural network

Ata ESHAGHZADEH*[a], Sanaz SEYEDI SAHEBARI[b] and Alireza DEHGHANPOUR[c]

[a]*Danesh Tadbir Zima Institute, Chaloos, Iran*
[b]*Roshdiyeh Higher Education Institute, Tabriz, Iran.*
[c]*Islamic Azad University, Science and Research Branch, Tehran, Iran.*

Research Article

Keywords:
Chromite deposit, Finite vertical cylinder, Forced Neural Networks, Gravity, Marquardt's algorithm.

ABSTRACT

In this paper, two modeling method are employed. First, a method based on the Marquardt's algorithm is presented to invert the gravity anomaly due to a finite vertical cylinder source. The inversion outputs are the depth to top and bottom, and radius parameters. Second, Forced Neural Networks (FNN) for interpreting the gravity field as try to fit the computed gravity in accordance with the estimated subsurface density distribution to the observed gravity. To evaluate the ability of the methods, those are employed for analyzing the gravity anomalies from assumed models with different initial parameters as the satisfactory results were achieved. We have also applied these approaches for inverse modeling the gravity anomaly due to a Chromite deposit mass, situated east of Sabzevar, Iran. The interpretation of the real gravity data using both methods yielded almost the same results.

Received Date: 20.09.2018
Accepted Date: 20.01.2019

1. Introduction

Non-uniqueness is a common problem in the inverse modeling of the residual gravity anomaly. IT can assign a set of the measured gravity field data on the ground to the geometrical distributions of the subsurface mass with various shapes or physical parameters such as density and depth. One way to eliminate this ambiguity is to put a suitable geometry to the anomalous body with a known density followed by inversion of gravity anomalies (Chakravarthi and Sundararajan, 2004). Although simple models may not be geologically realistic, they are usually are sufficient to analyze sources of many isolated anomalies (Abdelrahman and El-Araby, 1993*a.b*). The interpretation of such an anomaly aims essentially to estimate the parameters such as shape, depth, and radius of the gravity anomaly causative body such as geological structures, mineral mass and artificial subsurface structures.

Several graphical and numerical methods have been developed for analyzing residual gravity anomalies caused by simple bodies, such as Saxov and Nygaard (1953) and Bowin et al. (1986). The methods include, for example, Fourier transform (Odegard and Berg, 1965; Sharma and Geldart,1968); Mellin transform (Mohan et al., 1986); Walsh transforms techniques (Shaw and Agarwal, 1990); ratio techniques (Hammer, 1974; Abdelrahman et al., 1989); least-squares minimization approaches (Gupta, 1983; Lines and Treitel, 1984; Abdelrahman, 1990; Abdelrahman

Citation Info: Eshaghzadeh, A., Sahebari, A.S., Dehghanpour, A. 2020. 2D inverse modeling of the gravity field due to a chromite deposit using the Marquardt's algorithm and forced neural network. Bulletin of the Mineral Research and Exploration, 161, 33-47. https://doi.org/10.19111/bulletinofmre.589224

* *Corresponding author: Ata ESHAGHZADEH, eshagh@alumni.ut.ac.ir*

et al., 1991) and different neural networks (Eslam et al., 2001; Osman et al., 2006, 2007; Al-Garni, 2013; Eshaghzadeh and Kalantari, 2015; Eshaghzadeh and Hajian, 2018); effective quantitative interpretations using the least-squares method (Gupta, 1983) based on the analytical expression of simple moving average residual gravity anomalies are yet to be developed. The moving average method has mostly used for interpreting the potential fields (Abdelrahman et al., 2003; Abdelrahman et al., 2015; Abdelrahman and Essa, 2015). Abdelrahman and El-Araby (1993*a, b*) introduced an interpretive technique based on fitting simple models convolved with the same moving average filter as applied to the measured gravity. A simple method proposed by Essa (2007) is used to determine the depth and shape factor of simple shapes from residual gravity anomalies along the profile. Another automatic method, the least-squares method, was proposed by Asfahani and Tlas (2008), by which the depth and amplitude coefficient can be determined.

Nowadays Artificial Neural Networks (ANNs) are of main research concern, so that involving researchers of various disciplines and sciences. Topics contributing to this investigation contain biology, computing, electronics, mathematics, medicine, geophysics and etc (Bichsel, 2005). The new method, the artificial neural network, has been employed in recent years for different branch of geophysics especially potential fields. For example, the situation of buried steel drums as magnetic dipole source is evaluated using supervised artificial neural network (Salem et al., 2001). Eslam et al., (2001) specified depth and radius of subsurface cavities from microgravity data using back propagation neural networks. Hajian (2004) estimated depth and shape factor of the gravity anomaly source by applying Feed-Forward Back-Propagation Neural Networks. Chua and Yang (1998) defined a new approach in neural networks titled Cellular Neural Network (CNN), which is focused on 2D image processing. CNN was applied for separation of regional/residual potential sources in geophysics (Albora et al., 2001*a*, *b*). Forced Neural Networks for gravity anomaly analysis was proposed by Osman et al. (2006; 2007). Abedi et al. (2009) calculated the depth and radius of the simple geometry by the neural network from the gravity anomalies. Kaftan et al. (2011) applied Artificial Neural Network for evaluating Seferihisar geothermal area by the gravity data. Al-Garni (2013) used MNN inversion for estimating the depth of the gravity anomaly source related to simple geometry such as sphere, infinite horizontal cylinder and semi-infinite vertical cylinder. Eshaghzadeh and Kalantari (2015) have been proposed a new method based on feed-forward neural network for gravity field inverse modeling due to anticlinal structures. Eshaghzadeh and Hajian (2018) have introduced a new concept of the modularity for analysis the gravity field by modular neural network.

In this paper, a simultaneous non-linear inversion based on Marquardt optimization is developed to estimate the radius and depth to top and bottom parameters of a structure similar to the finite vertical cylinder. The Marquardt inversion method has been used for modeling the geological structures such as faulted beds (Chakravarthi and Sundararajan, 2005), anticlinal and synclinal structures (Chakravarthi and Sundararajan, 2007; 2008), multiple prismatic structures (Chakravarthi and Sundararajan, 2006). We also employ Forced Neural Networks (FNN) introduced by Osman et al. (2006; 2007) as a comparative method. The validity of the methods are tested on synthetic gravity data with and without random noise and also on a real gravity data set from Iran. Furthermore, the Euler deconvolution method is utilized to verify the estimated depths to top by the presented methods.

2. Forward Gravity Modeling

The gravity effects of a finite vertical cylinder is defined by Hammer (1974)

$$g(x) = KF(x) \qquad \text{(equation 1)}$$

Where k is amplitude coefficient as

$$F(x_i)=\frac{1}{\sqrt{x^2+z^2}}-\frac{1}{\sqrt{x^2+h^2}},\ K=\pi G\rho R^2 \qquad \text{(equation 2)}$$

where x is the horizontal location coordinate of measurement points, z and h represent the depths to the top and base planes of causative structure from ground surface respectively, G is the gravitational constant, R is the radius of the horizontal cross section of a vertical cylinder, and ρ is the density contrast (Figure 1).

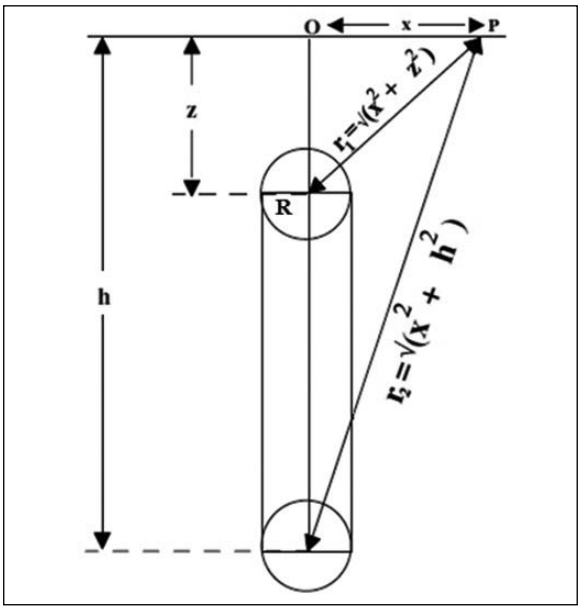

Figure 1- Geometries of the finite vertical cylinder.

3. Marquardt Method

The inversion of gravity anomalies is implicitly a mathematical process, trying to fit the computed gravity anomalies to the observed ones in the least-squares approach and then estimating the three parameters of the finite vertical cylinder model namely depth to top (z), depth to bottom (h) and radius (R). The process of the inversion begins with computing the theoretical gravity anomaly of the simple geometry using equation (1).

The difference between the observed gravity $g_{obs}(x_i)$, and calculated gravity anomaly of an initial assumed model $g_{cal}(x_i)$, can be estimated by a misfit function, J (Chakravarthi and Sundararajan, 2007), as

$$J=\sum_{i=1}^{N}[g_{obs}(x_i)-g_{cal}(x_i)]^2 \qquad \text{(equation 3)}$$

N is the number of observed gravity data. We have employed the Marquardt's algorithm (Marquardt, 1963) given by Chakravarthi and Sundararajan (2006) for minimizing the misfit function until the normal equations can be solved for over all modifications of the three unknowns structural parameters, i.e. depth to top (z), depth to bottom (h) and radius (R), as

$$\sum_{i=1}^{N}\sum_{k=1}^{2}\frac{\partial g(x_i)}{\partial a_j}\frac{\partial g(x_i)}{\partial a_k}(1+\delta\lambda)da_k = \sum_{i=1}^{N}[g_{obs}(x_i)-g_{cal}(x_i)]\frac{\partial g(x_i)}{\partial a_j},\ for\ \ j=1,2,3 \qquad \text{(equation 4)}$$

where da_k, k=1, 2 and 3 are the amendments to the three model parameters of the simple geometry structure, i.e. radius, depth to top and bottom. Also,

$$\delta=\begin{cases}1\ for\ \ k=j,\\ 0\ for\ \ k\neq j,\end{cases}$$

and λ is the damping factor. The advancements, da_k, k=1, 2 and 3 evaluated from equation (4) are then added to or subtracted from the available parameters estimated from last iteration and the process repeats until the misfit, J, in equation (3) descends below a predetermined allowable error or the damping factor obtains a large value which is greater than predefined amount or the repetition continues until the end of the considered number for iterations (Chakravarthi and Sundararajan, 2008).

Partial derivatives required in the normal system of equation (4) are calculated numerically by the relations derived from equation (1) considering to each parameter to be solved. The Partial derivatives of the finite vertical cylinder source than the three shape parameters, namely radius, depth to top and depth to bottom can be computed, respectively, as

$$\frac{\partial g}{\partial R}=\pi G\rho R\left[\frac{1}{\sqrt{x^2+z^2}}-\frac{1}{\sqrt{x^2+h^2}}\right] \qquad \text{(equation 5)}$$

$$\frac{\partial g}{\partial z}=\pi G\rho R^2 z\left[\frac{1}{\left(x^2+z^2\right)^{3/2}}\right] \qquad \text{(equation 6)}$$

$$\frac{\partial g}{\partial h}=\pi G\rho R^2 h\left[\frac{1}{\left(x^2+h^2\right)^{3/2}}\right] \qquad \text{(equation 7)}$$

3.1. Theoretical Model Evaluation by Marquardt Method

Figure 2a shows the observed and calculated gravity field variations with 1 m interval along a 100 m profile due to an initial finite vertical cylinder model with the parameters z=30 m, h=60 m and R=10 m and an assumed finite vertical cylinder model with parameters z=27 m, h=64 m and R=8 m (Figure 2b) where the maximum gravity is the center of the profile. The density contrast is given as Δρ=1000 kg/m^3. Hence, the assumed parameters and observed gravity field related to the initial model are the inputs to the inversion algorithm which coded in Matlab. During inversion, Δρ is constant and the model

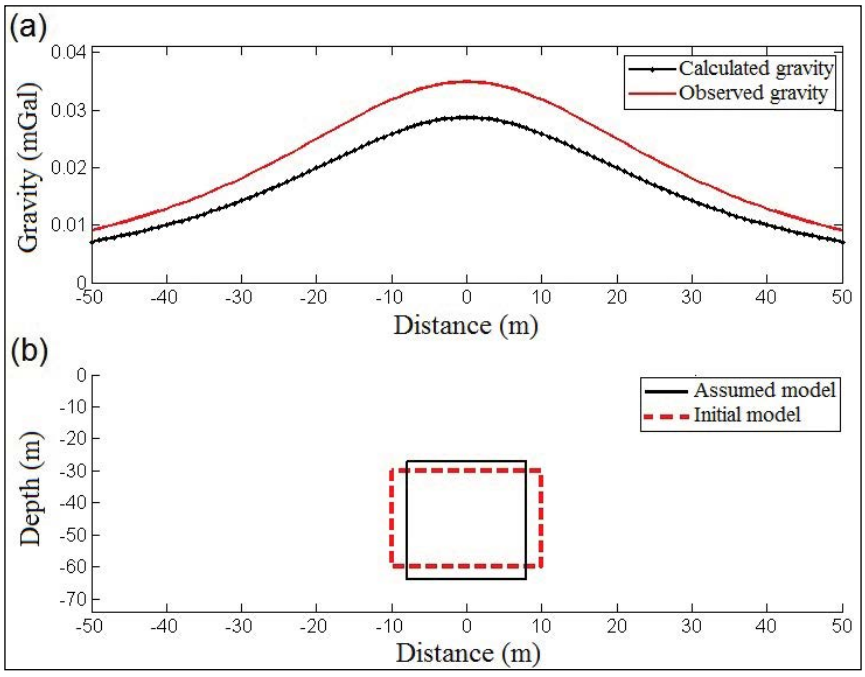

Figure 2- a) Observed and calculated gravity due to b) initial and assumed finite vertical cylinder models.

parameters, z, h and R are improved iteratively. The predefined values for error or misfit (J), iteration and damping factor (λ) are 0.00000001 mGal, 20 and 15, respectively. The initial damping factor is 0.5.

The misfit, J, reduces intensely from its initial value of 0.0021 mGal at the first iteration to 0.000042 mGal at the end of the 3rd iteration and then gradually reaches zero after the 16th iteration which is smaller than the allowable error value (Figure 3d). The

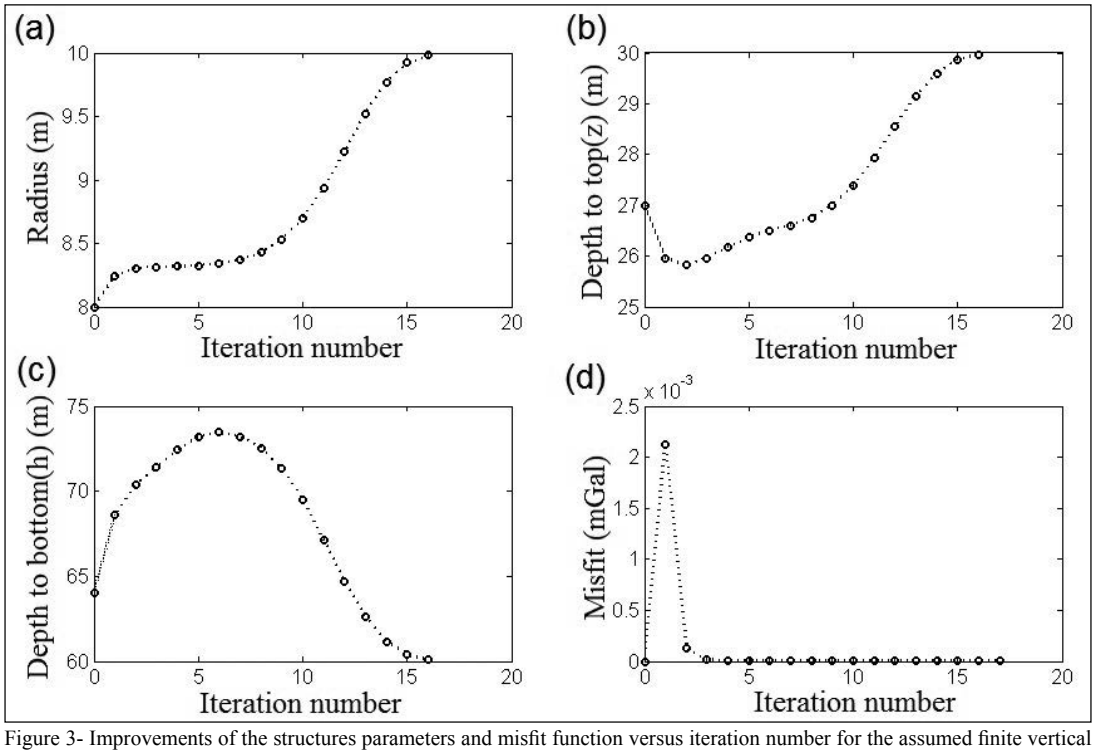

Figure 3- Improvements of the structures parameters and misfit function versus iteration number for the assumed finite vertical cylinder model in figure 2.

iteration terminated at 16th echo and therefore the estimated parameters at 16th iteration are the final results of the inversion.

Figures 3a, 3b and 3d illustrate the variations of the model parameters R, z and h during inversion with increasing the iteration number. The conclusive obtained parameters values are z=30 m, h=60 m and R=10 m. Figure 4a shows the computed gravity anomaly from the inferred structure which is shown in figure 4b as is completely similar initial model.

The efficacy of error has been evaluated by adding 10% random noise to the gravity response of the initial finite vertical cylinder model (Figure 5a) using the following expression:

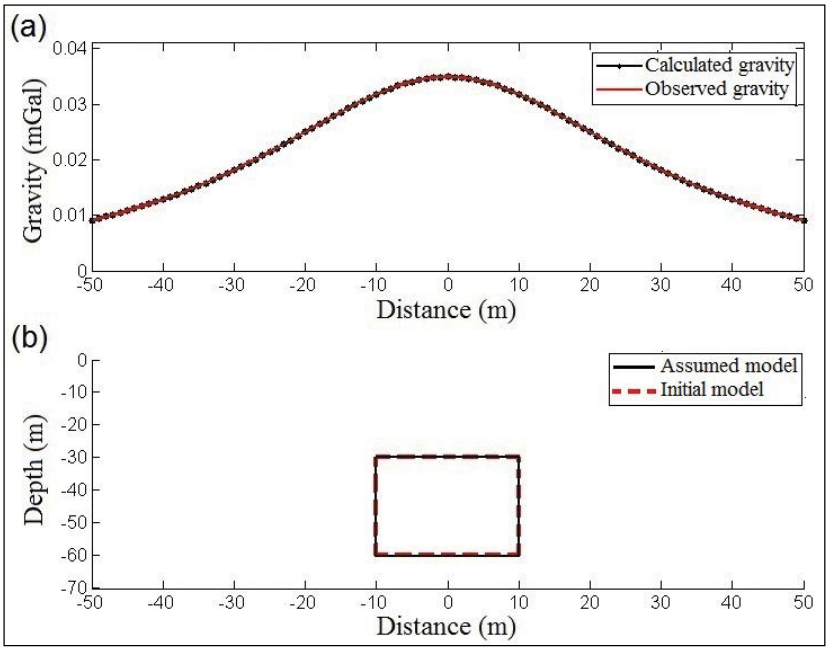

Figure 4- a) Observed and calculated gravity due to b) initial and estimated finite vertical cylinder model.

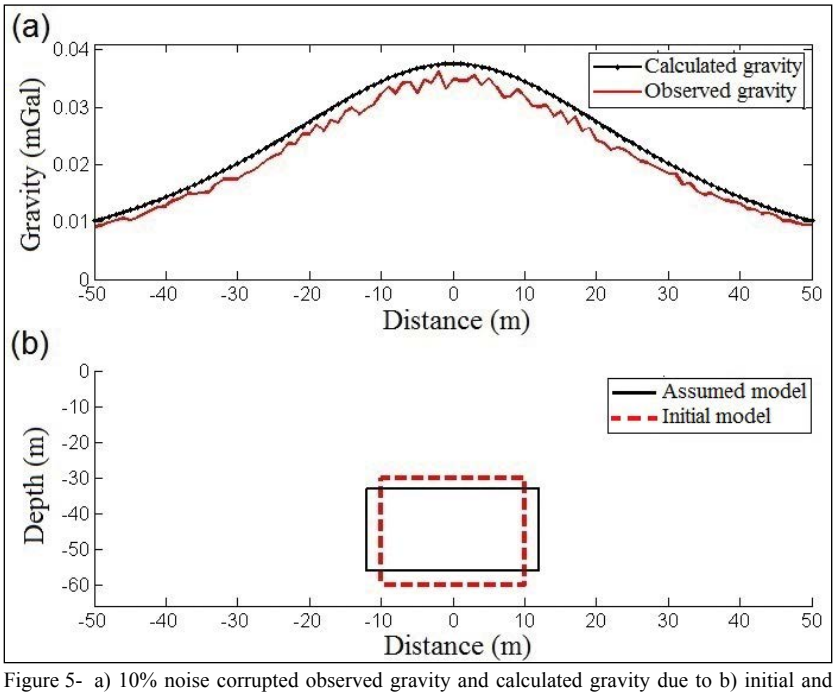

Figure 5- a) 10% noise corrupted observed gravity and calculated gravity due to b) initial and assumed finite vertical cylinder models.

$g_{nois}(x_i)=g_{obs}(x_i)[1+(RAN(i)-0.5)x0.1]$ (equation 8)

where $g_{nois}(x_i)$ is the noise corrupted synthetic data at x_i, and RND (i) is a pseudorandom number whose range is between 0 to 1.

The initial values for the parameters of the assumed finite vertical cylinder model are given as z=33 m, h=56 m and R=12 m (Figure 5b). The predefined values for error or misfit (J), iteration and damping factor (λ) are 0.00001 mGal, 100 and 15, respectively. The initial damping factor is 0.2. The misfit, J, reduces quickly from its initial value of 0.00051 mGal at the first iteration to 0.000049 mGal at the end of the 3th iteration and then incrementally attains 0.000042 mGal after the 32th iteration and this value remain constant to latest iteration (Figure 6d). The final evaluated values for the depth to top (z), depth to bottom (h) and radius (R) are 30.26 m, 60.04 and 10.06 m, respectively (Figure 6b, 6c and 6d). The percentage of error in the estimation of the model parameters, that is, z, h and R are about 0.87, 0.07 and 0.6 m, respectively.

Figure 7a shows the generated gravity anomaly of the final structure that is derived from the estimated parameters as shown in Figure 7b. The numerical results obtained from the interpretation of the synthetic gravity data, with and without random noise, are tabulated in table 1.

For evaluating the convergence of the Marquardt inversion, two different initial horizontal cylinder models were assumed to consider the gravity anomalies related to them with and without a random noise (Table 2). The estimated structural parameters approximately mimic the supposed ones.

Table 1- Numerical results evaluated from the initial and assumed structural parameters for the finite vertical cylinder model, with and without added noise.

Case	Without noise			With noise		
Parameter	z (m)	h (m)	R (m)	z (m)	h (m)	R (m)
Initial	30	60	10	30	60	10
Assumed	27	64	8	33	56	12
Estimated	30	60	10	30,26	60,04	10,06
Error %	0	0	0	0,87	0,07	0,6

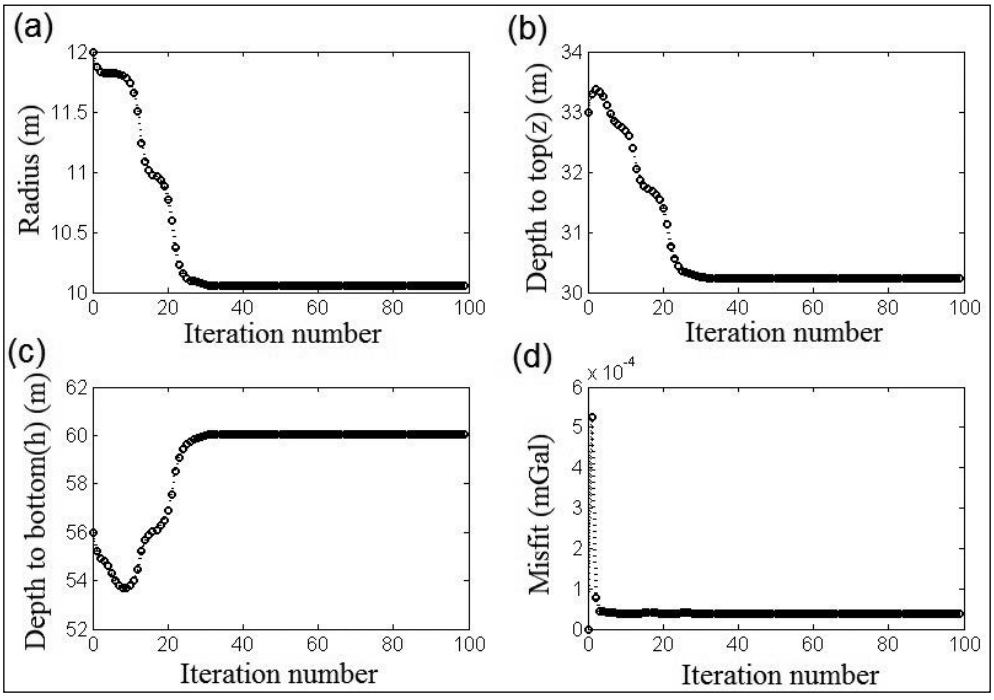

Figure 6- Improvements of the structures parameters and misfit function versus iteration number for the assumed finite vertical cylinder model in figure 5.

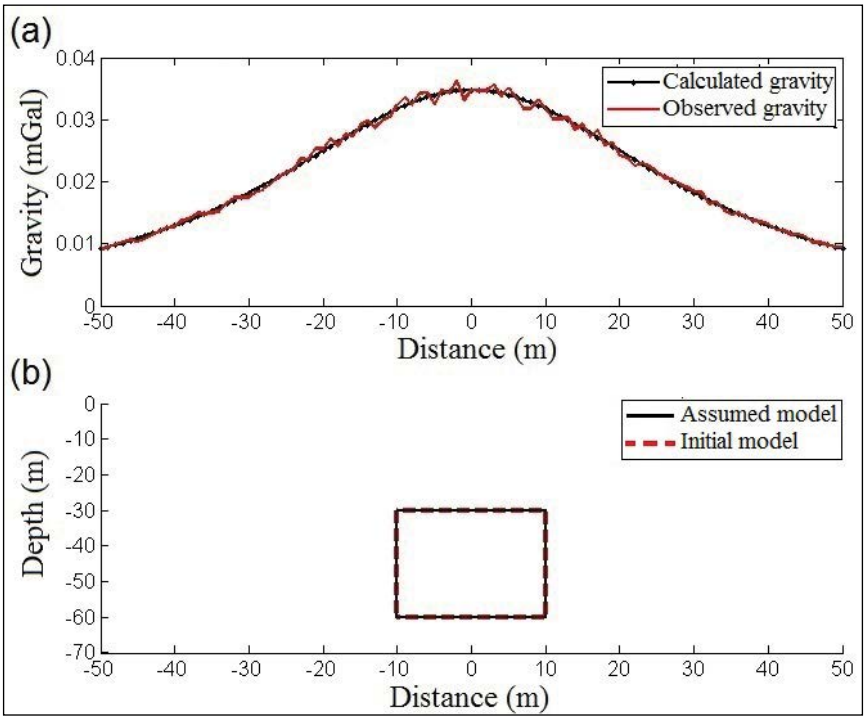

Figure 7- a) 10% noise corrupted observed gravity and calculated gravity due to, b) initial and estimated finite vertical cylinder models.

Table 2- Numerical results evaluated from the gravity responses of the two different finite vertical cylinder models. To model 1 and model 2 have been added 10% and 15% random noise, respectively.

		Model 1			Model 2		
Parameter		**z (m)**	**h (m)**	**R (m)**	**z (m)**	**h (m)**	**R (m)**
Initial		12	70	15	40	85	20
Assumed		16	65	11	34	78	16,5
Estimated	**Without noise**	12,02	70	14,99	40	85,02	20,01
	Error%	0,17	0	0,067	0	0,023	0,05
	With noise	11,94	70,8	15,11	39,1	86,5	18,9
	Error%	0,5	1,14	0,73	2,25	1,76	5,5

4. Forced Neural Network

In this study, we employ the Forced Neural Network (FNN) introduced by Osman et al. (2006, 2007) to determine the shape and density contrast of the target using the gravity anomaly as is assumed which the underground mass has been composed from the juxtaposed prisms.

FNN architecture is manufactured of several simple processing elements commonly known as neurons, which are connected together and performance in parallel (Figure 8). To estimate the efficient values of inputs and outputs, the various weights during the learning are attributed to these connections as these weights are multiplied by effective values of inputs and outputs (Osman et al. 2007). The primary objective of neural networks is to find out such weights that present the best output. Back propagation is one of the most well-known learning algorithms for neural networks.

In this approach, we need to compute the gravity anomaly due to a prismatic structure. There are some techniques for calculating the gravitational attraction of two-dimensional prism shaped masses, such as Talwani and Ewing (1960), Bhattacharyya (1964), Talwani (1965), Nagy (1966), Plouff (1976), Last and Kubik (1983) and Gerkens (1989). We apply the 2D prism equation developed by Last and Kubik (1983) to

estimate the gravity anomaly at point p because of any block located at (i,j) coordinates, which is given as

$$g_{pij} = 2G\Delta\rho\left[\begin{array}{l}(x_i - x + \frac{d}{2})\log(\frac{r_2 r_3}{r_1 r_4}) + d\log(\frac{r_4}{r_3}) - \\ (z_j + \frac{h}{2})(\theta_4 - \theta_2) + (z_j - \frac{h}{2})(\theta_3 - \theta_1)\end{array}\right], \text{(equation 9)}$$

where

$$r_1^2 = (z_j - \frac{h}{2})^2 + (x_i - x + \frac{d}{2})^2,$$

$$r_2^2 = (z_j + \frac{h}{2})^2 + (x_i - x + \frac{d}{2})^2,$$

$$r_3^2 = (z_j - \frac{h}{2})^2 + (x_i - x - \frac{d}{2})^2,$$

$$r_4^2 = (z_j + \frac{h}{2})^2 + (x_i - x - \frac{d}{2})^2,$$

and

$$\theta_1 = \tan^{-1}(x_i - x + \frac{d}{2})/(z_j - \frac{h}{2}),$$

$$\theta_2 = \tan^{-1}(x_i - x + \frac{d}{2})/(z_j + \frac{h}{2}),$$

$$\theta_3 = \tan^{-1}(x_i - x - \frac{d}{2})/(z_j - \frac{h}{2}),$$

$$\theta_4 = \tan^{-1}(x_i - x - \frac{d}{2})/(z_j - \frac{h}{2}),$$

Here G is the gravitational constant, $\Delta\rho$ is density contrast, d and h are the width and height of the each block, x_i and z_j indicate the coordinate of the each block. The equation (9) can be rewritten as

$$g_p = \sum_{h=0}^{i}\sum_{k=0}^{j}\Delta\rho_{hk} \times W_{phk} \qquad \text{(equation 10)}$$

Thus, there are i rows and j columns. By noting to the equation 10 can find that $\Delta\rho_{hk}$ are the weights of the neuron, i.e. each pixel and during the back propagation, the weights are updated and the output of the neuron exhibits the gravity anomaly (Figure 8). Hence, the density contrast are obtained. It is worth noting that in this method, from the linear activation function is used.

Because non-uniqueness in the responses, the results obtained from the FNN do not demonstrate the exact distribution of the structure. To model the causative mass correctly, a filter must serve until the value of the $\Delta\rho$ which is very close to the zero, corresponding to the density contrast which is obtained from geological features of the region under investigation, assign as zero, otherwise the value of $\Delta\rho$ is set to the density contrast of the geological region after back propagation (Osman et al., 2007). For obtaining more details, see Osman et al. (2006; 2007).

4.1 Theoretical Model Evaluation by FNN

Figure 9a displays the observed gravity related to a synthetic model assuming the density contrast 500 kg/m^3 in which the depth to top of the model is 2 m, depth to bottom is 10 m, the width of the upper part and lower part is 3 m, while the middle part is 9 m, as shown in figure 9b.

The gravity anomalies of this model are considered as input data to the FNN, then, shape, location, and density contrast parameters of the buried structure are estimated using trained FNN, as after adequate iteration is applied, constant values are assigned to the output of the neuron according to the density difference $\Delta\rho$, and this process is continued until the mean square error of the output, g_p which is shown in figure 8, becomes sufficiently little.

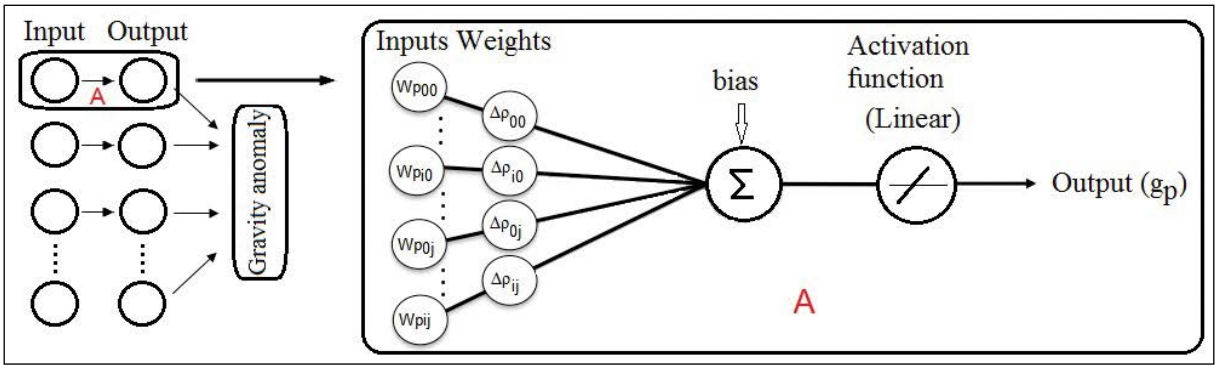

Figure 8- Sketch of the Forced Neural Network (FNN) architecture for gravity anomaly.

Figure 9c shows the evaluated structure by FNN which from the density contrast, shape and position points of view is similar the assumed one. The inverted gravity from FNN is illustrated in figure 9a.

5. Real Gravity Field Analysis

The site under survey is located in the east of Iran, around Sabzevar. The outcomes of the stones in the this area are mostly the alkali and ultrabasic igneous rocks and Ophiolite as the Chromite mineralization can be found in these rocks (Figure 10). In this region, the Chromite deposits are massive. Figure 11 shows the Bouguer gravity anomalies map of the area under consideration. The gravity measurement was done along 12 profiles with a station interval of about 10 m. The gravity data covering a 120×100 m area of the exploration region in Sabzevar.

For reaching to the residual gravity anomalies which is our desire, the regional gravity anomalies must be removed using a trend (degree two polynomial) from the Bouguer anomaly. Figure 12 displays the map of the computed local gravity field. The host rock of the chromite have the positive density contrast than the surrounding formation, therefore on the residual gravity anomalies map is appeared as the positive anomaly. The average density of the Chromite mass is about 4.5 gr/cm^3, whereas the density of the encompassing formation is between 3 gr/cm^3 to 3.5 gr/cm^3. Here, we analyze the residual gravity field variations along the profile AA′ which runs across the Chromite mineral mass in an approximately W–E direction as is shown in figure 12. The length of profile is 42 m and the gravity sampling interval is given as 2 m.

We applied the Marquardt inversion for the real gravity data where the causative mass shape was assumed as a finite vertical cylinder. The observed gravity field variations along profile AA′ is demonstrated in figure 13a. The initial values of the depth to top and bottom and radius parameters are given as z=8.5 m, h=80 m and R=11 m (Figure 13b). The density difference is chosen as 1500 kg/m^3. The

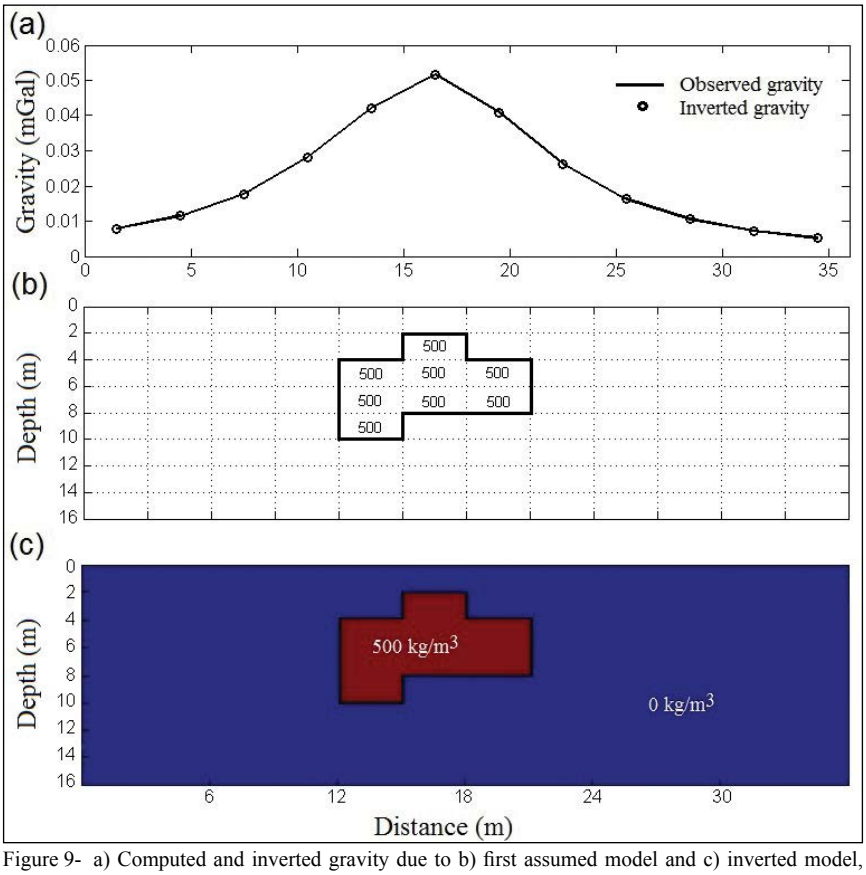

Figure 9- a) Computed and inverted gravity due to b) first assumed model and c) inverted model, respectively.

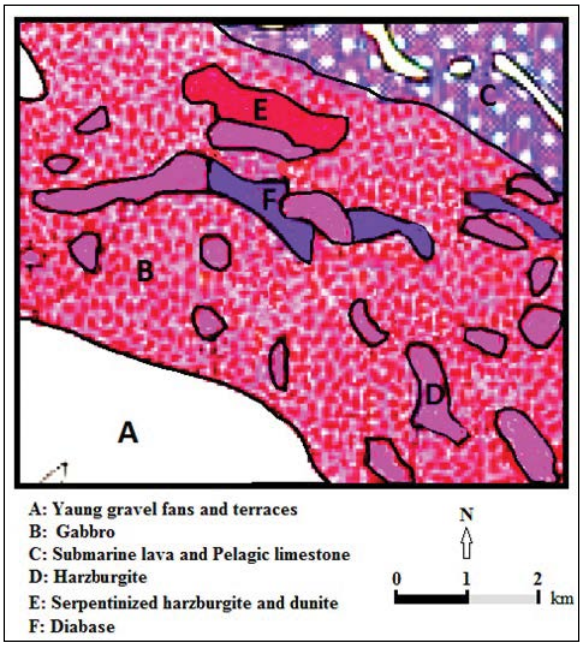

Figure 10- The geological map of the region under investigation.

gravity anomaly produced by the presumed initial values is represented in figure 13a. The assigned values for misfit (J), iteration and damping factor (λ) are 0.001 mGal, 50 and 20, respectively. The variability of each shape parameter and misfit of the finite vertical cylinder geometry model against the iteration number during inversion process is shown in figure 14.

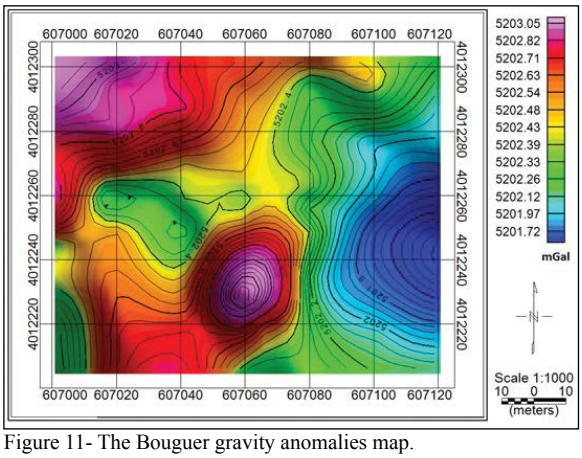

Figure 11- The Bouguer gravity anomalies map.

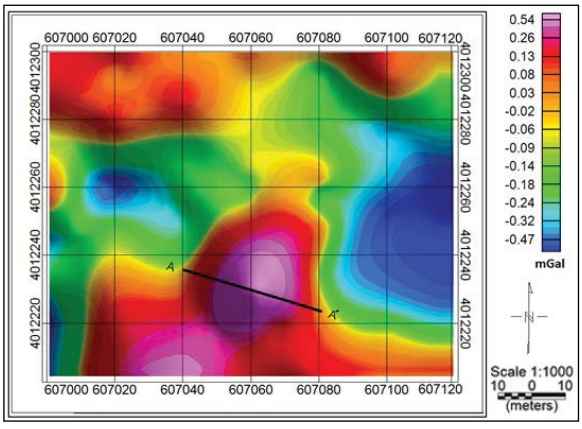

Figure 12-The residual gravity anomalies map. The profile AA′ is specified with a nearly W-E direction.

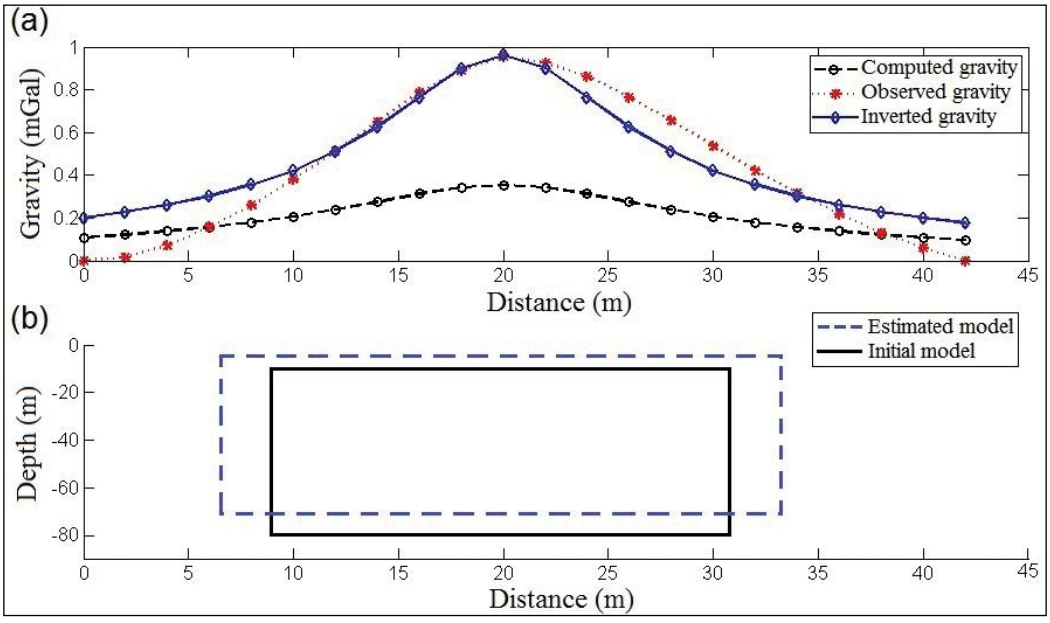

Figure 13- a) Observed gravity along profile AA′, calculated and inverted gravity due to b) initial and estimated finite vertical cylinder models.

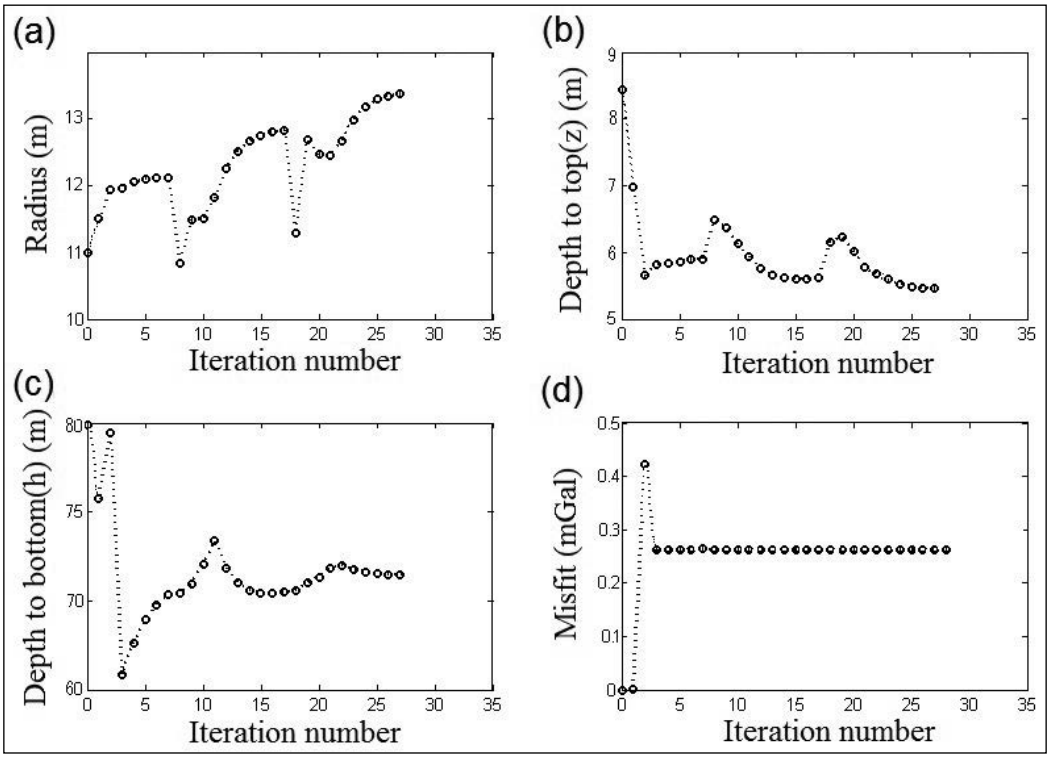

Figure 14- The variations of a) Radius b) depth to top c) depth to bottom d) misfit function versus iteration number for the real gravity data.

The performed iteration is 27, before it was ceased, as in the end of this iteration number, the damping factor obtained a value greater than the predefined value. The misfit abided constant after the 3th iteration while three other parameters have changed with each iteration as in the 27th iteration have been obtained the amounts 5.4 m, 72 m and 13.5 m for the depth to top, depth to bottom and radius, respectively. The inverted gravity due to the estimated parameters is brought in figure 13a whereas the inferred structure is shown in figure 13b. The assumed and inverted structural parameters are given in table 3.

Table 3- Numerical results evaluated from the real gravity data.

Parameter	**z (m)**	**h (m)**	**R (m)**	**z (m)**	**h (m)**	**R (m)**
Assumed	8,5	80	11	4	65	16
Estimated	5,4	72	13,5	5,45	71,8	13,6
Iteration	27			43		
Misfit (mGal)	0,265			0,0057		

The permanency and isotropy of the interpreted parameters from the real gravity data was investigated using different assumed values (Table 3). The estimated structural parameters illustrate a very slight differences that confirm the stability of the method.

The gravity profile AA′ in residual anomaly map is also analyzed for modeling with FNN approach. The length and width of each block was considered as 5 m and 10 m, respectively. To achieve a under surface model as a finely detailed map, the evaluated density distribution was interpolated, where figure 15 illustrate the estimated structure for the Chromite deposit mass based on the density contrast distribution. The central part of the modeled deposit have a density contrast of 1600 kg/m^3 and getting away from the center, this value slake as expected. By considering the inverted structure by FNN, the depth to top and bottom and radius parameters of the buried mass can consider as about 8 m, 70 m and 9 m, respectively.

For comparison, the generated gravity according to the interpreted mass using FNN and Marquardt inversion and also real gravity have been shown in figure 16. We have applied the standard error (SE) as a

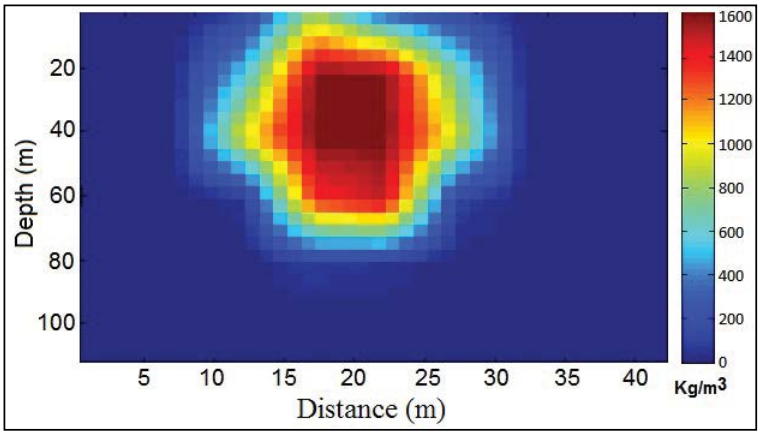

Figure 15- The inverted density distribution from analyzing the real gravity data using FNN.

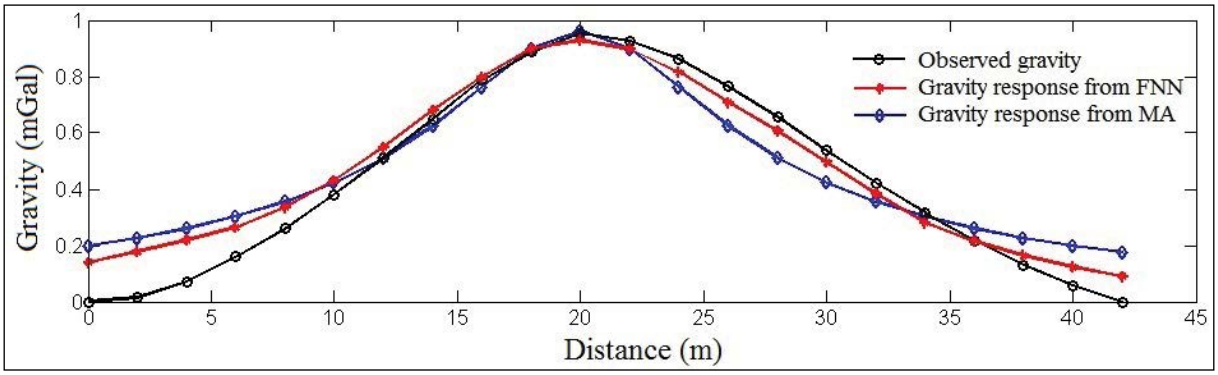

Figure 16- The observed gravity and gravity responses obtained from the FNN and Marquardt inversion (MA).

criteria in order to compare the observed and evaluated gravity values (Asfahani and Tlas, 2008):

$$SE = \sqrt{\frac{\sum_{i=1}^{N}\left[g_o(x_i) - g_c(x_i)\right]^2}{N}} \qquad \text{(equation 11)}$$

where g_o and g_c (i = 1, ..., N) are the observed and the evaluated values at the points x_i (i = 1, ..., N), respectively. The standard error for the FNN and Marquardt's algorithm methods are 0.09 and 0.126 mGal, respectively. Therefore, according to the computed SE, the inverted structure from FNN are closer to reality.

The Euler deconvolution method is a popular and well known technique in potential fields study which is widely used for estimating the depth of the anomaly source. In this study, we have employed the Euler method for calculating the depth of the Chromite mass by choosing a structure index of 1 and a window size of 5×5 points. Figure 17 show the solutions obtained from Euler deconvolution as plotted on the residual gravity anomaly map. The Euler solutions located on the gravity anomaly present a depth between 5 to 10 m for the buried deposit (red points in figure 17). Because the estimated depth to top by the all three methods are in a same range, thus, it was found that the introduced methods operate correctly. The attained results for the real gravity anomaly have been summarized in table 4.

Table 4- Evaluated parameters using the various methods.

	Parameters			
Methods	**z (m)**	**h (m)**	**R (m)**	**SE (mGal)**
FNN	8	70	9	0,09
Marquardt's algorithm	5,4	72	13,5	0,126
Euler	5-10	-	-	-

6. Conclusions

In this paper, we have introduced a optimization approach based on the Marquardt's algorithm and have also applied the Forced Neural Networks for the inverse modeling of the residual gravity anomaly due to the finite vertical cylinder geometric shape.

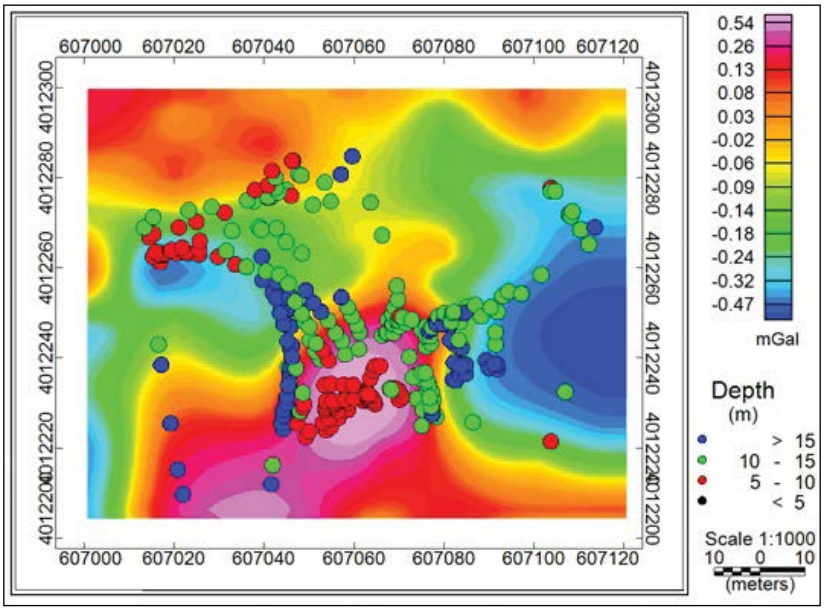

Figure 17- The depth solutions estimated by the Euler deconvolution method for the residual gravity anomalies.

To check the constancy and convergency of the parameters attained from the Marquardt inversion, the noise-free and noise corrupted theoretical gravity data related to the different initial models were used and it was eventuated that the inversion yields almost the same solutions in all cases. Moreover, the performance of the FNN was evaluated by the synthetic gravity data set. The stable and accurate solutions verify the reliability and applicability of the both Marquardt's algorithm and FNN methods as the powerful and useful inverse modeling tools.

The methods were used for estimating the buried structure parameters and determining the condition of the underground density distribution using the gravity anomaly of a Chromite deposit from Iran. The computed values for the depth to top, depth to bottom and radius parameters by the Marquardt inversion are 5.4 m, 72 m and 13.5 m, respectively and by the FNN method are about 8 m, 70 m and 9 m, respectively. Therefore, the acquired dimensions for the causative mass are very close and the inverted gravity from the final interpreted structure by these procedures conform to the real gravity along profile AA′ cross-section. The minimum standard error value was considered as a criterion for selecting the best mass shape, as the estimated parameters depict a acceptable structure naturally. As expected, the standard error amount between the inverted gravity from the FNN and real gravity is smaller than one between the inverted gravity from the Marquardt's algorithm and real gravity, because in reality a structure with invariable density whose feature be closely a geometric shape. In other words, the gravity causative mass has not a perfect geometry shape and is a heterogeneous body. In nonlinear inversion, we consider the gravity anomaly source as a regular geometry shape with a constant density, therefore we try to interpret the anomaly source with the most similar geometry shape where the error between the observed and computed gravity be least. Hence, existence of a mismatch between observed and computed data is unavoidable. Therefore, the estimated values for the depth to top (z), depth to bottom (h) and radius (R) parameters using the FNN are closer to the reality than those computed by the Marquardt inversion method. The evaluated depths to top have also good conformity with the Euler solutions.

References

Abdelrahman, E.M. 1990. Discussion on "A least-squares approach to depth determination from gravity data" by O. P. Gupta. Geophysics 55, 376-378.

Abdelrahman, E.M., El-Araby, T.M. 1993*a*. A least-squares minimization approach to depth determination from moving average residual gravity anomalies. Geophysics 58,1779–1784.

Abdelrahman, E.M., El-Araby, H.M. 1993*b*. Shape and depth solutions from gravity using correlation factors between successive least-squares residuals. Geophysics 59, 1785–1791.

Abdelrahman, E.M., Essa, K.S. 2015. A new method for depth and shape determinations from magnetic data. Pure and Applied Geophysics 172, 439–460.

Abdelrahman, E.M., Bayoumi, A.I., Abdelhady, Y.E., Gobashy, M.M., El-Araby, H.M. 1989. Gravity interpretation using correlation factors between successive least-squares residual anomalies. Geophysics 54, 1614-1621.

Abdelrahman, E.M., Bayoumi, A.I., El-Araby, H.M. 1991. A least-squares minimization approach to invert gravity data. Geophysics 56, 115-l 18.

Abdelrahman, E.M., El-Araby, T.M., Essa, K.S. 2003. A least-squares minimisation approach to depth, index parameter, and amplitude coefficient determination from magnetic anomalies due to thin dykes. Exploration Geophysics 34, 241–248.

Abdelrahman, E.M., Essa, K.S., El-Araby, T.M., Abo-Ezz, E.R. 2015. Depth and shape solutions from second moving average residual magnetic anomalies. Exploration Geophysics, 47/1, 58-66.

Abedi, M., Afshar, A., Ardestani, V.E., Norouzi, G.H., Lucas, C. 2009. Application of various methods for 2D inverse modeling of residual gravity anomalies. Acta Geophysica 58/2, 331-336.

Albora, A.M., Uçan, O.N., Özmen, A. 2001*a*. Residual separation of magnetic fields using a cellular neural network approach. Pure Appl Geophys,158,1797–1818.

Albora, A.M., Uçan, O.N., Özmen, A., Özkan, T. 2001*b*. Evaluation of Sivas-Divriği region Akdağ iron ore deposits using cellular neural network. J Appl Geophys 46,129–142.

Al-Garni, M.A. 2013. Inversion of residual gravity anomalies using neural network. Arab J Geosci 6, 1509–1516.

Asfahani, J., Tlas, M. 2008. An automatic method of direct interpretation of residual gravity anomaly profiles due to spheres and cylinders. Pure and Applied Geophysics 165/5, 981–994.

Bhattacharyya, B.K. 1964. Magnetic anomalies due to prism-shaped bodies with arbitrary polarization. Geophysics 29, 517–531.

Bichsel, M. 2005. Image processing with optimum neural networks. IEEE International Conference on Artificial Neural Networks, 513, IEEE, London, 374–377.

Bowin C., Scheer E., Smith W. 1986. Depth estimates from ratios of gravity, geoid, and gravity gradient anomalies. Geophysics 51, 123-136.

Chakravarthi, V., Sundararajan, N. 2004. Ridge regression algorithm for gravity inversion of fault structures with variable density. Geophysics 69, 1394–1404.

Chakravarthi, V., Sundararajan, N. 2005. Gravity modeling of 21/2-D sedimentary basins-a case of variable density contrast. Computers and Geosciences 31, 820–827.

Chakravarthi, V., Sundararajan, N. 2006. Gravity anomalies of multiple prismatic structures with depth-dependent density – A Marquardt inversion. Pure and Applied Geophysics 163, 229–242.

Chakravarthi, V., Sundararajan, N. 2007. Marquardt optimization of gravity anomalies of anticlinal and synclinal structures with prescribed depth-dependent density. Geophysical Prospecting 55, 571–587.

Chakravarthi, V., Sundararajan, N. 2008. TODGINV—A code for optimization of gravity anomalies due to anticlinal and synclinal structures with parabolic density contrast. Computers & Geosciences 34, 955–966.

Chua, L.O., Yang, L. 1988. Cellular neural networks. Theory. IEEE Trans Circuits Syst 35,1257–1272.

Eshaghzadeh, A., Kalantari, R.A. 2015. Anticlinal Structure Modeling with Feed Forward Neural Networks for Residual Gravity Anomaly Profile, 8th congress of the Balkan Geophysical Society DOI: 10.3997/2214-4609.201414210.

Eshaghzadeh, A., Hajian, A. 2018. 2-D inverse modeling of residual gravity anomalies from Simple geometric shapes using Modular Feed-forward Neural Network, Annals of Geophysics. 61,1, SE115.

Eslam, E., Salem, A., Ushijima, K. 2001. Detection of cavities and tunnels from gravity data using a neural network. Explor. Geophys 32, 204–208.

Essa, K.S. 2007. A simple formula for shape and depth determination from residual gravity anomalies. Acta Geophysica 55/2, 182–190.

Gerkens, A.J.C. 1989. Foundation of exploration Geophysics Elsevier.

Gupta, O.P. 1983. A least-squares approach to depth determination from gravity data. Geophysics 48, 357-360.

Hajian, A.R. 2004. Depth estimation of gravity data by neural network, M. Sc. thesis, Tehran University, Iran (unpublished).

Hammer. S. 1974. Graticule spacing versus depth discrimination in gravity interpretation. Geophysics 42, 60-65.

Kaftan, I., Salk, M., Şenol, Y. 2011. Evaluation of gravity data by using artificial neural networks case study: Seferihisar geothermal area (Western Turkey). Journal of Applied Geophysics 75, 711-718.

Last, B. J., Kubik, K. 1983. Compact gravity inversion. Geophysics 48, 713-721.

Lines, L.R., Treitel, S. 1984. A review of least-squares inversion and its application to geophysical problems. Geophys. Prosp 32, 159-186.

Marquardt, D.W. 1963. An algorithm for least-squares estimation of nonlinear parameters. Journal of the Society of Indian Applied Mathematics 11, 431–441.

Mohan, N.L., Anandababu, L., Rao, S. 1986. Gravity interpretation using the Melin transform, Geophysics 51, 114-122.

Nagy, D. 1966. Gravitational attraction of a right rectangular prism. Geophysics 31, 362–371.

Odegard, M.E., Berg, J.W. 1965. Gravity interpretation using the Fourier integral. Geophysics 30, 424-438.

Osman, O., Muhittin, A.A., Uçan, O.N. 2006. A new approach for residual gravity anomaly profile interpretations: Forced Neural Network (FNN). Ann. Geofis 49, 6.

Osman, O., Muhittin, A.A., Uçan, O.N. 2007. Forward modeling with Forced Neural Networks for gravity anomaly profile. Math. Geol 39, 593-605.

Plouff, D. 1976. Gravity and magnetic fields of polygonal prisms and application to magnetic terrain corrections. Geophysics 41, 727–741.

Salem, A., Ravat, D., Johnson, R., Ushijima, K. 2001. Detection of buried steel drums from magnetic anomaly data using a supervised neural network. J. Environ. Eng. Geophys 6,115-122.

Saxov, S., Nygaard, K. 1953. Residual anomalies and depth estimation. Geophysics 18, 913-928.

Sharma, B., Geldart, L.P. 1968. Analysis of gravity anomalies of two-dimensional faults using Fourier transforms. Geophys. Prosp 77-93.

Shaw, R.K., Agarwal, N.P. 1990. The application of Walsh transforms to interpret gravity anomalies due to some simple geometrically shaped causative sources: A feasibility study. Geophysics 55, 843-850.

Talwani, M. 1965. Computation with the help of a digital computer of magnetic anomalies caused by bodies of arbitrary shape. Geophysics 30,797–817.

Talwani, M., Ewing, M. 1960. Rapid computation of gravitational attraction of 3D bodies of arbitrary shape. Geophysics 25, 203–225.

Bulletin of the Mineral Research and Exploration

http://bulletin.mta.gov.tr

Usability of PC-ash as lightweight aggregate in foam concrete

Metin DAVRAZ[*a] and Şemsettin KILINÇARSLAN[b]

[a]*Süleyman Demirel University, Natural and Industrial Building Materials Application and Research Center, Isparta, Turkey*
[b]*Süleyman Demirel University, Faculty of Engineering, Civil Engineering Department, Isparta, Turkey*

Research Article

Keywords:
Foam concrete, Lightweight aggregate, PC ash, Compressive strength, Thermal conductivity.

ABSTRACT

Foam concretes can be produced with aggregate or without aggregate. In this study, the possibility of using PC ash as lightweight aggregate in the production of foam concrete was investigated. Waste-PC ash is emerging from the pulverized coal furnace about 10 tons/day in a textile factory located in the vicinity of Dinar (Afyonkarahisar). The chemical properties, particle size distribution and grain densities of PC-ash were determined. Foam concrete with a dry density of 450 kg/m^3 at a cement dosage of 250 kg/m^3 and w/c:0.65 was produced after the aggregate analysis. The PC-ash which is used in foam concrete mix is between 0 and 200 kg/m^3. 100 mm cube and 300x300x50 mm prism samples were prepared with this foam concrete. The compressive strengths of the cube samples and the thermal conductivity coefficient of the prism samples were tested at the 28th day. The average compressive strength of foam concrete samples with a density of 452 kg/m^3 was determined as 1.07 MPa and the thermal conductivity coefficient was determined as 0.097 W/mK. As a result, it has been determined that PC-ash as lightweight aggregate can be successfully used in production of precast element and light floor-screed.

Received Date: 24.10.2018
Accepted Date: 30.01.2019

1. Introduction

Foam concrete is a type of lightweight concrete. It is obtained by mixing the foam formed with the foam agent in the mortar composed of cement, water and aggregate. It contains 50% -80% of the volume of closed pores which aren't interconnected. Foam concrete is an environmentally friendly structure and insulation material which provides light, heat and impact sound insulation that can be used in place of the building elements used in the interior-exterior walls and floors of all buildings. Foam concrete has high flow ability in fresh condition, low density, function-dependent resistance and low thermal conductivity. The dry density of foam concrete is between 400 and 1600 kg/m^3. The compressive strength of foam concrete is between 1 and 15 MPa. Foam concrete can be easily pumped and placed. It does not require compression and vibration. It has excellent resistance to water and frost. Foam concrete mortar can be molded into blocks in enterprises, and if necessary, it can be prepared as mobile in the application area and can be easily carried with the help of a pump. Depending on its density, foam concrete can be used in the production of wall blocks, asmolene, panel, insulation leveling concrete, prefabricated building elements (Brady et al., 2001).

Foam concrete was first patented in 1923. However, it has become widespread in semi-reinforced and non-reinforced concrete construction applications in recent years (Ramamurthy et al., 2009). The first comprehensive review of cellular concrete was made by Valore in 1954. Detailed studies were

Citation Info: Davraz, M., Kılınçarslan, Ş. 2020. Usability of PC-ash as lightweight aggregate in foam concrete. Bulletin of the Mineral Research and Exploration, 161, 49-56. https://doi.org/10.19111/bulletinofmre.545562

* *Corresponding author: Metin DAVRAZ, metindavraz@sdu.edu.tr*

made related to the composition, properties, usage and structure of foam concrete by Rudnai (1963) and Short and Kinniburgh (1963). In recent years, Jones and McCarthy (2005) investigated the history of foamed concrete, used materials, properties and construction practices in some projects carried out worldwide. These investigations include functional properties such as fire resistance, thermal conductivity and acoustic properties. But, the data of subjects such as the fresh concrete properties of foam concrete, durability and air gap system are limited.

The success of foam concrete production depends on many factors such as choice of foam agent, material and admixture, foam preparation methods, mixing method etc. Ramamurthy et al. (2009) classified scientific studies such as foam concrete components, mixture design, production, fresh and hardened concrete properties. Based on this study, the results of these studies including the mix design, density and compressive strength of foamed concrete were presented in table 1.

Many researchers have been carried out on the use of filler, pozzolanic material or lightweight aggregates in foam concrete. A significant proportion of these studies have focused on the use of fly ash in foam concrete. Kunhanandan and Ramamurthy (2006) investigated the effect of sand and fly ash on hardened foam concrete properties. Researchers have suggested that the reduction in sand particle size leads to an improvement in the strength of foam concrete. In addition, it has been determined that the replacement of sand and fly ash causes higher strength for given density (Kunhanandan and Ramamurthy, 2006).

Jitchaiyaphuma et al. (2011) used fly ash in foam concrete mix at ratios 10%, 20%, 30% of cement weight. The w/c ratio in foam concrete with density of 800 kg/m^3 was kept constant. The compressive strengths of foam concrete samples were determined at 3, 7, 14, 28 and 60 days. The researchers concluded that as a result of the study, fly ash replaced by cement increased the compressive strength in the early period (Jitchaiyaphuma et al., 2011). Slabaugh et al. (2007)

Table 1- The compositions, compressive strengths and densities of foam concretes investigated years (Ramamurthy et al., 2009).

Author(s) and Year	**Cement dosage (kg/m^3) or compositions**	**s/c**	**w/c**	**FA/c**	**Density range (kg/m^3)**	**Compressive Strength (MPa, 28d)**
McCormick (1967)	335-446	0,79-2,8	0,35-0,57		800-1800	1,8-17,6
Tam vd. (1987)	390	1,58-1,73	0,6-0,8		1300-1900	1,81-16,72
Regan ve Arasteh (1990)	LWA	0,6	0,45-0,6		800-1200	4-16
Van Dijk (1991)	Cement, sand/FA				280-1200	0,6-10 (91days)
ACI 523.1R-1992	Cement paste				240-640 (DD)	0,48-3,1
	Cement-sand				400-560 (DD)	0,9-1,72
Hunaiti (1997)		3			1667	12,11
Kearsly ve Booyens (1998)	Cement-FA (replacement)				1000-1500	2,8-19,9
Durack ve Weiqing (1998)	270-398	1,23-2,5	0,61-0,82		982-1185 (KY)	1-6
	137-380		0,48-0,7	1,48-2,5	541-1003 (DD)	3-15 (77days)
Aldridge (2000)	Cement-sand				400-1600	0,5-10
Kearsly ve Wainwright (2001*a,b*)	Cement and FA				1000-1500	2-18
Tikalsky vd. (2004)	Cement, 149-420		0,4-0,45		490-660	0,71-2,07
	Cement, sand/FA 57-149		0,5-0,57		1320-1500	0,23-1,1
Jones ve McCarty (2005)	300	1,83-3,17	0,5		1000-1400	1-2
			1,11-1,56	1,22-2,11	1000-1400	3,9-7,3
Jones ve McCarty (2005)	500	1,5-2,3	0,3		1400-1800	10-26
			0,65-0,83	1,15-1,77	1400-1800	20-43
Nambiar ve Ramamurthy (2006)	Cement-sand mix (coarse)	With filler cement ratio varied from 1to3 and fly ash replacement for sand varied from 0% to 100%			800-1350 (DD)	1-7
	Cement-sand mix (fine)				800-1350 (DD)	2-11
	Cement-sand – Fly ash mix (coarse)				650-1200 (DD)	4-19

s/c : Sand-cement ratio s/c : water-cement ratio FA/c : Fly ash-cement ratio DD : Dry density (kg/m^3)

used foamed synthetic light aggregates (FSLA) as coarse aggregates in foamed concrete. As a result of the research, they obtained 20-25% lower density and more ductile foam concrete. Conversely, it has been stated that there is a reduction of 65-75% in the compressive strength of foam concrete (Slabaugh et al., 2007). Kearsly and Wainwright (2001*a, b*) have studied the properties of foamed concrete replaced by cement with both classified and unclassified fly ash (up to 75% by weight). It has been determined that there was little difference in the performance of classified and unclassified fly ashes (Kearsly and Wainwright, 2001*a, b*).

Expanded perlite, micronized pumice, vermiculite etc. lightweight aggregates can be used in foam concrete. However, the high unit costs of such lightweight aggregates limit their application areas and quantities. Materials such as micronized calcite, stone flour, very fine sieved natural sand, fly ash, etc., negatively changed thermal conductivity coefficient of foam concrete. Waste-PC ash is emerging from the pulverized coal furnace about 10 tons/day in a textile factory located in the vicinity of Dinar (Afyonkarahisar; figure 1). This waste is stored in the around Acıgöl as wild and cause environmental pollution. In this study, the possibility of using PC-ash as lightweight aggregate in the production of foamed concrete was investigated.

2. Materials and Methods

Firstly, the chemical properties, particle size distribution and grain densities of Pulverized Coal Fly Ash (PC- ash) were determined. Portland cement (CEM I 42.5 R) was used as binder for the production of foam concrete. The characteristics of the cement were given in table 2.

Chemical analysis of PC ash was performed by Göltaş AŞ Quality and Control Laboratory. Particle size distribution, loose bulk density, grain densities and water absorption tests of PC ash were performed in accordance with TS 3530 EN 933-1; TS EN 1097-3; TS EN 1097-6, respectively. The findings were interpreted according to TS EN 13055. Synthetic foam agent was used in foam concrete production. The foam agent was mixed with water at rate of 1/50 and foam was obtained from the foam generator at a density of 85 g/L. The w/c ratio of the mixture was chosen to be 0.65. The resulting foamed concrete mixture was poured into 100 mm cube molds and cured for 28 days in a climate cabinet at 95% relative humidity. In addition, the thermal conductivity samples were

Figure 1- The satellite image of textile factory (upper left) and ash storage area (lower right).

Table 2- Cement properties.

Chemical properties of clinker (%)		Physical properties of cement	
SiO_2	20,52	Volumetric expansion (mm)	≤ 1
Al_2O_3	4,00	Fineness (90m, %)	0,10
Fe_2O_3	3,45	Fineness (200m, %)	1,10
CaO	64,28	Specific surface area (cm^2/g)	3340
MgO	1,63	Initial setting time (min)	185
SO_3	2,53	Final setting time (min)	240
Na_20+K_2O	1,35	Specific gravity (g/cm^3)	3,12

Mechanical properties of cement (MPa)				
at 7 days	Flexure strength (MPa)	5,8	Compressive strength (MPa)	39,3
at 28 days	Flexure strength (MPa)	7,2	Compressive strength (MPa)	51,0

poured into 300x300x50 mm prism molds and then the samples were dried at 105°C until reaching the constant mass, when the cure time was completed.

The compressive strengths at 28th day of the samples were carried out by the compressive strength test press according to TS 13565 standard and the thermal conductivity values were determined by HFM device according to TS EN 12664 standards. The properties of the fly ash as described in TS EN 450-1 standard were given in table 3 and the PC ash chemical constituents were given in table 4. The proportions of total pozzolanic components (SiO_2+Fe_2O_3+Al_2O_3) were 81% in the PC ash. The content of MgO and SO_3 which can react harmfully with the cement in the ash was less than 4% and 3% respectively. In addition, equivalent alkaline substance (Na_2O+0.658*K_2O) was than 5%, and the loss of ignition value was lower than 10%.

The physical analysis findings of the PC ash were given in table 5. The water absorption value at 24 hours by weight of the aggregate was 35%.

The oven dry-grain density of PC ash was 1280 kg/m^3. This value was suitable the criteria described for light aggregates in TS EN 13055 (< 2000 kg/m^3). In addition, mineral based aggregates with an oven dry-grain density of < 2000 kg/m^3 and dry bulk density < 1200 kg/m^3 are defined as "lightweight aggregate" according to TS EN 206 standard.

The PC ash has a fairly uniform grain size distribution (Table 6, Figure 2). The maximum grain size was less than 2 mm, and the fineness module value was 0.54. This value indicates that the average grain size of the ash was around 0.5 mm. In addition, the amount of small particles in 90 microns was 12%.

Table 3- Fly ash properties according to TS EN 450-1standard.

Components	TS EN 450-1
SiO_2+Al_2O_3+Fe_2O_3 (%)	≥ 70
MgO (%)	≤ 4
SO_3 (%)	≤ 3
Amount of eq. alkaline subs. (%)	≤ 5
Total Chloride	≤ 0,1
Loss of ignition (LOI) (%)	≤ 10

Table 4- Chemical properties of PC ash.

Components	%
SiO_2	44,85
Al_2O_3	19,02
Fe_2O_3	17,11
CaO	9,05
Na_2O	0,33
K_2O	1,36
MgO	3,11
TiO_2	1,04
Cr_2O_3	0,09
SO_3	2,23
LOI	2,06

Table 5- Physical properties of PC ash.

Physical Properties of PC ash	
Specific gravity (g/cm^3)	2,590
Bulk density (100%-dried) (kg/m^3)	570
Apparent grain density (g/cm^3)	2,19
Oven dried grain density (g/cm^3)	1,28
Saturated surface dry -grain density (g/cm^3)	1,70
Water absorption (by weight, %)	34

Table 6- Particle size distribution of PC ash.

Particle Size Distribution		
Sieve (mm)	**Retained (%)**	**Cumulative passing (%)**
2,000	0,05	99,95
1,000	8,33	91,62
0,500	21,21	70,41
0,250	23,97	46,44
0,090	34,30	12,14
Pan	12,14	0,00

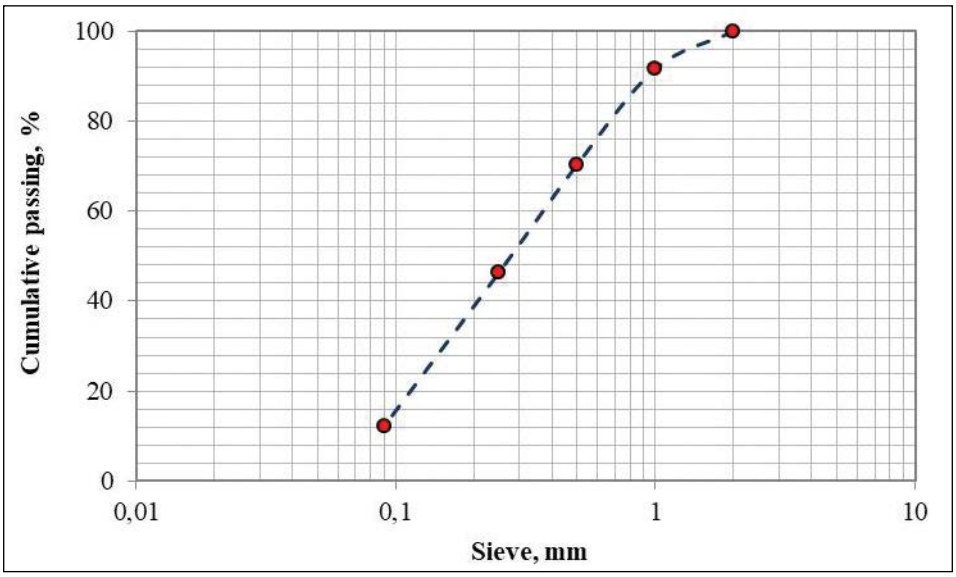

Figure 2- Particle size distribution curve of PC ash.

These particles may react with $Ca(OH)_2$ formed during the hydration of the cement to form additional C-S-H bonds.

3. Results and Discussions

3.1. Mechanical and Thermal Properties of Foam Concrete

PC ash was used at 0%, 11%, 22%, 33% and 44% by replacing with cement in the foam concrete. The components of the prepared foam concrete mixtures were given in table 7.

The densities (in fresh condition) of the P0, P50, P100, P150 and P200 samples were measured as 676, 674, 672, 670 and 667 kg/m^3, respectively. The cube samples were cured at 95% relative humidity for 28 days and then dried until reached constant volume. Subsequently, the masses of the samples were weighed and their dimensions were measured. The compressive strengths of 6 cube specimens from each sample group were tested. The density and compressive strengths of the samples were given in table 8.

As the amount of PC ash replacement by cement increased, the compressive strength of foam concrete samples decreased (Figure 3). The compressive strength of P200 sample with 200 kg/m^3 ash decreased by 44% compared to the control sample.

The compressive strengths of foam concretes in dry-densities of 400-500 kg/m^3 were reported by Tikalsky et al. (2004), Aldridge (2000) and ACI-523 (1992) as 0.7, 0.5 and 0.9 MPa, respectively. The results obtained in this study were consistent with the

The thermal conductivities of foam concrete samples were measured by the Lasercomp Fox 314 device. The density and thermal conductivity coefficient ($\lambda_{10\text{-dry}}$) test results of 3 samples from each group were given in table 9.

Table 7- Mixture designs of foam concrete samples.

Components	FC Samples				
	P0	P50	P100	P150	P200
Cement (kg/m^3)	450	400	350	300	250
PC ash (kg/m^3)	0	50	100	50	200
Water (kg/m^3)	162	162	162	162	162,5
Foam (kg/m^3)	58,6	56,7	54,7	52,8	50,9
Water / solid	0,36	0,36	0,36	0,36	0,36

Table 8- Dry densities and compressive strengths of hardened foam concrete samples.

S. No	P0		P50		P100		P150		P200	
	D	$f_{c\text{-}28d}$	D	$f_{c\text{-}28d}$	D	$f_{c\text{-}28d}$	D	$f_{c\text{-}28d}$	D	$f_{c\text{-}28d}$
1	452	1,95	465	1,80	454	1,59	451	1,45	452	1,12
2	450	1,89	452	1,73	455	1,59	464	1,30	448	1,13
3	452	1,94	458	1,81	451	1,73	455	1,37	457	1,03
4	453	1,93	448	1,82	453	1,69	463	1,48	443	1,10
5	457	1,87	454	1,77	448	1,62	457	1,28	453	1,06
6	458	1,93	458	1,77	455	1,60	460	1,35	457	0,98
Av.	454	1,92	456	1,78	453	1,64	458	1,37	452	1,07
D: *Dry density, kg/m³* $f_{c\text{-}28d}$: *Compressive strength at 25d, MPa*										

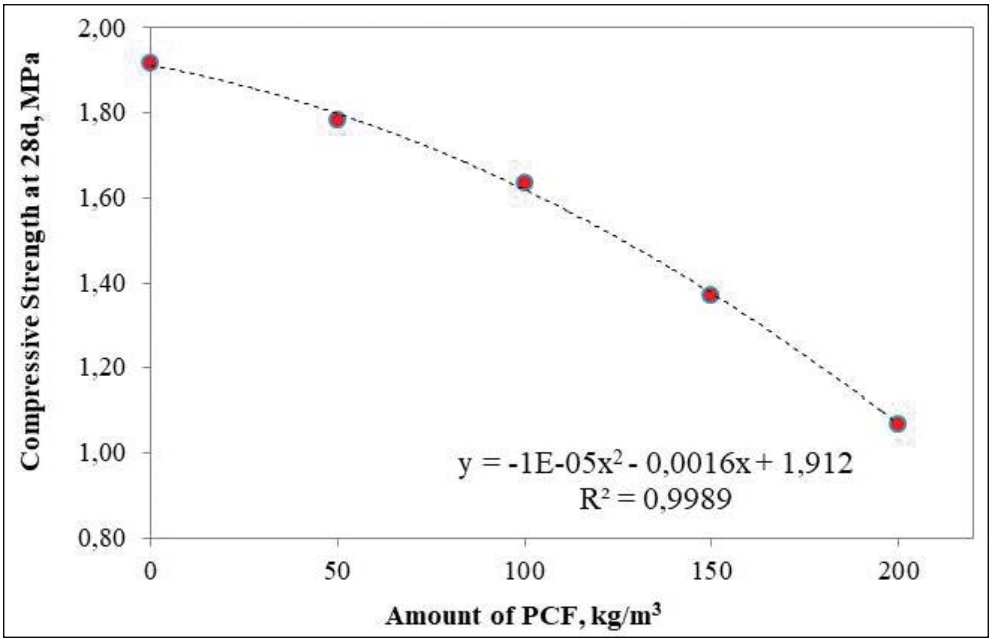

Figure 3- PC ash content-compressive strength relationship in foam concrete samples with equivalent densities.

Table 9- $\lambda_{10\text{-}dry}$ values of foam concrete samples.

No	**P0**		**P50**		**P100**		**P150**		**P200**	
	D	$\lambda_{10\text{-}dry}$	**D**	$\lambda_{10\text{-}dry}$	**D**	$\lambda_{10\text{-}dry}$	**D**	$\lambda_{10\text{-}dry}$	**D**	$\lambda_{10\text{-}dry}$
1	452	12,88	458	11,39	448	10,73	455	9,95	445	0,0948
2	452	12,85	454	11,31	448	10,73	457	9,91	455	0,0967
3	454	12,93	452	11,36	454	10,79	452	9,89	462	0,0979
Av.	**453**	**12,89**	455	**11,35**	450	**10,75**	455	**9,92**	**454**	**0,0965**
$\lambda_{10\text{-}dry}$: *Thermal conductivity coefficient of samples in 100% dry condition at dT = 10°C (W/mK)*										

As the amount of ash displaced by cement increases, the thermal conductivity values of foam concrete samples also decrease. The thermal conductivity of the P200 sample was 25% better than the control sample (Figure 4).

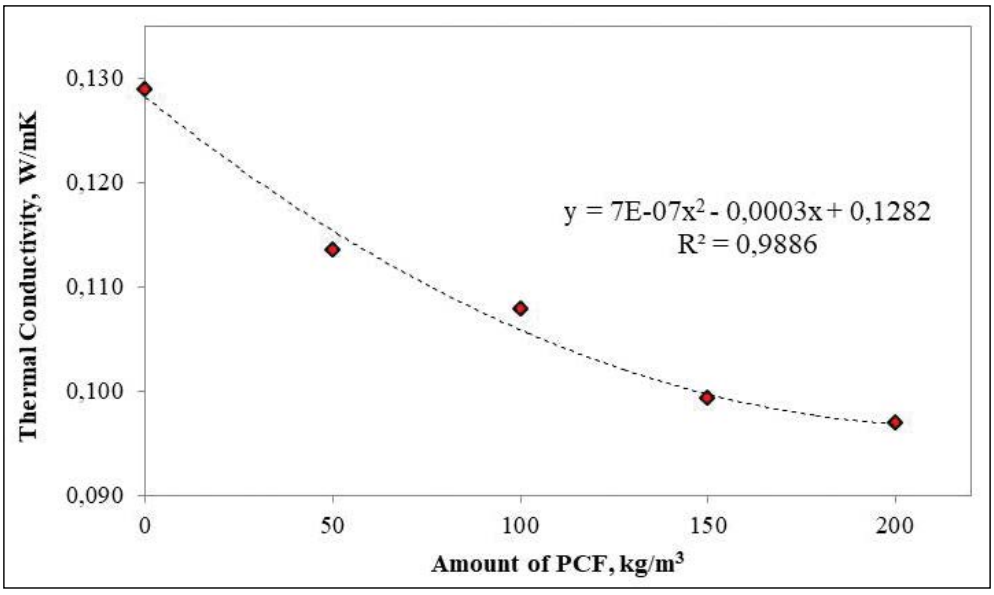

Figure 4- Relationship between PC ash content and thermal conductivity coefficient in the foam concretes with equivalent densities.

4. Conclusion

PC ash was classified as a lightweight aggregate when it was evaluated in terms of the physical properties (bulk density and oven particle density). The content of pozzolanic substance in PC ash was very high (81%) and other chemical properties were suitable for use in concrete. Moreover, PC ash provided the required criteria for F-class fly ashes. In the foam concrete, the aggregate should be the largest grain size less than 2 mm and the average grain size <0.6 mm. The largest grain size of PC ash is less than 2 mm and the fineness module is 0.5 mm.

In this study, PC ash was used as replacement of cement at 4 different rates in foam concrete with a density of 450 kg/m^3. Compared with the control mixture, the 28d-compressive strength of the mixture (P200) which is used the maximum PC was reduced by 44%. In addition, the P200 sample is 40% cheaper than the control mixture in terms of unit production costs for March 2018. Furthermore, according to the equivalent density values, the thermal conductivity of the P200 sample (0.097 W/mK) was 25% lower than the P0 sample (0.13 W/mK). This difference makes the P200 sample more advantageous in the production of precast wall and filler elements.

Considering the pozzolanic substance content of PC ash, it is possible to say that the increase in strength after 28 days according to the control mixture will accelerate under suitable cure conditions. In particular, if steam cure is applied, it can be expected that the resistance difference in the early ages will decrease significantly. As a result, the findings of this study revealed that PC ash that causes environmental pollution, can be used as an industrial raw material.

Reference

ACI 523. 1R. 1992. Guide for cast-in-place low density concrete. American Concrete Institute 1992.

Aldridge, D. 2000. Foamed concrete. Concrete 34 (4):20–2.

Durack J.M., Weiqing L. 1998. The properties of foamed air cured fly ash based concrete for masonry production. In: Page A., Dhanasekar M., Lawrence S., editors. In: Proceedings of 5th Australian masonry conference. Australia: Gladstone, Queensland 129-38.

Hunaiti Y.M. 1996. Composite action of foamed and lightweight aggregate concrete. Journal of Materials in Civil Engineering 3-111.

Jitchaiyaphum, K., Sinsiri, T., Chindaprasirt, P. 2011. Cellular Lightweight Concrete Containing Pozzolan Materials. Procedia Engineering Vol. 14, pp. 1157–1164.

Jones, M.R., McCarthy, A. 2005. Preliminary views on the potential of foamed concrete as a structural material. Magazine of Concrete Research 57: 21-31

Kearsly, E.P., Booyens, P.J. 1998. Reinforced foamed concrete, can it be durable. Concrete/Beton 91; 5-9.

Kearsly, E.P., Wainwright, P.J. 2001*a*. The effect of high fly ash content on the compressive strength of foamed concrete. Cement and Concrete Research 31 : 12-105.

Kearsly, E.P., Wainwright, P.J. 2001*b*. Porosity and permeability of foam Concrete. Cement and Concrete Research 35: 805-812

Kunhanandan, E.K., Ramamurthy, K. 2006. Influence of filler type on the properties of foam concrete. Cement and Concrete Composites 28: 475–480.

Mc Cormick, F.C. 1967. Rational propertioning of preformed foam cellular concrete. ACI Material Journal 64:9-104.

Ramamurthy, K., Nambiar, E.K., Ranjani, G. 2009. A classification of studies on properties of foam concrete. Cement and Concrete composite 31: 388-396.

Regan, P.E. Arasteh, AR., 1990. Lightweight aggregate foamed concrete. The Structural Engineer 68 (9): 73-167.

Rudnai, G. 1963. Lightweight concretes. Budapest, Akademikiado.

Short, A., Kinniburgh, W. 1963. Lightweight concrete. Asia Publishing House.

Slabaugh, S., Swan, C., Malloy, R. 2007. Development and Properties of Foam Concrete Synhetic Lightweight Aggregates. World of Coal Ash (WOCA) May 7-10, Covington Kentucky, USA.

Tikalsky, P.J. Pospisil, J., Mac Donald, W. 2004. A method assessment of the freeze – thaw resistance of performed foam cellular concrete, Cement and Concrete Research 34 (5), 889- 893.

Tam, C.T., Lim, TY., Lee, SI. 1987. Relationship between strength and volumetric composition of mosit-cured cellular concrete. Magazine of Concrete Research 39:12-8.

TS 13565, 2013. Lightweight sandwich masonry units with insulation layer. Turkish Standard Institute.

TS 3530 EN 933-1, 2012. Tests for geometrical properties of aggregates - Part 1: Determination of particle size distribution - Sieving method. Turkish Standard Institute.

TS EN 1097-3, 1999. Tests for mechanical and physical properties of aggregates- Part 3: Determination of loose bulk density and voids. Turkish Standard Institute.

TS EN 1097-6, 2013. Tests for mechanical and physical properties of aggregates - Part 6: Determination of particle density and water absorption. Turkish Standard Institute.

TS EN 12664, 2009. Thermal performance of building materials and products - Determination of thermal resistance by means of guarded hot plate and heat flow meter methods - Dry and moist products of medium and low thermal resistance. Turkish Standard Institute.

TS EN 13055, 2013. Lightweight aggregates. Turkish Standard Institute.

TS EN 206, 2017. Concrete - Specification, performance, production and conformity. Turkish Standard Institute.

TS EN 450-1, 2013. Fly ash for concrete - Part 1: Definition, specifications and conformity criteria. Turkish Standard Institute.

Van Dijk, S. 1991. Foamed concrete: A Dutch View. British Cement Association 49-53.

Bulletin of the Mineral Research and Exploration

http://bulletin.mta.gov.tr

Determination of the origin and recharge process of water resources in Salda Lake Basin by using the environmental, tritium and radiocarbon isotopes (Burdur/Turkey)

Simge VAROL[a*], Ayşen DAVRAZ[b], Fatma AKSEVER[b], Şehnaz ŞENER[b], Erhan ŞENER[c], Bülent KIRKAN[a] and Ahmet TOKGÖZLÜ[d]

[a]*Suleyman Demirel University, Water Institute, Isparta, Turkey*
[b]*Suleyman Demirel University, Department of Geological Engineering, Isparta, Turkey*
[c]*Suleyman Demirel University, Remote Sensing Centre, Isparta, Turkey*
[d]*Suleyman Demirel University, Department of Geography, Isparta, Turkey*

Research Article

Keywords:
Stable isotope, Tritium, Radiogenic isotope, Salda Lake.

ABSTRACT

The Salda Lake basin which is in the southwestern Turkey is an important water body in view of environmental values. We used stable isotopes (δD and $\delta^{18}O$), $\delta^{3}H$ and ^{14}C composition of the water samples to understand recharge process effective in the groundwater and lake water. Water samples were collected in dry and wet periods and the stable isotope (δD and $\delta^{18}O$) and radiogenic isotope (^{14}C) analysis were made in the basin. The $\delta^{18}O$ contents of groundwater and lake water ranged from -9,94‰ to 1,18‰ in dry period and from -10,24‰ to 0,30‰, in wet period. δD contents of groundwater and lake water varied from -67,42‰ to 1,20‰ and from -64,51‰ to -2,80‰, in dry and period wet respectively. The stable isotope data of samples indicate a meteoric origin for all samples. According to stable isotope data, groundwater samples seem to be recharged from higher elevations whereas the lake water is recharged from low elevations. The tritium ($\delta^{3}H$) content of the water samples ranges from 1.04 to 4.49 TU and from 1.91 to 4.18 TU in the dry period and wet period respectively. Long-term $\delta^{3}H$ observations are required to determine whether these $\delta^{3}H$ signals are associated with young recharge or with the groundwater with long residence time. In addition, the ^{14}C activities of the samples vary between 90 pmc and 110 pmc for Salda Lake waters and 530 pmc and 5990 pmc for the groundwater.

Received Date: 29.10.2018
Accepted Date: 13.02.2019

1. Introduction

Surface and groundwater perform an important function, the maintenance of the natural environment and ecosystems with a continuous recycling and renewal process of evaporation, precipitation and runoff in nature as well as supplying freshwater for human necessities such as agriculture, drinking water, industry and recreation (Çaldırak and Kurtuluş, 2018). Unfortunately, it is difficult to understand how the recharge processes in surface and groundwater. Therefore, the isotopes of oxygen $\delta^{18}O$ and hydrogen δD are used as major tracers for determining the origin and movement of groundwater (Subyani, 2004). The isotopic properties of oxygen and hydrogen are influenced by atmospheric and surface processes during recharge of the groundwater (Gupta and Deshpande, 2005). In addition to the environmental isotopes in groundwater studies as tracers of groundwater provenance and age, isotopes

Citation Info: Varol, S., Davraz, A., Aksever, F., Şener, Ş., Şener, E., Kırkan, B., Tokgözlü, A. 2020. Determination of the origin and recharge process of water resources in Salda Lake Basin by using the environmental, tritium and radiocarbon isotopes (Burdur/Turkey). Bulletin of the Mineral Reserach and Exploration, 161, 57-70. https://doi.org/10.19111/bulletinofmre.604352

* *Corresponding author: Simge VAROL, simgevarol@sdu.edu.tr*

are also used to study the quality of groundwater, geochemical evaluation, water-rock interaction, the origin of salinity, recharge processes and contaminant processes. Also, tritium isotope (δ^3H) is always introduced into the hydrological circulation and dated with the fallout from atmospheric nuclear weapon tests conducted mainly during the early 1960s. It can be indirectly used to evaluate the rate of groundwater circulation and renewal rate (Clark and Fritz, 1997; Mokadem et al., 2017). Furthermore, the relationships between the physicochemical parameters and the isotopic properties of water are very important in understanding the recharging process of natural resources. (Baykal et al. 1996; Çaldırak and Kurtuluş, 2018).

In this study, the Salda Lake basin is selected as the investigation area. Because, Salda Lake within the basin is an important surface water in terms of environmental. Firstly, Salda Lake is one of the largest and deepest (about 184m) enclosed saline lakes of Turkey (Kazancı et al., 2004). It is highly alkaline (pH 8–10) and magnesium rich. Also, the magnesite deposits located around of the lake, were related to ‘‘White Rock’’ which was also discovered on Mars (Russell et al., 1999). Furthermore, in the Salda Lake basin, the groundwater which is recharge to Salda Lake, is used intensely as drinking, domestic and irrigation purposes. Therefore, the main purpose of the study is to reveal the origin and recharging of groundwater and surface water in the basin using the environmental isotopic, radiocarbon and physicochemical properties of water.

2. Materials and Methods

2.1. Study Area

The Salda Lake basin which is in the southwestern Turkey at 42 59404 - 44 4624N and 1799785 - 734837E and covers an area of 207.14 km^2 (Figure 1). Basin is an important water body in view of environmental values. The Salda Lake basin is a depression basin with closed basin characteristics, formed by the effect of tectonism at the end of Neogene (Lise et al., 2013). The Quaternary alluvium in the Salda Lake basin covers up to 34.84 km^2. The thickness of the aquifer is 5 to 60 m in the Yeşilova and its surroundings. The aquifer system is composed of sand, gravel, clay and mudstone levels (Table 1). The mean annual precipitation and real evaporation are approximately 494.10 mm and 345.91mm/year in the basin, respectively (Varol et al., 2017).

2.2. Sampling and Analytical Methods

Total 34 water samples collected from wells, springs, stream and lake waters were analyzed in November 2015 (dry period) and June 2015 (wet period) for the determination of their hydrochemical characteristics and their stable isotope (δD, $\delta^{18}O$, δ^3H and ^{14}C) composition in the study area. All sample's locations were determined on Global Positioning System (GPS). Physical parameters (pH, temperature (T; °C) and electrical conductivity (EC; mS/cm)) of the water samples were measured in-situ with YSI Professional Plus multiparameter instrument (YSI 6050). Samples were collected in 100 ml clean polyethylene bottles and dispatched for analysis to the laboratory in an ice-filled box. The major cations were analyzed by ICP-MS (Inductively Coupled Plasma-Mass Spectrometer) at the Bureau Veritas Commodities Canada Ltd. (ACME Laboratory Vancouver, Canada, an ISO 9002 accredited company). CO_3^{2-} and HCO_3^-, anions were analyzed by titrimetric method; Cl^-, and SO_4^- were determined using ion chromatography at Water Chemistry Laboratory at Hacettepe University (Ankara, Turkey). The accuracy of the analysis can for major ions be estimated from the electrical balance (E.B.) since the sum of positive and negative charges in the water should be equal:

$$\text{Electrical Balance (\%)} = (\text{Sum cations} + \text{Sum anions}) / (\text{Sum cations} + \text{Sum anions}) \times 100 \quad [1]$$

Where cations and anions are expressed as meq/L and inserted with their charge sign. The sums are taken over the cations Na, K, Mg^{2+} and Ca^{2+}, and anions Cl, HCO^-_3 and SO_4^{2-} (Appelo and Postma 2005). In this study, E.B (%) was used to determine accuracy of the major ions analysis (Table 2).

Water samples for oxygen ($\delta^{18}O$), deuterium (δD), tritium (δ^3H), isotopic analysis was analyzed at the Hacettepe University International Karst Water Resources Research Center and for ^{14}C analysis was analyzed at Geochron Laboratories Massachusetts (U.S.A.). $\delta^{18}O$ and δD from isotopic compositions of the samples were determined using International Atomic Energy Agency (IAEA)-Equilibration method. Also, δ^3H was determined using IAEA-Liquid Siltation

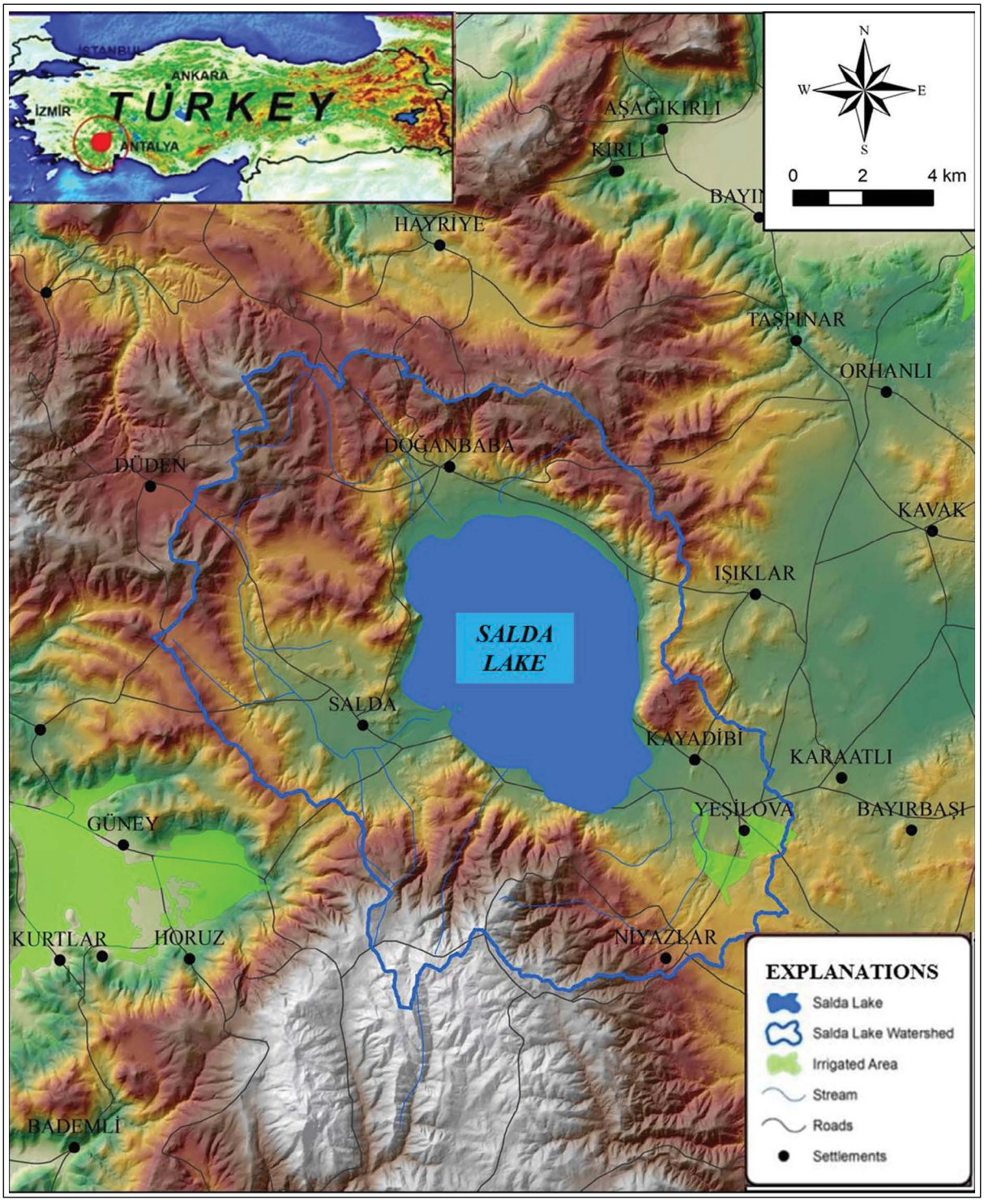

Figure 1- Location map of the study area (1/200.000 scale).

Counting (LSC) Technique. The amounts of Tritium (δ^3H) are determined as absolute concentrations, using tritium units (TU). The tritium unit is 1 TU = 0.1183 Bq/L. The precision of measurements is ±1 TU. Determination of natural radioactivity in drinking water samples were used EPA 900.0 method.

Table 1- Stratigraphic relation of the formations and hydrogeological properties.

Geochronology			Lithostratigraphy		Lithology
Time	**Period**	**Epoch**	**Formation**	**Symbol**	**Explanations**
CENOZOIC	Quaternary		Alluvium	Qal	Sand, gravel, mud and block deposits.
			Slope debris	Qym	Blocks and gravel deposits on mountain slopes and skirts
	Tertiary	Pliocene Miocene	Çameli formation	Plç	Claystone, siltstone, marl, clayey limestone, sandstone, mudstone and conglomerate
MESOZOIC	Cretaceous	Late Cenoniyen	Kızılcadağ Ophiolitic Melange	Kkzm	Serpentinite, serpentinized harzburgite, dunite, radiolarite, chert, basic volcanite, neritic limestone, pelagic limestone, dolomite
			Marmaris Peridotite	Kmo	Serpentinized ultramafic rocks, harzburgite, serpentinite, very olivine serpentinized dunites
			Dunite Member	Kmod	
		Liyas	Iğdır Metamorphic	Kmoi	Amphibolite, amphibole schist, marble, quartzite, metabasalt
			Orhaniye formation	JKo	Basic volcanics, radiolarite, chert intermittent micrite
	Jura Triyas		Dutdere Limestone	TRJd	Few megaladon recrystallized limestones

3. Results and Discussions

3.1. Geology

The interaction time of groundwater with the lithological units control the chemical compound of the groundwater. Therefore, firstly the lithological units in the study area have been investigated. The lithological units are observed as Autochthonous and allochthonous units within the study area. Allochthonous units are composed from Marmaris Peridotite and Dunite Member, Kızılcadağ Ophiolitic Melange, Iğdır Metamorphites, Dutdere Limestones and Orhaniye formation. The autochthonous units are Alluvium and slope debris with Çameli formation (Şenel et al., 1989) (Table 1, Figure 2). The lithological formations in the study area have different hydrogeological properties. Alluvium which is the most important aquifer in the study area has an area of roughly 34.84 km^2. When the well logs are examined, it is seen that the thickness of alluvium is between 5 and 60 m in the study area.

3.2. Hydrochemistry

3.2.1. Seasonal Evaluation of Physical Parameters

The physical parameters of water samples were made in-situ for two seasons and the measurements (pH, EC, T (°C)) shown in table 2. The EC_{25} of groundwater samples in wet and dry season ranges from 296 to 1075 µs/cm and ranges from 279 to 1119 µs/cm, respectively. The EC_{25} of surface water samples in wet and dry season ranges from 532 to 2275 µs/cm and ranges from 759 to 2358 µs/cm, respectively. The temperature (°C) of groundwater samples in wet and dry season ranges from 11,5 to 21,4 °C and ranges from 8,5 to 16,1°C, respectively. The temperature (°C) of surface water samples in wet and dry season ranges from 17,7 to 23,5 °C and ranges from 14.6 to 15,6 °C, respectively. Temperature (°C) changes in surface water samples are related to climatic conditions. The pH of groundwater samples in wet and dry season ranges from 7,38 to 9,33 and ranges from 7,4 to 11, respectively. The pH of surface water samples in wet and dry season ranges from 8,39 to 9,08 and ranges from 8,02 to 8,62, respectively (Table 2). The pH values increased in wet season for water samples (Table 2). Generally, seasonally increase in physical parameters of water samples is related to the high interaction between rock and rainwater (Makwe and Chup, 2013; Ngabirano et al., 2016). Carbonates, bicarbonates, hydrooxides, phosphates, silicates and borates reduce the number of hydrogen ions (H^+) in water and the water gains basic character. The increase in hydrogen ion usually causes acidic water. There is a close relationship between HCO_3^- and CO_3^{2-} ions which are the main sources of alkalinity in water and H^+ ion concentrations in water. When the pH of the water exceeds 8,2, the bicarbonate ions are separated

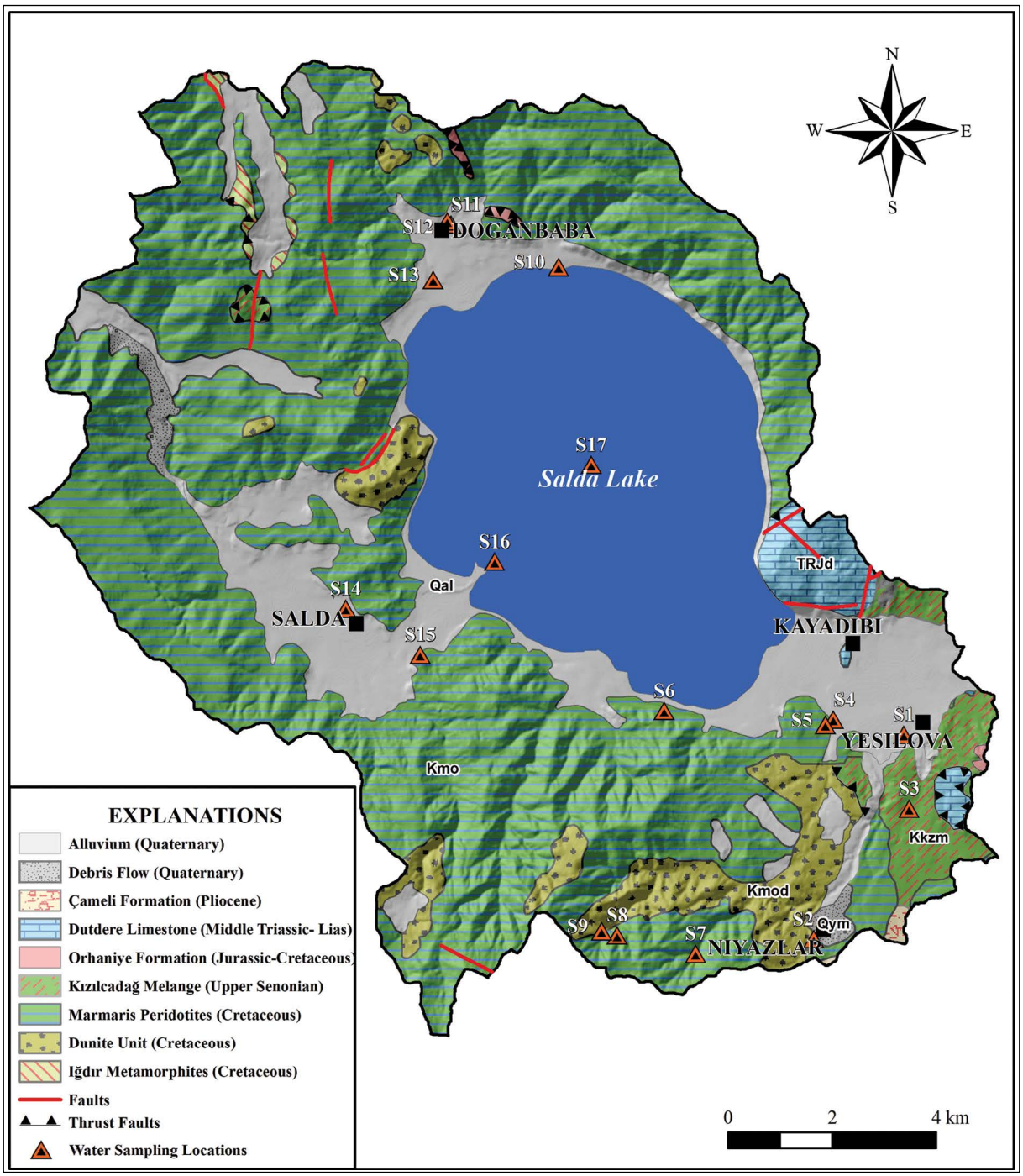

Figure 2- Geological map of the region [modified from Şenel et al. (1997).

into carbonate and hydrogen ions. In this condition, if the pH of the water is above 8,2, the CO_3^{2-} ions increase and if it is below this value, the HCO_3^- ion becomes the dominant ion. The presence of such a relationship is observed in the water samples in the study area. Electrical conductivity of water depends on the presence of ions in the water, total concentrations and temperature. The increase in temperature and ion concentration is proportional to the increase in electrical conductivity (Şahinci, 1991; Erguvanlı and Yüzer, 1987). Thus, due to the interaction of rock water, there is an increase in pH and EC values in groundwater and surface waters in the study area.

3.2.2. Seasonal Evaluation of Major Ions

The major chemical constituents of water samples were analyzed at two seasons (June 2015 and November 2015). In addition, the accuracy of major ion analysis results was evaluated with E.B (%).When the electrical balance results are examined, S1, S2, S5, S7, S14, S16 (for wet season), S10, S12, S13, S16 and S17 (for dry season) water samples have more than 5% error rate. Therefore, these samples have not been considered in chemical assessments. The results of the analysis are shown in table 2.

According to this, major carbonate rocks such as limestone and dolomitic limestone are the origin of Ca^{2+} and Mg^{2+} in water. The increase at Mg^{2+} in dry and wet seasons was observed at groundwaters discharged within the Kızılcadağ Ophiolite and Mélange. In the same way, Mg^{2+} increases in the surface waters associated with Kızılcadağ Ophiolite and Mélange. The major origin of Mg^{2+} in the groundwater and surface waters within the study area are ion exchange of minerals in rocks with water. The increase at K^+ which is another major ion was observed for both two seasons at S11. Likewise, this increase is related to ion exchange due to water-rock interaction.

HCO_3^- is the major anion component of the groundwater and surface waters. The HCO_3^- content of groundwater samples in wet and dry season range from 1,70 to 14,30 meq/L and 0,50 to 9,80 meq/L, respectively (Table 2). The major origin of HCO_3^- generally is due to the water- rock interaction and oxidation of organic matter. The Cl^- ion concentration at most of the samples in dry season increases related to water-rock interaction between rainwater with Kızılcadağ Ophiolite and Mélange in discharged waters from the contact of the Dutdere Limestone and Kızılcadağ Ophiolite and Mélange. The SO_4^{2-} originates from oxidation of sulphite (Ranjan et al., 2013). The SO_4^{2-} content of groundwater samples in wet and dry season range from 0,03 to 0,32 meq/L and 0,00 to 0,76 meq/L, respectively (Table 2). The SO_4^{2-} content of surface water in wet and dry season range from 0,06 to 0,34 meq/L and 0,10 to 0,35 meq/L, respectively (Table 2).

3.2.3. Hydrogeochemical Facies

Determination of hydrogeochemical facies it is important to determine the chemical background and origin of groundwater. It was developed by Piper (1944) to demonstrate the similarities and/or differences in the chemical properties of groundwater based on dominant cations and anions. Piper trilinear diagram were prepared for dry and wet seasons samples in the study area. According to the diagrams, the groundwater and stream water are "Mg^{2+}-CO_3^{2-}-HCO_3^-, Mg^{2+}-Ca^{2+}-CO_3^{2-}-HCO_3^- and Ca^{2+}-Mg^{2+}- HCO_3^- " facies, and lake water is Mg^{2+}- CO_3^{2-}-HCO_3^- facies in the basin (Figure 3).

Table 2- Physical and chemical parameters of water samples.

Season	Sample No	Sample Type	pH	EC (µs/cm)	EC_{25} (µs/cm)	T (^{o}C)	Ca^{2+} meq/L	Mg^{2+} meq/L	Na^{+} meq/L	K^{+} meq/L	CO_3^{-} meq/L	HCO_3^{-} meq/L	Cl^{-} meq/L	SO_4^{2-} meq/L	Σ Cation meq/L	Σ Anion meq/L	Electrical Balance %
JUNE 2015 (WET SEASON)	**S1**	Well	7,58	543	689	13,9	3,16	5,43	0,62	0,02	0,00	6,80	0,49	0,77	9,23	8,06	**6,74**
	S2	Spring	8,43	459	559	15,6	0,86	7,61	0,14	0,00	1,60	5,80	0,08	0,08	8,61	7,55	**6,56**
	S3	Spring	7,38	427	542	13,9	3,21	3,16	0,76	0,01	0,00	6,10	0,24	0,32	7,13	6,66	3,46
	S4	Stream	8,57	517	532	23,5	0,72	7,13	0,14	0,01	2,00	5,10	0,11	0,06	8,00	7,27	4,79
	S5	Stream	8,39	704	735	22,8	1,27	9,78	0,24	0,01	1,80	7,80	0,15	0,08	11,30	9,83	**6,97**
	S6	Spring	9,13	467,3	597	13,6	0,13	10,01	0,10	0,01	4,20	4,90	0,09	0,09	10,25	9,28	4,95
	S7	Spring	8,27	506	585	17,9	0,41	8,51	0,10	0,01	1,00	6,60	0,06	0,05	9,04	7,72	**7,87**
	S8	Spring	8,36	346,1	393	18,8	0,46	5,11	0,10	0,00	1,40	3,80	0,06	0,05	5,68	5,31	3,32
	S9	Spring	9,05	275,9	296	21,4	0,14	4,33	0,06	0,01	2,60	1,70	0,04	0,03	4,53	4,38	1,69
	S10	Spring	7,81	845	1020	16	0,62	15,12	0,14	0,01	0,00	14,30	0,10	0,10	15,89	14,51	4,54
	S11	Spring	7,73	399,9	539	11,5	0,96	6,62	0,24	0,13	0,00	7,30	0,09	0,12	7,95	7,52	2,80
	S12	Well	8,15	707	874	15	0,52	12,69	0,22	0,01	0,60	10,60	0,24	0,20	13,44	11,63	7,21
	S13	Stream	8,39	546	634	17,7	0,89	8,72	0,18	0,02	1,40	7,50	0,08	0,07	9,81	9,05	3,98
	S14	Well	8,35	925	1075	17,7	0,26	3,85	1,02	0,08	3,40	0,20	0,68	0,01	5,20	4,30	**9,57**
	S15	Spring	9,33	312,7	369	17	0,11	5,63	0,05	0,01	3,60	1,70	0,05	0,04	5,80	5,40	3,62
	S16	Salda Lake	-	-	-	-	0,20	25,06	7,13	0,60	19,20	12,20	4,94	0,35	32,98	36,70	**-5,34**
	S17	Salda Lake	9,08	2066	2275	20,2	0,17	27,13	8,53	0,68	19,20	12,20	5,06	0,34	36,51	36,80	-0,39
NOVEMBER 2015 (DRY SEASON)	**S1**	Well	7,4	489,9	631	13,3	3,20	5,41	0,49	0,01	0,00	7,20	0,55	0,76	9,11	8,52	3,35
	S2	Spring	8,63	395,7	578	8,5	0,79	7,18	0,12	0,01	1,60	6,00	0,09	0,07	8,10	7,76	2,12
	S3	Spring	7,53	427,5	539	14,2	3,03	2,96	0,63	0,01	0,00	6,00	0,24	0,30	6,63	6,54	0,64
	S4	Stream	-	-	-	-	-	-	-	-	-	-	-	-	-	-	-
	S5	Stream	-	-	-	-	-	-	-	-	-	-	-	-	-	-	-
	S6	Spring	9,31	422,1	557	12,3	0,09	8,54	0,08	0,01	4,40	4,20	0,10	0,09	8,72	8,79	-0,42
	S7	Spring	8,49	400,9	508	14	0,49	6,35	0,09	0,00	1,00	6,40	0,09	0,06	6,93	7,55	-4,29
	S8	Spring	8,57	294,9	372	14,2	0,41	4,60	0,08	0,00	1,20	3,40	0,07	0,05	5,09	4,72	3,79
	S9	Spring	9,25	219,7	279	13,9	0,14	3,62	0,05	0,00	2,20	1,90	0,05	0,04	3,81	4,19	-4,78
	S10	Spring	7,89	929	1119	16,1	0,65	16,18	0,14	0,01	0,00	15,00	0,12	0,04	16,99	15,17	**5,66**
	S11	Spring	7,95	618	760	15,2	1,06	9,25	0,27	0,15	0,00	9,80	0,23	0,14	10,72	10,17	2,68
	S12	Well	7,87	751	933	14,8	1,60	11,25	0,32	0,02	0,20	10,80	0,39	0,32	13,18	11,71	**5,90**
	S13	Stream	8,62	608	759	14,6	0,86	10,02	0,30	0,04	1,60	8,00	0,20	0,10	11,21	9,89	**6,26**
	S14	Well	9,84	247,4	307	14,9	0,13	2,41	0,87	0,04	2,40	0,50	0,81	0,00	3,44	3,71	-3,71
	S15	Spring	11	233,3	334	9,23	0,13	3,99	0,05	0,01	1,60	2,60	0,05	0,04	4,18	4,29	-1,37
	S16	Salda Lake	8,02	1912	2358	15,1	0,23	27,67	8,89	0,74	30,50	8,85	5,65	0,34	37,53	45,34	**-9,43**
	S17	Salda Lake	8,22	1921	2341	15,6	0,23	27,23	8,74	0,63	28,47	8,85	5,81	0,35	36,83	43,48	**-8,28**

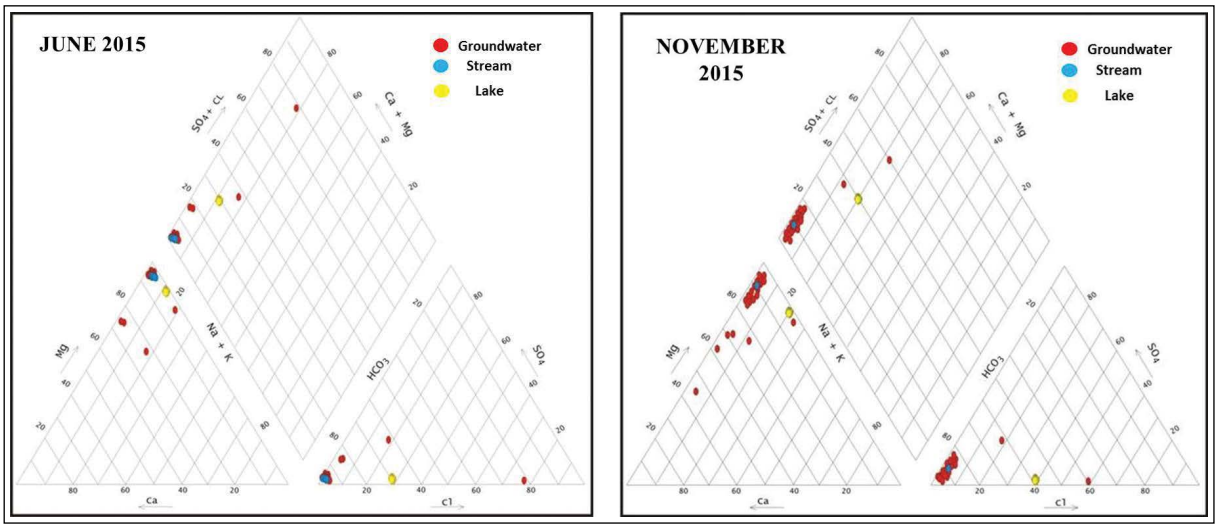

Figure 3- Piper diagrams prepared for dry and wet season (Piper, 1944).

3.3. Evaluation by Using the Stable Isotopes, Tritium and Radiocarbon of Water Samples

3.3.1. Evaluation the Stable Isotope (hydrogen and oxygen) Composition of Water Samples

The environmental isotopes of oxygen ($\delta^{18}O$), tritium ($\delta^{3}H$) and deuterium (δD) are excellent tracers for determining the origin of groundwater. The stable isotope analyses were made in wet and dry season in the Salda Lake basin. Table 3 contains data of isotopic compositions of groundwater and surface water.

The isotope compositions in water samples range from -10,24‰ to 0,30‰ $\delta^{18}O$ (wet season) and range from -10,08‰ to 1,86‰ $\delta^{18}O$ (dry season), respectively. The δD composition in water samples range from -64,51‰ to -2,80‰ (wet season) and range from -69,14‰ to 0,02‰ (dry season), respectively (Table 3).

The relationship between the $\delta^{18}O$ and δD values of water samples is plotted in figure 4. In this graphic is shown the Global Meteoric Water Line ($\delta D = 8\delta^{18}O + 10$) with d-excess value of 10‰ (Craig, 1961) and the Meteoric Water Line of Lake District in Turkey ($\delta D = 8\delta^{18}O + 14,6$) with d-excess value of 14.6‰ (Dilsiz, 2006).

According to the diagram (June 2015 in figure 4) large part of the water samples (S2, S4, S5, S6, S7, S16, S8, S10, S11, S12, S13, S14, S15) are located around the Global Meteoric Water Line ($\delta D = 8 * \delta^{18}O + 10$) and in addition S9 is in regions near the Lake Region Meteoric Water Line (Figure 4). This situation proves that the groundwater and surface waters in the study area are meteoric origin. The location of the S3 spring water deviates from the GMWL line to the right in June 2015. This indicates that water-rock interaction is dominant in S3. In addition, evaporation was observed to be dominant in S16 and S17 samples taken from Salda Lake during this period.

According to the diagram (November 2015 in figure 4) large part of the water samples (S2, S6, S7, S8, S9, S10, S11, S12, S13, S14 and S15) are located around the Global Meteoric Water Line ($\delta D = 8 * \delta^{18}O + 10$). This situation proves to be meteoric origin of groundwater and surface waters in the study area as in June 2015. Besides, it was determined that water rock interaction was more dominant especially in S1, S3, S4 and S5 samples compared to Nov 2015 and June 2015. In addition, evaporation was observed in S16 and S17 samples taken from Salda Lake during this period. In addition, evaporation was dominant in S16 and S17 samples taken from Salda Lake during this period (Figure 4).

3.3.2. Evaluation the D-Excess Values of Water Samples

Another evidence for the origin of recharge of groundwater within the study area is obtained from the value of the deuterium excess (d-excess). Locally, d-excess values due to differences in meteorological state at the source region of the vapour mass vary

Table 3- Isotopic composition of groundwater.

Season	Sample No	Sample Type	$d^{18}O$	δD	d-excess* (‰)	^{3}H (TU)	$d^{13}C$ ‰	^{14}C (year)
JUNE 2015 (WET SEASON)	S1	Well	-8,90	-60,01	11,19	-	-	-
	S2	Spring	-9,28	-59,77	14,47	3,28	-15,6	530
	S3	Spring	-7,69	-55,91	5,61	1,91	-	-
	S4	Stream	-8,10	-54,28	10,52	3,07	-14,4	700
	S5	Stream	-8,14	-56,30	8,82	2,66	-	-
	S6	Spring	-9,21	-63,03	10,65	2,48	-16,3	5820
	S7	Spring	-9,68	-63,34	14,10	3,16	-16,6	2130
	S8	Spring	-9,80	-61,86	16,54	-	-16,5	2260
	S9	Spring	-10,24	-64,51	17,41	3,71	-16,0	5990
	S10	Spring	-8,74	-57,60	12,32	-	-15,8	1020
	S11	Spring	-8,80	-58,16	12,24	3,18	-	-
	S12	Well	-8,62	-56,54	12,42	-	-	-
	S13	Stream	-8,23	-53,75	12,09	-	-	-
	S14	Well	-8,50	-57,58	10,42	-	-	-
	S15	Spring	-9,74	-62,10	15,82	-	-	-
	S16	Salda Lake	-1,41	-12,54	-1,26	-	-0,8	110
	S17	Salda Lake	0,30	-2,80	-5,20	4,18	-0,7	90
NOVEMBER 2015 (DRY SEASON)	S1	Well	-8,58	-61,04	7,60	2,53	-	-
	S2	Spring	-9,23	-66,04	7,80	2,97	-	-
	S3	Spring	-7,55	-59,23	1,17	1,74	-	-
	S4	Stream	-7,89	-52,81	10,31	3,01		
	S5	Stream	-7,77	-51,47	10,69	2,45		
	S6	Spring	-9,33	-64,54	10,10	2,34	-	-
	S7	Spring	-9,51	-64,18	11,90	3,12	-	-
	S8	Spring	-9,94	-67,42	12,10	3,04	-	-
	S9	Spring	-10,08	-69,14	11,50	3,67		
	S10	Spring	-9,05	-61,29	11,11	3,42	-	-
	S11	Spring	-8,87	-59,04	11,92	3,38		
	S12	Well	-8,99	-60,71	11,21	3,35	-	-
	S13	Stream	-8,56	-58,76	9,72	-	-	-
	S14	Well	-8,52	-57,39	10,77	1,04	-	-
	S15	Spring	-9,91	-63,55	15,73	2,77	-	-
	S16	Salda Lake	1,86	0,02	-14,86	4,02	-	-
	S17	Salda Lake	1,75	-1,68	-15,68	4,27	-	-

* *d-excess = δD - 8$\delta^{18}O$ (Dansgaard 1964)*

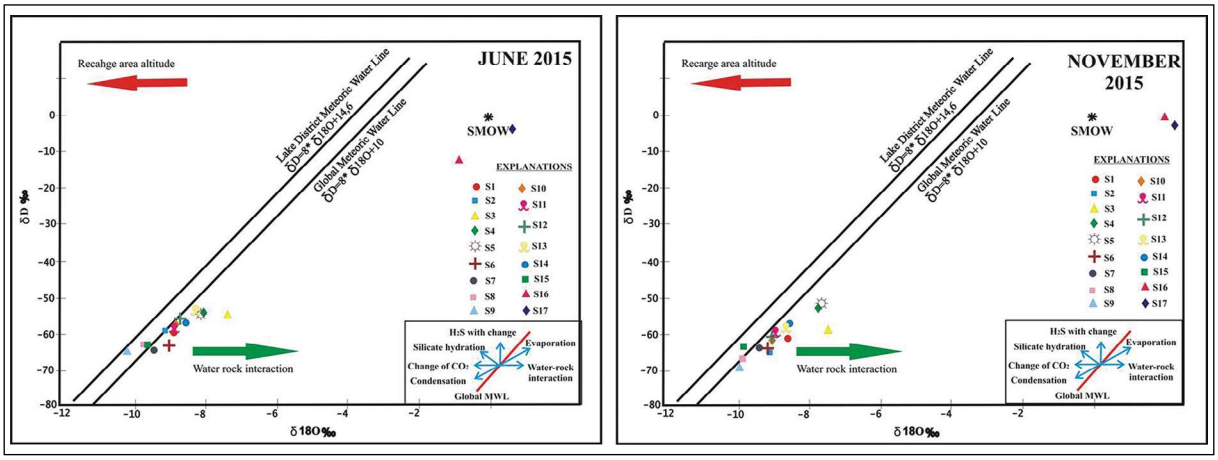

Figure 4- Graphic of δD and $\delta^{18}O$ for Salda Lake basin water samples in wet and dry season (June and November 2015).

(Merlivat and Jouzel 1979). The d-excess values are defined by the following equation (Dansgaard 1964);

$$d\text{-excess} = \delta D - 8\delta^{18}O \quad [2]$$

The d-excess values for the water samples in the study area varied from -5,2 to 17,41‰ and from -16,44 to 15,73‰ for wet and dry seasons, respectively (Table 3).

According to the results of the analysis, samples of S3, S5, S16 and S17 are lower than 10 and other waters are higher than 10 in wet seasons (June 2015). In dry seasons (November 2015), the samples with the numbers of S1, S2, S3, S13, S16 and S17 are lower than 10 while the other waters are higher than 10. According to this, waters with excess deuterium values of more than 10, atmospheric and marine origin precipitation waters with high velocity evaporation effect of the regions; Waters with values lower than 10 are originating from terrestrial rainfall under the influence of evaporation.

3.3.3. Evaluation the Tritium Values of Water Samples

$\delta^{18}O$-^{3}H relation; tritium is produced in the upper atmosphere. Tritium is a short-lived isotope of hydrogen with a half-life of 12,43 years. The tritium in groundwater indicates that the aquifer is being recharged with water that originated before or after 1950s (Schlosser et al., 1988; Busenberg and Plummer, 1993; Aggarwal et al., 2000). Activity of geogenic ^{3}H in most groundwater is negligible. Thus measurable ^{3}H in groundwater samples virtually always signifies modern recharge (Clark and Fritz, 1997).

The tritium concentrations in the groundwater and surface water samples are very low and ranging from 1,91 to 4,18 TU (wet season) and from 1,04 to 4,27 TU (dry season), respectively (Table 3). The diagram of tritium values versus $\delta^{18}O$ of water samples is shown figure 5. According to the results of the analysis (S2, S7 and S9) is recharge from higher elevations than the other samples in wet seasons at the study area. In addition, S8, S9, and S15 are recharge from higher elevations than the other samples in dry seasons. Also, S3 spring water in wet season is the deepest and the longest stay in the underground. In dry season same way, S3 and S14 waters are the deepest and the longest stay in the underground.

$d^{2}H$ - ^{3}H relation; tritium, one of the radioactive

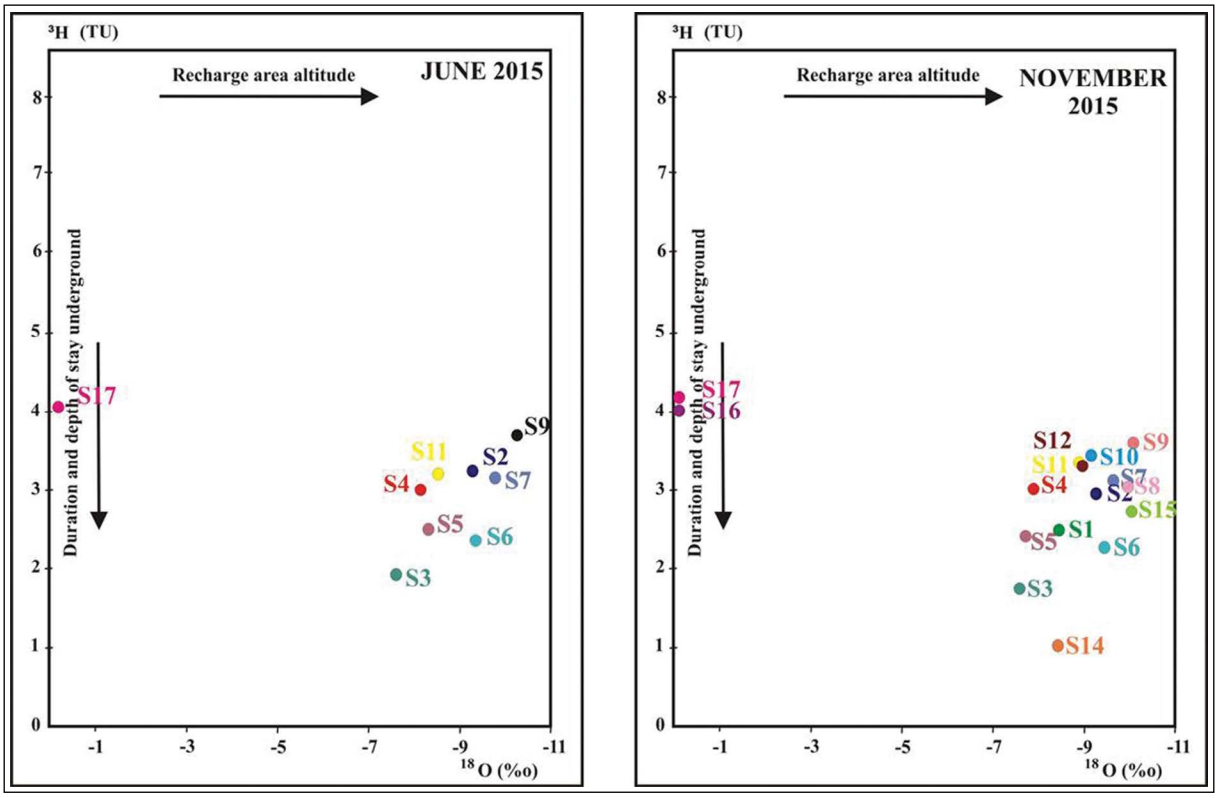

Figure 5- ^{3}H - $\delta^{18}O$ graphic (June and November 2015).

isotopes, undergoes continuous decay through natural half-life. Accordingly, if the content of tritium in the rainfall that supplies the groundwater is known, can be suggested ideas about determining the weighted average age of the groundwater or mixing conditions of different groundwater. The d^2H - ^3H chart reflects the relationship between recharge elevations in water and the duration of stay in the aquifer. In this graph, the recharge area elevation in the initial direction of the horizontal axis (d^2H) and the continuation of the aquifer in the initial direction of the vertical axis (^3H) are increasing (Afşin et al., 2007). Figures prepared with d^2H and ^3H values of the samples taken in June 2015 and November 2015 periods in the study area are presented in figure 6. According to ^3H values, in the wet season (June 2015), S9 has the youngest, shallowest and fastest circulating water feature. S3 is the oldest, deepest and slowest circulating water in the same period. Other water samples represent shallow and medium circulating waters with mixing and transitional water characteristics. According to the results of the dry season (November 2015) analysis, the water with the deepest and slowest circulation in the samples is taken from the well of S14. In the same period, the spring (S10) is the shallowest and fastest circulating groundwater. Lake water samples (S16, S17) represent shallow and medium circulating waters in the mixture and transitional waters.

EC_{25} - ^3H relation; the isotope of tritium (^3H), which is used for isotopic evaluation of water, is radioactive in proportion to the residence time of groundwater in the reservoir. Therefore, ^3H isotope is one of the most important parameters in determining the relative ages of groundwater. Similarly, the EC value of the samples also increases due to the residence time of the groundwater in the reservoir (Guner and Guner, 2002).

In periods (June (S17), November (S16, S17)), the high tritium and low EC_{25} values of the samples taken from the Salda Lake indicate that the transition times of these waters are short. S4, S5 and S7 samples in June 2015 and S10, S12 samples in November 2105 have low tritium and high EC_{25} values show that these spring waters are deeply circulated (Figure 7). Also, S2, S3, S6, S9 and S11 (June-2015) and S1, S2, S3, S6, S7, S8, S9, S11, S14 and S15 (Nov-2015) samples have low EC_{25} value and tritium content. This shows that the samples are deeply circulated.

3.3.4. Evaluation the Radiogenic Isotope Values of Water Samples

The main sources of the carbon element in the groundwater are (i) atmospheric CO_2, (ii) organic CO_2 resulting from the organic activities in the infiltration zone, (iii) geogenic CO_2, and (iv) carbonate (CO_3) ions that are absorbed by the dissolution of carbonate minerals. The main sources of geogenic CO_2 are metamorphism of carbonate rocks and ground-mantle CO_2 escape. Atmospheric and biogenic CO_2 contains ^{14}C, whereas geogenic and dissolved CO_2 do not contain ^{14}C at all. The carbon element provided by CO_2 sources in the groundwater is called Total Dissolved Inorganic Carbon (TDIC). ^{14}C age determination studies of groundwater are mostly used with ^{14}C origin of TDIC, and age determination based on dissolved organic carbon content is also possible (Bayarı et al., 2005). The ^{14}C activities of the samples vary between 90 pmc to 110 pmc for Salda Lake waters and 530 pmc to 5990 pmc for the groundwater. ^{13}C values were

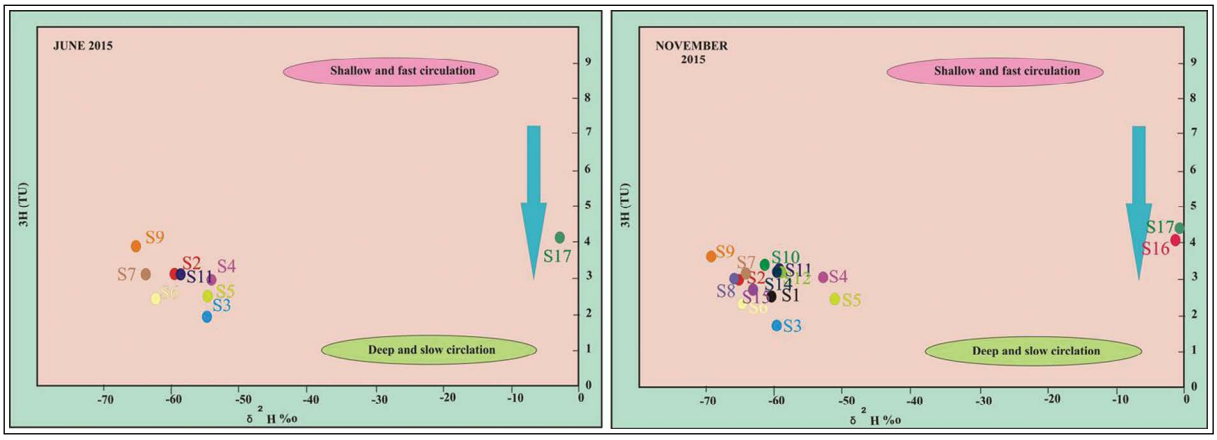

Figure 6- d^2H -^3H graphic (June and November 2015).

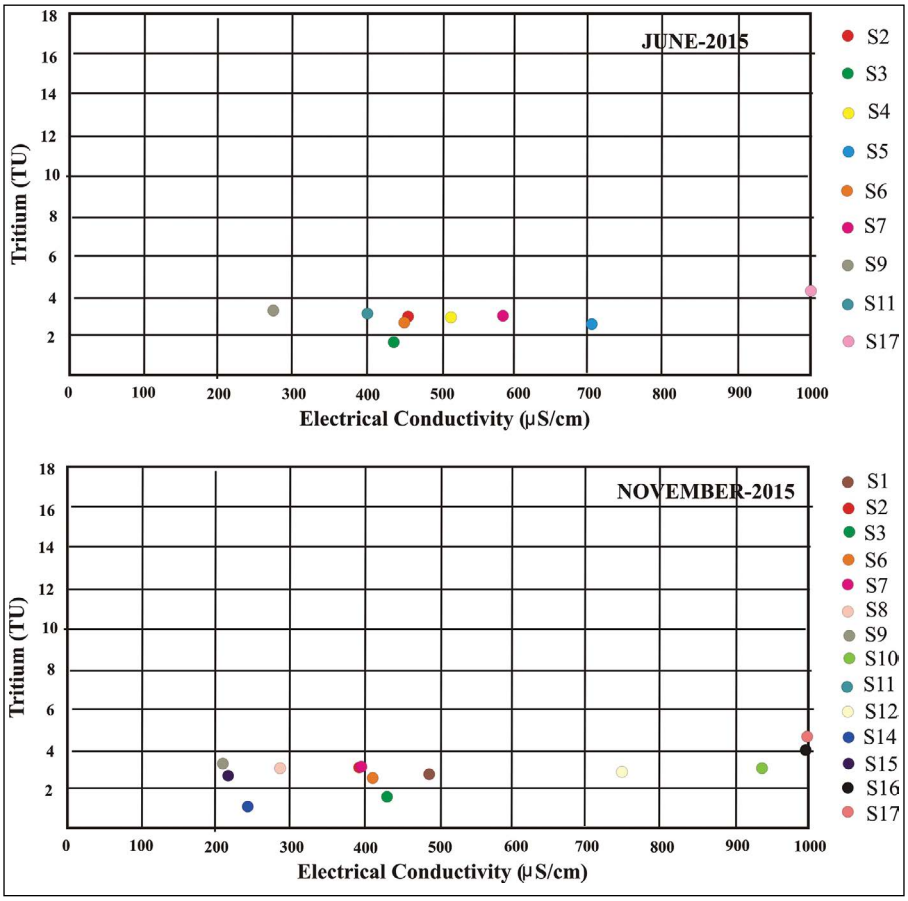

Figure 7- EC_{25} -^{3}H graphic (June and November 2015).

-15,6 to -16,6 in spring waters and -0,8 and -0,7 in lake waters (Table 3). According to this, CO_2 is the solution of marine limestone and fresh water carbonates in the lake waters, while in the groundwater it is geogenic (dissolved and mantle in the groundwater) (Figure 8)

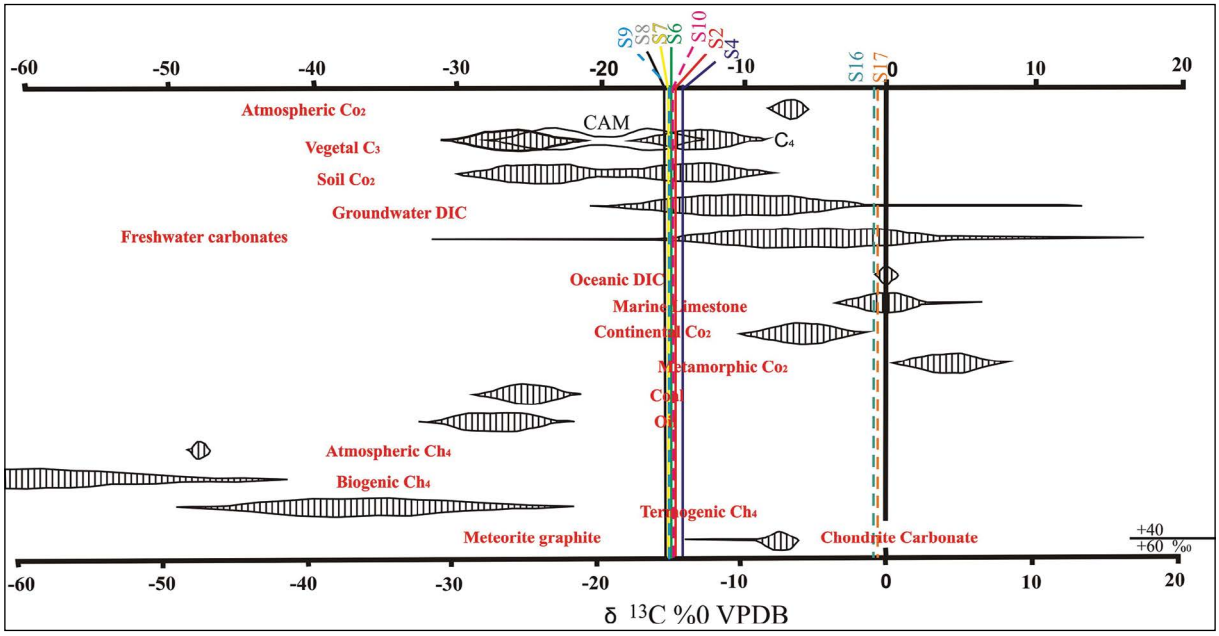

Figure 8- According to Clark and Fritz (1997), in terms of the origin of natural carbon compounds of ^{13}C values of investigated waters.

4. Conclusions

This study used water chemistry and isotope data to investigate origin, recharge processes (the recharge area, circulation depth) of groundwater and surface water in the Salda Lake basin. The groundwater chemical composition was "Mg^{2+}-CO_3^{2-}-HCO_3^-, Mg^{2+}-Ca^{2+}-CO_3^{2-}-HCO_3^- and Ca^{2+}-Mg^{2+}-HCO_3^-" facies. The lake water was Mg^{2+}-CO_3^{2-}-HCO_3^- facies in the basin. All the groundwater and surface water system is recharged by meteoric precipitation. Groundwaters in the study area are recharged from high elevations and lake waters are recharged from low elevations in the basin. According to this, waters with excess deuterium values of more than 10, atmospheric and marine origin precipitation waters with high velocity evaporation effect of the regions; waters with values lower than 10 are considered to be waters originating from terrestrial rainfall under the influence of evaporation. According to the tritium analysis results, S3 and S14 in the study area are recharge from higher elevations than the other samples in both seasons. In addition, according to radiogenic isotope, CO_2 is the solution of marine limestone and fresh water carbonates in the lake waters, while in the groundwater it is geogenic.

Acknowledgement

This study has been supported by The Scientific and Technological Research Council of Turkey (TUBITAK) with project No: 114Y084.

References

Afşin, M., Erdoğan, N., Gürdal, H., Gürel, A., Onak, A., Oruç, Ö., Kavurmacı, M., Durukan, G. 2007. İç Anadolu'daki Sıcak ve mineralli sular ve travertenlerin hidrojeokimyasal ve izotopik incelenmesi ve suların tıbbi ve biyolojik iklimlendirme değerlendirmesi. TÜBİTAK-ÇAYDAG, Proje No: 104Y197, Aksaray.

Aggarwal, P. K., Basu, A. R., Poreda, R. J., Kulkarni, K. M., Froehlich, K., Tarafdar, S. A., Ahmed, S. R. 2000. A report on isotope hydrology of groundwater in Bangladesh: implications for characterization and mitigation of arsenic in groundwater. International atomic energy agency-TC project BGD/8/016, 64.

Appelo, C.A.J., Postma, D. 2005. Geochemistry, Groundwater and Pollution. Rotterdam: A.A. Balkema.

Bayarı, S., Özyurt, N., Kilani, S. 2005. "Konya Kapalı Havzasının Yeraltı Sularında Karbon-14 Yaş Dağılımı", II. Ulusal Hidrolojide İzotop Teknikleri Sempozyumu, 26-30 Eylül 2005, Gümüldür, İzmir, 147-166.

Baykal, B. B., Gönenç, I.E., Meric, M., Tanik, A., Tunay, O. 1996. ``An alternative approach for evaluation of lake water quality: Lake Sapanca ± a case study from Turkey'', Water Science and Technology Vol. 34 No. 12, pp. 73-81.

Busenberg, E., Plummer, L.N. 1993. Concentrations of chlorofluorocarbons and other gases in groundwater at Mirror Lake, New Hampshire. In: Morganwalp, D.W., Aronson, D.A. (Eds.), USGS Toxic Substances Hydrology Program Technical Meeting, Colorado Springs, CO.

Çaldırak, H., Kurtuluş, B. 2018. Evidence of Possible Recharge Zones for Lake Salda (Turkey). Journal of the Indian Society of Remote Sensing. Springer.

Clark, I., Fritz, P. 1997. Environmental isotopes in hydrogeology. Lewis, Boca Raton, FL, s. 1-328

Craig, H. 1961. Isotopic variations in meteoric waters. Science 133, 1833-1834.

Dansgaard, W. 1964. Stable isotopes in precipitation. Tellus 16, 436-468.

Dilsiz, C. 2006. Türkiye'nin güneybatısındaki Pamukkale hidrotermal sahasının hidrokimyasal ve izotopik verilere dayanan kavramsal hidrodinamik modeli. Hidrojeoloji Dergisi 14: 562-572.

Erguvanlı, K., Yüzer, E. 1987. Yeraltı Suyu Jeolojisi. İTÜ Maden Fakültesi, yayın no: 23, İstanbul, 339p.

Güner, F.G., Güner, I.N. 2002. Sakarbaşı Karstik Kaynaklarının (Çifteler - Eşkişehir) Hidrojeoloji ve Çevresel İzotop Yöntemleriyle Hidrojeolojisinin Belirlenmesi, Hidrolojide İzotop Tekniklerinin Kullanımı Sempozyumu 21-25 Ekim 2002, Adana-Türkiye, sayfa: 199-213.

Gupta, S.K., Deshpande, R.D., 2005. Groundwater Isotopic Investigations in India: What has been Learned? Curr. Sci. 89(5):826-830.

Kazancı, N., S. Girgin, M. Dügel, On the limnology of Salda Lake, a large and deep soda lake in southwestern Turkey: future management proposals, Aquatic Conservation: Marine and Freshwater Ecosystems 14: 151-162, 2004.

Lise, Y., Gülle, İ., Kesici, E., Dişli, E., Akarsu, F., Küçükala, A., Çalışkan, B.K., Gül, S. 2013. Salda Gölü Sulak Havzası Biyolojik Çeşitlilik Araştırması, Orman ve Su Yönetimi Bakanlığı, Doğa Koruma ve Milli Parklar Genel Müdürlüğü.

Makwe, E., Chup, C.D. 2013. Seasonal Variation in Physico-Chemical Properties of Groundwater Around Karu Abattoir, Ethiopian Journal of Environmental Studies and Management Vol. 6 No.5, 489-497.

Merlivat, L., Jouzel, J. 1979. Global climatic interpretation of the deuterium-oxygen 18 relationship for precipitation. Journal of Geophysical Research: Oceans 84(C8):5029-5033.

Mokadem, N., Demdoum, A., Hamed, Y., Bouri, S., Hacı, R., Boyce, A., Laouar, R., Sâad, A. 2017. Hydrogeochemical and stable isotope data of groundwater of a multi-aquifer system: Northern Gafsa basin–Central Tunisia. Journal of African Earth Sciences 114, 174-191.

Ngabirano, H., Byamugisha, D., Ntambi, E. 2016. Effects of Seasonal Variations in Physical Parameters on Quality of Gravity Flow Water in Kyanamira Sub-County, Kabale District, Uganda. Journal of Water Resource and Protection 8, 1297-1309.

Piper, A. M. 1944. A Graphic Procedure in Geochemical Interpretation of Water Analyses, American Geophysical Union Transactions 25; 914-923.

Ranjan R.K., Ramanathan A.L., Parthasarthy P., Kumar A. 2013. Hydrochemical characteristics of groundwater in the plains of Phalgu river in Gaya, Bihar, India. Arab J Geosci 6: 3257–3267.

Russell, M.J., Ingham, J.K., Zedef, V., Maktav, D., Sunar, F., Hall, A.J. 1999. Search for Signs of Ancient Life on Mars: Expectations from Hydromagnesite Microbialites, Salda Lake, Turkey. Journal of the Geological Society of London, Vol. 156, No. 5, 1999, pp. 869-888.

Schlosser, P., Stute, M., Sonntag, C., Munnich, K.O. 1988. Tritiogenic 3He in shallow groundwater. Earth and Planetary Science Letters 94:245-256.

Subyani, A.M. 2004. Use of chloride-mass balance and environ- mental isotopes for evaluation of groundwater recharge in the alluvial aquifer, Wadi Tharad, west Saudi Arabia. Environmental Geology (46):741–749.

Şahinci, A. 1991. Doğal Suların Jeokimyası, Reform Baskısı, bölüm 2., s. 33, İzmir.

Şenel, M., Selçuk, H., Bilgin, ZR, Şen, AM, Karaman, T., Dinçer, MA, Durukan, E., Arbas, A., Örçen, S., Bilgi, C. 1989. Çameli (Denizli) - Yeşilova (Burdur) - Elmalı (Antalya) ve kuzeyinin jeolojisi. Maden Tetkik ve Arama Genel Müdürlüğü Rapor no: 9429 Ankara (unpublished).

Şenel, M., Akyürek, B., Can, N., Aksay, A., Pehlivan, N., Bulut, V., Aydal, N. 1997. 1: 100 000 ölçekli Türkiye Jeoloji Haritası, Denizli M23 (J9), Maden Tetkik ve Arama Genel Müdürlüğü yayını, Ankara.

Varol, S., Davraz, A., Şener, Ş., Şener, E., Aksever, F., Kırkan, B., Tokgözlü, A. 2017. Salda Gölü Sulak Alanının Hidrojeolojisi ve Hidrojeokimyasal Özelliklerinin İzlenmesi ve Kirlenme Durumunun Tespiti, TÜBİTAK ÇAYDAĞ proje raporu, Proje No: 114Y084.

Bulletin of the Mineral Research and Exploration

http://bulletin.mta.gov.tr

Investigation on geoarchaeological structure of ancient ports in the Lycia Region

Su Güneş KABAKLI[a*] and M. Erkan KARAMAN[b]

[a]*Akdeniz University, Department of Geological Engineering, Dumlupinar Boulevard, Campus,07058, Turkey*
[b]*Akdeniz University, Department of Geological Engineering, Dumlupinar Boulevard, Campus, 07058, Turkey*

Research Article

Keywords:
Phaselis, Sea level, Lycia, Aerial photographs, Satellite images.

Received Date: 18.06.2018
Accepted Date: 16.02.2019

ABSTRACT

The effects of geological events that occurred in ancient times, on ancient cities are undeniably great, so geoarchaeology has become an important mutidisciplinary science. Using geological methods in archaeological researchs offers a much more comprehensive understanding for history. Today, the methods of remote sensing and geographical information systems have facilitated archaeological researches to a greater extent than before. In this study, Phaselis, Andriake and Patara ancient cities were investigated. In the research, help was obtained from satellite images as a method. By comparing the ancient coast line and the modern coast line, it is tried to be understood to what extent the sea level change occurred.

1. Introduction

Archeology and geology have important places in the world cultural heritage. These two sciences work together to provide a wider perspective and provide access to get more information. Geoarchaeology is a bridge between human history and the history of the world. This allows us to better understand our planet.

One of the most important reasons for these changes at sea level is the plate movements. The Teke Peninsula, which is the focus region of this research, were highly affected by the changes in the sea level.

Also local differences in sediment structure and coastal dynamics had caused different coastline curves (Brükner et al., 2010).

Most extensive coastal changes in history have been observed in the delta regions of the Major coastal changes were observed in the coastal delta bay of the Mediterranean Sea. On the other hand, earthquakes and other natural phenomenas had effects on delta formations. (Brückner et al., 2005). Also, the river valleys always formed along weak structural lines or in depressions, grabens, and half-grabens (Kayan, 1999).

Many historical harbors were affected by the sea level changes in Anatolia in the ancient period. Troy, Ephesus, Miletus, Priene, Patara, Seleukeia Pieria are important ones among these ports (Erol and Pirazzoli, 1992). Some of these historical harbors have been flooded due to the rise of the sea level. On the other hand some historical harbors had been covered with alluviums. The most famous example is the Ephesus Ancient Port which is 8 km away from the coastline today. Strabon states that Priene was originally on the shore but it is about 6.5 km far from the sea shore today.

Citation Info: Kabaklı, S.G., Karaman, M. E. 2020. Investigation on geoarchaeological structure of ancient ports in the Lycia Region. Bulletin of Mineral Research and Exploration, 161, 71-79. https://doi.org/10.19111/bulletinofmre.545547

* *Corresponding author: Su Güneş KABAKLI, sugunesk@gmail.com*

Santorini volcanic eruption (Thera eruption) has affected the eastern Mediterranean for over 1000 years during the Bronze Age. Probably volcanic eruptions are the reasons of these severe earthquakes and tsunamis which have caused the disappearance of the Minoan civilization (Özdemir, 2004). Also, Thera eruption and following tsunami affected the western Turkey and Crete coasts (Minoura et al., 2000) (Figure 1).

It has been determined that there have been different descending and ascending event sequences in close regions. For example while rises at the sea level are observed in the Mediterranean coasts, large decreases at the sea level are observed in Londos at the island of Rhodes.

In Lycia Region, earthquakes are the most important reasons of sea level changes. A few earthquakes which are known to have affected the region are listed at the below table (Table 1) (Guidoboni et al., 1994).

Table 1- Important earthquakes in Lycia region.

Date	Center
2nd Millenium BC	Santorini (Volcanic Eruption)
199-198 BC	Rhodes
227 BC	Rhodes
23	Cibyra
68	Myra
142	Rhodes
344	Rhodes
417	Cibyra
474-478	Rhodes
515	Rhodes
530	Myra

2. Material Method

In this study, Lycian Region was investigated by using archaeological, geoarchaeological and geological data. In this direction, surface surveys were carried out in Phaselis, Patara and Andriake ancient cities. Using Global Positioning System (GPS), contemporary coastlines and possible coastlines of

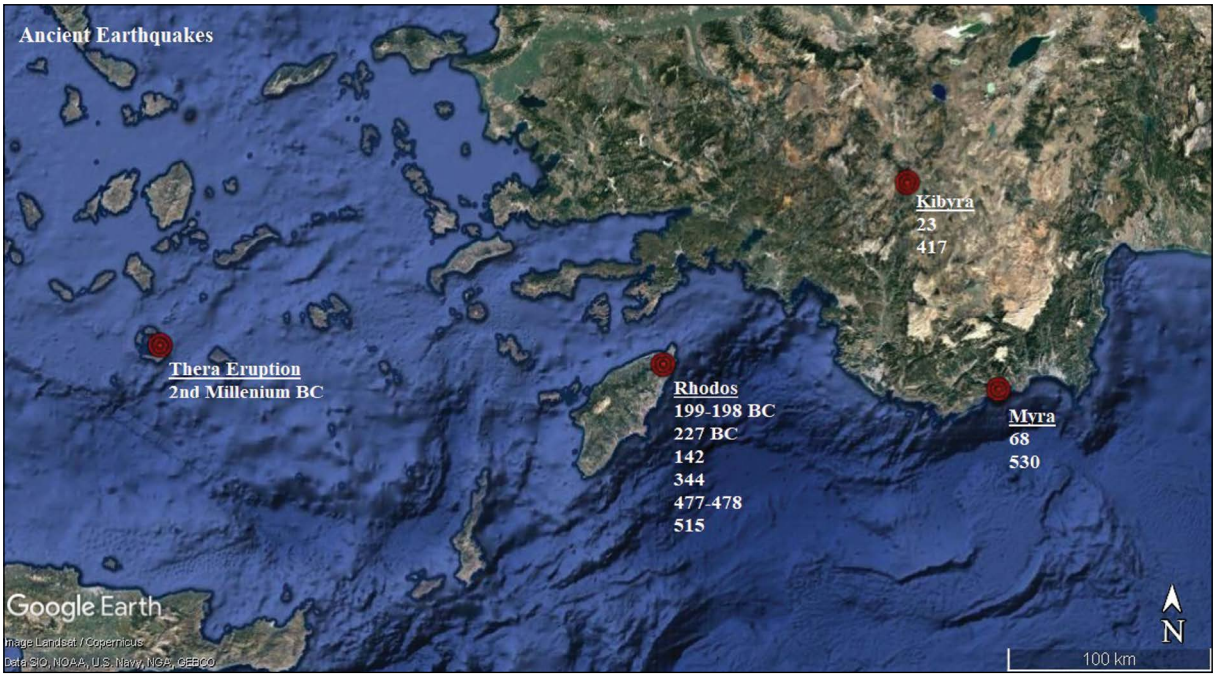

Figure 1- Important ancient earthquakes.

ancient times have been documented. During these surface investigations, the drone was flown above Phaselis and aerial photographs were taken. At the same time, a detailed underwater survey was conducted in the Phaselis coastline and many underwater parts of the buildings were photographed and documented.

The structure of the region has been studied in detail with the help of satellite images and geological maps and the desired result has been achieved by using GIS programs (QGIS and ArcGIS).

Firstly, research was carried out in the ancient city of Patara. In this research, it is aimed to determine the effects of the earthquakes that have occurred in the region. Moreover, it has been observed that alluviums carried by the Eşen River closed the port of the city. Much of the later work is concentrated in the Phaselis Ancient City. It was investigated how much Phaselis harbor was affected by earthquakes. During studies mainly it was concentrated to the underwater works. Photographs taken with underwater camera has a gretaer effect on the scope of the project.

The Andriake Ancient City, the port of Myra, also exposured the effects of the earthquakes. The research conducted around this region concentrates on the port which is in a swampy situation.

The data obtained from field studies conducted in ancient cities are compared with each other. The photographs were rearranged considering the geological structure of the region.

Territories, that could not be reached because of the land structure, were surveyed via satellite images. The geographical structure mentioned in ancient literatures and the present geography were compared.

3. Results

3.1. Patara

Patara Ancient City in Kaş, Antalya, is located on the southeast of the delta flood plain formed by the Eşen Stream (Xanthos). The north-south tectonic groove bordered by 100-120 meters and 300 meters high hills to the west is located in the estuary, which is 2 kilometers from the sea. This estuary determines the borders of Patara harbor bay. In Patara, epigraphic datas from 13th Century BC, proved that the city had been settled much earlier. The pottery of the Tepecik Acropolis located at the north of the settlement area and the finds of the mother goddess figurine as baked clay proves the existence of the settlement at the last phase of the Early Bronze Age (İşkan and Şahin, 2018).

Patara, which is the port of the famous Xanthos Ancient City, is also the biggest port of Lycia Region. Patara, the Ancient City port is now covered with alluviums. However, it is known that this region is the harbor of ancient times. Alluviums carried by the Eşen River have made the remaining part of the harbor a swamp. Nowadays, the area near the sea has been covered with alluviums. The sands of Patara beach are fine and smooth. This unique structure of the sand is due to the sandstone and limestone of the geological formation of the region. Patara Port was used 2500-3000 years ago from today. In this period, Eşen Bay was filled with sediments but Patara Bay was in a very convenient position to be a port. As Eşen Stream continued to carry sediments, it continued to be filled with sediments in Patara Bay continued to be filled with sediments. Thus, Patara Port was completely covered with alluvium (Öner, 2001).

According to Strabon ± 2000 years ago, Letoon was reached 10 stadion (1,8 km) from Eşen Creek. Today, this distance has increased to 4 km (Strabon, 2000).

It is mentioned in the historical literature that the ships could enter the port of Patara 15th century. In the following period, the port has become a marsh. In the same way, the lagoon in the eastern part of the Eşen Plain has also been a marsh. If we accept that these developments continue in the future, it will be possible for the eastern Kalkan Bay to turn into a lagoon and then a swamp in time (Öner, 2001).

In figure 2b, Patara and the geological formation of the region were taken into consideration to redraw the ancient port boundaries of the region with the help of the Adobe Photoshop program and Google Earth.

3.2. Phaselis

Phaselis Ancient city is located in Kemer, Çamyuva district. In figure 3, the location of Phaselis in the Mediterranean Sea can be observed. Phaselis

Figure 2- a) Patara shore line in today, b) Patara shore line in ancient times (Google Earth 2017 map based).

Ancient City was founded on the west coast of the Gulf of Pamphylia under the leadership of Lindos in around 691/690 BC (Tüner-Önen, 2012). From the 7th century BC to the mid-2nd century BC, Phaselis, mainly governed through democracy, managed to maintain its autonomy during the period of Persian hegemony in Anatolia in the Classical Period and, at times, during the Hellenistic Period (Arslan and Önen, 2016).

In Phaselis some of the harbor structures are underwater. Destructive earthquakes caused the buildings in Phaselis to be destroyed and the city to be flooded. In addition, cracks were observed on the ground under the sea in the coastal region of Phaselis. It is not clear when and for what reason these cracks were formed, and more information is needed to obtain by paleoseismological examinations in the region. Destructive earthquakes caused the buildings in Phaselis to be destroyed and the city to be flooded. In addition, cracks were observed on the ground under the sea in the coastal region of Phaselis. It is not clear when and for what reason these cracks were formed, and more information is needed to obtain by paleoseismological examinations in the region.

In the images which were taken by a drone over Phaselis, the remains of underwater structures of the ancient Breakwater are clearly visible (Figure 4,5).

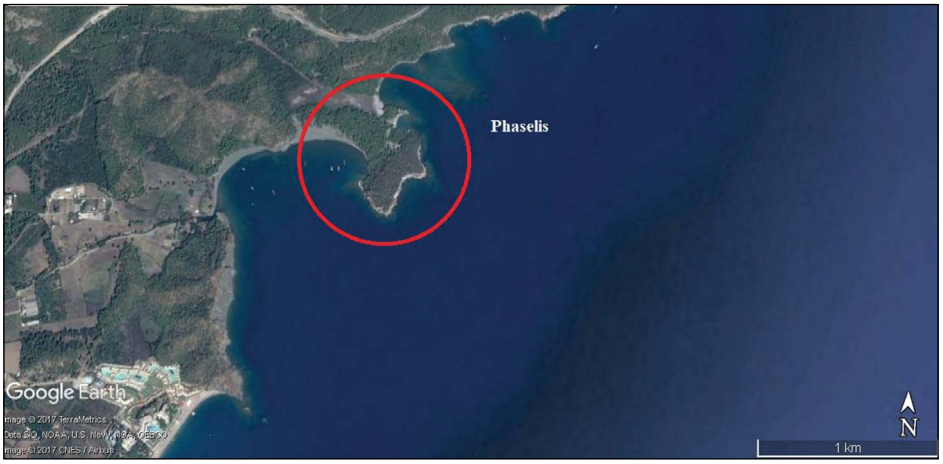

Figure 3- Phaselis (today) (Google Earth 2017 map based).

Figure 4- Location of the Phaselis breakwater.

Figure 5- Air photo of Phaselis breakwater (17.07.2016).

In Phaselis, there are many building remains under water (Figure 6). Above mentioned underwater fractures observed in Phaselis Shores are seen in Figure 7. It is not well known which eartquakes caused these fractures observed on the Phaselis cost. In order to have a certain knowledge, paleoseismological researches have to be carried out in the region.

3.3.Andriake

Andriake is located 4,7 km southwest of Myra. It lies between Kumdağ Tepe and Bozdağ Tepe. 3000-2000 years ago, the alluvials brought by Myros Stream filled the Myra River Delta by the time and turned it into a suitable plain for settlement (Çevik, 2015). It was one of the most active harbors in the region since the Hellenistic period. The defense system comprised

Figure 6- Building remains in underwater in Phaselis.

Figure 7- Underwater fracture in Phaselis.

of towers on the hills at the south side of the harbor settlement is dated to the Hellenistic period and was used in the Roman and Byzantine periods with some modifications (Akyürek, 2016).

The ancient city of Andriake was settled along a bay in the past, and around this bay was the ancient port of Andriake. Today, however, this port is in a swamp. Underneath this swamp a part of the harbor structures exists.

In figure 8, the result of the site surveys in Andriake and the studies about the geological formation of the region were provided basis to redraw the ancient port boundaries of the region with the help of the Adobe Photoshop program and Google Earth. In figure 9 we can see the shoreline of Andriake in today.

The geological basement of the region consists of limestone. Because of this, there is no river to carry sediments to Andriake harbor. It can be assumed that the sediments of Demre River reached to the harbor were carried from here by the coastal currents (Öner, 1998).

4. Discussion

Visible changes have been observed at the sea level in the research conducted in the Lycia Region.

Figure 8- Estimated shore line in ancient times (Google Earth 2017 map based).

Figure 9- Andriake shore line in today. (Google Earth 2017 map based).

However, these changes are not the same everywhere. While the ports of cities such as Kekova and Phaselis are underwater as a result of the sea level rise, the ports of the Andriake and Patara cities are now filled with alluvial deposits and are quite inland. The most important reason why the port structures remain underwater is earthquake. In Phaselis, underwater fractures may have been caused by earthquakes that left the harbor structures underwater. Although it is not possible to say anything definite about this issue, it is possible to trace the earthquake traces in the major structures.

5. Conclusion

Lycia Region, today's Teke Peninsula, has hosted various civilizations throughout history. The geographical and geological characteristics of the region are the most important reasons for this. The region has always maintained its popularity due to the fertile lands, the sea and the sheltered location of the bays. However, like everywhere else, it was greatly influenced by the earthquakes in Lycia. We can see the effects of these earthquakes from the ancient literatures and the remains of ancient buildings.

It can be easily estimated that the earthquake is a great disaster for ancient civilizations. However, because of the earthquakes the strength of the structures built afterwards had been increased. The important buildings (theater, parliament building (bouleuterion), bathhouse etc.) were more solid than the others. Today, we see that most of these important structures are still standing.

Due to the earthquakes, the changes in the landforms in the Lycian region were much faster than expected.

The impact of rapid changes in ground patterns in the Lycian Region is most commonly observed in coastal areas. These changes on the coasts affected sea level directly. These visible changes in the sea level are evidences of tectonic mobility. For this reason, we can say that some changes in the sea level in the Lycian Region for example in Kekova and Phaselis, are tectonic rather than eustatic.

Apart from the direct effect of earthquakes, plate movements and climate change also affect the sea level changes. However, these effects occur over a much longer period of time and this change is not visible and takes thousands of years. However, large climatic events accelerate this process. For example, climatic events, such as global warming, the ice age of the earth, which completely affect the fate of the earth, can cause great changes in sea level in a few years. Sudden and large changes in climate will affect sea level definitely.

Although the tides provide a significant change, they do not have much impact on the average sea level as they do not change the existing water volume and are merely gravitational events. However, the change in the volume of water and the change in sea level, can modify the magnitude of the tides. Sea level changes after the ice age have had significant impacts on the tides (Kayan, 2012).

Alluviums carried by rivers have a great effect on sea level changes. We have seen examples of this in Patara and Andriake, as previously mentioned. As the alluvium carried by the Eşen Stream collided with the waves coming from the sea, Patara Bay was completely occupied with marshes and the ancient port was filled with sand dunes and became a marsh. The existence of various building remains under this swamp in Andriake may indicate that water has risen and then filled with alluviums. However, it is not possible to reach a definite result without detailed research.

As a result of surface and underwater research in the Lycian Region, satisfactory results were produced in Phaselis, Andriake and Patara.

Particular, building blocks found in Phaselis under the sea, revealed the destructive effects of the earthquakes in the region. In addition, Phaselis's northern port is underwater and some cracks can be observed under the sea, extending to the main basement rock of the city. The block fragments belonging to the Breakwater in the northern port are observed under water. A Sarcophagus located on the shore of the Necropolis can be observed from the surface. The flooded block fragments of the city's ancient military port were documented with aerial photographs.

In Patara, earthquake traces were determined on ancient building remains. The ancient Patara coastline is now 2,30 km from away the sea and the ancient lighthouse is 573 m from away the coast. The ancient

port was filled with alluviums by the time and today there are only small ponds left from the port.

Andriake Port is covered with alluvium like the port of Patara. The harbor, which has become a swamp, is a home to various species of birds today.

In the light of all these data, it can be said that there has been a significant change in the coastal line from the ancient period to the present day. Considering the geological origin of the world, this change was experienced in a short period of time as nearly 2000 years. It will continue to change thereafter. On the basis of all these data, we can easily say that the coastal line changes in the Lycian Region are faster than normal. The reason for this is that there are continual earthquakes in the region.

Acknowledgement

Within the scope of this project, I would like to thank to Prof. Dr. Murat Arslan the Head President of The Department of Ancient History of Akdeniz University and Phaselis excavation team. They supported us in all aspects of the surface and underwater research conducted in the ancient city of Phaselis. In addition, I would like to express my gratitude to Akdeniz University Scientific Research Projects Unit for providing financial support to the Project.

References

Akyürek, E. 2016. Andriake: The Port of Myra in Late Antiquity,Trade In Byzantium Papers From The Third International Sevgi Gönül Byzantine Studies Symposium Istanbul, 24-27 June 2013, Magdalino, P., Necipoğlu (Ed.), N., Koç University's Research Center For Anatolian Civilizations (Anamed) 465-487.

Arslan, M., Önen, N. T. 2016. Phaselis, İşkan, H. Dündar, E. (Ed.). From Lukka to Lycia The Land of Sarpedon and St. Nicholas, Anatolian Civilizations Series, 300 - 317.

Brückner, H., Vött, A., Schriever, A., Handl, M. 2005. Holocene delta progradation in the eastern Mediterranean e case studies in their historical context. Méditerranée 104, 95-106.

Brückner, H., Kelterbaum, D., Marunchak, O., Porotov, A., Vött, A. 2010. The Holocene sea level story since 7500 BP – Lessons from the Eastern Mediterranean, the Black and the Azov Seas. Quaternary International 225(2), 160–179.

Çevik, N. 2015. Lykia Kitabı, Suna-İnan Kıraç Akdeniz Medeniyetleri Araştırma Enstitüsü, Monografi Serisi: 10, 576.

Erol, O., Pirazzoli, P.A. 1992. Seleucia Pieria: an ancient harbour submitted to two successive uplifts, Nautical Archaeology 21, 4, 317-327.

Guidoboni, E., Comastri, A., Triana, G. 1994. Catalogue of Ancient Earthquakes in the Mediterranean Area up to the 10th Century. Istituto Nazionale di Geofisica 504.

İşkan, H., Şahin, F. 2018. Patara denizcilik ve ticaretin başkenti, Magma Dergisi 40-51.

Kayan, İ. 1999. Holocene stratigraphy and geomorphological evolution of the Aegean coastal plains of Anatolia, Quaternary Science Reviews 18(4):541-548.

Kayan, İ. 2012. Kuvetarner'de Deniz Seviyesi Değişmeleri, Kuvaterner Bilimi. (Ed. N. Kazancı, A. Gürbüz. 570 s). Ankara Üniversitesi Yay. 350, 59-78.

Minoura, K., Imamura, F., Kuran, U., Nakamura, T., Papadapoulos, G. A., Takahashi, T., Yalçıner, A. C. 2000. Discovery of Minoan Tsunami Deposits. Geology 28, 59-62

Öner, E. 1998. Likya Limanlarının Kaderi (Teke Yarımadası Kıyılarında Jeoarkeolojik Araştırmalar). "XV. Araştırma Sonuçları Toplantısı 419-440, Ankara.

Öner, E. 2001. Eşen Çayı Delta Ovasının Alüvyal Jeomorfolojisi ve Jeoarkeolojik Değerlendirmeler, Türkiye Kuvaterneri Çalıştayı Makaleler Kitabı 103-121, İstanbul.

Özdemir, M. A. 2004. İklim değişmeleri ve Uygarlık Üzerine Yansımalarına İlişkin Bazı Örnekler, Afyon Kocatepe Üniversitesi Sosyal Bilimler Dergisi 6, 2, 1-20.

Strabon, 2000. Geographika, ed: Prof. Dr. Adnan Pekman, (Book: XII, XIII, XIV). Arkeoloji ve Sanat Yayınları Antik Kaynaklar Dizisi 1 a. İstanbul, 384 p.

Tüner-Önen, N. 2012. Yazıtlar Işığında Phaselis, International Young Scholars Conference I: Mediterranean Anatolia, Suna – İnan Kıraç Akdeniz Medeniyetleri Araştırma Enstitüsü, Congress, Symposium, Seminar Series: 3, 479-488.

Bulletin of the Mineral Research and Exploration

http://bulletin.mta.gov.tr

Geochemical features and petrogenesis of Gökçeada volcanism, Çanakkale, NW Turkey

Pınar ŞEN[a*], Ramazan SARI[b], Erdal ŞEN[c], Cahit DÖNMEZ[a], Serkan ÖZKÜMÜŞ[a] and Şahset KÜÇÜKEFE[b]

[a]*General Directorate of Mineral Research and Exploration, Department of Mineral Research and Exploration, 06800, Ankara, Turkey*
[b]*General Directorate of Mineral Research and Exploration, Northwest Anatolia Regional Directorate, Balıkesir, Turkey*
[c]*Hacettepe University, Department of Geological Engineering, 06800 Beytepe, Ankara, Turkey*

Research Article

Keywords:
Gökçeada, Volcanism, Crustal contamination, Petrogenetic modeling, Partial melting.

ABSTRACT

Gökçeada Island, which is situated west of Biga Peninsula, has widespread magmatism with variable ages. Lower-Middle Eocene Dağiçitepe volcanics are the oldest volcanic unit in the island and consist of lavas, tuff-tuffites. They are influenced by alteration and almost all minerals, except quartz, are transformed into other minerals. Lower Oligocene Gökçeada andesitic lava/domes exhibiting hypocrystalline porphyric texture, are the products of NE-SW trending domes/cryptodomes. The phenocrysts assemblages consist of plagioclase, hornblende, clinopyroxene ± biotite and quartz. Middle Miocene Eşelek volcanics, which occur as lavas and pyroclastic rocks, exhibit hypocrystalline porphyric and intersertal textures. They are composed of plagioclase, hornblende and clinopyroxene crystals. Rhyolitic Dağiçitepe volcanics and andesitic Gökçeada lava/domes have calc-alkaline, andesitic Eşelek volcanics have tholeiitic character. They have geochemical features similar to subduction-related magmas. Lower-Middle Eocene Dağiçitepe volcanics are the products of syn-collisional magmas that have undergone processes of crustal contamination due to thickened crust. Whereas, Lower Oligocene Gökçeada andesitic lava/domes are the products of post-collisional magmas and were derived from metasomatized lithospheric mantle. Middle Miocene Eşelek volcanics were also derived from lithospheric mantle but, the mantle source generating Eşelek volcanics were relatively depleted over time. Geochemical data demonstrate the decreasing role of subduction signature and crustal contamination during the genesis and evolution of Gökçeada volcanics from Lower-Middle Eocene to Middle Miocene.

Received Date: 06.08.2018
Accepted Date: 05.03.2019

1. Introduction

Northward subduction and the following closure of the northern branch of Neo-Tethys ocean beneath the Sakarya continent, a continental collision between the Anatolide-Tauride blocks and the Sakarya continent occurred (Şengör and Yılmaz, 1981; Okay and Tüysüz, 1999). This continent-continent collision, which caused the formation of the Izmir-Ankara-Erzincan suture zone, occurred in the early Paleocene in the west (Okay and Tüysüz, 1999). Following the collision between the Sakarya continent and the Anatolide-Tauride blocks in the Late Cretaceous in northwestern Anatolia, a widespread magmatism from Eocene to Pliocene has developed, and the Tertiary magmatism has occurred in the region as a result of this collision (Şengör and Yılmaz, 1981; Yılmaz, 1989; Harris et al., 1994; Genç and Altunkaynak, 2007; Altunkaynak and Genç, 2008; Karacık et al., 2008; Yılmaz Şahin et al., 2010; Altunkaynak et al., 2012*a, b*; Altunkaynak

Citation Info: Şen, P., Sarı, R., Şen, E., Dönmez, C., Özkümüş, S., Küçükefe, Ş. 2020. Geochemical features and petrogenesis of Gökçeada volcanism, Çanakkale, NW Turkey. Bulletin of the Mineral Research and Exploration. 161, 81-99, https://doi.org/10.19111/bulletinofmre.543419

* *Corresponding author: Pınar ŞEN, pinar.sen@mta.gov.tr*

and Dilek, 2013; Gülmez et al., 2013; Aysal, 2015). The Gökçeada volcanism, which is the subject of this study, is the product of magmatic activity that took place during Tertiary. Tertiary magmatism, which is exposed in Gökçeada, began in the Lower Eocene and its activity has continued until Middle Miocene in various phases.

In this study, the petrographical and geochemical features of Lower-Middle Eocene Dağiçitepe, Lower Oligocene Gökçeada lava/domes and the Middle Miocene Eşelek volcanic rocks are presented and the magmatic processes in the genesis and evolution of Gökçeada volcanic rocks are introduced with trace element ratio diagrams and petrogenetic models. Gökçeada has been investigated by various researchers in terms of geological and stratigraphic features (Akartuna, 1950; Akartuna and Atan, 1978; Temel and Çiftçi, 2002; Kesgin and Varol, 2003; Ilgar et al. 2008; Sarı et al., 2015). As a widespread volcanism was occurred on the island, recent studies have mainly focused on the geochronological, geochemical and petrological characteristics of these magmatic rocks (Elmas et al., 2017; Aysal et al., 2018).

2. Regional Geology

Gökçeada, which is the largest island of Turkey, is located at 20 km west of the Biga Peninsula. Metamorphic, magmatic and sedimentary rocks ranging from Mesozoic to Quaternary formed on the island (Figure 1). However, the geology is dominated by magmatic rocks, occupying large areas. Late Ediacaran/Early Paleozoic Çamlıca metamorphic rocks (Okay et al., 1990; Tunç et al., 2002) are the oldest rocks of the island and consist of sericitic-schist, chloritic-schist, slate and marble. Lower Eocene Karaağaç formation that is composed of submarine fan deposits unconformably overlies the Çamlıca metamorphics. The altered rhyolitic volcanic rocks outcropping in the NW of Gökçeada were first named by Sarı et al. (2015) as the "Dağiçitepe

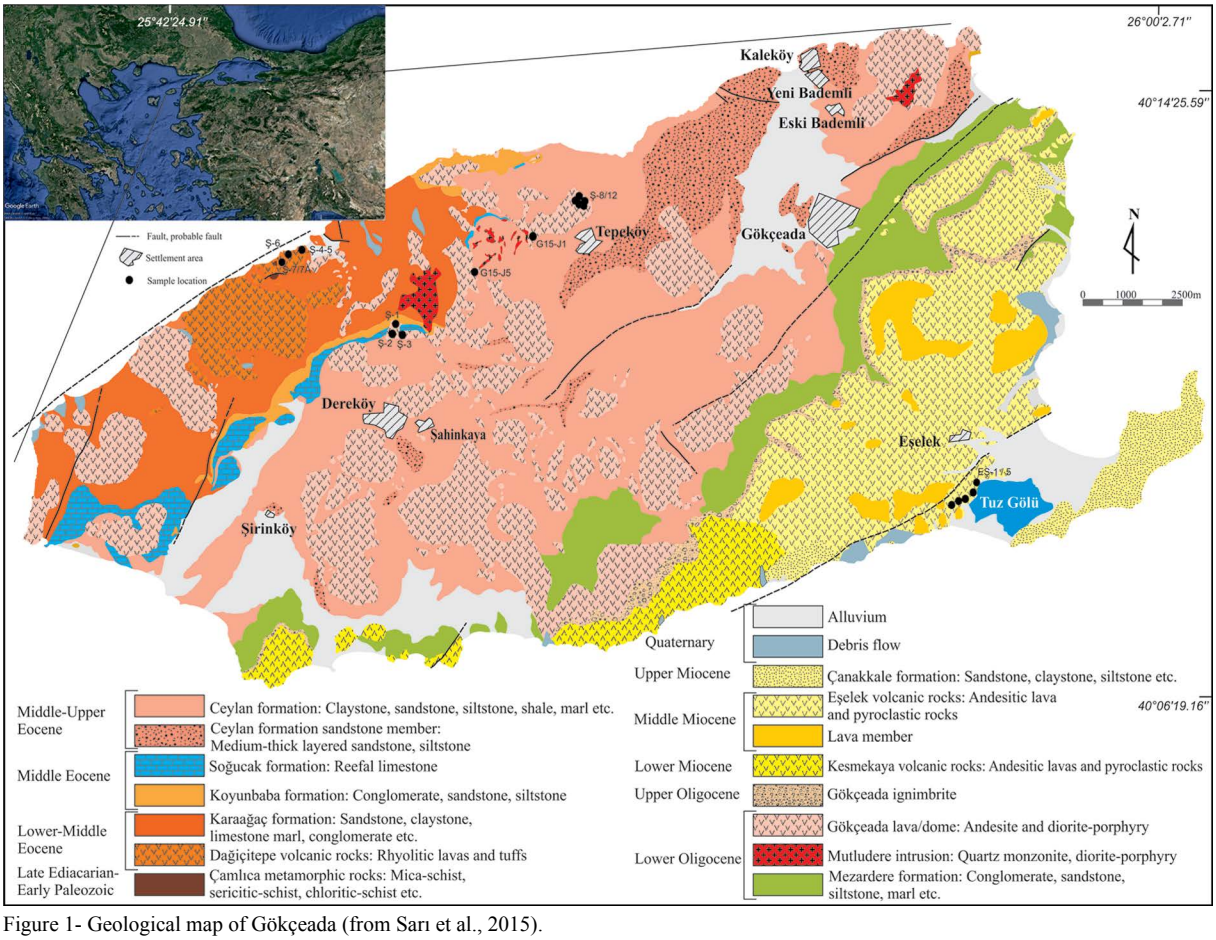

Figure 1- Geological map of Gökçeada (from Sarı et al., 2015).

volcanite member". The unit consisting of rhyolitic lava and tuff-tuffites is the oldest volcanic unit of the island**.** Elmas et al. (2017) defined these rhyolites and granitic plutons exposing in NW of the island as Marmaros Magmatic Assemblage and obtained an age of 26.2 ± 1.5 Ma from a rhyolite sample by the U-Pb LA-ICP-MS method. In the first stage of volcanic activity, the tuffs and then the lavas were erupted. The lavas of Dağiçitepe volcanic rocks were emplaced onto the Karaağaç formation by cutting Çamlıca metamorphic rocks. It is thought that they are Lower-Middle Eocene in age as the tuffs forming the unit are intercalated with the Karaağaç formation and lavas cut these deposits. Middle Eocene Koyunbaba formation, which is composed of shallow marine sandstones, unconformably overlies the Karaağaç formation and conformably underlies the reefal limestones. Middle-Upper Eocene Ceylan formation, which is formed by claystone-sandstone-shale alternation and deposited due to turbiditic currents in deep marine environment, conformably overlies the Soğucak formation. The unit is conformably overlain by the Mezardere formation. Lower Oligocene Mezardere formation (Ilgar et al., 2008) consists of the alternation of conglomerate with lesser amount of sandstone, siltstone and marl and it conformably overlies the Ceylan formation. Mezardere formation cut by the Gökçeada domes, is covered by the Gökçeada ignimbirite, and is cut and covered by the Eşelek volcanic rocks, too. The Mutludere intrusion, which is intruded into the sediments of the Karaağaç and Ceylan formations, has quartz-monzonite, diorite-porphyry composition (Sarı et al., 2015). As the Mutludere intrusion cut through the Upper Eocene sediments, it can be considered that the intrusion have been settled in the region after Eocene (Sarı et al., 2015). Andesite and diorite porphyry volcanic rocks occupying large areas on the island was named as the "Gökçeada domes" by Sarı et al. (2015). In this study, the domes will be called as the "Gökçeada andesitic lava/domes". Gökçeada andesitic lava/domes were emplaced into the Eocene sedimentary units in NE-SW trending dome-cryptodome and small lava flows in places. Gökçeada andesitic lava/domes were settled in Oligocene and their ages were detected as 28.6 ± 0.8 My by Sarı et al. (2015), and as 30.4 My and 34.3 My by Ercan et al. (1995) with radiometric age determinations using K/Ar method. These ages indicate that the magmatic activity occurred in the Lower Oligocene. However, Aysal et al. (2018) found that the U-Pb LA-ICP-MS zircon ages of the Gökçeada volcanic rocks were 25.66 ± 0.43 My and 26.0 ± 0.26 My. Pumice flows observed in east and south of Gökçeada were first named by Sarı et al. (2015) as the "Gökçeada ignimbrite". Gökçeada ignimbrite, which unconformably overlies the Ceylan and Mezardere formations, is unconformably overlain by Kesmekaya and Eşelek volcanic rocks. As the Gökçeada ignimbrite flows over the Lower Oligocene Mezardere formation and underlies the Middle Miocene Eşelek volcanic rocks, it is considered that the volcanic activity forming the ignimbrite occurred in the Upper Oligocene (Sarı et al., 2015). Lower Miocene Kesmekaya volcanic rocks composed of lava and block-and-ash flows are located on the Gökçeada ignimbrite. The andesitic lavas and pyroclastic rocks, which spread over large areas to the east of Gökçeada, were first mapped by Sarı et al. (2015) and named as the "Eşelek volcanic rocks". The pyroclastic deposits of the Eşelek volcanic rocks consist of lahar and block-and-ash flow deposits. Eşelek volcanic rocks overlies the Mezardere formation, Gökçeada ignimbrite and Kesmekaya volcanic rocks and unconformably underlies the Upper Miocene Çanakkale formation. Therefore, it is considered that the unit was formed in Middle Miocene. The Upper Miocene Çanakkale formation (Şentürk and Karaköse, 1987; Atabey et al., 2004) consists of less consolidated conglomerate, sandstone, siltstone and marl intercalations. The Quaternary deposits consist of debris flow and loose, unconsolidated conglomerate, sandstone, siltstone and mudstones unconformably overlie all formerly units.

3. Petrographical Features

Almost all of the samples from rhyolitic lavas of the Dağiçitepe volcanic rocks have been subjected to hydrothermal activity. All minerals, except quartz, were altered and transformed into other minerals. Only the external crystal forms of the original mineral are remained due to alteration (Figure 2a). Hornblende and biotite were completely opacified. While the great majority of the plagioclases were altered to sericite minerals, some of them were altered to pyrophyllite minerals (Figure 2a). The amount of glass in the groundmass is quite low. This is probably due to the subsequent development of secondary mineral formations. In addition to the silicification and carbonatization, the spherulites having a radiating structure that resulted from the intergrowth of quartz and feldspars due to silicification and devitrification, are observed (Figure 2a).

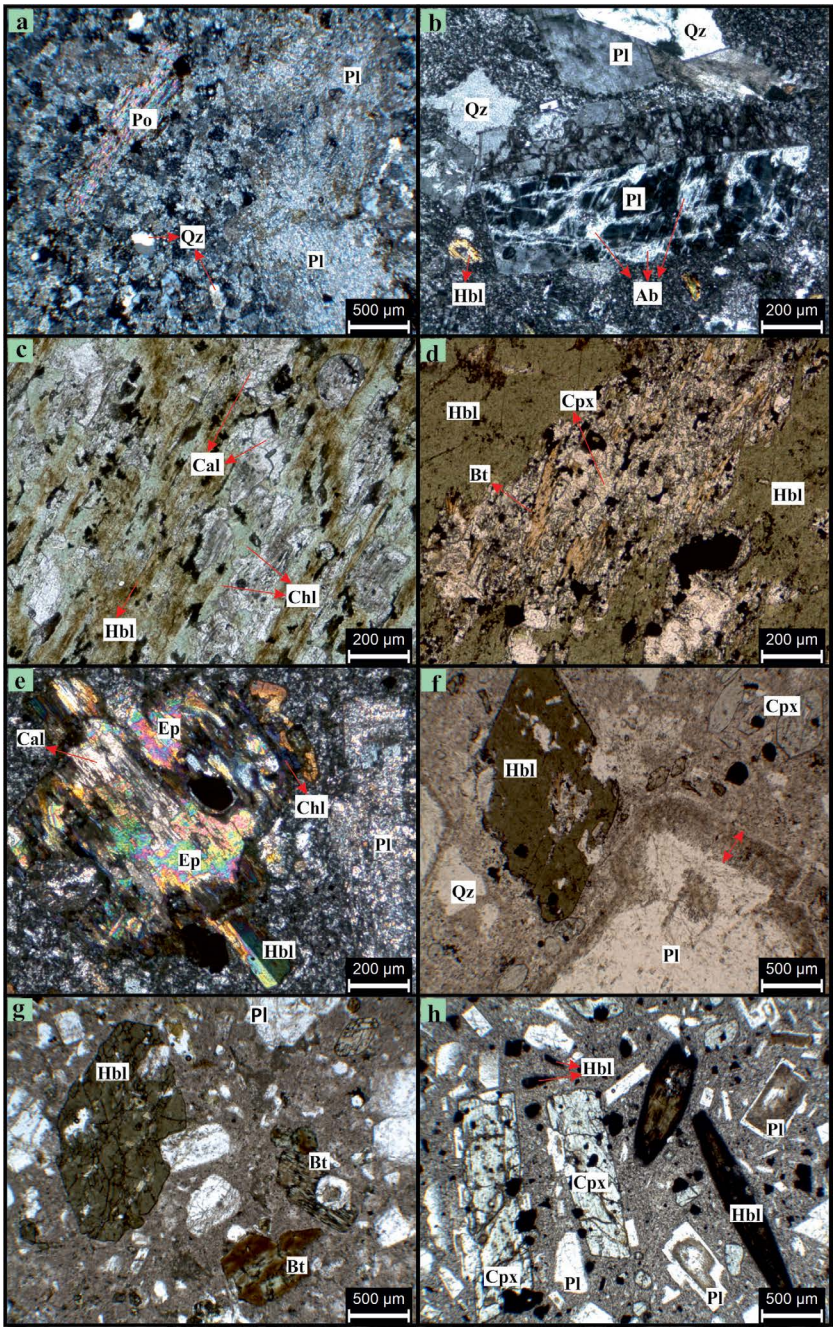

Figure 2- Photomicrographs of the Gökçeada volcanic rocks (Qz: quartz, Pl: plagioclase, Ab: albite, Hbl: hornblende, Cpx: clinopyroxene, Bt: biotite, Chl: chlorite, Ep: epidote, Cal: calcite and Po: pyrophyllite), a) quartz, sericitized plagioclase and secondary muscovite minerals in the devitrified groundmass, cross-polarized, Dağiçitepe volcanic rock Ş-5 sample, b) quartz, hornblende and albitized plagioclase phenocrysts in the silicified groundmass, cross-polarized, Gökçeada andesitic lava/domes Ş-9 sample, c) hydrothermally altered hornblende mineral, plane-polarized, Gökçeada andesitic lava/domes, d) relict clinopyroxene-based hornblende crystal and biotite minerals aligning in one direction, plane-polarized, Gökçeada andesitic lava/domes Ş-10 sample, e) pseudomorph epidote, calcite and chlorite aggregates, formed by hydrothermal alteration of sericitized plagioclase and clinopyroxene in silicified groundmass, cross-polarized, Gökçeada andesitic lava/domes Ş-1 sample, f) plagioclase with dusty zone, clear and euhedral clinopyroxene, resorbed quartz and hornblende minerals, plane-polarized, Gökçeada andesitic lava/domes Ş-10 sample, g) clear hornblende, plagioclase and partially chloritized biotite minerals, plane-polarized, Gökçeada andesitic lava/domes G15-J1, h) clear clinopyroxene, zoned plagioclase with glass inclusion, and partially or fully opacitized hornblende minerals, plane-polarized, Eşelek volcanic rock EŞ-2 sample.

Gökçeada andesitic lava/domes are andesitic volcanic products emplaced as NE-SW trending dome-cryptodome. Gökçeada andesitic lava/domes have hypocrystalline-porphyritic texture and their phenocrysts content vary between 40-75%. In general, the hydrothermal alteration is common and secondary minerals were formed. The groundmass significantly remained under the influence of silicification and carbonatization. For this reason, quartz minerals formed in the fractures and calcite are observed. There are three types of mineral assemblages in Gökçeada andesitic lava/domes; (1) plagioclase, hornblende, clinopyroxene ± quartz (crystal amount; 40-55%); (2) plagioclase, hornblende, clinopyroxene, biotite, quartz (crystal amount; 50-65%) and (3) plagioclase, hornblende, biotite ± quartz (crystal amount; 60-75%).

Plagioclase usually exhibits zoning and it was altered by sericitization, carbonatization and albitizations (Figure 2b). In plagioclase where alteration is less common, honeycomb textures and dusty zones are remarkable. Some plagioclase crystals are clustered as aggregate to form glomeroporphyric texture. The clear plagioclases exhibiting no alteration, zoning and inclusion, are rare.

Hornblende, particularly in the second and third assemblages, often occurs as clear crystals but it was also partially opacified along margins and cleavage planes. Whereas, almost all of the hornblendes in the first assemblage were either opacitized or carbonated (Figure 2c). Some hornblendes reaching up to 7 mm in grain size in the second assemblage contain relict pyroxene and biotite crystals occurred along the cleavage planes (Figure 2d).

Clinopyroxene, in the first assemblage, was subjected to intense alteration. Although it maintains its external crystal form, almost all of them are formed from secondary epidote, chlorite and calcite aggregates (Figure 2e). Except these samples, they commonly occur as clear crystals (Figure 2f).

Biotite, is usually seen as clear crystals, some have partially or completely altered to chlorite (Figure 2g).

Quartz occurs as anhedral aggregates, and present in the groundmass in large quantities. Some quartz have resorbed and rounded corners, some occur as subhedral crystals in the fractures.

Groundmass is mainly composed of anhedral quartz and plagioclase microlites and hornblende, clinopyroxene and opaque microcrystals as well. The amount of glass is low and the carbonatization, silicification and argillization are observed. Zircon and apatite are accessory minerals.

Eşelek volcanic rocks, represented by lava and pyroclastics in the east of Gökçeada, were first mapped and named by Sarı et al. (2015). The phenocryst amount of the andesitic lava samples from the Eşelek volcanic rocks is about 70%. All of them show hypocrystalline-porphyritic and intersertal texture. It consists of plagioclase, hornblende and clinopyroxene minerals.

Plagioclase; zoning, honeycomb textures and dusty zones, reflecting unstable conditions, are seen in the plagioclase crystals (Figure 2h).

Hornblende; the great majority of the hornblende crystals are completely opacitized, just the core of the coarse grains appear clear (Figure 2h).

Clinopyroxene; occur as clear pale green crystals.

The groundmass consists of microcrysts of clinopyroxene, hornblende, opaque minerals and plagioclase microlites. The glass amount is lower than crystals.

4. Analytical Techniques

Major-oxide, trace and rare earth element analyses were performed in the Department of Mineral Analysis and Technology of the General Directorate of Mineral Research and Exploration (MTA), Ankara, Turkey. The major-oxide analyses were determined on pressed pellets weighing approximately 3 gr sample, which are obtained by mixing cellulose as a binder (0.9 gr) and pressing under 40 kN pressure using the Thermo ARL brand XRF apparatus. Major element analyses were determined in the form of oxide % (SiO_2, Al_2O_3, Fe_2O_3 = total iron, MgO, CaO, Na_2O, K_2O, MnO, TiO_2, P_2O_5). The amount of loss on ignition (LOI) was determined as weight % of the sample calcified for 4 hours in an oven at 1050 ± 10 °C from the dried sample at 105 ± 5 °C for at least 4 hours.

Trace and rare earth element analyses were performed on the THERMO ICAP Q brand ICP-MS

device. 0,25 g of the sample were dissolved with HCl, HNO_3, $HClO_4$ and HF acids and the dissolved sample was analysed by completing it to 50 ml. The Certified Reference Material JG-1a was used for the quality control of analyses. The measured values of the certified standard reference material during the analysis are given in table 1.

5. Geochemical Features

Major-oxide, trace and rare earth element analyses of the Lower-Middle Eocene Dağiçitepe, Lower Oligocene Gökçeada lava/domes and Middle-Miocene Eşelek volcanic rocks are given in table 1. The major-oxide results have been normalized to 100% on an anhydrous basis and then these data are plotted on the Zr/TiO_2 vs SiO_2 diagram of Winchester and Floyd (1977) (Figure 3) in order to classify the rocks. According to this diagram, Dağiçitepe volcanic rocks fall into the rhyolitic, Gökçeada andesitic lava/domes and Eşelek volcanic rocks fall into the andesitic fields, and they generally exhibit sub-alkaline character. Based on the AFM diagram with calc-alkaline-tholeiitic dividing line (Irvine and Baragar, 1971), the Dağiçitepe volcanic rocks and Gökçeada andesitic lava/domes fall into calc-alkaline, Eşelek volcanic rocks fall into the tholeiitic fields (Figure 3).

Major-oxide and trace element variation diagrams against SiO_2 (Harker diagrams) are given in figure 4. Increasing SiO_2 in Gökçeada andesitic lava/domes is correlated with i) decreasing Fe_2O_3, MgO, CaO, Sr and V and ii) slight increasing K_2O, Na_2O and Ba. These observed variations in Fe_2O_3, MgO, CaO and Sr elements are related to the fractionation of olivine, pyroxene, Ca-plagioclase and Fe-Ti minerals. K_2O, Na_2O and Ba elements also show a tendency to increase against SiO_2. The variations between SiO_2 and major-oxides, trace elements suggest that fractional crystallization processes are effective in the evolution of Gökçeada andesitic lava/domes. Increasing SiO_2 in the Dağiçitepe volcanic rocks is slightly correlated with; i) decreasing Fe_2O_3, CaO and Sr and ii) increasing Ba. However, it is observed that the Eşelek volcanic rocks show a narrow variation against SiO_2.

Primitive mantle normalized trace element abundances patterns for the selected samples from Gökçeada are presented in figure 5. Gökçeada volcanic rocks are enriched in large ion lithophile elements (LILE: Cs, Rb, Ba, K, Th, U) relative to the primitive mantle. In general, all volcanic rocks exhibit similar trace element distribution patterns. As seen in diagrams, all samples have remarkable negative Nb, Ta and Ti, and positive Th, U, Pb and K anomalies. However, the Dağiçitepe volcanic rocks are distinguished from Gökçeada andesitic lava/domes and Eşelek volcanic rocks with their low Sr, P and Ti anomalies. This is due to fractionated nature and acidic character of the Dağiçitepe volcanic rocks, since Sr and P elements are taken up by Ca-plagioclase and apatite minerals during fractional crystallization. Therefore, the negative Sr and P anomalies in the Dağiçitepe volcanic rocks can be explained by Ca-plagioclase and apatite fractionation. Trace element patterns of Eşelek volcanic rocks show similar trends to those of Gökçeada andesitic lava/domes. The Eşelek volcanic rocks show different variations in Zr and Hf elements with respect to the Dağiçitepe volcanic rocks and Gökçeada andesitic lava/domes. Negative anomalies observed in Nb, Ta and Ti, and the positive anomalies in Th, U and Pb elements are typical geochemical characteristics of subduction-related magmas. In addition, contamination by crustal rocks during magma ascent to surface causes such anomalies (Gill, 1981; Thompson et al., 1983; Fitton et al., 1988).

Chondrite normalized rare earth element (REE) distribution diagrams (McDonough and Sun, 1995) of Gökçeada volcanic rocks are given in figure 6.

REE distribution patterns of the Gökçeada volcanic rocks show similar trends. The chondrite normalized (La/Yb)n ratios (McDonough and Sun, 1995) of the Dağiçitepe volcanic rocks, Gökçeda andesitic lava/domes and Eşelek volcanic rocks vary between 11,50-14,59, 13,82-18,17 and 8,23-8,68, respectively. This ratio points out the fractionated nature of the Dağiçitepe volcanic rocks and Gökçeada andesitic lava/domes, however, the fractionation is not effective in the Eşelek volcanic rocks as they have a lower (La/Yb)n ratio than others. Besides, slight depletion in heavy rare earth elements (HREE) in Dağiçitepe volcanic rocks relative to other volcanics in the study area and the presence of negative Eu anomalies are due to fractionated nature of these rhyolitic rocks.

Table 1- Major-oxide, trace and rare earth element analysis of Gökçeada volcanic rocks. (LOI: Loss On Ignition; wt.%: weight %)

	Dağiçitepe volcanic rocks (Lower-Middle Eocene)					Gökçeada andesitic lava/domes (Lower Oligocene)										Eşelek volcanic rocks (Middle Miocene)					JG-1a (Standard Reference Material)
Sample No	**Ş-4**	**Ş-5**	**Ş-6**	**Ş-7**	**Ş-7A**	**Ş-1**	**Ş-2**	**Ş-3**	**Ş-8**	**Ş-9**	**Ş-10**	**Ş-11**	**Ş-12**	**G15-J1**	**G15-J5**	**EŞ-1**	**EŞ-2**	**EŞ-3**	**EŞ-4**	**EŞ-5**	
SiO_2 (Wt. %)	70,1	70	70,3	73,5	72,3	59,5	56,1	57,8	62,6	62,4	62,5	61,1	62,4	60,3	60,9	58,2	58	58,5	58,2	58,2	
Al_2O_3	16,3	16,7	15,8	17	16,2	16,8	16,1	16,4	17,1	17,1	17	18	17,1	16,8	16,6	17,4	17,2	17,1	17,2	17,2	
CaO	2,7	2,6	1,9	0,1	0,1	4,5	7,1	5,2	3,6	4,8	5,1	2,6	4,8	4,4	4,6	5,8	6,9	7,1	7	7,1	
Fe_2O_3	1	1	1,4	1,1	1,2	5,6	5,6	5,8	4,8	4,6	4,7	4,6	4,7	5,6	4,7	7,3	7,3	6,9	7	6,9	
MgO	0,3	0,2	0,2	0,2	0,2	2,3	2,6	3	1,4	1,4	1,3	1,3	1,4	2,1	2,3	1,3	1,3	1,3	1,3	1,3	
MnO	0,1	0,1	0,1	<0.1	<0.1	0,2	0,1	0,1	0,1	0,1	0,1	0,1	0,1	0,2	0,1	0,1	0,1	0,1	0,1	0,1	
K_2O	4	4,3	4,2	3,4	4,4	3,8	3,3	3,6	3,9	3,5	3,7	5,5	3,5	3,3	3,4	2,9	2,9	2,9	3	2,9	
Na2O	0,2	0,2	2,8	0,3	2,9	3,5	2,5	3	4,8	4,1	3,9	5,1	4,2	3,1	3,6	3,1	3,3	3,3	3,3	3,3	
P_2O_5	<0.1	<0.1	<0.1	<0.1	<0.1	0,3	0,3	0,3	0,3	0,3	0,3	0,3	0,3	0,3	0,2	0,4	0,4	0,4	0,5	0,4	
TiO_2	0,2	0,2	0,2	0,2	0,2	0,6	0,6	0,6	0,5	0,5	0,5	0,5	0,5	0,6	0,5	1,1	1,1	1,1	1,1	1,1	
A.K.	4,8	4,5	2,8	3,7	2,05	2,7	5,5	3,35	0,6	0,75	0,5	0,7	0,65	2,6	2,75	2,05	1,05	0,85	1,05	0,95	
Total	99,7	99,8	99,7	99,5	99,55	99,8	99,8	99,15	99,7	99,55	99,6	99,8	99,65	99,3	99,65	99,65	99,55	99,55	99,75	99,45	
Sc (ppm)	1,26	1,19	1,19	1,17	1,41	11,04	11,14	11,45	9,40	8,41	8,74	8,76	8,12	9,44	11,06	15,02	14,81	14,92	15,02	14,09	7
V	30,94	27,97	31,94	27,40	27,06	181,60	185,10	190,80	184,50	186,00	177,70	181,70	167,00	204,40	196,90	248,20	256,50	246,10	247,70	238,90	20,56
Cr	69,57	44,37	102,30	62,10	61,34	44,90	39,41	49,17	57,39	196,50	55,24	34,54	79,65	99,38	100,30	33,78	31,23	37,66	34,30	23,72	15,42
Rb	163,4	159,2	149,3	118,8	166,1	132,8	127,5	155,8	162,5	140,2	138,7	231	131,9	149	139,9	108	105,3	104,4	100,4	96,3	142,33
Sr	65,76	104,8	182	65,54	128,4	835,6	647,6	749,1	685,7	903	877	631,8	845,4	1072	1059	812,9	822,3	854,1	831	804,4	154,21
Y	11,59	11,85	11,77	10,03	12,19	13,88	13,78	15,49	13,97	13,52	13,92	14,05	13,97	15,68	16,53	24,89	26,68	30,46	27,32	27,92	35,27
Zr	35,23	43,5	40,87	46,49	62,71	69,66	62,69	72,6	77,83	66,8	68,58	84,6	65,48	86,66	58,96	230,5	237,9	240,4	234,5	224,6	91,84
Nb	9,59	9,77	9,12	9,01	10,72	4,86	4,21	4,07	4,89	4,81	4,89	4,92	4,58	5,30	5,58	7,08	6,90	7,06	6,85	6,90	9,37
Cs	4,26	4,06	3,84	3,43	3,39	5,88	7,03	15,50	2,56	3,15	3,21	1,89	3,15	3,87	12,90	2,90	4,11	2,62	1,97	1,90	11,21
Ba	1083	1160	1135	1092	1409	1252	1096	1214	1252	1297	1325	1333	1531	1518	1775	1372	1193	1171	1162	1222	403,82
La	26,97	23,56	22,82	22,86	24,50	25,31	25,69	28,37	30,80	31,47	35,20	38,14	30,72	40,66	37,38	30,87	33,24	39,99	34,32	34,73	19,84
Ce	58,27	50,94	49,15	46,39	51,88	53,56	54,97	56,37	62,60	63,89	64,43	68,70	62,32	74,88	72,08	65,87	65,44	76,70	68,00	68,38	39,95
Pr	5,43	4,79	4,67	4,59	5,01	5,14	5,26	5,70	6,00	6,06	6,12	6,60	5,98	7,29	7,08	7,20	7,02	8,36	7,33	7,24	5,48
Nd	21,27	18,95	18,57	18,26	19,44	22,28	22,79	24,75	25,19	25,43	25,54	27,31	25,05	30,75	30,08	32,95	31,90	37,96	33,22	32,95	18,74
Sm	3,67	3,36	3,27	3,27	3,33	4,17	4,21	4,57	4,55	4,50	4,57	4,73	4,45	5,45	5,40	6,65	6,45	7,57	6,67	6,64	4,21
Eu	0,81	0,75	0,77	0,76	0,77	1,15	1,14	1,21	1,19	1,24	1,24	1,28	1,25	1,48	1,49	1,81	1,75	1,88	1,77	1,75	0,64
Gd	3,33	3,03	3,03	3,00	3,03	4,05	4,11	4,37	4,20	4,27	4,32	4,41	4,21	5,11	5,09	6,60	6,47	7,61	6,56	6,70	3,84
Tb	0,37	0,34	0,35	0,33	0,34	0,45	0,45	0,48	0,47	0,46	0,48	0,48	0,46	0,55	0,57	0,82	0,82	0,96	0,83	0,86	0,68
Dy	1,94	1,94	1,88	1,71	1,88	2,43	2,47	2,59	2,52	2,43	2,53	2,56	2,45	2,93	3,11	4,74	4,86	5,66	4,96	5,09	3,98
Ho	0,37	0,37	0,36	0,31	0,37	0,46	0,46	0,48	0,46	0,45	0,47	0,48	0,46	0,55	0,58	0,90	0,94	1,10	0,96	0,99	0,67
Er	1,21	1,26	1,19	1,01	1,25	1,38	1,43	1,47	1,45	1,40	1,48	1,51	1,45	1,70	1,83	2,78	2,98	3,42	3,05	3,16	2,11
Tm	0,17	0,19	0,17	0,15	0,19	0,18	0,19	0,20	0,19	0,19	0,20	0,21	0,20	0,23	0,25	0,37	0,40	0,47	0,41	0,43	0,24
Yb	1,27	1,39	1,28	1,07	1,42	1,22	1,27	1,34	1,34	1,30	1,37	1,43	1,34	1,60	1,72	2,51	2,75	3,14	2,81	2,87	3,51
Lu	0,20	0,21	0,20	0,17	0,22	0,19	0,19	0,20	0,20	0,20	0,21	0,22	0,20	0,24	0,26	0,37	0,41	0,47	0,42	0,43	0,38
Hf	1,22	1,46	1,39	1,49	2,00	1,73	1,59	1,85	2,02	1,79	1,88	2,24	1,82	2,42	1,79	5,02	5,04	5,21	5,04	4,86	2,78
Ta	0,75	0,75	0,70	0,68	0,76	0,51	0,48	0,46	0,45	0,45	0,46	0,47	0,44	0,50	0,49	0,61	0,60	0,63	0,59	0,60	2,41
Pb	17,11	17,52	19,38	14,27	18,34	16,17	9,93	15,14	20,84	26,69	18,49	20,99	17,16	23,48	24,05	19,71	17,55	20,71	14,96	14,65	19,57
Th	15,16	14,16	13,41	13,80	14,54	11,83	12,18	12,02	17,10	19,79	17,96	22,03	17,67	23,96	15,15	14,25	14,16	14,78	14,14	13,84	15,24
U	3,27	3,74	4,63	2,64	3,67	3,27	3,55	3,75	5,41	4,64	5,60	6,81	4,45	7,25	4,74	3,66	4,58	5,04	4,85	4,73	4,21

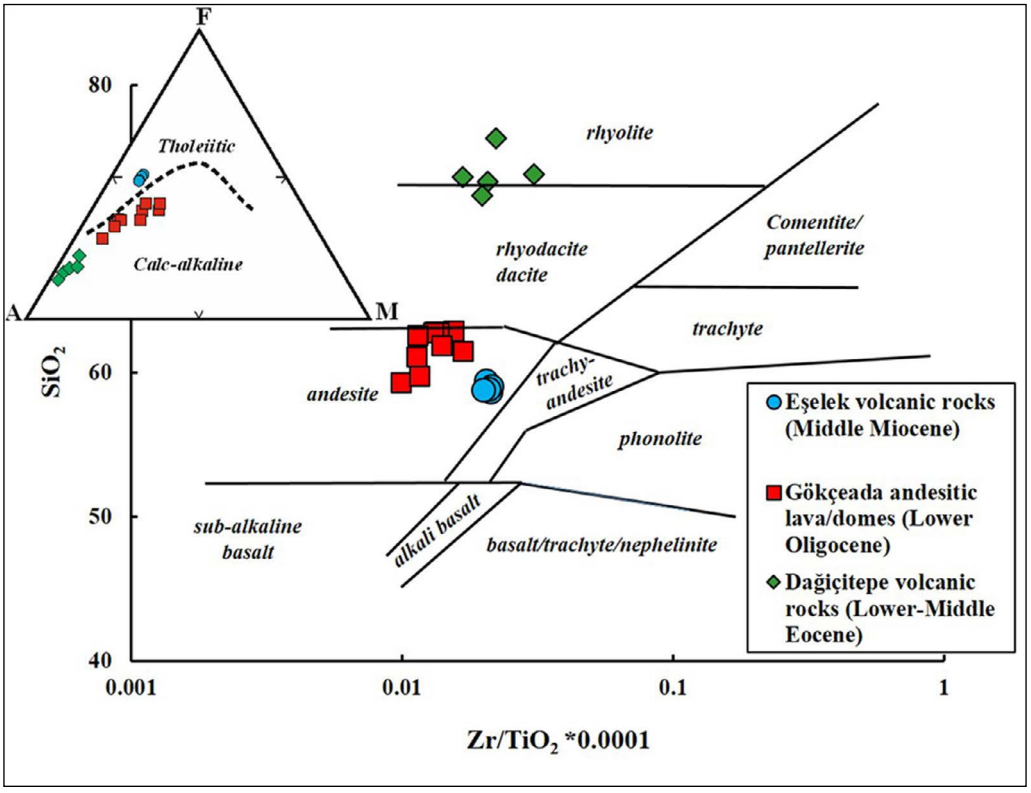

Figure 3- Zr/TiO_2 vs SiO_2 diagram of the Gökçeada volcanic rocks (Winchester and Floyd, 1977). The inset figure is the representation of sub-alkaline samples in the AFM diagram (Irvine and Baragar, 1971).

6. Discussion

6.1. Source Characteristics

Trace and rare earth element geochemistry demonstrate that subduction and/or crustal contamination processes (low Nb, Ta and Ti; high Th, U and Pb contents) are effective in the genesis and evolution of the Gökçeada volcanism. Therefore, trace element ratio and tectonic discrimination diagrams are drawn in order to clarify the tectonic setting and source characteristics of the Gökçeada volcanism. Elmas et al. (2017)'s data of Gökçeada volcanic rocks are also plotted onto diagrams. Ba/La vs Nb/La diagram is used to distinguish within-plate volcanism from orogenic volcanisms, because high Ba/Nb (>28) and Ba/Ta (>450) ratios are the characteristics of subduction-related magmas (Gill, 1981; Fitton et al., 1988) and high Nb/La (>1,5) ratio is the typical characteristic of within-plate volcanism subjected no and/or negligible crustal contamination (Haase et al., 2000). Gökçeada volcanic rocks have very high Ba/Nb (112-334) and Ba/Ta (1452-3608) ratios. As can be seen from Figure 7a, the Gökçeada volcanic rocks are located in the region represented by orogenic andesites. While the vertical trend observed in the Rb/Y vs Nb/Y diagram (Figure 7b) indicates the crustal contamination and/or subduction zone enrichment, within-plate enrichment results from a positive relationship between Rb and Nb (Edwards et al., 1991). Gökçeada volcanic rocks show a vertical trend in the direction of subduction enrichment and fall close to the field represented by Andean volcanic rocks. Also in Th/Ta vs Yb diagram, it is seen that the samples are concentrated in the field represented by arc magmatism (Figure 7c).

In (Nb/Zr)n vs Zr diagram (Figure 7d), while Dağiçitepe volcanic rocks are plotted in the collisional zone, Gökçeada andesitic lava/domes and Eşelek volcanic rocks are plotted in the subduction related zone. Additionally, all samples are plotted within the field of volcanic arc and syn-collisional granite field in Nb vs Y tectonic discrimination diagram of Pearce et al. (1984) suggested for granitic rocks (inset diagram in figure 7d). However, as the tectonic setting of granitic rocks falling at the intersection of within-plate granites (WPG), volcanic-arc granites (VAG), and syn-collisional granites (syn-COLG) is still controversial, this intersection field is regarded

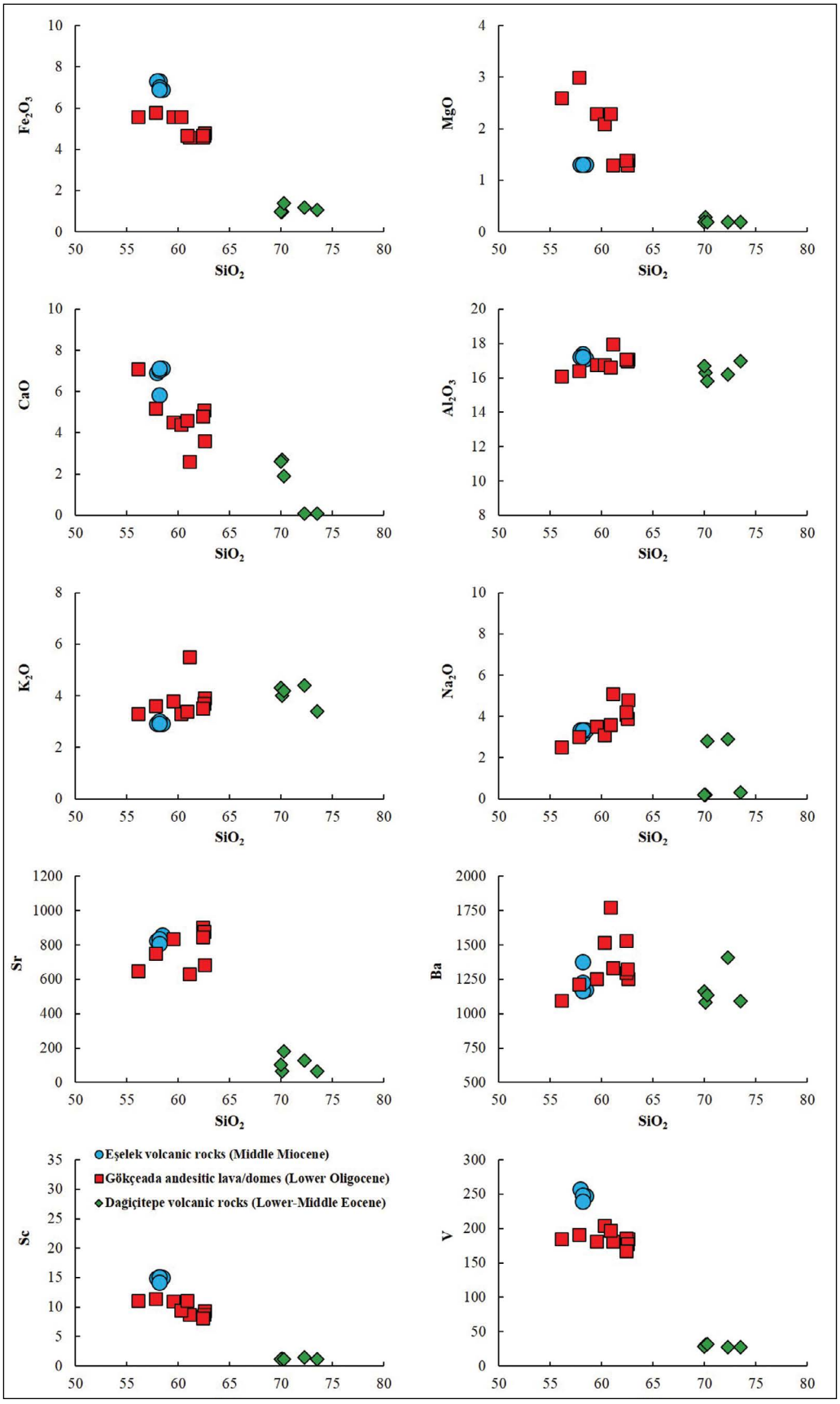

Figure 4- The major-oxide and trace element vs SiO_2 variation diagrams of the Gökçeada volcanic rocks.

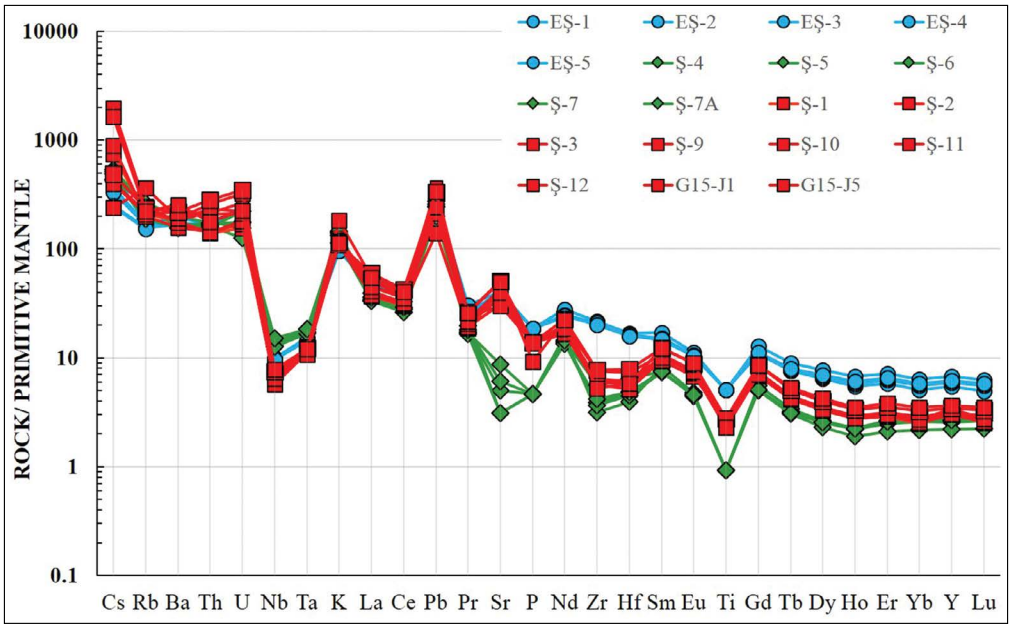

Figure 5- Primitive mantle-normalized (Sun and McDonough, 1989) trace element distribution patterns of Gökçeada volcanic rocks.

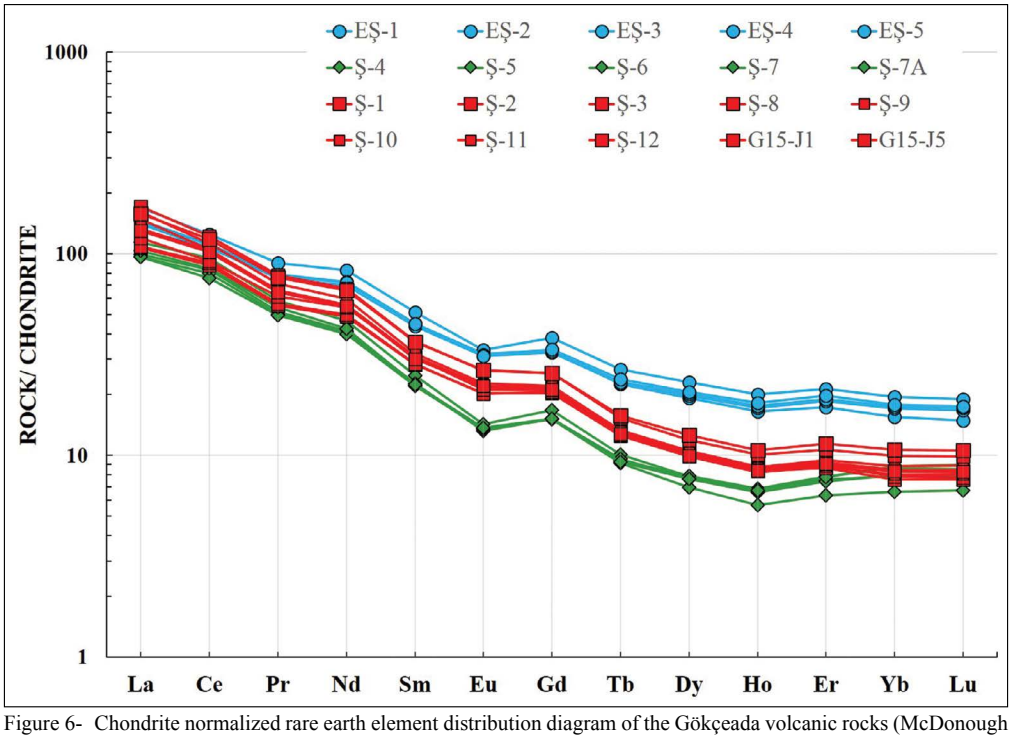

Figure 6- Chondrite normalized rare earth element distribution diagram of the Gökçeada volcanic rocks (McDonough and Sun, 1995).

as post-collisional granite (post-COLG) field (Pearce, 1996). According to this diagram, Dağiçitepe volcanic rocks and Gökçeada andesitic lava/domes slightly shifted from the field of post-collisional granite to volcanic arc granite (VAG) and syn-collisional granite (syn-COLG) field, Eşelek volcanic rocks are located in the post-collisional granite field (Figure 7d). According to the trends in figure 7d, it can be suggested that Dağiçitepe volcanic rocks are the products of collisional magmas, Gökçeada andesitic lava/domes and Eşelek volcanic rocks are the products of post-collisional magmas.

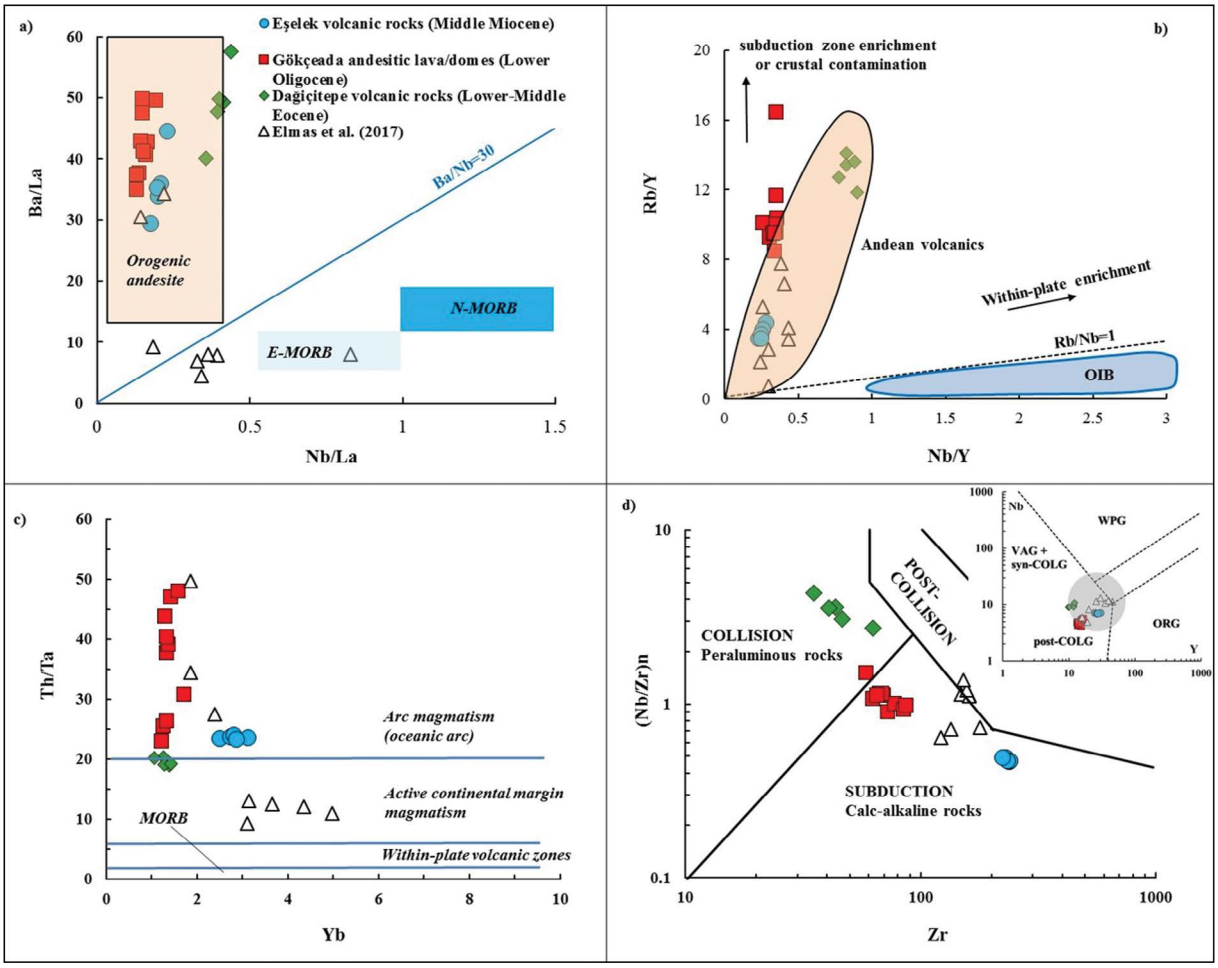

Figure 7- a) Ba/La vs Nb/La; b) Rb/Y vs Nb/Y (Edwards et al., 1991); c) Th/Ta vs Yb (from Zak et al., 2011 and Qian et al., 2013); d) (Nb/Zr)n vs Zr (Thiéblemont and Tegyev, 1994) diagrams of the Gökçeada volcanic rocks (inset figure from Pearce et al., 1984 and Pearce, 1996). Abbreviations: E-MORB: Enriched-Mid Ocean Ridge Basalt; N-MORB: Normal Mid Ocean Ridge Basalt; OIB: Ocean Island Basalts; post-COLG: Post-Collisional Granites; syn-COLG: syn-Collisional Granites; VAG: Volcanic Arc Granites; WPG: Within-plate Granites; ORG: Ocean Ridge Granites. The data of the Andean volcanic rocks are from Hickey et al. (1986; 1989) and Bryant et al. (2006).

6.2. Crustal Contamination

In order to determine the role of crustal contamination and fractional crystallization process in the evolution of Gökçeada volcanism, the AFC (assimilation - fractional crystallization) model of De Paolo (1981) has been applied in a Th/Y vs Nb/Y diagram. In the modeling, MORB (Mid Ocean Ridge Basalt) (Hofmann, 1988) and upper crust (UC) (McLennan, 2001) have been used as the initial starting composition and concomitant end-members, respectively. The ratios of the rate of assimilation to the rate of crystallization (-r values) are -0,1 and 0,7 (Figure 8). Gökçeada andesitic lava/domes and Eşelek volcanic rocks are shifted from the AFC trajectories in the direction of high Th/Y with almost constant Nb/Y ratios. This could be possibly due to the source characteristics rather than the involvement of crustal material to magmas during their ascent to the surface. However, the Dağiçitepe volcanic rocks are located close to the r=0,7, indicating the involvement of crustal material during their rise. Additionally, it can be concluded that the magmas generating Gökçeada volcanism retain the geochemical features of the subduction-related magmas, since almost all samples are located within the field of Andean volcanic rocks.

Low Ce/Pb ratio is one of the most characteristic features of the crustal contamination and/or sediment contamination to the mantle material, because the Pb content in crustal materials is remarkably higher than the mantle. Hofmann et al. (1986) have

shown that OIB and MORB (Ocean Island Basalt & Mid Ocean Ridge Basalt) mantle have a high and relatively constant Ce/Pb ratio (~25). On the other hand, the upper crust and GLOSS (Global Subducting Sediment) have low Ce/Pb values (~3,8 and ~2,9) (Taylor and McLennan, 1985; Plank and Langmuir, 1998; McLennan, 2001). The AFC modeling in the Th/Y and Nb/Y diagram indicates that high Th and low Nb contents in the Gökçeada volcanic rocks can be related to the source characteristics rather than the crustal contamination, since higher Th contents already indicate the involvement of subducted sediment (Plank, 2005; Labanieh et al., 2012). Therefore, in order to assess the reasons of high Th and Pb contents in the Gökçeada volcanic rocks and to reveal the role of sediment involvement in the genesis of volcanic rocks, binary mixing model of Langmuir et al. (1978) has been performed and a mixing curve has been calculated in a Ce/Pb vs Pb diagram between 'MORB' and 'sediment', with an average Pb content (0,7) and Ce/Pb ratio (25,7) for MORB (Normand and Garcia, 1999) and Pb content (27) and Ce/Pb ratio (2,2) for the gravity core sediment sample (N17/30) from Kermadec-Hikurangi volcanic arc system (Gamble et al., 1996) (Figure 9a). The Gökçeada volcanic rocks generally lie on the mixing curve in the direction of 'sediment' end-member. Accordingly, it can be concluded that the contribution of sediment having arc signatures plays an important role.

Figure 9b displays the Rb/Ba vs Rb/Sr diagram with binary mixing curve between '*basalt-derived melt'* and '*pelite-derived melt'* (Slyverster, 1998). It is clear from this figure that the Eşelek volcanic rocks and Gökçeada andesitic lava/domes are distributed close to the '*basalt-derived melt*' end-member, indicating derivation from a mantle source rather than crustal melting, because 'basalt-derived melt' and 'pelite-derived melt' end-members in the diagram represent mantle and crustal source, respectively (Sylvester, 1998; Li et al., 2015; Chen et al., 2017). Whereas, Dağiçitepe volcanic rocks shift to higher Rb/Sr ratios with no corresponding change in Rb/Ba. This could be because the fractionated and contaminated nature of the Dağiçitepe samples. This case is also supported by the variations observed in the Th/Y-Nb/Y diagram for Dağiçitepe volcanic rocks (Figure 8).

Consequently, the geochemical evaluations reveal that the Gökçeada volcanism have geochemical

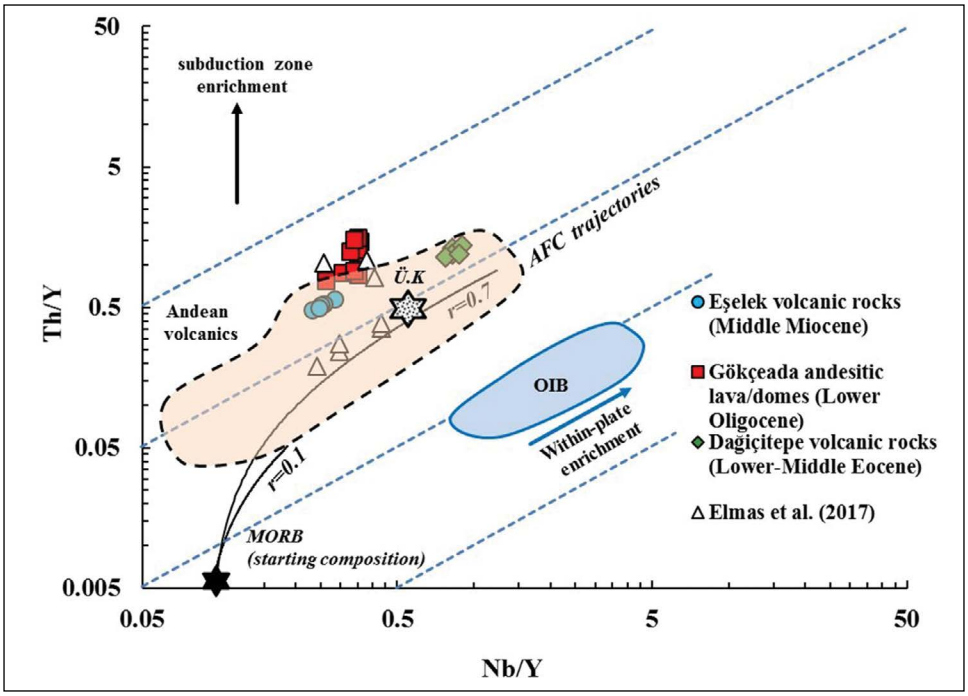

Figure 8- AFC modeling for the Th/Y vs Nb/Y diagram between Mid Ocean Ridge Basalts (MORB, Hofmann, 1988) and the upper crustal end-members. (Andean volcanic rocks are from Hickey et al. (1986; 1989) and Bryant et al., 2006). The r (the ratio of the rate of assimilation to the rate of crystallization) is shown as trajectories on the diagram.

variations similar to that of subduction-related magmatism and subduction processes in their genesis have played a major role (Figure 7). Further, the Dağiçitepe volcanic rocks are the products associated with collision-related magmas, and they have subjected to the crustal contamination during their ascent through the thickened crust. Gökçeada andesitic lava/domes and Eşelek volcanic rocks are the products of post-collisional magmas retaining subduction signatures.

6.3. Petrological Modeling

In order to determine the source mineralogy and melting depth of the Gökçeada volcanism, the non-modal batch-melting model of Shaw (1970) has been realized. In the model, the enriched lithospheric mantle component from McDonough (1990) has been chosen as the initial component (C0). Garnet bearing amphibole-peridotite for the source composition and has been used, and the non-modal batch melting

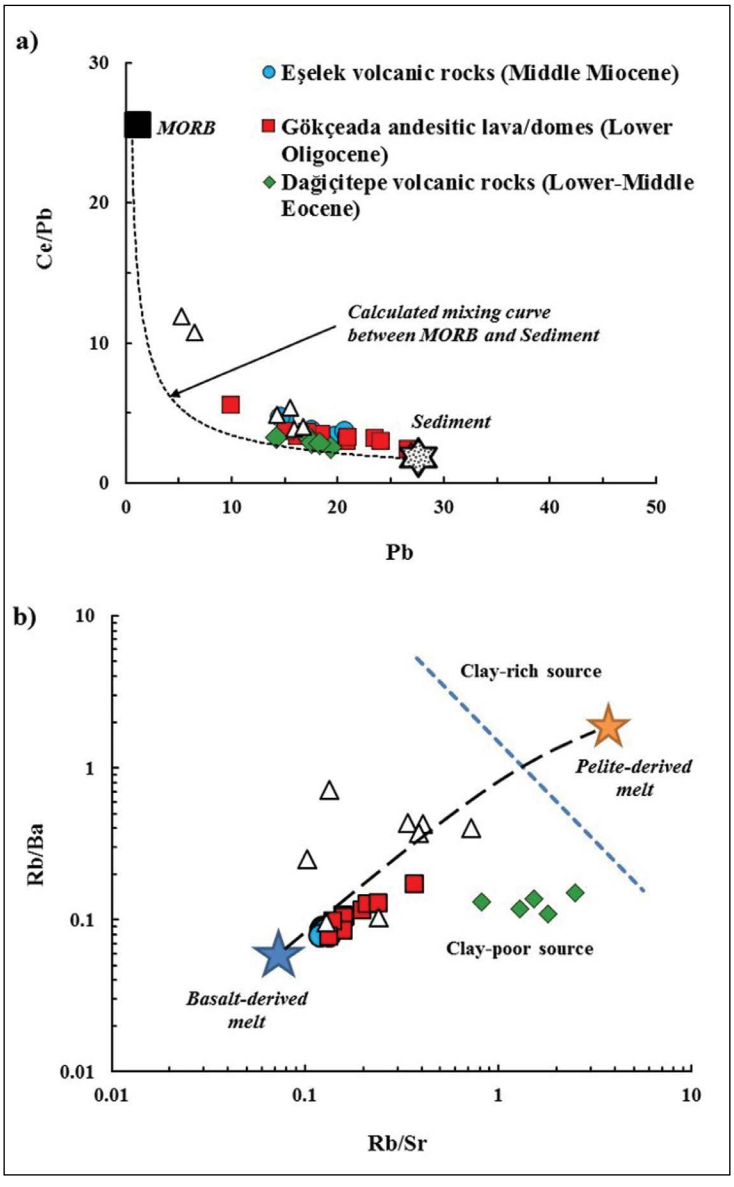

Figure 9- a) Ce/Pb vs Pb binary mixing diagram (Langmuir et al., 1978) (MORB and sediment values are from Normand and Garcia (1999) and Gamble et al. (1996), respectively); b) Rb/Ba vs Rb/Sr diagram of the Gökçeada volcanic rocks. (The mixing curve between the basalt-derived melt and pelite-derived melt from Sylvester (1998).

calculations have been performed. The mineral/melt partition coefficient (Kd) values for basaltic melts of the REEs are from Rollinson (1993), McKenzie and O'Nions (1991) and Adam and Green (2006; 2010). The modal mineralogy (X) and melting mode (Pi) values of the garnet-bearing amphibole peridotite melting facies and La, Sm and Yb concentrations of the enriched lithospheric mantle component are from McDonough (1990) and Ersoy et al. (2012). The data used in the modeling calculations are given in table 2. It can be concluded from the figure 10 that the Gökçeada andesitic lava/domes were derived from a garnet bearing amphibole-peridotite via variable degrees of partial melting, since they are clearly plotted on the melting curve drawn for the 3%, 5% and 7% garnet-bearing amphibole peridotite (Figure 10). The Eşelek volcanic rocks, on the other hand, represent a relatively depleted source with low La/Yb, Sm/Yb and (Tb/Yb)n ratios. The petrogenetic modeling diagrams show that metasomatic processes play a dominant role in the Lower Oligocene Gökçeada andesitic lava/domes. However, the mantle source generating the Middle Miocene Eşelek volcanic rocks became more depleted over time.

Table 2- Data used in the non-modal batch melting calculations. Abbreviations: Opx: orthopyroxene; Cpx: Clinopyroxene.

	Amphibole bearing garnet peridotite			
	Source Mode (X)			**Melting Mode (Pi)**
	7%	5%	3%	
Olivine	0,54	0,54	0,54	0,05
Opx	0,21	0,21	0,21	0,05
Cpx	0,12	0,14	0,15	0,3
Garnet	0,07	0,05	0,03	0,2
Amphibole	0,06	0,06	0,06	0,4
	Initial concentration (C0)	**Bulk Partition Coefficient (D0)**		**Melting Mode (P)**
La	2,6	0,0082		0,0292
Sm	0,47	0,0659		0,2284
Tb	0,07	0,127		0,5116
Yb	0,26	0,2282		1,1489

6.4. Geodynamic Effects

Late Cretaceous-Early Eocene tectonic evolution of the Western Anatolia is represented by the ophiolite emplacement, high pressure/low temperature metamorphism, subduction, arc magmatism and continent-continent collision (Okay et al., 2001). The consumption of the oceanic lithosphere of the northern branch of Neotethys by northward subduction beneath the Sakarya continent caused the continent-continent collision between the Sakarya continent and the Anatolide-Tauride platform. It is suggested that consumption of the northern branch of Neotethys and subsequent collision, which caused the formation of İzmir-Ankara Suture Zone occurred in the Paleocene-early Eocene (Harris et al., 1994; Okay and Tüysüz, 1999; Altunkaynak et al., 2012*b*). Tertiary magmatic activity in NW Anatolia is also the products of this collision (Şengör and Yılmaz, 1981; Yılmaz, 1989; Harris et al., 1994; Yılmaz et al., 1995). Additionally, the stratigraphic data (Akdeniz, 1980; Akyürek and Soysal, 1983; Yılmaz et al., 1997) also reveals that the collision was earlier than the Middle Eocene and the Eocene magmatism corresponded to the post-collisional magmatism (Harris et al., 1994; Genç and Yılmaz, 1997; Köprübaşı and Aldanmaz, 2004; Altunkaynak and Dilek, 2006; Altunkaynak, 2007; Altunkaynak et al., 2012*b*). Gökçeada has a widespread magmatism with variable ages and compositions. The genesis and evolution of the Lower-Middle Eocene Dağiçitepe volcanic rocks, Lower Oligocene Gökçeada andesitic lava/domes and Middle Miocene Eşelek volcanic rocks are related to the Late Cretaceous-Early Eocene tectonic evolution. The overall geochemical variations reveal that the geodynamic evolution of the region has been effective in the genesis and evolution of the volcanism. Accordingly;

(i) (Nb/Zr)n vs Zr tectonic discrimination diagram (Figure 7d) reveals that the Dağiçitepe volcanic rocks were generated in a collision related setting, and Th/Y vs Nb/Y and Rb/Ba vs Rb/Sr diagrams in which the assimilation and fractional crystallization processes are modeled reveal the effects of crustal contamination in their evolution. Accordingly, the Lower-Middle Eocene Dağiçitepe volcanic rocks carry the geochemical signatures of collisional magmas as it corresponds to the latest stages of the collision (e.g., crustal contamination).

(ii) Gökçeada andesitic lava/domes and Eşelek volcanic rocks are clearly fall into the subduction-related field (Figure 7d). Moreover, since both volcanisms are located close to the "*basalt-derived melt*" end-member, representing the mantle source in the Rb/Ba vs Rb/Sr diagram, the effects of crustal

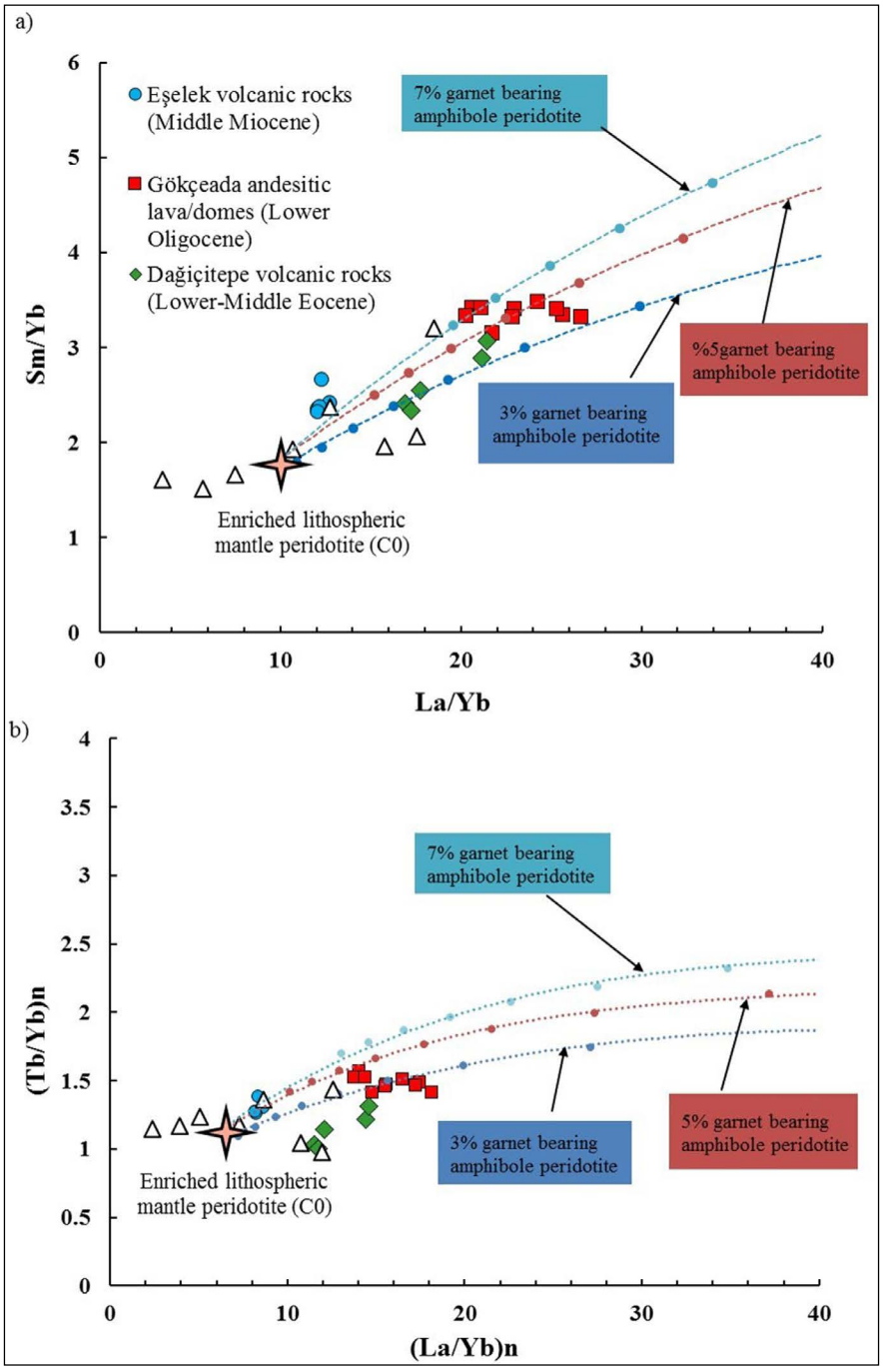

Figure 10- a) Sm/Yb vs La/Yb and b) (Tb/Yb)n vs (La/Yb)n diagrams of the Gökçeada volcanic rocks (Chondrite normalization values are from Thompson, 1982). The non-modal batch melting curves of garnet bearing amphibole peridotite were calculated using the equation of Shaw (1970). The data used in the modeling calculation are given in table 2.

contamination can be negligible. The petrogenetic modeling diagrams (Figure 10) also pointed out that both volcanisms were derived from a metasomatized lithospheric mantle source. Considering that the Eocene magmatism in NW Anatolia corresponds to the post-collisional magmatism, it can be concluded that the Gökçeada andesitic lava/domes and Eşelek volcanic rocks were generated in a post-collisional setting. However, the Eşelek volcanic rocks were derived from a relatively depleted source which became depleted over time.

7. Conclusion

In Gökçeada Island, there is a widespread magmatism with variable ages and compositions. Lower-Middle Eocene Dağiçitepe volcanic rocks, Lower Oligocene Gökçeada andesitic lava/domes and Middle Miocene Eşelek volcanic rocks on the island have calc-alkaline and tholeiitic compositions, respectively. In the rocks, which have geochemical characteristics of subduction magmas, the Lower-Middle Eocene Dağiçitepe volcanic rocks are the products of magmas in a collisional setting, hence they have experienced crustal contamination process is effective in the evolution of volcanic rocks. On the other hand, the Lower Oligocene Gökçeada andesitic lava/domes were derived from a metasomatized lithospheric mantle source in a post-collisional setting. The Middle Miocene Eşelek volcanic rocks were also derived from a lithospheric mantle, but the mantle source generating these volcanic rocks became relatively depleted over time. The geochemical data reveals that the effects of crustal contamination and subduction signatures in the evolution of the Gökçeada volcanism have decreased over time from Lower-Middle Eocene to Middle Miocene.

Acknowledgements

This study has been carried out within the project of "Batı Anadolu Polimetal Maden Aramaları (Western Anatolia Polymetallic Mineral Explorations)" in the Mineral Research and Exploration Department of General Directorate of Mineral Research and Exploration (MTA). We would like to thank to the Department of the Mineral Research and Exploration and the Northwest Anatolian Regional Directorate for their contributions during the study. We are grateful to Prof. Dr. Namık Aysal, Prof. Dr. Erdinç Yiğitbaş and the anonymous referee for their valuable and constructive reviews that greatly improved the manuscript.

References

Adam, J., Green, T. 2006. Trace element partitioning between mica- and amphibole-bearing garnet lherzolite and hydrous basanitic melt: 1. Experimental results and the investigation of controls on partitioning behaviour. Contributions to Mineralogy and Petrology 152, 1-17.

Adam, J., Green, T. 2010. Trace element partitioning between mica-and anphibole-bearing garnet lherzolite and hydrous basanitic melt: 2. Tasmanian Cainozoic basalts and the origins of intraplate basaltic magmas. Contribution to Mineralogy and Petrology, DOI 10.10007/s00410-010-0570-7.

Akartuna, M. 1950. İmroz adasında bazı jeolojik müşahadeler. Türkiye Jeoloji Kurumu Bülteni 2/2, 8-17.

Akartuna, M., Atan, O.R. 1978. Gökçeada'nın (Çanakkale) jeoloji ve sedimantoloji hakkında ön rapor. Maden Tetkik ve Arama Genel Müdürlüğü, Rapor No: 105, Ankara (yayınlanmamış).

Akdeniz, N. 1980. Başlamış Formasyonu. Journal of Geological Engineering 10, 39-47.

Akyürek, B., Soysal, Y. 1983. Biga yarımadası güneyinin (Savaştepe-Kırkağaç-Bergama-Ayvalık) temel jeoloji özellikleri. Maden Tektik ve Arama Dergisi 95, 1-12.

Altunkaynak, Ş. 2007. Collision-driven slab breakoff magmatism in Northwestern Anatolia, Turkey. Journal of Geology 115, 63–82.

Altunkaynak, Ş., Dilek, Y. 2006. Timing and nature of postcollisional volcanism in western Anatolia and geodynamic implications. In: Dilek, Y., Pavlides, S. (Eds.), Post collisional tectonics and magmatism in the Mediterranean region and Asia: Geological Society of America Special Paper 409, 321–351.

Altunkaynak, Ş., Genç, Ş.C. 2008. Petrogenesis and time-progressive evolution of the Cenozoic continental volcanism in the Biga Peninsula. Lithos, 102, 316-340.

Altunkaynak, Ş., Dilek, Y. 2013. Eocene mafic volcanism in northern Anatolia: its causes and mantle sources in the absence of active subduction. International Geology Review 55, 13, 1641-1659.

Altunkaynak, Ş., Dilek, Y., Genç, Ş.C., Sunal, G., Gertisser, R., Furnes, H., Foland, K. A., Yang, J. 2012*a*. Spatial, temporal and geochemical evolution of Oligo-Miocene granitoid magmatism in western Anatolia, Turkey. Gondwana Research 21, 961-986.

Altunkaynak, Ş., Sunal, G., Aldanmaz, E., Genç, Ş.C., Dilek, Y., Furnes, H., Foland, K. A., Yang, J., Yıldız, M. 2012*b*. Eocene Granitic Magmatism in NW Anatolia (Turkey) revisited: New implications from comparativezircon SHRIMP U–Pb and 40Ar-39Ar geochronology and isotope geochemistry on magma genesis and emplacement. Lithos 155, 289-309.

Atabey, E., Ilgar, A., Saltık, A. 2004. Çanakkale havzasının orta-üst Miyosen stratigrafisi, Çanakkale, KB Türkiye. Maden Tetkik ve Arama Dergisi 128, 79-97.

Aysal, N. 2015. Mineral chemistry, crystallization conditions and geodynamic implications of the Oligo–Miocene granitoids in the Biga Peninsula, Northwest Turkey. Journal of Asian Earth Science 105, 68-84.

Aysal, N.. Keskin, M., Kasapçı, C., Güngör, Y., Ündül, Ö., Peytcheva, I. 2018. Geochronology and geochemistry of the Gökçeada volcanics: Geodynamic significance of the Oligosen Magmatism on the Biga Peninsula, western Turkey. 8. Geochemistry Symposium Abstracts Book, 02-06 May 2018, Antalya, Turkey.

Bryant, J.A., Yogodzinski, G.M., Hall, M.I., Lewicki, J.L., Bailey, D.G. 2006. Geochemical constraints on the origin of volcanic rocks from the Andean Northern Volcanic Zone, Ecuador. Journal of Petrology 47, 6, 1147-1175.

Chen, B., Long, X., Wilde S.A., Yuan, C., Wang, Q., Xia, X., Zang, Z. 2017. Delamination of lithospheric mantle evidenced by Cenozoic potassic rocks in Yunnan, SW China: A contribution to uplift of the Eastern Tibetan Plateau. Lithos 284-285, 709-729.

DePaolo, D.J. 1981. Trace element and isotopic effects of combined wall-rock assimilation and fractional crystallisation. Earth Planetary Science Letter 53, 189-202.

Edwards, C., Menzies, M., Thirwall, M. 1991. Evidence from Muriah, Indonesia, for the interplay of supra-subduction zone and intraplate processes in the genesis of potassic alkaline magmas. Journal of Petrology 32, 555–592.

Elmas, A., Koralay, E., Duru, O., Schmidt, A. 2017. Geochronology, geochemistry, and tectonic setti,ng of the Oligocene magmatic rocks (Marmaros Magmatic Assemblage) in Gökçeada Island, northwest Turkey. International Geology Review 59, 4, 420-447.

Ercan, T., Satır, M., Dora, A., Sarıfakıoğlu, E., Yıldırım, T., Adis, C., Walter, H.J., Özbayrak, İ.H. 1995. Biga Yarımadası, Gökçeada, Bozcaada ve Tavşan Adaları'ndaki Tersiyer yaşlı volkanitlerin petrolojisi ve bölgesel yayılımı. Maden Tetkik ve Arama Dergisi 117, 55-86.

Ersoy, Y.E., Helvacı, C., Uysal, İ., Karaoğlu, Ö., Palmer, M.R., Dindi, F. 2012. Petrogenesis of the Miocene volcanism along the İzmir-Balıkesir Transfer Zone in western Anatolia, Turkey: implications for origin and evolution of potassic volcanism in post-collisional areas. Journal of Volcanology and Geothermal Research 241-242, 21-38.

Fitton, J. G., James, D., Kempton, P.D., Ormerod, D.S., Leeman, W.P. 1988. The role of lithospheric mantle in the generation of late Cenozoic basic magmas in the Western United States. Journal of Petrology Special Lithosphere Issue, 331-349.

Gamble, J., Woodhead, J., Wright, I., Smith, I. 1996. Basalt and sediment geochemistry and magma petrogenesis in a transect from oceanic island arc to rifted continental margin arc: the Kermadec-Hikurangi margin, SW Pacific. Journal of Petrology 37, 6, 1525-1546.

Genç, Ş.C., Yılmaz, Y. 1997. An example of Post-collisional Magmatism in Northwestern Anatolia: the Kızderbent Volcanics (Armutlu peninsula, Turkey). Turkish Journal of Earth Science 6, 33-42.

Genç, Ş.C., Altunkaynak, Ş. 2007. Eybek graniti (Biga yarımadası, KB Anadolu) üzerine: Yeni jeokimya verileri ışığında yeni bir değerlendirme. Yerbilimleri 28, 2, 75-98.

Gill, J.B. 1981. Orogenic andesites and plate tectonics. Springer - Verlag, New York, 392 p.

Gülmez, F., Genç, Ş.C., Keskin, M., Tüysüz, O. 2013. A post-collision slab-breakoff model for the orgin of the Middle Eocene magmatic rocks of the Armutlu-Almacık belt, NW Turkey and its regional implications. Geological Society, London, Special Publications 372, 107-139.

Haase, K.M., Mühe, R., Stoffers, P. 2000. Magmatism during extension of the lithosphere: geochemical constraints from lavas of the Shaban Deep, northern Red Sea. Chemical Geology 166, 225-239.

Harris, N.B.W., Kelley, S., Okay, A.İ. 1994. Post-collsion magmatism and tectonics in northwest Anatolia. Contributions to Mineralogy and Petrology 117, 241-252.

Hickey, R.V., Frey, F.A., Gerlach, D.C., Escobar, L.L. 1986. Multiple source basaltic arc rocks from the southern volcanic zone from of the Andes (34°-41°S): Trace element and isotopic evidence for contributions from subducted oceanic crust. Journal of Geophysical Research 91, B6, 5963-5983.

Hickey, R.V., Roa, H.M., Escobar, L.L., Frey, F. 1989. Geochemical variations in Andean basaltic and silicic lavas from the Villarica-Lanin Chain (39.5°S): an evaluation of source heterogeneity, fractional crystallization and crustal assimilation. Contribution to Mineralogy and Petrology 3, 361-386.

Hofmann, A.W. 1988. Chemical differentiation of the Earth: the relationship between mantle, continental crust, and oceanic crust. Earth and Planetary Science Letters 90, 297–314.

Hofmann, A.W., Jochum, K.P., Seufer, M., White W.M. 1986. Nb and Pb in oceanic basalts: new constraints on mantle evolution. Earth and Planetary Science Letters 79, 33-45.

Ilgar, A., Demirci, E.S., Duru, M., Pehlivan, Ş., Dönmez, M., Akçay, A.E. 2008. 1/100.000 ölçekli, Türkiye Jeoloji Haritaları Çanakkale H15 ve H16 Paftaları No: 100. Maden Tetkik ve Arama Genel Müdürlüğü, Ankara.

Irvine, T. N., Baragar, W. R. A. 1971. A guide to the chemical classification of the common volcanic rocks. Canadian Journal of Earth Science 8, 523-548.

Karacık, Z. Yılmaz, Y., Pearce, J., Ece, Ö.I. 2008. Petrochemistry of the South Marmara granitoids, northwest Anatolia, Turkey. International Journal of Earth Science 97, 1181-1200.

Kesgin, Y., Varol, B. 2003. Gökçeada ve Bozcaada'nın Tersiyer jeolojisi (Çanakkale), Türkiye. Maden Tetkik ve Arama Dergisi 126, 49-67.

Köprübaşı, N., Aldanmaz, E. 2004. Geochemical constraints on the petrogenesis of Cenozoic I-type granitoids in Northwest Anatolia, Turkey: evidence for magma generation by lithospheric delamination in a post-collisional setting. International Geology Review, 46, 705–729.

Labanieh, S., Chauvel, C., Germa, A., Q., X. 2012. Martinique: a clear case for sediment melting and slab dehydration as a function of distance to the trench. Journal of Petrology 53, 12, 2411-2464.

Langmuir, C.H., Vocke, R.D., Hanson, G.N., Hart, S.R. 1978. A general mixing equation with applications to İcelandic basalts. Earth and Planetary Science Letters 37, 380-392.

Li, D., He, D., Fan, C. 2015. Geochronology and Sr-Nd-Hf isotopic composition of the granites, enclaves, and mafic dykes in the Karamaya area, NW China: Insights into late Carboniferous crustal growth of West Junggar. Geoscience Frontiers 6, 2, 153-173.

McDonough, W.F.1990. Constraints on the composition of the continental lithospheric mantle. Earth and Planetary Science Letters 101, 1-18.

McDonough, W.F., Sun, S.S. 1995. The composition of the Earth. Chemical Geology 120, 223-253.

McKenzie, D.P., O'Nions, R.K. 1991. Partial melt distributions from inversion of rare earth element concentrations. Journal of Petrology 32, 1021-1091.

McLennan, S.M. 2001. Relationship between the trace element composition of sedimenatry rocks and upper continental crust. Geochemistry Geophysics Geosystems 2, DOI: 10.1029/ 2000GC000109.

Normand, M.D., Garcia, M.O. 1999. Primitive magmas and source characteristics of the Hawaiian plume: petrology and geochemistry of shield picrites. Earth and Planetary Science Letters 168, 27-44.

Okay, A.İ., Tüysüz, O. 1999. Tethyan sutures of northern Turkey. In: Durand, B., Jolivet, L., Horvath, F., Seranne, M. (Eds.), The Mediterranean Basin: Tertiary Extansion within the Alpine Orogen, Geological Society London Special Publications 156, 1, 475-515.

Okay, A.İ., Siyako, M., Bürkan, K.A. 1990. Biga Yarımadası'nın jeolojisi ve tektonik evrimi. Türkiye Petrol Jeologları Derneği Bülteni 2, 1, 83-121.

Okay, A.İ., Tansel, İ., Tüysüz, O. 2001. Obduction, subduction and collision as reflected in the Upper Cretaceous-Lower Eocene sedimentary record of western Turkey. Geological Magazine 138, 2, 117-142.

Pearce, J.A. 1996. Sources and settings of granitic rocks. Episodes 19, 4, 120-125.

Pearce, J.A., Harris, N.B.W., Tindle, A.G. 1984. Trace element discrimination diagrams for the tectonic interpretation of granitic rocks. Journal of Petrology 25, 956-983.

Plank, T. 2005. Constraints from thorıum/lanthanum on sediment recycling at subduction zones and the evolution of the continents. Journal of Petrology 46, 5, 921-944.

Plank, T., Langmuir, C.H. 1998. The chemical composition of subducting sediment and its consequences for the crust and mantle. Chemical Geology 145, 325-394.

Rollinson, H.R. 1993. Using geochemical data: evaluation, presentation, interpretation. Longman Scientific and Technical, John Wiley and Sons, Inc., New York, 352 p.

Sarı, R., Türkecan, A., Dönmez, M., Küçükefe, Ş., Aydın, Ü., Özmen, Ö. 2015. The geology of Gökçeada (Çanakkale). Bullettin of the Mineral Research and Exploration 150, 1-18.

Shaw, D.M. 1970. Trace element fractionation during anatexis. Geochimica Cosmochimica Acta 34, 237-243.

Sun, S.S., McDonough, W.F. 1989. Chemical and isotopic systematics of oceanic basalts: implications for mantle composition and processes. In: Saunders, A.D. and Norry, M.J. (eds.), Magmatism in ocean basins. Geological Society of London Special Publication 42, 313-345.

Sylvester, P.J. 1998. Post-collisional strongly peraluminous granites. Lithos 45, 29-44.

Şengör, A.M.C., Yılmaz, Y. 1981. Tethyan evolution of Turkey: a plate tectonic approach. Tectonophysics 75, 181-241.

Şentürk, K., Karaköse, C. 1987. Çanakkale Boğazı ve dolayının jeolojisi. Maden Tetkik ve Arama Genel Müdürlüğü Rapor No: 9333, Ankara, (unpublished).

Taylor, S., R., McLennan, S.M. 1985. The continental crust: its composition and evolution. An examination of the geochemical record preserved in sedimentary rocks. Blackwell Scientific Publications 46, pp.838.

Temel, R.Ö., Çiftçi, N.B. 2002. Gelibolu Yarımadası, Gökçeada ve Bozcaada Tersiyer Çökellerinin stratigrafisi ve ortamsal özellikleri. Türkiye Petrol Jeologları Derneği Bülteni 14, 17-50.

Thiéblemont, D., Tegyey, M. 1994. Une discrimination géochimique des roches différenciées témoin de la diversité d'origlisboaine et de situation tectonique des magmas calcoalcalins. Comptes Rendus de l'académie des Sciennces Paris 319, 87-94.

Thompson, R.N. 1982. Magmatism of the British Tertiary province. Scottish Journal of Geology 18, 49-107.

Thompson, R.N., Morrison, M.A., Dickin, A.P., Hendry, G.L. 1983. Continental flood basalts. arachnids rule OK? In: Hawkesworth, C.J. and Norry, M.J. (eds) Continental Basalts and Mantle xenoliths. Nantwich: Shiva, 158-185.

Tunç, İ.O., Yiğitbaş, E., Şengün, F. Wazeck, J., Hofmann, M., Linnemann, U. 2002. U-Pb zircon geochronology of northern metamorphic massifs in the Biga peninsula (NW Anatolia-Turkey): new data and a new approach to understand the tectonostratigraphy of the region. Geodinamica Acta 25, n3-4, Special Issue: Tectonics of the eastern Mediaterranean-Black Sea Region: Part A, dedicated in honor of Aral Okay's 60th birthday, DOI: 10.1080/09853111.2013.87824.

Qian, X., Feng Q., Chonglakmani, C., Monjai, D. 2013. Geochemical and geochronological constrains on the Chiang Khong volcanic rocks (northwestern Thailand) and its tectonic implications. Frontiers of Earth Science 7, 4, 508-521.

Winchester, J.A., Floyd, P.A. 1977. Gerochemical discrimination of different magma series and their differentiation products using immobile elements. Chemical Geology 20, 325-343.

Yılmaz, Y. 1989. An approach to the origin of young volcanc rocks of western Turkey. In: Şengör, A.M.C. (eds), Tectonic ovolution of the Tethyan region. Kluwer Academics, Hague-The Netherlands 159-189.

Yılmaz, Y., Genç, Ş.C., Yiğitbaş, E., Bozcu, M. Yılmaz, K. 1995. Geological evolution of the Late Mesozoic continental margin of Northwestern Anatolia. Tectonophysics 243, 155-171.

Yılmaz, Y., Tüysüz, O., Yiğitbaş, E., Genç Ş.C., Şengör, A.M.C. 1997. Geology and tectonic evolution of the Pontides. In: Robinson, A.G. (Ed.), Regional and Petroleum Geology of the Black Sea and surrounding region. American Association of Petroleum Geologists, Memoir 68, 183-226.

Yılmaz Şahin, S., Örgün, Y., Güngör, Y., Göker, A.F., Gültekin, A.H., Karacık, Z. 2010. Mineral and Whole-rock Geochemistry of the Kestanbol Granitoid (Ezine-Çanakkale) and its Mafic Microgranular Enclaves in Northwestern Anatolia: Evidence of Felsic and Mafic Magma Interaction. Turkish Journal of Earth Science 19, 101-122.

Zak, J., Kratinova, Z., Trubac, J. Mrlina, J. 2011. Structure, emplacement, and tectonic setting of Late Devonian granitoid plutons in the Teplá–Barrandian unit, Bohemian Massif. International Journal of Earth Science 100, 7, 1477-1495.

Bulletin of the Mineral Research and Exploration

http://bulletin.mta.gov.tr

Geology and formation of Nevruztepe Fe-Cu skarn mineralization (Kayseri-Turkey)

Deniz TİRİNGA[a*], Bülent ATEŞÇİ[b], Yılmaz ÇELİK[a], Güvenç DEMİRKIRAN[c], Cahit DÖNMEZ[a], Aytekin TÜRKEL[b] and Taner ÜNLÜ[d]

[a]*General Directorate of Mineral Research and Exploration, Department of Mining and Exploration, Çankaya/Ankara, Turkey*
[b]*General Directorate of Mineral Research and Exploration, Aegean Region Directorate, Bornova/İzmir, Turkey*
[c]*General Directorate of Mineral Research and Exploration, Eastern Mediterranean Region Directorate, Çukurova/Adana, Turkey*
[d]*Ankara University, Department of Geological Engineering, Gölbaşı/Ankara, Turkey (Emeritus)*

Research Article

Keywords:
Skarn, Magnetite, Copper, Kayseri, Yeşilhisar, Yahyalı pluton.

ABSTRACT

The Nevruztepe iron-copper prospect is a skarn near Yeşilhisar (Kayseri). It has been overlooked as a potential producer of copper. The skarn was generated in Permian to Jurassic carbonate rocks by the Eocene Yahyalı granitic pluton. Lithologic units, including skarns, dip about 15 degrees southward. Skarns are both prograde (garnet and diopside) and retrograde (epidote); both exoskarn and endoskarn exist. Most of the magnetite is in a quartz-sulfide stage in retrograde skarn that is cut by veins and lenses containing quartz-pyrite-chalcopyrite. Granite and mineralized skarn are rare at the surface. From 2013 to 2015, 31 drill holes (totaling 6.178,5 m) encountered skarn to a depth of 450 m. Mineralized zones vary from 1,2 to 54,7 m thick. Fe mean grade ranges from 12% to 49%; mean copper grades vary from 10 to 4650 ppm. The deposit contains 5.096.788 tonnes of mineralized material. Microscopy on samples of drill core shows that the ore minerals are primarily magnetite, hematite, and chalcopyrite. Some magnetite is altered to hematite. Experiments show that with grinding to 100 microns the iron can be beneficiated to 66%. Waste from separation of the magnetite is 0.16 to 0.19% Cu; with flotation this was beneficiated to 19% Cu.

Received Date: 12.08.2018
Accepted Date: 10.03.2019

1. Introduction

Kayseri-Adana basin is the second most important iron province of Turkey in terms of reserve and production amounts. The Mansurlu section of the basin is riched by large-reserved hematite deposits which are oxidation products of Early Cambrian aged volcanosedimentary type siderite deposits (Tiringa et al., 2009; 2016). The best known of these deposits are Karaçat and Attepe deposits.

In the northern Kayseri-Adana basin, the Yahyalı Pluton outcrops in a narrow belt from Kovalı village in the west, Yahyalı in the east, between Yeşilhisar and Yahyalı (Kayseri). This pluton intrudes into metamorphic units of the Yahyalı Nappe and skarn type iron and lead-zinc mineralization are formed along the contact (Hanilçi and Öztürk, 2011; Tiringa et al., 2014).

The closest mineralization to Nevruztepe Fe-Cu mineralization is Karamadazı iron deposit. Other mineralizations are called as Kovalı, Sayburnu, Kurbağapınarı and İsmailinkaya iron mineralization. All these mineralizations are actively mined as open pit, while Karamadazı iron deposit is still mining in

Citation Info: Tiringa, D., Ateşçi, B., Çelik, Y., Demirkıran, G., Dönmez, C., Türkel, A., Ünlü, T. 2020. Geology and formation of Nevruztepe Fe-Cu skarn mineralization (Kayseri-Turkey). Bulletin of the Mineral Research and Exploration. 161, 101-119. https://doi.org/10.19111/bulletinofmre.543189

* *Corresponding author: Deniz TİRİNGA, deniz.tiringa@mta.gov.tr*

galleries. In terms of type and ore paragenesis the mineralization, it has similarities with Karamadazı iron deposit.

In Karamadazı iron deposit, skarn formed as a result of contact metasomatism between quartz diorite and limestone (Oygür et al., 1978). Kuşçu et al. (2001) stated this represented typical exoskarn development and indicated that mineralization formed both endoskarn and exoskarn. The basic ore minerals in the deposit are hematite occasionally martitised and magnetite transformed to maghemite. Magnetites are accompanied by very small amounts of pyrite, chalcopyrite and pyrrhotite. The Karamadazı iron deposit has an orebody striking southeast in the form of lenses with occasional 120 m length and 20 m thickness. The deposit has proven+probable reserves calculated at 6,5 million tons with 54% Fe, 1,7% S and 11% SiO_2 (Oygür, 1986).

This study aims to determine the ore geology and formation of Nevruztepe mineralization based on mineralogic-petrographic, SEM and geochemical analysis results from drill core samples, and to attract attention to large and small iron deposits located between Yahyalı and Yeşilhisar counties, which may contain high grades of copper as well as iron. In this study, it is considered that the deposits in the region have been ignored in terms of obtaining copper from iron ore production recently, and will assess the benefit of adding this economic value for future mining activities.

1.1. Methods

Core samples are taken from ore-bearing zone to analyse trace element content and determine the grade of ore deposit. Geochemical analyses were performed in MTA General Directorate MAT Department Laboratories. Gold analyses were done with aqua regia solution and ICP-MS, silver is analysed by AAS and major oxide analyses are done with XRF. Trace element analyses were performed after triple acid solutions or aqua regia solution processes using and ICP-MS and ICP-OES.

Mineralogic-petrographic studies were performed in MTA General Directorate MAT Department Mineralogy-Petrography Laboratories with samples firstly prepared as thin and polished sections. Thin sections were examined with Leitz polarized microscope, to determine the mineralogic, petrographic and textural properties of the rocks. Ore microscopy studies of polished sections were performed with Leica brand reflected and transmitted light microscope. SEM analysis studies were performed using FEI Quanta 400 MK2 SEM and EDAX Genesis XM4i EDS detector. For SEM analysis, polished sections are coated by carbon.

2. Geology

The study area is located in the southeast section of the Central Anatolia region, near Kovalı village located between Yeşilhisar and Yahyalı in Kayseri (Figure 1). Mainly rocks belong to the Yahyalı Nappe, outcrop in the study area and surroundings (Figure 2). Apart from these, granitic rocks of Yahyalı Pluton, the Late Cretaceous Çiftehan formation of Bozkır Assemblage, cover sediments of Palaeocene Çamardı formation and lacustrine sediments with volcanic interlayers of the middle-late Miocene Ürgüp formation are observed (Figure 3). Granitic rocks belonging to the Yahyalı Pluton in the study area are observed in a small area, which is too small to be mapped, with the ancient workings of the Sayburnu mineralization.

The Karsavuran formation is the lowest unit in the study area and surroundings. Its lowermost units are calcschist and crystallized limestone interlayered with schists and thickens upwards into limestone levels before thin to pass into schists (Ayhan and Lengeranlı, 1986). The dominant lithology in the Ayraklıtepe formation is grey-dark grey dolomite, marble and dolomitic limestones. In central sections, metacarbonate, schist and quartzite alternations are observed (Ayhan and Lengeranlı, 1986). Mostly represented by yellow, green and brown schists, the Yellibel formation comprises recrystallized limestone and calcschist interlayers containing sericite-schist, quartz-sericite schist and phyllites in some locations (Ayhan and Lengeranlı, 1986). The Başoluk formation comprises grey and yellow coloured moderate-thick-bedded quartzites (Alan et al., 2007). The dominant lithology in the Karlığıntepe formation is grey-black coloured, fine-moderate-bedded recrystallized limestone (Ayhan and Lengeranlı, 1986). The upper sections are present in the study area represented by black, fine-moderate-bedded dolomitic levels containing micritic limestone (Tiringa et al., 2014).

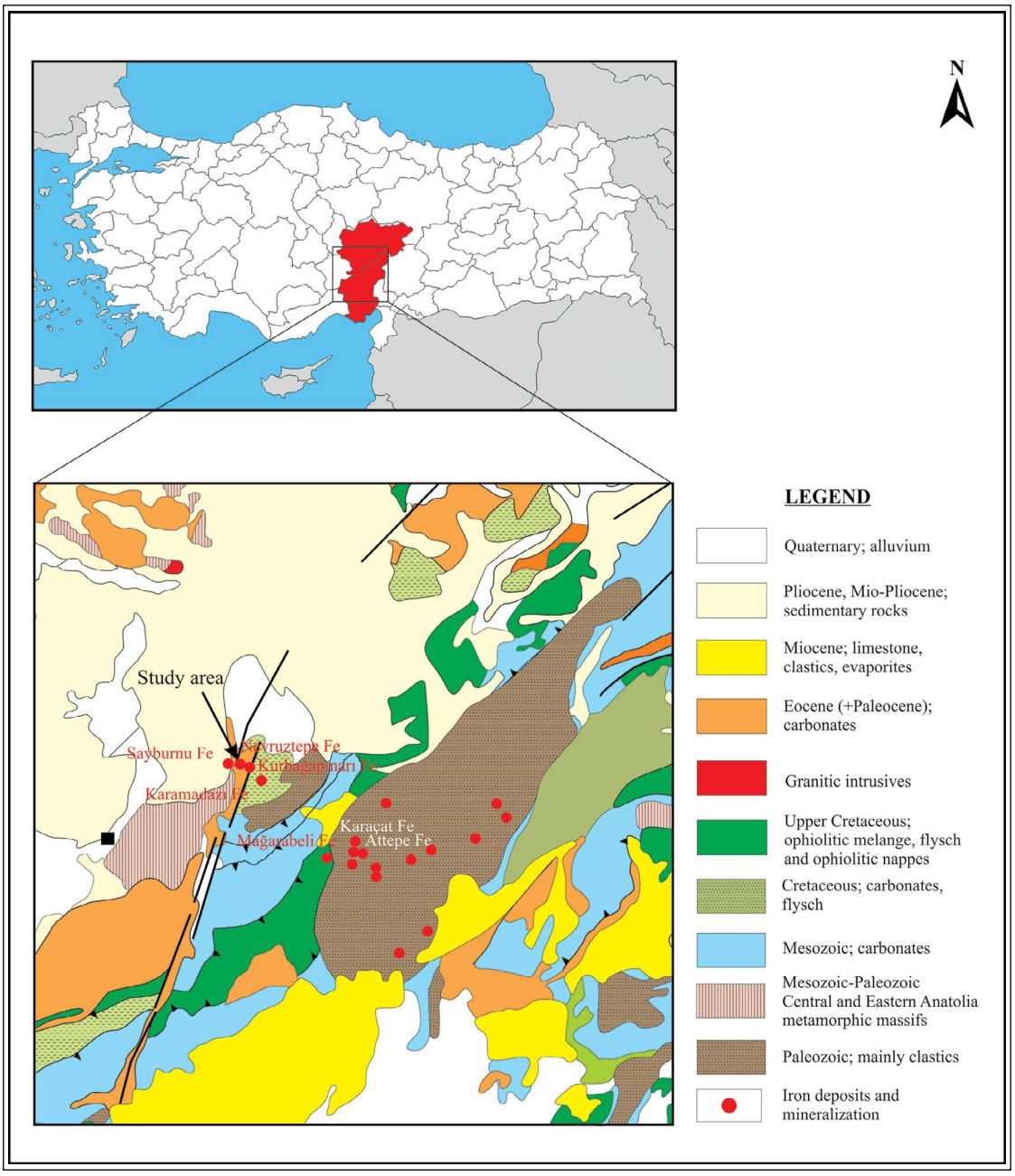

Figure 1- Location map showing regional geology of the study area and surroundings. Regional geology map taken from MTA General Directorate 1/500.000 scale geology map.

The Kocatepe formation contains recrystallized limestone, metapebblestones and quartzites at lower levels (Keskin and Alan, 2013). In upper sections it comprises maroon, green, grey, yellow-grey coloured marl, mudstone and siltstone which are slightly metamorphosed (Figure 4a).

The Tavşancıdağtepe formation comprises recrystallized clayey limestone at different levels, grey-black coloured metadolomite and grey-black coloured moderate-thick-bedded, locally very thick limestone and marble containing hematite zones, fractures filled with calcite and macro fossil shells (Keskin and Alan, 2013) (Figure 4b).

The Çiftehan formation in the Bozkır Assemblage contains serpentinites with limestone blocks, pelagic micritic mudstone, turbiditic and conglomeratic rocks, cherty limestone, radiolarite, diabase and granodiorite (Tekeli, 1980). The lowermost part of the formation

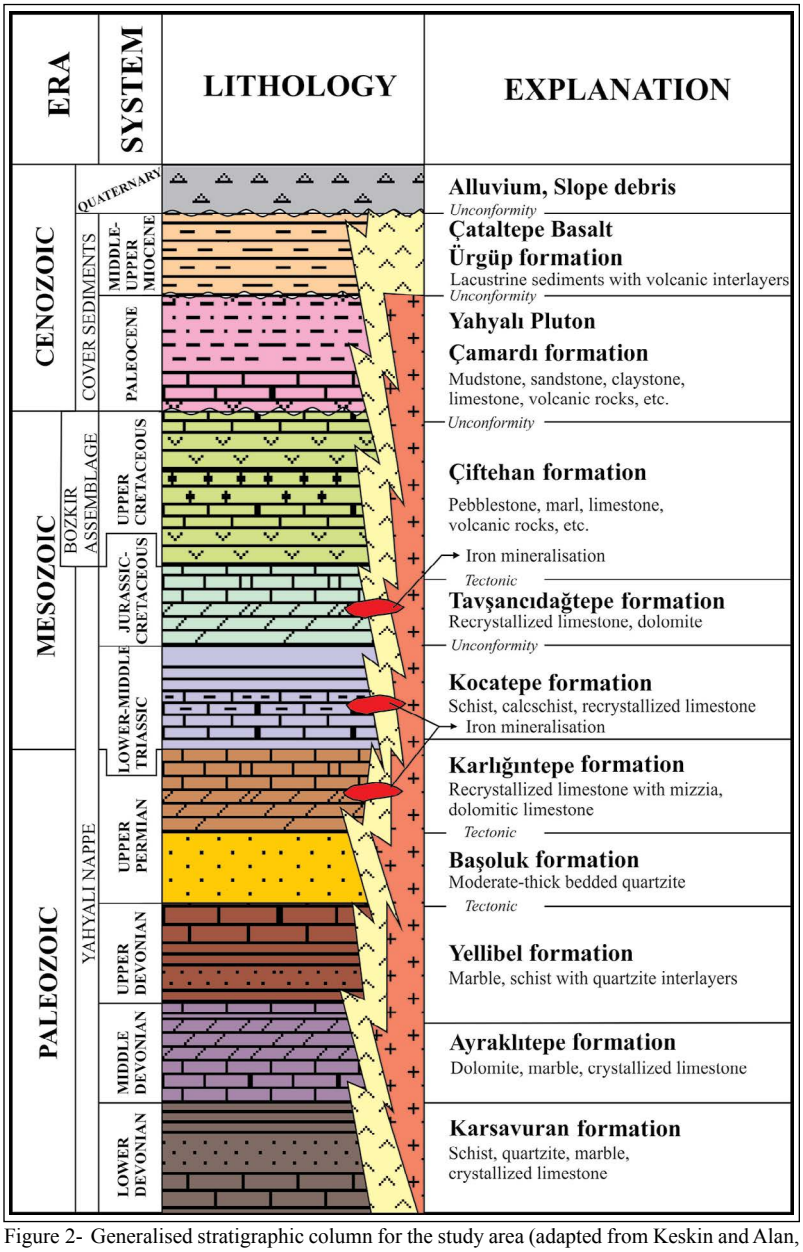

Figure 2- Generalised stratigraphic column for the study area (adapted from Keskin and Alan, 2013).

is red coloured basal pebblestone which poorly sorted pebbles up to 5 cm in size, and changes upwards to grey coloured clayey limestone and marl (Figure 4c). Marl-sandstone alternation overlies these units.

The Çamardı formation in the cover units mainly comprises marl, mudstone, siltstone, sandstone and clastic limestone. It contains rare spilitic interlayers and is cut by plutonic rocks (Keskin and Alan, 2013).

The Ürgüp formation includes red-brown coloured, poorly or without bedded pebblestone, sandstone, mudstone, gypsum, anhydrite, limestone and ignimbrite interlayers and was deposited in continental conditions (Keskin and Alan, 2013).

The clearest outcrop of the Yahyalı Pluton is between Yularıköy and Karakuşkayası Hill. Here, it thins towards the west, and after being observed northeast of Kovalı village, east of Sayburnu, the Kovalı dam lake and in old galleries in İsmalinkaya, it is covered by younger rock units. The Yahyalı Pluton consists of calcalkaline biotite granite, quartz diorite, diorite and granodiorite. The hypabyssal

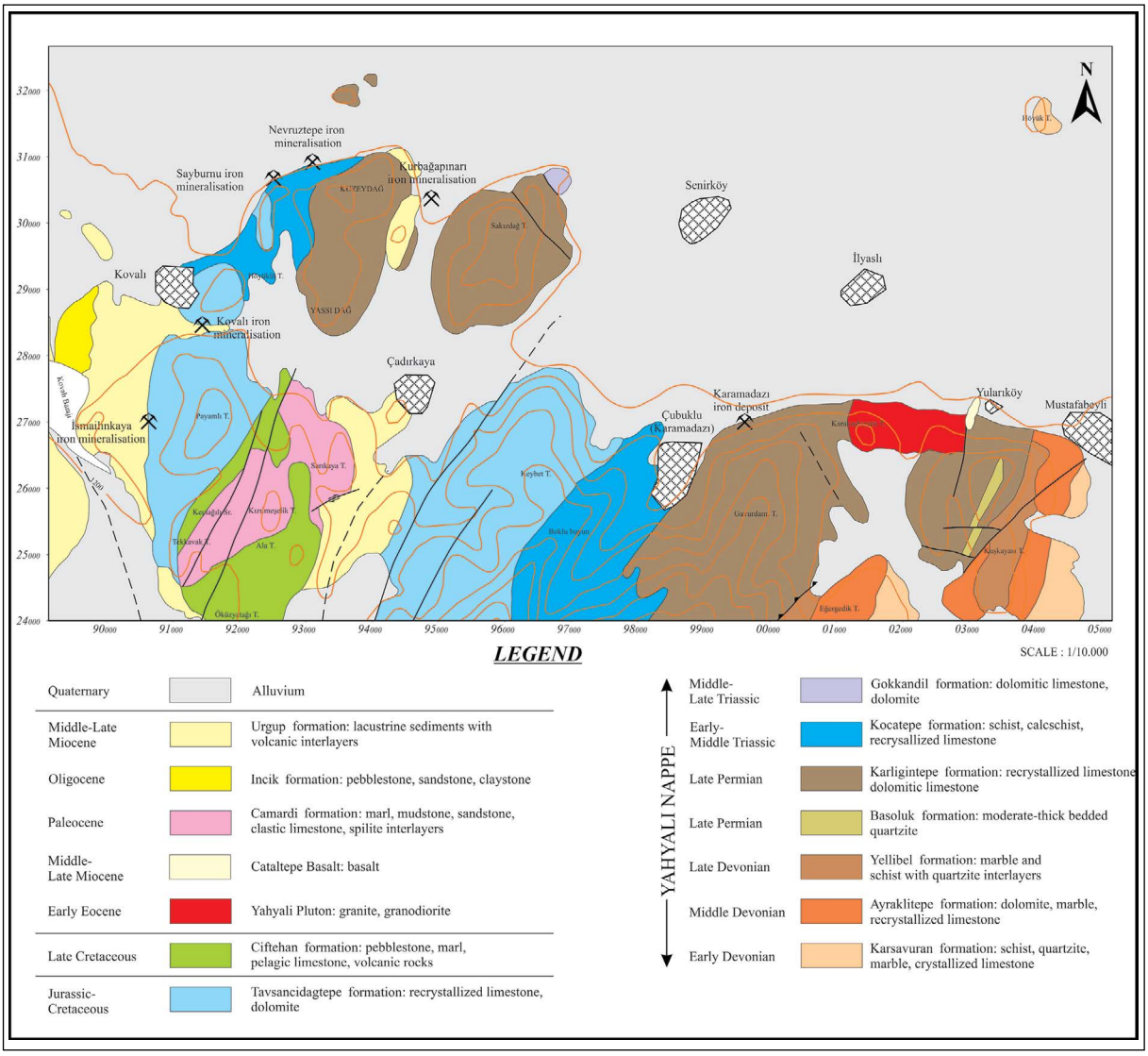

Figure 3- General geology map of the study area (taken from Keskin and Alan, 2013).

Figure 4- a) Recrystallised limestone containing quartzite-rich levels, b) Grey-coloured recrystallised limestones containing red-coloured iron zones, c) Sorted basal conglomerates belonging to the Çiftehan formation.

equivalents of these rocks of albite porphyrite, rhyolite, rhyodacite, dacite, trachydacite and andesite rocks are observed (Oygür et al., 1978). There is no reliable radiometric age data belong to the pluton. But based on the stratigraphic relationship in the field the magmatic intrusion formed during the Eocene-Oligocene (Oygür, 1986), while Keskin and Alan (2013) proposed its age is Early Eocene.

3. Petrography

3.1. Magmatic Rocks

Mineralogic and geochemical features of the Yahyalı Pluton indicates that it is derived from typical post-collisional environment from mantle-derived mafic magma source (Boztuğ et al., 2002). During injection of the magma into the crust or during diapiric elevation through the crust, the crust melted to create coeval felsic magma association emphasising the bimodal characteristic. Another study by Kuşçu et al. (2002) compared the mean iron-copper skarn granitoids in the Yahyalı Pluton and proposed that other iron skarn granitoids contained higher Rb, Sr and Th and lower Ni, Cr, Sc and V. As a result, they stated that the granitoid should be distinguished from typical iron skarn granitoids in the world due to containing more material from the continental crust. Based on all features, the Yahyalı Pluton appears similar to the Ulukışla island arc at the end of the Late Cretaceous or beginning of the Palaeocene described by Oktay (1982) and the bimodal characteristic of Horoz (Ulukışla-Niğde) Pluton developing in post-collisional environment (Çevikbaş et al., 1995).

In this study, according to petrographic investigations of drill core samples, the magmatic rocks in the Yahyalı Pluton comprised lithologies varying from gabbroporphyry to monzonite, with basic and intermediate composition plutonic and hypabyssal rocks (Figure 5a). Additionally, many aplite and pegmatite dykes cutting the pluton and mafic enclaves up to 30-40 cm in size are observed (Figure 5b). The rocks generally have porphyritic textures, though some have holocrystalline texture. The main components are plagioclase, feldspar, biotite and quartz. Alteration is commonly observed in all rock groups. The dominant alteration in granular texture plutonic rocks like granite, granodiorite and monzonite is seriticisation, on the other hand in porphyritic rocks at the margins of the pluton argillisation and carbonation are commonly observed. Lower grade silicification and chloritisation are observed (Table 1). Considering the alteration types, it can be said that phyllic and/or argillic zones are represented. Certain rock groups determined by petrographic investigations can be listed as follows.

Monzonite-monzonite porphyry: Granular and porphyritic texture, fine-moderate grained, plagioclase, alkali feldspar, quartz and biotite are the main components in samples. Alteration types are commonly observed as sericitisation and carbonation of plagioclase, argillisation of alkali feldspar, and chloritisation of biotite (Figures 5c and 5d).

Granite-granite porphyry, microgranite-microgranite porphyry: Rocks comprise quartz, alkali feldspar, plagioclase and biotite minerals and are fine-grained, holocrystalline and porphyritic texture. There is sericitisation, argillisation and carbonation developed in rocks, with cataclasm traces commonly observed.

Andesite: Rocks comprise plagioclase, amphibole, biotite, quartz and alkali feldspar minerals and are fine-grained with porphyritic texture. Sericitisation, argillisation, silicification, chloritisation and carbonation are observed in the rocks (Figures 5e and 5f).

Granodiorite-granodiorite porphyry: Granodiorites are the most common rock type observed in all samples. The rocks contain plagioclase, alkali feldspar, quartz, biotite and amphibole minerals and are fine-grained and granular texture. Alteration types of argillisation, sericitisation, carbonation, silicification and chloritisation are observed in the rocks (Figures 6a and 6b).

Diorite, diorite porphyry, quartz diorite, quartz diorite porphyry, microdiorite: Comprising plagioclase, biotite and amphibole minerals, the rock has fine and occasionally coarse-grain and granular texture. Alteration in the form of sericitisation, carbonation, argillisation, chloritisation, uralitisation and opacification has developed in the rock (Figures 6c and 6d).

Gabbroporphyry: One sample was defined as gabbro porphyry according to mineralogic composition, containing pyroxene, amphibole and plagioclase minerals. The rock is fine-grained with porphyritic texture, with groundmass of ophitic texture containing fine-grained plagioclase and amphibole minerals. The pyroxenes in the rock have undergone uralitisation, amphiboles have been carbonated and chloritised, while plagioclases have been argillised and sericitised (Figures 6d and 6e).

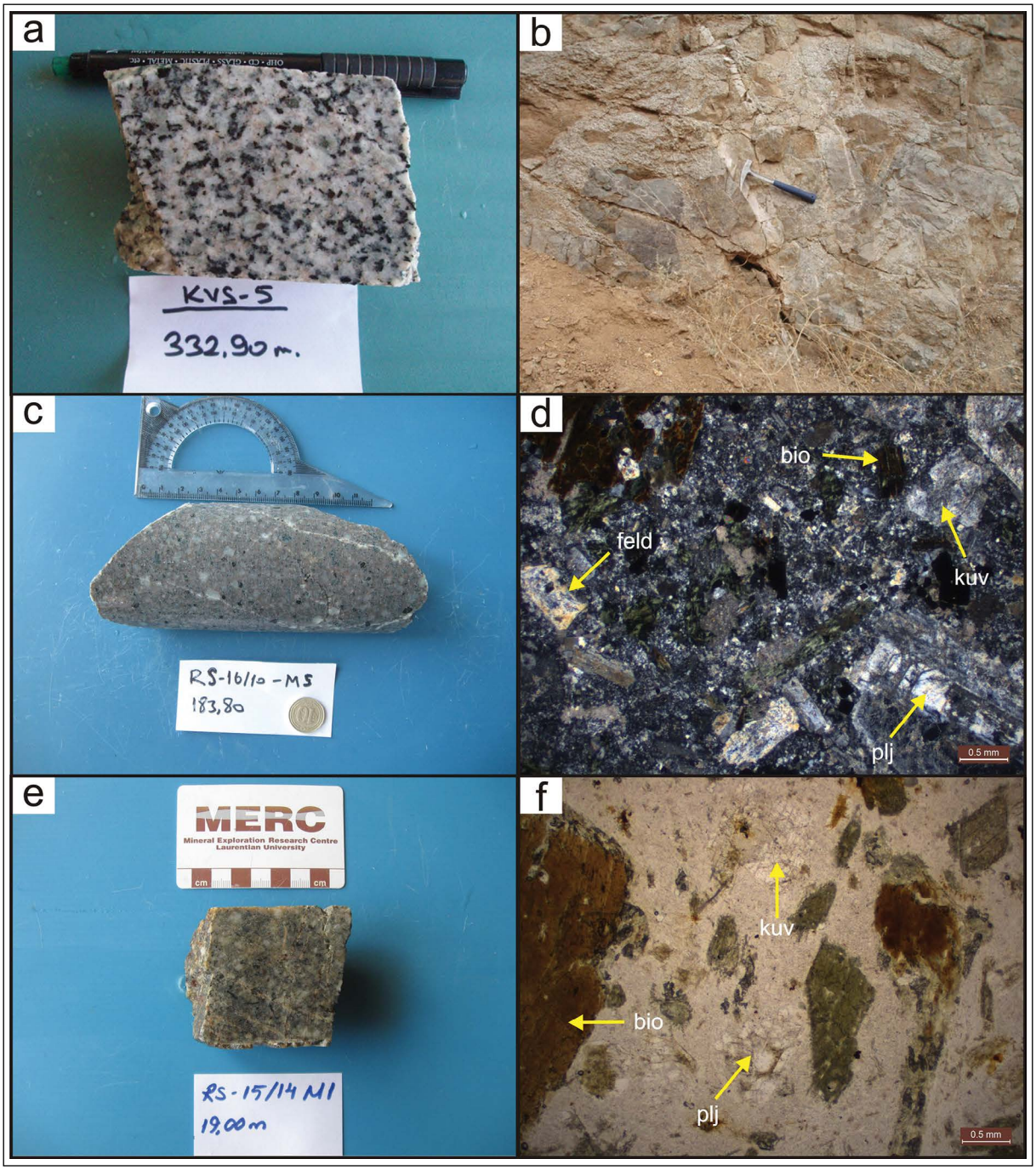

Figure 5- a) Granodiorite igneous rocks belonging to the Yahyalı Pluton, b) mafic enclaves and aplite veins commonly observed in the Yahyalı Pluton, c) monzonite core sample, d) polarising microscope image of monzonite sample (2.5 X, //), e) andesite core sample, f) polarising microscope image of andesite sample (2.5 X, /), plj: plagioclase, kuv: quartz, bio: biotite, feld: alkali feldspar.

3.2. Skarns

In the study area and surroundings, along the contact between limestone and granitoids, skarn zones are formed with very variable distribution. Due to skarn zones containing magnetite-chalcopyrite lenses with different thicknesses, mineralization has temporal and spatial relationship with contact metamorphism and formation of skarn. Skarn lithologies do not outcrop in the locations where mineralization is observed, and so could not be mapped at preferred scale. According to petrographic and geochemical investigations within

Table 1- Summary of petrographic investigation of core samples from the Yahyalı Pluton (plj: plagioclase, amf: amphibole, px: pyroxene, q: quartz, feld: feldspar, alk. feld: alkali feldspar, horn: hornblende, lök: leucoxene, kar: carbonatisation, ser: sericitisation).

Sample ID	Grain Size	Texture	Main Components	Alteration	Rock Name
KVS-3-M9	Fine grained	Porphyritic	plj.+amf.±apatite	clay, kar., silica	Andesite
KVS-5-M7	Fine grained	Porphyritic	plj.+amf.+biotite+q± sphene	ser., clay, chlorite, kar., epidote, silica	Andesite
KS-14/6-M8	Fine grained	Porphyritic	plj.+amf.+q	kar., silica, chlorite, clay	Andesite
KS-14/12-M1	Fine grained	Porphyritic	plj.+amf.+px	clay, kar., chlorite	Andesite
KS-14/14-M6	Fine grained	Porphyritic	plj.+biotite	chlorite	Andesite
RS-15/4-M5	Fine grained	Porphyritic	px+amf.+plj.±sphene	kar., opacite	Andesite
RS-15/9-M4	Fine-medium grained	Porphyritic	plj.±apatite	ser., clay, silica	Andesite
RS-15/10-M3	Fine-medium grained	Porphyritic	plj.+amf.+biotite± apatite±sphene	ser., clay, opacite, silica, kar.	Andesite
RS-15/15-M3	Fine-medium grained	Porphyritic	plj.+biotite+q±apatite	opacite, kar., ser., silica	Andesite
KVS-5-M1	Fine grained	Porphyritic	plj.+amf.+biotite±sphene	ser., clay, chlorite, kar., epidote, uralite, silica	Andesite (include gabbro anklave)
RS-15/14-M6	Medium grained	Porphyritic	plj.+biotite+amf.	ser., clay, chlorite, kar., silica, epidote	Andesite (include granular anklave)
KS-14/9-M4	Fine grained	Porphyritic	q+alk feld.+plj.	kar., clay	Granite
RS-15/14-M2	Fine-medium grained	Porphyritic	plj.+amf.+biotite+q	ser., clay, kar.	Andesite
RS-15/16-M5	Fine-medium grained	Porphyritic	plj.+biotite+q	opacite, chlorite, kar., ser., silica	Diyoriteporphyry
RS-16/2-M8	Fine-medium-coarse grained	Porphyritic	feld.+q	kar., silica	Granite
KVS-5-M18	Fine-medium-coarse grained	Porphyritic	plj.+biotite+amf.± apatite±lök.	ser., clay, kar., chlorite, silica	Diyoriteporphyry
RS-15/16-M3	Fine-medium grained	Porphyritic	plj.+amf.+biotite±apatite	opacite, clay	Diyoriteporphyry
RS-15/16-M4	Fine-medium grained	Porphyritic	plj.+biotite+amf.±apatite	opacite, clay, silica	Diyoriteporphyry
KVS-6-M4	Fine-medium-coarse grained	Porphyritic	plj.+horn.+biotite± sphene	ser., kar., epidote, chlorite, silica	Diyoriteporphyry (include monzonite anklave)
KVS-5-M9	Fine grained	Granular	plj.+q+alk feld.+biotite	ser., clay, kar.	Granite
KS-14/8-M6	Medium grained	Holocrystalline	q+alk feld.+plj.	kar.	Granite
KS-14/12-M6	Medium grained	Holocrystalline	q+alk feld.+plj.+biotite	clay, kar., ser	Granite
KS-14/13-M10	Fine grained	Holocrystalline	q+alk feld.+plj.+biotite	clay	Granite
KS-14/8-M9	Fine grained	Holocrystalline	q+alk feld.+plj.+biotite	kar., clay	Granodiorite
KS-14/9-M7	Medium grained	Holocrystalline	q+alk feld.+plj.+biotite	ser, clay	Granodiorite
KS-14/11-M3	Fine-medium grained	Holocrystalline granular	plj+alk feld.(ortoklaz) +q+biotite+amf.±apatite	ser., kar.	Granodiorite
KS-14/13-M12	Fine grained	Holocrystalline	q+alk feld.+plj.+biotite	kar., clay	Granodiorite
KVS-5-M13	Fine-medium-coarse grained	Holocrystalline granular	plj.+alk feld.(ortoklaz, mikroklin)+q+biotite±sphene	ser., clay, kar., epidote	Granodioriteporphyry
KS-14/8-M4	Medium grained	Hypocrystalline granular	q+alk feld.+plj.+ biotite+amf.	clay, kar.	Granodioriteporphyry
RS-16/4-M5	Fine-medium grained	Holocrystalline porphyritic	plj.+amf.+q	clay, kar.	Granodioriteporphyry
RS-16/7-M2	Fine-medium grained	Holocrystalline porphyritic	plj.+q+alk feld.+ biotite+amf.±titanit± zirkon±apatite	clay, kar., silica	Granodioriteporphyry
RS-16/10-M2	Fine-medium grained	Holocrystalline porphyritic	plj.+q+alk feld.+amf.+ biotite±zirkon	clay, kar.	Granodioriteporphyry
RS-16/10-M4	Fine-medium grained	Holocrystalline porphyritic	plj.+q+alk feld.+amf.+ biotite±zirkon±apatite	clay, kar., chlorite	Granodioriteporphyry
RS-15/7-M5	Fine grained	Granular	plj+q+biotite+amf.	kar	Quartzdiorite
KVS-5-M14	Fine-medium-coarse grained	Porphyritic	plj.+q+amf.+ biotite±sphene	ser., clay, kar., chlorite, silica	Quartzdiorite porphyry
KVS-1-M4	Fine grained	İdiomorph granular	plj.+amf.±apatite	karb., ser., chlorite, biotite, clay	Microdiorite
KVS-3-M3	Fine grained	Hypidimorph granular	plj.+alk feld.+amf.	clay, epidote, uralite, chlorite	Microdiorite
RS-15/15-M5	Fine grained	Porphyritic, subophitic	amf.+biotite±apatite	kar., ser., uralit, opacite	Microdiorite
RS-15/6-M3	Very fine grained	Granular	plj.+alk feld.+q+biotite	clay, ser., kar.,	Micromonzodiorite
RS-15/4-M4	Fine grained	Granular	plj.+alk feld.+px+amf. ±apatite±sphene	ser., clay, chlorite, epidote	Monzodiorite
RS-15/9-M6	Fine-medium grained	Granular	plj.+alk feld.+q+ biotite+amf.±apatite	ser., kar., chlorite, clay	Monzonite
KVS-3-M12	Fine-medium grained	Porphyritic	plj.+alk feld.+amf.+ q±sphene	ser., clay, uralit, chlorite, kar., epidote, silica	Monzonite porphyry

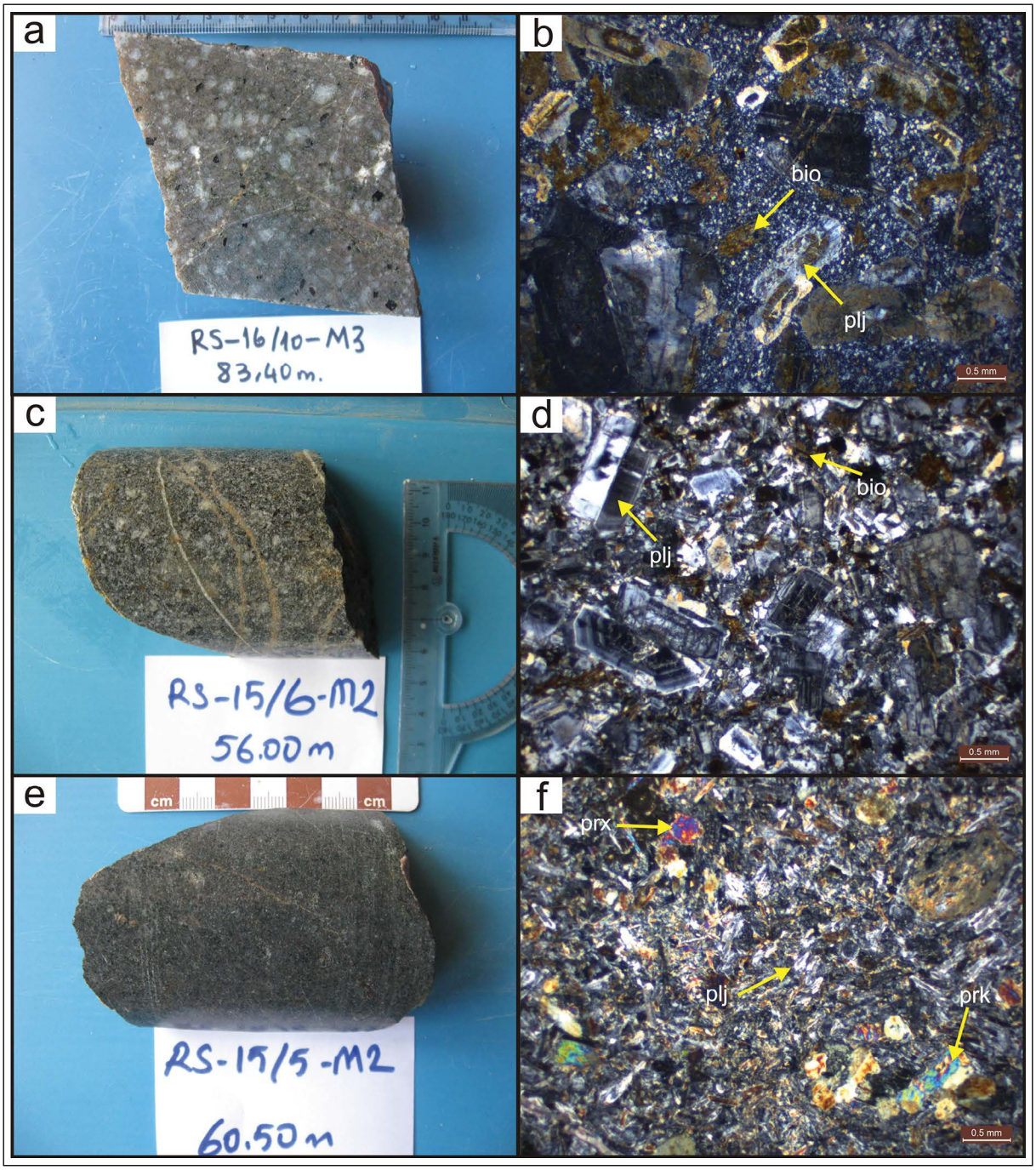

Figure 6- a) Granodiorite core sample, b) polarising microscope image of granodiorite sample (2.5 X, //), c) diorite porphyry core sample, d) polarising microscope image of diorite porphyry sample (2.5 X, //), e) gabbro porphyry core sample, f) polarising microscope image of gabbro porphyry sample (2.5 X, //), plj: plagioclase, prx: pyroxene, bio: biotite.

the scope of this study, skarns observed in Nevruztepe mineralization may be classified as calsic skarns based on wall rock composition, but the environment of skarn formation may be classified as both endoskarn and exoskarn. Garnet and epidote with rare diopside are observed as skarn minerals. The skarn minerals indicate an oxidising environment and magnetite-rich iron and copper skarn type (Murakami, 2005). As skarn minerals are very irregular in drill core and extremely overprinted, it is not possible to describe clear mineral zonation. SEM analysis of garnet has shown they have almandine (Fe_2+$3Al_2$ $(SiO_4)_3$) and andradite

$(Ca_3Fe_3+2(SiO_4)_3)$ (Figure 7). Murakami (2005) stated that garnet with almandine type contains aluminium formed by substitution of magmatic protoliths, and hence represent endoskarn. On the other hand, andradite formed by substitution of calcium-rich wall rocks and as a result, it represents exoskarn.

Macroscopically observed garnet in drill cores is brownish coloured and coarse grained and epidote is pistachio-green coloured (Figure 8). Data obtained from microscopic investigation of garnet, epidote and diopside skarn samples is summarised below.

Diopside skarn: The rock comprises small-grained pyroxene (diopside), quartz, amphibole, carbonate, plagioclase group minerals, chlorite, epidote and secondary components of titanite and opaque minerals with granoblastic-hornfels texture (Figures 9a and 9b).

Epidote skarn: The rock contains fine-rarely moderate grained epidote, quartz, carbonate, chlorite and secondary titanite, apatite and opaque minerals with granoblastic-hornfels texture (Figures 9c and 9d).

Garnet skarn: Rocks contain moderate-coarse grained garnet, fine-grained carbonate, amphibole and quartz with secondary components of opaque minerals with granoblastic-hornfels texture (Figures 9e and 9f).

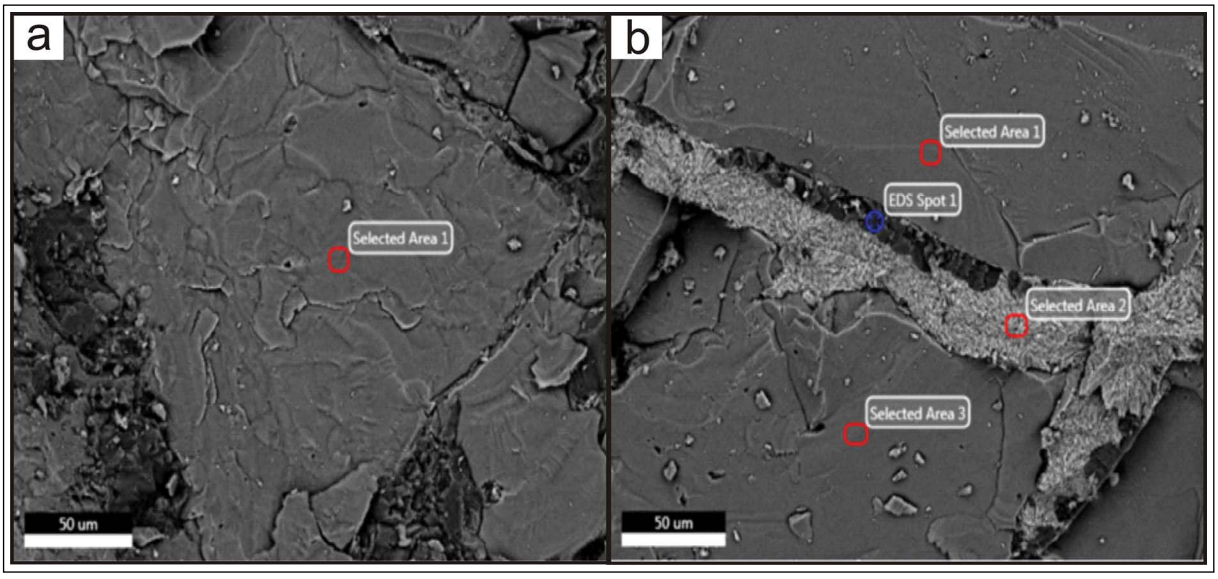

Figure 7- SEM images of core sample containing garnet, a) almandine garnet (1200 X), b) andradite garnet (1157 X).

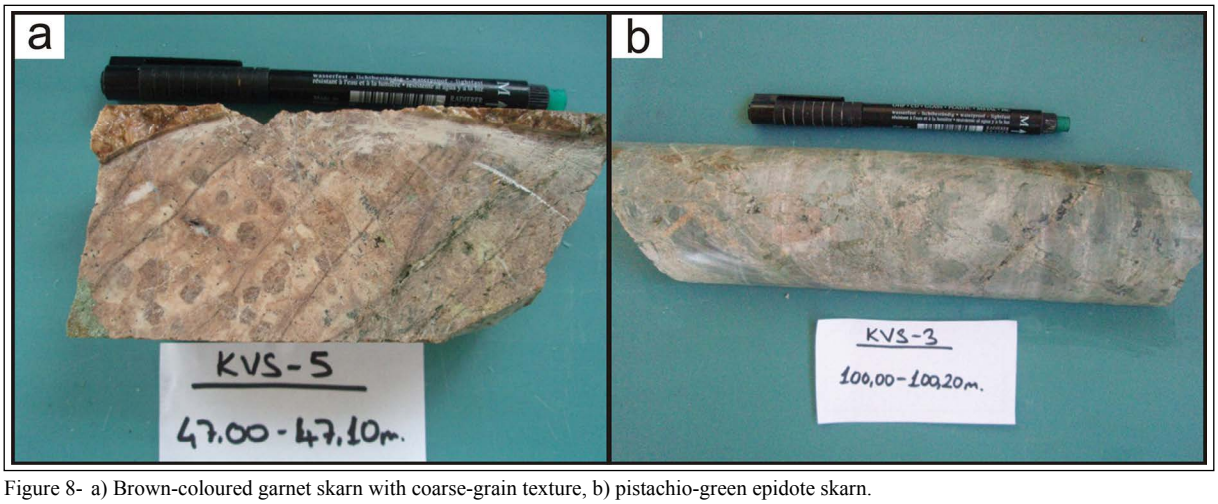

Figure 8- a) Brown-coloured garnet skarn with coarse-grain texture, b) pistachio-green epidote skarn.

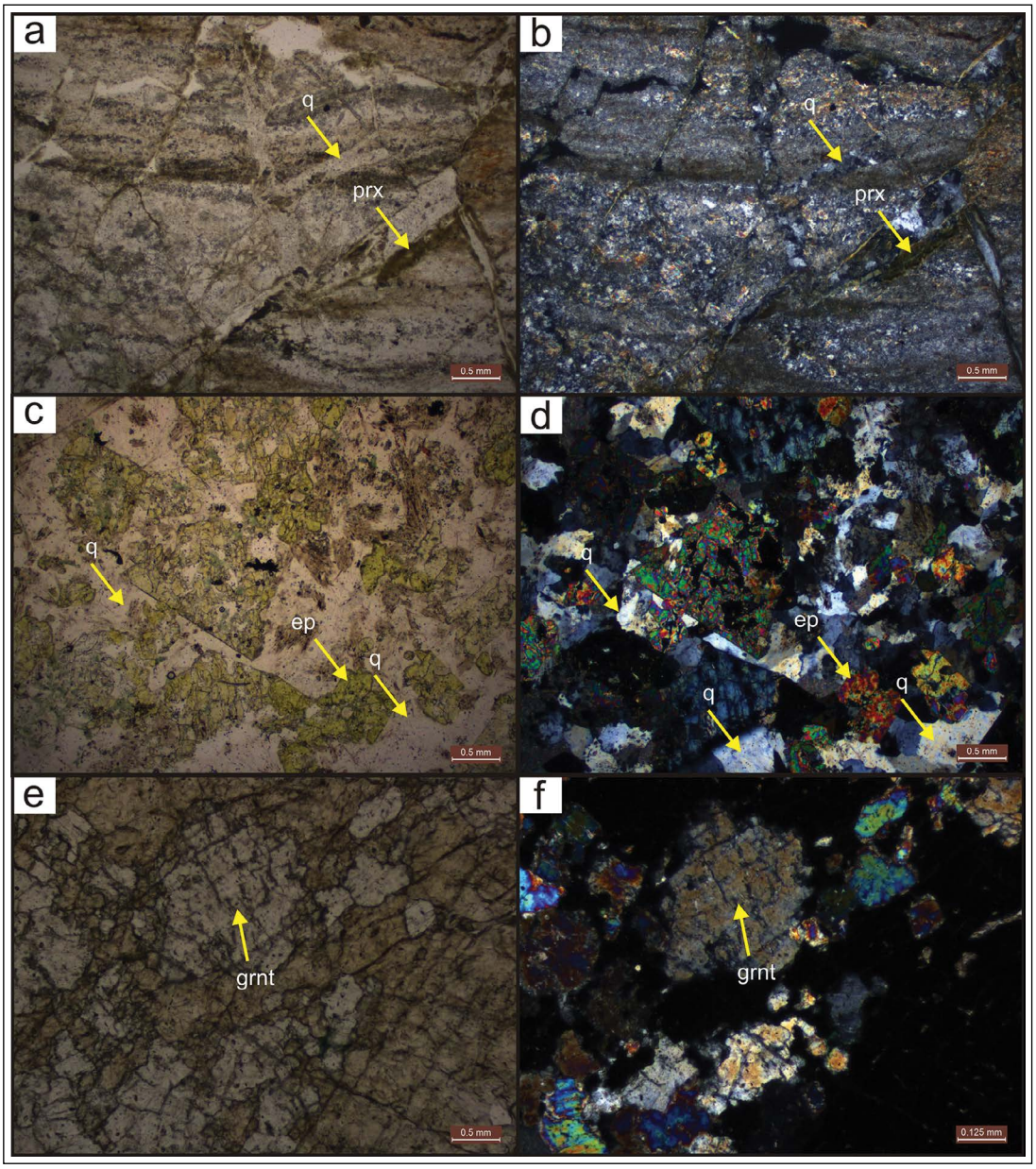

Figure 9- Pyroxene (diopside) and quartz minerals in diopside skarn rocks, a) (2.5 X, /), b) (2.5 X, //); epidote and quartz minerals in epidote skarn rocks c) (2.5 X, /), d) (2.5 X, //); garnet minerals in garnet skarn rocks e) (10 X, /), f) (10 X, //), prx: pyroxene, q: quartz, grnt: garnet, ep: epidote.

4. Ore Geology

4.1. General Features of Mineralization

Yahyalı Pluton intruded into members of Yahyalı Nappes as the Early-Middle Triassic Kocatepe formation and Jurassic-Cretaceous Tavşancıdağtepe formation. The pluton outcrops close to Yahyalı county in the east and laterally continues to west, Kovalı village. Along the contact between limestone and pluton, skarn zone was developed. The most known mineralization in this belt is Karamadazı iron deposit and it is currently operated. Nevruztepe mineralization as similar features with buried iron-copper mineralization within the same belt. In the study area, related with iron-copper mineralization, a total of 6.178,50 m of drilling was completed at 31 locations in between 2013-2016.

Nevruztepe mineralization has 750 m length along E-W trend, 500 m width and nearly 300 m thick (Figure 10). Mineralization dips toward south,

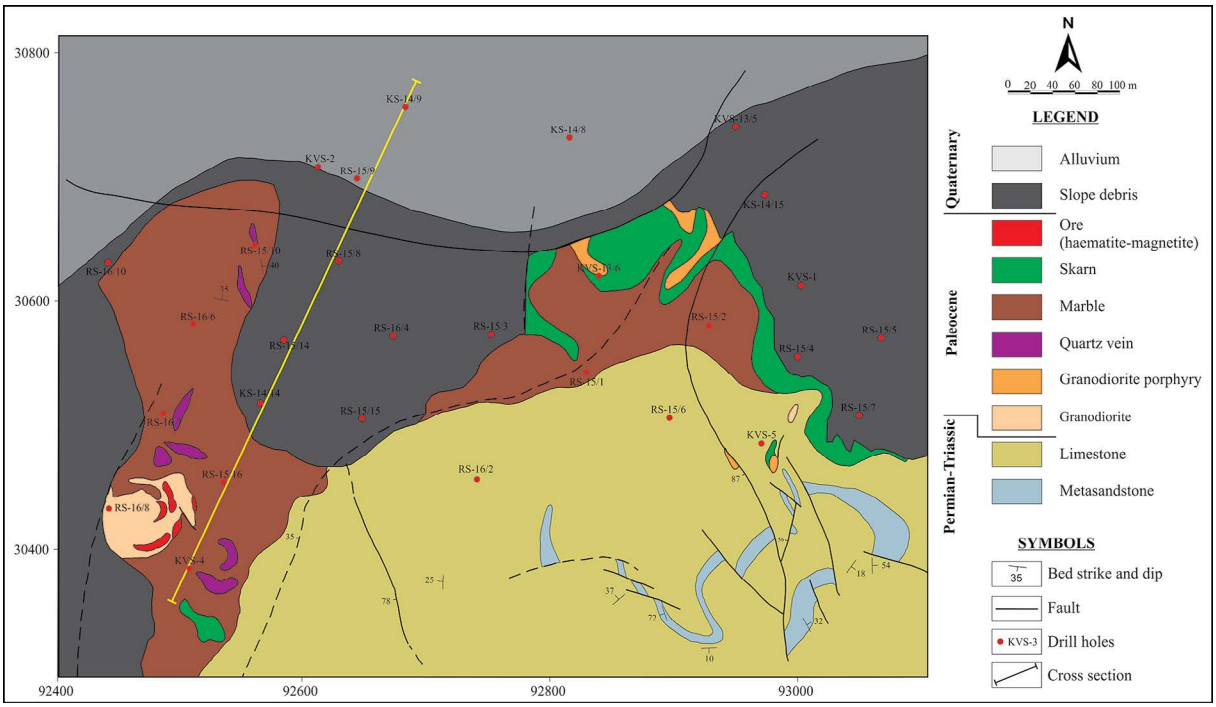

Figure 10- Detailed ore geology map of Nevruztepe Fe-Cu mineralization (Tiringa et al., 2018).

with the mineralization zone containing ore levels at different thicknesses up to 54,70 m. Mineralization is formed within skarn and magmatic intrusions. The distribution of mineralization within the magmatic intrusions is small pocket and lense shaped. Ore minerals are disseminated and/or formed in veins with different thicknesses in the skarn zone. Drill holes profiles along ore levels with different grades, and grade values correlated with mineralization level are observed on the cross-section in figure 11. Low-graded ore level extends laterally for long distances and high-graded ore levels are in lense-shaped along short distances. Copper is accompanied and enriched within iron levels.

Primary ore mineral is magnetite, which is generally anhedral and fine-grained. The main magnetite abundancy is observed along the margins, fractures and cleavages due to martitisation (Figure 12a). Hematite is observed in two forms. There is primary hematite with rod-shape as free grains, and secondary hematite is observed along fractures-cracks and cleavages due to martitisation. Along the fractures, limonitisation is also observed (Figure 12b). Ore levels contain pyrite, chalcopyrite, molybdenite, less amounts of sphalerite, bornite and malachite occasionally in limonitised zones. Pyrite is mostly euhedral and subhedral and partly interlocking with chalcopyrite (Figure 12c). Chalcopyrite is fine-grained and interlocked with pyrite, pyrrhotite and magnetite (Figure 12d). In some samples, sphalerite exsolution is observed within chalcopyrite (Figure 12e). Molybdenite is generally submicroscopic grain, with very few rod-shaped observed within gangue minerals (Figure 12f). Sphalerite is generally fine-grained and contain chalcopyrite exsolutions. Gangue minerals are all stained with limonite, comprising diopside, feldspar (plagioclase, orthoclase), epidote, clinozoisite, quartz, biotite, chlorite, calcite and reduced oxidised garnet. Biotite is chloritised and opacified, feldspars are argillised and carbonated.

Based on field observations and petrographic studies, four paragenetic stages are defined within Nevruztepe mineralization (Figure 13). The first stage is prograde skarn stage represented by garnet and diopside minerals. This stage is characterised by formation of disseminated magnetite within garnet minerals (Figure 14a). In the second stage called as retrograde stage, magnetite as main ore mineral with epidote are dominantly observed. In this stage, less amount rod-shaped primary hematite and disseminated pyrite, chalcopyrite and pyrrhotite are observed (Figure 14b). The third stage is quartz-sulphide stage,

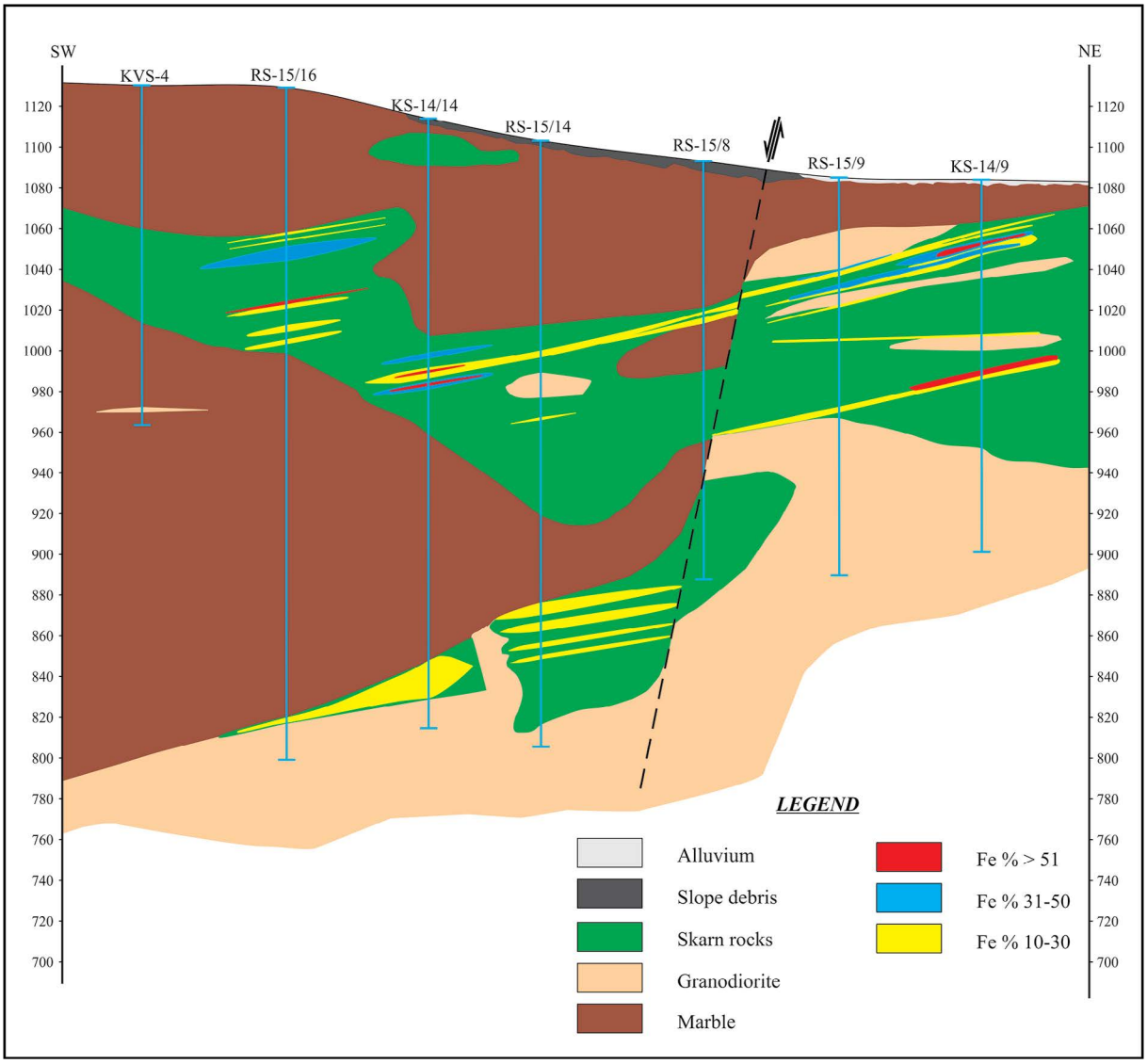

Figure 11- Geologic cross section showing drill core correlations (simplified lithologies, ore levels grouped according to grade and correlated).

and quartz-pyrite-chalcopyrite veins intensely cut by magnetites previously formed in this stage. Copper mineralization basically formed in this stage. Less amount pyrrhotite, sphalerite, molybdenite and calcite minerals are observed (Figure 14c). The fourth stage is quartz-carbonate stage. In this stage, rocks and previously formed mineralization are cut by quartz-carbonate veins. Magnetite is largely transformed to haematite due to martitisation. Limonitisation is commonly observed. Bornite, digenite, covelline and malachite transformations formed in this stage (Figure 14d).

4.2. Ore Geochemistry

Nevruztepe mineralization is low-medium grade iron-copper mineralization. Copper does not have economic importance without iron. As seen in table 2, the ore zone thicknesses are variable between 1,2 and 54,70 m, with mean Fe grade value from 12,25% up to 49,08%. Mean copper grades are also changed from 10 ppm to 4650 ppm. The elevation of SiO_2 content in iron increases the slag amount in blast furnace and energy expended by a proportional amount. As a result, the desire is that the SiO_2 content is not very high. In Nevruztepe mineralization, the mean SiO_2 is

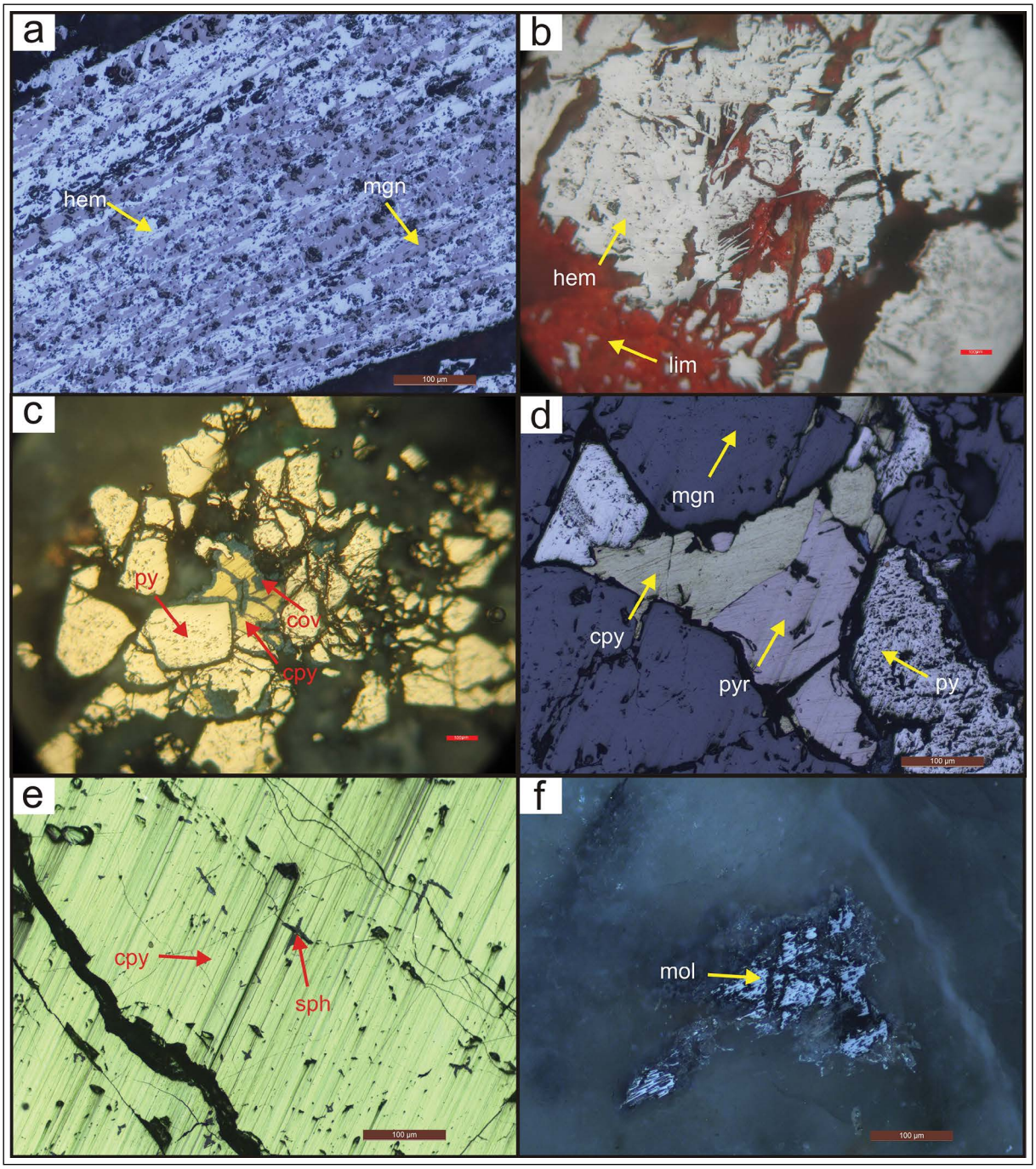

Figure 12- Microphotographs of ore microscopy studies, a) transformation of magnetite to hematite, b) hematites containing limonite in fractures, c) chalcopyrite partially transformed into covellite between pyrites, d) pyrite, chalcopyrite and pyrrhotite between magnetite, e) sphalerite separation in chalcopyrite, f) fine-grained molybdenite, mgn: magnetite, hem: hematite, lim: limonite, py: pyrite, cpy: chalcopyrite, cov: covellite, sph: sphalerite, mol: molybdenite.

high as much as 13,26% to 36,80%. The Al_2O_3 content of ore is from 0,80% to 8,78%.

Nevruztepe ore was studied by MTA with mineral processing and sample with 26,60% Fe and 0,12 ppm Cu grade ore, provided 59,66% efficiency for 66,35% Fe grade magnetite concentrate at 100-micron size. The waste from the experiment was enriched in copper content to reach 0,16-0,19% Cu grade. Flotation experiments of the waste obtained 19,48% Cu grade concentrate with 52,23% efficiency (Bayram and Bayrak, 2018).

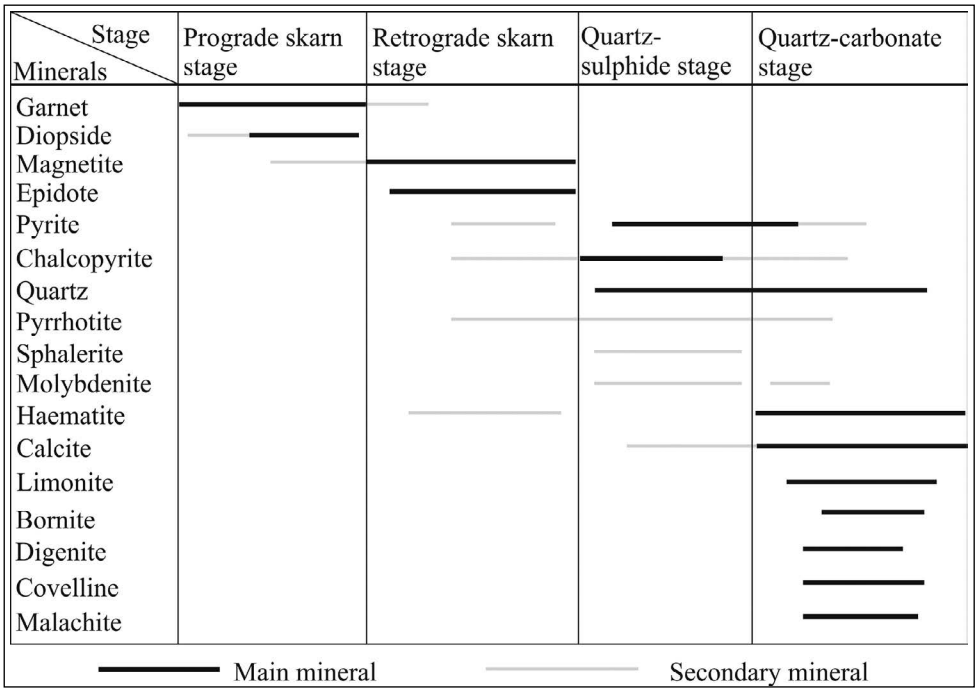

Figure 13- Mineral paragenesis and succession for Nevruztepe Fe-Cu mineralization.

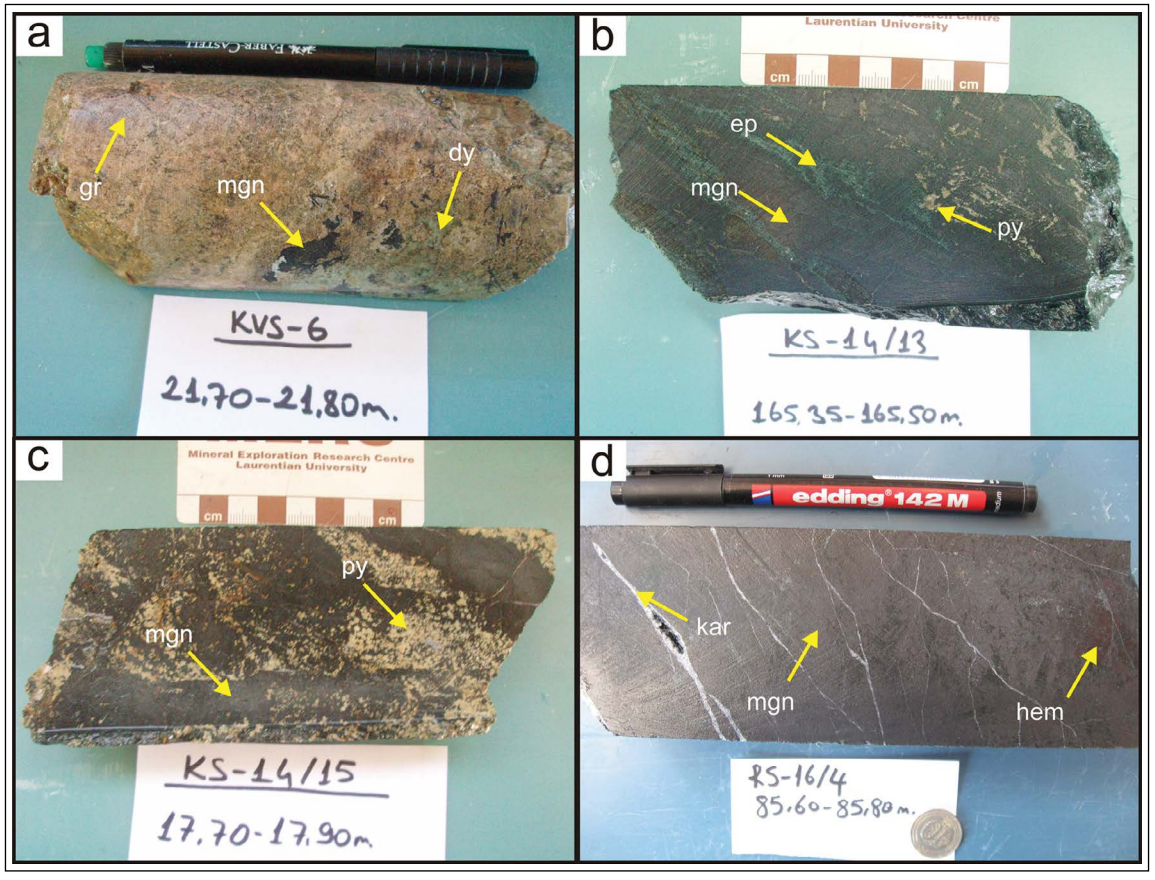

Figure 14- a) Disseminated magnetite from the prograde skarn stage, b) almost massive magnetite and secondary pyrites from the retrograde skarn stage, c) pyrite veins cutting magnetite in the quartz-sulphide stage, d) carbonate veinlets cutting magnetite and magnetite transformation hematites in the quartz-carbonate stage, gr: garnet, dy: diopside, ep: epidote, py: pyrite, kar: carbonate, mgn: magnetite, hem: hematite.

Table 2- Mean geochemical analysis results for mineralised levels cut by drill holes.

Drill ID	Sample number (n)	Thickness of ore level (m)	Fe	SiO_2	Al_2O_3	S	CaO	MgO	Na_2O	K_2O	TiO_2	P_2O_5	MnO	LOI	Cu
			%	%	%	%	%	%	%	%	%	%	%	%	ppm
KS-14/8	4	4,70	13,9	25,70	5,43	1,78	30,43	1,35	0,85	0,55	0,15	0,13	0,43	13,36	25
KS-14/9	17	15,80	34,65	21,04	4,28	0,10	12,21	3,19	0,15	0,36	0,20	0,11	0,18	11,78	2717
KS-14/14	19	28,90	27,61	28,54	2,98	1,59	19,71	2,28	0,22	0,26	0,13	0,10	0,39	4,44	1078
KS-14/15	12	12,50	49,08	13,36	1,43	0,88	11,27	0,93	0,10	0,11	0,10	0,10	0,25	1,56	35
RS-15/1	6	6,20	20,57	33,27	0,87	0,10	25,98	4,37	0,10	0,10	0,10	0,10	0,32	4,07	1011
RS-15/2	27	54,70	17,39	33,11	1,39	0,10	33,04	2,46	0,10	0,10	0,12	0,13	0,43	4,16	31
RS-15/3	3	3,20	26,92	22,90	5,73	0,10	7,23	13,60	0,17	0,83	0,20	0,10	0,10	10,47	
RS-15/4	10	9,20	17,11	36,80	1,52	0,10	24,19	8,96	0,11	0,11	0,11	0,10	0,36	3,42	10
RS-15/5	19	22,95	19,97	27,12	2,44	0,10	32,07	2,32	0,14	0,09	0,16	0,11	0,41	6,29	
RS-15/6	2	1,90	12,25	21,95	0,80	0,10	35,75	3,75	0,10	0,10	0,05	0,10	0,35	19,60	
RS-15/8	6	5,60	12,98	34,70	8,78	1,46	14,60	7,60	0,10	1,54	0,30	0,10	0,12	11,87	1095
RS-15/9	10	12,40	21,38	30,37	3,79	2,10	19,37	5,34	0,14	0,40	0,15	0,10	0,33	8,18	1172
RS-15/10	15	18,00	22,98	26,12	2,49	0,23	27,39	3,18	0,10	0,24	0,13	0,10	0,37	6,95	230
RS-15/14	12	17,20	13,45	32,48	1,88	0,10	33,28	4,88	0,10	0,10	0,12	0,10	0,42	7,70	69
RS-15/15	11	15,00	13,05	33,57	2,69	0,68	31,62	4,07	0,10	0,11	0,11	0,10	0,55	8,00	239
RS-15/16	22	28,20	25,66	25,03	4,80	2,46	19,79	2,17	0,57	0,32	0,21	0,11	0,31	7,53	979
RS-16/4	8	8,10	25,61	28,71	6,23	0,55	8,53	11,64	0,16	1,78	0,29	0,11	0,26	7,43	1060
RS-16/6	2	1,20	29,18			8,85									2990
RS-16/7	2	2,00	41,68			7,75									4650
Overall Average			24,44	27,92	3,38	1,53	22,73	4,82	0,19	0,41	0,15	0,10	0,32	8,04	1086

5. Discussion and Conclusion

Assessment of field observations and petrographic analyses indicates that the Nevruztepe Fe-Cu mineralization is formed by skarn processes developing Yahyalı Pluton intruded into limestones of the Yahyalı Nappe. Accordingly, Nevruztepe mineralization may be described as skarn type mineralization based on host rock, source rock, mineral paragenesis, and ore geometry parameters. As it is known, skarns deposits are formed related to regional metamorphism or contact metasomatic processes with the intrusion of magmatic intrusions into carbonate rocks. They form in intense tectonic areas where carbonate lithologies and magmatic activity is present (Einaudi et al., 1981 and Meinert et al., 2005). During skarnisation, secondary carbonates and less commonly calcium-rich silicate rocks are formed. This process is directly related with fluid movements and transporting of metals from cooling plutonic mass into surrounding rocks by the heat transfer routes, isochemical contact metamorphism and metasomatism (prograde skarn) (Pirajno, 2009). Skarn deposits are formed when pluton is hotter than 600 °C cool below 200 °C. The environmental temperature, salinity, Eh and pH determine the type of silicate minerals formed the skarn zone (Meinert et al., 1997).

Due to temperature differences between wall rock and pluton, skarn zones develop in not only wall rock but also Yahyalı Pluton itself. In the drill core samples from Nevruztepe mineralization, thickness of skarn zone observed as more than 100 meters. Metasomatic process is highly effective on wall rock and pluton. That is why it is not so easy to distinguish endo- and exoskarn zone in the field. SEM analyses determines garnet are aluminium-rich almandine and calcium-rich andradite. Murakami (2005) proposed that aluminium-rich garnet represents the endoskarn and calcium-rich garnet indicates the exoskarn. Accordingly, Nevruztepe mineralization may be classified as both endoskarn and exoskarn based on the environment where the skarn zones are formed.

Magnetite mineralization in Nevruztepe is observed more abundantly within epidote-rich skarn zones representing the retrograde stage, and fine-grained disseminated ones are formed in the garnet- and diopside-rich skarn zones representing the prograde stage. Development of magnetite in

both the prograde and retrograde stages shows that mineralization is coeval with skarn formation. Similarly, Kuşçu et al. (2001) stated that Karamadazı iron deposit is coeval with skarnization. Oygür et al. (1978) proposed that mineralization formed as a result of metasomatism developing after skarn formation. Observations both in the field and drill cores don't indicate iron-rich lithologies within wall rocks. As a result, the only lithology that could be source for mineralization is the Yahyalı Pluton with differentiation from granodiorite to gabbro. Kuşçu et al. (2001) did not find abnormal iron enrichment or dissemination in limestone as wall rock of skarn in the Karamadazı iron deposit and proposed that the mineralization may be only related to the magmatic source and precipitated from iron solutions within late stage skarn zones. Petrographic analysis shows that retrograde stage magnetites are accompanied by a small amount of rod-shaped hematite. The quartz-carbonate stage indicates martitisation mainly along cleavages, fractures and cracks.

Nevruztepe mineralization is a low-moderate grade iron mineralization. Ore continues up to 750 m altitude with low grade, plunging to south. High-grade parts are formed as small lenses without much lateral continuity. Due to containing Cu-rich zones up to 4650 ppm in addition to iron mineralization in drill cores, the mineralization may be evaluated for copper. Copper mineralization is found with magnetite in epidote skarn from the quartz-sulphide stage, cut by pyrite-pyrrhotine and chalcopyrite veins. However, in the retrograde stage developing earlier, small amounts of disseminated copper mineralization developed within magnetites. In the final quartz-carbonate stage, chalcopyrite is changed to malachite, digenite, bornite and covelline. Technological tests were performed on Nevruztepe Fe-Cu mineralization for the first time in the region by MTA and it was revealed that after obtaining iron, copper may be extracted from waste using flotation (Bayram and Bayrak, 2018).

Total resource estimations of Nevruztepe mineralization is calculated by MTA as 5,096,788 tons at 21,05% Fe grade for iron and 1,906,267 tons of 2,219.75 ppm grade for copper (Tiringa et al., 2018). Technological tests on samples taken from drill cores obtained 66,35% Fe-grade magnetite concentration with 59,66% efficiency at 100 microns and observed that the waste was enriched in copper 0,16-0,19% grades. Flotation experiments provided 52,23% efficiency for 19,48% Cu grade concentrate (Bayram and Bayrak, 2018).

The Karamadazı iron deposit, has almost similar geological and spatial features with Nevruztepe mineralization, is a skarn-type deposit formed by intrusion of the Yahyalı Pluton into carbonate lithologies. Skarnisation from pluton to wall rock is represented by garnet and diopside in the prograde stage and epidote in the retrograde stage. Ore is found within the epidote skarn, similar to Nevruztepe mineralization, observed as disseminated within garnet. Ore paragenesis comprises martitisation, less amounts of pyrite, chalcopyrite and pyrrhotine with great similarities to Nevruztepe mineralization. The Karamadazı iron deposit has 6.5 million tons reserve with 54% Fe, 1,7% S and 11% SiO_2 and currently mining activity is going on with underground operations (Oygür, 1986). In terms of ore geometry, Nevruztepe and Karamadazı display similarities and ore has nearly E-W striking and dipping towards south, comprising thin magnetite lenses.

Genesis, mineral paragenesis, ore minerals and succession of Nevruztepe Fe-Cu mineralization has similarities to the Handagai Fe-Cu deposit located in the north of the Great Xing'an belt in the northeast of China. The Handagai Fe-Cu deposit formed as a result of contact metasomatic processes based on geology, mineralogy and geochemical data, and is a calcic skarn formation with andradite-diopside-epidote-actinolite associations dominantly observed. Skarn formation is represented by four paragenetic stages called prograde skarn, retrograde skarn, quartz-sulphide and quartz-carbonate. Iron mineralization is observed commonly within chlorite which is formed in retrograde skarn stage. The Handagai Fe-Cu deposit is a newly-discovered deposit containing 3 million tons of iron with 30-58% grade and 18 thousand tons of copper reserve with 0,5-5,1% grade (Zhou et al., 2017).

The Astamal iron deposit within the Karadağ-Sabalan metallogenic belt in the east Azerbaycan state in northwest Iran is similar to the Nevruztepe mineralization. The Astamal iron deposit formed in a continent-continent collision environment developing after the closure of Neotethys in terms of tectonic environment linked to the intrusion of the Oligocene-aged granodioritic-quartz monzonitic Karadağ

batholith into Late Cretaceous-aged marbles. Beside the similarities of timing and lithologic features, Nevruztepe iron deposit has almost the same ore and skarn minerals, mineral paragenesis and copper production potential with Astamal iron deposit. Astamal iron deposit is the largest and richest iron deposit in northwest Iran with mean 60% grade 10 million ton iron reserve (Baghban et al., 2015).

Acknowledgements

This article is based on data obtained during studies within the scope of the Western and Central Anatolia Iron Exploration Project organised by General Directorate of MTA Department of Mining and Exploration from 2012-2016. The authors wish to thank the management of General Directorate of MTA for all aspects of their support and the Prof. Dr. Eric Cheney, Prof.Dr. Nurullah Hanilçi and the other reviewers for their criticisms and recommendations about the manuscript. The authors wish also to thank Zehra Deveci Aral for her contribution to the English translation of the manuscript.

References

Alan, İ., Şahin, Ş., Altun, İ., Bakırhan, B., Balcı, V., Böke, N., Saçlı, L., Pehlivan, Ş., Kop, A., Hanilçi, N., Çelik, Ö. F. 2007. Orta Toroslar'ın Jeodinamik Evrimi, Ereğli (Konya)-Ulukışla (Niğde)-Karsantı (Adana)-Namrun (İçel) Yöresi. Maden Tetkik ve Arama Genel Müdürlüğü Rapor No: 11006, 245, Ankara (unpublished).

Ayhan, A., Lengeranlı, Y. 1986. Yahyalı-Demirkazık (Aladağlar Yöresi) Arasının Tektonostratigrafik Özellikleri, Jeoloji Mühendisliği Dergisi 27, 31-45.

Baghban, S., Hosseinzadeh, M. R., Moayyed, M., Mokhtari, M. A. A., Gregory, D. 2015. Geology, mineral chemistry and formation conditions of calc-silicate minerals of Astamal Fe-LREE distal skarn deposit, Eastern Azarbaijan Province, NW Iran. Ore Geology Reviews 68, 79-96.

Bayram, A. İ., Bayrak, M. Y. 2018. Kayseri-Yeşilhisar Demir Cevherinin Zenginleştirme Çalışması. Maden Tetkik ve Arama Genel Müdürlüğü MAT Dairesi Arşivi, Ankara (unpublished).

Boztuğ, D, Çevikbaş, A., Demirkol, C., Tatar, S., Akyıldız, M., Otlu, N. 2002. Karamadazı Plütonunun (Yahyalı-Kayseri) Mineralojik-Petrografik ve Jeokimyasal İncelemesi. Türkiye Jeoloji Bülteni 45, 1, 41-58.

Çevikbaş, A., Boztuğ, D., Demirkol, C., Yılmaz, S., Akyıldız, M., Açlan, M., Demir, Ö., Taş, R. 1995. Horoz Plütonunun (Ulukışla-Niğde) Oluşumunda Dengelenmiş Hibrid Sistemin Mineralojik ve Jeokimyasal Kanıtları, TJK Bülteni 10, 62-77.

Einaudi, M. T., Meinert, L. D., Newberry, R. J. 1981. Skarn Deposits, Economic Geology, 75th Anniversary 317-391.

Hanilçi, N., Öztürk, H. 2011. Geochemical/Isotopic Evolution of Pb–Zn Deposits in the Central and Eastern Taurides, Turkey. International Geology Review 53, 13, 1478-1507.

Keskin, H., Alan, İ. 2013. Yahyalı (Kayseri)–Dündarlı (Niğde) Arasında Kalan Alanın Jeolojisi (Doğu Toroslar'ın Jeodinamik Evrimi ve Metalojenezi Projesi), Maden Tetkik ve Arama Genel Müdürlüğü Rapor No: 11612, 50, Ankara (unpublished).

Kuşçu, İ., Gençalioğlu Kuşçu, G., Göncüoğlu, M. C. 2001. Karamadazı Demir Yatağında Skarn Zonlanması ve Mineralojisi. Türkiye Jeoloji Bülteni 44/3, 1-14.

Kuşçu, İ., Gençalioğlu Kuşçu, G., Saraç, C., Meinert, L. D. 2002. Jeokimyasal Karakterizasyon Çalışmalarında Faktör Analizi Yönteminin Kullanımı: Çelebi Granitoyidi ve Karamadazı Graniti. Türkiye Jeoloji Bülteni 45/1, 125-140.

Meinert, L. D., Hefton, K. K., Mayes, D., Tasiran, I. 1997. Geology, zonation, and fluid evolution of the Big Gossan Cu-Au skarn deposit, Ertsberg District, Irian Jaya, Econ. Geol. 92, 509-534.

Meinert, L. D., Dipple, G. M., Nicolescu, S. 2005. World skarn deposits, Econ. Geol. 100th Ann. 299–336.

Murakami, H. 2005. How to Study Skarn Type Deposits. A short time expert seminar in MTA, Ankara.

Oktay, F. Y. 1982. Ulukışla ve Çevresinin Stratigrafisi ve Jeolojik Evrimi. Türkiye Jeoloji Bülteni, 25/1, 15-24.

Oygür, V., Yurt, F., Yurt, M. Z. 1978. Kayseri-Yahyalı-Karamadazı ve Kovalı Yöresi Demir Madenleri Jeolojisi, Maden Tetkik ve Arama Genel Müdürlüğü Rapor No. 6609, Ankara (unpublished).

Oygür, V. 1986. Karamadazı (Yahyalı-Kayseri) Kontak Metazomatik Manyetit Yatağının Jeolojisi ve Oluşumu, Jeo. Müh. Dergisi 27, 1-9.

Pirajno, F. 2009. Hydrothermal Processes and Mineral Systems, Australia, Springer 1250.

Tekeli, O. 1980. Toroslar'da Aladağlar'ın Yapısal Evrimi, Türkiye Jeoloji Bülteni 23/1, 11-14.

Tiringa, D., Ünlü, T., Sayılı, S. 2009. Kayseri-Yahyalı-Karaköy, Karaçat Demir Yatağının Maden

Jeolojisi. Jeoloji Mühendisliği Dergisi, Jeoloji Mühendisleri Odası Yayınları 33/1, 1-43.

Tiringa, D., Ateşçi, B., Türkel, A., Tufan, E., Akın, U., Yıldırım, G. 2014. AR: 201201149 ve AR: 201300002 (Kayseri-Yeşilhisar) ile AR: 201201150 (Kayseri-Yahyalı) Nolu Ruhsat Sahaları Maden Jeolojisi Ara Raporu. Maden Tetkik ve Arama Genel Müdürlüğü Rapor No: 11753, Ankara (unpublished).

Tiringa, D., Ünlü, T., Gürsu, S. 2016. Erken Kambriyen Yaşlı Karaçat Demir Yatağı (Mansurlu Havzası, Adana) ve Doğusunda Yüzeylenen Demir Yataklarının Kökenine Bir Yaklaşım. Maden Tetkik ve Arama Dergisi 152, 121-141.

Tiringa, D., Ateşçi, B., Çelik, Y., Türkel, A., Demirkıran, G., Niğdeli, S. F., Yurtseven, D., Yakıcı İçli, M., Aksoy, T. 2018. Kayseri-Yeşilhisar-Kovalı Yöresindeki AR: 201201149 (ER: 3286890) no'lu IV. Grup Ruhsat Sahasına Ait Demir ve Bakır Madenleri Buluculuk Talebine Esas Maden Jeolojisi ve Kaynak Tahmin Raporu. Maden Tetkik ve Arama Genel Müdürlüğü Rapor No: 13742, Ankara (unpublished).

Zhou, Z., Mao, J., Che, H., Ouyang, H., Ma, X. 2017. Metallogeny of the Handagai Skarn Fe-Cu Deposit, Northern Great Xing'an Range, NE China: Constraints on Fluid Inclusions and Skarn Genesis. Ore Geology Reviews 80, 623-644.

Bulletin of the Mineral Research and Exploration

http://bulletin.mta.gov.tr

Drilling and core data from the Gulf of Gemlik (SE Sea of Marmara): Holocene fauna and flora assemblages

Engin MERİÇ[a], Zeki Ü. YÜMÜN[b], Atike NAZİK[c*], Enis K. SAGULAR[d], M. Baki YOKEŞ[e], Yeşim BÜYÜKMERİÇ[f], Ayşegül YILDIZ[g] and Gülin YAVUZLAR[d]

[a]*Moda Hüseyin Bey Sokak No: 15/4, 34710 Kadıköy, İstanbul, Turkey*
[b]*Namık Kemal University, Çorlu Faculty of Engineering, Department of Environmental Engineering,59860, Çorlu, Tekirdağ, Turkey*
[c]*Çukurova University, Faculty of Engineering, Department of Geological Engineering, 01330, Balcalı, Adana, Turkey*
[d]*Süleyman Demirel University, Faculty of Engineering and Architecture, Department of Geological Engineering,32260 Çünür, Isparta, Turkey*
[e]*AMBRD Doğa Bilimleri, Hanımefendi Sokak 160/6 34384 Şişli, İstanbul, Turkey*
[f]*Bülent Ecevit University, Faculty of Engineering, Department of Geological Engineering, 67100 Zonguldak, Turkey*
[g]*Aksaray University, Faculty of Engineering, Department of Geological Engineering, 68100 Aksaray, Turkey*

Research Article

Keywords:
Foraminifer, Ostracod, Mollusc, Nannoplankton, Diatome, Gemlik Gulf

ABSTRACT

This study was conducted to determine fauna and flora assemblages of Holocene sequences from Gemlik Gulf (SE Marmara Sea) and to obtaine their similarities and differences between the assemblages of Gemlik and İzmit Bays. Total of 201 dark gray colored, fine to medium grained sandy clay samples were studied. In the drilled samples, 22 genera and 38 species were identified from the foraminifera characterizing the infralittoral zone. 40 genera and 58 species of foraminifera characterizing the upper circalittoral zone were identified. In addition, Black Sea originated Ammonia parasovica was found for the first time in cores taken from Gemlik Gulf. Nannofossil species characterizing the open-shallow marine environment *Emiliania huxleyi*, *Reticulofenestra parvula*, *Coronosphaera* spp., *Syracosphaera* spp., *Helicosphaera* spp. beside *Gephyrocapsa oceanica*, small *Gephyrocaps*a spp., S*cyphosphaera porosa* were obtained. A total of 27 genera and 37 species from ostracods were defined in the samples from gulf. Moreover, the quite abundant mollusc assemblage characterizing the shallow marine environment and fewer genera and species of diatoms were identified. The studied sequence is represented by NN21 *Emiliania huxleyi* biozone at the Holocene. Foraminifers and ostracods of the Gemlik Gulf are observed as Mediterranean-Aegean Sea originated assemblages. The mollusc shows the shallow marine community.

Received Date: 26.09.2018
Accepted Date: 03.04.2019

1. Introduction

The study area is the Gulf of Gemlik located in southeast of Marmara Region (Figure 1). In order to reveal information about the Black Sea-Marmara-Mediterranean connection, many studies have been carried out both with marine and non-marine data obtained from the drilling and bottom sediments in the Sea of Marmara and the Gulf of Gemlik (Meriç, (1995); Görür et al. (1997); İslamoğlu and Chepalyga, (1998); Çağatay et al. (2000, 2003, 2009); Aksu et al. (1999, 2002); Yaltırak and Alpar, (2002); Sperling et al. (2003); Kerey et al. (2004); Mudie et al. (2004); Meriç et al. (2005, 2009, 2018); Chepalyga (2007); Hiscott et al. (2007); Yanko-Hombach et al. (2007); McHugh et al. (2008); Marret et al. (2009); İslamoğlu, (2002, 2009); Brückner et al. (2010); Vidal et al. (2010); Gasperini et al. (2011); Nazik et al. (2011); Mertens et al. (2012); Taviani et al. (2014); Vardar et al. (2014); Filikçi et al. (2017).

Citation Info: Meriç, E., Yümün, Z. Ü., Nazik, A., Sagular, E. K., Yokeş, M. B., Büyükmeriç, Y., Yıldız, A., Yavuzlar, G. 2020. Drilling and core data from the Gulf of Gemlik (SE Sea of Marmara): Holocene fauna and flora assemblages. Bulletin of the Mineral Research and Exploration. 161, 121-149. https://doi.org/10.19111/bulletinofmre.581537

** Corresponding author: Atike NAZİK, anazik@cu.edu.tr*

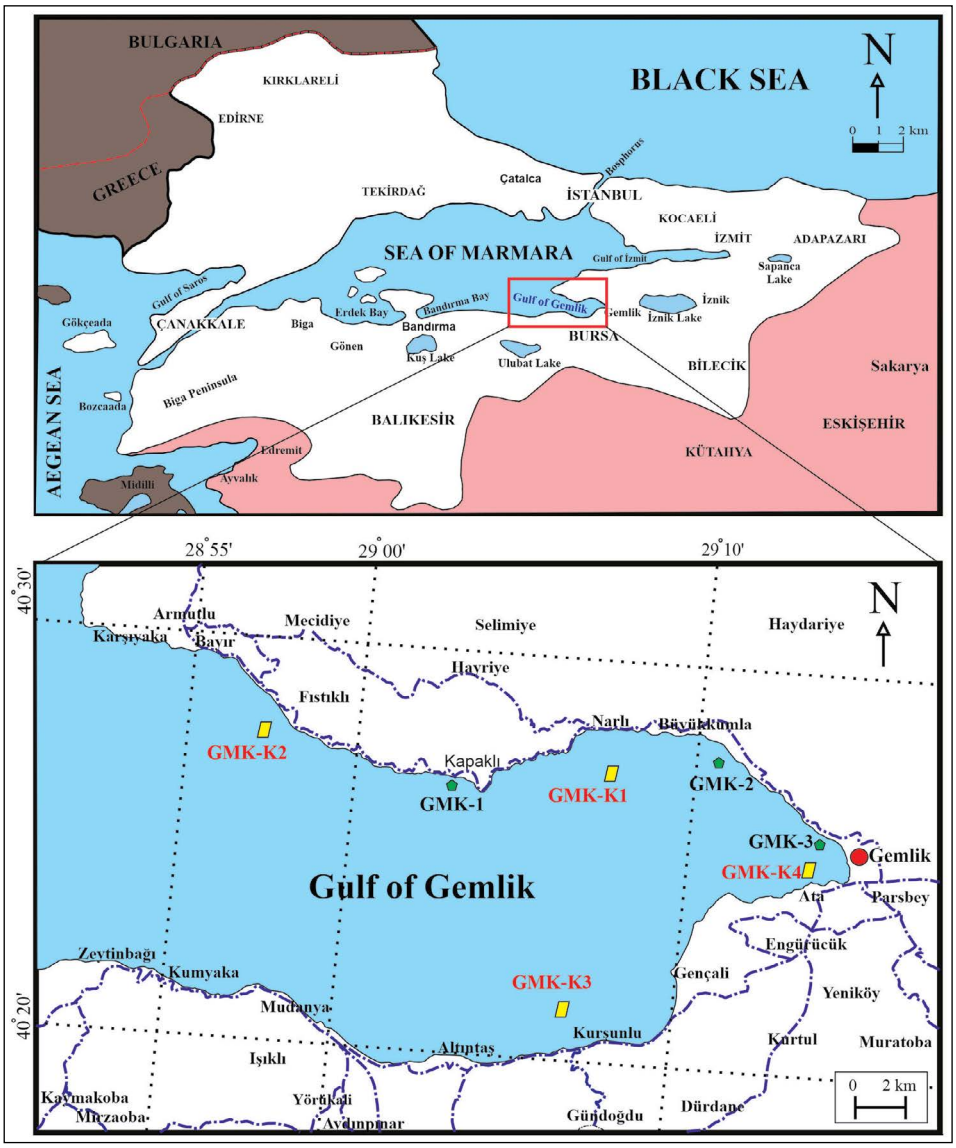

Figure 1- Location map of drilling and cores taken from the Gulf of Gemlik (GMK drilling, GMK-K core locations).

In this study, the foraminifer, ostracod, mollusc, nannoplankton and diatom assemblages in the deposits identified in three drilling holes (GMK-1, GMK-2, GMK-3) from the northeast and east of the Gulf of Gemlik and 4 cores taken from its north, northeast and southeast (GMK-K1, GMK-K2, GMK-K3, GMK-K4) were studied and compared with the Mediterranean-Marmara-Black Sea assemblages in order to reveal similarities and differences.

When previous studies carried out in the region are compared, the foraminifer, ostracod and mollusc faunas of the Sea of Marmara, and also the nannoplankton and diatom assemblages from the deep sediments of the Gulf of Gemlik, as indicated by the present study, are considered to be richer compared to those reported by Meriç et al. (2005).

2. Material and Methods

Sediment samples used in this study were taken from 3 drillings carried out in north, northeast and southeast of the Gulf of Gemlik (GMK-1, GMK-2, GMK-3) (Figures 1-3). Samples come from 4 cores ranging from between 0,70-1,00 m in length. These were collected from the north, northeast and southeast of the bay (GMK-K1, GMK-K2, GMK-K3, GMK-K4) during summer 2015 (Figures 1-4, 5 and table 1). The drilling samples mostly consist of blackish gray, clayey and sandy gravel, medium-grained sandy and

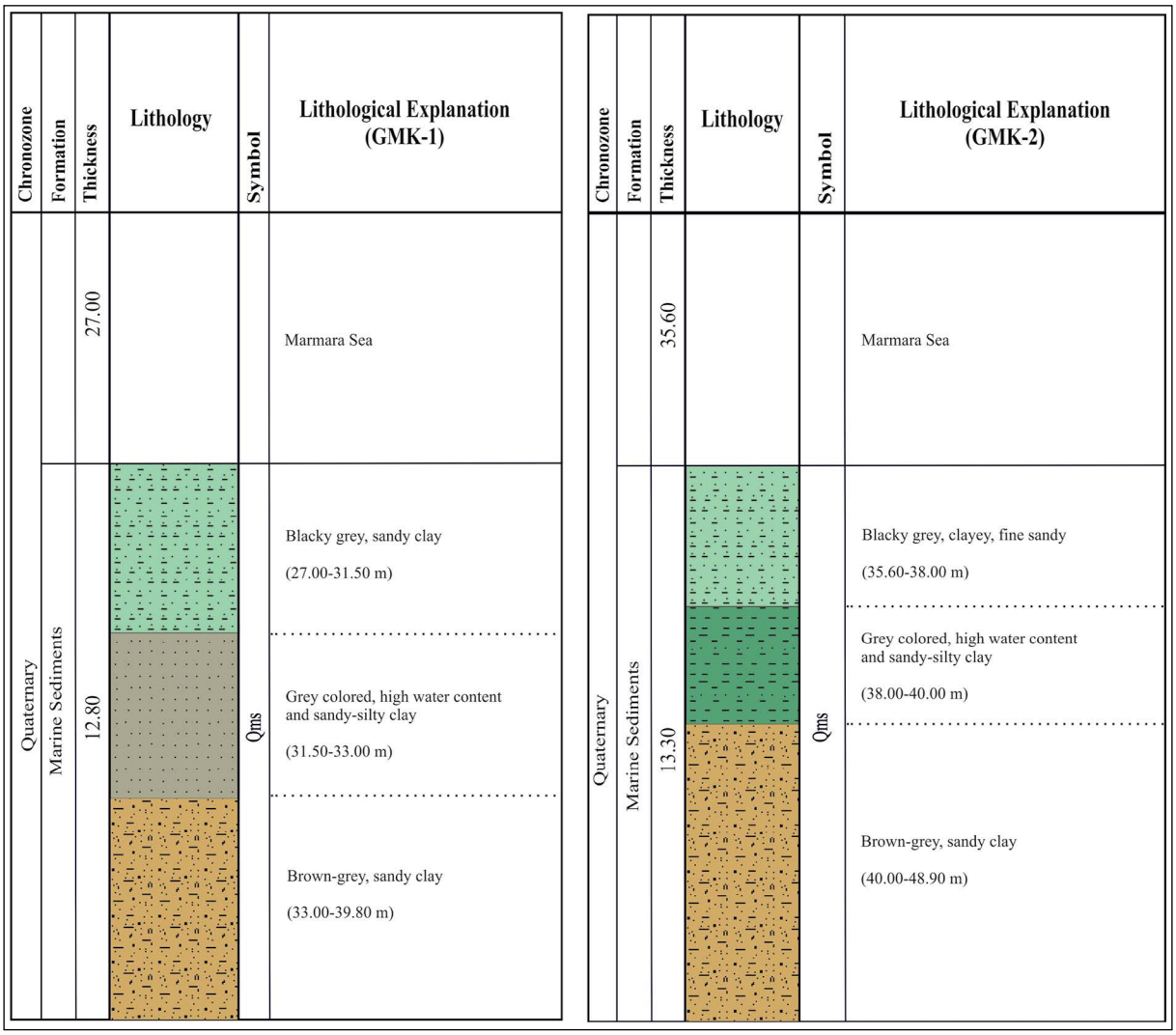

Figure 2- The columnar section of the locations in which drilling samples were taken in the Gulf of Gemlik (GMK-1, water depth 27,00 m and GMK-2, water depth 35,60 m) (not to scale).

silty clay with mollusc shells. The core samples are dark gray, fine sand (with high water content), silty and sandy clay units.

A total of 201 samples were studied as follows: 150 samples (with 10 cm intervals) from the cores of GMK-1 and GMK-2, 14 samples from GMK-3 drilling (with 20 cm intervals) and 37 samples taken from 4 cores (with 10 cm intervals).

To identify foraminifer, ostracod and molluscs, 10% hydrogen peroxide was added to wet sediment samples weighing 5 g, and then left for 24 hours. Afterwards, the samples were washed through a 0.063 mm sieve with pressurized water, allowed to dry in a 50 °C oven and further sieved through 2.00, 1.00, 0.500, 0.250, 0.125 mm size sieves and then examined under a binocular microscope.

The nannofossil smear-slides were prepared by the traditional method, as summarized by Perch-Nielsen (1985*a, b*). Preparations were examined under the light microscope with the help of 100x magnification oil-immersion objective lens and 10x ocular magnification (using the traditional method) and displayed by using approximately 40x magnification with an intermediate lens+digital camera. Imaging under polarized (PL), normal (NL), contrast (CL) light was as used by Perch-Nielsen (1985*a, b*) for microscope studies. In addition, the imaging methods under PL using a gypsum wedge (GL) was employed as suggested by Reinhardt (1972) and Romein (1979). Also, imaging

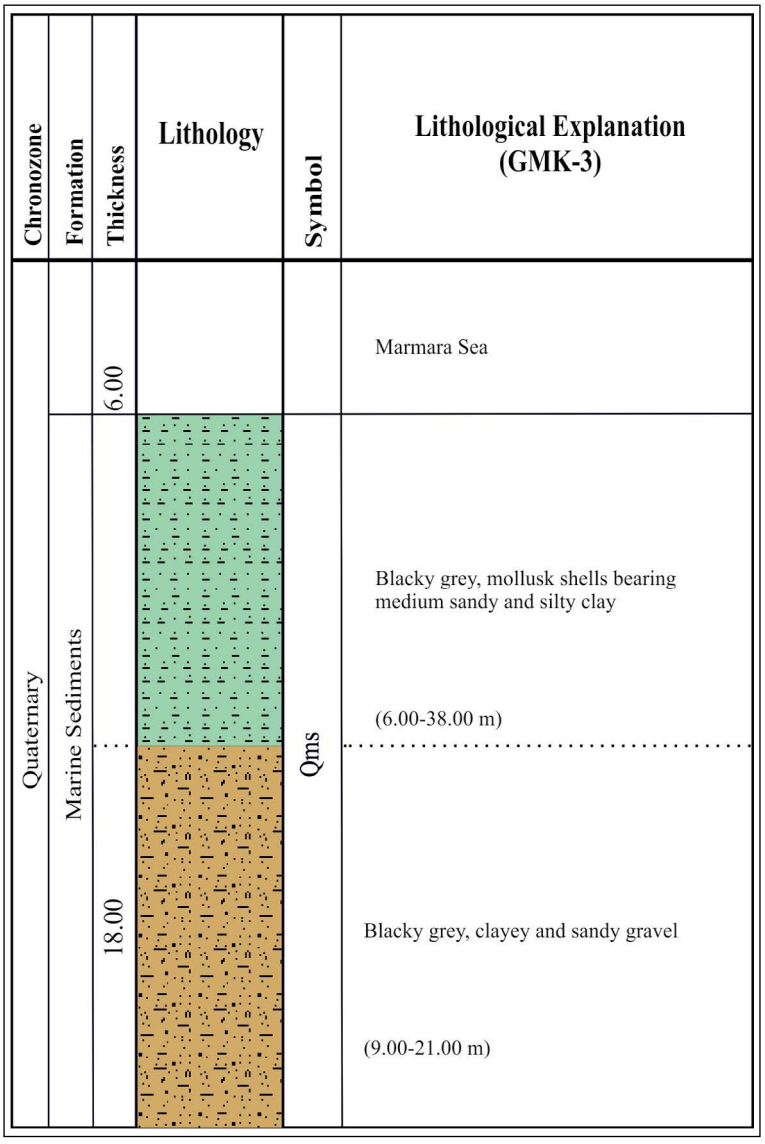

Figure 3- The columnar section of locations in which drilling samples in the Gulf of Gemlik were taken (GMK-3, water depth: 6 m) (not to scale).

under PL was carried out using a quartz wedge (QL), as recommended by Sagular (2009). Selected images of the nannofossil species identified are shown in plate 1.

Samples taken from the drilling holes for diatom analysis were first cleaned by using 10% HCl at the Department of Geological Engineering of the Faculty of Engineering in Aksaray University; this material was then prepared for paleontological study by mounting on a slide using entellan and a coverglass. The preparations were examined under 1600x magnification using a polarizing microscope and an oil-immersion objective with a Leica DM 2500 P. The fossil diatom genera and species were then identified and photographed (Plate 2)

3. Micro and Macro Faunal Findings

3.1. Foraminifera

In the samples from GMK-1, GMK-2 and GMK-3, a total of 22 genera and 39 species were identified as follows: *Textularia bocki* Höglund, *Adelosina cliarensis* (Heron-Allen and Earland), *A. mediterranensis* (Le Calvez and Le Calvez), *Spiroloculina dilatata* d'Orbigny, *S. excavata* d'Orbigny, *S. ornata* d'Orbigny, *Siphonaperta*

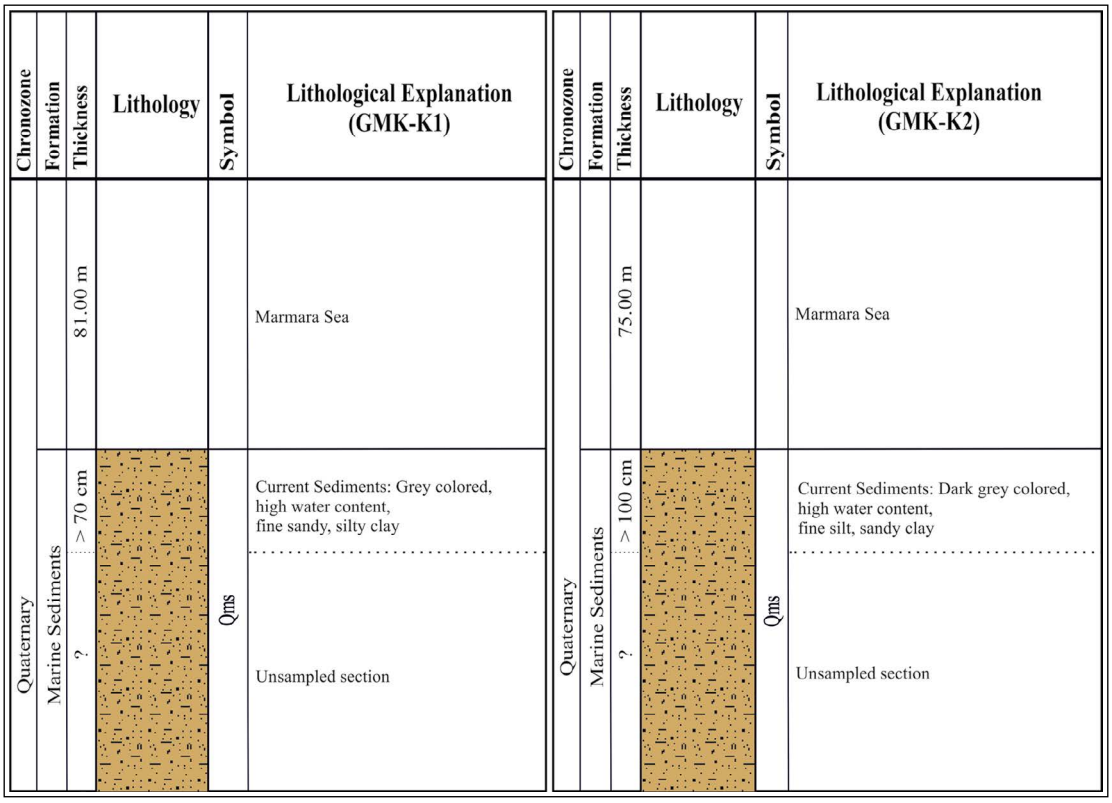

Figure 4- The columnar section of locations in which core samples in the Gulf of Gemlik were taken (GMK-K1, water depth 81,00 m and GMK-K2, water depth 75,00 m) (not to scale).

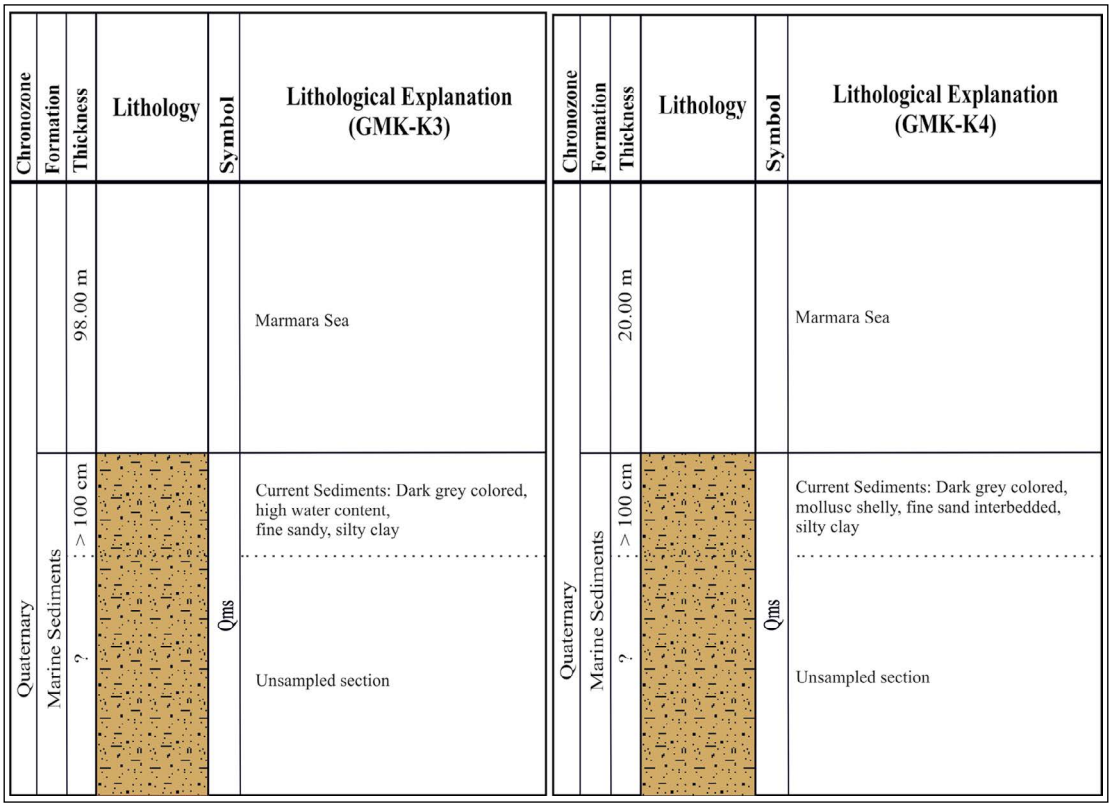

Figure 5- The columnar section of locations in which core samples in the Gulf of Gemlik were taken (GMK-K3, water depth 98,00 m and GMK-K4, water depth 20,00 m) (not to scale).

Table 1- Coordinates and other specifications of drilling and core locations.

Borehole and Cores	GMK-1: GS-84 6 Degree Coordinates		Water Depth	Sample Length
	Longitude	Latitude	(m)	(m)
GMK-1	666899.00 d E	4480487.00 m N	27,00	12,80
GMK-2	677320.00 d E	4480755.00 m N	35,60	13,30
GMK-3	682561.00 d E	4477768.00 m N	6,00	3,00
GMK-K1	672101.00 d E	4481326.00 m N	81,00	0,70
GMK-K2	658957.00 d E	4481138.00 m N	75,00	1,00
GMK-K3	669332.26 d E	4471289.16 m N	98,00	1,00
GMK-K4	681950.40 d E	4477270.34 m N	20,00	1,00

aspera (d'Orbigny), *Cycloforina contorta* (d'Orbigny), *C. rugosa* (d'Orbigny), *Massilina secans* (d'Orbigny), *Quinqueloculina bidentata* d'Orbigny, *Q. disparilis* d'Orbigny, *Q. jugosa* Cushman, *Q. lamarckiana* d'Orbigny, *Q. seminula* (Linné), *Miliolinella elongata* Kruit, *M. subrotunda* (Montagu), *Pseudotriloculina laevigata* (d'Orbigny), *P. oblonga* (Montagu), *P. rotunda* (d'Orbigny) *Triloculina marioni* Schlumberger, *Lagena laevis* (Montagu), *Polymorphina* sp., *Globobulimina affinis* (d'Orbigny), *Valvulineria bradyana* (Fornasini), *Rosalina bradyi* Cushman, *Lobatula lobatula* (Walker and Jacob), *Planorbulina mediterranensis* d'Orbigny, *Asterigerinata mamilla* (Williamson), *Nonion depressulum* (Walker and Jacob), *Ammonia compacta* Hofker, *A. parkinsoniana* (d'Orbigny), *Porosononion subgranosum* (Egger), *Elphidium advenum* (Cushman), *E. complanatum* (d'Orbigny), *E. crispum* (Linné), *E. depressulum* Cushman, *E. jenseni* (Cushman), *E. macellum* (Fichtel and Moll).

In contrast, in the samples from GMK-K1, GMK-K2, GMK-K3 and GMK-K4, a total of 40 genera and 58 species were found, namely: *Ammodiscus planorbis* Höglund, *Eggerelloides scabrus* (Williamson), *Bigenerina nodosaria* d'Orbigny, *Textularia bocki* Höglund, *T.* cf. *pala* Czjek, *Adelosina cliarensis* (Heron-Allen and Earland), *Spiroloculina excavata* d'Orbigny, *S. tenuiseptata* Brady, *Siphonaperta aspera* (d'Orbigny), *Cycloforina contorta* (d'Orbigny), *C. tenuicollis* (Wiesner), *Quinqueloculina seminula* (Linné), *Biloculinella depressa* (Wiesner), *B. wiesneri* (Le Calvez and Le Calvez), *Miliolinella subrotunda* (Montagu), *Pseudotriloculina laevigata* (d'Orbigny), *P. rotunda* (d'Orbigny), *Pyrgo elongata* (d'Orbigny), *P. inornata* (d'Orbigny), *Triloculina tricarinata* d'Orbigny, *Sigmoilinita costata* (Schlumberger), *S. edwardsi* (Schlumberger), *S. tenuis* (Czjcek), *Sigmoilopsis schlumbergeri* (Silvestri), *Dentalina inornata* d'Orbigny, *Neolenticulina peregrina* (Schwager), A*mphicoryna scalaris* (Batsch), *Lagena strumosa* Reuss, *Brizalina alata* (Seguenza), *B. spathulata* (Williamson), *Cassidulina carinata* Silvestri, *Rectuvigerina phlegeri* Le Calvez, *Bulimina aculeata* d'Orbigny, *B. costata* d'Orbigny, *B. elongata* d'Orbigny, *B. marginata* d'Orbigny, *Globobulimina affinis* (d'Orbigny), *G. pseudospinescens* (Emiliani), *Reussella spinulosa* (Reuss), *Fursenkoina acuta* (d'Orbigny), *Valvulineria bradyana* (Fornasini), *Discorbinella bertheloti* (d'Orbigny), *Hyalinea balthica* (Schröter), *Planorbulina mediterranensis* d'Orbigny, *Asterigerinata mamilla* (Williamson), *Nonion depressulum* (Walker and Jacob), *Nonionella turgida* (Williamson), *Chilostomella mediterranensis* Cushman and Todd, *Gyrodinoides lamarckiana* (d'Orbigny), *Aubignyna perlucida* (Heron-Allen and Earland), *Ammonia compacta* Hofker, *A. parasovica* Stshedrina and Mayer, *A. parkinsoniana* (d'Orbigny), *Porosononion subgranosum* (Egger), *Elphidium complanatum* (d'Orbigny), *E. crispum* (Linné), *E.* cf. *incertum* (Williamson), *E. macellum* (Fichtel and Moll) (Table 2). These genera and species were identified by using Meriç et al. (1995, 2005); Sakınç, (2008); Meriç et al. (2014). In total, 77 species were observed in the drillings and cores.

3.2. Ostracods

Ostracods were found in 82 samples of GMK-1, GMK-2, GMK-3 and 37 samples of GMK-K1, GMK-K2, GMK-K3, GMK-K4, in which a total of 27 genera and 37 species were identified (Table 3), according to Van Morkhoven (1963); Breman (1975); Bonaduce et al. (1975); Yassini (1979); Athersuch et al. (1989); Guillaume et al. (1985); Tunoğlu (1999, 2002); Şafak (1999); Guernet et al. (2003).

Table 2- The foraminifer contents of boreholes and cores.

FORAMINIFERA	BOREHOLES			CORES			
	GMK-1	GMK-2	GMK-3	GMK-K1	GMK-2	GMK-3	GMK-4
Ammodiscus planorbis Höglund				*		*	
Eggerelloides scabrus (Williamson)							*
Bigenerina nodosaria d'Orbigny				*	*		
Textularia bocki Höglund		*		*		*	
Textularia cf. *pala* Czjek				*	*	*	
Adelosina cliarensis (Heron-Allen and Earland)		*			*		
Adelosina mediterranensis (Le Calvez and Le Calvez)		*					
Spiroloculina dilatata d'Orbigny	*						
Spiroloculina excavata d'Orbigny	*	*		*	*	*	
Spiroloculina ornata d'Orbigny		*					
Spiroloculina tenuiseptata Brady				*	*	*	
Siphonaperta aspera d'Orbigny	*	*				*	
Cycloforina contorta (d'Orbigny)	*	*	*				*
Cycloforina rugosa (d'Orbigny)	*						
Cycloforina tenuicollis (Wiesner)				*			
Massilina secans (d'Orbigny)	*	*	*				
Quinqueloculina bidentata d'Orbigny	*						
Quinqueloculina disparilis d'Orbigny	*		*				
Quinqueloculina jugosa Cushman	*						
Quinqueloculina lamarckiana d'Orbigny		*					
Quinqueloculina seminula (Linné)	*	*	*	*	*	*	*
Biloculinella depressa (Wiesner)						*	
Biloculinella wiesneri (Le Calvez and Le Calvez)				*	*	*	
Miliolinella elongata Kruit		*					
Miliolinella subrotunda (Montagu)	*				*		
Pseudotriloculina laevigata (d'Orbigny)	*	*				*	
Pseudotriloculina oblonga (Montagu)	*		*				
Pseudotriloculina rotunda (d'Orbigny)	*						*
Pyrgo elongata (d'Orbigny)				*			
Pyrgo inornata (d'Orbigny)				*			
Triloculina marioni Schlumberger	*						
Triloculina tricarinata d'Orbigny				*			
Sigmoilinita costata (Schlumberger)					*		
Sigmoilinita edwardsi (Schlumberger)					*		
Sigmoilinita tenuis (Czjcek)					*	*	
Sigmoilopsis schlumbergeri (Silvestri)						*	
Dentalina inornata d'Orbigny						*	
Neolenticulina peregrina (Schwager)				*			
A*mphicoryna scalaris* (Batsch)				*	*		
Lagena laevis (Montagu)	*						
Lagena strumosa Reuss				*	*		
Polymorphina sp.	*						
Brizalina alata (Seguenza)				*	*	*	
Brizalina spathulata (Williamson)				*	*	*	*
Cassidulina carinata Silvestri				*	*	*	
Rectuvigerina phlegeri Le Calvez				*	*	*	
Bulimina aculeata d'Orbigny				*	*	*	
Bulimina costata d'Orbigny						*	

Table 2- continued.

Bulimina elongata d'Orbigny				*	*	*	
Bulimina marginata d'Orbigny				*	*	*	
Globobulimina affinis (d'Orbigny)	*			*	*	*	
Globobulimina pseudospinescens (Emiliani)						*	
Reussella spinulosa (Reuss)						*	
Fursenkoina acuta (d'Orbigny)					*		
Valvulineria bradyana (Fornasini)		*		*	*	*	
Rosalina bradyi Cushman	*						
Discorbinella bertheloti (d'Orbigny)				*	*	*	
Hyalinea balthica (Schröter)				*	*	*	
Lobatula lobatula (Walker and Jacob)	*	*	*				
Planorbulina mediterranensis d'Orbigny		*		*			
Asterigerinata mamilla (Williamson)	*					*	
Nonion depressulum (Walker and Jacob)	*						*
Nonionella turgida (Williamson)				*	*	*	
Chilostomella mediterranensis Cushman and Todd				*	*	*	
Gyrodinoides lamarckiana (d'Orbigny)				*	*	*	
Aubignyna perlucida (Heron-Allen and Earland)							*
Ammonia compacta Hofker	*	*	*		*		*
Ammonia parasovica Stshedrina and Mayer							*
Ammonia parkinsoniana (d'Orbigny)	*	*	*				*
Porosononion subgranosum (Egger)			*				*
Elphidium advenum (Cushman)	*		*				
Elphidium complanatum (d'Orbigny)	*	*	*		*		*
Elphidium crispum (Linné)	*	*	*				*
Elphidium depressulum Cushman	*	*					
Elphidium cf. *incertum* (Williamson)					*		*
Elphidium jenseni (Cushman)	*						
Elphidium macellum (Fichtel and Moll)	*		*				*

When the boreholes and cores were compared to each other in terms of the Gulf of Gemlik ostracod community, it was found that the number of genera and species are richer in the drilling samples of GMK-1 and GMK-2 and the core samples of GMK-K2 and GMK-K4 (Table 3). When the drilling locations are considered, it is observed that the northern and eastern parts of the bay are rich in ostracod fauna, similar to the ostracod fauna found in the bottom sediments of the Gulf of Gemlik, as emphasized by Meriç et al. (2005).

The ostracod community found in this study was compared with the ostracod communities in the Aegean islands, the Adriatic Sea, Algeria, Sea of Marmara (Gökçeada-Bozcaada-Çanakkale), the southern Marmara shelf, the Western Black Sea, and the İzmir, Edremit and Gemlik gulfs as reported by Nazik (2001), Meriç et al. (2002, 2005, 2008), Parlak and Nazik (2016), and in the studies mentioned above. There are numerous similarities in genera and species, with *Carinocythereis carinata* (Roemer), *Hiltermannicythere turbida* (Mueller), *H. Rubra* (Mueller), *Costa edwardsii* (Roemer), *Pterygocythereis jonesii* (Baird), *Palmoconcha agilis* (Ruggieri), *Cytheridea acuminata* (Bosquet) species being widespread. In addition, *Loxocauda pellucida* (Mueller), which is known from the Mediterranean, Aegean and Marmara Seas (from Pliocene to the Recent), was found only in the core samples. *Ilyocypris bradyi* Sars, indicative of fresh water inflow, was found at depths of 6,00-6,20 m; i.e. in the topmost part of the GMK-3 drilling. *Heterocypris salina* (Brady) was found at higher levels of the core of GMK-K4 drilling at depths of 20,10-20,20 m. As a result, it was inferred that the ostracod community obtained from the Gulf of Gemlik drillings and cores can be equated with the ostracods of Mediterranean-Aegean seas.

Table 3- The ostracod content of boreholes and cores.

OSTRACODA	BOREHOLES			CORES			
	GMK-1	GMK-2	GMK-3	GMK-K1	GMK-K2	GMK-K3	GMK-K4
Cytherella alvearium Bonaduce, Ciampo and Masoli		*			*		
Carinocythereis carinata (Roemer)	*	*					*
Carinocythereis rhombica Stambolidis	*	*					*
Aurila arborescens (Brady)			*				
Aurila convexa (Baird)		*					
Tyrrenocythere amnicola (Sars)							*
Hiltermannicythere rubra (Mueller)	*						*
Hiltermannicythere turbida (Mueller)	*						*
Pterygocythereis jonesii (Baird)	*	*					*
Cytheretta judaea (Brady)	*				*		
Costa batei (Brady)					*		
Costa edwardsii (Roemer)	*	*		*	*	*	*
Costa tricostata (Reuss)		*					
Callistocythere intricatoides (Ruggieri)	*						*
Callistocythere pallida (Mueller)	*						
Cyprideis torosa (Jones)	*		*				
Cytheridea acuminata (Bosquet)	*	*		*			*
Leptocythere sp.	*	*					
Leptocythere multipunctata (Seguenza)							*
Urocythereis crenulosa (Terquem)	*		*		*		
Buntonia sp.					*		
Semicytherura acuta Mueller	*						
Semicytherura incongruens (Mueller)	*	*					
Semicytherura inversa (Seguenza)	*						*
Paracytheridea depressa Mueller	*				*		
Cytheropteron sp.				*			
Palmoconcha agilis (Ruggieri)	*	*		*	*		*
Loxoconcha bairdi Mueller	*						
Loxoconcha stellifera Mueller	*	*	*		*		
Sagmatocythere versicolor (Mueller)					*		
Loxocauda pellucida (Mueller)				*		*	
Cushmanidea turbida (Mueller)	*	*			*		*
Pontocypris rara Mueller	*	*		*			
Argilloecia sp.					*		
Xestoleberis dispar (Mueller)	*						*
Heterocypris salina (Brady)							*
Ilyocypris bradyi Sars			*				

3.3. Nannoplanktons

The studies were carried out on mud/ unconsolidated mudstone samples from GMK-1, GMK-2, GMK-3 drillings and GMK-K1, GMK-K2, GMK-K3 and GMK-K4 cores. In general, the nannofossil assemblages including: *Gephyrocapsa oceanica,* small *Gephyrocapsa* spp.*, Scyphosphaera porosa* are present, in addition to *Emiliania huxleyi, Reticulofenestra parvula, Coronosphaera* spp.*, Bylosphaera* spp.*, Helicosphaera* spp. characterize an open-shallow marine environment. Biostratigraphic evaluation of this group allowed NN21 *Emiliania huxleyi* biozone to be determined. According to these data, Holocene marine deposition occurred.

In addition, both synsedimentary and reworked nannofossil assemblages, and their representative biozones and environmental characteristics were determined in mud samples belonging to the boreholes

and cores of the Gulf of Gemlik. In these stratigraphic interpretations, the data related from other coeval fossils, such as dinoflagellate cysts, ascidian spicules, diatom and sponge spicules were also used (see Table 4 and Plate 1). Some synsedimentary (Holocene) nannofossil species were simply reported as "coccospheres".

In mud samples of the GMK-1 drilling, 18 nannofossil species were observed, of which 12 are "synsedimentary", 5 of them "reworked from Cenozoic rocks" and a single one is "reworked from Cretaceous rocks". In these samples, 4 dinoflagellate cysts (*Thoracosphaera* spp.) were recognized, 2 of them are "synsedimentary" and the other 2 are "reworked" (Table 4). In mud samples from the GMK-2 drilling, 39 nannofossil species were recorded, of which 16 species are "synsedimentary", 20 of them were "reworked" from Cenozoic units, which of them are recorded as 3 dinoflagellate species, 2 are "synsedimentary" and 1 "reworked" (*Thoracosphaera* spp.) (Table 4) is. Finally, in the mud samples of the GMK-3 drilling, 15 nannofossil species were observed, 2 of them were "synsedimentary", 8 of them were reworked from the Cenozoic and 5 of them were reworked from the Cretaceous. Two "synsedimentary" dinoflagellate cysts (*Thoracosphaera* spp.) were also distinguished (Table 4). As shown in Table X, the nannofossil assemblages *Syracosphaera* spp. and *Coronosphaera* spp., in addition to *Emiliania huxleyi, Reticulofenestra parvula*, indicate the presence of the NN21 *Emiliania huxleyi* Zone. It is concluded that the sediments, excluding *Gephyrocapsa omega* individuals in the GMK-1 and GMK-2 drillings, represent shallow-open sea deposition during the Holocene period (Varol and Houghton, 1996; Young, 1998; Young et al., 2014). Although, there are few nannofossils in the samples from the GMK-3 drilling, the abundance

Table 4- The nannofossils assemblage and biostratigraphical distribution of boreholes and cores.

ORIGINAL CLASSIFICATION	CHRONOZONE	BIOZONE	Nannofossil species	BOREHOLES			CORES			
				GMK-1	GMK-2	GMK-3	GMK-K1	GMK-K2	GMK-K3	GMK-K4
SYNSEDIMENTARY	HOLOCENE	NN21 *Emiliania huxleyi* Zone	*Alisphaera* sp. (Gran and Braarud)		*					
			Anthosphaera sp. "coccosphere"		*					
			Braarudosphaera bigelowii (Gran and Braarud)	*	*		*	*	*	
			Cocolithus pelagicus (Wallich)				*		*	
			Coronosphaera binodata (Kamptner)	*	*		*	*	*	
			Coronosphaera mediterranea Lohmann	*	*		*	*	*	*
			Dictyococcites antarcticus Haq	*						
			Dictyococcites productus (Kamptner)	*	*		*	*	*	*
			Emiliana huxleyi (Lohmann)	*	*	*	*	*	*	*
			Emiliana huxleyi (Lohmann) "coccosphere"		*			*	*	*
			küçük *Gephyrocapsa* sp.		*			*	*	
			Gphyrocapsa oceanica Kamptner				*		*	
			Helicosphaera carteri (Wallich)	*	*		*	*	*	
			Helicosphaera hyalina Gaarder	*	*			*	*	
			Helicosphaera wallichii (Lohmann)				*	*		
			Papposphaera sp. Tangen "coccosphere"		*					
			Pontosphaera japonica (Takayama)		*		*			
			Pseudoemiliana lacunosa ovata (Kamptner)				*			
			Reticulofenestra parvula (Okada and McIntyre)	*	*	*	*	*	*	*
			Rhabdosphaera clavigera Murray and Blackman	*	*		*			
			Syracosphaera histrica Kamptner	*			*		*	
			Syracosphaera pulchra Lohmann	*	*		*	*	*	*
			Thoracosphaera granifera Fütterer	*	*	*	*	*	*	*
			Thoracosphaera tuberosa Kamptner	*	*	*	*	*		

Table 4- continued.

REWORKED	PALEOGENE-NEOGENE	?	*Arkhangelskiella specillata* Vekshina		*					
			Blackites spinosus (Deflandre and Fert)				*			
			Chiasmolithus grandis (Bramlette and Riedel)							*
			Clausicoccus fenestratus (Deflandre and Fert)		*					
			Cocolithus miopelagicus Bukry							*
			Cocolithus pelagicus (Wallich)	*	*	*				*
			Cruciplacolithus tenuis (Stradner)	*						
			Cyclicargolithus floridanus (Roth and Hay)	*	*		*			
			Dictyococcities hesslandii (Haq)		*	*	*	*	*	
			Dictyococcites scrippsae Bukry and Percival		*					
			Discoaster gemmifer Stradner							*
			Discoaster saipanensis Bramlette and Riedel			*				
			Ericsonia formosa (Kamptner)		*	*		*		
			Micrantolithus basquensis Martini		*					
			Neococcolithus dubius (Deflandre)		*					
			Pemma sp. Klumpp		*					
			Pontosphaera obliquipons (Deflandre)					*		
			Pontosphaera pectinata (Bramlette and Sullivan)	*	*					
			Prinsius martinii (Perch-Nielsen)			*				
			Reticulofenestra dictyoda (Deflandre)		*					
			Reticulofenestra gelida (Geitzenauer)					*		
			Reticulofenestra haqii Backman		*		*	*		
			Reticulofenestra hampdanensis Edwards			*				
			Reticulofenestra lockeri Müller				*	*		
			Reticulofenestra minuta Roth		*					
			Reticulofenestra minutula (Gartner)		*				*	
			Reticulofenestra pseudoumbilicus (Gartner)	*	*		*	*	*	*
			Scyphosphaera globulata Bukry and Percival		*					
			Sphenolithus abies Deflandre				*			
			Sphenolithus moriformis (Bronnimann and Stradner)		*	*				*
			Sphenolithus radians Deflandre		*	*				*
			Thoracosphaera heimii Lohmann	*	*		*	*		
			Toweius crassus (Bramlette and Sullivan)							*
	UPPER CRETACEOUS	?	*Aspidolithus parcus parcus* (Stradner)			*				
			Braarudosphaera bigelowii (Gran and Braarud)			*				
			Braarudosphaera discula Bramlette and Riedel					*		
			Cribrosphaerella ehrenbergii (Arkhangelsky)				*			
			Cyclagelosphaera reinhardtii (Perch-Nielsen)				*			
			Ellipsogelosphaera britannica (Stradner)							*
			Ellipsogelosphaera ovata (Bukry)						*	
			Microrhabdulus attenuatus Deflandre					*		
			Micula decussata Vekshina							
			Micula staurophora (Gardet)			*				
			Prediscosphaera cretacea (Arkhangelsky)			*			*	*
			Quadrum gartneri Prins and Perch-Nielsen							*
			Rhomboaster cuspis Bramlette and Sullivan					*		
			Stradneria crenulata Bramlette and Martini				*			
			Thoracosphaera saxea Stradner	*			*			
			Watznaueria barnesae Black	*	*	*	*	*	*	*

of dinoflagellate cysts such as *Thoracosphaera* spp. (*Th. granifera, Th. tuberosa*) that represent shallow-sea conditions indicates that the deposition, which generally represents the Holocene, records a steadily deepening marine environment. Although there are no nannofossils at some levels (as specified in the tables for the drilling samples), the presence of dinoflagellate cysts such as *Thoracosphaera* spp., which represent a shallow-marine setting (*Th. granifera*), suggests that there has been at least one short-period decrease in sea level during the Holocene.

In the mud samples of the GMK-K1 core, 18 nannofossil species were determined, of which 15 are "synsedimentary" and 3 are from Cenozoic and Cretaceous rocks, which of them are recorded as 3 dinoflagellate species (Thoracosphaera spp.), 2 of them are "synsedimentary" and 1 of them is "reworked" (Table 4). In the mud samples from the core GMK-K2 , 23 nannofossil species are "reworked", of which 12 are "synsedimentary", 11 are from the Cenozoic and Cretaceouss, which of them are recorded as 3 dinoflagellate species), 2 of them are "synsedimentary" and 1 of them is "reworked" (*Thoracosphaera* spp). Also, in mud samples from core GMK-K3 core, 20 nannofossil species are present, of which 14 are "synsedimentary", and 6 were reworked from the Cenozoic and Cretaceous. In addition, q 1 "synsedimentary" dinoflagellate species (*Thoracosphaera granifera*) was observed. In the mud samples of GMK-K4, 18 nannofossil species occur, of which 6 are "synsedimentary" and 12 were "reworked" from the Cenozoic and Cretaceous (Table 4).

In addition to an abundance of Emiliania huxleyi and Reticulofenestra parvula in the mud samples from GMK-K2 (75,00-76,00 m) and GMK-K3 (98,00 - 99,00 m), two deepest cores in Gemlik Bay, the existence of *Gephyrocapsa oceanica* and small *Gephyrocapsa* species (survivors after extinction of *Gephyrocapsa omega)* indicate that marine sedimentation began at the base of Holocene.

3.4. Diatoms

The number of genera and species of diatoms in the drilling and core samples is very small. In the drilling of GMK-2, *Stephanodiscus lucens* Hustedt occurs at 39,00-39,10 m also, *Perissonoe cruciata* (Janisch and Robenhorst) Andrews and Stocizel at 41,00-41,10 and 41,40-41,50 m. In the drilling of GMK-3, *Eunotia sp*. occurs at 7,20-7,40 m and *Campylodiscus echeneis* Ehrenberg at 8,20-8,40 m. (Plate 2). Between these, *Stephanodiscus lucens* is a planktonic freshwater form commonly found in the high-temperature waters. *Perissonoe cruciata* (Janisch and Robenhorst) is a warm-water form, which is common in marine, littoral environments. *Eunotia sp.* is common in waters with both low and high temperatures, and is also a benthic (epiphytic, epilitic) fresh water form; it is common in low-nutrient (oligosaprobic) waters, which have both low and high water temperatures (oligotropic, eutropic) and pH>7 (alkaline). *Campylodiscus echeneis* Ehrenberg is generally a marine form (Krammer-Lange Bertalot, 1988, 1991; Soinien and Könönen, 2004; Round et al., 2007; Lerin and Cambra, 2007; Lange Bertalot et al., 2011; Krizmanici et al., 2015).

In terms of the diatom flora, *Stenopterobia* sp., which is a cosmopolitan form, occurs in the cores of GMK-K3 between 98,30-98,40 m and 98,60-98,70 m, and individuals belonging to the same genus rarely occur at 21,90-22,00 m in GMK-K4 (Krammer, Lange-Bertalot, 1988 and URL) (Plate 2).

Stephanodiscus lucens Hustedt and *Eunotia* sp., which are encountered in small numbers amongst the diatom assemblages in the drilling samples, are freshwater forms and are likely to have been transported to the environment by rivers. *Perissonoe cruciata* (Janisch and Robenhorst) and *Campylodiscus echeneis* Ehrenberg are marine forms. Especially, *Perissonoe cruciata* (Janisch and Robenhorst) represents both a marine environment and a littoral warm-water environment.

The diatom species and genera described in boreholes and cores are widespread throughout the Holocene.

3.5. Molluscs

The drilled samples contain very rich gastropod and bivalve assemblages. In drilled samples of GMK-1, GMK-2, GMK-3, there is a rich community of gastropod, namely: *Gibbula albida* (Gmelin), *G. rarilineata* (Michaud*), Phorcus mutabilis* (Philippi), *Bittium latreillii* (Payraudeau), *B. reticulatum* (da Costa), *B. submammillatum* (de Rayneval and

Ponzi), *Turritella communis* Risso, *Similiphora similior* (Bouchet and Guillemot), *Epitonium clathrus* (Linné), *Melarhaphe neritoides* (Linné), *Rissoa auriformis* Pallary, *R. splendida* Eichwald, *Pussilina inconspicua* (Alder), *P. lineolata* (Michaud), *P. marginata* (Michaud), *Alvania geryonia* (Nardo), *Obtusella intersecta* (S. Wood), *O. macilenta* (Monterosato), *Hydrobia acuta* (Draparnaud), *Hyala vitrea* (Montagu), *Euspira intricata* (Donovan), *Tritia pygmaea* (Lamarck), *Clathromangelia strigilata* Pallary, *Sorgenfreispira brachystoma* (Philippi), *Mangelia scabrida* Monterosato, *Mangelia* sp., *Raphitoma* sp., *Eulimella acicula* (Philippi), *Parthenina juliae* (de Folin), *Megastomia conoidea* (Brocchi), *Odostomia megerlei* (Locard), *Ondina crystallina* Locard, *Turbonilla acutissima* Monterosato, *Retusa leptoeneilema* (Brusina,), *R. minutissima* (Monterosato), *R. obtusa* (Montagu), *Cylichna cylindracea* (Pennant) (Table 5a), and bivalves which are; *Nucula hanleyi* Winckworth, *N. sulcata* Bronn, *Lembulus pella* (Linné), *Mytilus galloprovincialis* Lamarck, *Musculus subpictus* (Cantraine), *Modiolula phaseolina* (Philippi), *Ostrea edulis* Linné, *Ctena decussata* (O. G. Costa), *Lucinella divaricata* (Linné), *Myrtea spinifera* (Montagu), *Kurtiella bidentata* (Montagu), *Acanthocardia paucicostata* (G. B. Sowerby II), *Parvicardium scriptum* (Bucquoy, Dautzenberg and Dollfus), *Papillicardium papillosum* (Poli), *Spisula solida* (Linné), *S. subtruncata* (da Costa), *Abra prismatica* (Montagu), *Atlantella pulchella* (Lamarck), *Timoclea ovata* (Pennant), *Gouldia minima* (Montagu), *Pitar mediterraneus* (Aradas and Benoit), *P. rudis* (Poli), *Ruditapes decussatus* (Linné), *Corbula gibba* (Olivi),

Table 5a- The mollusc content of the drillings.

MOLLUSCA		BOREHOLES		
		GMK-1	GMK-2	GMK-3
GASTROPODA	*Gibbula albida* (Gmelin)	*		*
	Gibbula rarilineata (Michaud)			*
	Phorcus mutabilis (Philippi)		*	
	Bittium latreillii (Payraudeau)	*	*	*
	Bittium reticulatum (da Costa)	*		*
	Bittium submammillatum (de Rayneval and Ponzi)	*	*	*
	Turritella communis Risso	*	*	
	Similiphora similior (Bouchet and Guillemo)	*		
	Epitonium clathrus (Linnaeus)	*		
	Melarhaphe neritoides (Linnaeus)	*		
	Rissoa auriformis Pallary		*	*
	Rissoa splendida Eichwald	*	*	*
	Pussilina inconspicua (Alder)	*	*	
	Pusillina lineolata (Michaud)	*	*	*
	Pusillina marginata (Michaud)	*		
	Alvania geryonia (Nardo)	*		
	Obtusella intersecta (S. Wood)	*	*	
	Obtusella macilenta (Monterosato)	*		
	Hyala vitrea (Montagu)		*	
	Hydrobia acuta (Draparnaud)	*		
	Euspira intricata (Donovan)	*	*	*
	Tritia pygmaea (Lamarck)	*	*	
	Tritia reticulata (Linnaeus)			*
	Sorgenfreispira brachystoma (Philippi)	*		
	Clathromangelia strigilata Pallary		*	
	Mangelia scabrida Monterosato	*	*	
	Raphitoma sp.	*	*	
	Eulimella acicula (Philippi)	*	*	
	Parthenina juliae (de Folin)	*		

Table 5a- continued.

GASTROPODA	*Megastomia conoidea* (Brocchi)		*	*
	Odostomia megerlei (Locard)	*	*	
	Turbonilla acutissima Monterosato	*		
	Retusa leptoeneilema (Brusina)	*		
	Retusa obtusa (Montagu)	*	*	
	Cylichna cylindracea (Pennant)	*	*	
BIVALVIA	*Nucula hanleyi* Winckworth		*	
	Nucula sulcata Bronn	*		
	Lembulus pella (Linnaeus)	*	*	*
	Musculus subpictus (Cantraine)	*		
	Modiolula phaseolina (Philippi)	*	*	*
	Ostrea edulis Linnaeus			*
	Ctena decussata (O. G. Costa)	*		
	Lucinella divaricata (Linnaeus)	*	*	*
	Myrtea spinifera (Montagu)	*	*	
	Kurtiella bidentata (Montagu)	*	*	
	Acanthocardia paucicostata (G. B. Sowerby II)	*		
	Parvicardium scriptum (Bucquoy, Dautzenberg and Dollfus)	*	*	*
	Papillicardium papillosum (Poli)	*		
	Spisula solida (Linnaeus)	*	*	
	Spisula subtruncata (da Costa)	*		
	Abra prismatica (Montagu)		*	
	Atlantella pulchella (Lamarck)	*	*	
	Timoclea ovata (Pennant)	*	*	
	Gouldia minima (Montagu)	*	*	*
	Pitar mediterraneus (Aradas and Benoit)	*		
	Pitar rudis (Poli)	*		
	Ruditapes decussatus (Linnaeus)	*		
	Corbula gibba (Olivi)	*		
	Hiatella arctica (Linnaeus)	*		
	Hiatella rugosa (Linnaeus)			*

Hiatella arctica (Linné), *H. rugosa* (Linné) were found (Table 5a) (Cossignani et al., 2011; Scaperrotta et al., 2009-2015) (Plates 3 and 4).

When the cores of GMK-K1, GMK-K2, GMK-K3 and GMK-K4 are considered in terms of mollusc assemblages; i.e. the following bivalves were identified: *Kelliella miliaris* (Philippi), *Spisula subtruncata* (da Costa), *Parvicardium exiguum* (Gmelin), *Loripes dentatus* (Defrance), *Timoclea ovata* (Pennant), *Corbula gibba* (Olivi), *Abra* sp., from gastropods; *Turritella communis* Risso, *Alvania cimicoides* (Forbes), *Panthenina intersincta* (J. Adams), *Bittium reticulatum* (de Costa), *Ecrobia* cf. *maritima*, *Rissoa* sp., *Turbonilla* sp.; the scaphopod, *Dentalium* sp. was also observed (Table 5b). The above assemblage is Holocene and characterizes a shallow-marine environment. Owing to the partial fossilization of the shells, they are considered to be of Early Holocene age (Nevesskaja, 1965, 1974; Perna, 2003; Nielsen et al., 2006; Taviani et al., 2014; Çağatay et al., 2015; Büyükmeriç, 2016).

4. Discussion and Conclusion

As a result of the studies, it is understood that the foraminifer assemblage of the Gulf of Gemlik was under the influence of the Mediterranean-Aegean Sea communities. It is remarkable that there is a great difference between the samples from the drilling and the cores in terms of the number of genera and species. Although, a total of 22 genera and 38 species, characterizing the infra-littoral zone in drilling samples were identified, 40 genera and 58 species were observed, which characterize the circa-littoral zone in the cores. In addition, to observing large

Table 5b- The mollusc content of core samples.

MOLLUSCA	CORES			
	GMK-K1	GMK-K2	GMK-K3	GMK-K4
Kelliella miliaris (Philippi)	*	*	*	*
Spisula subtruncata (da Costa)		*	*	*
Parvicardium exiguum (Gmelin)		*		*
Loripes dentatus J.L.M. Defrance				*
Timoclea ovata (Pennant)				*
Corbula gibba Olivi				*
Abra sp.				*
Turritella communis Risso		*		
Alvania cimicoides (Forbes)		*		
Parthenina interstincta (J. Adams)				*
Bittium reticulatum (da Costa)				
Ecrobia cf. *maritima* (Milaschewitsch)	*			
Rissoa sp.		*		
Turbonilla sp.				*
Dentalium sp.	*			

number of species of Black Sea origin, *Ammonia parasovica* in samples from GMK-K4, taken from the eastern part of the gulf, is another notable feature for the study area, and is the first record of this species in the Gulf of Gemlik. The same genus and species were encountered at different levels of the drillings of KS-2, S-5 and S-3, carried out in the Gulf of İzmit (Meriç et al., 1995). It is thought that this species of Black Sea origin continued its life in the Gulf of Gemlik after the Gulf of İzmit in Holocene. Both the boreholes and the core samples have a very rich fauna in terms of the ostracod assemblage. The ostracod assemblage of the boreholes and the core samples resembles each other. *Loxocauda pellucida*, which is known in the Mediterranean, Aegean and Marmara Seas, was encountered only in core samples. The ostracod genera and species identified belong to typical Mediterranean-Aegean Sea fauna.

The nannofossil assemblage in which *Emiliania huxleyi, Reticulofenestra parvula, Gephyrocapsa oceanica, Scyphosphaera porosa* species are present in the boreholes and cores, characterize an open shallow-marine environment, typical of the Holocene period, including the NN21 *Emiliania huxleyi* biozone in the samples studied. The nannoplankton community is richer than in terms of the number of genera and species in the Gulf of İzmit.

Although the drilling boreholes and cores represent a sparse community in terms of the diatom flora, its actual presence in the eastern Gulf of Gemlik is first emphasized by this study. When compared, it observed that there is a great difference between the diatom assemblage of the Gulf of Gemlik and that of the İznik Lake. The presence of fresh-water diatoms and ostracods in some boreholes and drilling samples also suggests that there was fresh water outflow to the marine Gulf of Gemlik at certain times.

The mollusc assemblage on the other hand includes characteristic Mediterranean genera and species. According to the data obtained, the Gulf of Gemlik remained under Mediterranean influence during the Holocene period. A remarkable feature is the great abundance of *Turritella communis in a* mud-rich environments between 27,10 to 40,00 m in GMK-1 and also between 35,10-40,80 m in the GMK-2 drilling. This shows that the life conditions were suitable in the Gulf of Gemlik for this species. This is the only species that adapted itself to the ambient low-oxygen conditions in the gulf. When all of the microfossil and the macrofossil findings were evaluated, it was determined that the Gulf of Gemlik assemblage is typical of the Mediterranean-Aegean Sea community during the Holocene period.

Acknowledgements

The authors would like to thank to Aynur Yümün (Yümün Mühendislik A.Ş.) for providing the drilling and core samples for this study. The authors are also thankful to Prof. Muhittin Görmüş (A.U.), Assoc. Prof. Burçin Aşkım Gümüş and an unknown referee who made significant contributions with their supportive criticism and suggestions during the revision of this article. Also, we would like to thank to Prof Alastair Robertson (The University of Edinburgh) who linguistically improved of last version of the manuscript.

References

Aksu, A.E., Hiscott, R.N., Yaşar, D. 1999. Oscillating Quaternary water levels of the Marmara Sea and vigorous out- £ow into the Aegean Sea from the Marmara Sea-Black Sea drainage corridor. Marine Geology 153, 275-302.

Aksu, A.E., Hiscott, R.N., Kaminski, M.A., Mudie, P.J., Gillespie, H., Abrajano, T., Yaşar, D. 2002. Last Glacial-Holocene paleoceanography of the Black Sea and Marmara Sea: stable isotopic, foraminiferal and coccolith evidence. Marine Geology 190, 119-149.

Athersuch J., Horne D.J., Whittaker J.E. 1989. Marine and brackish water ostracods. In Kermack D.M., Barnes R.S.K.(Ed.), Synopses of the British Fauna (New Series) 43, 345p.

Breman, E. 1975. The distribution of ostracodes in the bottom sediments of the Adriatic Sea. Vrije Universiteit te Amsterdam, Krips Repro, Meppel, 165 p.

Brückner, H., Kelterbaum, D., Marunchak, O., Porotov, A., Vott, A. 2010. The Holocene sea level story since 7500 BP - Lessons from the Eastern Mediterranean, the Black and the Azov Seas. Quaternary International 225, 160-179.

Bonaduce G., Ciampo G., Masoli M. 1975. Distribution of Ostracoda in the Adriatic Sea. Pubblicazioni della Stazione Zoologica di Napoli 40, 304 p.

Büyükmeriç, Y. 2016. Postglacial flooding of the Marmara Sea (Turkey): Molluscs and sediments tell the story. Geo-Marine Letters 36, 4, 307-321.

Chepalyga, A.L. 2007. The Late Glacial great flood in the Ponto-Caspian basin. In:Yanko-Hombach, V., Gilbert, A.S., Panin, N., Dolukhanov, P.M. (Ed.), The Black Sea Flood Question. Springer, Dordrecht, 119-148.

Cossignani, T., Ardovani, R., Micali, P., Tisselli, M., Cossignani, V., Cecalupo, A. 2011. Malacologia Mediterranea: Atlante delle Conchiglie del Mediterraneo. L'Informatore Piceno, Cupra Marittima, Italy, 536 p.

Çağatay, M.N., Görür, N., Algan, O., Eastoe, C., Tchapalyga, A., Ongan, D., Kuhn, T., Kuşçu, I. 2000. Late Glacial-Holocene palaeoceanography of the Sea of Marmara: timing of connections with the Mediterranean and the Black Seas. Marine Geology 167, 191-206.

Çağatay, M.N., Görür, N., Polonia, A., Demirbağ, E., Sakınç, M., Cormier, M.-H.,Capotondi, L., McHugh, C., Emre, Ö., Eriş, K. 2003. Sea level changes and depositional environments in the Izmit Gulf, eastern Marmara Sea, during thelate glacial-Holocene period. Marine Geology 202, 159-173.

Çağatay, M.N., Eris¸ , K., Ryan, W.B.F., Sancar, U., Polonia, A., Akcer, S., Biltekin, D., Gasperini, L., Görür, N., Lericolais, G., Bard, E. 2009. Late Pleistocene-Holocene evolution of the northern shelf of the Sea of Marmara. Marine Geology 265, 87-100.

Çağatay, M. N., Wulf, S., Sancar, Ü., Özmaral, A., Vidal, L., Henry, H., Appelt, O., Gasaperini, L. 2015. The tephra record from the Sea of Marmara for the last ca. 70 ka and its palaeoceanographic implications. Marine Geology 361, 96-110.

Filikçi, B., Eriş, K.K., Çağatay, N., Sabuncu, A., Polonia, A. 2017. Late glacial to Holocene water level and climate changes in the Gulf of Gemlik, Sea of Marmara: evidence from multi-proxy data. Geo-Marine Letters 37, 501-513.

Gasperini, I., Polonia, A., Çağatay, M. N., Bortoluzzi, C., Ferrante, V. 2011. Geological slip rates along the North Anatolian Fault in the Marmara Region. Tectonics, 30, TC6001.

Görür, N., Çağatay, M.N., Sakınç, M., Sumengen, M., Senturk, K., Yaltirak, C., Tchapalyga, A. 1997. Origin of the Sea of Marmara as deducted from the Neogene to Quaternary paleogeographic evolution of its frame, Int. Geol. Rev., 39, 342–352, doi:10.1080/00206819709465276.

Guernet, C., Lemeille, F., Sorel, D., Bourdillon, C., Berge-Thierry C., Manakou, M. 2003. Les ostracodes et le Quaternaire d'Aigion (golfe de Corinth, Grèce). Revue de Micropaleontologie 46, 73–93.

Guillaume, M.C., Peypouquet, J.P. et Tetart, J. 1985. Quaternaire et actuel. Atlas des Ostracodes de France, Ed: H.J. Oertli. Bulletin des centres de recherches exploration-production Elf-Aquitaine Mémoire 9, 337-377.

Hiscott, R.N., Aksu, A.E., Mudie, P.J., Kaminski, M.A., Abrajano, T., Yaşar, D., Rochon, N. 2007. The Marmara Sea gateway since ~16 Ky BP: non-catastrophic causes of palaeoceanographic

events in the Black Sea at 8.4 and 7.15 Ky BP. In:Yanko-Hombach, V., Gilbert, A.S., Panin, N., Dolukhanov, P.M. (Ed.), The Black Sea Flood Question. Springer, Dordrecht, 89-117.

İslamoğlu, Y. 2002. Neoeuxinian-Holocene molluscan fauna of the southern part of the Marmara Sea between Gemlik and Bandırma Bay (NW Turkey). Yılmaz, A. (Ed.). Oceanography of the Eastern Mediterranean and Black Sea, Similarities and Differences of Two Interconnected Basins. TÜBİTAK Publishers (ISBN: 975-288-451-2), Ankara, 953-960.

İslamoğlu, Y. 2009. Middle Pleistocene bivalves of the İznik lake basin (Eastern Marmara, NW Turkey) and a new paleobiogeographical approach. International Journal of Earth Sciences 98, 1981-1990.

İslamoğlu, Y., Chepalyga, A.L. 1998. The environmental changes determined with Molluscan assemblages during the Neoeuxinian-Holocene stages in the Sea of Marmara. Geological Bulletin of Turkey 41, 55-62.

Kerey E., Meriç, E., Tunoğlu, C., Kelling, G., Brenner, R.L., Doğan, A.U. 2004. Black Sea–Marmara Sea Quaternary connections: new data from the Bosphorus, Istanbul, Turkey. Palaeogeography, Palaeoclimatology, Palaeoecology 204, 3-4, 277-295.

Krammer, K., Lange-Bertalot, H. 1988. Bacillariophyceae. 2. Teil: Bacillariophyceae, Gustav Fischer Verlag, Band 2-2, Stuttgart, 611 p.

Krammer, K., Lange-Bertalot, H.1991. Bacillariophyceae. 3. Teil: Centrales, Fragilariaceae, Gustav Fischer Verlag, Band 2-3, Stuttgart, 599 p.

Krizmaniči, J., Ilıċ, M., Vidakoviči, D., Simiči, G.S., Petrovii, J., Cvetanovi, K. 2015. Diatoms of the Dojkinci River (Stara Planina Nature Park, Serbia). Acta Botanica Croatica 74, 2, 317– 331.

Lange Bertalot, H., Bak, M., Witkowski, A., Tagliavent, N. 2011. Eunotia and some related genera. Diatoms of Europe 6. Koeltz Scientific Books, Königstein.

Lerin, R., Cambra, J. 2007. Distribution and taxonomic notes of Eunotia Ehrenberg 1837 (Bacillariophyceae) in rivers and streams of Northern Spain. Limmetica 26, 2, 415-434.

Marret, F., Mudie, P., Aksu, A., Hiscott, R.N. 2009. A Holocene dinocyst record of a two-step transformation of the Neoeuxinian brackish water lake into the Black Sea. Quaternary International 197, 72-86

McHugh, C.M.G., Gurung, D., Giosan, L., Ryan, W.B.F., Mart, Y., Sancar, U., Burkle, L., Çağatay, M.N. 2008. The last reconnection of the Marmara Sea (Turkey) to the World Ocean: a paleoceanographic and paleoclimatic perspective. Marine Geology 255, 64-82.

Meriç, E. 1995. İstanbul Boğazı öncesinide Marmara Denizi-Karadeniz bağlantısının İzmit Körfezi-Sapanca Gölü-Sakarya Vadisi boyunca gereçekleştiğinin ön bulguları. Meriç, E. (Ed.). İzmit Körfezi Kuvaterner İstifi. İstanbul, 295-301.

Meriç, E., Yanko, V., Avşar, N. 1995. İzmit Körfezi (Hersek Burnu-Kaba Burun) Kuvaterner istifinin foraminifer faunası, Meriç, E. (Ed.). İzmit Körfezi Kuvaterner İstifi. İstanbul, 105-151.

Meriç, E., Avşar, N., Nazik, A. 2002. Bozcaada (Kuzey Ege Denizi) bentik foraminifer ve ostrakod faunası ile bu toplulukta gözlenen yerel değişimler, Yerbilimleri (Geosound) 40-41, 97-120.

Meriç, E., Avşar, N., Nazik, A., Alpar, B., Yokeş, B., Barut, İ. F., Ünlü, S. 2005. Gemlik Körfezi yüzey çökellerinin foraminifer, ostrakod ve mollusk faunası, foraminifer kavkılarında gözlenen morfolojik anomaliler ile bölgenin sedimentolojik, hidrokimyasal ve biokimyasal özellikleri. Maden Tetkik ve A*rama* Dergisi 131, 21-48. Ankara.

Meriç, E., Avşar, N., Tunoğlu, C., Nazik, A., Yokeş, B., Barut, İ.F., Yücesoy-Eryılmaz, F., Tuğrul, B., Görmüş, M., Öncel, M.S., Orak, H., Kam, E. ve Dinçer, F. 2008. Harmantaşı Mevkii (Saros Körfezi-Kuzey Ege Denizi) deniz içi kaynakları çevresinde foraminifer ve ostrakod topluluğuna bu alandaki çevresel koşulların etkisi. Maden Tetkik ve Arama Dergisi 136, 63-84.

Meriç, E., Nazik, A., Avşar, N., Alpar, B., Ünlü, S., Gökaşan, E. 2009. Marmara Denizi-Karadeniz su bağlantısında İzmit Kanalı'nın varlığının delilleri: İznik Gölü (Bursa-KB Türkiye) güncel sedimanlarının paleontolojik açıdan değerlendirilmesi. İstanbul Üniversitesi Yerbilimleri Dergisi 22, 1, 1-19.

Meriç, E., Avşar, N., Yokeş, M.B., Dinçer, F. 2014. Atlas of Recent benthic foraminifera from Turkey. Micropaleontology 60, 3-4, 188 p.

Meriç, E., Nazik, A., Yümün, Z. Ü., Büyükmeriç, Y., Avşar, N., Yıldız, A., Sagular, E. K., Koral, H., Gökaşan, E. 2018. Fauna and flora of drilling and core data from the İznik Lake: The Marmara and the Black Sea connection. Quaternary International 486, 156-184.

Mertens, K.N., Bradley, L.R., Takano, Y., Mudie, P.J., Marret, F., Aksu, A.E., Hiscott, R.N., Verleye, T.J., Mousing, E.A., Smyrnova, L.L., Bagheri, S., Mansor, M., Pospelova, V., Matsuoka, K. 2012. Quantitative estimation of Holocene surface salinity variation in the Black Sea using dinoflagellate cyst process length. Quaternary Science Reviews 39, 45-59.

Mudie, P.J., Rochon, A., Aksu, A.E., Gillespie, H. 2004. Late glacial, Holocene and modern dinoflagellate cyst assemblages in the Aegean-Marmara-Black Sea corridor: statistical analysis and re-interpretation of the early Holocene Noah's Flood hypothesis. Review of Palaeobotany and Palynology 128, 143-167.

Nazik, A. 2001. Ostracode faunas of bottom sediments from the continental shelf, South Marmara Sea, NW Turkey and their comparision with other shelf environments in the Mediterranean and Aegean regions. Geological Journal 36, 2, 111-123.

Nazik, A., Meriç, E., Avşar, N., Ünlü, S., Esenli, V., Gökaşan, E. 2011. Possible waterways between the Marmara Sea and the Black Sea in the late Quaternary: evidence from ostracod and foraminifer assemblages in lakes İznik and Sapanca. Geo-Marine Letters, 31, 2, 75-86.

Nevesskaja, L. A. 1965. Late Quaternary bivalve molluscs of the Black Sea, their systematics and ecology. Trudy Paleontologičeskogo Instituta, Akademiya Nauk SSSR 105, 390 p.

Nevesskaja, L. A. 1974. Molluscan shells in deep-water sediments of Black Sea. Degens E.T., Ross, D.A. (Ed.). The Black Sea-geology, chemistry and biology. American Association of Petroleum Geologists Memoir 20, 349-352.

Nielsen. J. K., Hanken, N-M., Nielsen, J. K., Haansen, K. S. 2006. Biostratigraphy and palaeoecology of the marine Pleistocene ofRhodes, Greece: Scleractinia, Serpulidae, Mollusca and Brachiopoda. Bulletin of Geosciences 80, 3,173-196.

Parlak, D., Nazik, A. 2016. Akdeniz (Antalya Körfezi) ve Ege Denizi (Ayvalık ve Kuşadası) ostrakodları ve biyocoğrafik dağılımı, Maden Tetkik Arama Dergisi 152, 63-65.

Perch-Nielsen, K. 1985*a*, Mesozoic calcareous nannofossils. Bolli, H. M., Saunders, J. B., Perch-Nielsen, K. (Ed.). Plankton Stratigraphy, Cambridge Earth Sciences Series, 329-426.

Perch-Nielsen, K. 1985*b*. Cenozoic calcareous nannofossils. Bolli, H. M., Saunders, J. B., Perch-Nielsen, K. (Ed.). Plankton Stratigraphy, Cambridge Earth Sciences Series, 427-554.

Perna, R. L. 2003. The Quaternary deep-sea protobranch fauna from the Mediterranean: composition, depth-related distribution and changes. Bollettino Malacologico 39, 1-4, 17-34.

Reinhardt, P. 1972. Coccolithen. Kalkiges nannoplankton seit jahmillionen. Neue Brehm Bücherei 453, 1-99.

Romein, A. J. T. 1979. Lineages in early paleogene calcareous nannoplankton. Utrecht Micropaleontological Bulletins 22, 1-231.

Round, F.E., Crawford, R.M., Mann, D.G. 2007. The Diatoms Biology and morphology of the Genera. Cambridge University Press, 747p.

Sagular, E.K. 2009. Fossil didemnid ascidian spicule records in the Plio-Quaternary marine clastics of the Antalya basin (Eastern Mediterranean) and their stratigraphic calibration to new nannofossil data. Geosciences Journal 13, 2, 121-131.

Sakınç, M. 2008. Marmara Denizi Bentik Foraminiferleri: Sistematik ve Otoekoloji. İstanbul Teknik Üniversitesi Rektörlüğü, İstanbul, 1638, 129 s.

Scaperrotta, M., Bartolini, S., Bogi, C. 2009-2015. Accrescimenti - Stadi di accrescimento dei Molluschi marini del Mediterraneo - Stages of growth of marine molluscs of the Mediterranean Sea, Vol. I-VI.

Sperling, M.R., Schmiedl, G., Hemleben, C., Emeis, K.C., Erlenkeuser, H., Grootes, P.M. 2003. Black Sea impact on the formation of eastern Mediterranean sapropel S1?Evidence from the Marmara Sea. Palaeogeography, Palaeoclimatology, Palaeoecology 190, 9-21.

Soininen, J., Könönen, K. 2004. Comparative study of monitoring South-Finnish rivers and streams using macroinvertebrate and benthic diatom community structure. Aquatic Ecology 38, 63-75.

Şafak, Ü. 1999. Recent ostracoda assemblage of the Gökçeada-Bozcaada-Çanakkale region, Yerbilimleri/Geosound 35, 149-172.

Taviani, M., Angeletti, L., Çağatay, M. N., Gasperini, L., Polonia, A., Wesselingh, F. P. 2014. Sedimentary and faunal signatures of the post-glacial marine drowning of the Pontocaspian Gemlik "Lake" (Sea of Marmara). Quaternary International 345, 11-17.

Tunoğlu, C. 1999. Recent ostracoda association in the Sea of Marmara, NW Turkey. Yerbilimleri 21, 63-87.

Tunoğlu, C. 2002. Karadeniz'in İstanbul Boğazı çıkışı ile Zonguldak ve Amasra kıyı alanlarında Güncel Ostrakod topluluğu. Yerbilimleri 26, 27-43.

URL,http//craticula.ncl.ac.uk/EADiatomKey/html/Stenopterobia.html

Van Morkhoven, F.P.C.M. 1963. Post Palaeozoic Ostracoda. Elsevir Amsterdam, (2), 478 pp.

Vardar, D., Öztürk, K., Yaltırak, C., Alpar, B., Tur, H. 2014. Late Pleistocene–Holocene evolution of the southern Marmara shelf and sub-basins: middle

strand of the North Anatolian fault, southern Marmara Sea, Turkey. Marine Geophysical Researches 35, 69-85.

Varol, O., Houghton, S.D. 1996. A review and classification of fossil didemnid ascidian spicules. Journal of Micropalaeontology 15, 135-149.

Vidal, L., Menot, G., Joly, C., Bruneton, H., Rostek, F., Çagatay, M.N., Major, C., Bard, E. 2010. Hydrology in the Sea of Marmara during the last 23 ka: implications for timing of Black Sea connections and sapropel deposition. Palaeoceanography 25, 1-16.

Yaltırak, C., Alpar, B. 2002. Evolution of the middle strand of North Anatolian Fault and shallow seismic investigation of the southeastern Marmara Sea (Gemlik Bay). Marine Geology 190, 307-327.

Yanko-Hombach, V.V., Gilbert, A.S., Dolukhanov, P., 2007. Controversy over Noah's flood in the Black Sea: geological and foraminiferal evidence from the shelf. Yanko-Hombach, V., Gilbert, A.S., Panin, N., Dolukhanov, P.M. (Ed.), The Black Sea Flood Question. Springer, Dordrecht, 149-203.

Yassini, l. 1979. The littoral system ostracodes from the Bay of Bou, İsmail, Algeries, Algeria: Revista Espanola de micropaleontologica, vol. XI, num. 3, 353-416.

Young, J.R. 1998. Neogene. Bown, P.R. (Ed.), Calcareous Nannofossil Biostratigraphy. British Micropalaeontological Society Publications Series. Chapman and Hall, London, 225-265.

Young, J.R., Bown P.R., Lees J.A. (Ed.) 2014. Nannotax3 website. International Nannoplankton Association. 21 Apr. 2014. URL: http://ina.tmsoc.org/Nannotax3.

PLATES

PLATE 1

Holocene nannofossil species found in drill and core samples of the Gemlik Bay (PL: polarized light, NL: normal light, CL: contrast light, GL: with gypsum wedge, QL: with quartz wedge; letter and number order on the upper left corner: drilling number and rock sampling depth, linear scale: 5 μm):

1. *Emiliania huxleyi*,

2. *Helicosphaera carteri*,

3. *Helicosphaera hyalina*,

4. *Syracosphaera histrica*,

5. *Braarudosphaera bigelowii*,

6. *Coronosphaera mediterranea*,

7. *Emiliania huxleyi*,

8. *Dictyococcites productus*,

9. *Reticulofenestra parvula*,

10. *Rhabdosphaera clavigera*,

11. *Thoracosphaera granifera*,

12. *Anthosphaera* sp.,

13. *Syracosphaera pulchra*,

14. *Gephyrocapsa oceanica*,

15. *Scyphosphaera porosa*,

16. *Coccolithus pelagicus*,

17. *Bonetia acuta* "Ascidian spicule",

18. *Reticulofenestra dictyoda* "reworked",

19. *Thoracosphaera tuberosa*,

20. *Pontosphaera pectinata* "reworked",

21. *Scyphosphaera globulata.*

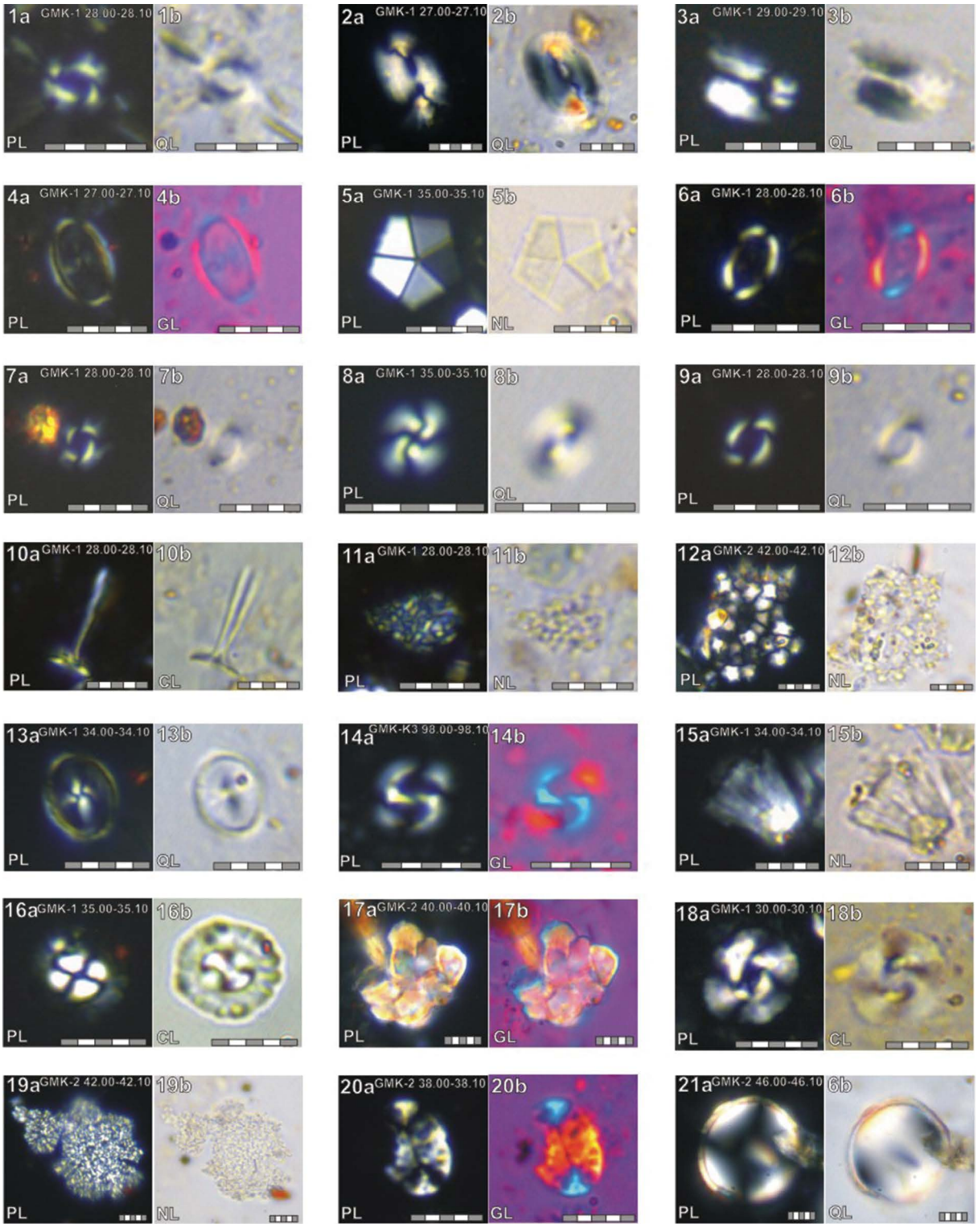
1a GMK-1 28.00-28.10
PL
1b
QL
2a GMK-1 27.00-27.10
PL
2b
QL
3a GMK-1 29.00-29.10
PL
3b
QL
4a GMK-1 27.00-27.10
PL
4b
GL
5a GMK-1 35.00-35.10
PL
5b
NL
6a GMK-1 28.00-28.10
PL
6b
GL
7a GMK-1 28.00-28.10
PL
7b
QL
8a GMK-1 35.00-35.10
PL
8b
QL
9a GMK-1 28.00-28.10
PL
9b
QL
10a GMK-1 28.00-28.10
PL
10b
CL
11a GMK-1 28.00-28.10
PL
11b
NL
12a GMK-2 42.00-42.10
PL
12b
NL
13a GMK-1 34.00-34.10
PL
13b
QL
14a GMK-K3 98.00-98.10
PL
14b
GL
15a GMK-1 34.00-34.10
PL
15b
NL
16a GMK-1 35.00-35.10
PL
16b
CL
17a GMK-2 40.00-40.10
PL
17b
GL
18a GMK-1 30.00-30.10
PL
18b
CL
19a GMK-2 42.00-42.10
PL
19b
NL
20a GMK-2 38.00-38.10
PL
20b
GL
21a GMK-2 46.00-46.10
PL
6b
QL

PLATE 2

Diatom species found in drill and core samples from the Gulf of Gemlik.

1. Stenopterobia sp., a) GMK-K3, 98,30-98,40 m, b). GMK-K3, 98,60-98,70 m, c) GMK-K4, 21,90-22,00 m.

2. Eunotia sp., GMK-3, 07,20-07,40 m.

3. Campylodiscus echeneis, GMK-3, 08,20-08,40 m.

4. Stephanodiscus lucens, GMK-2, 39,00-39,10 m.

5. Perissonoe cruciata, a. GMK-2, 41,00-41,10 m, b. GMK-2, 41,40-41,50 m.

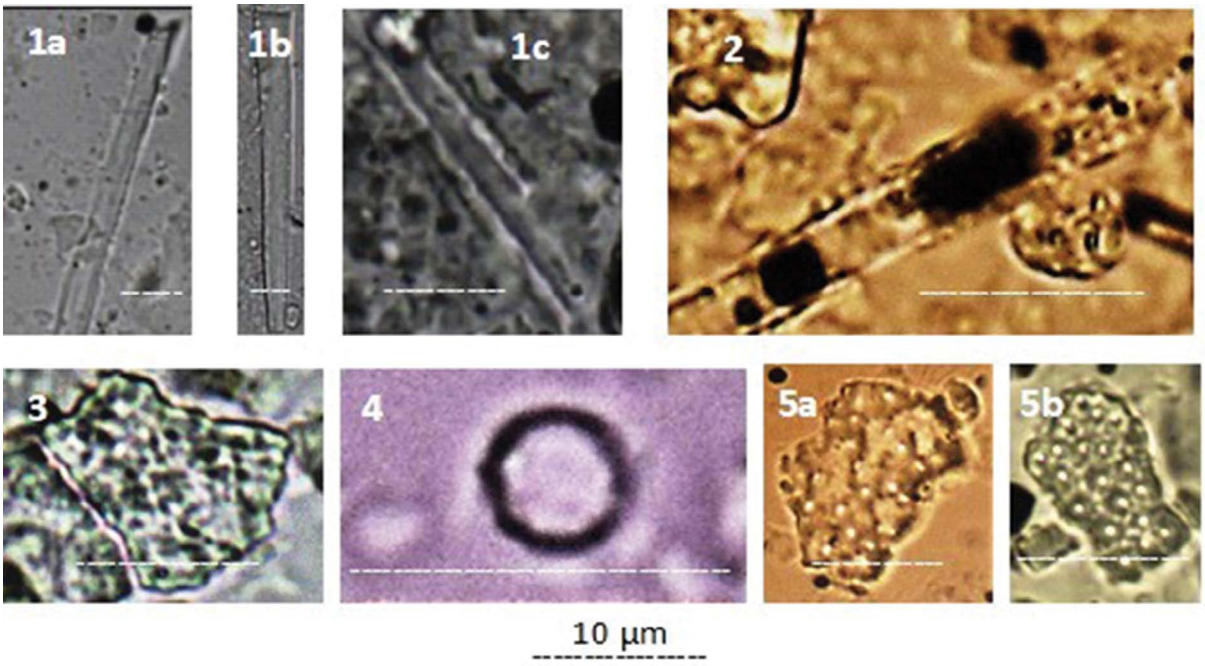
1a
1b
1c
2
3
4
5a
5b
10 µm

PLATE 3

Gastropod species found in drill samples from the Gulf of Gemlik.

1. *Phorcus mutabilis*, Gemlik-2, 40,20-40,30 m.

2. *Gibbula albida* Gemlik-1, 31,40-31,50 m.

3. *Melarhaphe neritoides*, Gemlik-1, 34,30-34,50 m.

4. *Rissoa splendida*, Gemlik-2, 38,00-38,10 m.

5. *Rissoa auriformis*, Gemlik-3, 07,20-07,40 m.

6. *Pussilina inconspicua*, Gemlik-2, 40,50-40,60 m.

7. *Pusillina lineolata*, Gemlik-1, 29,90-30,00 m.

8. *Pusillina marginata*, Gemlik-1, 30,50-30,60 m.

9. *Hyala vitrea*, Gemlik-2, 41,10-41,20 m.

10. *Euspira intricata*, Gemlik-1, 29,90-30,00 m.

11. *Epitonium clathrus*, Gemlik-1, 30,20-30,30 m.

12. *Similiphora similior*, Gemlik-1, 33,70-33,80 m.

13. *Bittium latreillii*, Gemlik-1, 33,50-33,60 m.

14. *Bittium reticulatum*, Gemlik-3, 07,20-07,40 m.

15. *Bittium submammillatum*, Gemlik-3, 06,40-06,60 m.

16. *Turritella communis*, Gemlik-2, 35,50-35,60 m.

17. *Tritia pygmaea*, Gemlik-1, 34,50-34,60 m.

18. *Sorgenfreispira brachystoma*), Gemlik-1, 35,10-35,20 m.

19. *Mangelia scabrida*, Gemlik-1, 34,00-34,10 m.

20. *Clathromangelia strigilata*, Gemlik-2, 35,50-35,60 m.

21. *Megastomia conoidea*, Gemlik-3, 06,20-06,40 m.

22. *Ondina crystallina*, Gemlik-2, 46,40-46,50 m.

23. *Eulimella acicula*, Gemlik-2, 41,80-41,90 m.

24. *Turbonilla acutissima*, Gemlik-1, 33,40-33,50 m.

25. *Parthenina juliae*, Gemlik-1, 37,60-37,70 m.

26. *Odostomia megerlei*, Gemlik-1, 34,60-34,70 m.

27. *Retusa leptoeneilema*, Gemlik-1, 34,70-34,80 m.

28. *Retusa obtusa*, Gemlik-1, 29,90-30,00 m.

29. *Cylichna cylindracea*, Gemlik-1, 30,30-30,40 m.

(Scale = 1 mm)

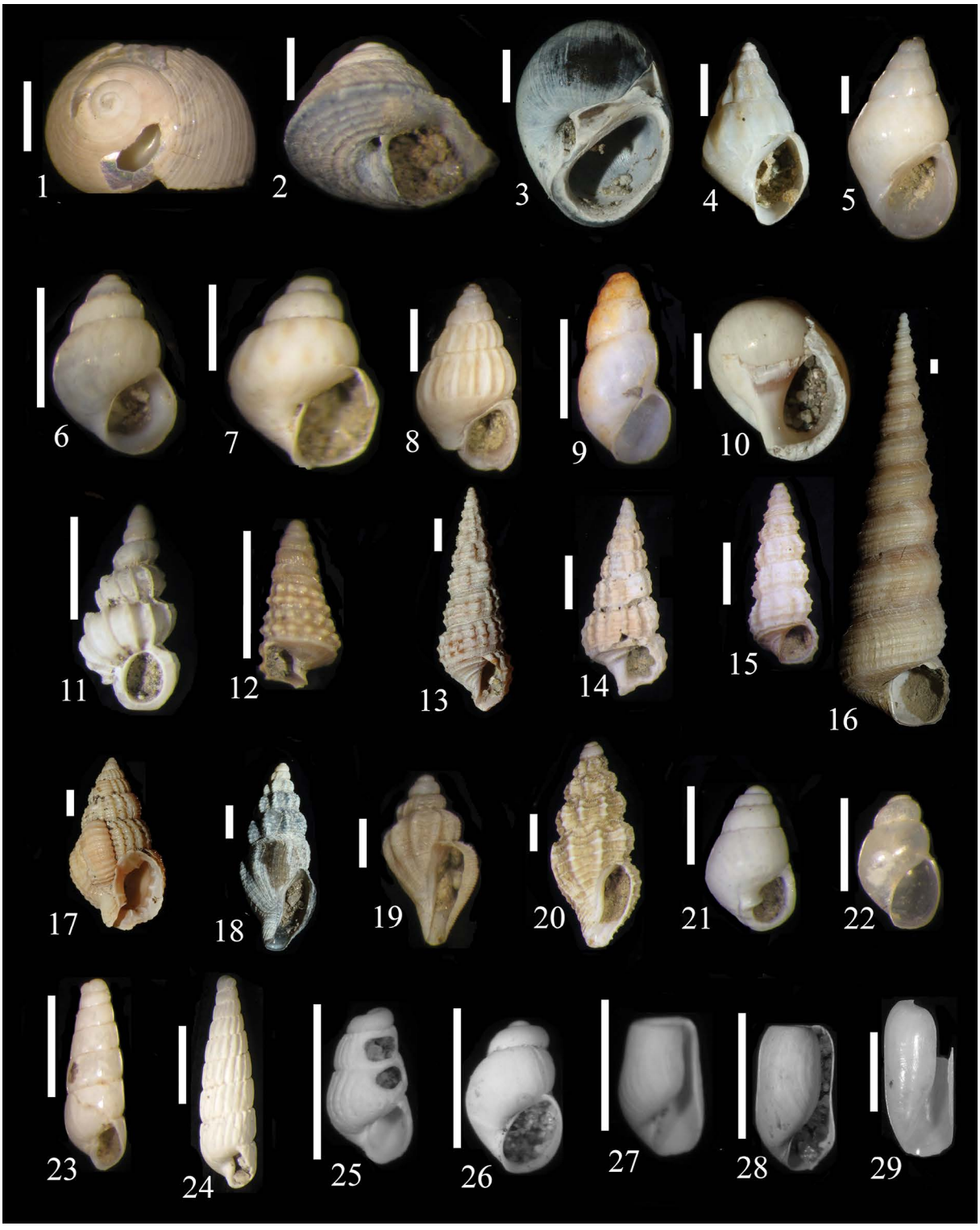
1
2
3
4
5
6
7
8
9
10
11
12
13
14
15
16
17
18
19
20
21
22
23
24
25
26
27
28
29

PLATE 4

Bivalve species found in drill samples from the Gulf of Gemlik.

1. *Nucula hanleyi*, Gemlik-2, 42,00-42,10 m.

2. *Nucula sulcata*, Gemlik-1, 35,00-35,10 m.

3. *Lembulus pella*, Gemlik-2, 39,20-39,30 m.

4. *Mytilus galloprovincialis*, Gemlik-3, 08,80-09,00 m.

5. *Ostrea edulis*, Gemlik-3, 06,20-06,40 m.

6. *Musculus subpictus*, Gemlik-1, 29,00-29,10 m.

7. *Modiolula phaseolina*, Gemlik-2, 44,60-44,70 m.

8. *Ctena decussata*, Gemlik-1, 34,00-34,10 m.

9. *Lucinella divaricata*, Gemlik-1, 28,10-28,20 m.

10. *Myrtea spinifera*, Gemlik-1, 27,80-27,90 m.

11. *Kurtiella bidentata*, Gemlik-1, 28,80-28,90 m.

12. *Acanthocardia paucicostata*, Gemlik-1, 27,90-28,00 m.

13. *Parvicardium scriptum*, Gemlik-1, 27,70-27,80 m.

14. *Papillicardium papillosum*, Gemlik-1, 3,30-33,40 m.

15. *Spisula solida*, Gemlik-2, 36,80-36,90 m.

16. *Spisula subtruncata*, Gemlik-1, 34,10-34,20 m.

17. *Abra prismatica*, Gemlik-2, 37,70-37,80 m.

18. *Atlantella pulchella*, Gemlik-1, 32,80-32,90 m.

19. *Timoclea ovata*, Gemlik-1, 27,80-27,90 m.

20. *Gouldia minima*, Gemlik-1, 33,60-33,70 m.

21. *Pitar mediterraneus*, Gemlik-1, 34,20-34,30 m.

22. *Pitar rudis*, Gemlik-1, 34,20-34,30 m.

23. *Ruditapes decussatus*, Gemlik-1, 34,20-34,30 m.

24. *Corbula gibba*, Gemlik-2, 42,10-42,20 m.

25. *Hiatella arctica*, Gemlik-1, 33,40-33,50 m.

26. *Hiatella rugosa*, Gemlik-3, 6,40-6,60 m.

(Scale = 1 mm)

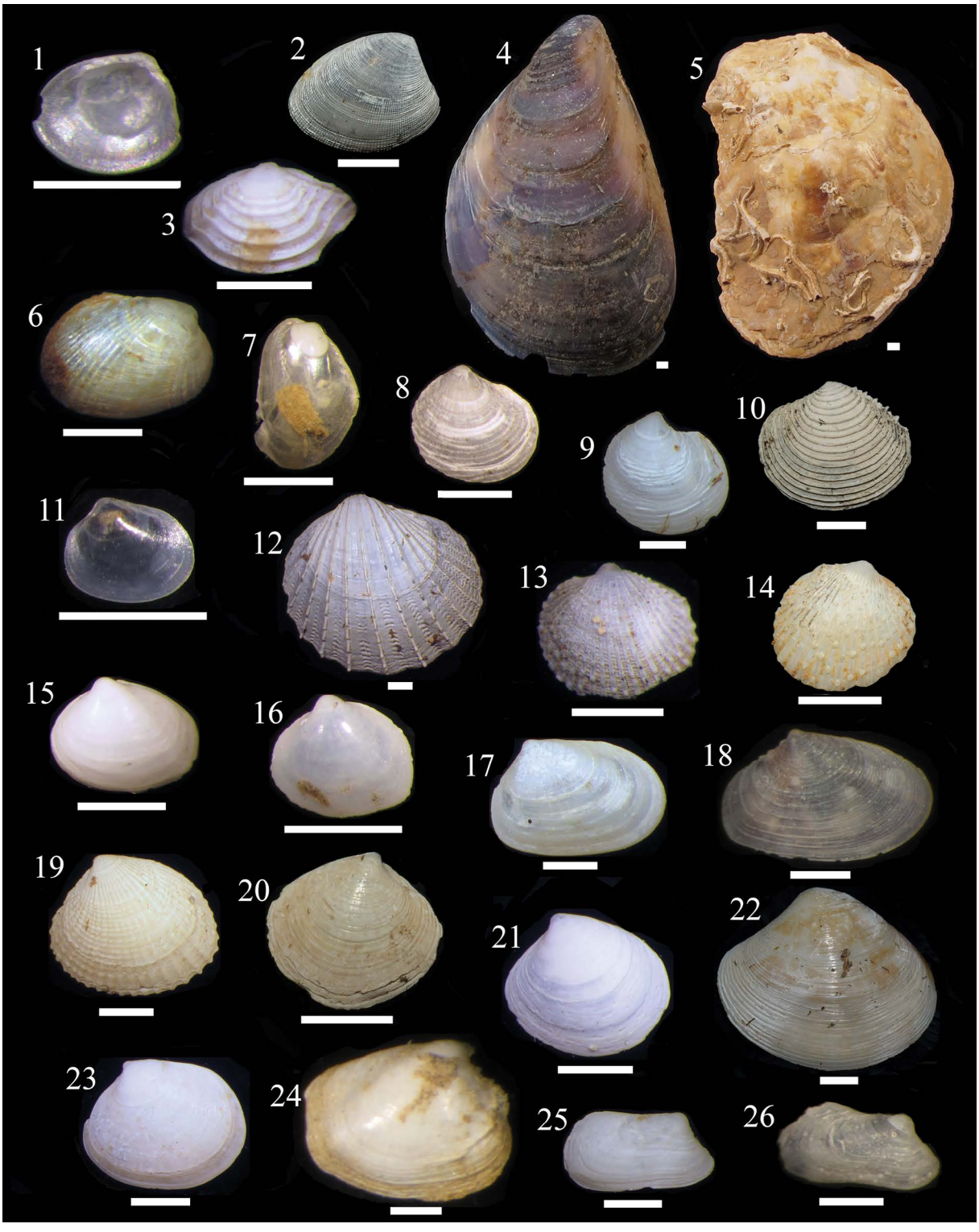
1
2
4
5
3
6
7
8
10
9
11
12
13
14
15
16
17
18
19
20
21
22
23
24
25
26

Bulletin of the Mineral Research and Exploration

http://bulletin.mta.gov.tr

Precise monitoring of temporal topographic change detection via unmanned air vehicle

Serkan KARAKIŞ[a], Umut Güneş SEFERCİK[a*], Turhan BİLİR[b] and Can ATALAY[a]

[a]*Bulent Ecevit University, Engineering Faculty, Dept. of Geomatics Engineering, 67100, Zonguldak, Turkey*
[b]*Istanbul University-Cerrahpasa, Engineering Faculty, Dept. of Civil Engineering, 34320, Istanbul, Turkey*

Research Article

Keywords:
Digital photogrammetry, UAV, DiffDTM, Monitoring.

ABSTRACT

Nowadays, fast developing space-borne and airborne remote sensing technologies became indispensable for land related engineering disciplines such as mapping, geology, environment, mining and forestry. The new technologies, provide more qualified and rapid achievable outcomes, are adopted permanently. The description of the topographic surface became easier by means of very high resolution (VHR), rapid achievable and accurate point clouds acquired by digital photogrammetry and airborne laser scanning (ALS). Optical unmanned air vehicle (UAV), one of the most actual photogrammetric techniques, is much in demand for varied purposes. UAVs provide high resolution data using the advantage of lower flight altitudes. In this study, a construction activity and its environmental influences in Bulent Ecevit University Central Campus were monitored by an optical hand-made UAV. In the application, the temporal change was detected by generating contour-lines, digital terrain models (DTMs) and differential DTMs (DiffDTM) of the topography. By DiffDTMs, temporal changes on the topography were visualized in color height scale where the contour-lines presents the change of morphological structure.

Received Date: 24.10.2018
Accepted Date: 25.01.2019

1. Introduction

In recent years, space-borne and airborne remote sensing technologies have been developing rapidly and monitoring of topographic displacements and deformations, depending on construction activities or natural disasters has become possible by temporal change detection analysis. With the development of airborne laser scanning (ALS) technology, three-dimensional (3D) description of the topographic surface became easier by means of very high resolution (VHR), rapid achievable and accurate point clouds that could not been provided by previous remote sensing technologies (Deng et al., 2007; Darwin et al., 2014; Höhle, 2017; Manfreda et al., 2018*a*). Considering high surface description potential, point cloud thought was adapted to photogrammetric image processing following ALS (Teizer et al., 2005; Rosnell and Honkavaara, 2012). Photogrammetric sensing acquires aerial photos by CCD/CMOS sensor-integrated multispectral digital cameras and point clouds can be provided with original colors in correlated parts of stereo imagery (Rosnell and Honkavaara, 2012; Swatantran et al., 2016).

The resolution of point cloud has a significant role on the quality of 3D topographic description and unmanned air vehicle (UAV) imaging (Ai et al., 2015) is the best way to increase the resolution with the advantage of lower flight altitudes. In UAV imaging, the properties of used camera and the terrain slope effect the final 3D model quality (Manfreda et al., 2018*b*).

Citation Info: Karakis, S., Sefercik, U. G., Bilir, T., Atalay, C. 2020. Precise monitoring of temporal topographic change detection via unmanned air vehicle. Bulletin of the Mineral Research and Exploration. 161, 151-156. https://doi.org/10.19111/bulletinofmre.524179

* *Corresponding author: Umut Güneş SEFERCİK, ugsefercik@hotmail.com*

In this study, we aimed to monitor the 3D temporal topographic change in a construction area with a handmade UAV. With this purpose, we preferred a study field in Bulent Ecevit University Main Campus due to avoid official restrictions about UAVs in urban areas.

According to this aim, the paper was organized as follows; in section 2, the properties of the study area is given. Next, utilized materials and used methods were presented in section 3. Results are placed in section 4 followed by the conclusions.

2. Study Area

The selected study area is a place that a new Engineering Faculty is being constructed. It covers approx.100 m × 100 m (1 ha) area and the orthometric height is around 65 m. Figure 1 shows Main University Campus of Bulent Ecevit University and preferred study area on the high resolution (12 Megapixel) image that we obtained by a UAV flight. The area was periodically monitored during the excavation and the stereo-images derived from the first and last flights were used in the applications.

3. Materials and Methods

3.1 Used Materials

The UAV, used in the study, is a handmade octocopter and has very simple equipment. Hence, it can be easily produced and utilized for large variety of applications. The main body was built by carbon-fiber arms and the equipment were mounted on it. The main contents of the UAV consist of brushless motors, a flight control unit, a global positioning system (GPS) for coarse positioning, a data control card, an electronic stability control (ESC), a battery and a remote controller receiver which communicates with outer remote sensing transmitter. The produced UAV and main contents are presented in figure 2.

In the study, 12 Megapixel Canon EOS450D DSLR camera, which can be full-size mounted to the

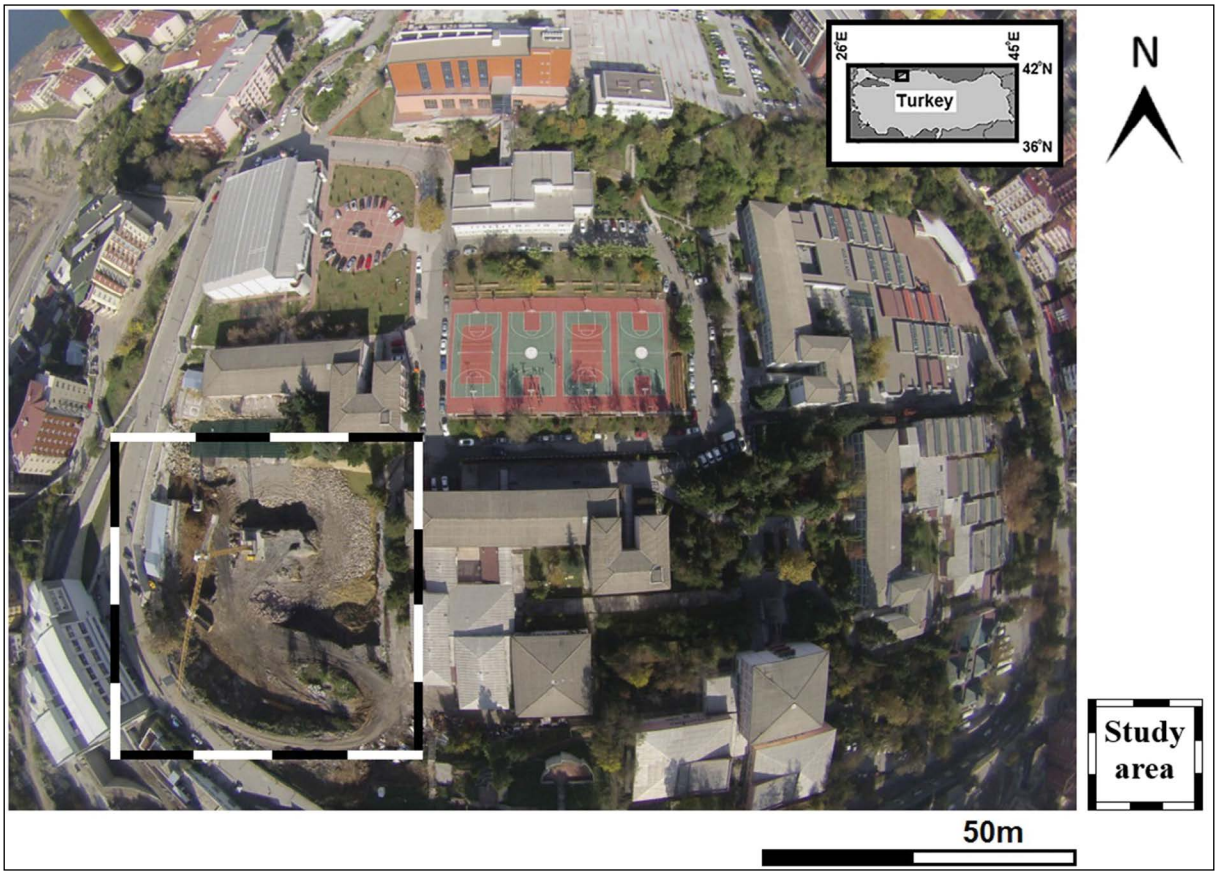

Figure 1- High resolution UAV image of Bülent Ecevit University Central Campus.

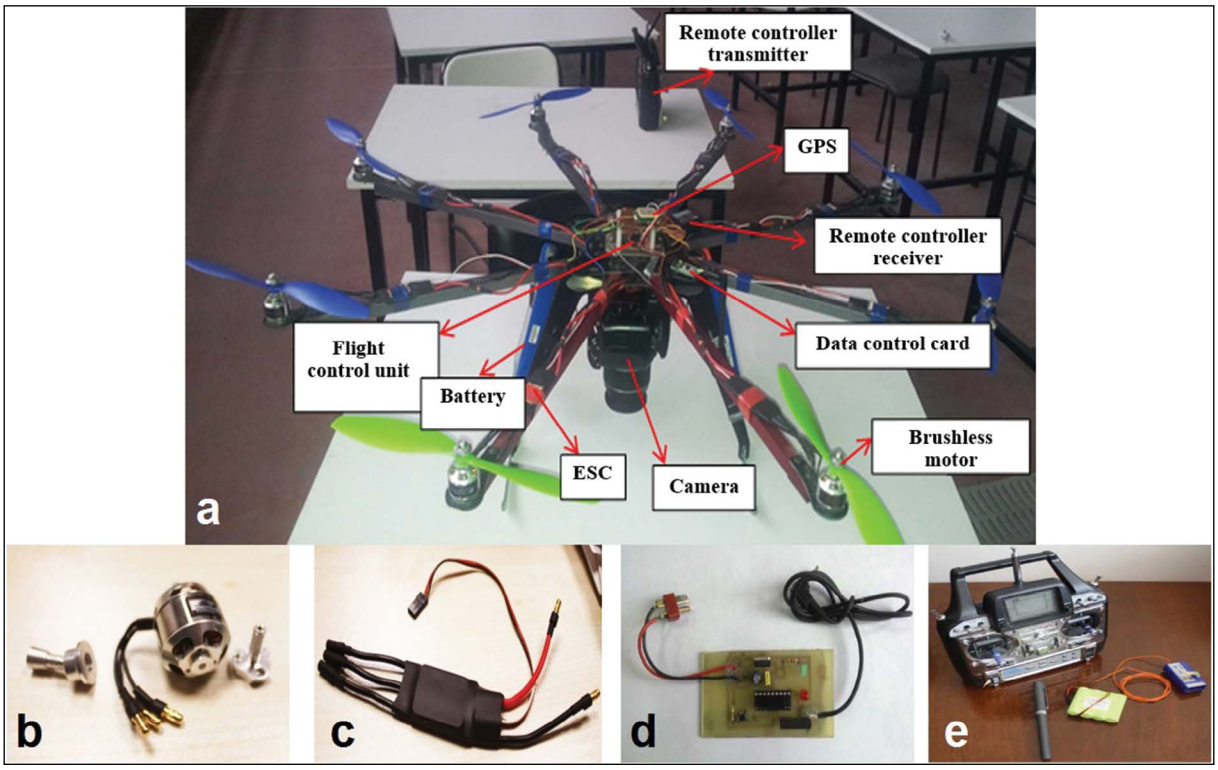

Figure 2- UAV and the main equipment; a) produced octocopter, b) brushless motor, c) electronic speed controller (esc), d) electronic timer, e) remote controller transmitter.

octocopter's body, was used. The properties of the camera are given in table 1.

Table 1- Technical properties of Canon EOS450D DSLR Camera.

Resolution (megapixel)	12
Maximum frame size (pixel)	4272 × 2848
Sensor size (mm)	22,2 × 14,8
Pixel size (μ)	5
Maximum shutter speed (sn)	1/4000
Weight (g)	475
Camera size (mm)	129 × 98 × 62
Processor	Digic III

Octocopter is operated with 8 bands remote controller which transfers data with modulation. Each band increases the movement variation of the UAV. In our UAV, 5 bands were used as motor cycle (take-off and landing), right and left motion, forward and back motion, direction motions and flight mode selections. Other 3 bands were utilized for taking photos and other processes.

The brushless motors used in the UAV are efficient and has regular moment/speed relation. They are operational in risky weather and topographic conditions and do not require permanent maintenances. On the other hand, these motors are costly and controlling of them are not easy. In contrast to brush direct current (DC) motors, switching process is realized electronically in brushless DC motors by ESCs. For the motion control of the UAV, micro controllers were utilized. The missions of the micro controllers can be summarized as; getting data from control unit and sensors and real time processing of derived data. For micro controller processes, open source software Arduino was used. Required edits were performed in "C" programming language (Karakış, 2012).

In UAV flight, the balance of the device was provided by a group of sensors. The main missions of these sensors can be summarized as; providing flight stability and correct maneuvers. In our UAV flights, we used gyro, acceleration and pressure sensors and inertial measurement unit (IMU) which is the essential inertial element in airborne and space-borne missions (Watts et al., 2012; Sørensen et al., 2017). To taking aerial photos, an electronic timer was integrated to the UAV. The taking interval was determined as 1

second considering possible facings of the octocopter during the flight. The 1 second interval was preferred regarding the trial flights.

Considering the payload and required flying time, an 11,1 Volt and 8000 mill ampere hours (mAh) de-charge capacity Lithium Polymer battery was preferred to achieve higher energy. By successful integration of all these equipment, the aerial images were achieved with approx. 3 cm ground sampling distance (GSD).

3.2. Image Geometric Correction Methods

For the geometric processing of the aerial stereo-images during photogrammetric processing, 5 ground control points (GCPs) were established and measured on the ground by real time kinematic global navigation satellite systems (RTK GNSS). In the production of 3D model, interior, mutual and absolute orientations were completed. Afterwards, model points were obtained by stereoscopic assessment of the images and contour-lines were generated using the model points.

For determining the temporal change detection in the topography, 10 cm gridded digital terrain models (DTMs) were generated by vector-raster transformation utilizing moving average interpolation method in LISA software considering ground and grade elevations derived before and after the construction. The differential DTM (DiffDTM) was created using DTMs generated by ground and grade elevation data by following equation;

$$DiffDTM = DTM_{grade} - DTM_{ground} \quad (1)$$

4. Results

The generated contour-lines depending upon ground and grade elevations are presented in figure 3 separately. In the figure, approx. 4 m topographic elevation change by excavation is seen. However, the temporal topographic change cannot be detected clearly from contour-lines in most cases because of insufficient contour interval and vector structure. In figure 4, generated raster DTMs before and after excavation are shown with height scales. Raster DTMs present whole area by 10 cm pixels with ±3 cm planimetric and ±5 cm vertical absolute accuracy that's why the correct change of topography can be achieved. The accuracies of the models were estimated by point-based GNSS measurements in the scope of root mean square errors of geolocation differences. Increased number of fringes after excavation is very clear in figure 4b.

Figure 5 shows the DiffDTM of the area with height scale. Considering DiffDTM, a temporal topographic change reaches up to -4.5 m. Using DiffDTM, the achieved areal and volumetric changes are shown in table 2.

Table 2- Areal and volumetric changes in the study area.

Excavation volume (m^3)	5089,9
Filling volume (m^3)	337,8
Excavation area (m^2)	2924,5
Filling area (m^2)	369,2

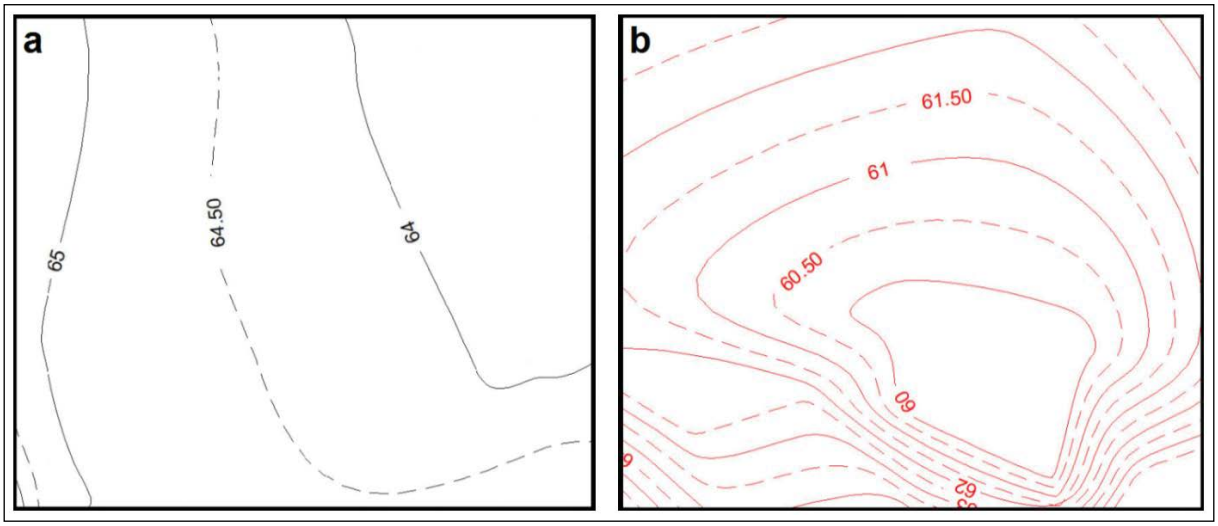

Figure 3- Contour-lines of a) ground and b) grade elevations.

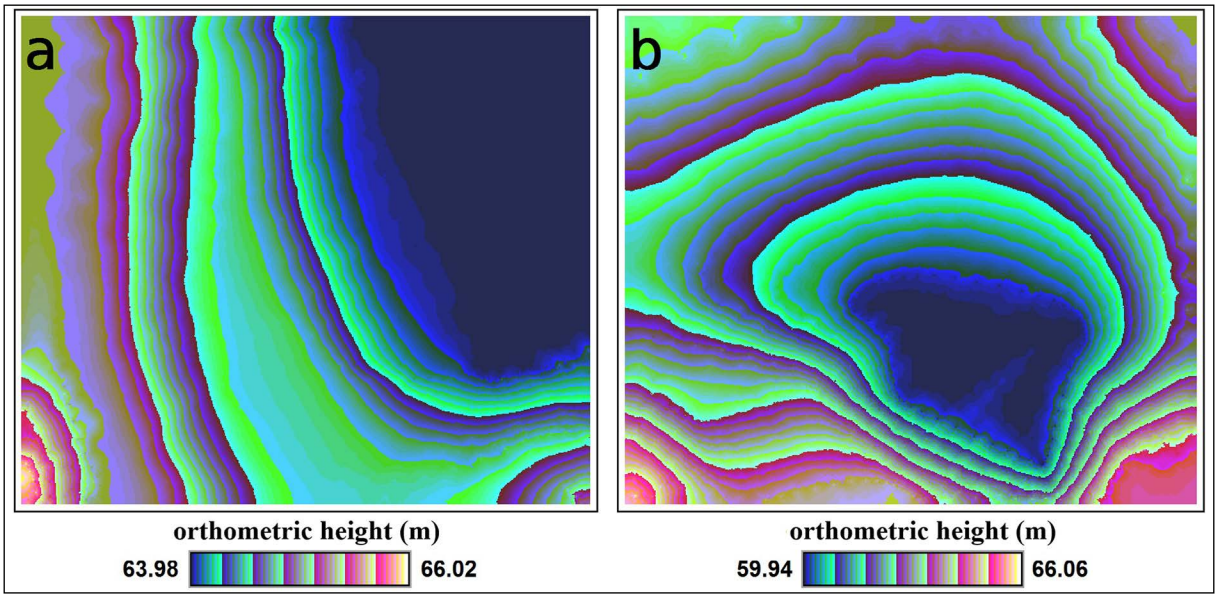

Figure 4- DTMs of (a) ground and (b) grade elevations.

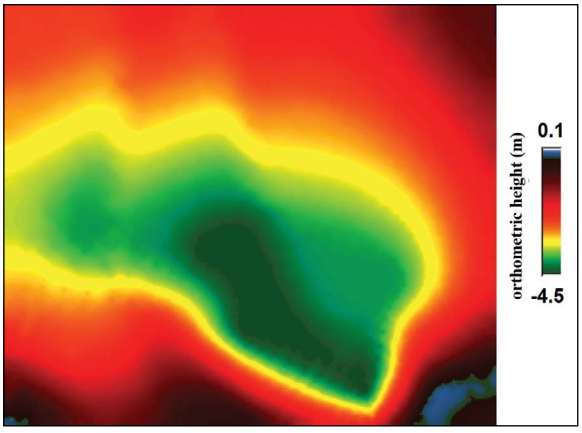

Figure 5- UAV-based DIFFDTM of the construction area.

As can be seen in the results, all of areal and volumetric temporal topographic change information can be easily achieved by a handmade UAV. For visual validation, the grade elevation contour-lines were processed on Google Earth image (Figure 6). By this way, first and last status of the study area can be clearly determined (please compare with figure 1).

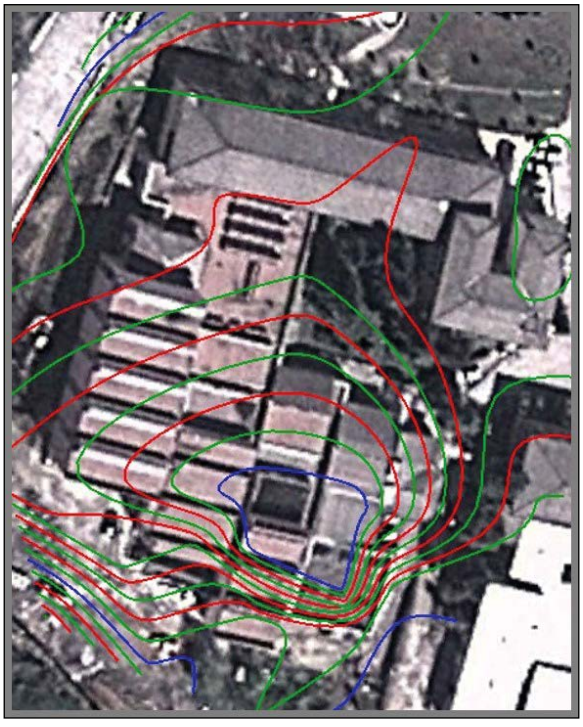

Figure 6- Grade elevation contour-lines on Google Earth.

5. Conclusion

In this research, high potential of unmanned air vehicle technique on areal and volumetric temporal topographic change detection was demonstrated. The application was performed in a construction area in Zonguldak Bulent Ecevit University Main Campus. The study area was monitored by a DSLR camera equipped handmade unmanned air vehicle during the construction activities. The geometries of obtained stereo models was corrected using ground control points which were measured by real time kinematic global navigation satellite systems. The ground and

grade elevation data of the topography were achieved utilizing first and last flight data and digital terrain models were generated separately. By generating the differential digital terrain model, the areal and volumetric topographic changes were clearly calculated. The study demonstrated that unmanned air vehicle technology is very beneficial for precisely calculation of filling and excavation amounts in every demanded period in the construction areas.

References

Ai, M., Hu, Q., Li, J., Wang, M., Yuan, H., Wang, S. 2015. A robust photogrammetric processing method of low-altitude UAV images. Remote Sens 7:2302–2333. doi: 10.3390/rs70302302

Darwin, N., Ahmad, A., Zainon, O. 2014. The potential of unmanned aerial vehicle for large scale mapping of coastal area. IOP Conf Ser Earth Environ Sci 18:. doi: 10.1088/1755-1315/18/1/012031.

Deng, Y., Wilson, J.P., Bauer, B.O. 2007. DEM resolution dependencies of terrain attributes across a landscape. Int J Geogr Inf Sci 21:187–213. doi: 10.1080/13658810600894364.

Höhle, J. 2017. Generating topographic map data from classification results. Remote Sens 9: doi: 10.3390/rs9030224.

Karakış, S. 2012. İnsansız Hava Aracı Yardımıyla Büyük Ölçekli Fotogrametrik Harita Üretim Olanaklarının Araştırılması. Harita Dergisi 147:13–20.

Manfreda, S., McCabe, M.F., Miller, P.E., Lucas, R., Pajuelo Madrigal, V., Mallinis, G., Ben Dor, E., Helman, D., Estes, L., Ciraolo, G., Müllerová, J., Tauro, F., De Lima, M.I., De Lima, J.L.M.P., Maltese, A., Frances, F., Caylor, K., Kohv, M., Perks, M., Ruiz-Pérez, G., Su, Z., Vico, G., Toth, B. 2018*a*. Use of Unmanned Aerial Systems for Environmental Monitoring. Remote Sens 10(4):641. doi: 10.3390/rs10040641.

Manfreda, S., Dvorak, P., Mullerova, J., Herban, S., Vuono, P., Arranz Justel, J.J., Perks, M. 2018*b*. Accuracy Assessment on Unmanned Aerial System Derived Digital Surface Models, Preprints 2018, doi: 10.20944/preprints201809.0579.v1.

Rosnell, T., Honkavaara, E. 2012. Point cloud generation from aerial image data acquired by a quadrocopter type micro unmanned aerial vehicle and a digital still camera. Sensors 12:453–480. doi: 10.3390/s120100453.

Sørensen, L.Y., Jacobsen, L.T., Hansen, J.P. 2017. Low cost and flexible UAV deployment of sensors. Sensors (Switzerland) 17:1–13. doi: 10.3390/s17010154.

Swatantran, A., Tang, H., Barrett, T., DeCola, P., & Dubayah, R. 2016. Rapid, high-resolution forest structure and terrain mapping over large areas using single photon lidar. Sci Rep 6:1–12. doi: 10.1038/srep28277.

Teizer, J., Kim, C., Bosche, F. N., Haas, C. T., Caldas, C. 2005. Real-time 3{D} Modeling for Accelerated and Safer Construction using Emerging Technology. 539–543.

Watts, A.C., Ambrosia, V.G., Hinkley, E.A. 2012. Unmanned aircraft systems in remote sensing and scientific research: Classification and considerations of use. Remote Sens 4:1671–1692. doi: 10.3390/rs4061671.

Bulletin of the Mineral Research and Exploration

http://bulletin.mta.gov.tr

An example study on re-evaluation of historical earthquakes: 1789 Palu (Elazığ) earthquake, Eastern Anatolia, Turkey

Mehmet KÖKÜM[a*] and Fatih ÖZÇELİK[b]

[a]*Fırat University, Faculty of Engineering, Geological Engineering, Elazığ, Turkey*
[b]*Fırat University, Faculty of Humanities and Social Sciences, Department of History, Elazığ, Turkey*

Research Article

Keywords:
East Anatolian Fault, Palu-Elazığ, 1789 Earthquake.

Received Date: 02.01.2019
Accepted Date: 28.05.2019

ABSTRACT

The East Anatolian Fault (EAF) is an active left-lateral strike-slip fault extending between Karlıova (Bingöl) in the northeast and Iskenderun Bay in the southwest. The Palu, which is the subject of the study area, is located on the Palu segment of the EAF. The Palu segment starts from the northeast of Palu, and is approximately 77 km long, and reaches the Lake Hazar after passing the Baltaşı Plain. Maximum shaking intensity in the earthquake listed in historical catalogs is estimated to have been Mercalli Intensity VIII, with conflicting accounts of as few as 8.000-10.000 to as many as 50.000 people killed. An examination of contemporary documents, books and administrative archives in the State Archives Head of Presidency Republic of Turkey for the district reveal that the extent of damage and the number of fatalities in the earthquake have been considerably inflated by these historical catalogs.

1. Introduction

The county of Palu near Elazığ in eastern Turkey is located on the Murat (Eastern Euphrates) River, and history of the Palu date backs to 5000 BC (Figure 1). Palu has been damaged by many major earthquakes in the historical and instrumental period, some of which have required relocation of the city as a consequence of being located on the East Anatolian Fault (EAF) (Şaroğlu et al., 2018) (Figures 1b and 2). Several historical earthquake catalogs record a major earthquake as having occurred between May 28 and June 2 1789 in Palu county (Pınar and Lahn, 1952; Soysal et al., 1981; Ambraseys and Finkel, 1995). Some of these accounts mention that 51.000 people lost their lives citing Abich (1878). Others cite the lower fatality count of 8.000-10.000 mentioned in *Tarih-i Lebibâ* (Emecen, 1982) listed by the contemporary historian Taylesanizâde with damage in Harput, Mazgirt (Tunceli), Çemişgezek (Tunceli), Peri (Tunceli), Palu (Elazığ), Keban Mine (Elazığ).

The purpose of his review is to question the credibility of the apparently inflated number of fatalities recorded for the 1789 earthquake (Ambraseys and Finkel, 1995). Because reported population of Palu is higher than the reasonable values. The population density of Palu region in 1789 was considerably lower than Istanbul in the 10 September 1509 Istanbul earthquake (population ~160.000), when 4.000-5.000 fatalities and 10.000 injured were reported (Ambraseys and Finkel, 1995), or in Erzincan when an earthquake on 23 July 1784 killed 5.000 people as a result of the collapse of 88-90% of its 8.000 dwellings (Soysal et al., 1981; Ambraseys and Finkel, 1995; Vogt, 2001). Palu was not a major city in 1789 and its population is uncertain. Kinneir (1818) cited by Ambraseys

Citation Info: Köküm, M., Özçelik, F. 2020. An example study on re-evaluation of historical earthquakes: 1789 Palu (Elazığ) earthquake, Eastern Anatolia, Turkey. Bulletin of the Mineral Research and Exploration. 161, 157-172. https://doi.org/10.19111/bulletinofmre.603929
* *Corresponding author: Mehmet KÖKÜM, mkokum@firat.edu.tr*

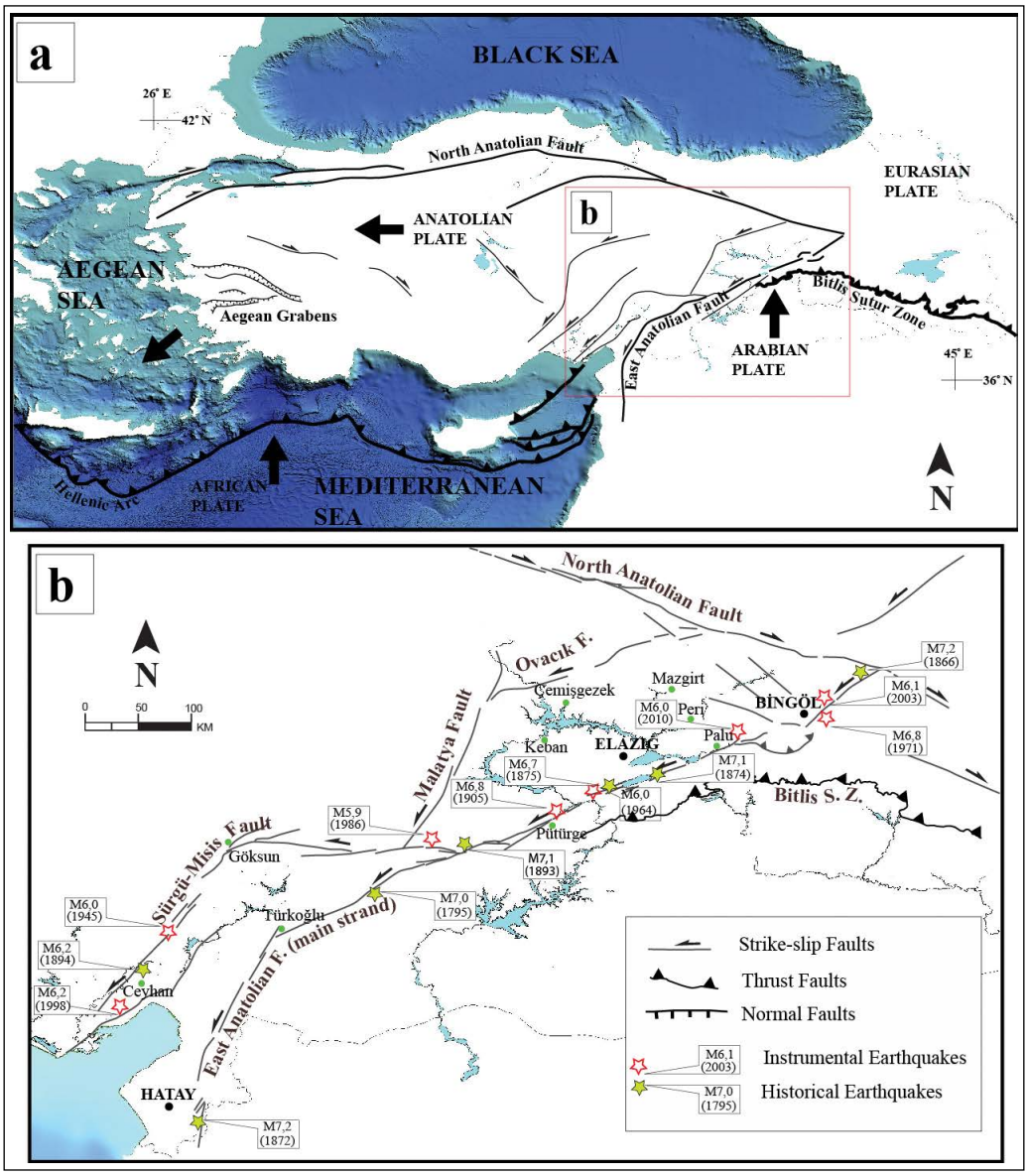

Figure 1- a) Simplified main tectonic features of Turkey and westward motion of Anatolian plate. Faults in Turkey (Emre et al., 2013) and faults located nearby of Turkey (Duman et al., 2016). Big black arrow indicates plate motion with respect to the Eurasian plate (Reilinger et al., 2006), b) Tectonic map of Eastern Anatolia, and historical and instrumental seismicity along the EAF. Historical earthquakes modified from Duman and Emre (2013) (Ambraseys, 1989; Ambraseys and Finkel, 1995; Ambraseys and Jackson, 1998; Tan et al., 2008; Palutoğlu and Şaşmaz, 2017). Instrumental seismicity (http://www.koeri.boun.edu.tr/sismo/zeqdb).

and Finkel, (1995) estimates the population of Palu 11 years after the earthquake (then in the province of present-day Diyarbakır) as approximately 8.000. Palu district was incorporated into Harput province after an administrative change in 1845-1846, and its 1845-1859 population is recorded as 35.436 people (Aksın, 1999). Thus, even 60 years after the earthquake, the population of Palu district is fewer than the number of people claimed to have died in the earthquake.

We summarize the geological and seismological setting of the 1789 earthquake, and provide contemporary information from hitherto unused sources (documents, books and related works) archived in Ankara in the State Archives Head of Presidency Republic of Turkey (henceforth refered to as the Ankara State Archives) and show that the actual deathtoll in the earthquake was much smaller than hitherto reported.

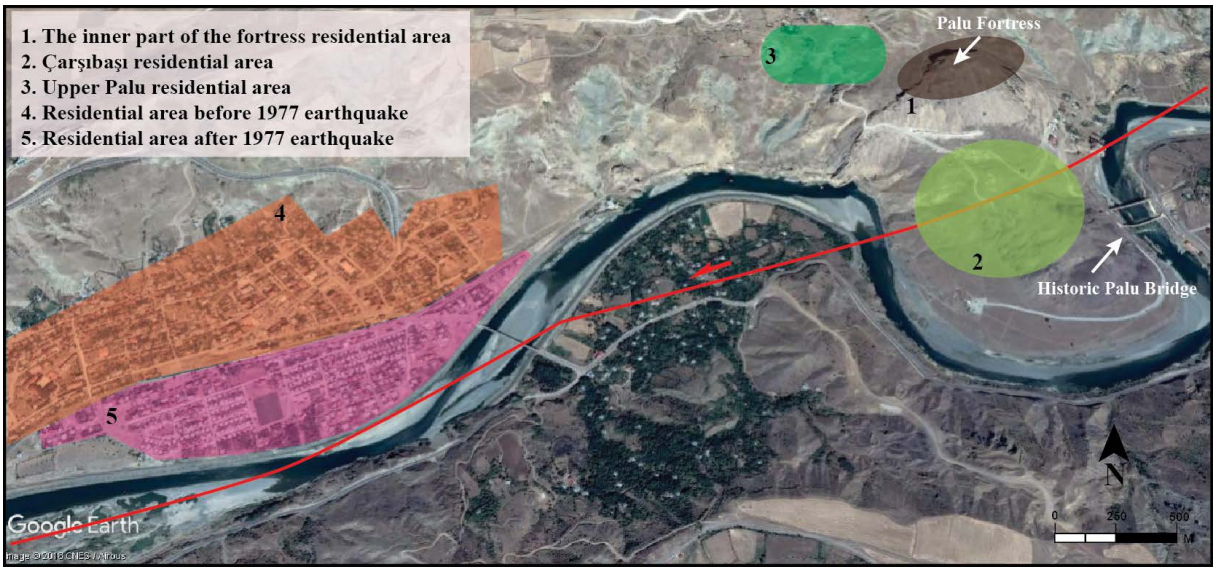

Figure 2- Google Earth image of Palu and changes in its location during history (modified after Şaroğlu vd., 2018). Each color and number represent relocated area.

2. Regional Geology

2.1. Geological Properties of Palu and its Surrounding Area

Various types of rock units ranging from Cretaceous to Holocene are exposed in the study area (Figure 3). The oldest units are the volcanic and granitic rocks of the late Cretaceous Elazığ Magmatites exposed in the northeastern part of the map. The upper Maastrichtian-lower Eocene Hazar Group consists of mainly sandstone-shale and marl intercalations is very common in the southern part of the map. The middle Eocene Maden Complex and middle Eocene-Oligocene Kırkgeçit formation are mostly composed of mudstone banded volcanic rocks, and basal conglomerate and reef limestones, respectively. The geological types of contacts of these two formations are tectonically controlled by East Anatolian Fault (Figure 3 and 4). The Quaternary Palu Formation consists of poorly sorted weakly cemented conglomerates and cross-bedded coarse-grained sandstones. The youngest and most widespread unit in the study area are Holocene alluviums, mostly composed of old river sediments dominated by free gravel and sand lithology. The present-day location of the town of Palu is located close to the river and the EAF and is sited on river alluvium, a seismically more hazardous location compared to its former locations on rock approximately 1 km to the east or to the north (Şaroglu et al., 2018) (Figure 2 and 4).

2.2. Regional Tectonic Meaning of the East Anatolian Fault

Turkey lies between in the zone of convergence between the northward moving Arabian and African plates and the Eurasian plate (Figure 1a). The Anatolian plate moves to west westward with respect to Eurasian plate at approximately 2 cm/yr. The reason of the westward movement of the Anatolian plate is still controversial either the Anatolian plate is being pushed by the Arabian plate in the east, or the pulling of the Anatolian plate along the Hellenic arc in the west (McKenzie, 1972; Dewey and Şengör, 1979; Le Pichon and Angelier, 1979; Barka and Kadinsky-Cade, 1988; Taymaz et al., 1991; Reilinger et al., 1997; McClusky et al., 2000). The North and East Anatolian faults accommodate westward movement of the Anatolian plate with respect to the Eurasian plate (McKenzie, 1972).

The EAF has been studied by many researchers since the early 1960s. Altınlı (1963) mapped the fault between Karlıova and Bingöl on 1/500.000 scale maps prepared by MTA. The EAF was connected with North Anatolian Fault (NAF) in the north and Dead Sea Fault (DSF) in the south by Allen (1969). The Bingöl earthquake on 22 May 1971 attracted international attention to activity on the fault. In the studies after the earthquake accomplished by Seymen and Aydın (1972) and Arpat and Saroğlu (1972; 1975), EAF was mapped for the first time on a regional scale and some

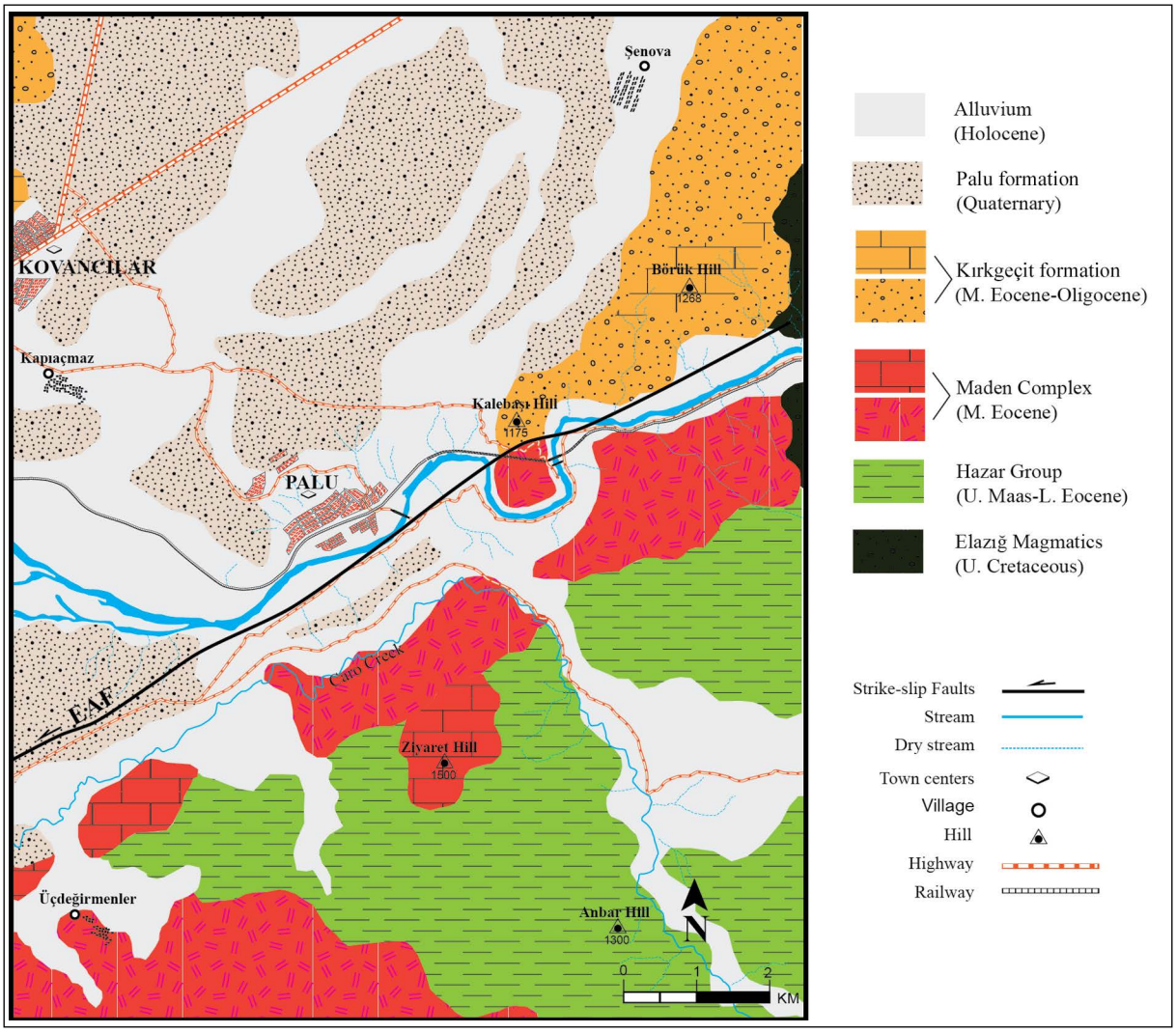

Figure 3- Geological map of Palu (modified from Herece, 2008).

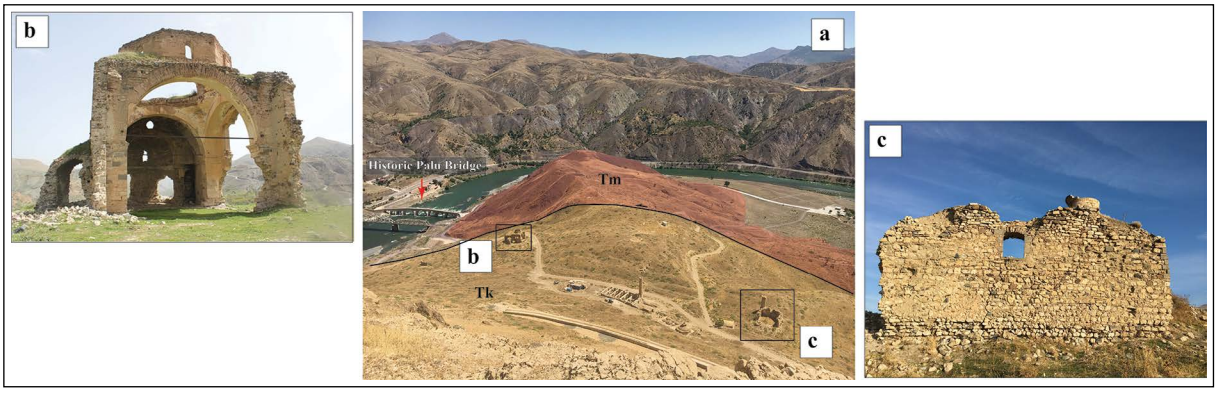

Figure 4- The settlement of historical Palu, where it is called Çarşıbaşı neighbourhood (for location see figure 2), a) the EAF looking south (black straight line) separates the Maden complex from the Kırkgeçit formation. EAF represent by, b) historic Surp Lusaroviç Church in Çarşıbaşı neighborhood and historical structures that survived recent historical earthquakes (looking northwest) and c) Historic Küçük Mosque (looking northwest).

fault-related morphological structures (compression and depression areas) were identified for the first time.

2.3. General Characteristics of the East Anatolian Fault

Several authors have proposed segmentation of the >900-km-long EAF into subsegments based on its geometry and seismic behaviour: five were proposed by Hempton and Dewey (1981) six by Şaroğlu et al., (1992), fourteen by Barka and Kadinsky-Cade (1988) and eleven by Herece (2008). A recent study (Duman and Emre, 2013) divides the EAF into three main sections with several subsegments: the southern (main) branch, the northern strand (Sürgü-Misis fault) and the Karasu trough (Figure 1b). The southern (main) strand includes the Karlıova Triple Junction in the northeast with the North Anatolian Fualt and Varto Fault, and the Amik Triple Junction in the southwest where it joins the Dead Sea Fault and the Cyprus Arc. The southern (main) strand with a length about 580 km includes the Karlıova, Ilıca, Palu, Pütürge, Erkenek, Pazarcık and Amanos segments. The northern strand with length about 350 km includes the Sürgü, Çardak, Savrun, Çokak, Toprakkale, Yumurtalık, Karataş, Yakapınar, and Düziçi-İskenderun segments. The Karasu trough is defined as a releasing bend associated with the linkage of the EAF and Dead Sea Fault, and is subdivided into the Narlı, Yesemek, Reyhanlı and Antakya segments (Figure 1b).

Several researchers working in different parts of the EAF have proposed left-lateral offsets ranging from 9 to 30 km. Arpat and Şaroğlu (1972) defined 22 km offsets on the Maastrichtian mudstone in the Göynük valley, and 27 km offsets along the Palu-Lake Hazar area. İnceöz and İnce (1999) and Aksoy et al. (2007) suggest 9 km offset for the Palu-Lake Hazar region. Çelik (2008) proposed 30 km offset in the middle Eocene Maden Comp. for the same region. Gülen et al. (1987) suggest that the Maraş thrust fault is offset 25 km by the EAF in the south.

In many studies related to the age of the EAF (Herece and Akay, 1992; Şaroğlu et al., 1992; Çetin et al., 2003; Aksoy et al., 2007; Çolak et al., 2012; Köküm and İnceöz, 2018, Köküm, 2019), the initiation of slip on the EAF is believed to be no older than the late Pliocene (~ 3.6 my). The slip rate of the EAF using different methods has variously been reported as 4 to 35 mm/year. Considering the age of the EAF, and lithological and morphological offsets along the fault, the long-term slip rate is calculated as 4-11 mm/year (Arpat and Şaroğlu, 1975; Öncel, 2000; Çetin et al., 2003; Aksoy et al., 2007; Çelik, 2008; Herece, 2008). From moment summations of significant earthquakes between 1955-1990 Taymaz et al. (1991) calculated the slip rate as 25-35 mm/year. Bulut (2017) summing moments of earthquakes with Mw>3 derives a slip rate of 12.4 mm/year in the northeast and 4.3 mm/year in the southwest. The slip rate determined from GPS measurements in the past two decades is calculated as 9-11 mm/yr (Oral et al., 1995; McClusky et al., 2000; Reilinger et al., 2006; Aktuğ et al., 2016). InSAR and GPS data in the past decade between Lake Hazar-Palu on the EAF (~ 100 km) indicate a present day rate of 10 mm/year (Ergintav et al., 2019).

2.4. Seismicity of the East Anatolian Fault

Many destructive earthquakes have occurred on the EAF in historical and instrumental periods (Figure 1b). The only earthquake to have formed a surface rupture on the EAF in the last century is the 22 May 1971 Bingöl (M 6.8) earthquake (Arpat and Şaroğlu, 1972). Other damaging earthquakes occurred on 8 March 2010 Mw=6.1 at Okçular (Elazığ)), 1 May 2003 Mw=6.4 at Bingöl, 27 June 1998 Mw=6.2 at Adana and 5 May 1986 M 6.0 at Malatya.

The historical earthquake catalog summarized most recently by Soysal et al., (1981) includes several severe earthquakes with uncertain magnitude but with estimated maximum Mercalli intensities as follows: 995 Palu-Sivrice (VI), 1114 Ceyhan-Antakya, Maraş (IX), 1268 Kozan-Ceyhan and its region (IX), 1737 Antakya (VII), 1789 Palu-Elazığ (VIII), 1855 Ceyhan-Adana (VI), 1872 Antakya-Samandağ (IX), 1874 Maden-Elazığ, Diyarbakır (VIII), 1875 Karlıova-Bingöl, Palu-Elazığ (VIII), 1889 Palu-Elazığ (VI).

A paleoseismological study at the northeast end of the Lake Hazar-Palu segment reports surface ruptures in earthquakes in 130, 400-450, 1513, 1874 and 1875 Çetin et al. (2003). No surface ruptures were found that could be associated with the historically recorded 995 and 1789 earthquakes.

2.4.1. Geometry and Seismic Activity of Palu Segment

In the study conducted by Duman and Emre (2013), the Palu segment with a length of 77 km is bounded by the Gökdere restraining bend and the Lake Hazar releasing bend (Figure 5). The Palu segment is

divided into three sub-sections (Duman and Emre, 2013). The eastern and central part are separated from each other by a left stepover south of Yamaçova near the epicenter of the 8 March 2010 Mw=6.1 Okçular (Elazığ) earthquake. The Palu segment, which passes east of Palu district, starts south of Yamaçova village in the northeast and continues to Örencik along the 22 km in a narrow zone with approximately N58°E strike. The surface fault is well exposed in the limestones of the Kırkgeçit Formation around Kalebaşı hill (Figure 6). The fault is obscured beneath reservoir of the Keban dam near Örencik, but it can be followed again in the north of the Orta Hill. The N65°E trending southern segment is nearly 30 km between Örencik and Lake Hazar. The southern segment observed in a narrow zone for 15 km between Örencik and Orta Hill, whereas it is divided into several strands with a wide deformation zone from the Kartaldere where it enters Lake Hazar (Figure 5). The length of the fault beneath Lake Hazar is approximately 20 km (Duman and Emre, 2013). There are significant earthquakes on the Palu segment according to historical and recent catalogs.

Çetin et al. (2003) defined the Palu segment with small faults parallel to the main fault in a 54 km long and 5 km wide zone. The Orta Hill Fault with N59°E strike is described as a left-oblique normal fault, and is defined as the main strand of this segment. The surface trace of the Orta Hill Fault is obscured near Örencik, but can be followed on Orta Hill to a trough near Kartaldere with N65-70°E strike. It then divides into two branches: The Havri and Gezin Faults. The northern Havri Fault on which Çetin et al. (2003) infer a 10-11 mm/year slip rate continues into Lake Hazar (Eris et al., 2017). The southern Gezin Fault on which earthquakes occurred in 1874 and 1875 is a normal fault, with a negligible strike-slip component.

The 1874 Maden-Elazığ/Diyarbakır (VIII) earthquake caused a surface rupture of the Palu segment and is one of the most important EAF earthquake sequences for which we have significant information. Ambraseys and Jackson (1998) state that the first earthquake of this sequence occurred on January 14 of 1874, and that the village of Sarıkamış (10 km northeast of Kartaldere village) was totally destroyed, with significant damage to nearby villages. The mines in Maden and the village of Örencik (Gülüşkür) were affected by this earthquake and it was felt in Diyarbakır. An aftershock occurred in Keban on April 29 of 1874, but no damage is reported for this event reported. The mainshock occurred in the morning on 3 May 1874 at 07.00 and lasted about 1 minute. The region north and south of the Lake Hazar was severely shaken. Habusu village was destroyed with damage to all villages in Uluova district. Ambraseys (1989) gave the epicenter of this earthquake as Gezin (Maden)

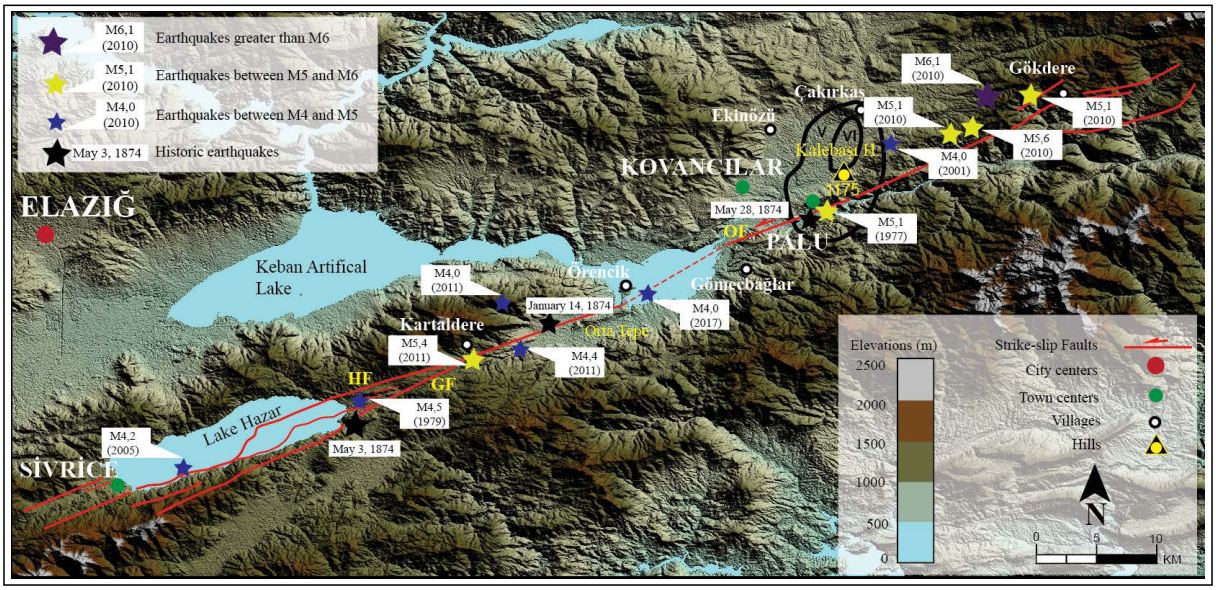

Figure 5- Tectonic map of the area with historical (Ambraseys, 1989; Ambraseys and Jackson, 1998) and instrumental seismicity on the Palu segment of EAF (http://www.koeri.boun.edu.tr/sismo/zeqdb) (modified after Çetin et al., 2003 and Emre et al., 2013). Fault geometry in Lake Hazar from (Eriş et al., 2017). Black closed curves show macrosesimic map based on damage distrubition from 1977 Mw=5.1 Palu earthquake (Şaroğlu et al., 1987).

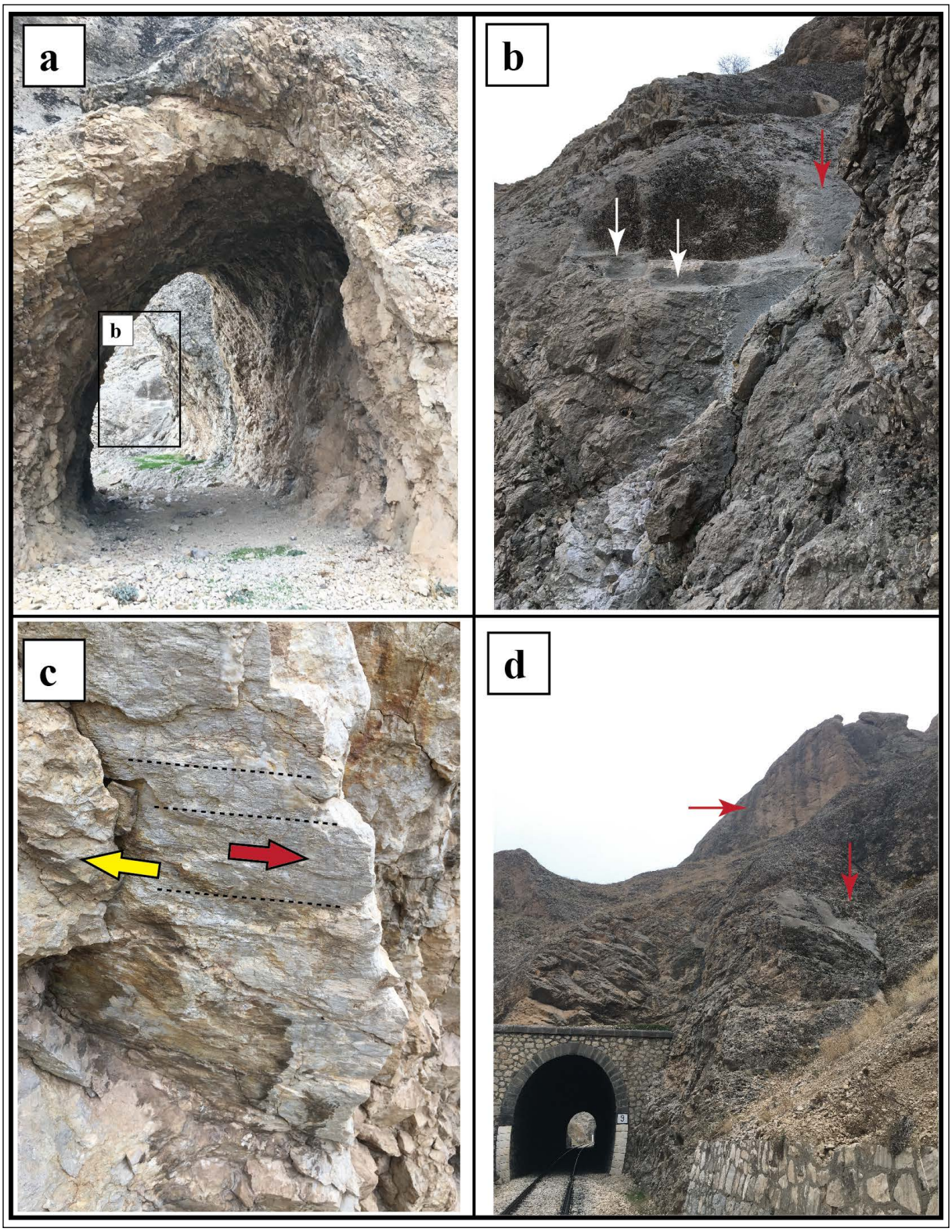

Figure 6- Slickensided fault surface within to limestones in Kırgeçit formation near Kalebaşı hill, a) historical hand excavated tunnel built to descend into the valley of the Murat River to supply water for the castle (looking north), b) stairs were offset by the EAF (looking north), c) faulted limestones near railway (looking northeast), d) fault surfaces near railway (looking northeast).

located in the northeast of the Lake Hazar. Çetin et al. (2003) described the surface rupture of this earthquake in their paleoseismological study on the Palu segment. Herece (2008) notes that a seasonal stream east of Yeşilova village may have been offset 2.6 m in a left-lateral sense in 1874. In the same region, Duman and Emre (2013) document 3.5 m displacement on a seasonal stream on the Orta Hill, with 2.6 m of left-lateral slip on the northeastern end around the Kayalık hill end of the Palu segment.

The Mw=5.1 earthquake of March 26, 1977 occurred on this same segment, causing loss of life and property in and around Palu. Although no significant surface rupture was observed as a result of the 1977 earthquake, small cracks were observed in railway fill material. In addition, the maximum damage in the macro-seismic map ased on spatial damage caused by the earthquake was not parallel to the EAF and occurred almost in the N-S direction (Şaroğlu et al., 1987) (Figure 5). Çetin et al. (2003) calculated a mean recurrence interval of 360 years for surface rupturing earthquakes this segment. Duman and Emre (2013) calculated the recurrence interval on the same segment as 350-400 years.

3. Information about the 1789 Earthquake

The entry on the 1789 earthquake listed by Ambraseys and Finkel (1995) is as follows:

"*The earthquake occurred in the third hour of the night on Hijri 10-19 Ramadan 1203 (29 May-2 June 1789) and destroyed many places in the district of Tunceli. As a result of the earthquake, the villages of Harput, Mazgirt, Çemişgezek, Peri, Palu and Keban Mine were destroyed and ruined. In the earthquake during the tarawih prayer in Great Mosque in Peri all the worshippers died under the ruins. From all these places, 8.000-10.000 people lost their lives in the earthquake (Tarih-i Lebibâ). In a document sent to inform the authorities in İstanbul, 51.000 people died in a tract of land… 21 hours (of march) long and 21 hours (of march) wide (an area of a radius about 75 km) (Abich, 1878). The earthquake interrupted the operation of the mines in Palu and Çarsancak and the need to supply coal was coming up to the region from other places (M. 15 January 1790, DVN. MHM., 190). The earthquake destroyed many Armenian churches, the miners working in the Keban mine applied with a petition to repair their churches which were destroyed in the earthquake in the middle of 1795. In another application dated September 1793, to the kadi and notables of Divriği, says that a petition submitted by the Armenian patriarch and by Armenians living in the village of Nikan, on the river Euphrates in the kaza of Divriği, requested permission to rebuild their churches as they had been before they were ruined in an earthquake (C. DRP., 32–1597). A European traveler passing through the region 11 years later comments that Palu (pop. 8.000) was subjected to 'constant earthquakes', perhaps an indication of continuing aftershocks.*"

The information about the number of fatalities in the two source accounts "Tarih-i Lebibâ and Abich (1878)" are contradictory.

A hitherto unused source of information about the 1789 earthquake reported by Dikran S. Papazyan is "History of Palu's Havav Village" by Housemadyan (2009). Havav village, also known as Ekinözü recently, is located 10 km north of Palu, and in Housemadyan (2009) its history is compiled from Papazyan, traditional information and from an oral history of the village handed down through generations. This narrative is mixed with the legend, in which the oral history of the village, passed from generation to generation and reached the author, is also included. In 1789, Havav (Ekinözü) was the largest Armenian village in the region. The village had two schools, two churches, a monastery and two fountains before 1915. There were 500 houses in the village during the Ottoman period.

The ruler of Havav at the end of the 18th century, Hacı Tıhad exploited the wars and unstable situation of the Ottoman Empire, and was able to build large mansion within the village despite protests from the villager community. Shortly after its completion, a major earthquake occurred and nearly half of the village of Havav, including Hacı Tıhad's mansion, was destroyed. The people of Havav resisted reconstruction of the mansion, and Hacı Tıhad was forced to settle in the village of Gömeçbağlar (Til), four hours from Havav (Housemadyan, 2009 from Papazyan) (Figure 5). In this account the date of the earthquake is not specified exactly, but it is written that it occurred in the late 18th century. During this period, the earthquake likely to affect Havav (Ekinözü) village was the 1789 Palu earthquake. Also, as a result of the earthquake, it is written that almost half of the village and the

mansion in the village were destroyed. The owner of the mansion moves to another village. In other words, as a result of the earthquake, the owner of the mansion did not lose his life. There is no information concerning loss of life in this account.

3.1. Examination of Official Documents of the Earthquake Period

The aim of this study is to determine the effects of the Palu earthquake in that period using documents, books and reports archived in the Precidency State Archives, Ankara and to investigate the accuracy of the information obtained from the historical earthquake catalogs as a source. Archive documents were first examined by us regarding the earthquake. As an archive document, the Sher′iyye Registers are one of the possible sources of data regarding the earthquake. The "Catalogs of the Religous Courts" include reports from Kadis, administrators who are responsible of the judicial, administrative and municipal affairs of the settlements where they are located. The books in which these officials record and official documents are also the Sher′iyye Registers. Because the "Catalogs of the Religous Courts" are contemporary sources of political, social and legal life for the period of the Ottoman Empire 472 years from the mid-15th century to the first quarter of the 20th century, it would be unexpected that the effects of the 1789 Palu earthquake, had it resulted in 51.000 fatalities, would have escaped notice (Soysal et al., 1981; Ambraseys and Finkel, 1995). Considering the conditions of the period, it must have caused a great destruction in and around the earthquake center. For this purpose, Diyarbakır and Keban (Elazığ) Sher′iyye Registers, which are present and compatible with the history and location of the earthquake, were examined.

Since the Palu district in 1789 was administratively linked to the province of Diyarbakır, the first source we investigated were the "Diyarbakır Catalogs of the Religous Courts No. 352 Öz (Öz, 2013). The registry dated "*Hijri 1136-1264 / Gregorian 1724-1848*" embraces the date of the earthquake. It was anticipated that had Diyarbakır been affected by a large earthquake this registry would mention its effects, however, there is no information regarding the reconstruction of the city, the registration of the inheritance of any person who died due to the earthquake, the appointment of successors to replace dead officials, and/or historical restoration of buildings, there are no requests for assistance from the state of any one who suffered losses in the earthquake, and no record of any decision related to this earthquake. Nor is there information about any earthquake-related repairs in Diyarbakır for the first half of the 19th century (Yılmazçelik, 1990).

The Keban province of Elazığ is one of the areas likely to have felt the earthquake, and the Şer′iyye register for "*Hijri 1190-1209, Gregorian 1776-1794*" (Yüksel, 1987) includes information related to mines and their operations, extraction, processing, furnaces, coal transfers and transportation to and from the mines in Keban. This register is devoid of information concerning damage to any mine and mine furnace at the time of the earthquake. Concerned that the "Catalogs of the Religous Courts" might omit mention of earthquake matters we searched elsewhere in the catalogs, and found that a 1782 entry indeed contains a request from a plaintiff desirous of state assistance for the repair of earthquake damage in the preceding year.

It was mentioned above that there are mining areas in the area which is likely to be operational in the 1789 Palu Earthquake. Two different studies on mines in the region are among the sources examined (Tızlak, 1991; Yüksel, 1997). The information common to both works is expressed as follows:

"According to the information given by a western traveler who visited the region at the end of the 19th century, the people believe that the Keban mine started to be operated in 1812. However, according to the information provided by the archival documents, it was found out that the Keban mine started to be operated in about 1708. It is known that the production activity in Keban mine was continuously maintained until 1730. However, due to the damage and loss of life caused by the earthquake in the region at that time, the mine operations were interrupted for a period of 20 years as a result of the destruction of 70 smelter furnaces. In 1751, Spinach Mustafa was sent to Keban mine and as a result of 7 years of repair activities with his great efforts, the mine was put back into operation. Production has continued uninterruptedly since 1758".

In the above summary of Keban mine operations, there is no indication of damage by an earthquake in 1789. Nor did Aksın (1999) who examined the physical, administrative, demographic, social and economic life of Harput using similar archival documents mention evidence for earthquake damage in 1789.

An important source of earthquake information within the Ottoman Empire is the work by Vogt (2001) who compiled eyewitness accounts of earthquakes as related by foreign ecclesiastical sources. According to the author's own words, "foreign ecclesiastics *are not only living in cities but also in remote regions*". For example, the Armenian patriarch relates that the newly appointed Governor with his entourage were shaken by the 23 July 1784 earthquake while they were on way to Erzurum. Despite the presence of a large Armenian population in the area affected by 1789 Palu earthquake Vogt (2001) makes no mention of the 1789 Palu earthquake.

The existence of the 1789 earthquake is indeed mentioned in the Ankara State Archives (M. 15 January 1790). The "Ottoman Empire Council of Ministers resolutions" (Book 190, January 15, 1790, MD 190) contains the following statemet (Figure 7):

"...coal transport was interrupted because Palu and Çarsancak (Peri) were affected by earthquake..."

A short information included in the munitions book numbered 190 expressed that the transportation of oak coal that was provided for the mines was interrupted from the Palu and Çarsancak (Peri) settlements as a result of the earthquake that occurred in 1789. Also in the Cevdet/Darphane classification (C. DRP. 32–1597) the Palu administrator requests a tax amnesty from the central government as a result of damage in the earthquake, the central government responded by reducing the tax instead of eliminating it, and increased the amount of oak fuel that Palu would supply for the

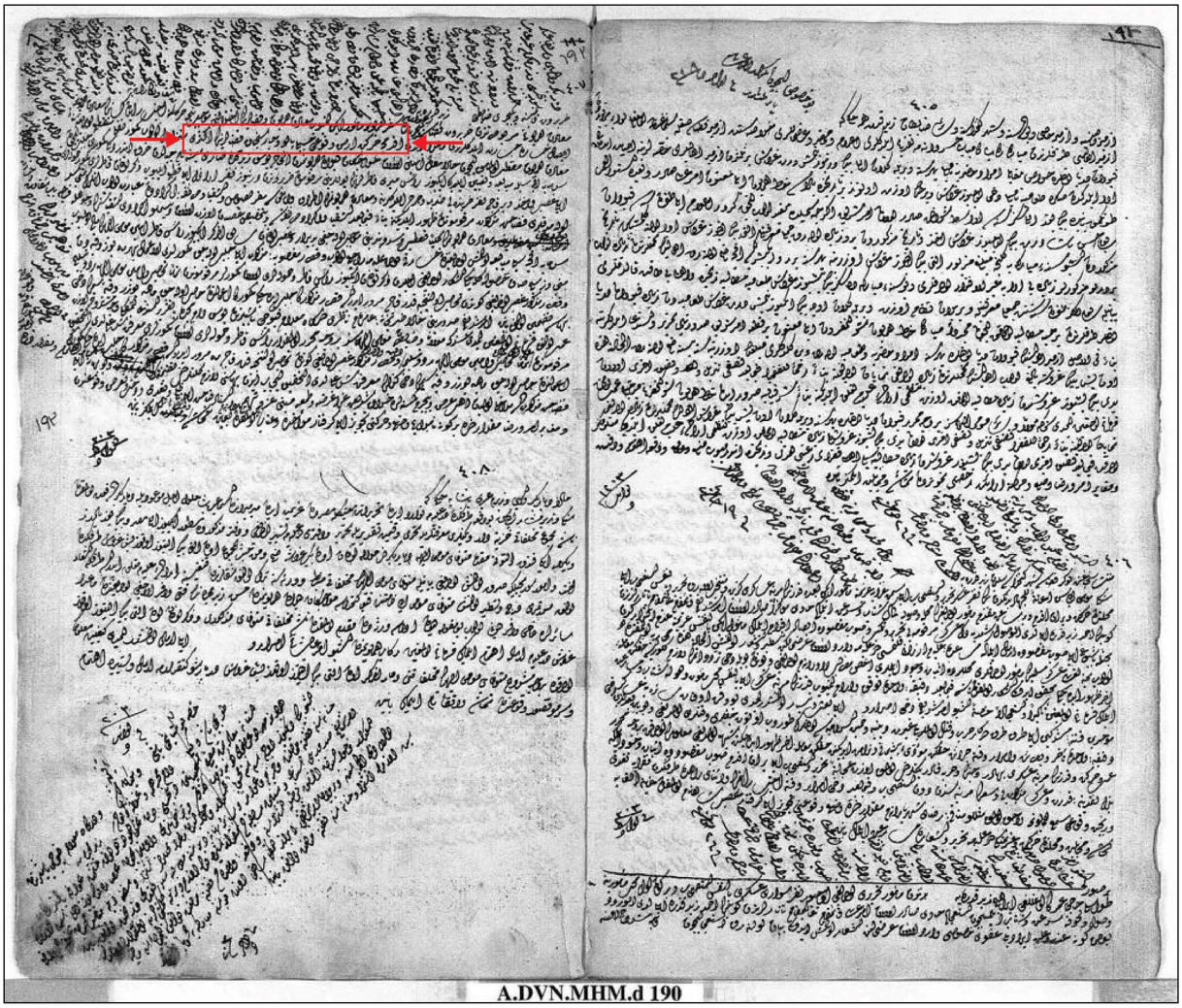

Figure 7- A page from the Ankara State Archives (*Head of Presidency Republic of Turkey M. 15 January 1790*) mentioning the 1789 earthquake. The relevant line is marked in red.

mines. As can be seen from this, there is no doubt that an earthquake occurred in Palu in 1789, but there is no information about the effects of earthquake.

3.2. The Assessment of the Earthquake

3.2.1. The Occurance Date and Center of the Earthquake

The earliest mention of the date of the earthquake is to be found in *Tarih-i Lebibâ* written by Taylesanizâde Master Hafız Abdullah. A major earthquake occured in 1789, on a day between the 10th and 19th days of Ramadan (May 28-June 2, 1789) at three o'clock at night (9 in the evening), and Harput, Mazgirt, Çemişgezek, Palu, Keban and their villages were affected (Emecen, 1982). This work provides a five-day possible window for the earthquake- 28 May and 2 June 1789. In addition, the Ankara State archive (M. 15 January, 1790) states that Palu was the region worst affected by the earthquake.

3.2.2. Magnitude estimates for the 1789 Earthquake

If we assume that 1789 earthquake occurred on the Palu segment of the EAF, and that it ruptured the entire segment we may derive a maximum estimate for the earthquake (Figure 5). The length of the Palu segment is estimated as 54 km (Çetin et al., 2003) or 77 km Duman and Emre (2013). Depending on the length of the active strike-slip fault, the magnitude of the earthquake is expressed by Wells and Coppersmith (1994) with the following formula;

M=a+b*log (SRL)

Mw=5,16+(1,12 x log(L)) (for strike-slip faults)

where Mw is moment magnitude and L is the length of a strike slip fault

Mw=5,16+(1,12 x log(54))

Mw=7,10

Mw=5,16+(1,12 x log(77))

Mw=7,27 is calculated

The magnitude calculation of the 1789 earthquake with the maximum displacement with the assumption that the last earthquake occurred on the Palu segment in 1513 is expressed by Wells and Coppersmith (1994) with the following formula;

M= a+b*log (MD)

Mw=6,81+(0,78 x log(MD))

where MD is the amount of maximum displacement.

1789-1513= 276 year

Using a 10 mm/yr nominal slip rate the time interval yields a potential

276 year*10 mm/year= 2,76 m (MD)

2.76 m slip deficit in 1789 for which slip

scaling relations from Wells and Coppersmith (1994) indicate

Mw=6.81+0.78log(2.76) = 7.15.

The findings of earthquakes forming surface ruptures in 130, 400-450, 1513, 1874 and 1875 were encountered in the Palu segment, while no surface fractures of 995 and 1789 earthquakes in the historical records were found (Çetin et al., 2003). Researchers claimed that these earthquakes may happen on the Karlıova-Bingöl segment, or that traces of earthquakes may have been erased or they do not found these ruptures. Depending on the length of the active strike-slip fault proposed by Wells and Coppersmith (1994), the magnitude of the earthquake to be produced must be Mw = 7.1 and/or 7.2 for the Palu segment.

4. Discussion and Conclusions

Two conflicting deathtolls are recorded for the 1789 earthquake that are unexpectedly high given the probable total population of settlements at the time. The first, for 8.000-10.000 deaths, comes from the contemporary source *Tarih-i Lebibâ,* which was written in Istanbul using unknown primary accounts from the provinces, and the second, for 51.000, is recorded by the German geologist Otto Wilhelm Hermann von Abich (1878) in his travels at least 8 decades after the earthquake. Contemporary administrative documents in the Ankara State Archives and compiled from local traditions by Housemadyan (2009) suggest that both estimates are severely inflated.

These inflated numbers may be compared with the deathtoll in the 10 September 1509 Istanbul earthquake in which the deathtoll was no more than 3% of the population (4.500-5.000 in a population of 160.000) (Ambraseys and Finkel, 1995, or in the 23 July 1784 Erzincan earthquake where 5.000 people lost their lives (Soysal et al., 1981; Ambraseys and Finkel, 1995; Vogt, 2001). Abich (1878) includes questionable information for at least one other

earthquake. He states that 5.000 people fell into fissures caused by the 1582 Bitlis earthquake which is clearly an exaggeration.

Specifically, the following archival records contain no information substantiating severe loss of life or damage in 1789 in Palu, Diyarbakır, Keban-Ergani Mines or Harput: *Diyarbakır Catalogs of the Religous Courts No. 313 and 352, Catalogs of the Religous Courts dated 1776-1794, Diyarbakır in the First Half of the 19th Century (1790-1840), Mining in the Harput, Keban-Ergani Region in the 19th Century, Keban-Ergani Mines in the Ottoman Period the Mining Operating Book of 1776–1794, Seismicity Throughout History in the Ottoman Lands-Examples from Western Sources and Expressions of Witnesses.*

The Ankara archive (*M. 15 January 1790, Registers of Important Affairs (M. 15 January 1790, DVN. MHM., 190) and the Cevdet Darphanesi (C. DRP., 32–1597*) includes mention of disruption of transport to local mines after the earthquake, adjustments to tax revinues, and severe damage in Palu, but provides no quantitative details concerning loss of life and damage to buildings. That damage was not excessive can be deduced from the absence of a request for reconstruction assistance to the central administration by the Çarsancak (Peri) administrator.

Ambraseys and Finkel (1995) equate Armenian labor being diverted in 1793 and 1795 from the Keban mine to repair destroyed churches, with damage in the 1789 earthquake. We counter that it is possible that earthquake damage may have been invoked as an arbitrary reason for church reconstruction. The reason for a 4-5 year delay between damage and repair remains unexplained.

Using scaling relations (Wells and Coppersmith, 1994) we calculate the maximum probable magnitude of an earthquake on the Palu segment as $7.1<Mw<7.2$. However, the absence of a 1789 surface ruture north of Lake Hazar (Çetin et al., 2003) remains problematic. Our investigations indicate that the locus of the 1789 earthquake was near Palu and therefore did not occur on the Karlıova-Bingöl segment as suggested by these authors. This result suggests that 1789 earthquake may have not created a surface rupture suggesting its magnitude may have been M 6.5 close to Palu.

Damaging earthquakes are common in the region of the Palu settlement as testified by its destruction and relocation several times in past millennia (Şaroğlu et al., 2018) (Figures 1b and 2). In recent moderate earthquakes (1977 Mw= 5.1 Palu and 2010 Mw=6.1 Okçular) loss of life and property was significant, and as a result of its current location and geological setting (Sunkar, 2011). Considering the factors, damages caused by earthquakes in the historical period cannot be measured with the magnitude of the earthquakes.

In conclusion, extant archival documents indicate that previous fatality estimates for the 1789 Palu earthquake have been grossly inflated. Our study shows much hitherto unused information is available in Ottoman archives and that these data have an important role in correcting our knowledge of historical earthquakes in Turkey.

References

Abich, H. 1878. Geologische Forschungen in den kaukasischen Landern. 3. cilt. Viyana.

Aksın, A. 1999. 19. Yüzyılda Harput, Elazığ, Ceren, 1999, 314, ISBN: 975-94229-0-5, 168.

Aksoy, E., İnceöz, M., Koçyiğit, A. 2007. Lake Hazar Basin: A Negative Flower Structure on the East Anatolian Fault System (EAFS), SE Turkey. Turkish Journal of Earth Sciences 17, 319-338.

Aktuğ, B., Özener, H., Doğru, A., Sabuncu, A., Turgut, B., Halıcıoğlu, Yılmaz, O., Havazli, E. 2016. Slip rates and seismic potential on the East Anatolian Fault System using an improved GPS velocity field. Journal of Geodynamics 94-95, 1-12.

Allen,C.R. 1969. Active Faulting in Northern Turkey. Contribution No:1577, Division of Geological Sciences, California. Institute. Technology, 32.

Altınlı, İ.E. 1963. Explanatory text of the Geological Map of Turkey of 1:500 000 scale; Erzurum sheet. Publ. Bulletin of Mineral Research and Exploration Inst., Ankara.

Ambraseys, N. N. 1989. Temporary seismic quiescence: SE Turkey. Geophysical Journal 96, 311–331.

Ambraseys, N. N., Finkel, C. 1995. The Seismicity of Turkey earthquake of 19 December 1977 and the seismicity of the Adjacent Areas 1500–1800. Eren Yayıncılık ve Kitapcılık, İstanbul. 240.

Ambraseys, N. N., Jackson, J. A. 1998. Faulting associated with historical and recent earthquakes in the Eastern Mediterranean region. Geophysical Journal International 133, 390–406.

Arpat, E., Şaroğlu, F. 1972. The East Anatolian Fault System; Thoughts on its Development. Bulletin of Mineral Research and Exploration 78, 33-39.

Arpat, E., Şaroğlu, F. 1975. Türkiye'deki bazı önemli genç tektonik olaylar, Türkiye Jeoloji Kurumu Bülteni 18, 1, 91-101.

Barka, A.A., Kadinsky-Cade K. 1988. Strike-slip fault geometry in Turkey and influence on earthquake activity. Tectonics 7, 3, 663-684.

Bulut, F. 2017. Doğu Anadolu Fayı boyunca Sismik ve A-sismik Tektonik Hareketler: Hazar Gölü Doğu'sunda Sismik Boşluk mu yoksa Krip mi? Afyon Kocatepe Üniversitesi, Fen ve Müh. Bil. Der. (FEMÜBİD) 015803, 257-263. DOI: 10.5578/fmbd.53986.

Çelik, H. 2008. Doğu Anadolu Fay Sistemi'nde Sivrice Fay Zonu'nun Palu-Hazar Gölü (Elazığ) arasındaki bölümünde atımla ilgili yeni arazi bulgusu. Fırat Üniv. Fen ve Müh. Bil. Dergisi 20 (2), 305-314.

Çetin, H., Güneyli, H., Mayer, L. 2003. Paleosismology of the Palu-Lake Hazar Segment of the East Anatolian Fault Zone, Turkey. Tectonophysics 374, 163–197.

Çolak, S., Aksoy, E., Koçyiğit, A., İnceöz, M. 2012. The Palu-Uluova Strike-Slip Basin in the East Anatolian Fault System, Turkey: Its Transition from the Palaeotectonic to Neotectonic Stage. Turkish Journal of Earth Sciences 21,1–24.

Dewey, J.F., Şengör, A.M.C. 1979. Aegean and surrounding regions: complex multiplate and continuum tectonics in a convergent zone. Geological Society of America Bulletin 90, 84–92.

Duman, T.Y., Emre, Ö. 2013. The East Anatolian Fault: geometry, segmentation and jog characteristics. Geological Society London, Special Publications, 372.

Duman, T.Y., Çan, T., Emre, Ö., Kadirioğlu, F.T., Baştürk, N.B., Kılıç, T., Arslan, S., Özalp, S., Kartal, R.F., Kalafat, D., Karakaya, F., Azak, T.E., Özel, N.M., Ergintav, S., Akkar, S., Altınok, Y., Tekin, S., Cingöz, A., Kurt, A.İ. 2016. Seismotectonics database of Turkey. Bulletin of Eartquake Engineering, DOI 10.1007/s10518-016-9965-9

Emecen, E. F., 1982. Tarih-i Lebiba' ya Dair. Turkish Journal of History 0 (33), 237.

Emre, Ö., Duman, T.Y., Özalp, S., Elmacı, H., Olgun, Ş., Şaroğlu, F. 2013. Açıklamalı Türkiye Diri Fay Haritası Ölçek: 1/1.250.000. Maden Tetkik ve Arama Genel Müdürlüğü Özel Yayın serisi-30, Ankara.

Ergintav, S., Çetin, S., Şentürk, S., Özdemir, A., Doğan, A., Çakır, Z., Karabulut, H., Şaroğlu, F. 2019. Doğu Anadolu Fayı, Hazar-Palu Segmenti Üzerinde Gerçekleşen Krip Davranışının Sorgulanması. Uluslararası Katılımlı 72. Türkiye Jeoloji Kurultayı 28 Ocak–01 Şubat 2019, Ankara, Türkiye, s. 33-34.

Eris, K.K., Akçer, S., Çağatay, M.N., Ülgen, U.B., Ön, Z.B., Gürocak, Z., Arslan, T.N., Akkoca, D.B., Damcı, E., İnceöz, M., Okan, Ö.Ö. 2017. Late Pleistocene to Holocene paleoenvironmental evolution of Lake Hazar, Eastern Anatolia,Turkey. Quaternary International 486, 4-16. https://doi.org/10.1016/j.quaint.2017.09.027

Gülen, L., Barka, A., Toksöz, M.N. 1987. Kıtaların çarpısması ile ilgili komplex deformasyon: Maras üçlü eklemi ve çevre yapıları. Hacettepe Üniversitesi Yerbilimleri Bülteni 14, 319-336.

Hempton, M.R., Dewey, J.F. 1981. Structure and tectonics of the Lake Hazar pull-apart basin, SE Turkey. Transactions, American Geophysical Union EOS, 62, 1033.

Herece, E., Akay, E. 1992. Karlıova-Çelikhan arasında Doğu Anadolu fayı. Türkiye 9. Petrol Kongresi Bildiriler, 361-372, Ankara.

Herece, E. 2008. Doğu Anadolu Fayı (DAF) Atlası. Maden Tetkik ve Arama Genel Müdürlüğü Özel Yayın serisi, Ankara, 13, 359.

Housemadyan, 2009. Palu-Yerel Tarih. 1 Ocak 2019 tarihinde,

https://www.houshamadyan.org/tur/haritalar/diyarbakir-vilayeti/palu/yerlesim-birimi/yerel-tarih.html adresinde erişildi.

http://www.koeri.boun.edu.tr/sismo/zeqdb (2018, 30 Kasım)

İnceöz, M., İnce, S. C. 1999. Doğu Anadolu Fay Zonu'nun (DAF) Palu çevresinde yapısal ve Morfotektonik özellikleri. Aktif Tektonik Araştırma Grubu İkinci Toplantısı (ATAG-2) Ekim, 1999, İstanbul Teknik Üniversitesi, İstanbul. Bildiriler 98–110.

Köküm, M. 2019. Landsat TM Görüntüleri Üzerinden Doğu Anadolu Fay Sistemi'nin Palu (Elazığ)-Pütürge (Malatya) Arasındaki Bölümünün Çizgisellik Analizi. Gümüşhane Üniversitesi Fen Bilimleri Enstitüsü Dergisi (GÜFBED/GUSTIJ) (2019) 9 (1): 119-127. DOI: 10.17714/gumusfenbil.419865.

Köküm, M., İnceöz, M. 2018. Structural analysis of the northern part of the East Anatolian Fault System. Journal of Structural Geology 114, 55-63. https://doi.org/10.1016/j.jsg.2018.06.016.

Le Pichon, X., Angelier, J. 1979. The Hellenic arc and trench system: a key to the neotectonic evolution of the eastern Mediterranean area. Tectonophysics 60, 1–42.

McClusky, S., Balassanian, S., Barka, A., Demir, C., Ergintav, S., Georgiev, I., Gürkan, O., Hamburger, M., Hurst, K., Kahle, H., Kastens, K., Kekelidze, G., King, R., Kotzev, V., Lenk, O., Mahmoud, S., Mishin, A., Nadriya, M., Ouzounins, A., Paradissis, D., Peter,Y., Prilepin, M., Reilinger, R., Sanli, I, Seeger, H., Tealeb, A., Toksöz, M.N., Veis, G. 2000. Global Positioning System constraints on plate kinematics and dynamics in the eastern Mediterranean and Caucasus. J. Geophy. Res. 105, 5695-5720.

McKenzie, D.P. 1972. Active tectonics of the Mediterranean region. Geophysical Journal of the Royal Astronomical Society 30, 109–185.

Oral, M.B., Reilinger, R.E., Toksöz, M.N., King, R.W., Barka, A., Kınık, İ., Lenk O. 1995. Global Positioning System Offers Evidence of Plate Motions in Eastern Mediterranean. EOS Transac. 76 (9).

Öncel, A.O. 2000. Fraktal Analiz İle Türkiye'deki Doğrultu Atımlı Fayların Yapısal Ve Sismolojik özelliklerinin Belirlenmesi. Deprem Araştırma Bülteni 84, 5–109.

Öz, D. 2013. 352 Nolu Diyarbakır Şer'iye Sicilinin Transkripsiyon ve Değerlendirilmesi (H. 1136-1264/M. 1724-1848). Dicle Üniversitesi Sosyal Bilimler Ens. Yüksek Lisans Tezi, Diyarbakır (unpublished).

Palutoğlu, M., Şaşmaz, A. 2017. 29 November 1795 Kahramanmaraş Earthquake, Southern Turkey. Bulletin of the Mineral Research and Exploration (155):10-10. DOI: 10.19111/bulletinofmre.314211

Pınar, N., Lahn, E. 1952. Türkiye Depremleri İzahlı Kataloğu. Bayındırlık Bakanlığı Yapı ve İmar İşleri Reisliği Yayınlarından 6, 36, 1952.

Reilinger, R.E., McClusky, S.C., Oral, M.B., King, R.W., Toksoz, M.N. 1997. Global Positioning System measurements of present-day crustal movements in the Arabia–Africa–Eurasia plate collision zone. Journal of Geophysical Research 102, 9983–9999.

Reilinger, R., McClusky, S., Vernant, P., Lawrence, S., Ergintav, S., Çakmak, R., Özener, H., Kadirov, F., Guliev, I., Stepanyan, R., Nadariya, M., Hahubia, G., Mahmoud, S., Sakr, K., ArRajehi, A., Paradissis, D., Al-Aydrus, A., Prilepin, M., Guseva, T., Evren, E., Dmitrotsa, A., Filikov, S.V., Gomez, F., Al-Ghazzi, R., Karam, G. 2006. GPS constraints on continental deformation in the Africa-Arabia-Eurasia continental collision zone and implications for the dynamics of plate interactions. J. Geophys. Res. 111, B05411.

Seymen , İ., Aydın, A. 1972. The Bingöl Earthqyake Fault and its Relation to the North Anatolian Fault Zone. Bulletin of the Mineral Research and Exploration 79, 1-8.

Soysal H, Sipahioğlu S, Kolçak D, Altinok Y. 1981. A catalogue of earthquakes for Turkey and surrounding area (BC 2100-AD 1900). Final report, Project number Tbag 341, The Scientific and Technical Research Council of Turkey (TUBİTAK), Ankara.

Sunkar, M. 2011. 8 Mart 2010 Kovancılar-Okçular (Elazığ) Depremi; Yapı Malzemesi ve Yapı Tarzının Can ve Mal Kayıpları Üzerindeki Etkisi. Türk Coğrafya Dergisi 56, 23-37.

Şaroğlu, F., Emre, Ö., Boray, A. 1987. Türkiye'nin Diri Fayları ve Depremsellikleri Maden Tetkik ve Arama Genel Müdürlüğü Rapor no: 8174, Ankara (unpublished).

Şaroğlu, F., Emre, O., Kuşçu, I. 1992. The East Anatolian Fault Zone of Turkey. Annalae Tectonicae 6, 99–125.

Şaroğlu, F., Ardahanlıoğlu, A., Demirci, E. 2018. Yer Değiştir(mey)en Kent: PALU/ELAZIĞ. Mavi Gezegen Popüler Yerbilim Dergisi 25, 18-34.

Tan, O., Tapırdamaz, M. C., Yörük, A. 2008. The earthquake catalogues for Turkey. Turkish Journal of Earth Sciences 17, 405–418.

Taymaz, T., Eyidoğan, H., Jackson, J. 1991. Source parameters of large earthquakes in the east Anatolian fault zone (Turkey). Geophysical Journal International 106, 537–550.

T.C. Cumhurbaşkanlığı Devlet Arşivleri Başkanlığı (M. 15 Ocak 1790) DVN. MHM. d.190.

T.C. Cumhurbaşkanlığı Devlet Arşivleri Başkanlığı Cevdet Darphanesi (C. DRP) 32–1597 (H. 28 Rebiülahir 1204).

Tızlak, F. 1991. Keban-Ergani Yöresinde Madencilik (1780-1850). Fırat Üniversitesi Sosyal bilimler Enstitüsü Doktora Tezi, Elazığ (unpublished).

Vogt, J. 2001. Osmanlı Topraklarında Tarih Boyunca Depremsellik: Batılı Kaynaklardan ve Tanıkların İfadelerinden Örnekler, Osmanlı İmparatorluğu'nda Doğal Afetler. Ed. Elizabeth Zachariadou, Çev. Gül Çağalı Güven–Saadet Öztürk, Tarih Vakfı Yurt Yayınları, İstanbul, 13-58.

Wells, D.L., Coppersmith, K.J. 1994. New Emprical Relationships among Magnitude, Rupture Length, Rupture width, Rupture Area and Surface Displacement. Bulletin of Seismological Society of America 84, 4, 974-1002.

Yıldız, A. 1994. 135/313 No' lu Şer'iyye Siciline Göre (1135/1722-1213/1798) Yıllarında Amid (Diyarbakır) Sancağında Sosyal ve Ekonomik Durum, Uludağ Üniversitesi Sosyal Bilimler Enstitüsü Yüksek Lisans Tezi, Bursa (unpublished).

Yılmazçelik, İ. 1990. 19. Yüzyılın ilk Yarısında Diyarbakır (1790-1840). TTK Yayınları, Ankara.

Yüksel, H. 1987. Hicri 1190 (M.1776) – Hicri 1209 (M. 1794) Tarihli Keban Şer'iyye Sicilinin Transkripsiyon ve Değerlendirilmesi. Ankara Üniversitesi Sosyal Bilimler Enstitüsü, Yüksek Lisans Tezi, Ankara.

Yüksel, H. 1997. Osmanlı Döneminde Keban–Ergani Madenleri–1776–1794 Tarihli Maden Emini Defteri. Dilek Matbaası, Sivas.

Bulletin of the Mineral Research and Exploration

http://bulletin.mta.gov.tr

Early Miocene seed like plant remain fossils and facies associations from the Nallıhan district (NW Turkey)

Muhittin GÖRMÜŞ[a,b*], Yusuf Kağan KADIOĞLU [a,b], Baki Erdoğan VAROL[a] Muhammed Sami US[a,c]

[a]*Ankara University, Department of Geological Engineering, Ankara, Turkey*
[b]*Ankara University, YEBİM, Ankara, Turkey*
[c] *Munzur University, Department of Geological Engineering, Tunceli, Turkey*

Research Article

Keywords:
Nallıhan, NW Turkey, Miocene, plant remain fossils, EPMA.

ABSTRACT

Seed like fossils recognized by their distinctive orbicular in shape are seen in the early Miocene of the Nallıhan area (NW Türkiye). We examined more than one hundred specimens and facies associations for interpreting of fossil morphology and its paleoenvironment. The fossils as dark crystallized dots on the bedding surface of clayey limestones are characterized by a thick edged lenticular shape with a smooth one side and concave another side with circular nucleus. Their internal structures have circular a few whorlings, too often radial calcitic lamellae on the upper side and a few circular coiling at the bottom side. SEM, EPMA and RAMAN data of soft nucleus, hard part, filling materials and surrounding sediments support its plant origin. The Paleogene aged Kızılbayır formation and early Miocene aged Karadoruk and Akpınar formations include the following facieses: non-channelized red sandstone and mudstone (F1), channelized "confined" reddish-beige pebbly sandstone and conglomerate (F2), medium to coarse siliciclastics (F3), mudstones interbedded with sandstones (F4), thin bedded clayey limestone bearing plant fossils (F5) medium to thick bedded limestone (F6) and rhythmic siliciclastics - clayey limestone including coal occurrences (F7). Abundant plant fossils indicate a planted shallow lake margin with low topography during the early Miocene.

Received Date: 13.09.2018
Accepted Date: 10.06.2019

1. Introduction

The Beypazarı-Ayaş Miocene Basin is a well-known terrestrial area extending from the west of Ayaş to the east of Nallıhan (W, NW Ankara) (Figure 1). Due to the significance of Miocene sediments from the mentioned basin to palaeontologists, stratigraphers, sedimantologists and field geologists, the majority of previous literature has been associated with the sediments stratigraphy, sedimantology and coal occurrences (Siyako, 1983; Inci et al., 1988; Helvacı and Bozkurt, 1994; Yağmurlu and Helvacı, 1994; Yağmurlu et al., 1988, 1990; Karadenizli, 1995). However, plant remains fossil occurrences and their origin within the Miocene lacustrinal sediments have not been fully understood and no studies have been carried out to investigate the Miocene aged seed like fossil records. The first record of the Miocene plant remain fossils in Turkey is assumed to be a significant discovery for the Miocene palaeogeography and sedimantological approaches. The problems are what they are, where they were deposited, and what the facies associations are? The aims of the study are to present the first seed like plant remain fossil records from the Miocene sediments of the north- western Turkey, to define their morphological features based

Citation Info: Görmüş, M., Kadıoğlu, Y. K., Varol, B. E., Us, M. S. 2020. Early Miocene seed like plant remain fossils and facies associations from the Nallıhan district (NW Turkey). Bulletin of the Mineral Research and Exploration. 161, 173-192. https://doi.org/10.19111/bulletinofmre.609697

* *Corresponding author: Muhittin GÖRMÜŞ, mgormus@ankara.edu.tr*

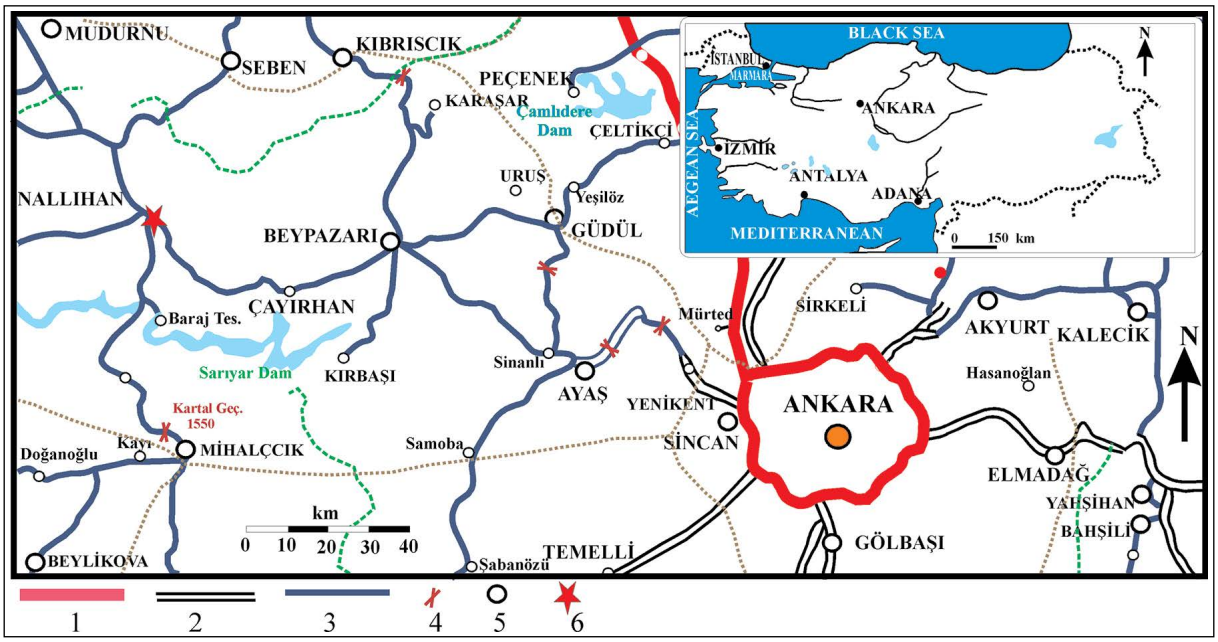

Figure 1- Location map of the study area. 1) highway, 2) divided road, 3) road, 4) mountain pass, 5) settlement, 6) study area.

on field and laboratory observations with thin sections, SEM, EPMA and RAMAN data and to discuss their palaeoenvironmental and facies associations.

2. Geological Setting

At the both sides (east and west) of the Beypazarı-Ayaş Miocene Basin, the Palaeozoic metamorphics are seen at the basement. The lithostratigraphy of the investigation area from basement to top include the following geological units: The Palaeogene aged Kızılbayır formation comprising of red terrestrial siliciclastics; early Miocene aged Karadoruk formation, limestones, clayey limestones in lithologies; siliciclastics of the Akpınar formation, Acısu formation including dirty white coloured clayey limestones and tuffits; Plio-Quaternary clastics and alluvium (Figures 2-3). The names of the formations are based on Siyako (1983).

The Miocene sediments including various mainly lacustrinal lithologies overlie unconformably the Mesozoic carbonates and Palaeogene red clastics in the studied area (Figures 2, 3). Although many studies deal with the Miocene basin (Siyako, 1983; İnci et al., 1988; Helvacı and Bozkurt, 1994; Yağmurlu and Helvacı, 1994; Yağmurlu et al., 1988, 1990; Karadenizli, 1995), geological units (Stchepinsky, 1941 *a, b*; Tekin, 1977; Altınlı, 1978; Kalafatcıoğlu and Uysallı, 1964; Saner, 1980; Önal et al., 1988) and palaeontological, sedimantological data (Kazancı, 1979, 1980; Tunç, 1980; 1984; Varol, 1980; Varol and Kazancı, 1980; 1981; Alkaya, 1987, 1989 *a, b*), seed fossils from the Miocene sediments have not been mentioned. Figure 4 shows selected field views of the studied Kızılbayır, Karadoruk and Akpınar formations and their lithologies.

In the area, a few small anticline and syncline axis, one to a few kilometres in length extends from west to east. They are more or less parallel to the North Anatolian Fault known as a strike-slip fault in the Bolu-Gerede area, the Sekli overthrust and Davutoğlan Fault that is near to the study area (Kalafatcıoğlu and Uysallı, 1964; Saner, 1980; Önal et al., 1988; Siyako, 1983). Neotectonic compressional tectonism in north-south direction affected the all Palaeogene to Miocene sediments.

3. Methodology

The plant remain fossils come from the clayey limestones of the Karadoruk formation outcropping around Sarıkafa and Çoban Hill, 15 km east of the Nallıhan (NW Ankara) (Figures 2-3). Red to yellowish coarse to medium sized clastics of the Kızılbayır formation (Siyako, 1983) are at the base of anticline exposing at the northern part of the studied area. The

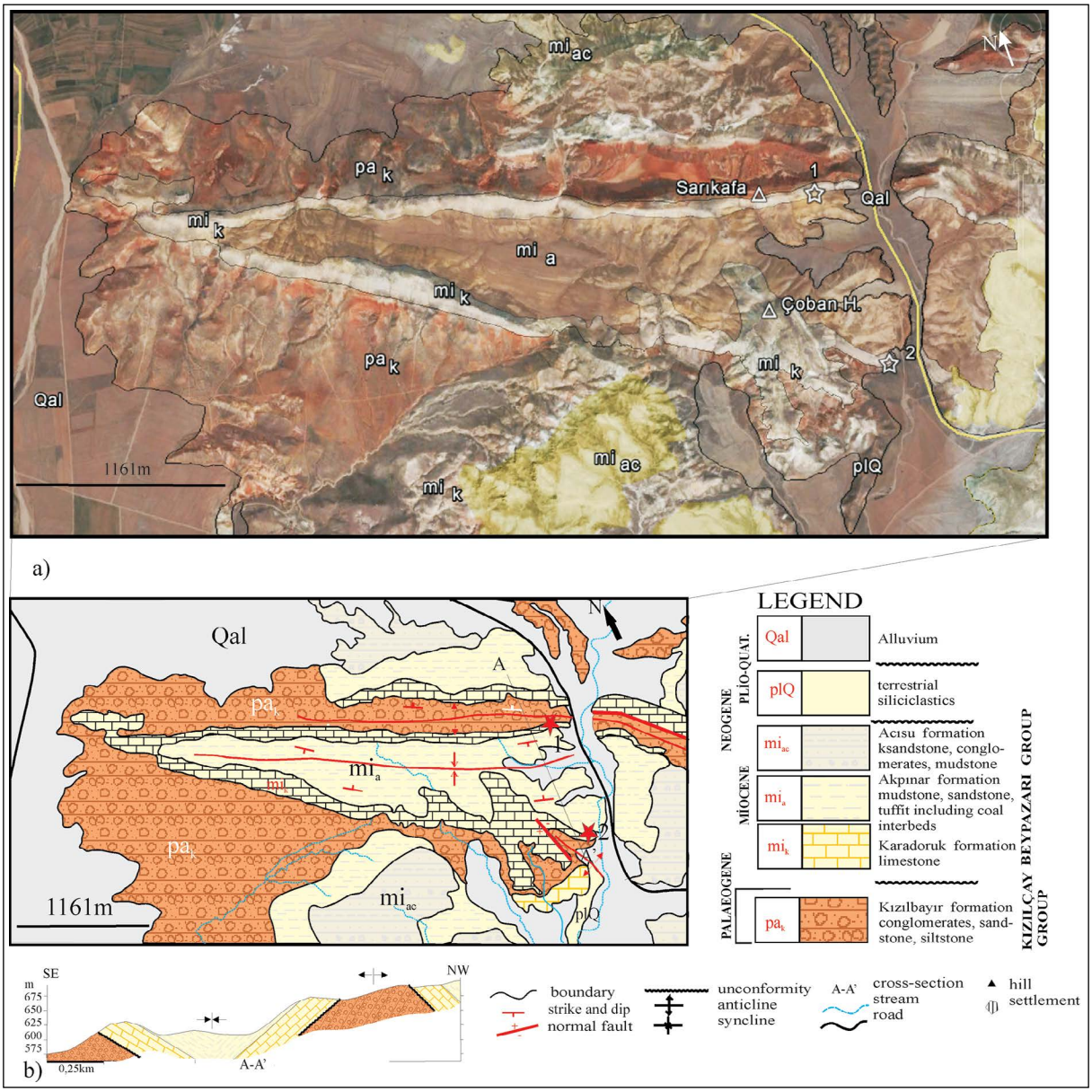

Figure 2- GoogleEarth view, a) and geological map of the study area, b) stars 1 and 2 show the Miocene plant remain fossil locations.

following syncline limbs including seed fossils appear in the middle part of the area (Figures 2-3). On the northern limb of a syncline near to Sarıkafa, white, gray coloured limestones of the Karadoruk formation conformably overlie the Kızılbayır formation. Total thickness of the Karadoruk formation herein is about 25 meters. On the southern limb of the syncline near to Çoban Hill, the Karadoruk formation thickness is about 30-40 meters. Two measured sections were performed at the north and south limbs of the syncline in the Karadoruk formation. Another section is approximately 500 meters far from the south limb of the syncline (Figures 2-3). 30 hard rock samples, 3 mudstone samples and more than one hundred plant remain specimens were collected. Hard rock thin sections from the measured sections and spot samples, and individual seed thin sections comprising their vertical and horizontal views were prepared. Mudstone samples including coal occurrences were evaluated for aging of the sediments based on the spore and pollen data (written and oral communication, Dr. Zühtü Batı, TPAO, 2017). SEM photographs have been taken in the Institute of Nuclear Science of the Ankara University. Electron microprobe (EPMA) analyses

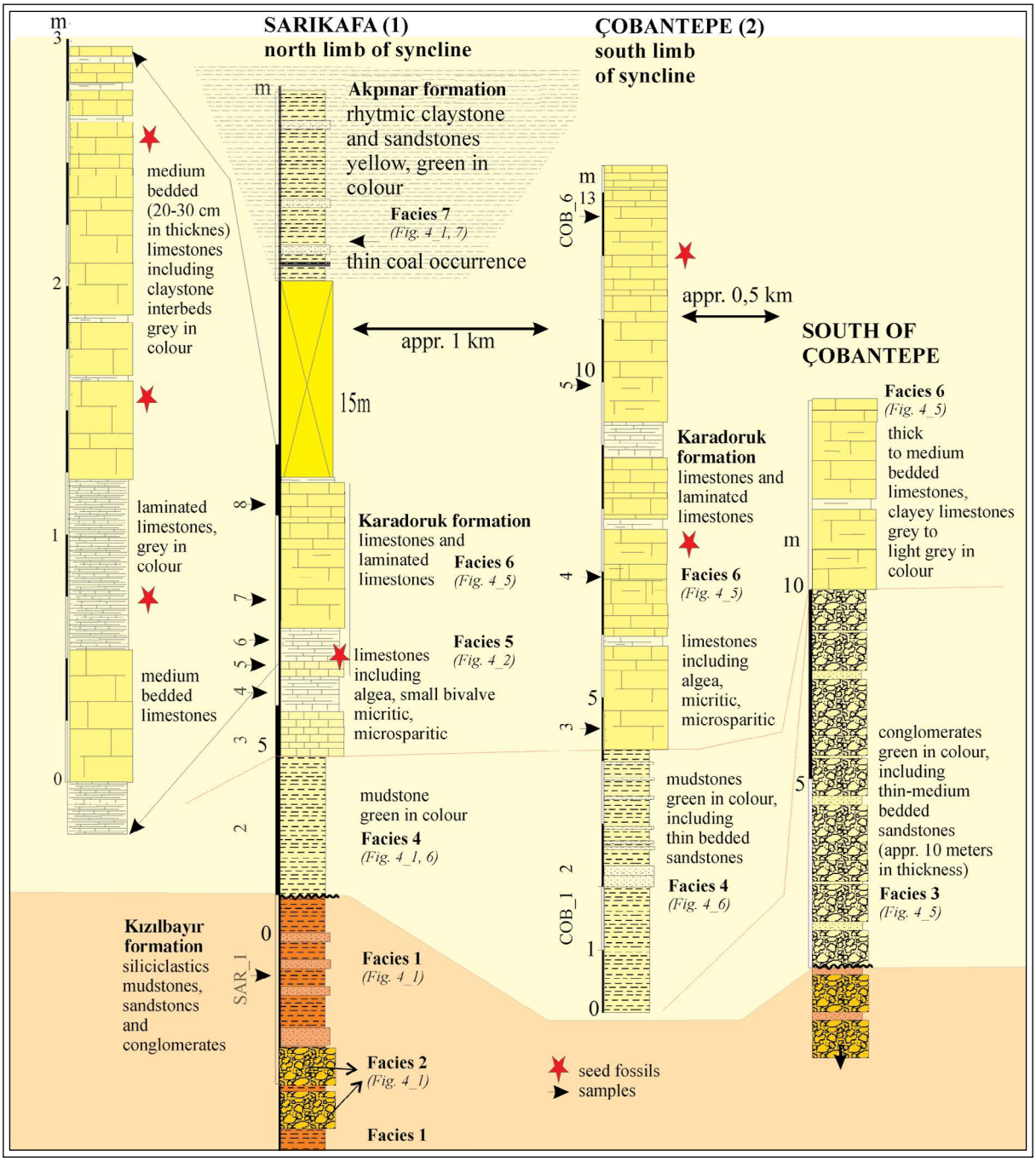

Figure 3- Correlation of measured sections in the investigation area.

were performed on polished thin sections using a JEOL JXA–8230 instrument which is equipped with 5 wavelengths–dispersive spectrometers at the Earth Sciences Application and Research Centre (YEBIM) of Ankara University. Operating conditions were 20 kV accelerating voltage, 10 nA beam current and a 2 µm spot size. Detection limits for Na, Mg, Al, Si, Fe, Mn, K, Ca and Ti are below 0,04 wt% oxide. Natural oxide and mineral reference materials were used for calibration and measurements. Matrix effects were corrected using the ZAF software provided by JEOL. Carbon coating were made by using Quorum Q150T ES machine at YEBIM. The seed specimens were also studied in thermo confocal Raman Spectroscopy in order to identify the natural chemical bond composition for comparison with the lived seed. Confocal Raman Spectrometer is a well-known method for the analyses of minerals however; it has not yet been widely

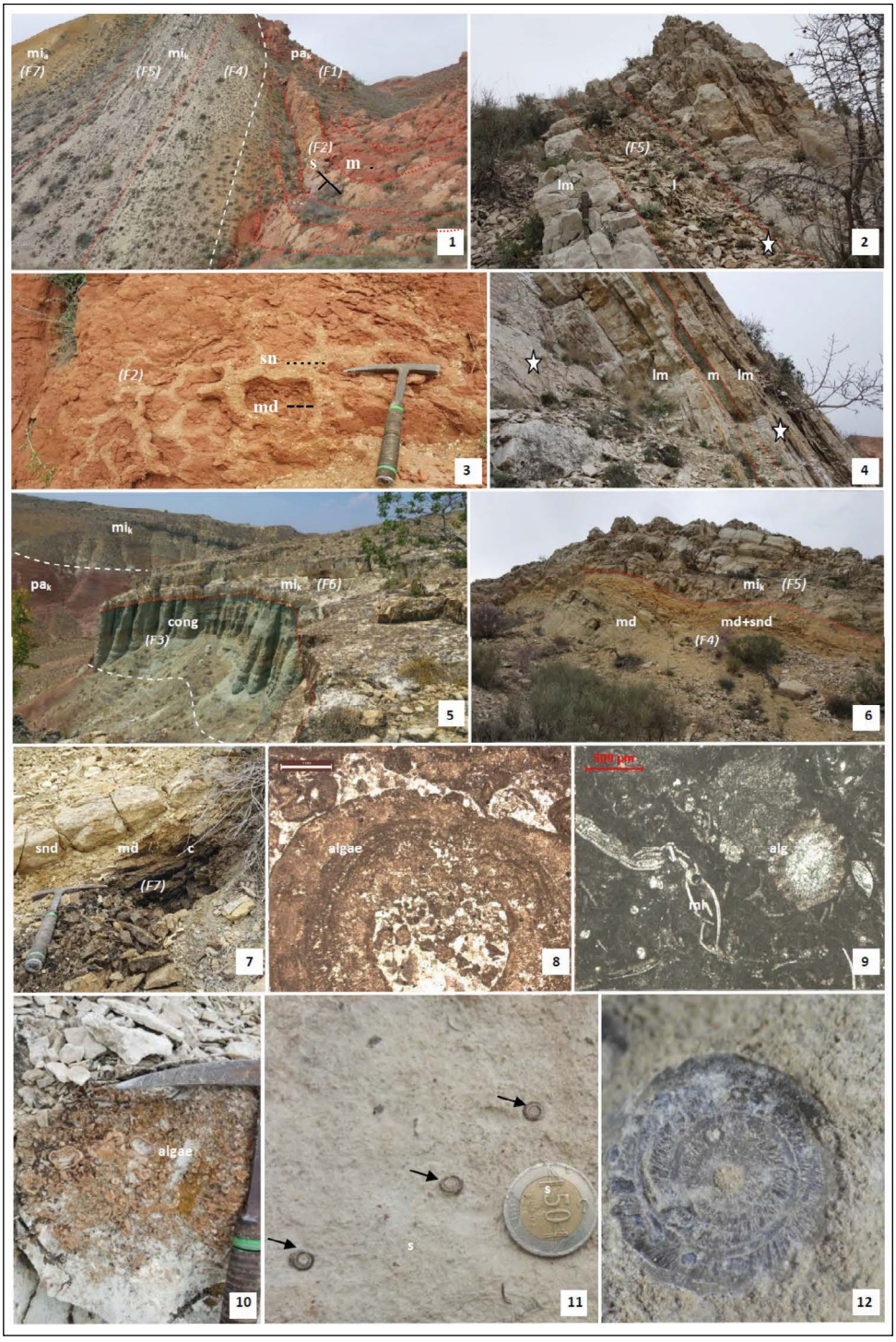

Figure 4- Field and thin section views of the geological units from the study area. 1) A view of the Kızılbayır formation (pa_k), Karadoruk formation (mi_k) and Akpınar formation (mi_a) looking towards to west of the northern limb of the syncline; s. sandstone beds, m. mudstone beds, 2) alternating of limestones (lm) and laminated limestone (l) looking towards to east of the northern limb of the syncline; 3) mud-crack within the Kızılbayır formation-facies 1; sn. sands, md. muds, 4) Seed like plant remain fossils limestone levels including mudstone interbed (m); 5) Karadoruk formation (mi_k) including conglomerates at the base of the Miocene, Kızılbayır formation (pa_k); 6) Karadoruk formation (mi_k) including mudstone and mud-sand litologies at the base of the formation; 7) a view from the base of Acısu formation (mi_{ac}) showing coal (c), mudstone (md) and sandstone (snd) layers; 8-9) thin section views from the base of Karadoruk formation, algea (alg), small mollusc shells (ml); 10) silicified algea bed from the Karadoruk formation; 11-12) seed fossil external views within limestone around Sarıkafa Hill.

applied on fossil seed identification and determination. Raman measurements were performed with a Thermo equipped with a laser operating at a wavelength of 633 nm. An electrical cooled charge coupled device (CCD) detector was employed to acquire spectra, and the laser spot was focused on seed surface with 10X or 50X long focused objectives, which allow a 65 and 13 mm working distance, respectively, and a lateral resolution of 5 and 2 µm respectively. Polarization of the incident laser beam was selected parallel to the preferential domain orientation of samples and spectra were collected in a strict backscattering geometry. The seed like fossils have been kept in the Geology Department of the Ankara University by the first author.

4. Early Miocene Seed Like Plant Remain Fossils and Their Geochemical Analysis

Plant remain fossils from the early Miocene sediments in the east of the Nallıhan district provide a unique opportunity to explore ancient terrestrial bio communities and facies associations. Figure 5 shows a schematic three dimensional external and internal views together with their thin section views of the fossils.

4.1. External Views

They are mainly on the bedding surface of the cream to beige coloured clayey limestones as dark crystallized dots (Figures 4.11-4.12). Their colour is nearly black in many specimens (Figures 6-9). But, some individuals colour is yellowish to brown (Figure 6-7). Mold and cast of the seed fossils are light beige in colour (Figure 7). They are more or less in the same size changing from 5 to 7 mm in diameter and 0,5-1,2 mm in thickness (Figures 7, 9). One side of the seed like plant remain fossils has a smooth surface while another side comprises concave in shape (Figures 5-6). Annular external view is composed of compressed the initial part, and thicker edges. The shape of the plant remain fossils is

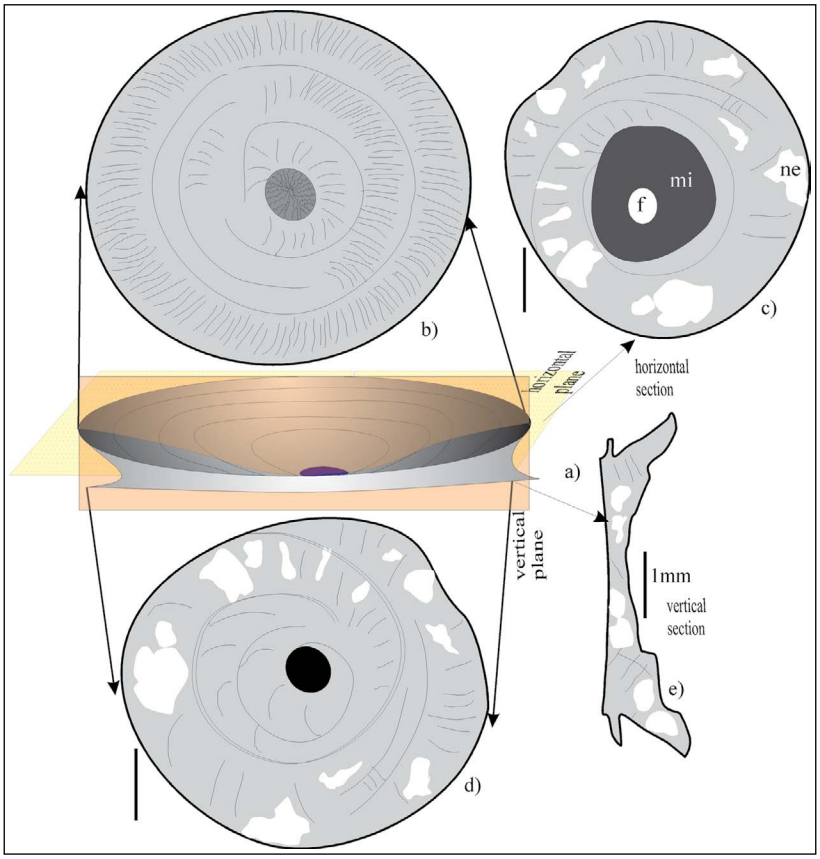

Figure 5- Schematic views of a seed like plant remain fossil, a) schematic block diagram, b) external view (upper concave part) with a nucleus view, c) vertical thin section view, d) external view (lower flattened part), e) horizontal view, f) initial part without nucleus, mi. micritic filling, ne. neomorphic filling.

similar to a tray or a pan. At its centre, there has been a circular initial cave in many specimens (Figure 9). One of the specimens includes a soft nucleus in the middle of the seed (Figure 6). Later 4 or 5 orbicular lines comprise too often calcitic radial and curved internal lines. When we pour the hydrochloric acid on it, all tests was melt. It means coating part of the seed is re crystallized. As mentioned above, one of the specimen includes a semi soft nucleus in the initial part.

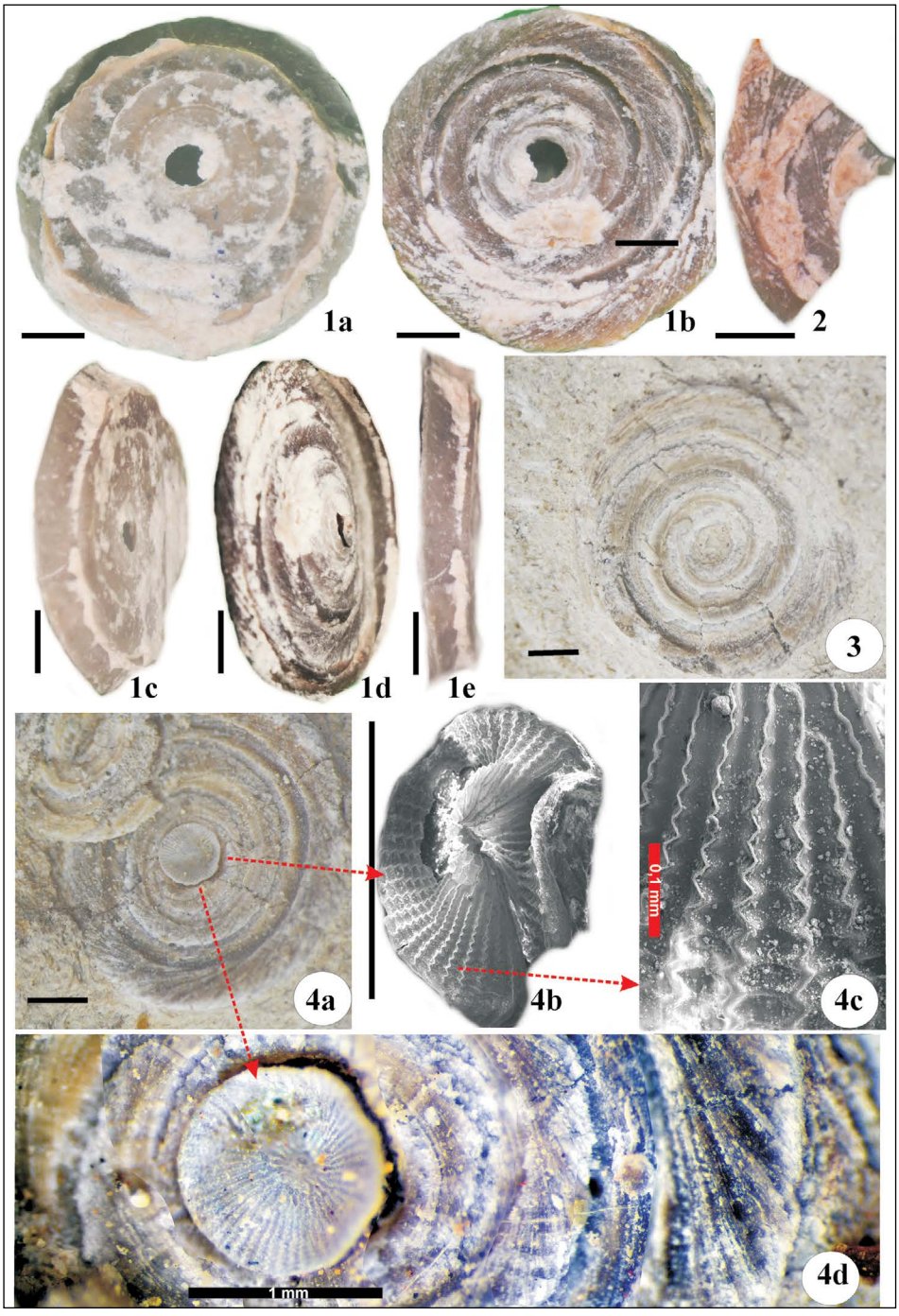

Figure 6- External and SEM views of seed like plant remain fossils and its nucleus details. 1a) flattened part view, 1b) concave part view, 1c-d-e) side views, 2) closest view of concave part, 3) a seed like plant remain fossil within clayey limestone, 4a) a seed plant remain fossil including a nucleus part, 4b-c) closer SEM views of the nucleus, 4d) closer external view of the nucleus (scale 1 mm).

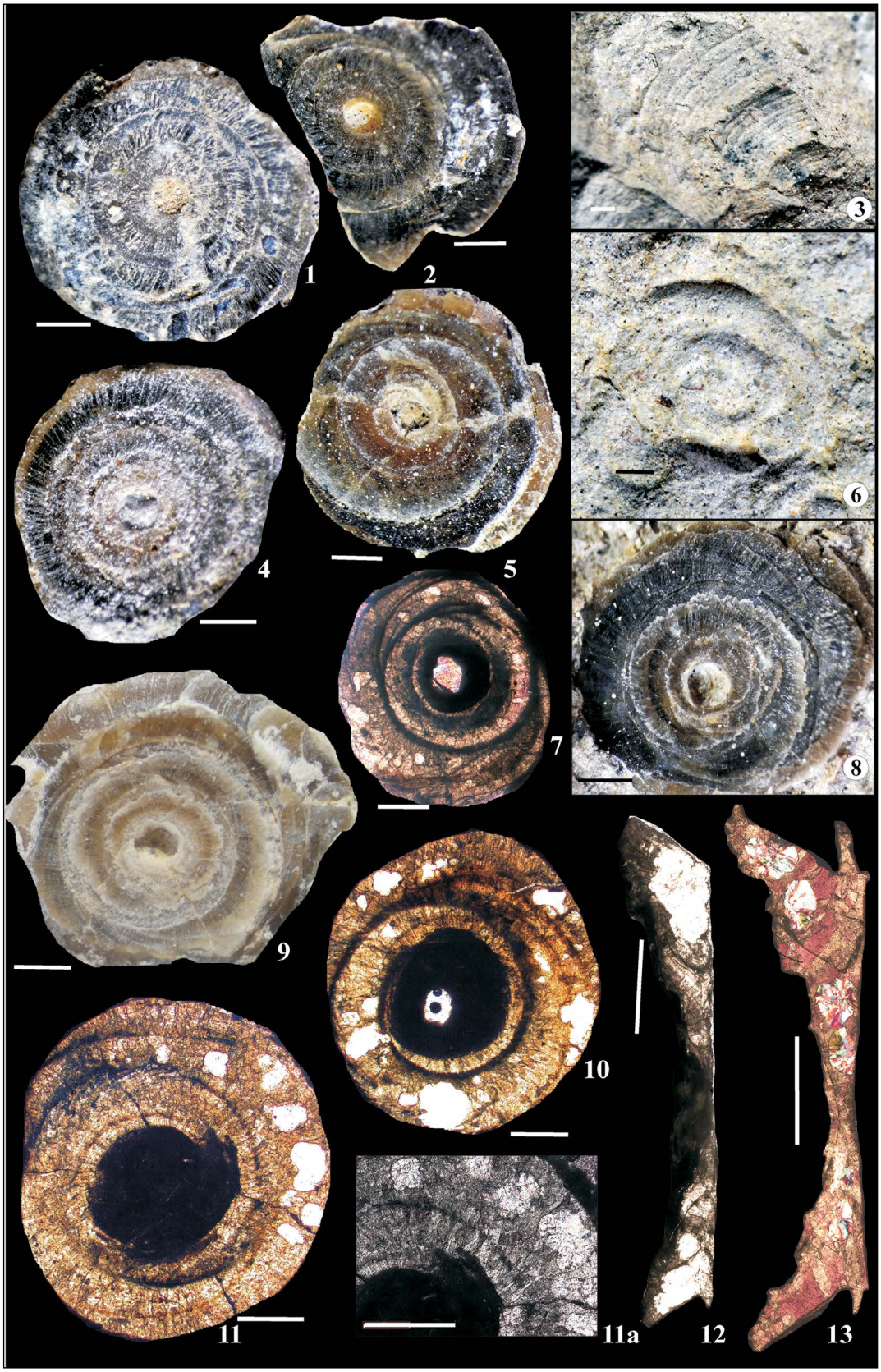

Figure 7- Seed like plant remain fossil views. 1,2,4,5,8,9 external views, 3,6 mold and cast of the seed like fossils, 7,10,11 horizontal views, 12,13 vertical views, scale shows 1 mm, all specimens are from the northern and southern limb of the syncline between Sarıkafa and west of the Çoban Hill.

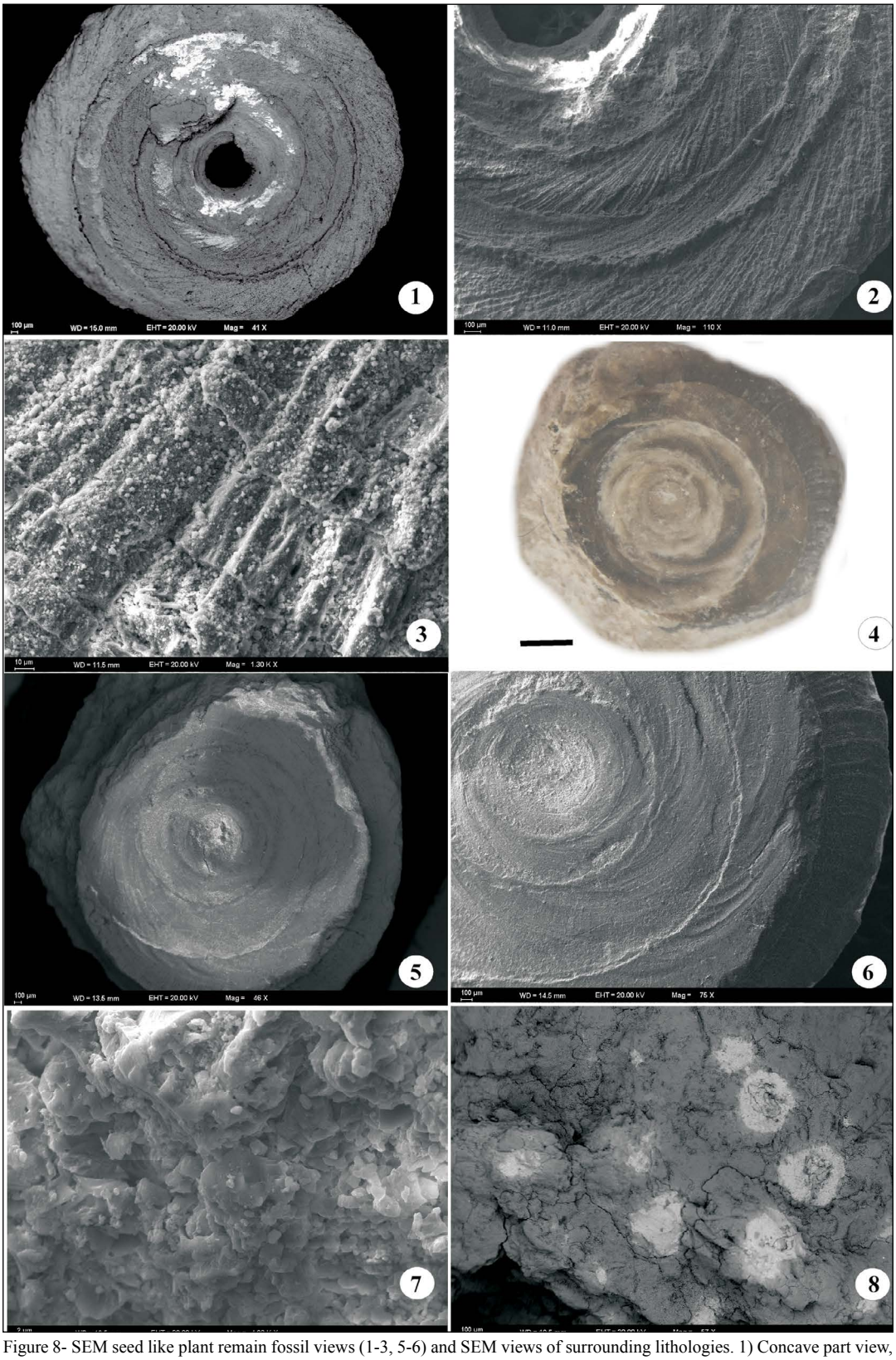

Figure 8- SEM seed like plant remain fossil views (1-3, 5-6) and SEM views of surrounding lithologies. 1) Concave part view, 2) details of radial ornament, 3) closer view of the radial part, 4) flattened part view, 5) flattaned part SEM view, 6) closer view of the initial part, 7) closer view of clayey limestone, 8) closer view of dark nodules with iron richness within clayey limestones.

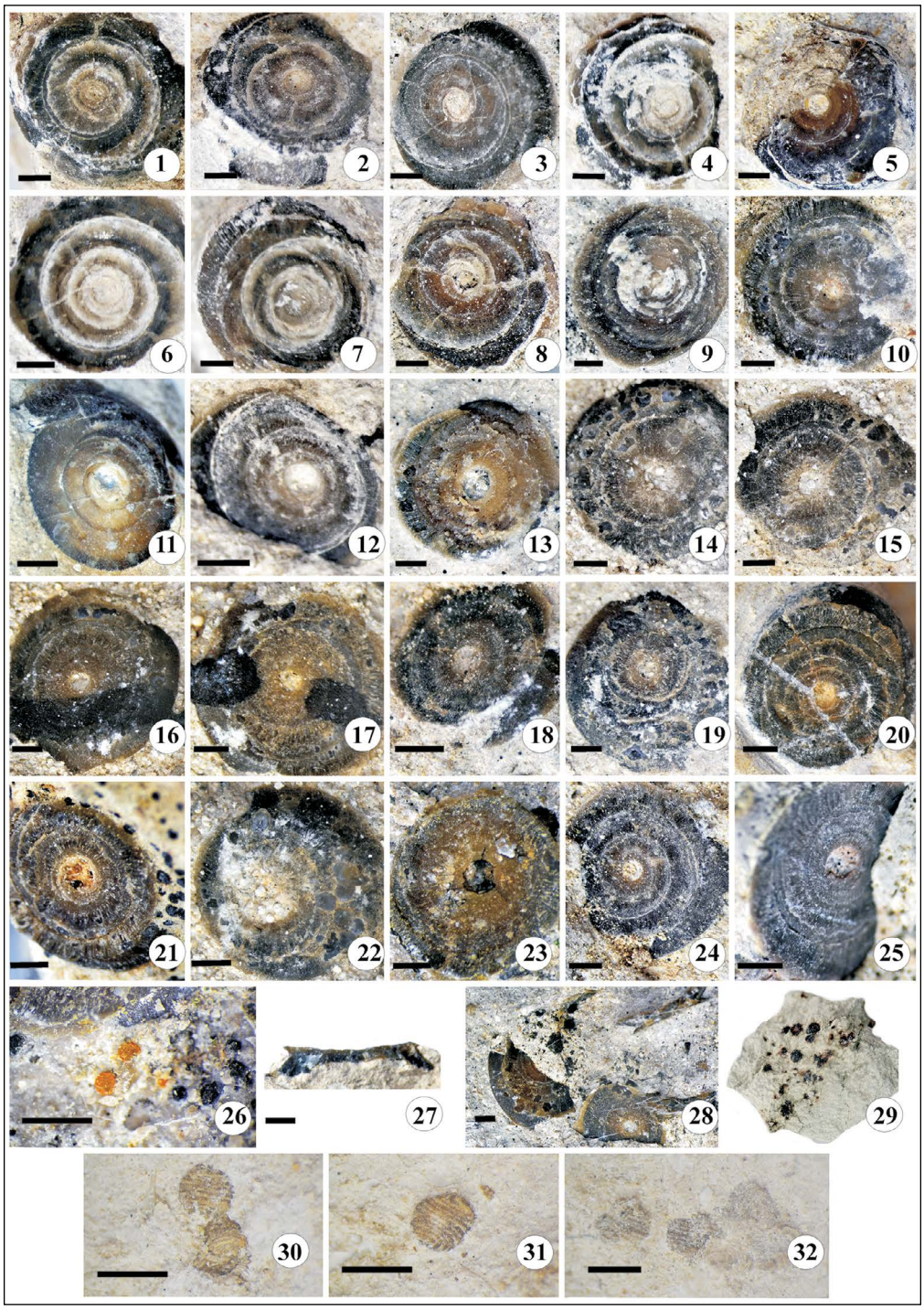

Figure 9- Various seed like plant remain fossil views (1-25), 26) Sulfur (S) nodules within clayey limestone, 27) side view of a seed fossil, 28) side and oblique views of seed fossils within clayey limestone, 29) iron nodules within clayey limestones, 30-32) *Chara globularis* within clayey limestone.

4.2. Internal Views

Micritic initial part and sometimes neomorphic cave up to 0,5 mm in size are in the centre of the fossil. They have calcitic circular, curved radial internal structures. Within the individual thin sections, calcitic small caves within the whorls are also usual. Circular whorlings are clearly seen. As mentioned before, only one specimen includes a nucleus at the centre. The nucleus is about 1 mm in diameter and

includes radial internal lines (Figure 6.4). The lines are Z in shape (Figure 6.4c).

4.3. Associated Flora and Age

Associated flora is *Pediastrum* spp., *Botryococcus braunii, Ovoidites* spp., *Tricolpopollenites* spp., *Pinus* spp. Gramineae and Polypodiaceae. They were determined within the claystones and coals overlying the limestones with seed fossils. *Pediastrum* spp. is abundant form within the sediments. It is organic green algae. *Botryococcus braunii, Pinus* spp. Gramineae are rare (maximum up to 10 individuals) while *Ovoidites* spp. and Polypodiaceae are seen as usual forms (between 20-50). *Tricolpopollenites* spp. is between 5-20. Due to appearances of Gramineae pollens in the western Anatolia at the beginning of Miocene, the age of the sediments may be accepted as early Miocene and their paleoenvironments as shallow lacustrinal paleoenvironment having so many river transportation due to abundance of Polypodiaceae (written and oral communication Dr. Zühtü Batı, TPAO, 2017).

4.4. Geochemical Results

The nucleus, seed, surrounding lithologies and flora were analyzed geochemically to bring out the differences between similar organisms and seed fossils (Figures 10-11-12, Tables 1-2). According to SEM EDS analysis results, two points (A and B) in the nucleus include more carbon element (Figure 10). Point C is composed of Ca contents (Figure 10). Point D in the hard part of *Chara globularis* which is seen with the seed fossils also has similar composition with point C. Within the clayey limestones, very small nodules, point E and matrix of clayey limestones comprise Si, Al and Fe contents. Particularly dark nodules, point F includes rich Fe element (Figure 10).

The EPMA analysis results (Table 1) are as follows: N changes between 47,79 and 48,56% within the seed test. It decreases within the clayey matrix from 43,29 and 43, 31%. CaO within the seed is higher than CaO values of clayey matrix. Besides V_2O_5, Mn, FeO and SO_3 were found within the plant remain fossils in higher values. They are undetermined or very low values within the matrix. In contrary, MgO and SiO_2 has low values within the seed while the clayey matrix contain more Mg and Si elements (Table 1, Figure 11).

RAMAN analyses in the nucleus part show that it is an organic part of the seed. Because surface of three analyzed points A, B, C on the nucleus were burnt after analysis and two points of nucleus comprise organic composition (Figure 12). All obtained geochemical data show that the fossils are related to the Miocene are seed like plant remain fossils.

4.5. Comparison

In comparison with the similar organisms such as snails, differences are presented in table 3. Properties on the shape, size, ornament, geochemical compositions of nucleus and hard parts of the organisms show that our specimens are not gastropoda or other animal organisms.

Table 1- EPMA results for the seed like plant remain fossils, points 1 and 2: hard part of the seed, points 3 and 4: initial part cemented with clayey fillings without nucleus.

	1	2	3	4
Elements	mass%	mass%	mass%	mass%
N	48,56	47,79	43,31	43,29
F	2,07	2,03	2,1	2,03
CaO	47,41	47,72	42,71	40,21
Na_2O	0,02	0,07	0,09	0,02
MgO	0,32	0,28	0,45	0,44
Al_2O_3	0,16	0,23	2,12	2,83
SiO_2	0,28	0,37	6,22	8,14
P_2O_5	0,07	0,01	0,06	0,11
SO_3	0,5	0,43	0,37	0,21
Cl	0,01	0,02	0,01	0,02
K_2O	0,02	0,02	0,99	1,39
TiO_2	0,05	0,05	0,1	0,06
V_2O_5	0,01	0,04	0,01	nd
Cr_2O_3	0,03	0,03	0,09	0,11
Mn	0,06	0,04	nd	nd
FeO	0,66	0,52	0,36	0,42
CoO	0,02	nd	0,03	0,01
NiO	0,11	0,1	0,01	nd
CuO	0,03	0,06	0,05	0,01
ZnO	0,05	nd	nd	0,04
Ga	nd	0	nd	0,07
Rb_2O	0,11	0,04	nd	nd
SrO	0,16	0,11	0,33	0,41
Ba	nd	0,03	0,1	0,05
PbO	0,18	0,09	0,05	nd
	100,89	100,08	99,56	99,87

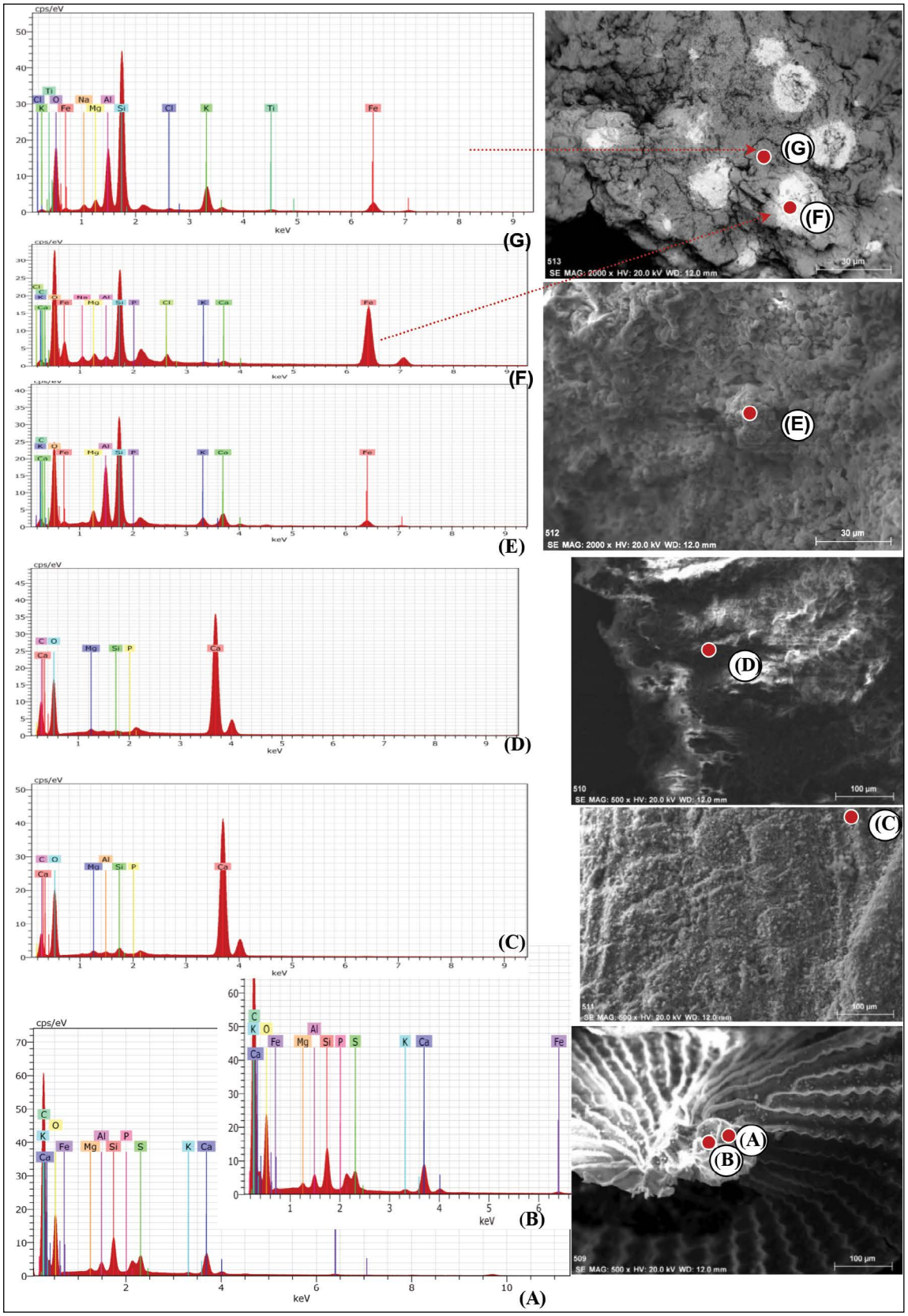

Figure 10- SEM EDS analysis diagrams, A-B) nucleus of a seed like plant remain fossil, C) hard part of a seed like plant remain fossil, D) *Chara* test, E) tiny silicified nodules, F) nodules with iron richness, G) surrounding lithology.

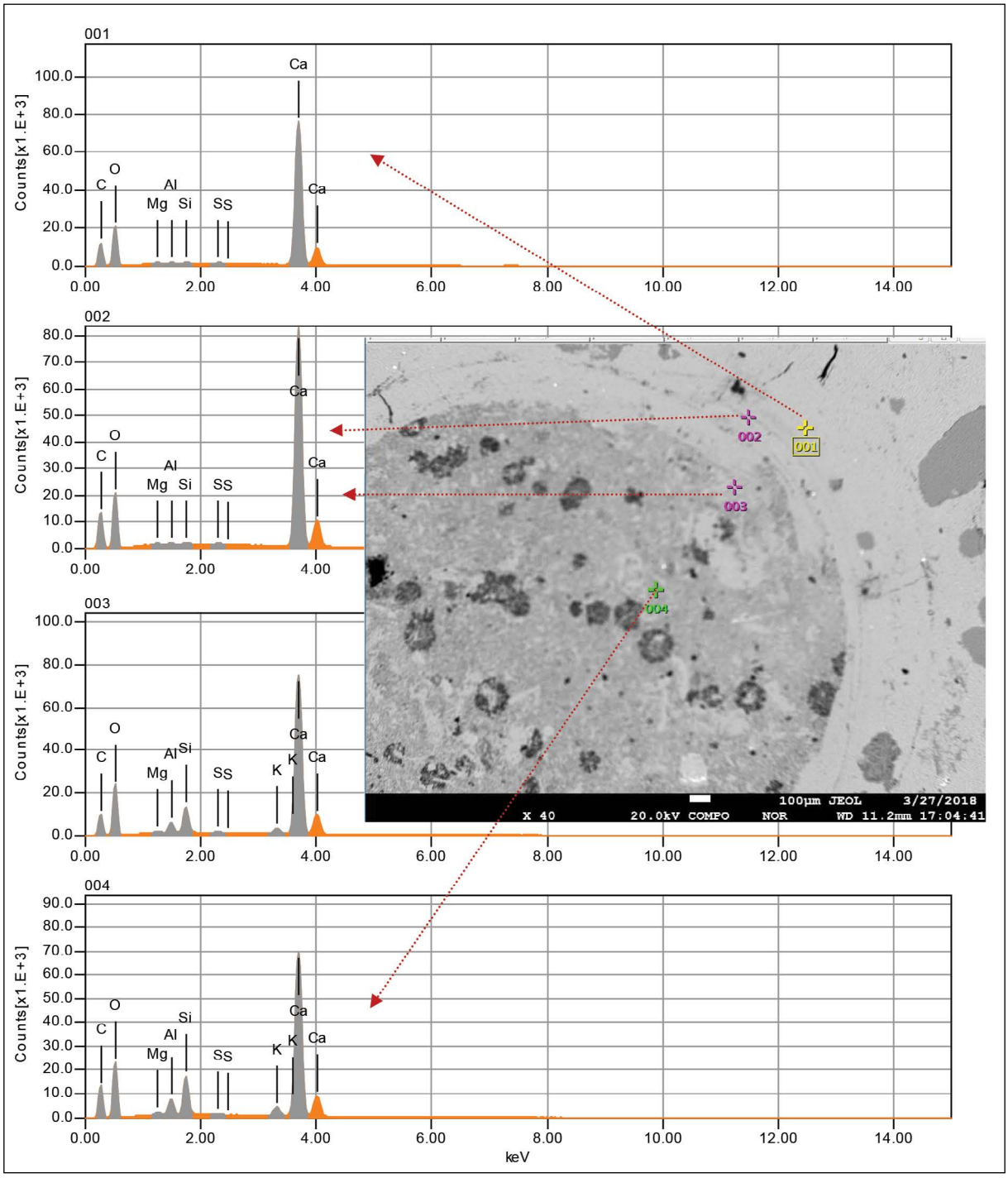

Figure 11- A seed like plant remain fossil EPMA analysis results (points 1-3 seed fossil hard parts, point 4 filling material in the initial part).

5. Facies Associations

The facies association studies mainly concentrate on the three main litostratigraphic units known as Kızılbayır formation, Karadoruk formation and Akpınar formation. The Kızılbayır formation comprises red bed coloured medium to coarse sized siliciclastic deposits and divided into two facies (F1 and F2). These are non-channelized red sandstone and mudstone (F1) and channelized "confined" reddish-beige pebbly sandstone and conglomerate (F2). Clayey limestones of the Karadoruk formation

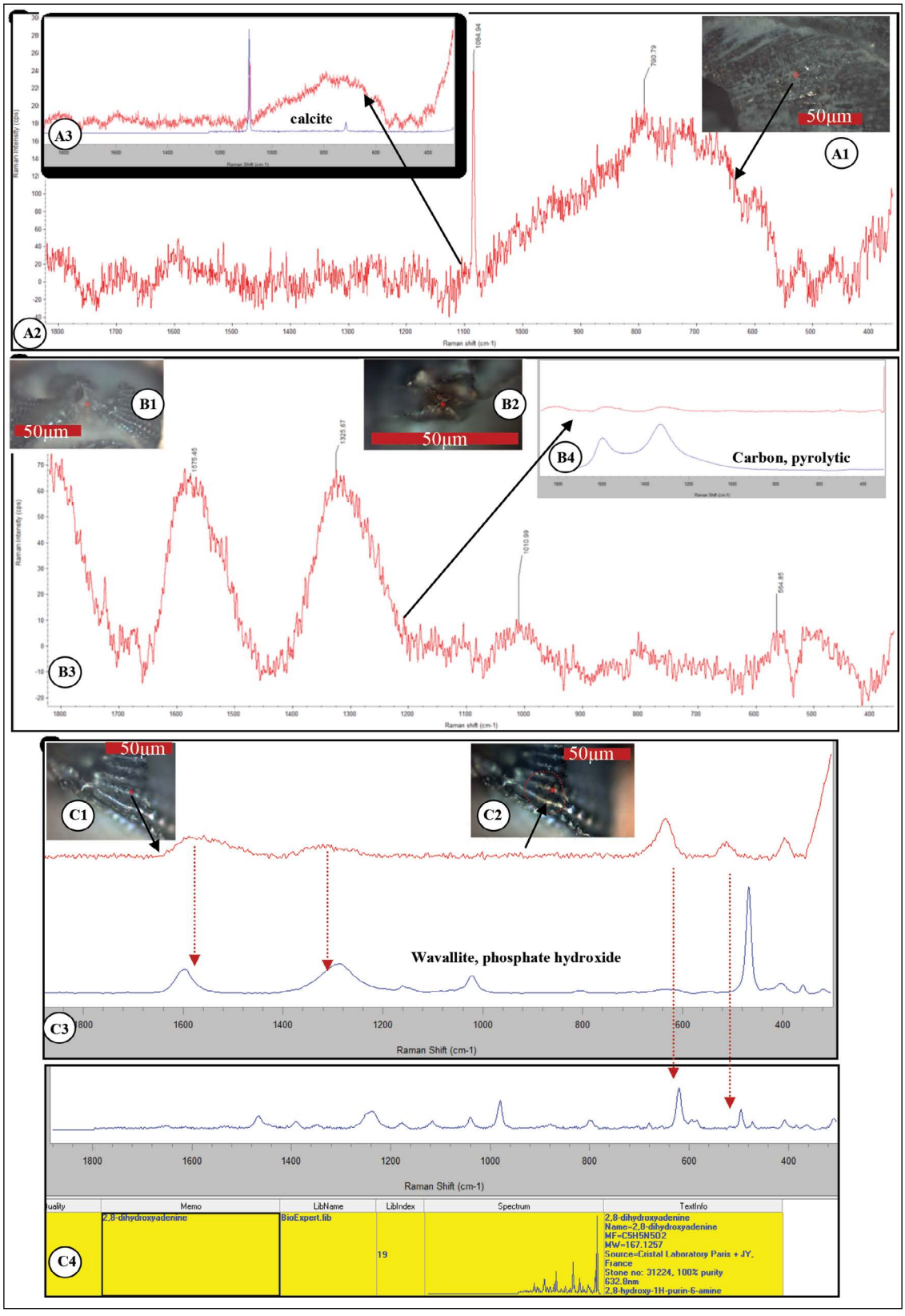

Figure 12- RAMAN analysis results of seed like fossil nucleus (point views A1, B1-before analysis, B2-after analysis, laşer burnt point view, C1-before analysis, C2-after analysis, laser burnt point view) (Raman shifts A2, B3) (Comprasion shift views between standart mineral shifts-blue in colour and obtained shift values-red in colour, A3, B4, C3, C4).

Table 2- SEM EDS results for the seed like plant remain fossils, Nuc_1 and 2. nucleus; *Chara* test, Seed_1 and 2, surrounding parts of nucleus, Ndl_1 and 2. nodules within the clayey layers.

	Nuc_1	Nuc_2	Chara	Seed_1	Seed_2	Ndl_1	Ndl_2
O	56,62	55,08	57,86	57,96	50,07	35,73	40,50
C	**34,09**	**30,29**	12,46	7,98	0,21	0,18	–
Ca	3,90	4,89	**28,99**	**30,43**	4,31	0,51	–
Si	1,75	2,80	–	0,89	**18,90**	12,56	**30,80**
S	1,72	2,16	–	–	–	–	–
P	0,76	1,38	0,40	0,91	3,17	3,88	–
Al	0,44	1,35	–	0,60	11,68	1,42	14,41
Fe	0,40	0,62	–	–	5,96	**37,98**	1,38
K	0,20	0,38	–		2,09	0,20	5,15
Mg	0,11	1,05	0,28	1,24	3,61	2,60	3,40
Na						3,32	3,07
Cl						1,61	0,63
Ti							0,66
Total	100,00	100,00	100,00	100,00	100,00	100,00	100,00

conformably rest on the basal siliciclastic red bed unit. However coarse clastics of the formation overlie unconformably the basement at the south of the investigation area. The Karadoruk formation and overlying siliciclastics of the Akpınar formation include the following facies association's namely as medium to coarse siliciclastics (F3), mudstone dominated siliciclastics (F4), plant remain-bearing placket, thin bedded clayey limestone (F5) medium to thick bedded limestone (F6) and rhythmic siliciclastics - clayey-marly limestone including coal occurrences (F7) in ascending order (Figure3).

5.1. Non-Channelized Red Sandstone and Mudstone (F1)

Thickness of the facies is more than 100 meters. They have large lateral persistence (200 -500 m), but display little thickness variations which are generally between 30-40 cm. The sandstones are fine grained in size, represented by a non-channelized depositional character composed of homogenous and stacked beds with sharp and gradational bases that are separated by thin (5-15 cm thick) immature palaeosol levels**.** In some places, upper parts of the beds confined fine laminate sets, mostly horizontal and climbing laminations.

Table 3- Properties comparison between gastropoda and seed like plant remain fossils of this study.

Properties	**Gastropoda (flattened)**	**Seed like fossil (this study)**
Hand specimen view	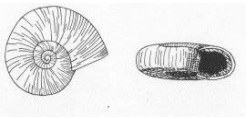 http://bioteaching.com/the-steinheim-basin-snail-series-part-1/	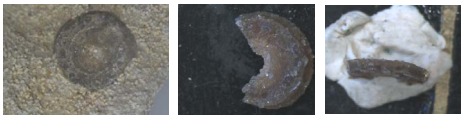 see Figs. 5-9
Size	4-7mm, micromolluca	4-5 mm
Shape	compact spiral shape both sides are more or less same views	One side is smooth, another side is concave
Ornament	stripes on the both sides	many stripes on concave side less stripes on smooth side
Coiling	planspiral, low trochospiral, heights of last whorls increase in size	circular, planspiral
Nucleus	-	circular nucleus with radial lines with Z in shape, see Fig. 6.4
Seed shell composition	Calcite	Calcite
Seed nucleus composition	No nucleus	Calcite and organic material (see Fig. 12)
Thin section view	neomorphic sparite	Neomorphic sparite with small porosites
Associated flora	Other lacustrinal mollusca and organisms	algea, *Chara globularis*, spor and pollens
Environment	Lake	Lake

The sandy beds are sometimes cut by small (10-20 cm) ephemeral channels filled with fine-pebbles. In some parts, the pebbles show patch distributions on the sandy matrix or penetrated as injections within the sandstones. Mudstone interlayers are thinner (15-25 cm thick) than sandstones and contain root casts and mud cracks filled with sandy materials (Figures 4.1, 4.3).

Interpretation: Determined sedimentary structures in the F1, represented by lack of channelization "non-confined" and narrow flood plain are cut by laterally wedge-shaped lobate sandstones. The extensive sharp bases sandy deposition, little thickness variations and horizontal and climbing laminations indicate that the sheet flood-type flows deposited (Lopez-Gomez and Arche, 1993; Martinius et al., 2002; Hampton and Horton, 2007). On the other hand, dispersive or patchy pebble accumulations within the fine-medium-grained sandy matrix would be reflection of high flows flashing that occurred in the seasonal periods of the arid/semi-arid. High rates of sediment accumulation and tectonic subsidence of the Beypazarı Paleogene basin would provide suitable accommodation space and depositional conditions leading to long-term maintenance of a sheet flow system rather than braided and meandering fluvial systems (Hartley, 1993; Hampton and Horton, 2007).

5.2. Channelized "Confined" Reddish-Beige Pebbly Sandstone and Conglomerate (F2)

The facies is characterized by channel – fill deposits bedding with erosional bottom surface. The conglomerates and sandstones lenticular in shape were developed and show lateral extent between 20 and 50 metres, and they merge or interfinger with the sheet red sandstone and floodplain mudstone (F1). Bedding thickness varies from 40 cm to 100 cm (Figure 4.1). Of which pebbly sandstones having with matrix-supported texture exhibit weak stratification, poor sorting character and a wide spectrum of grain sizes with respect to channelized conglomerate with clast-supported texture. Channelized conglomerates record fining/coarsening upward trend, lensoidal – shaped channel lag pebbles, scour - fill structure and planar cross-stratification (Figure 4.1). Where cross-stratification orientations suggest that the flow regime took place in the direction of from NE to SW.

Interpretation: The channelized "confined" facies (F2) would be result of seasonal climate with high rate sedimentation which favoured for the construction of the ephemeral stream and/or ephemeral flashing high flow regime (Abdullatif, 1989) involving a mixed load of pebble, sand, silt and mud. The channel-fill deposits characterized by planar cross- stratification, pebbly channels and upward - coarsening conglomeratic bar sheets could be linked with basin margin alluvial fan or a braided – stream distributary network (Nemec and Postma, 1993).

5.3. Medium to Coarse Siliciclastics (F3)

They expose at the bottom of Karadoruk formation at the south of Cobantepe Hill (Figure 4.5). The facies lithologies are mainly green coloured coarse siliciclastics, medium to thick in bedding. Bedding thickness changes between 1,5 and 2 meters. Total thickness of the facies is about 20 meters. Matrix and clast supported textures, poor sorting character and a wide spectrum grain sizes are seen within the green to red conglomerates and sandstones.

Interpretation: Its restricted geometry, lithological characteristics and unconformity relation with the underlying Kızılbayır formation show that they were derived from the terrestrial areas by rivers. They may be compared with lake margin alluvial fan or a braided – stream distributary network (Nemec and Postma, 1993).

5.4. Mudstones Interbedded with Sandstones (F4)

The facies is between the basal conglomerates (F3) and plant remains-bearing clayey limestone (F5). Rhythmic green coloured mudstones and brown coloured sandstones are the main lithologies of the facies (Figure 4.6). Thickness of the bedding changes from 5 cm to 1 meters. Total thickness of the facies changes between 5 and 15 meters. Thin sections of sandstones of the unit include very small bivalve cross-sections and algae.

Interpretation: Its restricted geometry, lithological characteristics and fauna-flora such as algae and very small mollusc contents show that they were related to very shallow part of the lake. They were probably deposited within the inner part of the lake.

5.5. Placket, Thin Bedded Clayey Limestone Bearing Plant Remain Fossils (F5)

Its measurable thickness of the facies is about 40 metres. The facies is mainly composed of alternating beds of limestones and laminated limestones (Figure 4.2). The alternating beds are organized as upward –fining sets, each one consists of several beds separated by greenish mudstone interlayer's (0.5-20 cm thick) (Figure 4.4).

At the northern limb of the syncline in the middle of the study area (Figures 4.1, 4.2, 4.4), succession of the Karadoruk formation starts with cream coloured siltstones. The total thickness of the base deposits changes between 5 to 10 meters. Siltstones and clayey limestones, including algae are dominant (Figures 4.8, 4.9, 4.10). Clayey limestones and limestones, including many fractures and laminated limestones towards the upper part of the formation have mainly thin to medium beddings, 2- 30 cm in thickness. Grey to yellowish grey coloured siltstone interbeds, a few cm in thickness are seen within the laminated limestones. Seed fossils are clearly observed on the bedding limestone surfaces, up to %1-2 in ratio (Figures 4.11-4.12). Plant remain fossils (?Menispermacea) is well fossilized and disseminated within the limestone beds mixed with various amount of woody plant, root materials and fresh water pelecypod fossils. The limestone facies contains very low rate of clayey minerals (≥% 10 and). Low-magnesium calcite is formed the main mineralogical composition in this facies, which precipitated as micrite matrix and void-filling spar cement particularly in the open space of the mud crack and root cast.

At the southern part of the syncline in the middle of the study area (Figures 4.5, 4.6), greenish coloured siltstones, and mudstones including tuffit interbeds are at the base of the Karadoruk formation. Its succession continuous with yellowish coloured rhythmic mudstones and clayey limestones, totally 5 meters in thickness. In the succession, the bed thickness is from 5 to 15 cm. Limestones and clayey limestones are at the upper part of the formation. Silicified nodules known as beekyte are seen within the limestones at the upper part of the succession. Seed fossils as seen at the northern side of the syncline are within the bed surface of the limestones at the upper parts of the Karadoruk formation.

Interpretation: The facies represents a transgression of the lake upon the Palaeogene terrain that started with a major climatic changes evolved from arid-semiarid (terrestrial red bed deposits) to humid (lacustrine limestone) environments (Mueller et al., 2016). Fining-upward limestone cycles dissected by thin mudstone precipitations suggest that lake level fluctuations existed during the initial phase of the transgression. Abundant plant remain (?Menispermacea) fossil is indication of planted shallow lake margin with low topography (Yabe, 2009). On the other hand, very low terrigenous contribution into the lake waters support to existence of an oligotrophic lake through the carbonate precipitation. It is thought that the lake received poor nutrient supply and had little aquatic plants mixed with flowering plant (?Menispermacea) on the land.

5.6. Medium to Thick Bedded Limestone (F6)

They are seen at the top of the Karadoruk formation. They have facies changes with plant remain (?Menispermacea)-bearing clayey limestone. It is characterized with silicified nodules and thick beddings (Figures 4.5). Their colour is light beige. The total thickness is between 20 and 30 meters.

Interpretation: Clayey limestones outcrops widespreadly in the Beypazari basin and known as lacustrinal sediments (Siyako, 1983; Yağmurlu and Helvacı, 1994; Karadenizli, 1995). Lithological characteristics in the study area show that they were deposited within lake.

5.7. Rhythmic Siliciclastics - Clayey Limestone Including Coal Occurrences (F7)

The Akpınar formation fine to medium sized siliciclastic includes rhythmic mudstones, clayey marly limestones, siltstones and sandstones, 20 cm in bed thickness. Black to dark brown coloured coal occurrences, 2-3 cm in thickness are within the mudstones and sandstones (Figure 4.7). They are mainly yellowish in colour and overlie conformably the deposits of the Karadoruk formation. Whole facies is thicker than 30 metres and it is distinguished from the basal limestones by greyish yellow appearance, abundant plant material but lack of the seed like fossils.

Interpretation: Lignite-bearing basal level and high rate terrigeneous influx supported by clayey/ marl limestones were deposited during the time of drastically changes of the lake hydrology, presumably evolved from shallow oligotrophic to deeper eutrophic lake (Cayelan and Rydin, 2011), where the progressively deepening commenced with swamp environment, and then low-drainage river, running on the low topography, carried suspension load into the lake environment.

6. Discussion

The Miocene seed like fossils look like nummulits, and may be confused with annular benthic foraminifera. But the studied seed like fossils' shape and internal structures are so different than *Nummulites* and/or other living organisms and fossils. It may also be assumed as small gastropods. But its initial part view, vertical and horizontal structures are also so different from the gastropods (Table 3). Some Eocene, Miocene fossil seeds may be compared with our fossil seed data (Friis, 1985; Burge and Manchester, 2008; Herrera et. al., 2011; Wang et. al., 2013; Collinson et al., 2012; Pan et al., 2012; Lin et al., 2013; Huang et al., 2015; Hounslow et. al., 2016).

The mean size of our seed like plant remain fossils is around 6 mm and its mean diameter is about 0,7 mm. The size and its structure seem to be a Eocene species of Menispermaceae (Collinson et al., 2012). It may be compared with *Karinschmidtia rotulae*. However, its initial part is so different.

Due to the following reasons, our fossil findings are the first possible seed records from the lower Miocene sediments (?Menispermaceae): (1) Its shape-concave upper part, flattened bottom side, narrow thickness (Figure 6.1), (2) inner side of concave part includes radial, often lines (Figures 6.1b, 2; 8.2), it is impossible for gastropoda inside view, (3) having a semi-organic nucleus part with Z shaped often radial lines (Figure 6.4), (4) nucleus composition comprise organic material based on geochemical data (Figures 11-12), (5) associated flora and fauna, particularly seeing lacustrinal *Chara* (Figure 9.30-32), spore, pollen and coal occurrences (Figure 4.7), (6) they are seen on the clayey limestone beds (Figure 4.11).

The facies associations studied here provide a good example to interpret the environmental and paleoclimatic evaluations of the early Miocene succession in the Beypazarı –Nallıhan basin. The first depositional pocket (F1,2,3) was generated by fluvial system located near the centre of the basin, formed by low- sinuosity channels, braided river and seasonally channelized or non-channelized ephemeral flows supplied the high rate of siliciclastic sediments (Bridge and Gabel, 1992). Whereas basin margin setting alluvial fans might be active by alluvial fans during the flushing period of wet seasons (Abdul Aziz et al., 2003). The transition from the fluvial to lake deposition was highlighted by a drastic climatic changes developed from dry to humid, which was responsible for the onset of the new tectonic regime across the basin and constrained the establishment of a lake dominated -new drainage system along with topographic lowering and consequent retraction of the fluvial system. Shallow lake environment (facies 4-6) was initially filled by clayey limestone received abundant plant material (?Menispermacea) from the flat–edged lake margin. In the final stage (Akpınar and Karadoruk formations) lake relatively became deeper and rimmed by local swamps along the lake margin (facies 7). In this time period, high inflow of suspended load had involved a massive precipitation of marly limestones in the deeper part of the lake. Sedimentation and hydrological changes in a lake realm are related to humidity and other climate factors (Runge 2012).

7. Conclusions

The study focuses on Miocene plant remain fossil occurrences and their palaeoenvironment. So, the seed like plant remain fossil data from the east of Nallıhan area provide useful information on the terrestrial occurrences to interpret the early Miocene lake history. EPMA, RAMAN and SEM EDS results support seed like fossil appearances in the area. According to field and laboratory observations, seven facies associations were determined from the upper Paleogene to lower Miocene sediments. The Kızılbayır formation in the investigation area includes basin margin alluvial fan or a braided and meandering fluvial systems at the bottom related to arid/semi-arid conditions (F1, F2). The lacustrinal sediments of the Karadoruk and Akpınar formations comprise various lithofacies (F3-F7). The lake water is assumed as an oligotrophic lake through the carbonate precipitation, which received poor nutrient supply and having little aquatic plants contrasting to flowering plant

(?Menispermacea) on the land. Deeper eutrophic lake including swamp coal occurrences are seen towards the upper part of the Miocene.

Acknowledgement

The authors thanks to Ankara University BAP Coordination Unit, project no: 13B4343014 and Zühtü Batı (TPAO) for spore and pollen determinations.

References

Abdul Aziz, H., Sanz-Rubio, E, Calvo,C.P., Hilgen, F.J., Kingsman, W. 2003. Paleoenvironmetal reconstruction of a middle Miocene alluvial fan to cyclic shallow lacustrine depositional system in the Calatayud Basin (NE Spain). Sedimentology 50, 211-236.

Abdullatif, O. M. 1989. Channel-fill and sheet-flood facies sequences in the ephemeral terminal River Gash, Kassala, Sudan. Sedimentary Geology 63, 171-184.

Alkaya, F. 1987. Beypazarı yöresi KimmericiyenBerriasiyen ammonit faunası ve stratigrafisi. Melih Tokay Jeoloji Sempozyumu '87 Bildiri özetleri, Ankara, 114-117.

Alkaya, F. 1989*a*. Nallıhan (Ankara) Yöresi Titoniyen-Beriaziyen Ammonit Stratigrafisi. Selçuk Üniversitesi Mühendislik Mimarlık Fakültesi Dergisi 2, 1 – 13.

Alkaya, F. 1989*b*. Soğukçam (Bolu) Yöresi Kimmericiyen-Alt Titoniyen Ammonit Faunası ve Stratigrafisi. Yerbilimleri 15, 55 -73.

Altınlı, İ.E. 1978. Geology of eastern territiory of Nallıhan. İstanbul Üniversitesi Fen Fakültesi Mecmuası 42, 29-44.

Bridge, J .S., Gabel, S. 1992. Flow and sediment dynamic in a low sinuosity, braided river: Calamus river, Neblaska Sandhills. Sedimentology 39, 125-142.

Burge, D.O., Machester, S.R. 2008. Fruit morphology, fossil history, and biogeography of Paliurus (Rhamnaceae). International Journal of Plant Sciences 169 (8) 1066–1085.

Cayeland, C.C., Rydin, E. 2011. Lake trophic status can be determined by the depth distribution of sediment phosphorus. Limnology and Oceanography 56 (6) 2051–2063.

Collinson, M.E., Manchester, S.R., Wilde, V. 2012. Fossil fruits and seeds of the middle Eocene Messel biota, Germany. Abhandlungen der Senckenbergischen Naturforschenden Gesellschaft 570, 1 – 251.

Friis, E.M. 1985. Angiosperm Fruits and Seeds from the Middle Miocene of Jutland (Denmark). Det Kongelige Danske Videnskaberne Selskab, Biologiske Skrifter 24, 3, København, 169p.

Hampton, B.A.**,** Horton, B.K. 2007. Sheetflow fluvial processes in a rapidly subsiding basin, Altiplano plateau, Bolivia, Sedimentology 54, 1121–1147.

Hartley, A.J. 1993. Sedimentological response of an alluvial system to source area tectonism: the the Seilao Member of the Late Cretaceous to Eocene Purilactis Formation of northern Chile. In: Marzo M, Puigdefabregas C (Eds) Alluvial sedimentation. International Association Special Publication 17, 489-500.

Helvacı, C., Bozkurt, S. 1994. Beypazarı (Ankara) granitinin jeolojisi, mineralojisi ve Petrojenezi., Türkiye Jeoloji Bülteni 37 (2), 31-42.

Herrera, F., Manchester, S. R., Hoot, S. B., Wefferling, K. M., Carvalho, M. R., Jaramillo, C. 2011. Phytogeographic implications of fossil endocarps of Menispermaceae from the Paleocene of Colombia. American Journal of Botany 98 (12), 2004–2017.

Hounslow, M.W., White, H.E., Drake, N.A., Salem, M.J., El-Hawat, A., McLaren, S. J., Karloukovski, V., Noble, S.R., Hlal, O. 2016. Miocene humid intervals and establishment of drainage networks by 23 Ma in the central Sahara, southern Libya. Gondwana Research http://dx.doi.org/10.1016/J.gr.

Huang, Y.J., Ji, X.P., Su, T., Wang, L., Deng, C.L., Li, W.Q., Luo, H.F., Zhou Z.K. 2015. Fossil seeds of Euryale (Nymphaeaceae) indicate a lake or swamp environment in the late Miocene Zhaotong Basin of southwestern China. Science Bulletin 60, 1768-1777.

http://bioteaching.com/the-steinheim-basin-snail-series-part-1

İnci, U., Helvacı, C.,Yağmurlu, F. 1988. Stratigraphy of Beypazarı Neogene basin, Central Anatolia, Turkey. Newsletter Stratigraphy 18 (3), 165-182.

Kalafatcıoğlu, A., Uysallı, H. 1964. Beypazarı-Nallıhan-Seben civarının jeolojisi. Maden Tetkik Arama Enstitüsü Dergisi 62 (1), 1-11.

Karadenizli, L. 1995. Beypazari havzası (Ankara batısı) Üst Miyosen – Pliyosen jipsli serilerinin sedimantolojisi. Türkiye Jeoloji Bülteni 38 (1), 63-74.

Kazancı, N. 1979. Haramiköy konglomeralarının sedimanter özellikleri (Nallıhan KD/Ankara). Türkiye Jeoloji Kurumu Bülteni 22, 69-76.

Kazancı, N. 1980. Seben Bölgesinin Sedimantolojisi. Ankara Üniversitesi Fen Fakültesi Jeoloji Müh. Bölümü, Doktora Tezi (unpublished).

Lin, T. A., Yu, S., Liao, T., Xu, G. 2013. Fossil Seed from the Miocene Shihti Formation of Taiwan. Terrestrial Atmospheric and Oceanic Sciences 24 (4), part II, 731-735.

Lopez-Gomez, J., Arche, A. 1993. Sequence stratigraphy analysis and paleogeographic interpretation of the Buntsandstein and Muschelkalk Facies (Permo-Triassic) in the Iberian Ranges. Palaeogeography, Palaeoclimatology, Palaeoecology 103, 179- 201.

Martinius, A.W., Geel, J.L., Aribas, J. 2002. Lithofacies characterization of fluvial sandstones from outcrop gramma-ray logs (Larance Basin, Spain). The influence of provenance 8, 51-62.

Mueller, S., Hounslow, M.W., Kürschner, W.M. 2016. Integrated stratigraphy and palaeoclimate history of the Carnian Pluvial Event in the Boreal realm; new data from the Upper Triassic Kapp Toscana Group in central Spitsbergen (Norway). Journal of the Geological Society 173, 186-202.

Nemec, W., Postma, G. 1993. Quaternary alluvial fans in southwestern Crete: sedimentation processes and geomorphic evolution. In: Marzo, M., Puigdefàbregas, C. (Eds.), Alluvial Sedimentation Special Publications, International Association of Sedimentologists 17, 235–276.

Önal, M, Helvacı, C., İnci, U., Yağmurlu, F., Meriç, E., Tansel, İ. 1988. Çayırhan (KB) Ankara kuzeyindeki Soğukçam kireçtaşı, Nardin formasyonu ve Kızılçay gurubunun stratigrafisi, yaşı, fasiyes ve depolama ortamları. Türkiye Petrol Jeologları Derneği Bülteni 1/2, 132-163.

Pan, A.D., Currano, E.D., Jacobs, B.F., Feseha, M., Tabor, N., Herendeen, P.S. 2012. Fossil Newtonia (Fabaceae: Mimoseae) seeds from the Early Miocene (22–21 Ma) MushValley in Ethiopia. International Journal of Plant Sciences 173 (3), 290–296.

Runge, J. 2012. The African Neogene – Climate , Environments and People Palaeoecology of Africa. International Yearbook of Lanscape Evolution and Paleoenvironment , 34, CRC Press Taylor &Francis Group London, UK.

Saner, S. 1980. Mudurnu-Göynük havzasının Jura ve sonrası çökelim nitelikleriyle paleocoğrafya yorumlanması. Türkiye Jeoloji Kurumu Bülteni 23, 39-52.

Siyako, F. 1983. Beypazarı (Ankara) kömürlü Neojen havzasının ve çevresinin jeoloji raporu. Maden Tetkik ve Arama Genel Müdürlüğü, Rapor No:7431, Ankara (unpublished).

Stchepinsky, V. 1941*a*. Beypazarı-Nallıhan-Bolu bölgesinin jeolojisi ve mineral zenginlikleri. Maden Tetkik Arama Genel Müdürlüğü Enerji Hammadde Etüt ve Arama Dairesi Başkanlığı Rapor No: 1332 Ankara (unpublished).

Stchepinsky, V. 1941*b*. Beypazarı-Nallıhan-Bolu-Gerede bölgesinin genel jeolojik etüdü. Maden Tetkik Arama Genel Müdürlüğü Enerji Hammadde Etüt ve Arama Dairesi Başkanlığı Rapor No: 1363 Ankara (unpublished).

Tekin, F. 1977. Atca-Kızılöz-Yeşilyurt (Ankara ili) dolayının jeolojik incelemesi. İstanbul Üniversitesi Fen Fakültesi Temel Jeoloji Kürsüsü, Yüksek Lisans Tezi (unpublished).

Tunç, M. 1980. Davutoğlu (Beypazarı) – Seben (Bolu) arasında kalan ve Aladağçay boyunca olan bölgenin jeolojisi. Ankara Üniversitesi, Jeoloji Mühendisliği Bölümü Doktora Tezi (unpublished).

Tunç, M. 1984. Seben. (KB Ankara) yöresindeki Üst Kretase tortullarının biyostratigrafi incelemesi. Cumhuriyet Üniversitesi, Mühendislik Fakültesi Yerbilimleri Dergisi 1,19-30.

Wang, H., Blanchard, J., Dilcher, D.L. 2013. Fruits, seeds, and flowers from the Warman clay pit (middle Eocene Claiborne Group), western Tennessee, USA. Palaeontologia Electronica 16(3), 1-73.

Varol, B. 1980. Seben bölgesinin sedimantolojik etüdü: Ankara Üniversitesi Fen Fakültesi Jeoloji Mühendisliği Bölümü, Doktora Tezi (unpublished).

Varol, B., Kazancı, N. 1980. Seben Bölgesi Volkanotortulları (BOLU GD). Türkiye Jeoloji Kurumu Bülteni 23, 53 – 58.

Varol, B., Kazancı, N. 1981. Nallıhan-Seben (Bolu) bölgesinde Üst Jura-Alt Kretase karbonat istifinin lito ve biyofasiyes özellikleri. Türkiye Jeoloji Kurumu Bülteni 24 (2), 31-38.

Yabe, A. 2009. Early Miocene terrestrial climate inferred from plant megafossil assemblages of the Joban and Soma areas, Northeast Honshu , Japon. Bulletin of the Geological Survey of Japan 59, 397-413.

Yağmurlu, F., Helvacı, C. 1994. Sedimentological characteristics and facies of evaporite- bearing Kirmir Formation (Neogene), Beypazarı Basin, Central Anatolia, Turkey. Sedimentology 41, 1-14.

Yağmurlu, F., Helvacı, C., Inci, U. 1988. Depositional setting and geometric structure of Beypazarı lignite deposits, Central Anatolia. International Journal of Coal Geology 10, 337-360.

Yağmurlu, F., Helvacı, C., İnci, U. 1990. Tectonic characteristics and structural of the Beypazarı and Nallıhan Neogene basin, Central Anatolia. METU Journal of Pure and Applied Sciences 21 (1-3), 127-143.

Bulletin of the Mineral Research and Exploration

http://bulletin.mta.gov.tr

Utilization of pumice of Burdur region and zeolite of Bigadiç-Balıkesir region as fine aggregate in construction materials

Özge BEYCAN TATANOĞLU[a] and Niyazi Uğur KOÇKAL[b]*

[a]*Vocational School, Construction Technology Program, Antalya Akev University, Turkey*
[b]*Department of Civil Engineering, Akdeniz University, Turkey*

Research Article

Keywords:
Zeolite, Pumice, mineralogy, Chemical composition, Bulk density, Thermal conductivity.

ABSTRACT

Volcanic originated pumice and zeolite aggregates have low density owing to their considerable porous structure. Porosity is usually correlated with insulation properties. In order to examine the effects of this lightweight aggregates on dead load of structure and insulation properties of standard construction materials, samples were produced by using pumice and zeolite at varying percentages by volume and control samples were manufactured with crushed sand. The samples were exposed to normal (standard) curing, hot water curing and steam curing to observe the effect of different curing regimes on their behavior. Bulk density and thermal conductivity tests were carried out on samples. Both bulk density and thermal conductivity values of the lightweight mortar samples were smaller than those of control sample. Besides, chemical compositions of aggregates and cement, analyses were also performed. Silica content of pumice and zeolite were %54,09 and %75,14 by mass respectively.

Received Date: 23.10.2018
Accepted Date: 19.06.2019

1. Introduction

Cement, aggregate and water are the main components of most used construction materials namely concrete and mortar which are also called cement based materials (CBM). Aggregates have the largest share of % 60-70 by volume in CBM mixtures and any of their properties such as density, porosity, strength, durability, chemical structure directly affect CBM properties. Crushed stone and sand are the common used aggregates in conventional CBM due to their abundance beside their beneficial properties. However, their density values are between 2,60-2,70 g/cm^3 and with the improvements in structural engineering, high buildings have begun to be constructed and dead load were becoming more of a problem than in the past. In addition to this, the majority of the human population have started to live in the metropolitans and given birth to vertical architecture. As a result, the protection of the private area has become difficult and the sound insulation has come to the forefront. From an environmental point of view, too much energy is consumed to heat and cool the buildings, thus increasing the carbon dioxide emission (Koçkal, 2016). Recent studies have been carried out by researchers on construction materials which had low density and functional for heat and sound insulation (Patnai et al., 2015, Degrave-Lemeurs et al., 2018).

Materials used for improvement of CBM properties demonstrate considerable diversity. Zhang and Poon (2015) used lightweight expanded clay aggregate to reduce the density of CBM and furnace bottom

Citation Info: Beycan Tatanoğlu, Ö., Koçkal, N. U. 2020. Utilization of pumice of Burdur region and zeolite of Bigadiç - Balıkesir region as fine aggregate in construction materials. Bulletin of the Mineral Research and Exploration. 161, 193-202. https://doi.org/10.19111/bulletinofmre.593558

* *Corresponding author: Niyazi Uğur KOÇKAL, ukockal@yahoo.com*

ash for producing thermal insulation properties. As far as their conclusions, lightweight expanded clay aggregate CBM containing furnace bottom ash is suitable for structural use and with the increase of furnace bottom ash thermal conductivity decreased. In terms of improving thermal properties of CBM, some researchers used waste materials such as pet and rubber pieces (Yeşilata et al., 2009) and in other study was carried out to use coconut fibres in order to prevent effect of solar heat radiation (Mintorogoa et al., 2015). However, lightweight aggregates mostly possess structural properties besides insulation ones. Morover, plenty of natural or artificial lightweight aggregates for instance; pumice (Widodo et al., 2017), zeolite (Najimi et al., 2012), perlite (Şengül et al., 2011), vermiculite (Schackow et al., 2014), sintered fly ash (Koçkal and Özturan, 2010; Koçkal and Özturan 2011*a*, *b;* Koçkal, 2015) expanded clay (Fantilli et al., 2016) etc. were incorporated to develop CBM characteristics.

The purpose of this research is to investigate usability of volcanic originated pumice and zeolite particles as aggregate to improve bulk density and the thermal properties of mortars which are classified under CBM. Meanwhile, how different curing regimes affect these properties are also discussed.

2. Materials and Method

2.1. Materials

CEM-I 42.5 R Portland cement without any type of admixture was used as binder in the mortar mixtures, its specific gravity was 3,03 g/cm^3. The meaning of notation R is for rapid setting and it obligates this characteristic to be ground ultra fine and high content of C_3S which is one of the four main compounds compared to conventional cements.

The pumice aggregate was supplied from Burdur (Ağlasun) region and zeolite aggregate was obtained from Balıkesir (Bigadiç) region. The location map of aggregate sources were given in figure 1. The physical properties of aggregates were tested according to ASTM C 128, ASTM C 29 and ASTM C 97. The results of specific gravity, water absorption, porosity, modulus of fineness, loose and rodded unit weight were given in a previous study (Beycan and Koçkal, 2017). According to TS EN 933-1 and ASTM C-136, sieve analysis of aggregates were performed and the results are given in table 1.

It is clearly noticed that all the aggregates were smaller than 4mm. Owing to the % 80 passing value of particles through 1-mm sieve, pumice and zeolite aggregates were accepted ultra fine aggregates. Crushed sand had the coarsest particles containing %37 of total particles under 1mm. Seraj et al. (2017) performed an investigation with different particle size of pumice aggregate and remarked that reducing particle size increased the rates of cement hydration, pozzolanic reaction, and compressive strength gain, while also increasing mixture viscosity.

Figure 1- Location map of the aggregate sources (Bigadiç and Ağlasun).

X-ray fluorescence (XRF) analysis was performed at the Izmir High Technology Institute Material Research Center. For each component, an average of 1,5 g powder sample was prepared and the SPECTRO-IQ II device was used. X-ray fluorescence (XRF) analysis was conducted to obtain chemical composition of fine aggregates and cement which are given in table 2 with loss on ignition values. The loss on ignition measures the mass loss of volatile materials such as carbon dioxide and water but also alteration level in the materials under high temperature exposure. The major oxides of pumice aggregate were SiO_2 and Al_2O_3 with the percentage of 54,09%, 21,68 by weight respectively. The major oxides measured in the zeolite aggregate were the same as those of the pumice aggregate. But the percentages were different and in order of 75,14% and 14,71. Both fine aggregates had high SiO_2 content. There are several studies in which minerals with high SiO_2 content, if they are ground as fine as cement, they can be used as cement replacement materials (Chen et al., 2017). On the other hand the major oxide of crushed sand was CaO with the percentage of 54,01%. When evaluated L.O.I. value of samples, it was seen that zeolite and crushed sand had higher values within the group.The reasons of high L.O.I. values in zeolite and crushed sand could be explained as follows: Zeolites were chemically known as aqueous alumina silicates. Coombs et al. (1997) stated that zeolites had a large number of water molecules attached to the clinoptilolite mineral. At high temperatures, the attached water evaporated and therefore the L.O.I value of zeolite was high. Crushed sand was a calcium carbonate ($CaCO_3$) originated aggregate and under high temperature exposure, $CaCO_3$ decomposed into CaO and CO_2. As a result of CO_2 output, L.O.I. value was high (Topçu and Demir, 2007).

The mineral phases of fine aggregates were detected with the help of X-ray diffraction method (XRD), which is based on the principle of breaking X-rays in a characteristic order, depending on the specific atomic sequences of each crystal phase. XRD analysis results are exhibited on figure 2 and 3. ($Si_{29,04}Al_{6,96}O_{96,40}Na_{1,92}Ca_{1,57}Ba_{0,32}K_{0,56}Mg_{0,72}$) chemical formulated clinoptilolite was the common mineral phase appeared in zeolite, quartz (Si_3O_6) and orthoclase ($Si_{12}Al_4K_4O_{32}$) were encountered rarely.

Clinoptilolite had microporous structure and high surface area. The basic units of the crystal structure of clinoptilolite, SO_4 and AlO_4 tetrahedrals, combined to form a secondary structure and it is illustrated in figure 4. The secondary structure united with different combinations and created a porous and channeled form. These channels and porosities constituted a significant surface area by providing void volume of 30% - 35% (Ersoy, 2000).

Major phase crystalline of pumice was feldspar ($Si_{9,04}Al_{6,96}Sr_{3,36}Na_{0,12}O_{32}$) and another mineral was coesite ($Si_{16}O_{32}$) identified in structure. Feldspar is a monoclinic crystal. Feldspars are the most common mineral in the rocks and compose nearly 60% of the earth's crust (Xu et al., 2017). When the previous studies were examined, it was seen in figure 5, the main mineral phase was feldspar in the petrographic analyzes performed on pumice (Döyen and Aksoy, 2013).

Table 1- Sieve analysis of aggregates.

Cumulative Passing(%)	Aperture Size (mm)	4	2	1	0,5	0,25	0,125	0,063
	Pumice	100	91	76	63	44	26	13
	Zeolite	100	100	77	53	27	8	1
	Crushed Sand	100	62	37	25	15	9	4

Table 2- Chemical composition of constituents (by weight%).

Constituents	Na_2O	MgO	Al_2O_3	SiO_2	SO_3	K_2O	CaO	Fe_2O_3	L.O.I.[a]	T.A.M.O.[b]
Cement	0,1	1,77	4,28	19,28	2,95	0,58	61,36	2,65	4,01	80,64
P	8,23	1,89	21,68	54,09	0,18	6,10	4,03	2,48	3,55	75,77
Z	<0,11	1,22	14,71	75,14	0,01	2,80	4,21	1,28	10,94	89,85
CS	0,08	1,02	0,64	3,94	-	-	54,01	0,11	40,81	54,01

[a] Loss on ignition

[b] Total amount of major oxide

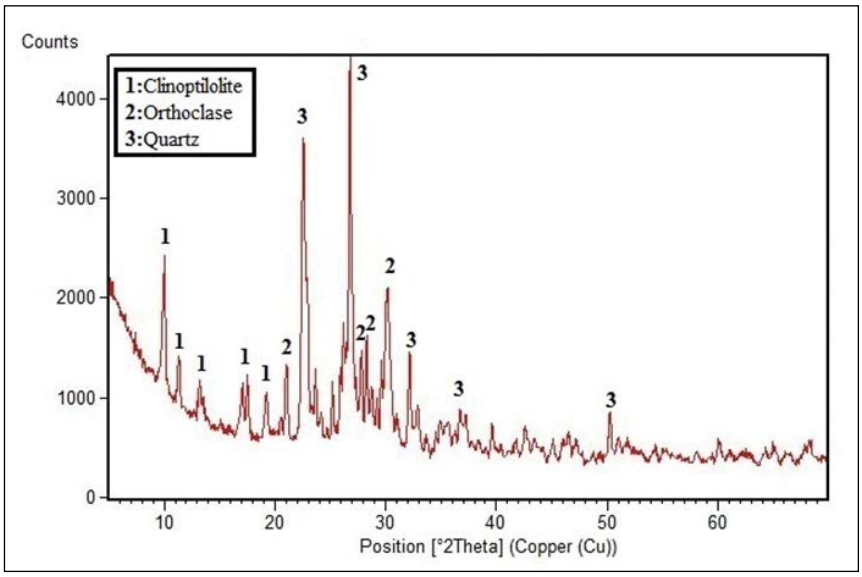

Figure 2- XRD patterns of zeolite.

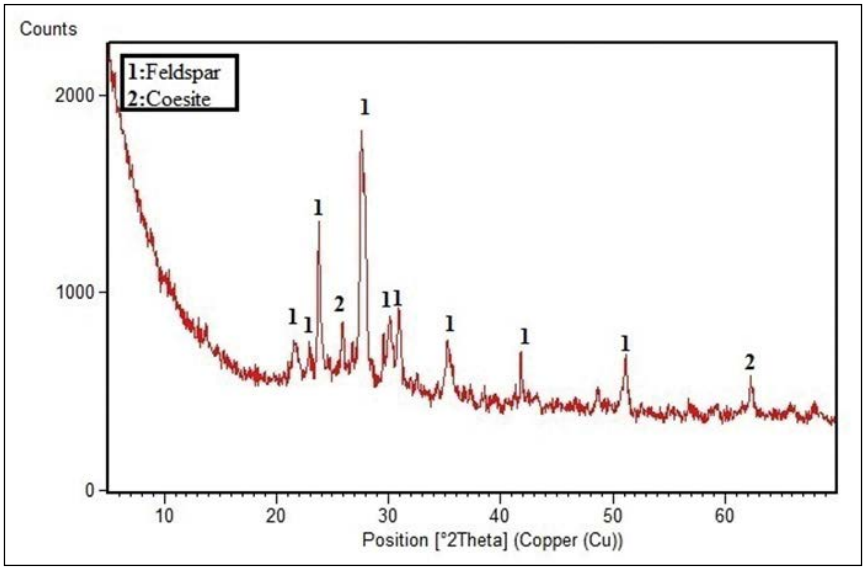

Figure 3- XRD patterns of pumice.

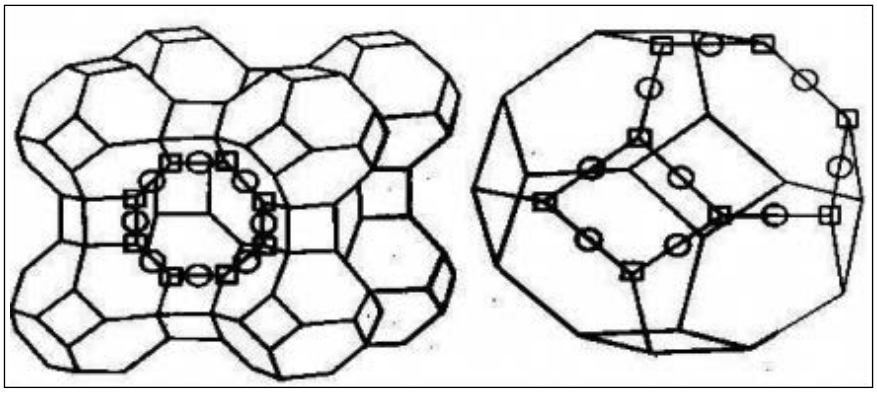

Figure 4- Connecting zeolite to tetrahedral (Akay et al., 2018 figure 1).

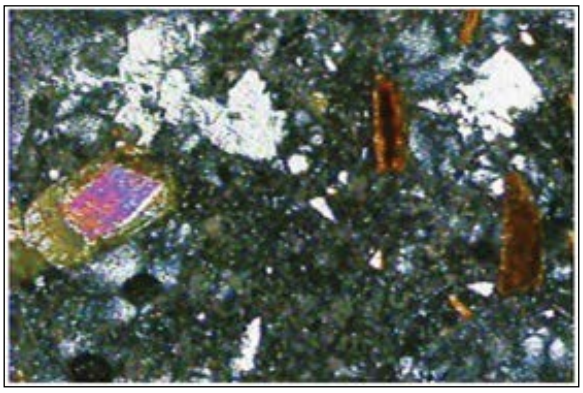

Figure 5- Feldspar mineral in pumice sample (gray) (Döyen and Aksoy, 2013).

Bilgin and Kantarcı (2018) investigated the technologic properties of zeolite formations in Balıkesir Bigadiç region. Three different zeolite samples were examined and in XRD analyzes the main mineral phase was found to be clinoptilolite. However, in petrographic analysis, quartz minerals were more visible (Figure 6).

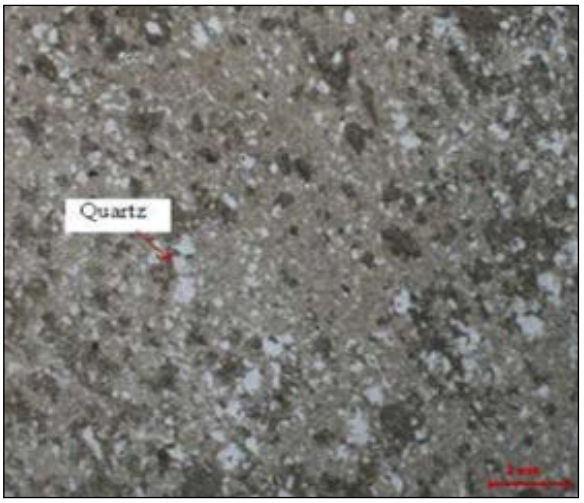

Figure 6- Quartz mineral in zeolite sample (Bilgin and Kantarcı, 2018).

Zeolite and pumice aggregates were used with five different replacement ratios by volume in mortars (Table 3). With the guidance of trial mixes, the pumice aggregate was put into mixtures in saturated surface dry condition for proper workability. The zeolite aggregate was in air dry condition before mixing and additional water for absorption was introduced into the mixture. Water-cement ratio was selected as 0.6, so that the cement paste could surround the aggregate surface and maintain sufficient workability. The cement content was kept constant as 300 kg/m^3 in all mixtures.

Mortars were placed into the 40x40x160mm prismatic steel molds, after demoulding at 24h, the samples were exposed to three different curing regimes; normal curing (NC), hot water curing (HC) and steam curing (SC). NC samples were maintained in a lime saturated water tank to cure at 20 ± 2°C for 7 days, HC samples were immersed 60°C in lime saturated water for 2 days and at the end of that exposure then placed into NC tank in until 7th day, SC samples were stored in steam curing cabinet at 90% relative humidity (RH) and 50°C for 7 days.

Table 3- Mix design ratios of mortars.

Design Code	Replacement Ratio by Volume (%)		
	Zeolite	Pumice	Sand
A	70	30	–
B	60	40	–
C	50	50	–
D	40	60	–
E	30	70	–
CS	–	–	100

2.2. Experimental Methods

The unit weight test on fresh mortars was performed as follows: The fresh mortar was poured into container in two stages and in every stage it was rodded 25 times with a steel bar. After that, the container was weighed and achieved the result by dividing this weight to the volume.

The workability of mortars were measured with ASTM C230 flow-table test (Figure 7). The mortar was placed into special cone specified in the standard. Afterwards the cone was raised upward slowly and the arm was rotated for certain times to spread the mortar on the table. The flow diameter was obtained by measuring the diameter from both x and y axis and taking the average of them.

The bulk density values were obtained by testing 40x40x160 mm prism samples according to ASTM C 642 (Figure 8). Oven dry (OD) bulk density and saturated surface dry (SSD) bulk density were calculated below:

$$OD = W1 / (W2 - W3) \quad (1)$$

Figure 7- The workability test aparatus.

Figure 8- The test set up for determination of bulk density.

$$SSD = W1/(W1-W3) \quad (2)$$

W1 is the mass of oven-dried sample in air (g), W2 is the mass of surface-dry sample in air (g) and W3 is the mass of surface-dry sample in water (g) (Koçkal, 2016).

Thermal conductivity values of mortars were determined by the guarded hot plate method ASTM C 177. The side surfaces of the samples were covered with glass wool to prevent heat scattering. In this experiment, thermographic camera was used to monitor the temperature difference of thermally insulated sample surfaces until a constant temperature value has been reached (Figure 9).

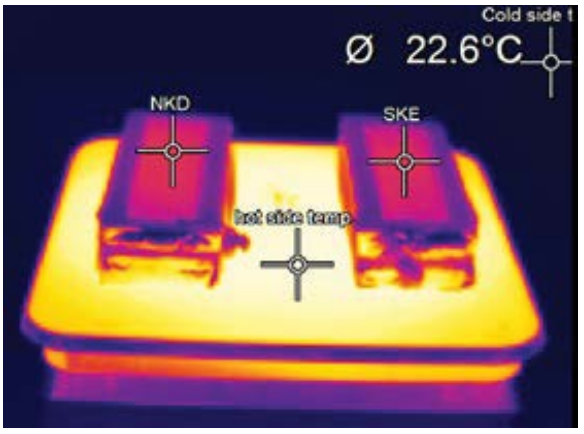

Figure 9- Thermographic camera image of mortars with different lightweight aggregate combinations.

The thermal conductivities of the samples were calculated relatively according to the control sample herein below:

$$RTC=((HST-CCS)x100)/CM \quad (3)$$

RTC is the relative thermal conductivity (%), HST is the hot side temperature and kept constant at 100°C, CCS is the constant temperature of the steam cured control sample top surface temperature (°C). CM is the constant temperature top surface of lightweight mortar sample (°C).

3. Results and Discussion

The flow-table test results and unit weight values are given in table 4. With the increase of pumice aggregate ratio, unit weight values increased smilarly, in contrast to flow diameter. However, compared to the control sample all lightweight mortar samples had lower unit weight and better workability. Gündüz and Uğur (2005) reported that using fine and coarse pumice aggregate reduced the unit weight of conventional CBM and in addition to this, the elasticity modulus was decreased in contrast to the capability of energy absorbsion namely toughness.

On the other hand, the reason of better workability with increasing zeolite volume was attributed to mixing procedure. The zeolite aggregates absorbed water was added into the mixing water and this fact directly affected fresh properties of mortars. Besides, some researchers indicated that in some cases, incorporation of zeolite reduced fresh properties

of CBM such as the value of flow table test and V box test. The results of workability properties of CBM including natural zeolite, carried out by Ramezanianpour et al. (2015) and they showed that use of natural zeolite increased water demand of CBM. Ranjbar et al. (2013) investigated the effect of using zeolite as a replacement material with cement on fresh properties of self compacted CBM. According to the experimental results, zeolite which was ground as fine as cement, impact workability negatively.

Table 4- Physical properties of fresh mortars.

Mix	Unit Weight (g/dm^3)	Flow Diameter (cm)
A	1765	>25
B	1814	15,75
C	1817	14,4
D	1843,7	14,35
E	1866,5	14,26
CS	2421,9	12,4

SSD bulk density and OD bulk density values are shown in figure 10 and 11. SSD bulk densities of lightweight mortars were varying from 1,755 to 1,879. Morover, the positive effect of lightweight aggregates is perfectly seen with OD bulk density values between 1,358 and 1,575 when compared with the value of control sample which is 2,177. SCA mortar had the lowest SSD and OD bulk density. Actually, the samples produced with same aggregate combination ratio, generally had the lowest both SSD and OD bulk density when they were cured in steam curing. Ba et al. (2011) carried out a study on the development of voids and pore characteristic of samples exposed to steam curing for different durations. According to the mercury intrusion porosimetry method, coarse porosity increased with duration of initial steam curing.

Owing to increasing pumice aggregate volume in mortar samples, bulk densities increased. Hot water curing regime especially affected OD bulk density of in a positive manner. Arel (2016) remarked that hot-water curing regime affects compressive strength initialy more pronounced than steam and standard curing regimes. It can be deduced from this explanation that hot water curing regime contributes to the formation of absolute structure. Another parallel research was published by Koçkal et al. (2018). They noticed that the mechanical properties of mortars such as flexural and compressive strength were increased with the increase of OD bulk densities of mortars.

Relative thermal conductivity test results are illustrated in figure 12. Because of the thermal conductivity increases in accordance with the amount of moisture (Young, 1988), before the experiments, the samples were kept in 90 ^{o}C heated oven for 24h to evaporate pore water. OD bulk density values were in a correlative relationship with the relative thermal conductivity values of the samples. SCA sample with the smallest OD bulk density had the lowest relative thermal conductivity value.

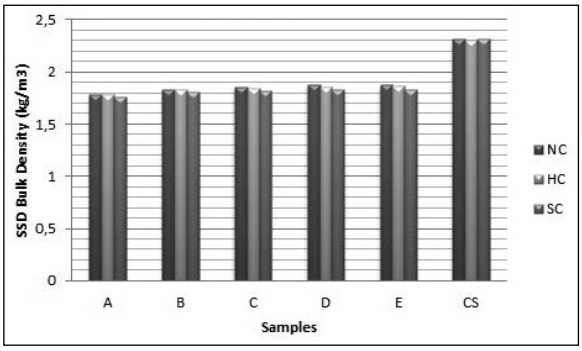

Figure 10- SSD bulk density values.

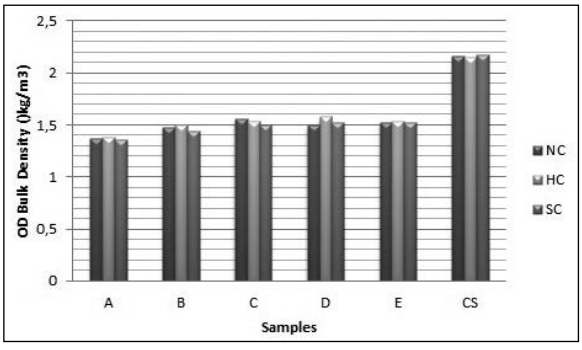

Figure 11- OD bulk density values.

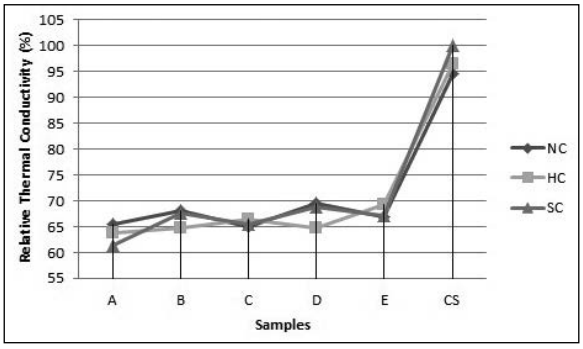

Figure 12- Development of relative thermal conductivity of mortars subjected to different curing conditions.

The lowest and the highest relative thermal conductivity values were 61,30% and 69,55% respectively. It can be seen that the aggregate type had an influence on thermal properties of mortars and pumice aggregate concentration was directly proportional to the relative thermal conductivity of mortars (Zhu et al., 2015). Even though, among lightweight mortars, the relative thermal conductivity increased with the incremental ratio of pumice, the thermal properties were better than the control mortars. The study was arranged by Amel et al. (2017) supporting that fact. The researchers prepared CBM samples with dune sand and pumice aggregate. The heat transfer and bulk density values of CBM samples were decreased with increasing rate of pumice aggregate.

The samples including high volume of zeolite aggregate, had lower relative thermal conductivity. Porosity is generally correlated with thermal conductivity. Nagrockiene and Girskas (2016) examined the properties of CBM modified with natural zeolite addition and it is stated that natural zeolite increased the closed porosity.

4. Conclusions

Following conclusions can be drawn from the experimental study:

- Volcanic originated lightweight aggregates can be preferred in special applications to produce building materials with special qualities.

- Utilisation of pumice and zeolite as fine aggregate resulted benefits in fresh properties of mortars. According to the value of flow table test, workability of lightweight mortars were improved resulting in reduction of labor demand and costs.

- Both OD and SSD bulk density of the lightweight mortar samples were smaller than those of control sample. Thus, zeolite and pumice aggregate can be used as an alternative construction material to reduce the self weight of structures.

- There was a corelation between OD bulk density and relative thermal conductivity values. SCA sample with the smallest OD bulk density had the lowest relative thermal conductivity value.

- The relative thermal conductivity values of lightweight mortars were approximately 40% smaller than those of the control sample. On the other hand, there wasn't any proof about the significant effect of different curing regimes on the relative thermal conductivity.

Acknowledgments

This research was supported by Scientific Research Projects Coordination Unit of Akdeniz University by the project number of 1278.

References

Akay, O.E., Gizlenci, Ö.S., Sönmez, K. 2018. Bir kurutma sisteminde kullanılan zeolit kurutma yatağının adsorpsiyon performansının deneysel olarak incelenmesi. KSÜ Mühendislik Bilimleri Dergisi 21(1):100-106.

Amel, C.L., Kadri, E., Sebaibi, Y., Soualhi, H. 2017. Dune sand and pumice impact on mechanical and thermal lightweight concrete properties. Construction and Building Materials 133: 209–218.

Arel, H.S. 2016. Effects of curing type, silica fume fineness, and fiber length on the mechanical properties and impact resistance of UHPFRC. Results in Physics 6: 664-674.

ASTM C 177, Standard Method for Steady-State Heat Flux Measurements and Thermal Transmission Properties by Means of the Guarded Hot Plate Apparatus, American Society for Testing and Materials, Annual Book, West Conshohocken, PA, 2004.

ASTM C 642, Standard test method for density, absorption, and voids in hardened concrete, American Society for Testing and Materials, Annual Book, Pennsylvania, USA, 2013.

ASTM C128-15, Standard Test Method for Relative Density (Specific Gravity) and Absorption of Fine Aggregate, ASTM International, West Conshohocken, PA, 2015.

ASTM C136 / C136M-14, Standard Test Method for Sieve Analysis of Fine and Coarse Aggregates, ASTM International, West Conshohocken, PA, 2014.

ASTM C230, Standard Specification for Flow Table for Use in Tests of Hydraulic Cement, ASTM International, West Conshohocken, PA, 2014.

ASTM C29 / C29M-17a, Standard Test Method for Bulk Density ("Unit Weight") and Voids in Aggregate, ASTM International, West Conshohocken, PA, 2017.

ASTM C97 / C97M-18, Standard Test Methods for Absorption and Bulk Specific Gravity of Dimension Stone, ASTM International, West Conshohocken, PA, 2018.

Ba, M., Qian, C., Guo, X., Han, X. 2011. Effects of steam curing on strength and porous structure of concrete with low water/binder ratio. Construction and Building Materials 25: 123–128.

Beycan, O., Koçkal, N.U. 2017. Properties of mortars with ultrafine aggregates. International Journal of Advances in Mechanical and Civil Engineering 4: 64-67.

Bilgin, Ö., Kantarcı, S. 2018. Bigadiç (Balıkesir, Türkiye) Civarında Gözlenen Höylandit/Klinoptilolit Zeolit Oluşumlarının Teknolojik Özelliklerinin İncelenmesi. Journal of Balıkesir University Institute of Science and Technology 20(1):589-601.

Chen, J.J., Li, L.G., Ng, P.L., Kwan, A.K.H. 2017.Effects of superfine zeolite on strength, flowability and cohesiveness of cementitious paste. Cement and Concrete Composites 83: 101-110.

Coombs, D.S. , Alberti, A., Armbruster, T., Artioli, G., Colella, C., Galli, E., Grice, C. D., Liebau, F., Minato, H., Nickel, E.H., Passaglia, E., Peacor, D.R., Quartieri, S., Rinaldi, R., Ross, M., Sheppard, R.A., Tillmans, E., Vezzalini, G. 1997. Recommended nomenclature for zeolite minerals: Report of the subcommittee on zeolites of the international mineralogical association, commission on new minerals and mineral names. The Canadian Mineralogist 35:1571-1606.

Degrave-Lemeurs, M., Glé, P., Hellouin de Menibus, A. 2018. Acoustical properties of hemp concretes for buildings thermal insulation: Application to clay and lime binders. Construction and Building Materials 160: 462–474.

Döyen, A., Aksoy, E. 2013. Isparta ve Gelincik Pomza Yataklarının Jeolojisi ve Beton Yapımına Uygunluğunun Araştırılması. Selcuk University Journal of Engineering, Science and Technology 28:25-34.

Ersoy, B. 2000. Clinoptilolite (Natural zeolite): properties, use and the importance of Turkey. Afyon Kocatepe University Journal of Sicience 2(1):41-52. (In Turkish, with English summary.)

Fantilli, A.B., Chiaia, B., Gorino, A. 2016. Ecological and mechanical assessment of lightweight fiber-reinforced concrete made with rubber or expanded clay aggregates. Construction and Building Materials 127: 692–701.

Gündüz, L., Uğur, I. 2005. The effects of different fine and coarse pumice aggregate/cement ratios on the structural concrete properties without using any admixtures. Cement and Concrete Research 35: 1859 – 1864.

Koçkal, N.U. 2015. Optimizing production parameters of ceramic tiles incorporating fly ash using response surface methodology. Ceramics International 41: 14529-14536.

Koçkal, N.U. 2016. Investigation about the effect of different fine aggregates on physical, mechanical and thermal properties of mortars. Construction and Building Materials 124: 816-825.

Koçkal, N.U., Özturan, T. 2010. Effects of lightweight fly ash aggregate properties on the behavior of lightweight concretes. Journal of Hazardous Materials 179: 954–965.

Koçkal, N.U., Özturan, T. 2011*a*. Characteristics of lightweight fly ash aggregates produced with different binders and heat treatments. Cement and Concrete Composites 33: 61-67.

Koçkal, N.U., Özturan, T. 2011*b*. Optimization of properties of fly ash aggregates for high-strength lightweight concrete production. Materials and Design 32: 3586-3593.

Koçkal, N.U., Beycan, O., Gülmez, N. 2018. Effect of binder type and content on physical and mechanical properties of geopolymer. Sådhanå 43:49.

Mintorogoa, D.S., Widigdoa, W.K., Juniwatia, A. 2015. Application of coconut fibres as outer eco-insulation to control solar heat radiation on horizontal concrete slab rooftop. Procedia Engineering 125: 765 – 772.

Nagrockiene, D., Girskas, G. 2016. Research into the properties of concrete modified with natural zeolite addition. Construction and Building Materials, 113: 964–969.

Najimi, M., Sobhani, J., Ahmadi, B., Shekarchi, M. 2012. An experimental study on durability properties of concrete containing zeolite as a highly reactive natural pozzolan. Construction and Building Materials 35:1023–1033.

Patnai, A., Myubu, M., Muniyasamy, S., Botha, A., Anandijwala, R.D. 2015. Thermal and sound insulation materials from waste wool and recycled polyester fibers and their biodegradation studies. Energy and Buildings 92: 161-169.

Ramezanianpour, A.A., Mousavi, R., Kalhori, M., Sobhani, J., Najimi, M. 2015. Micro and macro level properties of natural zeolite contained concretes. Construction and Building Materials 101: 347–358.

Ranjbar, M.M., Madandoust, R., Mousavi, S.Y., Yosef, S. 2013. Effects of natural zeolite on the fresh and hardened properties of self-compacted concrete. Construction and Building Materials 47: 806–813.

Schackow, A., Effting, C., Folgueras, M.V., Güths, S., Mendes, G.A. 2014. Mechanical and thermal properties of lightweight concretes with vermiculite and EPS using air-entraining agent. Construction and Building Materials 57: 190–197.

Şengül, O., Azizi, S., Karaosmanoğlu, F., Taşdemir, M.A. 2011. Effect of expanded perlite on the mechanical properties and thermal conductivity of lightweight concrete. Energy and Buildings 43: 671–676.

Seraj, S., Cano, R., Ferron, R.D., Juenger, M.C.G. 2017. The role of particle size on the performance of pumice as a supplementary cementitious material. Cement and Concrete Composites 80: 135-142.

Topçu, İ.B., Demir, A. 2007. Research of fire and high temperature effects on concretes produced with waste crushed tile. ICSW 2007, The Twenty-Second International Congerence on Solid Waste Technolgy and Management, Philadelphia,USA.

TS EN 933-1 Tests for geometrical properties of aggregates - Part 1: Determination of particle size distribution - Sieving method, Turkish Standarts 2012.

Widodo, S., Ma'arif, F., Gan, B.S. 2017. Thermal condactivity and compressive strength of lightweight mortar utilizing pumice breccia as fine aggregate. Procedia Engineering, 471: 768-773.

Xu, L., Tian, J., Wu, H., Deng, W., Yang, Y., Sun, W., Gao, Z., Hu, Y. 2017. New insights into the oleate flotation response of feldspar particles of different sizes: Anisotropic adsorption model. Journal of Colloid and Interface Science 505: 500–508.

Yeşilata, B., Işıker, Y., Turgut, P. 2009.Thermal insulation enhancement in concretes by adding waste PET and rubber pieces. Construction and Building Materials 23: 1878–1882.

Young, J.F. 1988. A review of the pore structure of the cement paste and concrete and its influence on permeability, American Concrete Institute, Detroit pp. 1-18.

Zhang, B., Poon, C.S. 2015. Use of Furnace Bottom Ash for producing lightweight aggregate concrete with thermal insulation properties. Journal of Cleaner Production 99: 94-100.

Zhu, L., Dai, J., Bai, G., Zhang, F. 2015. Study on thermal properties of recycled aggregate concrete and recycled concrete blocks. Construction and Building Materials 94: 620–628.

1. Aims of Publication

- To announce and share researches in all fields of geoscientific studies in Turkey with geoscientists worldwide.
- To announce scientific researches and practices on geoscientific surveys carried out by the General Directorate of Mineral Research and Exploration (MTA) to the public.
- To use the journal as an effective media for international publication exchange by keeping the journal in high quality, scope and format.
- To contribute to the development of Turkish language as a scientific language.

2. Scope

At least one of the following qualifications is required for publishing the papers in the Bulletin of Mineral Research and Exploration.

2.1. Research Articles

2.1.1. Original Scientific Researches

- These articles cover and contribute to the main subjects of the earth sciences, the original scientific researches and its results related to all aspects of disciplines in geoscience like exploration and evaluation of the underground sources and environmental problems, and
- The studies, which apply new aspects and methods for the solution of problems about the earth sciences and researches, which apply new aspects and methods for the solution of the problems, in the engineering sciences carried out in MTA.

2.1.2. Review Articles

These papers include comphrehensive scholarly review articles that summarize and critically assess previous geoscientific researches with a new perspective and reveal a new approach.

2.2. Discussion/Reply

- This type of article is intended for the discussion of papers that have already been published in the latest issue of the Bulletin. The discussion/reply type articles, which criticize all or a part of a recently published article, are published in the following first issue if it is submitted within six months after the publication of the Bulletin.
- The discussions are sent to the corresponding author of the original paper to get their reply before publication. The discussions abut the paper with two or more authors are sent only to the corresponding author.
- If the review article is not published within the prescribed preiod then it is published alone. Later sent replies are not published. Re-criticising of the replies is not allowed.
- The authors should obey the rules of scientific ethics and discussions in their discussion/reply papers. The papers in this category should not exceed four printed pages of the journal including figures and tables etc. The format of the papers should be compatible with the "Spelling Rules" of the Bulletin.

2.3. Short Notes

- The short notes part of the Bulletin covers short, brief and concisely written research reports for papers including the data obtained from ongoing and/or completed scientific researches and practices related to geoscience and new and/or preliminary factual findings from Turkey and worldwide.
- The short notes will follow a streamlined schedule and will normally be published in the following first or second issue shortly after submission of the paper to the Bulletin.
- This type of articles should not exceed four printed pages of the journal including figures, tables and an abstract.

3. Submission and Reviewing of Manuscripts

- Manuscript to be submitted for publishing in the Journal must be written clearly and concisely in Turkish and/or English and prepared in the Bulletin of Mineral Research and Exploration style guidelines. All submissions should be made online at the http://dergi.mta.gov.tr website.
- The manuscript submitted for reviews must not have been published partially or completely previously in another journal.
- The rejected manuscripts are not returned back to

author(s) whereas a letter of statement indicating the reason of rejection is sent to the corresponding author.

- Submitted manuscripts must follow the Bulletin style and format guidelines. Otherwise, the manuscript which does not follow the journals' style and format guidelines, is given back to corresponding author without any reviewing.
- Every manuscript which passes initial Editorial treatise is reviewed by at least two independent reviewers selected by the Editors. Reviewers' reports are carefully considered by the Editors and associated editors.
- The manuscript that need to be corrected with the advices of reviewer(s) is sent back to corresponding author(s) to assess and make the required corrections suggested by reviewer(s) and editors. The authors should prepare a letter of well-reasoned statement explaining which corrections are considered or not.
- If there are any suggestions given by editors and referees that are not accepted and corrected by the author, then it should be sent to the Editor's Office with corrected copies of the report explaining the reason for not accepting these suggestions and corrections.
- Figures and tabless should be 1/3 of the main text.
- To be published in the Bulletin of Mineral Research and Exploration, the printed lenght of the manuscript should not exceed 30 printed pages of the journal including an abstract, figures and tables. The publication of longer manuscripts will be evaluated by Editorial Board if it can be published or not.
- The authors must do the reviewer's corrections and proposals in 60 days and must upload to the system.
- At the printing stage after the last control, the first print of the manuscript are sent to the author/ authors in pdf version and asked from the author/ authors to make the press control.

4. Publication Language and Periods

- The Bulletin of Mineral Research and Exploration is published at least twice a year and each issue is published both in Turkish and English. Thus, the manuscripts are accepted in Turkish or English. The spelling and punctuation guidelines of Turkish Language Institution are preferred for the Turkish issue. However, the technical terms related to geology are used in accordance with the decision of the Editorial Board.

5. Spelling Draft

Manuscripts should be written in word format in A4 (29,7 x 21 cm) size and double-spaced with font size Times New Roman 10-point, margins of 25 mm at the sides, top and bottom of each page.

The formulas requiring the use of special characters and symbols must be submitted by the symbols part of the Microsoft Office Word Program on computer.

Initial letters of the words in sub-titles must be capital. The first degree titles in the manuscript must be numbered and left-aligned, 10 point bold Times New Roman must be used. The second degree titles must be numbered and left-aligned, they must be written with 10 point normal Times New Roman. The third degree titles must be numbered and left-aligned, they must be written with 10 point italic Times New Roman. The fourth degree titles must be left-aligned without having any number; 10 point italic Times New Roman must be used. The text must continue placing a colon after the title without paragraph returns (See: Sample article: http://bulletin.mta.gov.tr).

One line spacing must be left after paragraphs within text.

Paragraphs must begin with 0,5 mm indent.

The manuscript must include the below sections respectively;

o Title Page

o The Name and Surname of the author and * sign (Adress, e-mail adres must be given at the bottom of the page)

o Abstract

o Key Words

o Introduction

o Body

o Discussion

o Conclusion

o Acknowledgements

o References

5.1. Title Page

The title must be short, specific and informative and written with small letters font size Times New Roman 10-point bold. The title mustn't contain the subjects insufficiently processed in the article.

5.2. Author(S)'S Name, Addresses and Email Address

- The name and surname of the author/authors must be written without affiliations. Name must be written in small letters, the surname must be written in capital letters.
- At the affiliation (work adres) written after the name and the surname of the author/authors only the name of the company must be written, the author's job mustn't be written.
- Information about the adresses must be given at the next line as 10-point and italic.
- ORCID number should be taken from www.orcid.org and placed below the address.
- At the articles with two or more than two authors, the numbers must be written above the surnames of the authors, the informations about their adresses must be given at the next line by leaving one space line. Also, at this part the corresponding author must be indicated by the (*) symbol and the telephone, FAX and e-mail address of the corresponding author must be given.
- Abbreviations must not be made while writing the name of the uthor and the affiliation adres. Adresses must be given in Turkish in the Turkish version, in English in the English version.
- At the end of the article the name of the corresponding author and contact informations must be added.

5.3. Abstract

- The abstract must be understandable before having a look at the text.
- The abstract should state briefly the overall purpose of the research, the aim of the article, its contributions to the known theories, new data, principle results and major conclusions.
- Tha abstract must contain short and brief sentences.
- Addressing other sections and illustrations of the text or other writings must be avoided.
- The information, which have not been mentioned in the text, must not be in the abstract.
- The article must be written as one paragraph, preferably. Please provide an abstract which doesn't exceed 200 words.
- The abstract must be written with 10-point, normal Times New Roman in single-spaced lines.
- "Abstract" must not be given for the writings that will be located in "Short Notes" section.
- The English abstract must be under the title of "Abstract".

5.4. Key Words

Immediately after the abstract, please provide up to 5 key words and with each words seperated by comma. These key words will be used for indexing purposes.

5.5. Introduction

- The introduction section should state the objectives of the work, research methods, location of the study area and provide an adequate and brief background by avoiding a detailed literature survey.
- Non-standard or uncommon classifications or abbreviations should be avoided. But if essential, then they must be defined at their first mention and used consistently thereafter. Seperate paragraphs could be organized for each of the subjects at the introduction part. If it is necessary, the subtitle can be given for each of them (for example method, material, terminology etc.).
- When pre-information is needed for facilitating the understanding of the text, this section can also be used (for example, statistical data, bringing out the formulas, experiment or application methods, and others).

5.6. Body

- In this chapter, there must be data, findings and opinions that are intended to convey to the reader about the subject. The body section forms the main part of the article.
- The data used in other sections such as "Abstract", "Discussions", and "Results" are caused by this section.
- While processing the subject, the care must be taken not to go beyond the objective highlighted in the "Introduction" section. The knowledge, which

do not contribute to the realization of the purpose of the article or are useless for conclusion, must not be included.

- All data used and the opinions put forward in this section must prove the findings obtained from the studies or they must be based on a reference by citation.
- The guidance and methods to be followed in processing subjects vary according to the characteristics of the subjects mentioned. Various topic titles can be used in this section as many as necessary.

5.7. Discussions

- Discussion of the data and findings that are objectively transferred in the Main Text section of the article should be done in this section. This must be written as a seperate section from the results section.

5.8. Conclusions

- The main conclusion of the study provided by data and findings of the research should be stated concisely and concretely in this section.
- The subjects that are not mentioned sufficiently and/or unprocessed in the body section must not be included in this section.
- The conclusions can be given in the form of substances in order to emphasize the results of the research and to make the expression understandable.

5.9. Acknowledgements

- In this section, the significant contributions made in the realization of investigation that form the topic of the paper is specified. While specifying contributions, the attitude diverted the original purpose of this section away is not recommended. Acknowledgements must be made according to the following examples.
- This study was carried out within scope of .....project.
- I/we would like to thank to …… for contributing to the development of this article with his/her critiques.
- Academic and/or authoritorial affiliations are written for the contributions made because of requirement of ordinary task.
- For example:
- “Prof. Dr. İ. Enver Altınlı has led the studies”.
- “The opinions and warnings of Dr. Tandoğan Engin are considered in determining the chemistry of chrome minerals.”
- The contributions made out of the requirement of ordinary task:
- For example:
- “I would like to thank to Professor Dr. Melih Tokay who gives the opportunity to benefit from unpublished field notes”; “I would like to thank to the preliminary-Plan Chief Engineer Ethem Göğer, State Hydraulic Work, 5th Zone”. Academic and / or task-occupational titles are indicated for such contributions.
- The contributions, which are made because of requirement of ordinary task but do not necessitate responsibility of the contributor mustn’t be specified.
- For example:
- Sentences such as “I would like to thank to our General Manager, Head of Department or Mr. / Mrs. President ……who has provided me the opportunity to research” must not be used.

5.10. References

- All references cited in the text are to be present in the reference list.
- The authors must be sure about the accuracy of the references. Publication names must be written in full.
- Reference list must be written in Times New Roman, 9-point type face.
- The reference list must be alphabetized by the last names of the first author of each work.
- If an author’s more than one work is mentioned, ranking must be made with respect to publication year from old to new.
- In the case that an author’s more than one work in the same year is cited, lower-case alphabet letters must be used right after publication year (for example; Saklar, 2011*a, b*).
- If the same author has a publication with more than one co-author, firstly the ones having single author

are ranked in chronological order, then the ones having multiple authors are ranked in chronological order.

- In the following examples, the information related to works cited is regulated in accordance with different document/work types, considering punctuation marks as well.
- If the document (periodic) is located in a periodical publication (if an article), the information about the document must be given in the following order: surnames of the author/authors, initial letters of author's/ authors' first names. Year of publication. Name of the document. Name of the publication where the document is published, volume and/ or the issue number, numbers of the first and last pages of the document.

For example:

Pamir, H.N. 1953. Türkiye'de kurulacak bir hidrojeoloji enstitüsü hakkında rapor. Türkiye Jeoloji Bülteni 4, 1, 63-68.

Barnes, F., Kaya, O. 1963. İstanbul bölgesinde bulunan Karbonifer'in genel stratigrafisi. Maden Tetkik ve Arama Dergisi 61,1-9.

Robertson, A.H.F. 2002. Overview of the genesis and emplacement of Mesozoic ophiolites in the Eastern Mediterranean Tethyan region. Lithos 65, 1-67.

- If more than one document by the same authors is cited, firstly the ones having single name must be placed in chronological order, then the ones having two names must be listed in accordance with chronological order and second author's surname, finally the ones having multiple names must be listed in accordance with chronological order and third author's surname.
- If the document is a book, these are specified respectively: surnames of the author/authors, initial letters of author's/authors' first names. Year of publication. Name of the book (initial letters are capital). Name of the organization which has published the book, name of the publication wherethe document is published, volume and/ or the issue number, total pages of the book.

For example

Meriç, E. 1983. Foraminiferler. Maden Tetkik ve Arama Genel Müdürlüğü Eğitim Serisi 23, 280p.

Einsele, G. 1992. Sedimentary Basins. Springer-Verlag, p 628.

- If the document is published in a book containing the writings of various authors, the usual sequence is followed for the documents in a periodic publication. Then the editor's surname andinitial letters of their name /names are written. "Ed." which is an abbreviation of the editor word is written in parentheses. Name of the book containing the document (initial letters are capital). Name of the organization which has published the book. Place of publication, volume number (issue number, if any) of the publication where the document is published, numbers of the first and last page of the document.

For example:

Göncüoğlu, M.C., Turhan, N., Şentürk, K., Özcan, A., Uysal, Ş., Yalınız, K. 2000. A geotraverse across northwestern Turkey. Bozkurt, E., Winchester, J.A., Piper, J.D.A. (Ed.). Tectonics and Magmatism in Turkey and the Surrounding Area. Geological Society of London Special Publication 173, 139-162.

Anderson, L. 1967. Latest information from seismic observations. Gaskell, T.F. (Ed.). The Earth's Mantle. Academic Press. London, 335-420.

- If name of a book where various authors' writings have been collected is specified, those must be indicated respectively: book'seditor/editors' surname/surnames, and initial letters of their name/ names. "Ed." which is an abbreviation of the editor word must be written in parentheses. Year of Publication. Name of the book (initial letters are capital). Name of the organization which has published the book, total pages of the book.

For example:

Gaskel, T.F. (Ed.) 1967. The Earth's Mantle. Academic Press, 520p.

- If the document is an abstract published in a Proceedings Book of a scientific activity such as conference/symposium/workshop …etc. , information about the document must be given in the following order: surnames of the author/authors, initial letters of author's/authors' first names. Year of publication. Title of the abstract. Name, date and place of the meeting where the Proceedings Book is published, numbers of the first and last pages of the abstract in the Proceedings Book.

For example:

Yılmaz, Y. 2001. Some striking features of the Anatolian geology. 4. International Turkish Geology Symposiums 24-28 September 2001, London, 13-14.

Öztunalı, Ö., Yeniyol, M. 1980. Yunak (Konya) yöresi kayaçlarının petrojenezi. Türkiye Jeoloji Kurumu 34. Bilim Teknik Kurultayı, 1980, Ankara, 36

- If the document is one of the unpublished documents as report, lecture notes, and so on., information about the document must be given by writing the word "unpublished" in parentheses to the end of information about the document after it is specifiedin accordance with usual order which is implemented for a document included in a periodic publication.

For example:

Özdemir, C. Biçen, C. 1971. Erzincan ili, İliç ilçesi ve civarı demir etütleri raporu. General Directorate of Mineral Research and Exploration Report No: *4461*, 21 p. Ankara (unpublished).

Akyol, E. 1978. Palinoloji ders notları. EÜ Fen Fakültesi Yerbilimleri Bölümü, 45 p., İzmir (unpublished).

- The followings must be specified for the notes of unpublished courses, seminars, and so on: name of the document and course organizer. Place of the meeting. Name of the book, corresponding page numbers.

For example:

Walker, G. R. Mutti, E. 1973.Turbidite facies and facies associations. Pacific Section Society for Sedimentary Geology Short Course. Annaheim. Turbitides and Deep Water Sedimantation, 119-157.

- If the document is a thesis, the following are written: surname of the author, initial letter of the author's first name. Year of Publication. Name of the thesis. Thesis type, the university where it is given, the total number of pages, the city and "unpublished" word in parentheses.

For example:

Seymen, İ. 1982. Kaman dolayında Kırşehir Masifi'nin jeolojisi. Doçentlik Tezi, İTÜ Maden Fakültesi, 145 s.İstanbul (unpublished).

- Anonymous works must be regulated according to publishing organization.

For example:

MTA. 1964. 1/500.000 ölçekli Türkiye Jeoloji Haritası, İstanbul Paftası. Maden Tetkik ve Arama Genel Müdürlüğü, Ankara.

- The date, after the name of the author, is not given for on-printing documents; "in press" and / or "on review" words in parenthesis must be written. The name of the article and the source of publication must be specified, volume and page number must not be given.

For example:

- Ishihara, S. The granitoid and mineralization. Economic Geology 75th Anniversary (in press).

- Organization name, web address, date of access on web address must be indicated for the information downloaded from the Internet. Turkish sources must be given directly in Turkish and they must be written with Turkish characters.

For example:

- ERD (Earthquake Research Department of Turkey). **http://www.afad.gov.tr**. March 3, 2013.

- While specifying work cited, the original language must be used; translation of the title of the article must not be done.

6. Illustrations

- All drawings, photographs, plates and tables of the article are called "illustration".
- Illustrations must be used when using of them is inevitable or they facilitate the understanding of the subject.
- While selecting and arranging the illustrations' form and dimensions, page size and layout of the *Bulletin* must be considered, unnecessary loss of space must be prevented as much as possible.
- The pictures must have high quality, high resolution suitable for printing.
- The number of illustrations must be proportional to the size of the text.
- All illustrations must be sent as separate files independent from the text.

- While describing illustrations in the text, abbreviations must be avoided and descriptions must be numbered in the order they are mentioned in the text.
- Photographs and plates must be given as computer files containing EPS, TIFF, or JPEG files in 600 dpi and higher resolutions (1200 dpi is preferred) so that all details can be seen in the stage of examination of writing.

6.1. Figures

- Drawings and photos (except for the plates in the text) will be evaluated together as "Figure" and they must be numbered in the order they are mentioned in the text.
- The figures published in the Bulletin of Mineral Research and Exploration must be prepared in computer considering the dimensions of single-column width 7.4 m or double-column width 15.8 cm. Figure area together with the writing at the bottom should not exceed 15.8x21in maximum.
- Unnecessasry details must not be given in figures or care must be taken not to use much space for information transfer.
- Figures must be arranged in such a way to be printed in black/white or colored.
- The figure explanations being justified in two margins must be as follows:

Figure 1- Sandıklı İlçesinin (Afyon); a) güneybatısının jeolojik haritası, b) İnceleme alanının genel dikme kesiti (Seymen 1981), c) Türkiye'nin önemli neotektonik yapıları (Koçyiğit 1994'den değiştirilerek).

Figure 1- a) Sandıklı ilçesinin güneybatısının jeolojik haritası, b) İnceleme alanının genel dikme kesiti (Seymen, 1981), c) Türkiye'nin önemli neotektonik yapıları (Koçyiğit 1994'den değiştirilerek).

- Drawings must be made by well-known computer programs painstakingly, neatly and cleanly.
- Using fine lines, which can disappear when figures shrinks, must be avoided. Symbols or letters used in all drawings must be in Times New Roman and not less than 2 mm in size when shrink.
- All standardized icons used in the drawings must be explained preferably in the drawing or with figure caption if they are too long.
- Linear scale must be used for all drawings. Author's name, figure description, figure number must not be included into the drawing.
- Photos must be in quality and quantity that will reflect the objectives of the subject.

6.2. Plates

- Plates must be used when needed a combination of more than one photo and the publication on a special quality paper.
- Plate sizes must be equal to the size of available magazine pagespace.
- Figure numbers and linear scale must be written under each of the shapes located on the Plate.
- The original plates must be added to the final copy which will be submitted if the article is accepted.
- Figures and plates must be independently numbered. Figures must be numbered with Latin numerals and plates with Roman numerals (e.g., Figure1, Plate I).
- There must be no description text on Figures.

6.3.Tables

- All tables must be prepared preferably in word format in Times New Roman fonts.
- Tables together with table top writing must not exceed 15x8 cm in size.
- The table explanations being justified in two margins must be as follows:

Table 1- Hydrogeochemical analysis results of geothermal waters in the study area.

7. Nomenclature and Abbreviations

- Non-standard and uncommon nomenclature abbreviations should be avoided in the text. But if essential, they must be described as below: In cases where unusual nomenclatures and unstandardized abbreviations are considered to be compulsory, the followed way and method must be described.
- Full stop must not be placed between the initials of words for standardized abbreviations (MER, SHW, etc.).
- Geographical directions must be abbreviated in English language as follows: N, S, E, W, NE …etc.
- The first time used abbreviations in the text are presented in parenthesis, the parenthesis is not used for subsequent uses.

- The metric system must be used as units of measurement.
- Figure, plate, and table names in the article must not be abbreviated. For example, "as shown in generalized stratigraphic cross-section of the region (Figure 1……..."

7.1. Stratigraphic Terminology

Stratigraphic classifications and nomenclatures must be appropriate with the rules of International Commision on Stratigraphy and/or Turkey Stratigraphy Committee. The formation names which have been accepted by International Commision on Stratigraphy and/or Turkey Stratigraphy Committee should be used in the manuscript.

7.2. Paleontologic Terminology

Fossil names in phrases must be stated according to the following examples:

o For the use of authentic fossil names;

e.g. Limestone with *Nummulites*

o When the authentic fossil name is not used;

o e.g. nummulitic Limestone

o Other examples of use;

e.g. The type and species of *Alveolina / Alveolina* type and species

- Taxonomic ranks must be made according to the following examples:
- The names of the fossils should be stated according to the rules given below:

o For the first use of the fossil names, the type, spieces and the author names must be fully indicated;

Alveolina aragonensis Hottinger, 1960, not reference

Alveolina cf. *aragonensis* Hottinger, 1960, not reference

Alveolina aff. *aragonensis* Hottinger, 1960, not reference

o When a species is mentioned for the second time in the text;

A.aragonensis

*A.*cf.*aragonensis*

*A.*aff. *aragonensis*

It is accepted as citiation if stated as *Alveolina aragonensis* Hottinger (1960). Cited Hottinger (1960), stated in the Reference section.

- The statement of plates and figures (especially for the articles of paleontology):

a for the statement of species mentioned in the body text; ***Borelis vonderschmitti*** (Schweighauser, 1951)

(Plate, Figure, Figure in the body text).

b. When cited for other articles;

1951 ***Neoalveolina vonderschmitti*** Schweighauser, page 468, figure 1-4, figure in body text.

1974 ***Borelis vonderschmitti*** (Schweighauser), Hottinger, page 67, plate 98, figure 1-7.

c. For the citation in the text

(Schweighauser, 1951, page, plate, figure, figure in the body text)

(Hottinger, 1974, page, plate 97, figure 67, plate 98, figure 1-7, figure in the body text).

Ordo: Foraminiferida Eichwald, 1830 Super family: Alveolinacea Ehrenberg, 1939 Family: Borelidae Schmarda, 1871 Type genus: *Borelis* de Montfort, 1808 Type species: *Borelis melenoides* de Montfort, 1808; *Nautilus melo* Fitchel and Moll, 1789	Not reference, Not stated in the Reference section
Borelis vonderschmitti (Schweighauser, 1951) (Plate, Figure, Figure in Body Text)	Schweighauser, 1951 not reference
1951 *Neoalveolina vonderschmitti* Schweighauser, page 468, figure 1-4	Cited Scweighauser (1951), stated in the Reference section.
1974 *Borelis vonderschmitti* (Schweighauser), Hottinger, page, 67, plate 98, figure 1.7	Cited Hottinger (1974), stated in the Reference section.

8. Citations

All the citiations in the body text must be indicated by the last name of the author(s) and the year of publication, respectively. The citations in the text must be given in following formats.

- For publications written by single author:

- It is known that fold axial plain of Devonian and Carboniferious aged units around Istanbul is NS oriented (Ketin, 1953, 1956; Altınlı, 1999).

- Altınlı (1972, 1976) defined the general characteristics of Bilecik sandstone

- For publications written by two authors:

- The upper parts of the unit contain Ilerdian fossils (Sirel and Gündüz, 1976; Keskin and Turhan, 1987, 1989).

- For publications written by three or more authors:

According to Caner et al. (1975) Alıcı formation reflects the fluvial conditions.

The unit disappears wedging out in the East direction (Tokay et al., 1984).

- If reference is not directly obtained but can be found in another reference, cross-reference should be given as follows:

- It is known that Lebling has mentioned the existence of Lias around Çakraz (Lebling, 1932: from Charles, 1933).

9. Reprints

The author(s) will receive 2 two hard copies of the related issues.

10. Copyright and Conditions of Publication

- It is a condition of publication that work submitted for publication must be original, previously unpublished in whole or in part.

- It is a condition of publication that the authors who send their publications to the Bulletin of Mineral Research and Exploration hereby accept the conditions of publication of the Bulletin in advance.

- All copyright of the accepted manuscripts belong to MTA. The author or corresponding author on behalf of all authors (for papers with multiple authors) must sign and give the agreement under the terms indicated by the Regulations of Executive Publication Committee. Upon acceptance of an article, MTA can pay royalty to the authors upon their request according to the terms under the "Regulations of Executive Publication Committe" and the "Regulations of Royalty Payment of Public Office and Institutions"

All the information and forms about the Bulletin of Mineral Research and Explorations can be obtained from http://bulletin.mta.gov.tr